Proton, Deuteron, and Triton Emission in ^{14}N + Ag Interactions at an Energy of 52 MeV per Nucleon*

V. Yu. Alexakhin, M. I. Gostkin, K. K. Gudima[1]**, M. P. Ivanov, A. Kugler**[2]**, I. V. Kuznetsov, S. I. Merzlyakov, C. L. Morris**[3]**, E. A. Pasyuk, Yu. E. Penionzhkevich, S. Yu. Porokhovoy, Yu. G. Sobolev, and V. D. Toneev**

Joint Institute for Nuclear Research, Dubna, Moscow oblast, 141980 Russia
Received October 1, 1999; in final form, February 7, 2000

Abstract—The inclusive energy spectra and multiplicities of *p*, *d*, and *t* from the reactions ^{14}N(Ag, *X*), *X* = *p*, *d*, *t* at *E*/*A* = 52 MeV are measured. The experimental data are compared with the results obtained within the Dubna version of the cascade model and are analyzed on the basis of the moving-source model. © *2000 MAIK "Nauka/Interperiodica".*

1. INTRODUCTION

The emission of fast light charged particles is an interesting problem in heavy-ion physics, especially in the energy range between 20 and 100 MeV/nucleon. In this energy range, reaction mechanisms are thought to change from mean-field phenomena at low energies, where the projectile energy is comparable with the nuclear binding energy and with the Coulomb barrier, to localized interaction regions, where single nucleon–nucleon scattering becomes important, at higher energies. In spite of numerous investigations (see, for example, [1–8]), the problems are still open, and investigations of light-charged-particle emission (measurements of light-particle spectra, multiplicity, angular distributions, and correlations for a wide range of kinematical variables) have been continued till now [9–11].

In this paper, we present new experimental data on the spectra and multiplicities of light charged particles emitted in ^{14}N + Ag interactions at 52 MeV/nucleon and analyze them within the moving-source model and within the cascade model modified for low energies (40–60 MeV/nucleon).

2. DESCRIPTION OF THE EXPERIMENT

The measurements were performed in a 52-MeV/nucleon ^{14}N beam from the U-400M cyclotron of the JINR Flerov Laboratory of Nuclear Reactions. The average beam current was about 1 nA. A 0.1-mm-thick Ag target was placed inside an evacuated beam pipe with the 0.4-mm-thick stainless steel walls at the

center of the BGO ball. A 4π spectrometer, LAMPF BGO-ball [12], consisting of 30 phoswich detectors was used to detect the reaction products. The detectors of the array were of pentagonal and hexagonal shapes and were tightly packed to form a truncated polyhedron of 32 faces of approximately equal solid angles. Two of the 32 faces were open for beam entry and exit. The detectors were distributed around an inner radius of 6.1 cm from the center of the array to the center of each crystal face and were arranged in six groups centered at the laboratory scattering angles of θ = 37°, 63°, 79°, 102°, 116°, and 142°. Five detectors located at the scattering angle of 37° were not used in these measurements. Each detector had a solid angle of about (1/32) × 4π sr and a 0.05-mm-thick nickel entrance window and consisted of a 3-mm-thick NE102 plastic scintillator optically coupled to the front of a 5.6-cm-thick bismuth germanate (BGO) crystal with a photomultiplier tube 7.62 cm in diameter on the back. The crystal was sufficiently thick to stop protons of energy up to 185 MeV. The phototube signals from each detector were split for energy and time measurements. The time resolution of each detector was about 1 ns. The timing measurements were used to reject random coincidences. Since the decay constant for the BGO scintillator was much larger than that for the plastic scintillator (250 versus 1.5 ns), it was possible to measure the energy lost of outgoing particles. The anode signal was time-sliced to provide both Δ*E* (fast) and *E* (slow) signals for identifying both charged (pions, protons, deuterons, etc.) and neutral (neutrons and photons) particles. A detailed description of the raw data analysis can be found in [12]. Figure 1 shows an example of the two-dimensional Δ*E*–*E* distribution. One can see that protons, deuterons, and tritons are clearly identified. Background measurements made without a target were subtracted from the measurements with a target. A coinci-
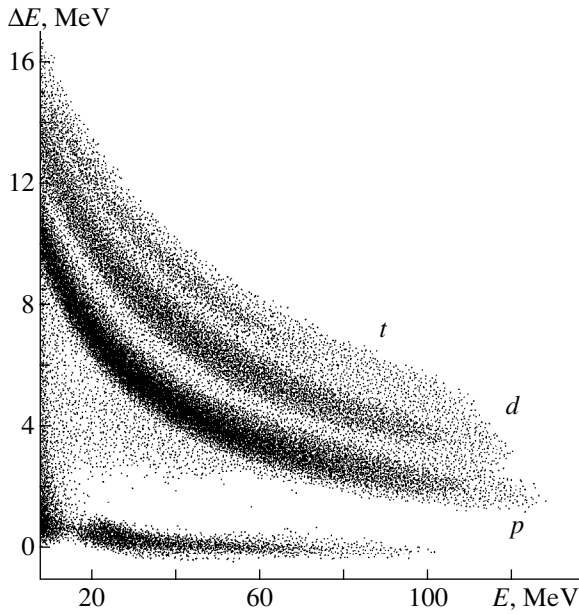

Fig. 1. Two-dimensional ΔE–E distribution.

dence of at least two detectors in the BGO-ball was used as an event trigger.

In [12, 13], the energy calibration of the BGO crystals was obtained by using the elastic peak for $\pi^+ + {}^{12}C$ scattering. An alternative calibration that used the reaction $\pi^+ d \longrightarrow pp$ yielded similar results. The BGO crystals showed the same energy response to pions and to muons. For this reason, cosmic-ray muons were used to calibrate the BGO-ball detectors. We used the conventional GEANT code based on Monte Carlo techniques [14] to calculate the energy lost by cosmic muons in actual detectors. We used the known muon-energy spectrum from [15] for this simulation. Cosmic-ray muons of average energy about 2 GeV that traveled along the axis of the crystal, traversing its center, deposited about 60 MeV in the BGO crystal. For calibration, we selected events for which the muon passed through the center of the BGO ball. The measured energy-loss spectra were in a good agreement with the results of the simulations. This calibration procedure could be performed simultaneously with the data acquisition, in time intervals between beam macrobursts. This provided real-time corrections to the data set. The data were corrected for the energy losses in the target and in the other materials between the target and the

Moving-source parameters

Particle	v/c	T, MeV	N_0	σ, b
p	0.129 ± 0.001	16.8 ± 0.1	3455 ± 8	2.65 ± 0.2
d	0.129 ± 0.001	16.8 ± 0.1	1529 ± 8	1.17 ± 0.1
t	0.129 ± 0.001	16.8 ± 0.1	689 ± 8	0.53 ± 0.1

detectors, for the efficiency loss due to particle interactions in the scintillator, and for the dead time. A typical dead time was less than 20% in this experiment.

3. RESULTS

The inclusive energy spectra of protons, deuterons, and tritons were measured at five angles of 63°, 79°, 102°, 116°, and 142°. The measured spectra are presented in Fig. 2. The energy spectra exhibit an exponential fall, which becomes steeper with increasing detection angle. The slopes of the proton, deuteron, and triton spectra are nearly identical at large angles (in excess of 100°). For angles in the forward hemisphere, however, they behave rather differently.

We have parametrized the spectra of light particles, assuming equilibrium (Maxwellian) emission in the rest frame moving at some velocity intermediate between the target and projectile velocities:

$$\frac{d^2\sigma}{d\Omega dE} = N_0\sqrt{(E - U_C)} \tag{1}$$

$$\times \exp\{-[E - U_C + E_1 - \sqrt{2E_1(E - U_C)}\cos\theta]/T\}.$$

Here, U_C is the kinetic energy gained from the emitting system owing to the Coulomb repulsion; $E_1 = \frac{1}{2}mv^2$, where m is the particle mass and v is the source velocity in the laboratory frame; T is the source temperature; θ is the detection angle; and N_0 is normalization factor. In the present analysis, the temperature and velocity parameters were determined from a fit, while the Coulomb barrier was chosen to be $U_C = 0$ because our measurements were performed in the region where $E \gg U_C$. The values of v, T, and N_0 for protons, deuterons, and tritons were obtained by fitting the spectrum of each particle separately. They are given in the table. The values of the temperatures T are in fairly good agreement with the systematization from [9].

We have also estimated the total cross sections for light-particle emission according to the relation

$$\sigma = 2N_0(\pi T)^{3/2}, \tag{2}$$

which was obtained by integrating (1).

The experimental energy spectra and moving-source calculations for proton, deuteron, and triton emission are compared in Fig. 2. The moving-source parametrization provides a good description for these particles at backward angles, but it overestimates the high-energy part of the spectra at forward angles.

Using the values of the moving-source velocity that were obtained from a fit, we have analyzed the invariant cross sections for proton, deuteron, and triton emission. Figure 3 displays contour plots of the invariant cross sections for protons, deuterons and tritons versus longitudinal and transverse velocities. Also shown are the contour lines for an isotropic source with parameters
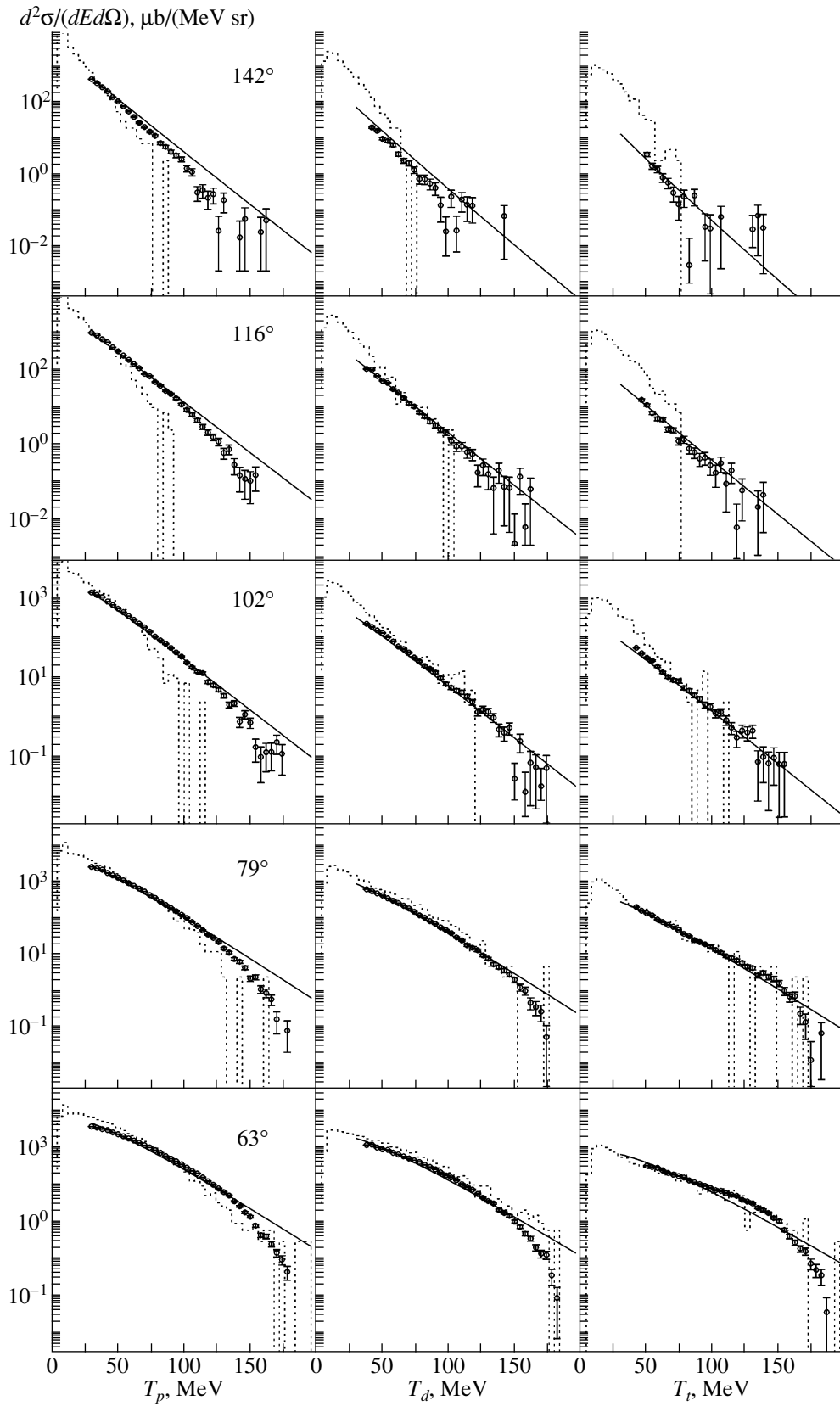
$d^2\sigma/(dEd\Omega)$, µb/(MeV sr)

Fig. 2. Inclusive energy spectra of protons, deuterons, and tritons measured at the scattering angles of θ = 63°, 79°, 102°, 116°, and 142°: (circles) data from the present experiment, (solid lines) moving-source parametrization with (1), and (dotted lines) results of the DCM calculation.
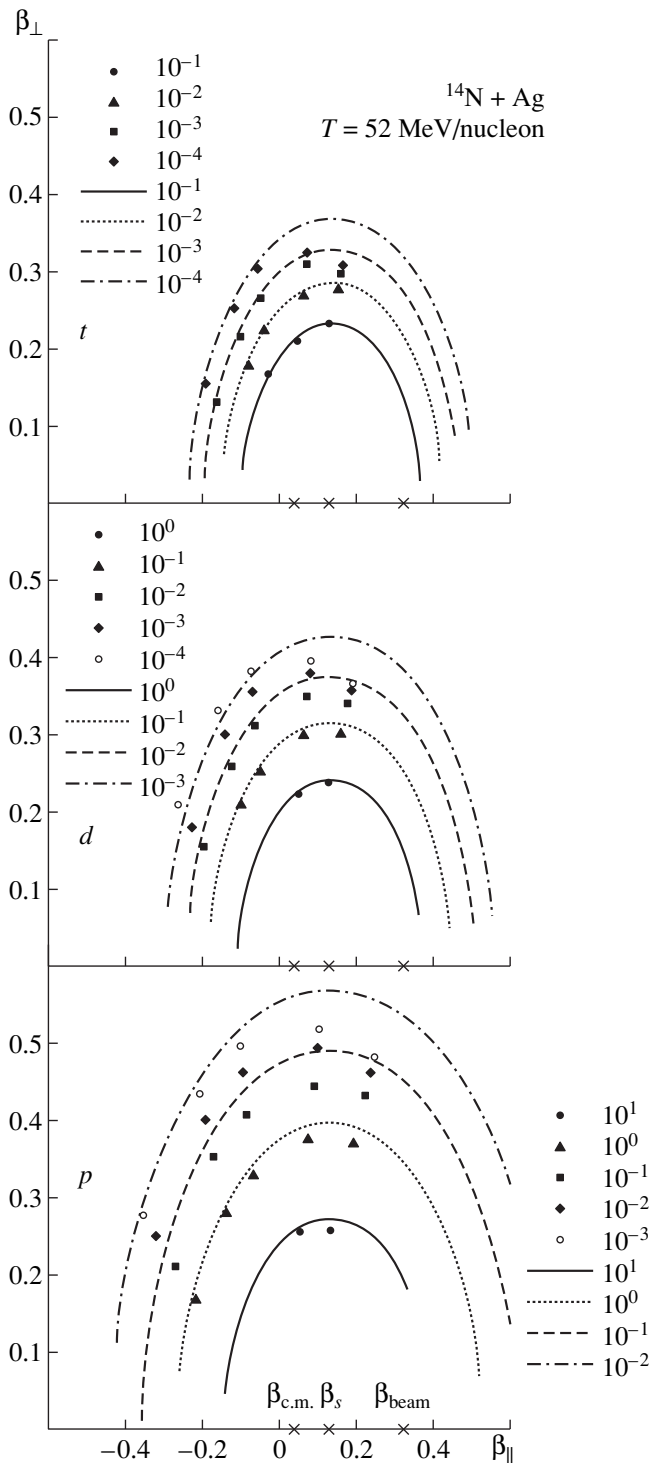
Fig. 3. Invariant cross sections for p, d, and t in the $(\beta_\parallel, \beta_\perp)$ plane. Circles, triangles, squares, diamonds, and open circles represent experimental data on the cross sections $\sigma_{inv} = (1/pc)d^2\sigma/(dEd\Omega)$ in $\mu b/(\text{MeV}^2 \text{ sr})$. Contour lines depict the calculated cross sections under the assumption of an isotropic source with the parameters from the table. The cross section grows by a factor of 10 between subsequent contour lines. The crosses on the $\beta_\parallel$ axis indicate the center-of-mass velocity ($\beta_{c.m.}$), the moving-source velocity (β_s), and the beam velocity (β_{beam}).

obtained from the moving-source parametrization. It is obvious that the intermediate data can be described with the mechanism of emission from a single source moving with a velocity between the velocity of the center-of-mass frame and the beam velocity.

We have also compared experimental spectra with the results of the calculations within the Dubna version of the cascade model (DCM), which was originally proposed for describing particle and light-fragment production in $N + A$ and $A + A$ reactions at high energies [16, 17]. In this model, inelastic nucleus–nucleus interactions are treated as successive quasifree two-particle collisions described by a set of coupled relativistic kinetic equations of the Boltzmann type. In our approach, the mean-field evolution is treated in a simplified way. We take a scalar nuclear potential, defined in the local Thomas–Fermi approximation, to describe initial-state interaction, changing only the depth of the potential well according to the number of knock-on nucleons [18]. This procedure allows one to take into account nuclear binding and the Pauli exclusion principle. This approximation is sufficiently good for hadron–nucleus or peripheral nucleus–nucleus collisions, where there is no large disturbance of the mean field, but it is questionable for violent central collisions of two nuclei.

The model is also capable of describing the production of fast composite particles d, t, ^{3}He, and ^{4}He by taking into account the final-state interaction of cascade particles in the framework of the dynamical coalescence model [17] on an event-by-event basis. The values for the coalescence radii in the momentum space, initially estimated from experimental spectra of particles produced in interactions of neon nuclei with uranium at 400–2100 MeV/nucleon, turned out to be independent of both the primary energy of nucleus and the mass numbers of colliding nuclei.

Upon completing the cascade stage of the reaction, light particles may be emitted both from the equilibrium and nonequilibrium states of excited residual nuclei at a subsequent slower stages of interaction. We have taken into account the preequilibrium emission effects within the exciton model [19]. For ^{14}N + ^{108}Ag interactions at 52 MeV/nucleon, 100000 events were generated.

In the experiment, two particles that hit the same detector at the same time could not be separated and were lost from the data set. The calculated energy spectra were filtered by simulating the experimental biases, and a misidentification correction function (MCF) was obtained from a comparison of these spectra with pure DCM calculations. The measured p, d, and t spectra were corrected using this function and were normalized then to the calculated one at a single energy of 60 MeV and at an angle of 63° for the proton spectrum. This single normalization coefficient was used for all measured spectra at all angles.
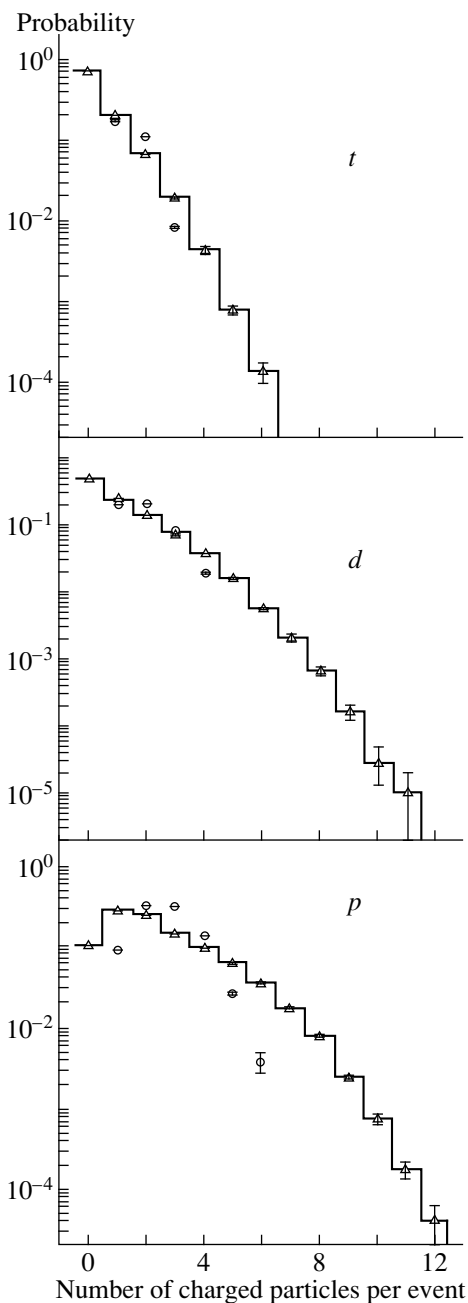
Fig. 4. Multiplicity distributions of light particles: (circles) data from the present experiment and (solid line with triangles) results of the DCM calculation.

The inclusive spectra shown in Fig. 2 are in quite satisfactory agreement with the measured data. The DCM slightly underestimates high-energy part of the proton yield at large angles. This is also reflected in the deuteron and triton spectra, which are overestimated at the same angles. The momentum coalescence radii in this model (90 MeV/c for a deuteron and 108 MeV/c for a triton [17, 18]) are independent of both the beam energy and colliding nucleus size. The difference noted shows that nucleon correlations in the coordinate space

may be important in this energy range. We note that the DCM reproduces the abundance of different light particles correctly.

The inclusive spectra of composite particles can be related to the spectra of protons by a power law [20] due to thermodynamic consideration. Composite particles are formed by the coalescence of free nucleons which happen to occupy the same region of the momentum space similarly to the dynamical model. The size of this region is defined by coalescence radius ρ_0. We have extracted this parameter from the measured spectra. It is equal to 136 ± 4 MeV/c and 162 ± 4 MeV/c for the deuteron and the triton, respectively. Using these coalescence radii, we estimated the radii of deuteron- and triton-formation sources. The values equal 1.45 ± 0.04 fm and 1.22 ± 0.03 fm for the deuteron and the triton, respectively. These values are in rough agreement with the compilation of radii of fragment-formation sources from [21]. It is worth noting that the coalescence radius extracted in this way corresponds to the spectra integrated over the impact parameter and will depend on both the beam energy and the combination of colliding nuclei; therefore, this is only a rough estimate.

We also compared a measured probability of the number of light particles of specific kind per event with DCM calculations in Fig. 4. The agreement for composite particles (d, t) is rather good, while for protons one can see a disagreement for higher multiplicities, which could be explained by uncertainty in the MCF.

The next step in this research is to use a forward detector to measure projectile-like particles. This should allow the impact parameter to be determined, so that the contributions of peripheral and central collisions to the particle spectra can be separated, and more detail of the dynamics of reaction mechanisms can be provided.

ACKNOWLEDGMENTS

REFERENCES

1. T. C. Awes *et al.*, Phys. Rev. C **25**, 2361 (1982).
2. C. B. Chitwood *et al.*, Phys. Rev. C **34**, 858 (1986).
3. K. O. Oganesyan *et al.*, Nucl. Phys. A **583**, 389 (1995).
4. V. Yu. Alexakhin *et al.*, Acta Phys. Slov. **46**, 639 (1996).
5. B. V. Jacak *et al.*, Phys. Rev. C **35**, 1751 (1987).
6. R. Barbera *et al.*, Nucl. Phys. A **518**, 767 (1990).
7. J. Pochodzalla *et al.*, Phys. Rev. C **35**, 1695 (1987).
8. B. Jakobsson *et al.*, Phys. Lett. **102B**, 121 (1981).
9. H. Fuchs and K. Möring, Rep. Prog. Phys. **57**, 231 (1994).
10. V. Zagrebaev and Y. Penionzhkevich, Prog. Part. Nucl. Phys. **35**, 575 (1995).

11. G. Lanzano *et al.*, Phys. Rev. C **58**, 281 (1998).

12. E. A. Pasyuk *et al.*, Phys. Rev. C **55**, 1026 (1997).

13. V. Yu. Alexakhin *et al.*, Phys. Rev. C **57**, 2409 (1998).

14. CERN Program Library, W5013.

15. Review of Particle Properties, Phys. Lett. B **204**, 61 (1988).

16. K. K. Gudima and V. D. Toneev, Yad. Fiz. **27**, 658 (1978) [Sov. J. Nucl. Phys. **27**, 351 (1978)].

17. K. K. Gudima and V. D. Toneev, Nucl. Phys. A **400**, 173 (1983).

18. K. K. Gudima and V. D. Toneev, Preprint No. GSI-93-52 (Darmstadt, 1993); V. D. Toneev, in *Proceedings of the Second TAPS Workshop on Gamma Rays and Particle Production in Heavy Ion Reactions, Guardamar, Spain, 1993*, Ed. by J. Díaz, G. Martínez, and Y. Schutz (World Sci., Singapore, 1994), p. 590.

19. K. K. Gudima, S. G. Mashnik, and V. D. Toneev, Nucl. Phys. A **401**, 329 (1983).

20. S. Nagamiya, J. Randrup, and T. J. M. Symons, Annu. Rev. Nucl. Part. Sci. **34**, 155 (1984).

21. V. V. Avdeichikov, in *Proceedings of the Fourth International Conference on Nucleus–Nucleus Collisions, Kanazava, Japan, 1991*, Contributed papers, p. 177.

Synthesis of Superheavy Nuclei in ^{48}Ca + ^{244}Pu Interactions*

Yu. Ts. Oganessian[1], **V. K. Utyonkov**[1], **Yu. V. Lobanov**[1], **F. Sh. Abdullin**[1], **A. N. Polyakov**[1],
I. V. Shirokovsky[1], **Yu. S. Tsyganov**[1], **G. G. Gulbekian**[1], **S. L. Bogomolov**[1], **B. N. Gikal**[1],
A. N. Mezentsev[1], **S. Iliev**[1], **V. G. Subbotin**[1], **A. M. Sukhov**[1], **O. V. Ivanov**[1], **G. V. Buklanov**[1],
K. Subotic[1], **M. G. Itkis**[1], **K. J. Moody**[2], **J. F. Wild**[2], **N. J. Stoyer**[2],
M. A. Stoyer[2], **and R. W. Lougheed**[2]

Received April 14, 2000

Abstract—This article reports the results of experiments aimed at producing hypothetical long-lived super-heavy elements located near the spherical-shell closures with $Z \geq 114$ and $N \geq 172$. For the synthesis of super-heavy nuclei, we used a combination of neutron-rich reaction partners, with a ^{244}Pu target and a ^{48}Ca projectile. The sensitivity of the present experiment exceeded by more than two orders of magnitude previous attempts at synthesizing superheavy nuclides in reactions of ^{48}Ca projectiles with actinide targets. We observed new decay sequences of genetically linked alpha decays terminated by spontaneous fission. The high measured alpha-particle energies, together with the long decay times and spontaneous fission terminating the chains, offer evidence for the decay of nuclei with high atomic numbers. The decay properties of the synthesized nuclei are consistent with the consecutive alpha decays originating from the parent nuclides $^{288,\,289}$114, produced in the 3n- and 4n-evaporation channels with cross sections of about a picobarn. The present observations can be considered experimental evidence for the existence of the "island of stability" of superheavy elements and are discussed in terms of modern theoretical approaches. © *2000 MAIK "Nauka/Interperiodica".*

1. INTRODUCTION

The stability of heavy nuclei is largely determined by nuclear shell structure, whose influence is considerably increased near closed proton Z and neutron N shells. Beyond the domain of the heaviest known nuclei, the macroscopic–microscopic nuclear theory predicts the existence of an "island of stability" of long-lived superheavy elements. Calculations performed over more than 30 years within various versions of the nuclear shell model predict a substantial enhancement of the stability of heavy nuclei when approaching the closed spherical shells $Z = 114$ and $N = 184$. Neutron and proton shell closures are expected to occur there, resulting in the formation of spherical superheavy nuclei, the first spherical nuclei beyond ^{208}Pb ($Z = 82$ and $N = 126$).

However, more generally, an enhancement of nuclear binding energy can also be observed in deformed nuclei—in particular, in the theoretically predicted intermediate region of increased nuclear stability in the vicinity of the deformed-shell closures $Z = 108$ and $N = 162$ (for an overview, see, for example, [1–3]). These predictions were corroborated by the experimental observation of the new region of nuclear stability near $Z = 108$ and $N = 162$ [4] and synthesis of the heaviest elements up to $Z = 112$ [4–6]. These results gave more credibility to the predicted existence of spherical superheavy elements, thus opening prospects for the production of heaviest nuclei and for the study of their physical and chemical properties [7]. Super-heavy nuclei close to the predicted magic neutron shell $N = 184$ can be synthesized in complete fusion reactions of target and projectile nuclei with significant neutron excess. The isotopes of element 114 that show the highest neutron excess (with neutron numbers 174 and 175) and which are consequently relatively stable are expected to be produced in the fusion reaction of ^{244}Pu with ^{48}Ca ions [8].

With a doubly magic ^{48}Ca projectile, the resulting compound nucleus ^{292}114 should have an excitation energy of about 33 MeV at the Coulomb barrier. Accordingly, nuclear shell effects are still expected to persist in the excited nucleus, thus increasing the survival probability of the evaporation residues (EVRs), as compared to "hot-fusion" reactions ($E^* \approx 45$ MeV), which were used for the synthesis of heavy isotopes of elements with atomic numbers $Z = 106$, 108, and 110 [4]. Additionally, the high mass asymmetry in the entrance channel should decrease the dynamical limitations on nuclear fusion that arise in more symmetric reactions [9].

Despite these advantages, previous attempts at synthesizing new elements in ^{48}Ca-induced reactions with

---

actinide targets gave only upper limits on their production [10]. In view of the more recent experimental data on the production of the heaviest nuclides (see, for example, [4–6] and references therein), it became obvious that the sensitivity level of the above experiments was insufficient to reach the goal. Our present experiment with ^{244}Pu + ^{48}Ca interactions was designed to attempt the production of element 114 at the picobarn cross-section level, thus exceeding the sensitivity of the previous experiments by at least two orders of magnitude.

In the reaction of ^{244}Pu with ^{48}Ca ions at an energy close to the Coulomb barrier, ^{292}114 compound nuclei could be expected to deexcite via the emission of three or four neutrons. According to the macroscopic–microscopic calculations by Smolańczuk *et al.*, who adequately reproduced radioactive properties (alpha decay and spontaneous fission) of the known heavy nuclei [1, 11], the even–even isotopes ^{288}114 and ^{290}114 are expected to have the partial alpha-decay half-lives of $T_\alpha = 0.14$ and 0.7 s, respectively. Their predicted spontaneous fission (SF) half-lives are considerably longer: $T_{SF} = 2 \times 10^3$ s and 4×10^5 s, respectively. For their daughter nuclei—the isotopes of element 112—the main decay mode should still be alpha decay, although differences between T_α and T_{SF} are considerably less: $T_{SF}/T_\alpha \approx 4$ for ^{284}112 and about 70 for ^{286}112. The alpha-decay granddaughters—the isotopes of element 110—are expected to decay primarily via spontaneous fission.

For the odd isotopes—in particular, for ^{289}114—the predictions are less definitive; the odd neutron can lead to the hindrance of alpha decay and, especially, spontaneous fission. Here, one expects competition between the two decay modes in the daughter products with $Z \leq 112$ and somewhat longer chains of sequential alpha decays with longer half-lives than in the case of the neighboring even–even isotopes. Furthermore, all these nuclei are located close to the area of beta stability [12].

We note that the macroscopic–microscopic T_α calculations by Möller *et al.* [12] for $^{288–290}$114 give values exceeding those from [1, 11] by orders of magnitude (e.g., T_α of 7×10^4 s for ^{289}114). This, however, does not change the expected decay pattern for these isotopes of element 114 and their daughters. One could expect a sequence of two or more alpha decays terminated by spontaneous fission as the decay chain recedes from the stability region around $N = 184$.

We present here results of the experiments aimed at the synthesis of $Z = 114$ nuclei in the vicinity of predicted spherical nuclear shells in the complete fusion reaction induced by ^{244}Pu + ^{48}Ca collisions.

2. EXPERIMENTAL TECHNIQUE

The production of an intense ion beam of the rare and expensive isotope ^{48}Ca (0.187% of abundance in natural Ca), which was extremely important for achiev-

ing the high sensitivity in these experiments, required the upgrade of the U400 cyclotron and the development of an external multicharge ion source (ECR-4M). A ^{48}Ca^{+5} beam was extracted from the ECR-4M ion source and injected into the Dubna U400 heavy-ion cyclotron operated in a continuous mode. A typical intensity of the ion beam on the target was 4×10^{12} pps at the material-consumption rate of about 0.3 mg/h. The beam energy was determined with a precision of about 1 MeV by measuring the energies of scattered ions and by a time-of-flight technique.

Another important feature of the experiments was the use of a target from the unique isotope ^{244}Pu (98.6%), which was provided by LLNL. The target material (a total of 12 mg in the form of PuO$_2$) was deposited onto each of nine 1.5-μm Ti foils to a thickness of about 0.37 mg/cm^2, so that heavy recoil atoms would be knocked out of the target layer and transported through the separator to the detectors. Each target had an area of 3.5 cm^2 in the shape of an arc segment with an angular extension of 40° and an average radius of 60 mm. These targets were mounted on a disk that was rotated at 2000 rpm across the beam direction in a hydrogen gas filling the volume of the separator. This reduced the thermal and radiation load of the target. In the course of the experiment, the target withstood ^{48}Ca beam intensities up to 7×10^{12} pps, having accumulated a total beam dose of 2×10^{19} ions, without damage or significant loss of target material.

We used a ^{48}Ca bombarding energy of about 236 MeV at the middle of the ^{244}Pu layer. With allowance for the energy loss in the target (~3.4 MeV), some difference in the thickness of nine target sectors, the beam energy resolution, and the variation of the beam energy during the long-term irradiation, the excitation energy of the compound nucleus ^{292}114 was in the range 31.5–39 MeV [13]. With this excitation energy, the compound nuclei would deexcite by evaporation of three or four neutrons and gamma-ray emission. For each particular recoiling nucleus, we could determine a sector of a target where the reaction occurred and a ^{48}Ca bombarding energy at this time. That allowed us to restrict the excitation energy interval for each event.

Evaporation residues recoiling from the target were separated in flight from the primary beam, scattered target and beam particles, and various transfer-reaction products by the Dubna Gas-Filled Recoil Separator [14], consisting of a dipole magnet and two quadrupole lenses (Fig. 1). A rotating entrance window (1.5-μm Ti foil) separated the hydrogen-filled volume of the separator (at a pressure of 1 torr) from the vacuum of the cyclotron beam line. The average charge state of recoil $Z = 114$ atoms in hydrogen was estimated to be about 5.6 [15]. The recoils passed through a Mylar window (about 1 μm), which separated the hydrogen-filled volume from the detector module (Fig. 2) filled with pentane (at about 1.5 torr) and then through a time-of-flight
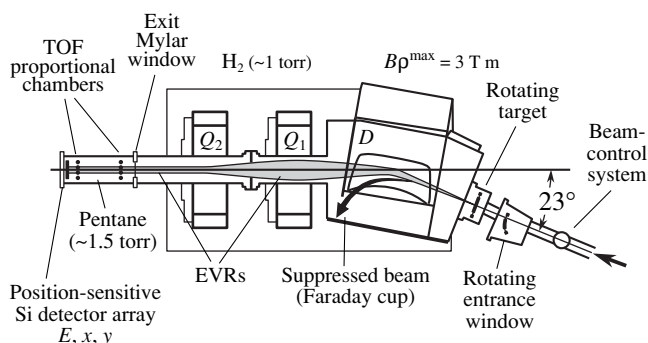
Fig. 1. Layout of the Dubna Gas-Filled Recoil Separator (dipole magnet D followed by the quadrupole doublet $Q_1 Q_2$).

Fig. 2. Detection system of the Dubna Gas-Filled Recoil Separator.

(TOF) system and were finally implanted in the detector array installed in the focal plane of the separator.

The TOF detector was used to measure the time of flight of recoiling nuclei (with a detection efficiency of about 99.7%) and to distinguish the signals arising in the focal-plane detector due to particles passing through the separator from those due to the radioactive decay of previously implanted nuclei. The focal-plane detector consisted of three 40×40 mm^2 silicon Canberra Semiconductor detectors, each with four 40-mm-high $\times$ 10-mm-wide strips having position sensitivity in the vertical direction. The detection efficiency for full-energy alphas from decays of EVRs implanted in these detectors is about 53%. To increase the detection efficiency for alphas escaping the focal-plane detector, we arranged eight detectors of the same type, but without position sensitivity, in a box surrounding the focal-plane detector. Employing these side detectors increased the alpha-particle detection efficiency up to about 87% of 4π.

Main sources of events with a TOF signal are the scattered target nuclei and targetlike transfer-reaction products. Background events without a TOF signal, which can imitate alpha particles from decay of implanted nuclei, can be due to fast light particles produced in direct nuclear reactions. A set of three similar "veto" detectors was mounted behind the detector array in order to eliminate signals from low-ionizing light particles, which could pass through the focal-plane detector (300 μm) without being detected in the TOF system.

Alpha-energy calibrations were periodically performed using the alpha peaks from nuclides produced in the bombardments of ^{nat}Yb and enriched $^{204, 206-208}$Pb targets with ^{48}Ca ions [14]. The reaction induced by ^{206}Pb + ^{48}Ca interactions is convenient for calibration purposes, since the known nuclide ^{252}No, decaying by both alpha emission and SF, is produced in it with a 0.5-μb cross section. The in-beam energy spectrum of alpha particles recorded by the focal-plane detector in the ^{206}Pb + ^{48}Ca reaction is shown in Fig. 3a. In the right part of Fig. 3a, the energy spectrum of the ^{252}No EVRs
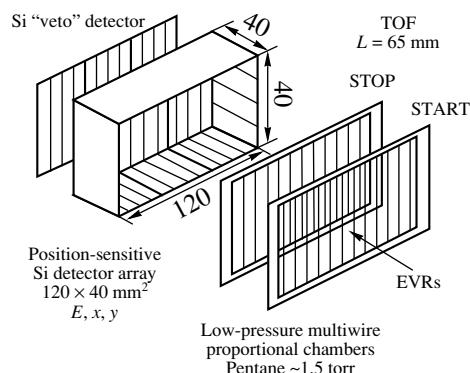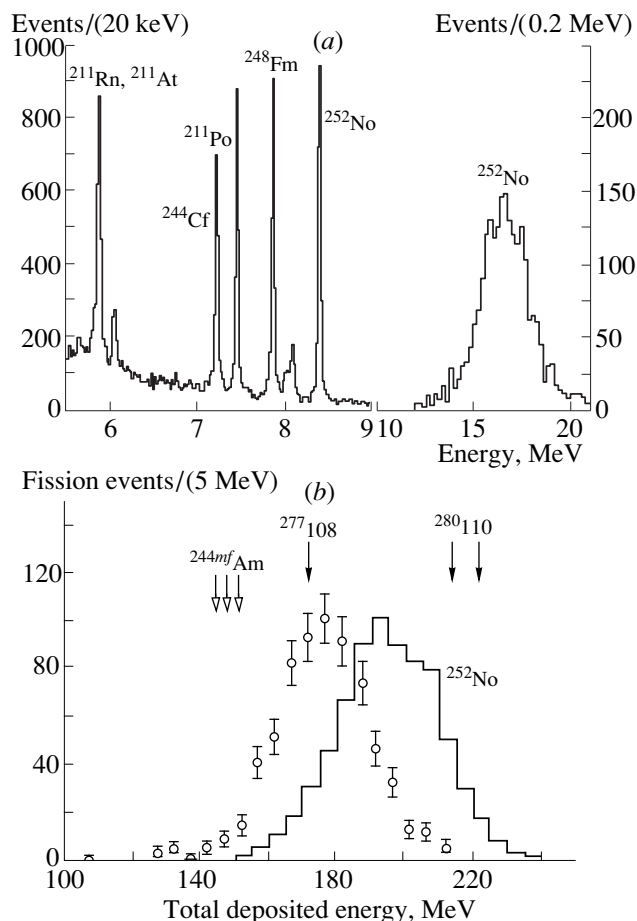
Fig. 3. (a) Energy spectrum of alpha particles detected in ^{206}Pb + ^{48}Ca interactions at the bombarding energy of about 217 MeV. The long-lived activities of ^{211}Rn, ^{211}At, and ^{211}Po were produced in the ^{nat}Yb + ^{48}Ca calibration reactions. (b) Spectrum of total energies deposited by the fission fragments of ^{252}No implants as measured by both the focal-plane and the side detectors. The histogram presents the ^{252}No total-kinetic-energy distribution [16] obtained with an external source. Open and solid arrows show the total measured deposited energies of fission events assigned to ^{244mf}Am, ^{277}Hs ($Z = 108$), and ^{280}110 produced in the ^{244}Pu + ^{48}Ca reaction.

is shown, corresponding to the events correlated in position and time with subsequent alpha particles of this nuclide. Note that the experimental energy spectrum of ^{252}No recoils measured by semiconductor detectors is distorted by the pulse-height defect, which is about one-third of the initial implantation energy of the heavy nuclei. The energy resolution for the detection of alpha particles in the focal-plane detector was about 50 keV. For alpha particles escaping from the focal-plane detector at different angles and absorbed in the side detectors, the energy resolution was about 190 keV because of energy losses in the entrance windows and dead layers of both detectors and the pentane. We determined the position resolution of the signals of correlated decays of nuclei implanted in the detectors in the experiments of 1998. For sequential alpha–alpha decays, the FWHM position resolution was 1.0 mm; for correlated EVR–alpha signals, 1.4 mm; and for correlated EVR–SF signals, 1.2 mm. Values of 1.1 mm, 0.8 mm, and 0.5 mm, respectively, were obtained in later experiments due to improvement of the detection system.

For the fission-energy calibration, we measured an energy spectrum of fission fragments from the SF of ^{252}No implanted in the focal-plane detector. Fission fragments of ^{252}No implants produced in the ^{206}Pb + ^{48}Ca reaction were absorbed with their full energy in sensitive layers of detectors with a probability of 65%. The initial measured total deposition energies should be corrected for the pulse-height defect of detectors and energy losses of escaping fragments in the entrance windows, detectors' dead layers, and pentane. With this aim in view, we compared the average measured deposited energy with the total-kinetic-energy (TKE) value of 194.3 MeV measured for SF of ^{252}No in [16]. The measured total-deposited-energy distribution for SF of ^{252}No implants is shown in Fig. 3*b* together with the TKE distribution obtained with an external source [16].

For the ^{244}Pu + ^{48}Ca reaction at a beam intensity of 4×10^{12} pps, the overall counting rate of the detector system was about 15 s^{-1}. The collection efficiency of the separator was estimated from the results of test experiments mentioned above. About 40% of the recoiling $Z = 114$ nuclei formed in the ^{244}Pu target would be implanted in the focal-plane detector.

3. EXPERIMENTAL RESULTS

The experiments were performed during November and December 1998, and from June to October 1999. Over a time period of 94 days, a total of 1.5×10^{19} ^{48}Ca projectiles of energy about 236 MeV were delivered to the target.

In the analysis of the experimental data, we sought new alpha-decay sequences with $E_\alpha \geq 8$ MeV [1, 11]. Note that, according to the concept of the "stability island" of superheavy elements, as long as any alpha-

decay chain leads to the edge of the stability region, it should be terminated by spontaneous fission.

In the course of the ^{244}Pu + ^{48}Ca bombardment, we observed five spontaneous-fission events, all of which could be genetically linked to preceding events, so that we could trace their origin. These events can be classified by their nature in two distinct groups.

First, we point out those SF decays that occur within milliseconds following the implantation of the heavy recoil. Two such events, with measured energies $E = 149$ and $E = 153$ MeV, were detected 1.13 and 1.07 ms, respectively, after the implantation of the corresponding position-correlated recoil nuclei. For one of them, fission fragments were recorded by both the focal-plane ($E = 141$ MeV) and side ($E = 12$ MeV) detectors. Based on the lifetime, we assign these events to the spontaneous fission of the 0.9-ms ^{244mf}Am isomer, a product of transfer reactions with the ^{244}Pu target. Such transfer-reaction products are expected to be suppressed by the gas-filled separator by a factor of about 10^5 [14]. The measured total deposited energies for SF of the ^{244mf}Am implants are shown in Fig. 3*b* by open arrows.

Three other SF events terminate alpha-decay sequences of relatively long-lived nuclei.

Two such SF events were observed as two coincident fission-fragment signals with energies $E = 221$ (156 + 65) MeV and $E = 213$ (171 + 42) MeV. The terms in each sum indicate energies deposited in the focal-plane and side detectors, respectively (see Fig. 3*b*). We scanned the data backwards in time from these events in searches for preceding alpha particles and/or EVRs, in the same positions. The latter were defined as the events characterized by the measured energies, TOF signals, and estimated resulting mass values, which were consistent with those expected for a complete-fusion EVR, as determined in the calibration reactions. The full decay chains including these two fission events are shown in Fig. 4*a*.

Taking into account the energy resolution of the detectors and statistical uncertainty in lifetimes determined from a few detected events, we can say that the two decay chains are consistent. The first alpha particles have similar energies, $E_\alpha = 9.87$ MeV and $E_\alpha = 9.80$ MeV, and were detected in the focal-plane detector 0.77 and 4.58 s after the implantation of the recoil nuclei in strips 2 and 8, respectively. The second alpha particles in corresponding chains, having the energies $E_\alpha = 9.21$ MeV and $E_\alpha = 9.13$ MeV, were observed at the same locations after 10.34 and 18.01 s. Finally, 14.26 and 7.44 s later, the SF events were observed. All events in the two decay chains appeared within time intervals of 25.4 and 30.0 s and position intervals of 0.5 and 0.4 mm (Fig. 4*a*), respectively.

By applying a Monte Carlo technique [17] and the procedure described in [18] (see below), we calculated the probabilities that these decay sequences were caused by the chance correlations of unrelated events at any position of the detector array and at the positions

where the candidate events occurred. The results of the two calculations were similar; the probability that both decay chains consist of random events is less than 5×10^{-13}, calculated in the most conservative approach.

Actually, we observed two identical three-member decay sequences. If we assume that they consisted of four decays, the probability of missing one alpha event in both decay chains would be less than 3%.

The formation of nuclei, which gave origin to the observed decays, corresponded to "instant" ^{48}Ca beam energies of 237.6 and 237.0 MeV in the middle of the target. Taking into account the target thickness and beam energy resolution, we find that this corresponds to 33.6–39.7 and 33.2–39.1 MeV of the excitation energies of the ^{292}114 compound nucleus, respectively. This would favor deexcitation of the compound nucleus by evaporation of four neutrons and alpha emission, which finally leads to the even–even nucleus ^{288}114.

Indeed, the observed chains, including two alpha-decays and terminated by SF, match the decay scenario predicted for the even–even nuclide ^{288}114 [1, 11]. The detected sequential decays have $T_{1/2}$ vs. E_α values that correlate well with the decays of the even–even isotopes of elements 114 and 112. To illustrate this, Fig. 4a presents the expected half-lives corresponding to the measured alpha-particle energies for the genetically related nuclides with the specified atomic numbers. For the calculation of half-lives with a given Q_α value, the formula by Viola and Seaborg with parameters fitted to the T_α values of 58 even–even nuclei with $Z > 82$ and $N > 126$, for which both T_α and Q_α were measured [11], has been used. The calculated alpha-decay half-lives are in agreement with the detected decay times. Conversely, substituting the $T_{1/2}$ and E_α values corresponding to the detected decays into this formula results in atomic numbers of $114.4^{+1.6}_{-0.8}$ and $110.2^{+1.5}_{-0.8}$ for the mother and daughter nuclides, respectively. The measured total energies deposited in the detector array for both fission events exceed the average value measured for ^{252}No by about 40 MeV (see Fig. 3b). Despite the relatively wide distributions of the total kinetic energies in spontaneous fission, this also indicates the fission of a rather heavy granddaughter nucleus, with $Z > 106$ [19].

From the above considerations, we can conclude that the detected decay chains originate from the parent even–even nuclide ^{288}114, produced in the ^{244}Pu + ^{48}Ca reaction via the 4n-evaporation channel.

The next SF event (the first, in chronological order) was also observed as two coincident signals (two fission fragments) with energy deposited in the focal-plane detector $E = 120$ MeV and that in the side detector $E = 52$ MeV, $E_{tot} = 172$ MeV (see Fig. 3b). The entire position-correlated decay chain is shown in Fig. 4b. An alpha particle was detected in the focal-plane detector 30.4 s after the implantation of a recoil nucleus in the middle of the eighth strip. The energy of this first alpha particle was $E_\alpha = 9.71$ MeV. A second alpha particle,
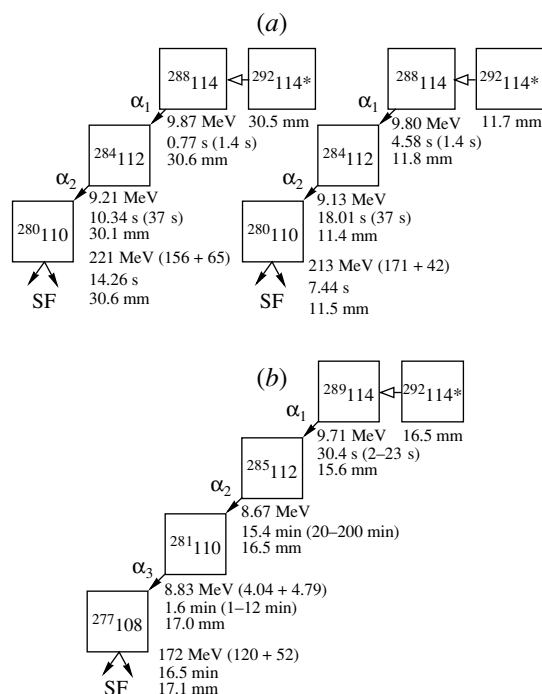

Fig. 4. Time sequences in the observed decay chains. The expected half-lives corresponding to the measured E_α values for given isotopes are shown in parentheses following the measured lifetimes. Hindrance factors of 1 and 10 were assumed for the alpha decay of nuclei having odd numbers of neutrons. The positions of the observed decay events are given with respect to the top of the strip.

having an energy $E_\alpha = 8.67$ MeV, was observed at the same location 15.4 min later. A third alpha particle, escaping the front detector, leaving an energy $E_{\alpha 1} = 4.04$ MeV, and absorbed in the side detector with $E_{\alpha 2} = 4.79$ MeV ($E_{tot} = 8.83$ MeV), was measured 1.6 min later. Finally, 16.5 min later, the SF event was observed [20].

All five signals (EVR, α_1, α_2, α_3, SF) appeared within a position interval of 1.6 mm (Fig. 4b), which strongly indicates that there is a correlation among the observed decays. Assuming that the decay sequence for a valid event will terminate with SF, we developed a Monte Carlo technique to estimate the probability for the candidate event to be due to random correlations [17]. Simulated SF events (about 10^5) were inserted into the data distributed at random positions and times over the entire detector array and entire experiment duration. We scanned the 34 min preceding each random fission in searches for three alpha-particle-like signals with energies 8.5–10.0 MeV and one EVR-like event preceding the alpha events. All four of these events had to be within 2.0 mm of the simulated fission and meet the position criteria at a confidence level greater than 95% to be considered a possible random correlation. The probability per fission of finding such a correlated event was determined to be $P_{err} = 0.006$. With the given energy window and no time restriction within the 34-min interval, we found that the majority
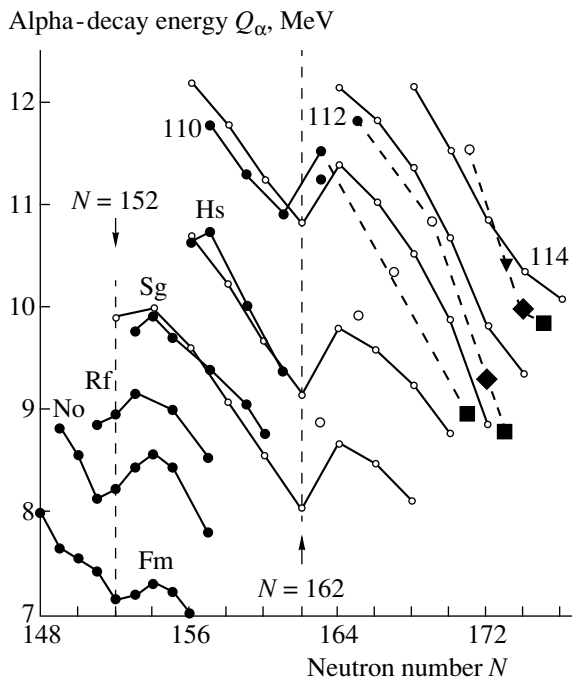
Alpha-decay energy Q_α, MeV

Fig. 5. Alpha-decay energy vs. the number of neutrons for the isotopes of even-*Z* elements with $Z \geq 100$ (solid circles) [4–6, 21–23]. Open circles, triangle, and solid squares and diamonds show data from [24], [25], and the present study. Open circles connected by solid lines represent theoretical Q_α values [1, 11] for even–even $Z = 106–114$ isotopes.

of these random sequences preceding the simulated SF events could not be proposed as the decay of $Z = 114$ or nearby elements. By applying the Geiger–Nuttall relationship, we imposed a lifetime window for each α event. Requiring that the hindrance factor be between 1 and 10 for each α energy reduced P_{err} to 6×10^{-4}.

For strip 8, wev performed another P_{err} calculation at the position, where the candidate event occurred, following the procedure described in [18]. For a position-correlation window of 1.6 mm, the signals from EVR-like events were observed with a frequency of 1.3 h^{-1}. The signals of α-like events with $E = 8.1$–10.5 MeV occurred with a frequency of 1 h^{-1}. Thus, a calculation from event rates alone, even without applying the Geiger–Nuttall relationship, shows that the probability that this decay sequence was caused by the chance correlation of unrelated events in strip 8 is 6×10^{-3}.

In this experiment, we observed a four-member decay sequence. If we assume that it actually consisted of five decays (the spontaneous fission was due to ^{273}106), the probability of missing any one of the four alpha-particle events is about 34%, but the probability of missing any particular alpha-particle event in the chain and observing the other three is only about 8.5%.

All events of the decay chain are correlated in time and position and match the predicted pattern of superheavy-nucleus decay. For the whole decay chain, the basic rule for alpha decay, defining the relation between Q_α and T_α, is

fulfilled. This can be seen in Fig. 4*b*, where the expected half-lives are shown, which correspond to the measured alpha-particle energies for the specified nuclides. The half-lives were calculated using the formula by Viola and Seaborg with the same parameters as above [11], with hindrance factors of 1 and 10 for the alpha decay of odd nuclei.

This decay sequence evidently originates from a different parent nucleus than the chains that were assigned to the decay of ^{288}114. Most probably, this decay chain could originate from the neighboring even–odd isotopes of element 114. The excitation energy of the ^{292}114 nucleus in our experiment was insufficient to evaporate five neutrons, so that the best candidate for the parent nucleus is the heavier even–odd isotope ^{289}114, produced in the 3*n*-evaporation channel. Indeed, the alpha-decaying nuclides in this chain are characterized by lower decay energies than the corresponding members of the chain attributed to the decay of ^{288}114, while SF terminates the decay sequence at a later stage. The decay properties of the observed nuclei are also in agreement with calculations [1, 11] (see Fig. 5).

A priori, one cannot exclude that the investigated excitation energy range of 31.5–39 MeV was not optimal for the production of this isotope and that the probability of the evaporation of three neutrons from the compound nucleus could be even higher at lower excitation energy. However, the excitation function for the 3*n*-evaporation channel should be quite sensitive to the actual fusion barrier, and reducing the energy in the subbarrier region could substantially decrease the complete-fusion cross section. To check this assumption in November and December 1999, we performed a further experiment using a lower projectile energy to seek additional decays of ^{289}114. In the 31-day bombardment by about 231-MeV ^{48}Ca projectiles, a total beam dose of 4.6×10^{18} was accumulated. The corresponding excitation energy of ^{292}114 compound nuclei was in the range of 28.5–34.5 MeV. Only one fission event of the 0.9-ms ^{244mf}Am isomer with $E_{tot} = 156$ MeV was detected 2.26 ms after the implantation of the corresponding position-correlated recoil nucleus in this bombardment. The measured total energy for this SF event is also shown in Fig. 3*b* by open arrows.

In the present series of experiments, we observed three decay sequences: one was attributed to the decay of the odd–even isotope ^{289}114 and two to the decay of the even–even nuclide ^{288}114. Recent semiempirical calculations [26] predict the cross-section maxima for to the emission of three and four neutrons at the ^{292}114 compound nucleus excitation energies of 30 and 38 MeV, respectively. From the present observations, we estimate the cross sections for producing both nuclides in this reaction to be about a picobarn. The bombardment performed at the lower projectile energy results in only an upper production limit of 2 pb (at a 95% C.L.), thus indicating that the maximum 3*n*-evaporation cross section probably does not exceed the cross section for the 4*n* channel.

Experimental and calculated Q_α values for the alpha-decay chains of $^{288}114$ and $^{289}114$

Z	A	Q_{exp}, MeV	Q_{theor}, MeV			
			YPE + WS	FRDM + FY	SHFB	RMF
110	280	≤9.4 (SF)*	9.8	9.05	9.8	8.98
110	281	8.96 ± 0.18		8.55	9.44	8.68
112	284	9.30 ± 0.05	9.8	8.69	9.4	9.30
112	285	8.80 ± 0.05		8.59	8.76	9.02
114	288	9.98 ± 0.05	10.3	9.16	9.4	9.83
114	289	9.85 ± 0.05		8.87	10.16	9.38

Note: The following notation is used in the table: YPE + WS is the macroscopic–microscopic Yukawa-plus-exponential model with Woods–Saxon single-particle potentials [11]. FRDM + FY is the macroscopic–microscopic finite-range droplet model with folded Yukawa single-particle potentials [12]. SHFB is the self-consistent Skyrme–Hartree–Fock–Bogoliubov model with pairing [27]. RMF is the self-consistent relativistic mean-field model [28].

* The Q_α limit was calculated from experimental $T_{1/2}$ value by using the Seaborg–Viola formula with the parameters from [11].

4. DISCUSSION

The lifetimes of the new isotopes, in particular, $^{285}112$ and $^{281}110$, appear to be approximately 10^6 times longer than those of the known nuclei $^{277}112$ [5] and $^{273}110$ [4, 5], which have eight fewer neutrons. We can also note that $^{289}114$, $^{285}112$, and $^{281}110$ are about 10^4 to 10^5 times more stable than $^{285}114$, $^{281}112$, and $^{277}110$, the alpha-decay products of the $^{293}118$ element [24], which was recently produced in the bombardment of ^{208}Pb with ^{86}Kr ions using the Berkeley separator BGS [24].

The $^{288}114$ and $^{284}112$ elements are the heaviest known alpha-decaying even–even nuclides, following the production of $^{260, 266}$Sg ($Z = 106$) [21, 4, 7] and the observation of alpha decay of ^{264}Hs ($Z = 108$) [22].

The radioactive decay properties of the newly observed nuclides are in qualitative agreement with macroscopic–microscopic nuclear theory [1, 11], which predicts both alpha-decay and spontaneous-fission properties of heavy nuclei. Alpha-decay energies of synthesized nuclei and previously known isotopes of even-Z elements with $Z \geq 100$, together with theoretical Q_α values [1, 11] for even–even isotopes of $Z = 106$–114 elements, are shown in Fig. 5. The properties of the new nuclides also agree with those of the neighboring odd isotope $^{287}114$ [25], which was produced in March and April 1999, in the bombardment of a ^{242}Pu target with 7.5×10^{18} ^{48}Ca ions at the VASSILISSA separator.

The experimental data exactly reproduced the decay scenario predicted for $^{288}114$—i.e., two consecutive alpha decays terminated by spontaneous fission. A comparison of the measured decay properties of the new even–even superheavy nuclei $^{288}114$ ($E_\alpha = 9.84 \pm 0.05$ MeV, $T_{1/2} = 1.9^{+3.3}_{-0.8}$ s), $^{284}112$ ($E_\alpha = 9.17 \pm 0.05$ MeV, $T_{1/2} = 9.8^{+17.9}_{-3.8}$ s), and $^{280}110$ ($T_{1/2} = 7.5^{+13.7}_{-2.9}$ s) with theoretical calculations [1, 11] indicates that nuclei in the vicinity of spherical-shell closures with $Z = 114$ and $N = 184$ could be even more stable than is predicted by theory. It can be seen in Fig. 5 that alpha-

decay energies of the heaviest new even–even nuclides with $Z = 112$ and 114 are 0.4–0.5 MeV less than the corresponding predicted values. The heaviest even–odd nuclides follow this trend as well. Such a decrease in Q_α values leads to an increase in partial alpha-decay lifetimes by an order of magnitude. Calculations are far less definite regarding spontaneous fission; however, we note that the observed spontaneous-fission half-life of $^{280}110$ exceeds the predicted value [11] by more than two orders of magnitude.

The alpha-decay properties of the synthesized nuclei can also be compared with predictions of other theoretical models, in particular, with calculations performed in Hartree–Fock–Bogolyubov approach with various Skyrme forces [27] and relativistic mean-field calculations [28]. Alpha-decay energies of the synthesized isotopes, together with theoretical Q_α values [11, 12, 27, 28], are shown in the table. Some theoretical calculations using macroscopic–microscopic models [1, 11, 12] predict the $^{298}_{184}114$ element to be the next spherical doubly magic nucleus; however, recent self-consistent models [27, 28] give preference to the more proton-rich nuclei $^{292}_{172}120$ or even $^{310}_{184}126$. While the macroscopic–microscopic models explain the relatively small Q_α values and corresponding long half-lives of the synthesized nuclei by the influence of spherical $Z = 114$ and $N = 184$ shell closures, the self-consistent Skyrme–Hartree–Fock–Bogolyubov model predicts an interesting shell structure in the neutron system but no shell effect at $Z = 114$. The last model reproduces well the measured Q_α values for the decay chain originating from $^{289}114$ and passing through the [611]1/2$^+$ levels (excited for $N = 175$, 171 and ground state for $N = 173$). The ground state of $^{289}114$ is calculated to be a high-Ω isomeric state, [707]15/2$^-$ [27].

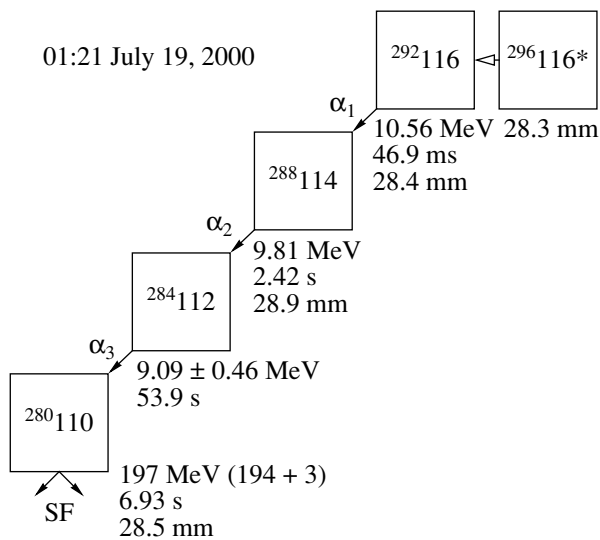The relativistic mean-field model [28] describes well the observed alpha-decay chain of $^{289}114$ (the

01:21 July 19, 2000

Fig. 6. Time sequence in the decay chain observed in the ^{248}Cm + ^{48}Ca reaction.

break in the measured Q_α values, missed in the calculations, was explained by assuming the decay of ^{289}114 to one of the numerous low-lying excited states in ^{285}112). This model perfectly reproduces the measured Q_α values for the decay chain of the even–even nuclide ^{288}114, suggesting the influence of deformed $Z = 114$ and $N = 174$ shell closures for its explanation, although a spherical $Z = 114$ shell cannot be excluded.

All the above theoretical approaches predict the existence of the "island of stability" in the region of superheavy elements. The principal result of the present work is the observation of the considerable growth of lifetimes of superheavy nuclei with $Z \geq 110$ with increasing neutron number. A comparison of the present data with calculations shows that theoretical predictions agree with experimental results not only qualitatively but also quantitatively. In this respect, the decay properties of the new nuclides observed in the present experiments conform to theoretical expectations and can be considered a proof of the existence of enhanced stability in the region of superheavy elements.

ACKNOWLEDGMENTS

Note added in proof. On June 14, 2000, we started an experiment aimed at the synthesis of $Z = 116$ superheavy nuclei in the complete fusion reaction induced by ^{248}Cm + ^{48}Ca collisions.

After an integrated beam dose of 6.6×10^{18} had been delivered to the targets, we observed a decay chain consisting of three consecutive alpha decays and a spontaneous fission that can be assigned to the implantation and decay of the $Z = 116$ heavy nuclide (see Fig. 6). The implantation of a heavy recoil in the focal-plane detector was followed, after 46.9 ms, by an α-particle decay with $E_\alpha = 10.56$ MeV. This sequence switched the ion beam off, and further decays—two alpha particles and a spontaneous fission—were detected under low-background conditions. All events in this decay chain appeared within a time interval of 63.3 s and a position interval of about 0.5 mm, which points to a strong correlation between them. The probability that the decay chain consists of random events is less than 10^{-10}.

The energies and decay times of the descendant nuclei are in agreement with those observed in the decay chains of the even–even isotope ^{288}114 produced in ^{244}Pu + ^{48}Ca interactions. Thus, the first alpha decay with $E_\alpha = 10.56$ MeV should be attributed to the parent nuclide ^{292}116 produced in ^{248}Cm + ^{48}Ca interactions via the $4n$-evaporation channel.

The experiments are now in progress.

REFERENCES

1. R. Smolańczuk, Phys. Rev. C **56**, 812 (1997).
2. P. Möller and J. R. Nix, J. Phys. G **20**, 1681 (1994).
3. S. Čwiok *et al.*, Nucl. Phys. A **611**, 211 (1996).
4. Yu. A. Lazarev *et al.*, Phys. Rev. Lett. **73**, 624 (1994); **75**, 1903 (1995); Phys. Rev. C **54**, 620 (1996).
5. S. Hofmann *et al.*, Z. Phys. A **350**, 277 (1995); GSI Nachrichten, No. GSI 02-95 (Darmstadt, 1995), p. 4; Z. Phys. A **350**, 281 (1995); **354**, 229 (1996).
6. A. Ghiorso *et al.*, Phys. Rev. C **51**, R2293 (1995).
7. A. Türler *et al.*, Phys. Rev. C **57**, 1648 (1998).
8. Yu. Ts. Oganessian, in *Proceedings of the International Conference on Nuclear Physics at the Turn of the Millen-*

nium "Structure of Vacuum and Elementary Matter," Wilderness, South Africa, 1996 (World Sci., Singapore, 1997), p. 11.

9. W. J. Swiatecki, Nucl. Phys. A **376**, 275 (1982); J. P. Blocki, H. Feldmeier, and W. J. Swiatecki, Nucl. Phys. A **459**, 145 (1986).

10. E. K. Hulet *et al.*, Phys. Rev. Lett. **39**, 385 (1977); J. D. Illige *et al.*, Phys. Lett. **78B**, 209 (1978); R. J. Otto *et al.*, J. Inorg. Nucl. Chem. **40**, 589 (1978); A. Ghiorso *et al.*, LBL Report, LBL 6575, 1977; Yu. Ts. Oganessian *et al.*, Nucl. Phys. A **294**, 213 (1978); P. Armbruster *et al.*, Phys. Rev. Lett. **54**, 406 (1985).

11. R. Smolańczuk, J. Skalski, and A. Sobiczewski, in *Proceedings of the International Workshop XXIV on Gross Properties of Nuclei and Nuclear Excitations "Extremes of Nuclear Structure," Hirschegg, Austria, 1996* (GSI, Darmstadt, 1996), p. 35.

12. P. Möller, J. R. Nix, and K.-L. Kratz, At. Data Nucl. Data Tables **66**, 131 (1997).

13. W. D. Myers and W. J. Swiatecki, Nucl. Phys. A **601**, 141 (1996).

14. Yu. Ts. Oganessian *et al.*, in *Proceedings of the 4th International Conference on Dynamical Aspects of Nuclear Fission, Castá-Papiernička, Slovak Republic, 1998* (World Sci., Singapore, 2000), p. 334; Yu. A. Lazarev *et al.*, in *Proceedings of the International School-Seminar on Heavy Ion Physics, Dubna, Russia, 1993*, JINR Report E7-93-274 (Dubna, 1993), Vol. II, p. 497.

15. Yu. A. Lazarev *et al.*, JINR FLNR Scientific Report 1995–1996, E7-97-206 (Dubna, 1997), p. 30.

16. J. F. Wild *et al.*, J. Alloys Compd. **213/214**, 86 (1994).

17. N. J. Stoyer *et al.*, LLNL Preprint UCRL-JC-136927, 1999; submitted for publication in Elsevier Science.

18. V. B. Zlokazov, JINR Preprint No. E7-99-273 (Dubna, 1999); submitted for publication in Eur. Phys. J.

19. M. G. Itkis *et al.*, Nuovo Cimento A **111**, 783 (1998); private communication.

20. Yu. Ts. Oganessian *et al.*, Phys. Rev. Lett. **83**, 3154 (1999).

21. A. G. Demin *et al.*, Z. Phys. A **315**, 197 (1984); G. Münzenberg *et al.*, Z. Phys. A **322**, 227 (1985).

22. Yu. Ts. Oganessian *et al.*, Z. Phys. A **319**, 215 (1984); G. Münzenberg *et al.*, Z. Phys. A **324**, 489 (1986); F. P. Heßberger *et al.*, in *Proceedings of the Tours Symposium on Nuclear Physics III, Tours, France, 1997* (American Inst. Phys., New York, 1998), p. 3.

23. *Table of Isotopes*, Ed. by R. B. Firestone and V. S. Shirley (Wiley, New York, 1996, 8th ed.).

24. V. Ninov *et al.*, Phys. Rev. Lett. **83**, 1104 (1999).

25. Yu. Ts. Oganessian *et al.*, Eur. Phys. J. A **5**, 63 (1999).

26. R. N. Sagaidak, JINR FLNR Scientific Report 1997–1998 (Dubna, 2000) (in press).

27. S. Ćwiok, W. Nazarewicz, and P. H. Heenen, Phys. Rev. Lett. **83**, 1108 (1999).

28. M. Bender, Phys. Rev. C **61**, 031302 (2000).

====== **NUCLEI** ======
Theory

Multidimensional Dynamical–Statistical Model for Describing the Fission of Excited Nuclei

I. I. Gontchar, A. É. Gettinger, L. V. Guryan, and W. Wagner[1)]
Omsk State University of Railway Transport, pr. Marksa 35, Omsk, 644046 Russia
Received November 15, 1999

Abstract—A multidimensional stochastic model for describing the decay of excited nuclei is presented. The model takes into account the dynamics of thermal fluctuations of collective variables, the dissipation of the kinetic energy of collective motion, and the emission of light particles from excited nuclei. The potential energy of a deformed nucleus is calculated within the liquid-drop model with a sharp surface and within the finite-range-interaction model. The friction parameters are calculated on the basis of the one-body-dissipation model. The inertia parameters are found in the Werner–Wheeler approximation. The drift components of forces are determined in terms of the entropy of an excited nucleus. The latter in turn is computed within the Fermi gas approximation with allowance for the deformation dependence of the density-level parameter. The fission probability, the mean multiplicity of neutrons emitted prior to scission (prescission neutrons), and the variances of the mass distributions of fission fragments at the most probable kinetic-energy value are calculated on the basis of the model developed here and are compared with experimental data. The dependences of these quantities on the model parameters are considered in detail. © *2000 MAIK "Nauka/Interperiodica".*

1. INTRODUCTION

Over the past 10–20 years, investigations into the process of excited-nucleus fission have focused primarily on the dissipative properties of fissile nuclei. The main objective pursued by such investigations has been to extract, from experimental data, information about the magnitude of nuclear friction and about its deformation or temperature dependence (or both deformation and temperature dependences). If the height of the fission barrier, B_f, is greater than the nuclear temperature T, fission appears to be a purely fluctuation process [1]. For such cases, the most adequate description is obtained within diffusion models based on the Fokker–Planck equation [2] or on stochastic differential equations that belong to the class of Langevin equations and which are physically equivalent to the Fokker–Planck equation. Within such models, nuclear friction determines both the rate of collective-energy dissipation and the intensity of fluctuations, thereby controlling the fission rate. Although the first studies along these lines relied on the Fokker–Planck equation (see the review article of Adeev *et al.* [3]), a decided preference is being given now to the second version (for an overview, see [4–7]).

In order to realize the pursued goal—that is, to extract information about nuclear friction from experimental data—we have to meet two conflicting demands. First, it is necessary to analyze (and, hence, to calculate within one theoretical model or another) various observables like fission probabilities, multiplic-

ities of particles emitted from a fissile nucleus prior to its scission into fragments (prescission particles), and kinetic energies of fragments. Second, a global analysis for a large number of reactions at various excitation energies must dispense with individually varying adjustable parameters for each reaction and at each energy value.

In order to meet the first demand, it is necessary increase the number of collective coordinates, but this leads to a sharp growth of machine time, giving no way to satisfy the second demand. The emerging situation is illustrated by the results obtained in [8–10].

Wada *et al.* [8] presented the results of their calculations for the fission probability P_f, the mean multiplicity $\langle n_{\mathrm{pre}} \rangle$ of prescission neutrons, and the first and the second moment of the kinetic-energy distribution of fragments. In order to calculate these observables, they developed a two-dimensional stochastic model, but the machine time proved to be so large that they were able to perform calculations only for two cases, that of ^{19}F + ^{181}Ta interactions at $E^*_{\mathrm{tot}} = 80.7$ MeV and that of ^{16}O + ^{184}W interactions at $E^*_{\mathrm{tot}} = 195.8$ MeV, E^*_{tot} being the total excitation energy of a compound nucleus.

A one-dimensional stochastic model relying on the approximation of a fast relaxation of the collective momentum was used in [9] as a basis for calculating the multiplicities of prescission neutrons and the fission probabilities for compound nuclei from ^{178}W to ^{251}Es over the excitation-energy interval between 40 and 200 MeV. These calculations were performed with the aid of the computer code DESCEND [11], which can

be used by experimentalists for data analyses. However, the code is unable to compute the mass or kinetic-energy distributions of fragments since the underlying model does not provide such possibilities.

Finally, Vanin *et al.* [10] proposed a two-dimensional stochastic model and, on the basis of this model, calculated the mass distributions of fragments over a wide range of values of the fissility parameter Z^2/A of compound nuclei. However, the model from [10] takes no account of the collective motion of a nucleus in the vicinity of the ground state, nor does it includes particle emission, which accompanies fission, competing with it. Because of these limitations, only one observable was computed in [10].

Among theoretical studies devoted to a dynamical simulation of the fission process with allowance for its fluctuation character, only that which is reported in [12] makes mention of full three-dimensional calculations, but no comparison with experimental data is drawn there.

Thus, the problem of constructing a multidimensional fission model that makes it possible to compute a number of observables for the fission process over a wide region of Z^2/A and E_{tot}^* within reasonable times becomes pressing.

This article is organized as follows. In Section 2, the ingredients of our model are described: the algorithms (Subsection 2.1), the parametrization of the nuclear shape (Subsection 2.2), the equation of motion (Subsection 2.3), the potential energy (Subsection 2.4), thermodynamic quantities like entropy and temperature (Subsection 2.5), the single-particle level-density parameter (Subsection 2.6), particle emission (Subsection 2.7), a transition to the statistical branch (Subsection 2.8), the inertia and friction parameters (Subsection 2.9), and the conditions of nuclear scission into two fragments (Subsection 2.10). In Section 3, we analyze the effect of collective-fluctuation dynamics (Subsection 3.1), of the single-particle level-density parameter (Subsection 3.2), of the potential energy (Subsection 3.3), and of the emission of prescission particles (Subsection 3.4) on the observables. Section 4 is devoted to a comparison of the results of our calculations for the fission probability (Subsection 4.1), the prescission-neutron multiplicity (Subsection 4.2), and the variance of the mass distribution of fission fragments (Subsection 4.3) with experimental data. The conclusions drawn from our analysis are summarized in Section 5.

2. DESCRIPTION OF THE MODEL

The multidimensional stochastic model is implemented as a package SAND that appears to be the result of a further development of the computer code DESCEND reported in [11]. The applicability range of the model in its up-to-date version is associated with the possibility of obtaining a statistically significant number of fission events over a reasonable time of simulation. In practice, this imposes the constraint $Z^2/A > 31$ on the fissility parameter of compound nuclei for which the calculations have been performed. However, this constraint is not very stringent since, for light compound nuclei, there is virtually no stage of descent from the barrier. In simulating their decay, we can therefore successfully apply one of the versions of statistical calculations (see, for example, [13, 14]).

The physical concepts underlying our model are illustrated in Fig. 1. The fission process is described in terms of a few collective variables associated with the main deformation modes. They form a system that has a small number of degrees of freedom and which will be referred to as a particle. It interacts with a system having a great number of different degrees of freedom of the nucleus (heat bath). In this case, the dynamics of the collective variables is similar to the dynamics of a Brownian particle since, in a single event of particle interaction with a heat bath, its energy changes insignificantly. In contrast to conventional Brownian motion, the fluctuation of the particle energy affects the heat-bath energy; therefore, the temperature T is a function of the collective variables. On average, the particle is near the ground state (see the probability density Π in Fig. 1*a*) and has a collective energy $\langle E_{\text{coll}} \rangle$ that is determined by the temperature T and which is small in relation to E_{tot}^*. The only way to describe the fluctuations quantitatively is to fix the particle coordinates and momenta at discrete time points separated by a fixed interval τ (these consecutive particle states are connected by broken-line segments in Fig. 1*b*).

While fluctuating, a hot nucleus emits particles, so that its excitation energy decreases. If the particle overcomes the potential barrier as the result of unidirectional fluctuations, the fission event occurs (the possibility of returns into the ground state is small). This process is associated with the tail of the distribution in Fig. 1*a*. But if the excitation energy of the particle occurring to the left of the ridge is decreased because of emission to such an extent that it becomes less than the barrier height, there arises an evaporation residue. The same compound nucleus at the same initial excitation energy E_{tot}^* can complete its evolution according to either scenario. The values of the corresponding probabilities are especially close if the neutron binding energy B_n is commensurate with the height of the fission barrier.

2.1. Algorithm

The algorithm of the SAND package is very close (but not identical) to the algorithm underlying the DESCEND code, which was schematized in Fig. 35 from [6] and in Fig. 1 from [11]. Our model features two branches—a dynamical and a statistical one. Within the dynamical branch, the evolution of collec-
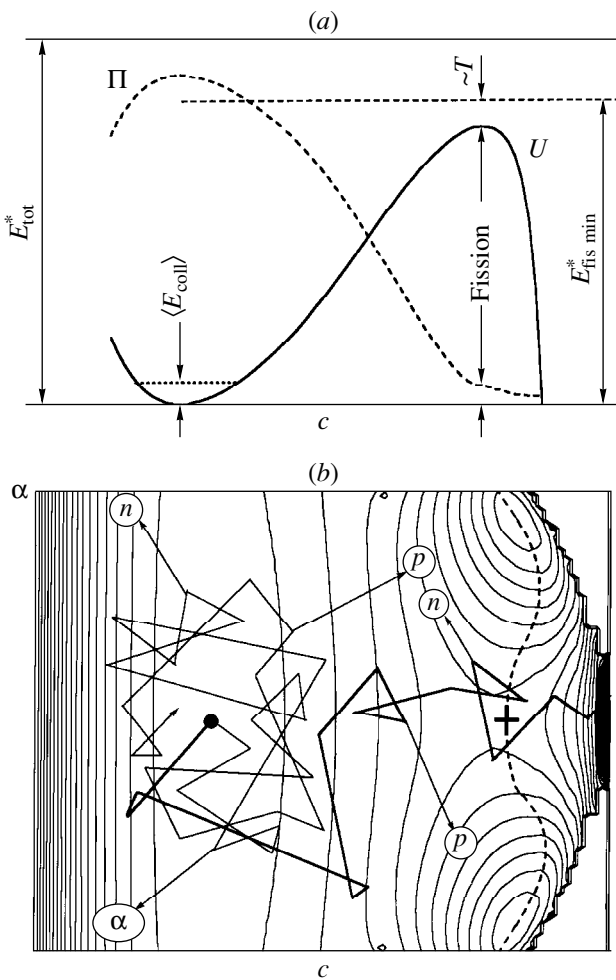
(a)

(b)

Fig. 1. Schematic representation of physical concepts underlying the model developed in the present study: *(a)* potential energy U and probability density Π versus the elongation of the nucleus, c, at a fixed value of the asymmetry parameter α (also shown in this panel are the total excitation energy, E_{tot}^*; the mean energy of collective motion, $\langle E_{\text{coll}} \rangle$; the minimal excitation energy at which fission can still occur, $E_{\text{fis min}}^*$; and the probability-density tail leading to fission) and *(b)* chart of the potential energy in terms of the coordinates c and α. In Fig. 1*b*, the closed circle on the left of the figure, the cross on the right of the figure, the dashed curve, and broken lines represent, respectively, the ground state, the fission barrier, the ridge separating the region of the ground state from the region of descent to the scission line, and trajectories of particles simulating the collective motion of the nucleus (segments of the broken lines connect successive positions of a particle at regular time intervals of duration τ; also shown are events of proton, neutron, and alpha-particle emission; the thick and thin broken lines end in a fission event and in an evaporation event, respectively).

tive degrees of freedom is described on the basis of the Langevin equation. The statistical branch is intended for describing the decay of nuclei that have lost a significant part of their initial excitation energy via particle emission. The initial segment of each trajectory

from the ground state is simulated within the dynamical approach, while particle emission is described statistically. After some delay time and under some additional conditions (for details, see Subsection 2.8), the process can be analyzed within the purely statistical approach, where both particle emission and the fission process are described statistically. If, after a transition to the statistical branch, the nucleus undergoes fission, the corresponding trajectory goes over to the dynamical branch. For the initial conditions, use is then made of equilibrium coordinate and momentum distributions at the ridge, which is displayed in Fig. 1*b* (the momentum values returning the particle into the energy position near the ground state are naturally rejected). In this way, we take into account the motion of the nucleus from the saddle point to the scission point (more precisely, from the ridge to the scission line), bearing in mind that this descent is accompanied by the emission of additional particles and by the formation of the fragment mass asymmetry. Only this (last) segment of the particle trajectory, without particle emission, was considered in [10].

2.2. Parametrization of Nuclear Shapes

The nuclear shape is specified with the aid of the (c, h, α) parametrization (detailed description of the parametrization and corresponding formulas can be found in [15, 16]), which proved to be quite successful. The physical meaning of the parameters c, h, α is clarified in Fig. 2. The first corresponds to the elongation of the nucleus; the second determines the quadrupole deformation of the nucleus for compact shapes and controls neck thickness (but is not equal to it) for shapes featuring a neck. As to the third parameter α, it determines the octupole deformation of compact shapes and governs the mass asymmetry of would-be fragments for shapes with a neck.

Full dynamical calculations in three-dimensional configuration space consume too much machine time. In order to sidestep this difficulty, we perform a dynamical simulation in terms of the coordinates c and α along the dynamical bottom of the fission valley (in the following, this will be referred to, for the sake of brevity, as a dynamical trajectory) in the (c, h) subspace.

The dissipative trajectory is determined in the following way. At $\alpha = 0$, we perform a dynamical calculation of the trajectory of particle descent from the saddle point of the potential energy to the scission point and to the ground state without fluctuations. If the initial momenta or displacements (or both of them) are not great, the system retains information about them only for a very short time interval; therefore, the interpretation in terms of one dissipative trajectory is legitimate. Such trajectories are depicted in Fig. 3. It turns out that the dissipative trajectory virtually coincides with the static bottom of the fission valley (this bottom is defined as the line that descends from the saddle point to the scission point and from the former to the ground
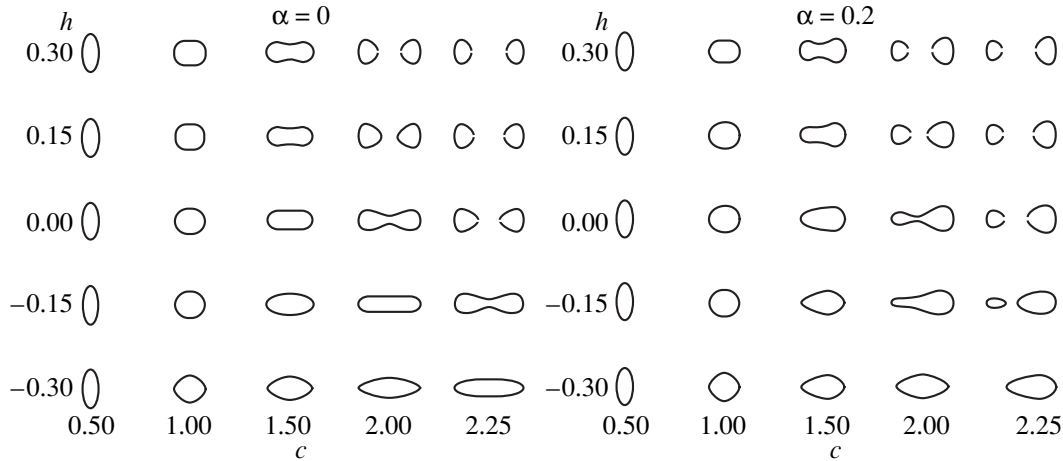
Fig. 2. Nuclear shapes corresponding to various values of the parameters c, h, and α.

state and which is characterized by the highest gradient of the potential energy) when the system moves toward the ground state and deviates from it significantly when the system moves toward the scission. Thus, the dissipative trajectory is determined not only by the coordinate dependence of the potential energy but also by the behavior of the inertia and friction tensors.

Four panels of Fig. 3 show the dynamical and static bottoms for two nuclei calculated within two models. Figures 3a and 3b illustrate the results of the calculations within the liquid-drop model, while Figs. 3c and 3d depict analogous results for the model employing finite-range nuclear interaction. For either model, we perform a comparison of the results for the relatively light ^{200}Pb nucleus ($Z^2/A = 33.62$) with a short descent and the rather heavy ^{222}Th nucleus ($Z^2/A = 36.49$) with a much longer descent. The relative arrangement of the static bottom of the fission valley and the dissipative trajectory in each panel of Fig. 3 is identical to that in Fig. 4 from [3] (at a qualitative level). It turns out that all dissipative trajectories lead to approximately the same point of the scission line in the (c, h) plane ($c = 2.15$, $h = -0.05$), irrespective of the nuclear species and of the potential-energy form.

The use of dissipative trajectories results in that the values of all observables are obtained at the most probable (mean) kinetic energy of fragments.

2.3. Equations of Motion

The motion of a Brownian particle that simulates the dynamics of collective nuclear motion is described with the aid of stochastic differential equations. In a discrete form, they are given by

$$p_i^{(n+1)} = p_i^{(n)} - \{[d_{qi}(m^{-1})_{jk}]^{(n)} p_j^{(n)} p_k^{(n)}/2$$
$$+ \gamma_{ij}^{(n)}(m^{-1})_{jk}^{(n)} p_k^{(n)} - K_i^{(n)}\}\tau + g_{ij}^{(n)} w_j^{(n)} \tau^{1/2}, \quad (1)$$

$$q_i^{(n+1)} = q_i^{(n)} + (m^{-1})_{ij}^{(n)} p_j^{(n)} \tau, \quad (2)$$

where q_i ($i = 1, 2$) are the collective coordinates (that is, $q_1 = c$ and $q_2 = \alpha$); p_i are the collective momenta conjugate to these coordinates; m_{ij} and γ_{ij} are, respectively, the inertia and the friction tensor; K_i is the drift force, which is determined primarily by nuclear deformation; τ is the time step of the simulation; w_j is a random number normally distributed with the variance value of two; and the superscript n indicates that the value of a given quantity is taken at the instant $n\tau$.

2.4. Potential Energy of a Deformed Nucleus

The potential energy $U(q)$—that is, the minimal energy that the system can have at a given deformation q—is an important ingredient of any dynamical simulation. First, it determines the internal excitation energy $E^*(q)$ via the energy-conservation law and, hence, the nuclear temperature T. Second, the potential energy determines the drift force K_i. Shell corrections are not taken into account since we consider only the fission of hot nuclei. In this study, we present the results obtained by calculating the potential energy by two methods, within the liquid-drop model with a sharp boundary [17] and within the model employing finite-range nuclear interaction [18] with the parameters borrowed from [19].

Among the distinctions between the potential energies as calculated on the basis of the liquid-drop model, on one hand, and on the basis of the finite-range-interaction model, on the other hand, those that are of prime importance for our problem are the following.

First, the fission barriers in the finite-range-interaction model are noticeably lower than in the liquid-drop model. Figure 4 illustrates this distinction and also confirms the quality of our calculations within the finite-range-interaction model. It is obvious that, in calculations within this model, the fission probability must be
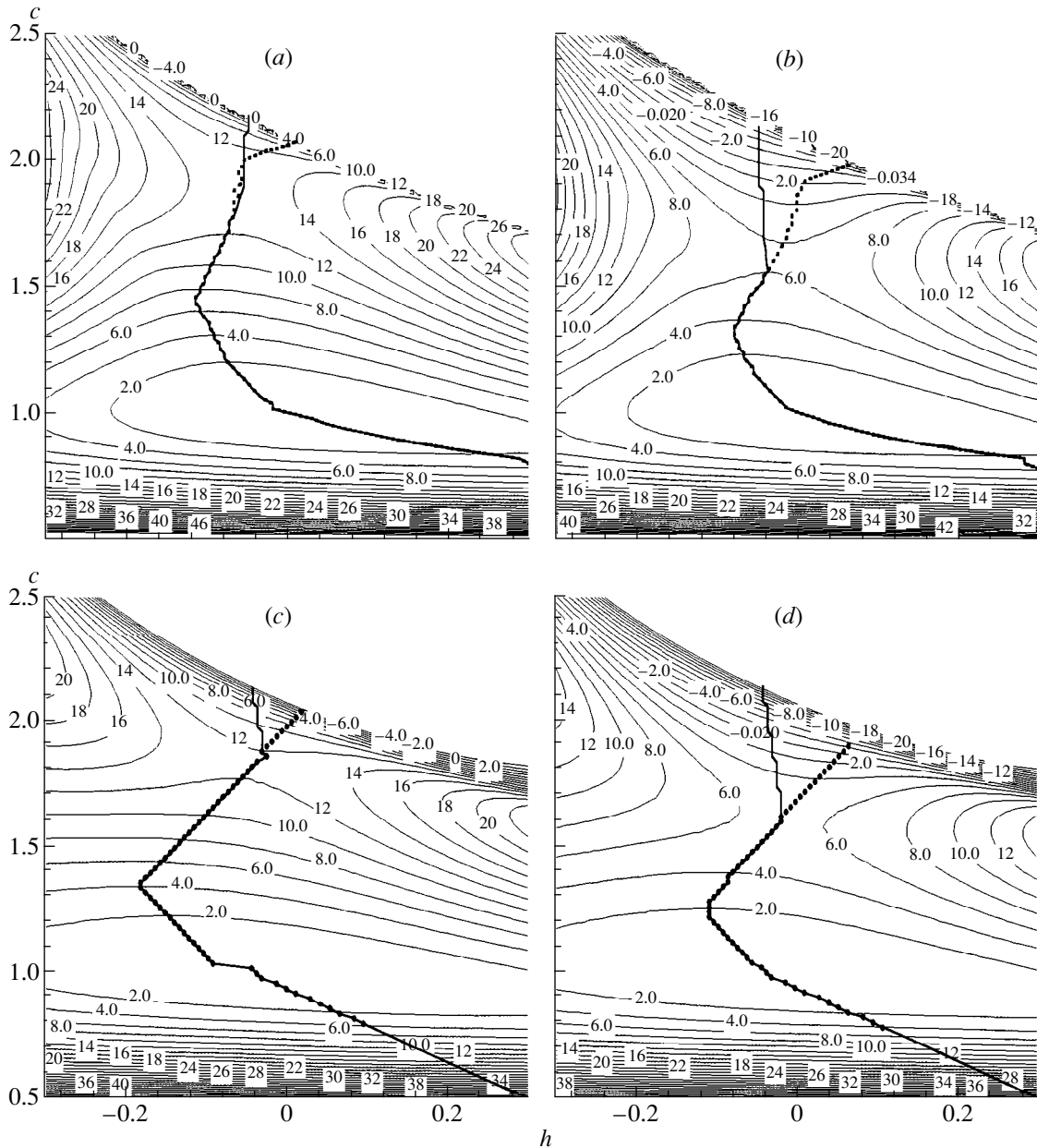
Fig. 3. Dynamical and static bottoms of the fission valley: (*a*, *b*) results of the calculations on the basis of the liquid-drop model for [200]Pb and [222]Th, respectively, and (*c* and *d*) results of the calculations on the basis of the finite-range-interaction model for [200]Pb and [222]Th, respectively. Dotted and thick solid lines correspond to, respectively, static bottoms and dynamical bottoms (dissipative trajectories) of the fission valley. The static bottom of the valley seems to be nonorthogonal to isolines of the potential energy because different scales were chosen along the different coordinate axes.

higher than in the liquid-drop model. The relative difference of the barrier heights decreases with increasing Z. It is generally believed that the effect associated with the difference of barrier heights calculated on the basis of the liquid-drop model and of the finite-range-interaction model becomes insignificant for nuclei heavier than radon–uranium nuclei.

Second, the saddle-point stiffnesses with respect to the mass-asymmetry coordinate are noticeably lower within the finite-range-interaction model than within the liquid-drop model. This distinction is illustrated in Fig. 5*a*. The special features of the saddle-point stiffnesses and their relation to the variance of the mass distribution are well known (see, for example, [13]), and we will not dwell upon this. We only note that the position of the Businaro–Gallone point calculated within the finite-range-interaction model agrees with experimental data from [21]. It is more interesting to discuss stiffnesses near the scission point (Fig. 5*b*). In just the same way as in the case of the saddle point, the liquid-
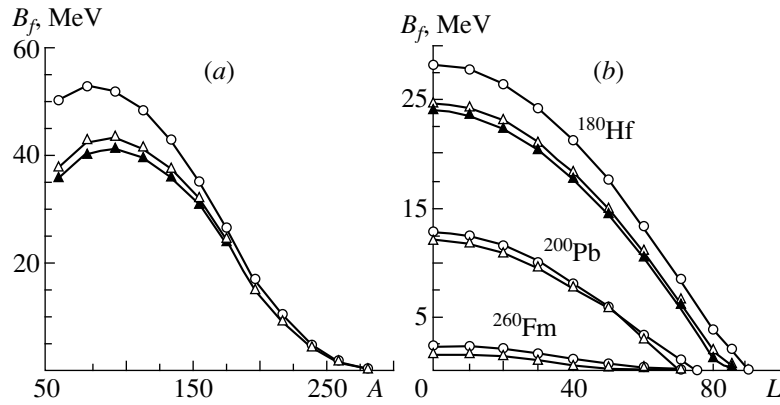
Fig. 4. Fission barriers computed on the basis of (open circles) the liquid-drop model [17], (open triangles) the finite-range-interaction model, and (closed triangles) the approximating Sierk code [20]: (*a*) results for zero orbital angular momentum along the beta-stability valley and (*b*) results for three nuclei versus orbital angular momentum (for lead and fermium, the results of our calculations are indistinguishable on the scale of the figure from the results presented in [20]).

drop model yields here higher values of the stiffness than the finite-range-interaction model. In either model, these stiffnesses increase monotonically with increasing Z^2/A. This must lead to a decrease in the variance of the mass distribution of fragments if the system does not retain information about preceding (more compact) states.

We now compare the saddle-point stiffness $C_{\alpha sd}$ (Fig. 5a) and the stiffness near the scission point, $C_{\alpha sc}$ (Fig. 5b). In the region $35 > Z^2/A > 30$, there is the value $(Z^2/A)_c$ at which the two stiffnesses coincide. Since the saddle-point stiffness is greater for $Z^2/A < (Z^2/A)_c$, the effect of descent from the barrier top must lead to a decrease in the variances of the mass distributions. However, the descent for these nuclei is short, so that the effect in question will manifest itself only slightly. For $Z^2/A > (Z^2/A)_c$, the saddle-point stiffnesses are smaller than those near the scission point. Because of this, the dynamics effect—that is, the memory of earlier states—must lead to an increase in the variances of the mass distributions in this region. In relation to what was said on the subject in the review article [3], there has not been much new physics in the above discussion.

A comparison of the stiffnesses calculated on the basis of the two models shows that the variances of the mass distributions must be greater within the finite-range-interaction model than within the liquid-drop model.

We will now discuss some details of the potential-energy calculation that are associated with the inclusion of particle emission in our model. After each particle-emission event, the Langevin trajectory goes over from one sheet of the potential energy to another. A complete rescaling of $U(q)$ would lead to a significant growth of the time of simulation; for this reason, we adopted a compromising solution. The dissipative trajectory in the coordinates c and h is determined only for the compound nucleus. When we use the liquid-drop model, the potential energy is rescaled for each nuclide

in the emission chain. In the case where we use the finite-range-interaction model, the chart of the dimensionless coefficients of the surface (B_s), the Coulomb (B_c), and the rotational (B_r) components of the potential energy are calculated for the compound nucleus; at the same time, the potential energy for each nuclide in the
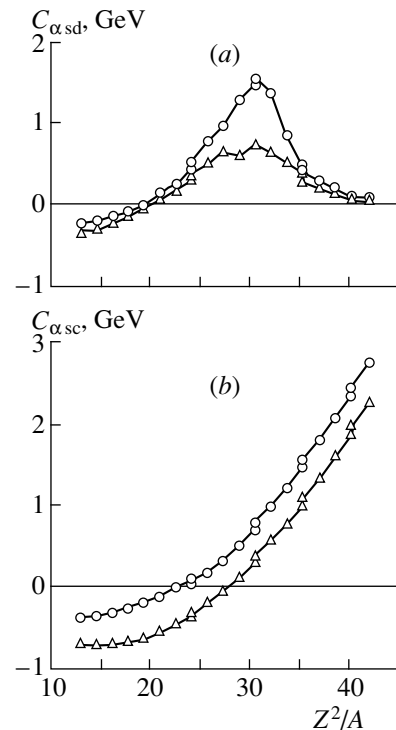
Fig. 5. Stiffnesses C_α in the mass-asymmetry coordinate as a function of Z^2/A that were calculated as $d_{\alpha\alpha}U$ (second derivative of the deformation energy with respect to α) at constant values of c and h: (*a*) results for the saddle point and (*b*) results for a shape characterized by a neck of radius of $0.1R_0$ at the bottom of the dynamical fission valley. The notation for the points is identical to that in Fig. 4.

Fig. 6. Isolines of (*a*) the deformation energy and (*b*) the entropy in the (c, α) plane along the bottom of the dynamical fission valley. The lines are drawn with a step of 2 MeV for $U(c, \alpha)$ and with a step of 0.5 MeV for $S(c, \alpha)$. The charts computed on the basis of the liquid-drop model and the finite-range-interaction model (abbreviated as LDM and FRIM in the corresponding panels) are depicted on the right and on the left, respectively. The entropy values are counted from zero corresponding to the ground state and are taken with a reversed sign. To avoid encumbering the figures, the level values are indicated only for a few lines. For convenience of a comparison, only values corresponding to negative and positive α are presented for, respectively, the liquid-drop and the finite-range-interaction model. The calculations have been performed up to the line corresponding to zero neck radius for the liquid-drop model and up to the line corresponding to $0.1R_0$ for the finite-range-interaction model.

emission chain is constructed on the basis of these coefficients in just the same way as for the liquid-drop model. A test has shown that this approximate method is quite acceptable. If a nuclide from the emission cascade has ten neutrons less than the compound nucleus, its calculated barrier exceeds the true barrier by no more than 5% (the calculation was performed in the range $15 < Z^2/A < 45$).

2.5. Thermodynamic Quantities

It is well known that the drift force K_i acting in the thermodynamic system must be calculated as the derivative of the thermodynamic potential but not as the derivative of the potential energy [22]. Following [9], we calculate here the drift force K_i in terms of the derivatives of the entropy S at a constant excitation energy:

$$K_i = T(dS/dq_i). \tag{3}$$

The entropy $S(q)$ is calculated within the Fermi gas model as

$$S(q) = 2\{a(q)[E_{\text{tot}}^* - U(q) - E_{\text{kin}}]\}^{1/2}, \tag{4}$$

where E_{kin} is the kinetic energy of collective nuclear motion, while $a(q)$ is the single-particle level-density parameter, which is discussed in the next subsection.

The examples of the potential-energy and entropy charts obtained on the basis of the liquid-drop and the finite-range-interaction model are presented in Fig. 6. They are conventional for the macroscopic case. It should be emphasized, however, that our calculations were performed not at a fixed value of one of the shape parameters, as was done, for example, in [10], but along the dissipative trajectory. In such situations, there sometimes arise unpleasant surprises {see, for example, [23], where the weak maxima (instead of minima) of the potential energy appeared at $\alpha = 0$}. This is not so in our case.

A comparison of the left- and the right-hand parts of the charts in Fig. 6 shows that the liquid-drop model leads to the softer potential and entropy in the ground-state region. This is the well-known effect that arises upon taking into account the surface diffuseness; its manifestations—lower barriers and smaller stiffnesses—have already been discussed. It is, however, interesting that the situation changes as the system approaches the descent from the saddle to the scission point: the value of U and the difference $S_{\text{gs}} - S$ decrease faster in the finite-range-interaction model. We cannot explain this qualitatively.

The temperature of the nucleus is specified by the conventional relation of the Fermi gas model

$$T(q) = \{[E_{\text{tot}}^* - U(q) - E_{\text{kin}}]/a(q)\}^{1/2}. \tag{5}$$

It determines the amplitudes of the fluctuation forces, g_{ij}, through the Einstein relation

$$g_{ik}g_{kj} = T\gamma_{ij}, \tag{6}$$

where summation over the dummy indices is implied.

2.6. Single-Particle Level-Density Parameter

This parameter, which appears in expressions (4) and (5) for the entropy and the temperature, respectively, is an important ingredient of our model. It is well known [24, 25] that the parameter a depends on the deformation and can be represented in the form

$$a(q) = a_v A + a_s A^{2/3} B_s(q). \quad (7)$$

In this equation, the dimensionless coefficient B_s, which determines the surface area, depends on the deformation; for a sphere, it is equal to unity within the liquid-drop model identically and deviates from unity only by 2% at $A = 200$ within the finite-range-interaction model.

Among a great number of sets of the coefficients a_v and a_s—these sets were analyzed by Smirenkin *et al.* [26]—we choose two sets for our calculations: one from the study of Ignatyuk *et al.* [25] and the other from the study of Toke and Swiatecki [27]. The set of coefficients from [25], $a_v = 0.073$ MeV^{-1} and $a_s = 0.095$ MeV^{-1}, results in the minimal value of the parameter a and in the weakest dependence of this parameter on the deformation, whereas the set of coefficients from [27], $a_v = 0.0685$ MeV^{-1} and $a_s = 4a_v$, corresponds to the maximal value of the parameter a and the strongest dependence of this parameter on the deformation. Figure 7 illustrates the aforementioned results. For the finite-range-interaction model, the temperature dependence of the Gibbs free energy $G(T)$ was obtained in [28]. Of the coefficients in that dependence, that which is associated with B_s proved to be the most important one. This coefficient, a_{B_s} (x_{as} in the notation adopted in [28]), can be related to the coefficient a_s (which characterizes the deformation dependence of the single-particle level-density parameter) with the aid of the formula

$$K_i = T[dS(q, E^*_{tot})/dq_i] = [dG(q, T)/dq_i]. \quad (8)$$

Here, the derivative of entropy is calculated at a constant total energy and a constant volume (the compressibility of nuclear matter is neglected), while the derivative of the Gibbs free energy is taken at a constant temperature and a constant pressure. As a result, we obtain

$$a_s = a_{B_s} a_2, \quad (9)$$

where $a_2 = 21.13$ MeV is the surface-energy coefficient in the mass formula used in the finite-range-interaction model. Substituting the value of $a_{B_s} = 0.00481$ MeV^{-2} into (9), we arrive at $a_s = 0.102$ MeV^{-1}. This is much closer to the value of $a_s = 0.095$ MeV^{-1} from [25] than to 0.274 MeV^{-1} from [27]. In a major part of our calculations, we therefore used the level-density parameter from [25].
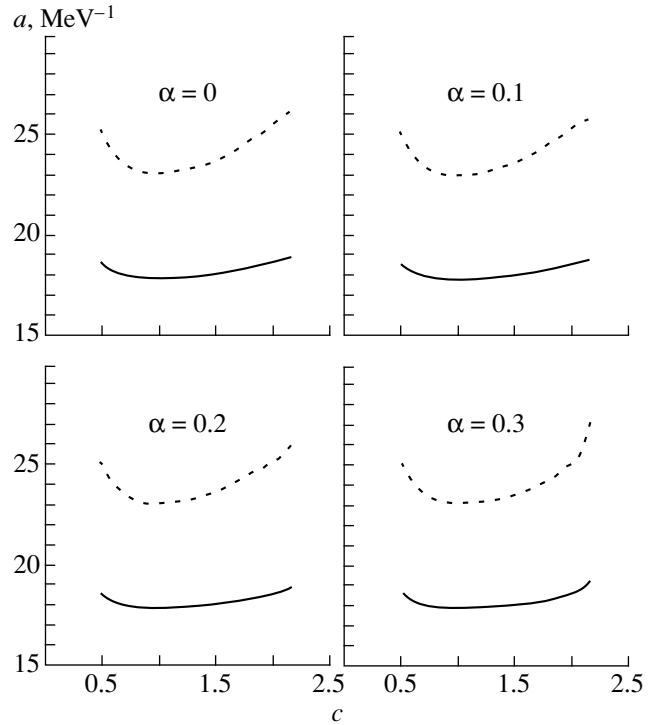

a, MeV^{-1}

Fig. 7. Level-density parameter a as a function of the nuclear-elongation parameter c for four values of the mass asymmetry α: (solid curves) results obtained with the deformation-dependence coefficients in Eq. (7) from [25] and (dashed curves) results obtained with the deformation-dependence coefficients in Eq. (7) from [27]. The calculations illustrated in this figure were performed for ^{200}Pb along the dissipative trajectory.

2.7. Particle Emission

The emission of particles (neutrons, protons, alpha particles, deuterons, and giant dipole photons) is taken to be discrete in our model, as was proposed for the first time in [29]. This approach is based on the assumption that the small probability $d\Pi$ to emit a particle is proportional to the time step of simulation, τ, and to the total statistical particle-emission width Γ_{tot}; that is,

$$d\Pi = \Gamma_{tot} \tau/\hbar. \quad (10)$$

An alternative approach (so-called continuous limit)—it is employed in many studies (for an overview, see [4, 6])—is less justified physically. In this approach, it is assumed that, over one time step of the simulation, the fissile system being considered emits a small fraction of the corresponding particle and that this fraction is proportional to the duration of the step.

The particle-emission widths are calculated as in [11]. The binding energies of the particles involved are calculated on the basis of the corresponding macroscopic mass formula (either within the liquid-drop or within the finite-range-interaction model).
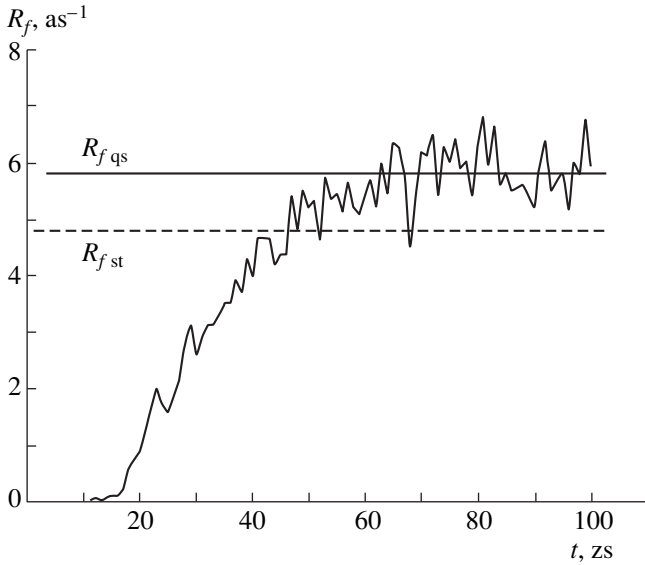
R_f, as^{-1}

Fig. 8. Fission rate as a function of time: (broken line) results of a dynamical simulation, (horizontal solid line) quasi-steady-state fission rate, and (dashed line) statistical fission rate calculated by formula (11). The calculations were performed for ^{220}Rn at $E_{tot}^* = 100$ MeV and $N_f = 16 \times 10^3$ (1 zs = 10^{-21} s).

2.8. Transition to a Statistical Branch

In the quasi-steady-state regime, the probability of the collective-coordinate fluctuation that leads to a fission event is proportional to $\exp(S_{sd} - S_{gs})$ (the subscripts sd and gs indicate that the value of corresponding quantity is calculated, respectively, at the saddle point and in the ground state). When particles are emitted, the excitation energy decreases, and so does the difference of the entropies (a negative quantity) in the exponent. This means that the nucleus can slightly fluctuate about the ground state for so long a time that a dynamical computer simulation becomes impossible. In this case, we must go over to a statistical simulation. For the first time, this transition was proposed in [29]. A similar method was also used in [8, 12].

Each trajectory is simulated dynamically from the ground state at zero collective momenta. A transition to the statistical stage is implemented if the following conditions are satisfied: (i) The particle at a given instant occurs near the ground state—that is, to the left of the ridge (see Fig. 1*b*); (ii) $S_{gs} - S_{sd} > 2$; and (iii) the trajectory was simulated dynamically for a time interval of duration not less than 50 zs (1 zs = 10^{-21} s).

At the statistical stage of the simulation, the probability that the deexcitation of the system proceeds via particle emission or fission is calculated by the conventional Neumann method. In the calculation of the quasi-steady-state rate of fission, the fact that the process is multidimensional is of great importance. This rate is calculated by the formula

$$R_{f\,st} = (\omega_K/2\pi)$$
$$\times \{[T_{sd}\det\{m_{sd}\}|\det\{S''_{gs}\}|]/[T_{gs}\det\{m_{gs}\}$$
$$\times \det\{S''_{sd}\}]\}^{1/2}\exp(S_{sd} - S_{gs}), \qquad (11)$$

where $\det\{m\}$ is the determinant of the matrix of the inertia parameters, while $\det\{S''\}$ is the determinant of the matrix of the second derivatives of the entropy with respect to the collective coordinates. In Eq. (11), ω_K is the so-called Kramers frequency equal to the only positive root of the equation

$$\det\{\omega_K^2 m + \omega_K\gamma + S''T\} = 0 \qquad (12)$$

(for details, see [30]). In this equation, all quantities that depend on the nuclear deformation are calculated at the saddle point.

In accordance with the classical theorem of equal distribution for two degrees of freedom, we have $\langle E_{kin}\rangle = T$ near the ground state and near the saddle point. In the region of relatively high excitation energies—and our model is intended precisely for this case—the temperature is much lower than the excitation energy; hence, all energy-dependent quantities in (11) and (12) are calculated at $E_{kin} = 0$.

Formula (11) is a generalization of the analogous formula for the quasi-steady-state rate of fission [30]. The validity of this generalization was checked numerically. For this, particle emission was forbidden in the dynamical branch of the code, and each of the $N_{tot} = 20000$ trajectories was simulated up to $\tau_d = 100$ zs. All trajectories that traversed the scission line within this time interval were used for numerical calculations of the fission rate. An example of such a test is presented in Fig. 8. As can be seen, the fission rate calculated by formula (11) is consistent, to within 15%, with the long-time limit of the dynamical calculations.

2.9. Parameters of Inertia and Friction

The inertia parameters m_{ij} are calculated within the approximation of layered flow with a negligibly small vorticity (so-called Werner–Wheeler approximation [31]). This is the irrotational-flow approximation, which is widely used in dynamical models of the fission process (see, for example, [8, 10]). It should be recalled, however, that its accuracy becomes poorer when higher harmonics are excited.

The friction parameters γ_{ij} are calculated in the model of one-body dissipation [32–34]. In this model, it is assumed that the motion of nucleons is fully chaotic. The relevant expression for the rate at which the dissipated energy increases in the case of a weakly deformed nucleus (mononucleus without a neck) is determined by the so-called wall expression [32]

$$\dot{E}_{dmn} = \rho_n\langle v\rangle\oint d\sigma(\dot{n} - D)^2. \qquad (13)$$

Near the scission configuration, where the two manifest would-be fragments are connected by a thin neck (window), which has the cross-sectional area πr_w^2, the rate at which the dissipated energy increases is given by the "wall + window" formula [33, 34]

$$\dot{E}_{ddn} = \sum_{b=1,2} \rho_n \langle v \rangle \oint_b d\sigma (\dot{n} - D_b)^2$$
$$+ \frac{1}{4}\rho_n \langle v \rangle \pi k_w^2 (u_t^2 + 2u_r^2) + \frac{16\rho_n \langle v \rangle}{9\pi r_w^2}\dot{V}_1^2. \qquad (14)$$

In (13) and (14), ρ_n is the density of nuclear matter; $\langle v \rangle$ is the mean velocity of chaotic nucleon motion (it is equal to three-quarters of the Fermi velocity); D_b is the normal component of the velocity of the directed motion of nucleons near the surface element $d\sigma$; and u_t and u_r are the velocities of the relative motion of would-be fragments in the directions, respectively, parallel and orthogonal to the window plane (for our case the former is zero). The last term on the right-hand side of (14)—it is proportional to the square of the rate at which the volume of one of the would-be fragments changes—has a strong effect on the friction-tensor component that is associated with the mass-asymmetry mode. It should be noted that Vanin *et al.* [10], who calculated the mass distributions of fragments, disregarded this term.

For the intermediate case where a neck has already appeared, but where its radius r_w is not yet too small in relation to the radius of the maximal cross section of the smaller fission fragment, r_f, the rate at which the dissipated energy increases has not yet been obtained exactly within the model of one-body dissipation. For this reason, we use here the rather arbitrary interpolation of expressions (13) and (14) that was proposed by Blocki *et al.* [34]. It has the form

$$\dot{E}_d = \dot{E}_{dmn}f + \dot{E}_{ddn}(1 - f), \qquad (15)$$

where $f = \sin^2[\pi r_w/(2r_f)]$.

The formula for calculating the friction parameters was also obtained by means of interpolation and is given by

$$\gamma_{ij} = \gamma_{ij\,mn}f/2 + \gamma_{ij\,dn}(1 - f)/2, \qquad (16)$$

where

$$\gamma_{ij\,mn} = \rho_n \langle v \rangle \pi \int dz \xi (d_i \rho_s^2)(d_j \rho_s^2), \qquad (17)$$

$$\gamma_{ij\,dn} = \rho_n \langle v \rangle \Big\{ \pi \sum \int dz \xi [d_i \rho_s^2 + (d_i z_b)(d_z \rho_s^2)]$$
$$\times [d_j \rho_s^2 + (d_j z_b)(d_z \rho_s^2)] + \pi r_w^2 (d_i |z_1 - z_2|)(d_j |z_1 - z_2|)$$
$$+ [32/(9\pi r_w^2)]\Big[\int_1 dz [d_i \rho_s^2 + (d_i z_w)\rho_s^2(z_w)] \Big]$$
$$\times \Big[\int_1 dz [d_j \rho_s^2 + (d_j z_w)\rho_s^2(z_w)] \Big] \Big\}. \qquad (18)$$

In formula (17), integration is performed from $-c$ to c—that is, over the entire body of the fissile system. In the first term on the right-hand side of (18), summation is performed over would-be fragments, while integration is carried out over one of these—that is, from the coordinate $-c$ to the neck coordinate z_w for the left fragment and from c to z_w for the right fragment. The quantities z_1 and z_2 represent the coordinates of the centers of mass of, respectively, the left and the right fragment, $\xi = [(d_z \rho_s^2)^2/4 + \rho_s^2]^{1/2}$.

2.10. Conditions for the Scission of a Nucleus into Two Fragments

The stage of a dynamical simulation is terminated if the condition for a transition to the statistical branch or the scission condition is satisfied. For the latter, we use the vanishing of the neck radius between the two would-be fragments. At $\alpha = 0$, this condition gives a straight line in the (c, h) plane. When we determined dissipative trajectories for various nuclei, it turned out that these trajectories are different, but that they lead to approximately the same point on the scission line in (c, h) plane—namely, to the $(c = 2.15, h = 0.05)$ point. It follows that, upon the transition to the (c, α) plane, we again have a single scission line for all nuclei. This is where all charts in Fig. 6 terminate. Some other authors assume different scission conditions (for details, see the discussion in [35, 36]).

The scission conditions are of paramount importance for describing the kinetic-energy distribution of fragments; as to mass distributions, they are less sensitive to these conditions. To test this, we performed calculations within the liquid-drop model for ^{261}Fm at $E_{tot}^* = 200$ MeV, the scission condition being changed from $c = 2.00$ to $c = 2.15$ along the dissipative trajectories. Concurrently, the neck radius was also changed. It appeared that the variance of mass distributions changed within 3%, which is considerably smaller than the statistical uncertainty in our calculations (about 4% for σ_M^2). Changes in the fission probability and in the multiplicity of prescission particles in response to the above variation in the scission condition are also within the statistical uncertainty of the calculation. The question of the statistical uncertainty peculiar to any stochastic simulation is discussed in detail elsewhere [35].

3. EFFECT OF VARIATIONS IN MODEL PARAMETERS ON OBSERVABLES

Prior to proceeding to compare the results of our calculations with experimental data, it would be reasonable to discuss the effect of particle dynamics and emission, as well as the effect of the adjustable model parameters, on the values of the observables. In developing our model, we aimed at simultaneously reproducing experimental data on three basic variables: fis-
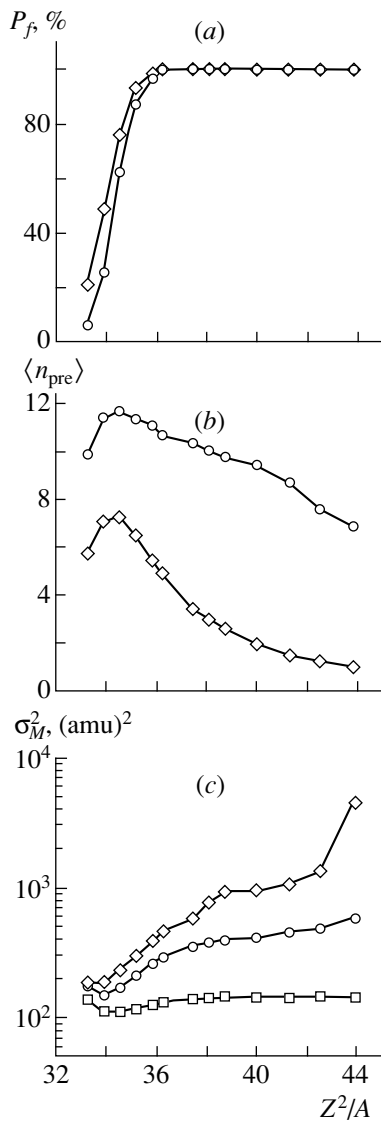
Fig. 9. (*a*) Fission probability, (*b*) mean multiplicity of prescission neutrons, and (*c*) variances of mass distributions as functions of the fissility parameter Z^2/A: (○) results of a dynamical simulation, (◇) results of a statistical calculation up to the saddle point, and (□) results of a statistical calculation up to the scission point. All calculations were performed at $E^*_{tot} = 150$ MeV and zero orbital angular momentum for beta-stable nuclei.

sion probabilities, P_f; mean multiplicities of prescission neutrons, $\langle n_{pre} \rangle$; and variances of fragment mass distributions, σ^2_M. For the variable model parameters, we took the potential energy (that in the liquid-drop model or that in the finite-range-interaction model) and the level-density parameter (that from [25] or that from [27]).

3.1. Dynamics of Collective Fluctuation Motion

In order to clarify the effect of dynamics on the observables, we compare the results of the dynamical

and statistical calculations in Fig. 9. All calculations in this subsection are performed within the liquid-drop model with the level-density parameter from [25] at zero orbital angular momentum L and $E^*_{tot} = 150$ MeV.

The statistical calculations of the fission probability and of the multiplicity of prescission neutrons are based on the Neumann method, as in the statistical branch. The only distinction is that, in calculating the fission rate, we use, instead of the above generalization of the Kramers formula (11), the N. Bohr–Wheeler formula in the version corresponding to the above generalization:

$$R_{fBW} = T_{sd}/(2\pi\hbar) \exp(S_{sd} - S_{gs}). \quad (19)$$

In this case, only so-called prefission neutrons—that is, neutrons that have been emitted prior to the saddle point and which have competed with fission—appear as prescission neutrons. The statistical calculation of the variance of the mass distributions is based on the formula

$$\sigma^2_{Mst} = \langle M \rangle^2 (d_\alpha V_1)^2 / |d^2 S/d\alpha^2|. \quad (20)$$

This calculation was performed for the saddle point and for the scission point. In the first case, the mean fragment mass $\langle M \rangle$ and the second derivative of the entropy, $|d^2S/d\alpha^2|$, were borrowed from the above statistical calculations—in other words, $\langle M \rangle$ was determined by the number of prefission neutrons, while $|d^2S/d\alpha^2|$ was determined by the temperature and the stiffness at the saddle point. The derivative of the volume of a would-be fragment with respect to the mass-asymmetry coordinate, $d_\alpha V_1$, was computed at the saddle point. In the second case, all quantities were borrowed from the dynamical calculation at the scission point.

In the literature, the statistical limit of the variance of the mass distribution is often calculated by the formula

$$\sigma^2_{Mst} = \langle M \rangle^2 T (d_\alpha V_1)^2 / C_\alpha \quad (21)$$

or by some analogous formula (see, for example, [3, 13, 14, 23]). Our test calculation showed that formulas (20) and (21) yield indistinguishable results. The reason for this is that the level-density parameter depends only slightly on α (see Fig. 7).

We now analyze the results presented in Fig. 9*a*. The main distinction between the statistical calculation of P_f and the dynamical calculation is that the delaying effect of the friction is taken into account in the former case. As might have been expected, friction lowers the fission probability. This circumstance ceases to be operative for $Z^2/A > 36$; at the excitation energies considered here, the probability of the evaporation-residue formation is negligible for these nuclei.

The effect of friction on the mean multiplicity of prescission neutrons can also be understood by inspecting data in Fig. 9*b*. Its dissipative role is more important than the fluctuation role: the fission process is slowed down, and a greater number of prefission neutrons are

emitted. Either curve $\langle n_{\text{pre}}\rangle(Z^2/A)$ shows a peak associated with a strong competition between neutron emission and fission at $B_n \approx B_f$. The details and consequences of this competition are discussed in [37]. The decrease in the multiplicities with increasing Z^2/A is due to the enhancement of the fission probability because of the reduction of the fission barrier.

The values of σ_M^2 determined dynamically are markedly different from those calculated by the statistical formula (20) for the saddle point ($\sigma_{M\,\text{sd}}^2$) and for the scission point ($\sigma_{M\,\text{sc}}^2$) (see Fig. 9c, where the scale on the ordinate is logarithmic). For light nuclei, we have $\sigma_M^2 \approx \sigma_{M\,\text{sd}}^2$ because there is virtually no stage of descent here, so that the fissile system remembers its mass distribution at the saddle point. With increasing Z^2/A, the results of two statistical and one dynamical calculations diverge ever more pronouncedly. The greatest value is always obtained for $\sigma_{M\,\text{sd}}^2$. There are two reasons for this. First, an increase in Z^2/A shifts the saddle point to the region of more compact forms that are more susceptible to a mass-asymmetry deformation (see the saddle-point stiffnesses in Fig. 5a). Second, these are results of the purely statistical calculation in which the energy carried away by prefission neutrons is not great; therefore, the temperature at the saddle point is much closer to the initial temperature.

The same two reasons are responsible for the very small values of $\sigma_{M\,\text{sc}}^2$—that is, the stiffness C_α at the scission point is maximal (see, for example, Fig. 2 from [23]), whereas the temperature is minimal, because it is determined by all particles emitted dynamically. The intermediate position of the dynamical value of the variance of the mass distribution is due to the fact that, at the scission point, the fissile system retains information about some segment of descent.

Qualitatively, these effects are similar to those discussed in [23, 28]. However, the quantitative results of the calculation of σ_M^2 depend strongly on whether particle emission is taken into account (as in this study) or not (as in [10, 23, 28]). The effect of particle emission on σ_M^2 is comprehensively discussed in Subsection 3.4.

It is worth noting that, in Fig. 9c, the values of $\sigma_{M\,\text{sc}}^2$ are virtually independent of the argument at $Z^2/A > 36$. This results from the effect of two factors compensating each other. On one hand, the stiffness of the α mode at the scission point increases with increasing Z^2/A (see Fig. 5b), and this must lead to a decrease in $\sigma_{M\,\text{sc}}^2$. On other hand, the mean multiplicity of prescission particles, $\langle n_{\text{pre}}\rangle$, decreases (see Fig. 9b); hence, the temperature at the scission point increases, and this compen-
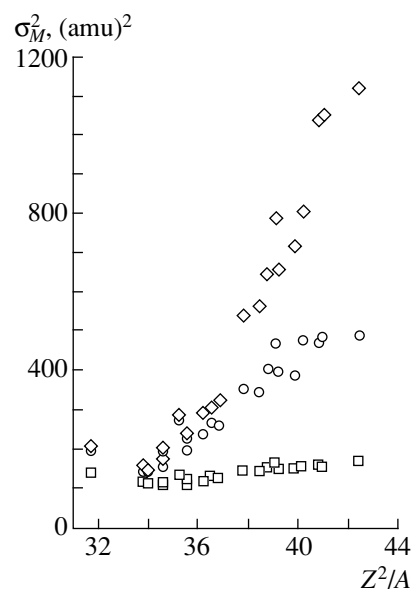

Fig. 10. Variances of fragment mass distributions as functions of the fissility parameter Z^2/A. The calculations were performed on the basis of the liquid-drop model with the level-density parameter from [25] for reactions that are induced by ^{12}C and $^{16,\,18}$O nuclei and which were studied experimentally in [13]. The spin distributions of compound nuclei were computed by formulas (1)–(4) from [11]. The notation for the points is identical to that in Fig. 9. That the results of a full dynamical simulation (open circles) differ significantly from the results obtained in the statistical limit at the saddle point (open diamonds) is due to the fact that the reactions under study were characterized by the laboratory energy of the incident particle, E_{lab}, and not by the total excitation energy E_{tot}^*.

sates for the aforementioned reduction to a considerable extent.

The calculations whose results are illustrated in Fig. 9 were performed at zero orbital angular momentum. The brings about the question of how these results will change if the calculations are performed for the actual situation where the reaction is induced by a heavy ion—that is, for a comparatively wide angular-momentum distribution. For the fission probability and for $\langle n_{\text{pre}}\rangle$, this question was analyzed in detail elsewhere [9]. For the variances of mass distributions, Fig. 10 illustrates the answer to this question. The meaning of its parts and the notation used are identical to those in Fig. 9. The calculations were performed for reactions induced by ^{12}C and ^{16}O at laboratory energies E_{lab} corresponding to the experimental data reported in [13]. The spin distribution of compound nuclei was calculated according to the procedure that was used in [11] and which approximates the results obtained within the surface-friction model [39] (see also the review article [6] and references therein). The results presented in Fig. 10 are in accord with those in Fig. 9c not only qualitatively but even quantitatively. From a comparison of these two figures, it follows that it is not the orbital
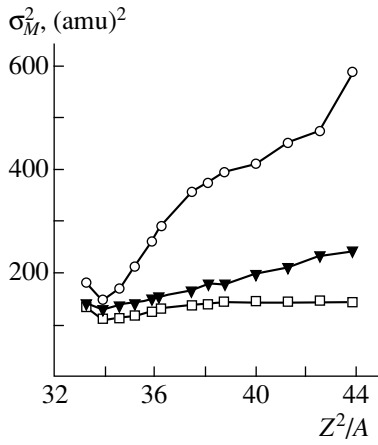
σ_M^2, (amu)^2

Fig. 11. Variances of fragment mass distributions as functions of the parameter Z^2/A: (open circles) results of a full dynamical simulation, (open boxes) results obtained in the statistical limit up to the scission point, and (closed inverted triangles) results of a dynamical simulation without the last term in expression (18). The calculations were performed at $E_{tot}^* = 150$ MeV and zero orbital angular momentum for beta-stable nuclei.

angular momentum that exerts the decisive effect on the formation of the mass distribution.

We now discuss the effect of the friction-tensor structure on the ability of the system to retain information about its previous states. In (18), the three terms correspond to three different physical effects: collisions of nucleons with the moving wall (first), a transition of nucleons from one would-be fragment to the other through the window (second), and the reaction of the system to the change in the volume of one of the would-be fragments (third).

The last (third) term was discarded in the pioneering study of Blocki *et al.* [32], but it appeared in the more recent studies reported in [33, 34]. Even at a qualitative level, the role of this term in the problem of mass distributions is obvious. First, this term must contribute to the friction-tensor components associated with the coordinate α and only for asymmetric configurations. Second, this contribution increases as the system approaches the scission point since it is inversely proportional to πr_w^2.

Quantitatively, the role of the last term on the right-hand side of (18) is illustrated in Fig. 11, which shows, in addition to the results of a full dynamical simulation, the variances of mass distributions as calculated dynamically by taking into account all terms on the right-hand side of (18), with the exception of the last one, and the statistical limiting values at the scission point. As can be seen, the results of the full dynamical calculation for the variances are noticeably different from those computed without the third term, which is inversely proportional to the window area—the latter are always smaller than the former. This directly fol-

lows from the fact that the system retains more information about the α distribution at the stage of descent, this distribution being broader than the analogous distribution at the scission point. The greater the friction along α, the earlier (the closer to the saddle point) the stage that is remembered. At the greatest values of Z^2/A, the results of dynamical calculations with and without the third term differ by a factor of three. Thus, the experimentally observed growth of the variance of mass distributions with increasing Z^2/A is due primarily to the last term in (18). It can be seen from Fig. 11 that, without this term in the friction tensor, the variances of mass distributions are found to be rather close to their statistical limiting values corresponding to the scission point.

It is interesting that Vanin *et al.* [10], who disregarded this term in (18), obtained approximately the same values of the variance of the mass distributions as in our study without this term. The values of the saddle-point temperatures in our study and in [10] are also close: this temperature is $T = 1.5$ MeV in [10], where there is no particle emission; in our study, the initial excitation energy is equal to 150 MeV, but emitted particles take away a sizable part of it. The parametrizations of the nuclear shape were quite different in our study and in the study of Vanin *et al.* [10], who used Cassini ovaloids, which were first applied to nuclear physics problems in [40, 41]. From the above, we can conclude that the results of the calculations for the variances of mass distributions are not very sensitive to the choice of parameters.

3.2. Single-Particle Level-Density Parameter

The effect of the single-particle level-density parameter is illustrated in Fig. 12, which displays the following quantities as functions of the excitation energy of the compound nucleus: six observables (P_f, $\langle n_{pre} \rangle$, $\langle E_n \rangle$, $\langle \alpha_{pre} \rangle$, $\langle p_{pre} \rangle$, and σ_M^2) and three auxiliary quantities (the mean internal excitation energy $\langle E_{sc}^* \rangle$, the mean temperature $\langle T_{sc} \rangle$, and the mean value of the parameter Z^2/A taken at the scission point). The calculations were performed for two values of the level-density parameter, that from the study of Ignatyuk *et al.* [25] (a_{Ig}) and that from the study of Toke and Swiatecki [27] (a_{TS}). As might have been expected, the fission probability shows the highest sensitivity to the density-level parameter. In order to interpret qualitatively the data in Fig. 12, it is necessary to recall that a_{TS} is greater than a_{Ig} in absolute value and that a_{TS} grows much faster with increasing nuclear deformation.

The last circumstance directly explains why the curve for $P_f(E_{tot}^* | a_{TS})$ lies higher in Fig. 12*a* than that for $P_f(E_{tot}^* | a_{Ig})$ at all excitation energies. Accordingly, the mean number of prescission neutrons (Fig. 12*b*) that was calculated with a_{TS} proves to be less since the

fission channel is open to a greater extent than in the calculation with a_Ig, so that the rate of the fission process is higher. Although the number of prescission neutrons is small at low excitation energies, their multiplicities calculated with a_TS and with a_Ig exhibit the greatest distinctions—there are 20% more prescission neutrons in the a_Ig version than in the a_TS version. With increasing excitation energy, this difference disappears. The mean energies of prescission neutrons (Fig. 12c) also appear to be greater in the calculation with a_Ig. However, the reason is associated here not with the coordinate dependence of the density-level parameter but with its absolute value—$\langle E_n \rangle \approx 2T$, and the temperature at the same excitation energy is inversely proportional to $a^{1/2}$. By and large, a transition from one version of the level-density parameter to the other changes the two characteristics of prescission neutrons quite modestly. As can be seen from Fig. 12d, the multiplicity of prescission charged particles is affected even more weakly. The absolute values of the mean multiplicities $\langle \alpha_\mathrm{pre} \rangle$ and $\langle p_\mathrm{pre} \rangle$ are sufficiently large at high excitation energies. This circumstance is responsible for the decrease in fission probability in Fig. 12a.

Figure 12e displays the variances of the mass distributions of fragments. It is interesting that the choice of version for the parameter a affects these variances quite sizably. In the calculations with a_TS, it appears to be 20–30% greater at excitation energies in the range 150–400 MeV. At a qualitative level, this can be explained by the stronger coordinate dependence of a_TS. This leads to two effects. First, the enhancement of the fission probability inhibits the cooling of the nucleus, so that the temperature, which determines the variances of mass distributions to a considerable extent, is higher in the version of the calculation with a_TS. This effect can take place at the same point of the descent from the saddle point. Second, the enhancement of the fission probability results in that the system remembers earlier stages of the descent, where the temperature was higher and where stiffness C_α was smaller. The first of the effects under discussion is illustrated in Figs. 12f and 12g. It turns out that the maximal value of the ratio $\langle E^*_\mathrm{sc} \rangle (a_\mathrm{TS}) / \langle E^*_\mathrm{sc} \rangle (a_\mathrm{Ig})$ is 1.7. For the temperature, however, this strong effect proves to be quenched because a_TS is greater than a_Ig in absolute value; in addition, T is proportional to $(E^*)^{1/2}$. As a result, the maximal value of the ratio $\langle T_\mathrm{sc} \rangle (a_\mathrm{TS}) / \langle T_\mathrm{sc} \rangle (a_\mathrm{Ig})$ appears to be only 1.1. It is reasonable to assume that the difference of $\sigma^2_M (a_\mathrm{TS})$ and $\sigma^2_M (a_\mathrm{Ig})$ is partly due to the memory of earlier stages of descent. A density-level-parameter effect on observables that is analogous to that illustrated in Fig. 12 was found in our calculations for ^{250}Cf and ^{255}No, but these results are not quoted here.

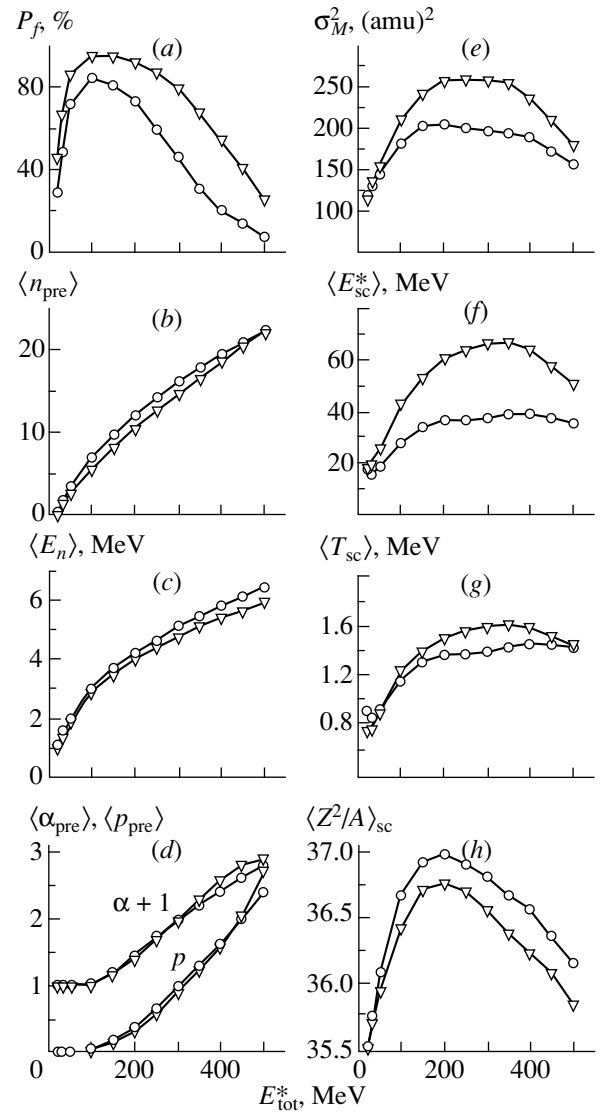It is interesting to discuss the dependence of the variances of mass distributions on the excitation energy

Fig. 12. (a) Fission probabilities P_f; (b) multiplicities of prescission neutrons, $\langle n_\mathrm{pre} \rangle$; (c) their mean kinetic energies $\langle E_n \rangle$; (d) multiplicities of prescission protons and alpha particles, $\langle p_\mathrm{pre} \rangle$ and $\langle \alpha_\mathrm{pre} \rangle$, respectively; (e) variances of fragment mass distributions, σ^2_M; (f) mean internal excitation energy at the scission point, $\langle E^*_\mathrm{sc} \rangle$; (g) mean temperature at the scission point, $\langle T_\mathrm{sc} \rangle$; and (h) mean value of the fissility parameter at the scission point, $\langle Z^2/A \rangle_\mathrm{sc}$, as functions of the initial excitation energy E^*_tot for ^{218}Ra at zero orbital angular momentum. All calculations were performed on the basis of the liquid-drop model with the level-density parameter from (open circles) [25] and (inverted open triangles) [27].

of a compound nucleus (Fig. 12e). The first fact that attracts attention is that σ^2_M ceases to grow even at $E^*_\mathrm{tot} \approx 200$ MeV. To the best of our knowledge, this effect was first observed experimentally by Ortlepp et al. [42].
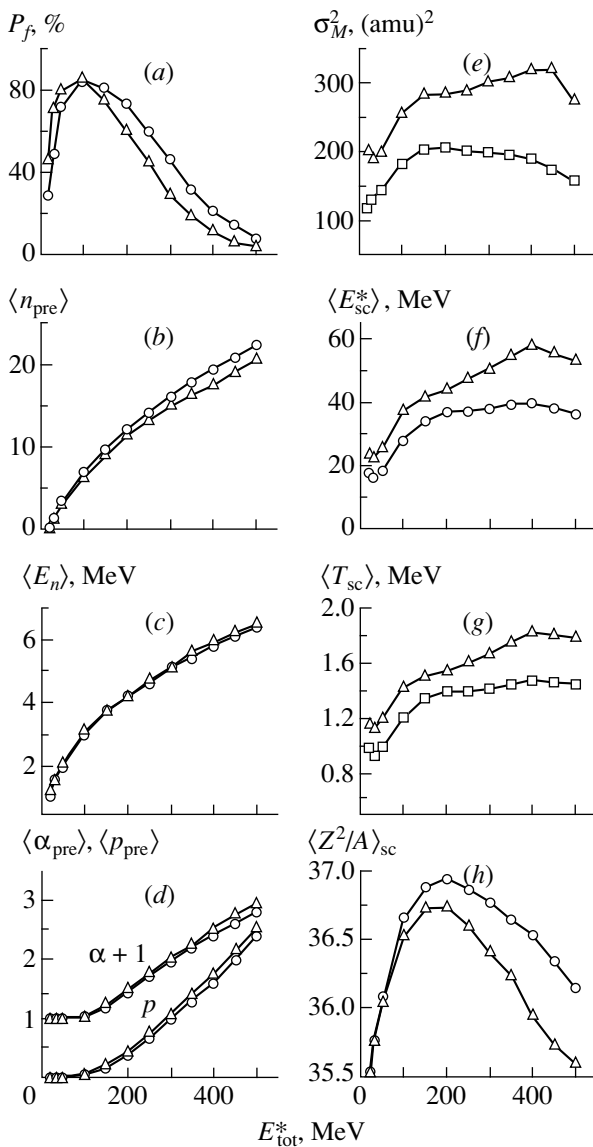
Fig. 13. As in Fig. 12, but the relevant calculations were performed on the basis of the (open circles) liquid-drop and (open triangles) finite-range-interaction model. The level-density parameter as given by Ignatyuk *et al.* [25] was used everywhere in this figure.

The growth of σ_M^2 for $E_{tot}^* < 150$ MeV can easily be explained by the increase in the temperature at which the mass distribution is formed; that this dependence then flattens is due to energy losses via particle emission. However, the reduction of σ_M^2 for $E_{tot}^* > 300$ MeV can hardly be understood on the basis of energy considerations alone without resort to information about the nucleonic composition of fissile nuclides. In order to explain this reduction, the mean value of the parameter Z^2/A for fissile nuclides at the scission point is presented in Fig. 12h. From the data in this figure, we can see that particle emission first shifts a nuclide consider-

ably toward greater values of the fissility parameter (for a compound nucleus, we have $Z^2/A = 35.5$). It should be recalled (see Fig. 9c) that, for $Z^2/A > 32$, the variance of the mass distribution is a monotonically increasing function of Z^2/A. Thus, the growth of $\sigma_M^2(E_{tot}^*)$ in the region $E_{tot}^* < 150$ MeV is due not only to the growth of temperature but also to the increase in the parameter Z^2/A of fissile nuclides. As the initial excitation energy of a compound nucleus increases further, the parameter $\langle Z^2/A \rangle_{sc}$ decreases sharply, since the probability of charged-particle emission increases. This occurs at $E_{tot}^* \approx 200$ MeV (see Figs. 12d and 12h). When the mean number of prescission protons and alpha particles approaches unity, $\sigma_M^2(E_{tot}^*)$ begins to decrease sizably. From Figs. 12d and 12e, we can see that this occurs at $E_{tot}^* \approx 300$ MeV.

3.3. Potential Energy

The effect of the potential-energy option on the observables is illustrated in Fig. 13, whose parts have the same meaning as those in Fig. 12.

It could be expected that, within the finite-range-interaction model, the fission probability would be greater at all values of E_{tot}^*, but it can be seen from Fig. 13a that, in fact, this is not the case. The point is that the neutron and the charged-particle binding energy within the finite-range-interaction model are, respectively, 0.2 MeV greater and 0.4 MeV less than the analogous values within the liquid-drop model. Accordingly, the calculation on the basis of the finite-range-interaction model yields fewer prescission neutrons (see Fig. 13b) and more charged particles (see Fig. 13d). As a result, the parameter $\langle Z^2/A \rangle_{sc}$ is less in the finite-range-interaction model than in the liquid-drop model at any value of E_{tot}^* (see Fig. 13h). When this effect proves to be stronger than the effect associated with the reduction of the fission barrier in the finite-range-interaction model in relation to the liquid drop model, the fission probability becomes less in the finite-range-interaction model than in the liquid-drop model.

The variances of the mass distributions (see Fig. 13e) are greater in the finite-range-interaction model than in the liquid-drop model by 20–100%, depending on E_{tot}^*. This is due to two factors: (i) The values of the stiffness C_α are smaller in the finite-range-interaction model (see Fig. 5). (ii) The values of $\langle E_{sc}^* \rangle$ and $\langle T_{sc} \rangle$ are greater in the finite-range-interaction model owing to a higher multiplicity of prescission neutrons (their mean energies are independent of the potential-energy option—see Fig. 13c). It is interesting to note that the curve of

$\sigma_M^2(E_{\text{tot}}^*)$ in Fig. 13*e* reproduces the curves of $\langle E_{\text{sc}}^* \rangle(E_{\text{tot}}^*)$ (Fig. 13*f*) and $\langle T_{\text{sc}} \rangle(E_{\text{tot}}^*)$ (Fig. 13*g*) in minute detail.

3.4. Effect of Prescission-Particle Emission on the Variances of Mass Distributions

The majority of theoretical studies devoted to a systematic analysis of mass distributions take no account of particle emission [3, 10, 38]. We have already discussed some particle-emission-induced features in the behavior of the variances of mass distributions (see Subsections 3.2 and 3.3). It is of interest, however, to single out explicitly the particle-emission effect on σ_M^2. With this aim in view, the results of a conventional dynamical calculation (that is, a calculation involving particle emission) are contrasted in Fig. 14 against the results that this model produces if particle emission is quenched in some ad hoc manner. As might have been expected, only at low initial excitation energies do the calculations allowing for particle emission lead to mass-distribution variances close to those found without including particle emission—the difference of these variances becomes significant even at $E_{\text{tot}}^* = 100$ MeV (see Fig. 14*a*). Thus, the model proposed in [10] is hardly reliable, since particle emission is disregarded there. Figure 14*a* also displays the statistical limits computed for the mass-distribution variances prior to the scission point. At any value of E_{tot}^*, the variances calculated dynamically are much greater than the statistical ones.

In Subsection 3.2, we have discussed three factors that can affect the variance σ_M^2. These are a decrease in the temperature of a fissile nuclide, changes in its nucleonic composition, and the memory effect consisting in that any mass mode retains a piece of information about some segment of the trajectory at the descent stage preceding scission. The first two factors stem from particle emission. As to the last factor, which has nothing to do with particle emission, its role has been elusive so far. We are now in position to reveal the role of this factor. In Fig. 14*b*, we display, for this purpose, the dimensionless parameter

$$\varepsilon_{\sigma\,\text{st}} = 2(\sigma_M^2 - \sigma_{M\,\text{st}}^2)/(\sigma_M^2 + \sigma_{M\,\text{st}}^2), \qquad (22)$$

which makes it possible to estimate quantitatively the sensitivity of the mass-distribution variance to the version of the calculation (a similar parameter was used in [6, 43]). If $\varepsilon_{\sigma\,\text{st}} \ll 1$, the effect of dynamics is insignificant. If the dynamical and the statistical results are not commensurate, $|\varepsilon_{\sigma\,\text{st}}| \approx 2$. The parameter $\varepsilon_{\sigma\,\text{st}}$ was evaluated here for the two versions of the calculation, with and without particle emission. It turned out that $\varepsilon_{\sigma\,\text{st}} \sim 1$, irrespective of whether the emission of particles is present (or absent). This is precisely the quantitative
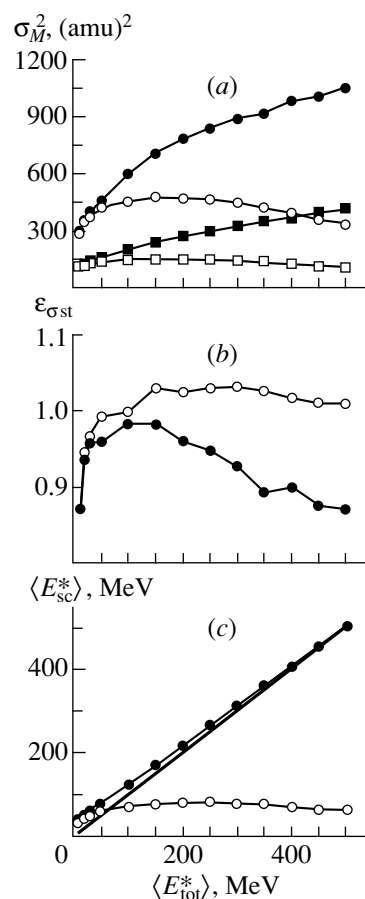

Fig. 14. (*a*) Variances of fragment mass distributions: (open circles) results of a full dynamical simulation, (open boxes) results obtained in the corresponding statistical limit at the scission point, (closed circles) results of a dynamical simulation without particle emission, and (closed boxes) results obtained in the corresponding statistical limit (without particle emission) at the scission point. (*b*) Relative difference between the results of the dynamical and statistical calculations, $\varepsilon_{\sigma\,\text{st}}$ [see Eq. (22)], (open circles) with and (closed circles) without particle emission. (*c*) Mean excitation energy at the scission point: (open circles) results of a full dynamical simulation, (closed circles) results of a dynamical simulation without particle emission, and (thick solid straight line) $\langle E_{\text{sc}}^* \rangle = E_{\text{tot}}^*$. All calculations were performed for ^{251}No on the basis of the liquid-drop model with the level-density parameter from [25].

measure of the memory effect. We do not deem that it is worthwhile to explore what is concealed behind a 10% distinction between the $\varepsilon_{\sigma\,\text{st}}$ values resulting from the two versions of the calculation.

Figure 14*c* shows the mean internal excitation energies at which fissile nuclides arrive at the scission point. It can be seen that, if the initial energy is high, its major part is carried away by prescission particles. It is interesting to compare values that are obtained for the energy at the scission point without taking into account particle emission (closed circles) with the data on the
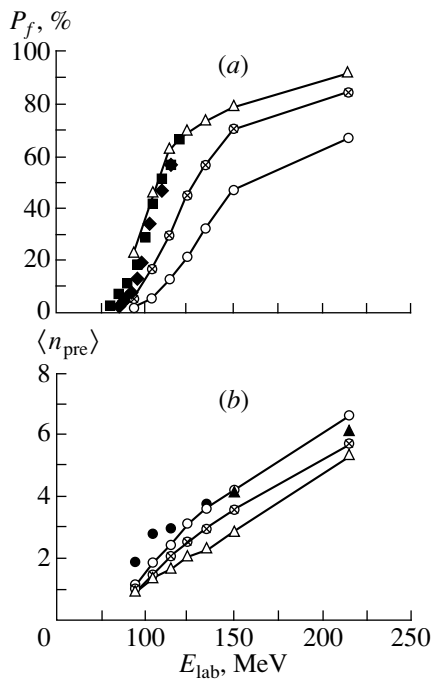
Fig. 15. (*a*) Fission probabilities and (*b*) mean multiplicities of prescission neutrons for the reaction $^{19}F + ^{181}Ta \longrightarrow$ ^{200}Pb as functions of the projectile energy. The experimental data were borrowed from (closed boxes) [44], (closed diamonds) [45], (closed circles) [46], and (closed triangles) [47]. The calculations were performed on the basis of the liquid-drop model with the level-density parameter from (open circles) [25] and (crossed circles) [27] and (open triangles) on the basis of the finite-interaction-range model with the level-density parameter from [27].

solid straight line corresponding to $\langle E_{sc}^* \rangle = E_{tot}^*$. The excess of the values computed for $\langle E_{sc}^* \rangle$ over the data on this straight line is nothing but the energy dissipated at the stage of descent. This excess is about 30 MeV at the lowest values of E_{tot}^* and tends to zero at greater values. This seems to suggest that, in the calculation disregarding particle emission, the growth of E_{tot}^* leads to a faster descent (since the drift force pushing the particle to the scission point gains in strength owing to the coordinate dependence of the single-particle level-density parameter), so that the energy does not have time to dissipate.

4. COMPARISON WITH EXPERIMENTAL DATA

4.1. Fission Probability

Figure 15*a* shows the fission probabilities computed for the reaction $^{19}F + ^{181}Ta \longrightarrow ^{200}Pb$, which was studied experimentally by two groups of researchers (see [44, 45]). The calculations were performed with three parameter sets: the level-density parameter of Ignatyuk *et al.* [25] for the liquid-drop model and the level-den-

sity parameter of Toke and Swiatecki [27] for the liquid-drop model and for the finite-range-interaction model. The last version complies best of all with experimental data. This agreement for one excitation-energy value was first obtained Wada *et al.* [8], who also relied on the finite-range-interaction model and used the Toke–Swiatecki level-density parameter and one-body dissipation.

4.2. Multiplicities of Prescission Neutrons

Figure 15*b* shows the mean multiplicities of prescission neutrons according to the same versions of the calculation as those that produced data in Fig. 15*a*. Also displayed in Fig. 15*b* for the sake of comparison are experimental data from [46, 47]. As might have been expected, the best agreement with experimental data on these multiplicities is achieved within that version—the liquid-drop model with the level-density parameter presented by Ignatyuk *et al.* [25]—which leads to the poorest agreement with data on the fission probability. On the contrary, the version that relies on the finite-range-interaction model and on the level-density parameter presented by Toke and Swiatecki [27] and which leads to the best results for the fission probability underestimates substantially the multiplicity of prescission neutrons. It should be recalled that, for the same reaction at $E_{tot}^* = 80.7$ MeV, Abe *et al.* [5] obtained theoretically the value of $\langle n_{pre} \rangle = 2$, which is in accord with the experimental result. Possibly, the reason behind this discrepancy between the above theoretical results is due to the use of different methods in [5] and in our model (continuous limit and discrete emission, respectively).

4.3. Variances of Mass Distributions

A comprehensive set of experimental data on the variances of the mass distributions of fragments originating from the fission of nuclei with excitation energies in the range 40–150 MeV is presented in [13]. Of a great number of the reactions quoted there, we chose those that are induced by the projectile nuclei ^{12}C and $^{16, 18}O$, because the probability that experimental data feature quasifission events is higher in the case of heavier projectiles. This is indicated by the authors of [13] as well. Although the set of reactions that we chose is rather poor, it covers the range $Z^2/A = 28$–42.

The results of the calculations performed with four sets of parameters are presented in Fig. 16, along with experimental data from [13]. Only data on reactions induced by carbon projectiles are subjected to analysis here. It can be seen that, even in the version relying on the liquid-drop model and using the level-density parameter from [25] (Fig. 16*a*), the agreement with the data is reasonably good. The resulting description undergoes virtually no changes when we use the Toke–Swiatecki level-density parameter (see Fig. 16*b*): at
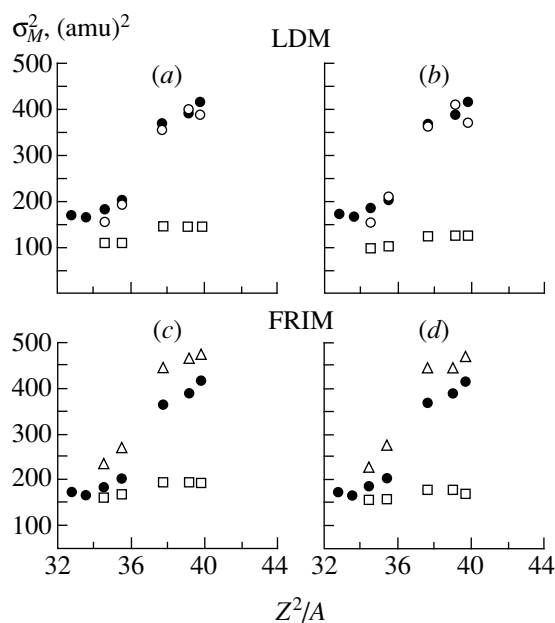
Fig. 16. Variances of mass distributions of fragments originating from the interactions of 97-MeV ^{12}C nuclei with ^{183}W, ^{198}Pt, ^{197}Au, ^{206}Pb, ^{232}Th, ^{233}U, and ^{239}Pu targets versus the fissility parameter Z^2/A. Closed circles represent experimental data from [13]. Open symbols show the results of the calculations (boxes) in the statistical limit at the scission point and on the basis of (circles) the liquid-drop and (triangles) the finite-range-interaction model (LDM and FRIM, respectively). These calculations were performed with the level-density parameter from (a, c) [25] and (b, d) [27].
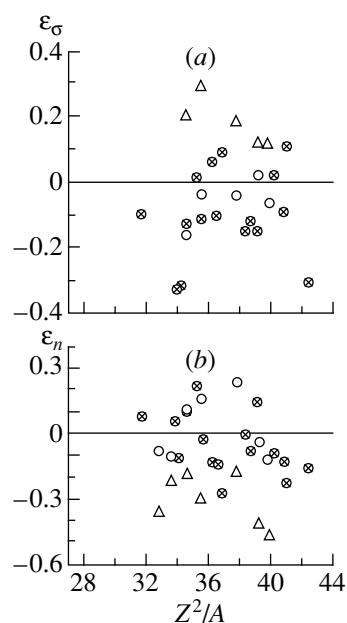
Fig. 17. Normalized deviations of the (a) calculated variances of fragment mass distributions and of the (b) calculated multiplicities of prescission neutrons from relevant experimental data {the quantities ε_σ and ε_n plotted along the ordinate are given by (23) and (24), respectively, and the experimental data were borrowed from [13]}. Open circles (open triangles) correspond to the calculations on the basis of the liquid-drop model with the level-density parameter from [25] (finite-range-interaction model with the level-density parameter from [27]) that were performed for carbon-projectile-induced reactions quoted in the caption under Fig. 16. Crossed circles represent similar results where the calculations relying on the liquid-drop model and on the level-density parameter from [25] were performed for the interactions of 128-MeV ^{16}O projectiles with ^{183}W, ^{182}W, ^{198}Pt, ^{197}Au, ^{206}Pb, ^{232}Th, ^{233}U, and ^{239}Pu targets; 145-MeV ^{16}O projectiles with ^{249}Cf targets; 108-MeV ^{16}O projectiles with ^{204}Pb and ^{208}Pb targets; 103-MeV ^{18}O projectiles with ^{232}Th and ^{246}Cm targets; and 158-MeV ^{18}O projectiles with ^{197}Au, ^{238}U, and ^{169}Tm targets. For the carbon-projectile-induced reactions, the number of points in Fig. 17b is greater than the number of points on Fig. 17a by two units, since the restrictions on statistics are much more stringent in the cases of the variances than in the case of mean multiplicities.

such low excitation energies—from 60 to 80 MeV—the sensitivity of the results to variations in the level-density parameter is extremely weak (see Fig. 12e).

Statistically significant calculations of the variances of mass distributions could not be performed here for two reactions leading to compound nuclei ^{195}Hg ($Z^2/A = 32.8$) and ^{210}Po ($Z^2/A = 33.6$), because the fission probabilities are very low in those cases at the E^*_{tot} and angular-momentum values corresponding to the prevalent experimental situation.

The use of the finite-range-interaction model (Figs. 16c, 16d) instead of the liquid-drop model (Figs. 16a, 16b) leads to σ^2_M values exceeding somewhat the experimental results; however, there are no dramatic changes in the situation here, such as those that were observed for the fission probability in Fig. 15a. Also displayed in Fig. 16 are the statistical limiting values of σ^2_M that correspond to the scission point. These lie much lower than the experimental values.

Figure 17a displays the results of our calculations along with the relevant experimental data from [13] for reactions induced by ^{12}C and $^{16, 18}$O projectiles. The calculations for oxygen-projectile-induced reactions were

performed only within the liquid-drop model with the level-density parameter presented by Ignatyuk *et al.* [25]. For carbon-projectile-induced reactions, we show the same data as in Figs. 16a and 16d. We deem it more instructive to depict (Fig. 17a), instead of mass-distribution variances, the quantity

$$\varepsilon_\sigma = 2(\sigma^2_{M\,\text{calc}} - \sigma^2_{M\,\text{expt}})/(\sigma^2_{M\,\text{calc}} + \sigma^2_{M\,\text{expt}}), \quad (23)$$

which measures the relative deviation of the calculated variances, $\sigma^2_{M\,\text{calc}}$, from the corresponding experimental values, $\sigma^2_{M\,\text{expt}}$. If we discard three points that correspond to ^{16}O + $^{182, 183}$W and ^{16}O + ^{249}Cf interactions and

which are characterized by relative-deviation values of $\varepsilon < -0.3$, the overall agreement with data is better within the liquid-drop model than within the finite-range-interaction model. To conclude our comparison of the computed mass-distribution variances with those measured experimentally, we note that, for any parameter set (including potential energy and level-density parameter) used here, the agreement between the results of the present calculations and experimental data is much better that the agreement achieved in the theoretical study of Vanin *et al.* [10].

4.4. Discussion of the Results Obtained from a Comparison of Theoretical and Experimental Results

Unfortunately, we were unable to find experimental data on the energy dependences of all three observables for the same reaction. This gap can be partly filled owing to data on $\langle n_{\mathrm{pre}} \rangle$ that are quoted in Table 3 from [13]. Those are not data obtained directly from experiments, but they come from the systematics developed in [21, 48]. A comparison with those data in Fig. 17*b* is drawn in just the same way as the comparison with data on σ_M^2 in Fig. 17*a*—that is, in terms of the quantity

$$\varepsilon_n = 2(\langle n_{\mathrm{pre}} \rangle_{\mathrm{calc}} - \langle n_{\mathrm{pre}} \rangle_{\mathrm{syst}})/(\langle n_{\mathrm{pre}} \rangle_{\mathrm{calc}} + \langle n_{\mathrm{pre}} \rangle_{\mathrm{syst}}). \tag{24}$$

It can be seen that the situation prevalent here is identical to that for the reaction $^{19}\mathrm{F} + {}^{181}\mathrm{Ta} \longrightarrow {}^{200}\mathrm{Pb}$ (see Fig. 15*b*): the calculation relying on the liquid-drop model and employing the level-density parameter from [25] leads to a fairly good agreement with $\langle n_{\mathrm{pre}} \rangle_{\mathrm{syst}}$ (basically, we have here $|\varepsilon_n| < 0.2$), whereas the calculation on the basis of the finite-range-interaction model with the Toke–Swiatecki level-density parameter [27] yields strongly underestimated multiplicity values (for three points of seven, the relative deviation ε_n falls below –0.3).

Thus, it proved to be impossible to attain full agreement with data for all three observables (fission probabilities, multiplicities of prescission neutrons, and the variances of the mass distributions of fragments) by using a unified parameter set. The liquid-drop model leads to a better agreement for $\langle n_{\mathrm{pre}} \rangle$ and σ_M^2, whereas the finite-range-interaction model better reproduces fission probabilities. At the same time, the calculation of the mass-distribution variances within the finite-range-interaction model yields results that are also compatible with experimental data. It should be borne in mind, however, that, upon lifting the limitation of our calculations that constrains the motion to the dissipative trajectory (see Subsection 2.2), the variances of mass distributions may become greater, as often occurs when the number of degrees of freedom is increased. This will improve the agreement between the results of the calculations performed within the liquid-drop model and data on the mass-distribution variances and impair the

agreement between data on these variances and the results of the relevant calculations on the basis of the finite-range-interaction model. That results of the calculations relying on the finite-range-interaction model describe the variances of mass distributions more poorly is partly due to allowing for a fewer number of emitted prescission neutrons within this framework, but the eventual reasons behind the failure of the model in dealing with the above variances have yet to be clarified conclusively: recall that, at present, it has been firmly established that the finite-range-interaction model faithfully reproduces the position of the Businaro–Gallone point [21] and that this model provides a correct description of the mass distribution of fragments originating from the fission of light nuclei ($Z^2/A < 30$) [14, 21].

That the multiplicities of prescission neutrons are underestimated within the finite-range-interaction model may be associated with neutrons emitted in the fusion process (see [49, 50]). The problem of estimating the contribution of these neutrons to the total multiplicity of prescission neutrons has not yet been solved unambiguously. If it turns out that the fraction of such neutrons is indeed great, the calculation on the basis of the finite-range-interaction model leads to the best description of data for all three observables discussed in the present article.

5. CONCLUSIONS

The basic results of our study can be summarized as follows:

(i) A multidimensional stochastic model that is intended for describing the decay of excited nuclei and which takes into account the fluctuation–dissipation character of collective nuclear motion and the emission of light particles from an excited nucleus has been developed. The potential energy of a nucleus has been calculated within the model of a liquid drop with a sharp surface [17] or within the model employing a nuclear interaction of finite range [18–20]. The friction parameters have been calculated on the basis of the one-body-dissipation model [32–34], while the parameters of inertia have been determined by the Werner–Wheeler method [31]. Drift forces have been found in terms of the entropy, which was computed with allowance for the deformation dependence of the single-particle level-density parameter.

(ii) Systematic calculations of the fission probabilities P_f, the mean multiplicities $\langle n_{\mathrm{pre}} \rangle$ of prescission neutrons, and the variances σ_M^2 of fragment mass distributions have been performed for various values of the fissility parameter Z^2/A of a compound nucleus and various values of its excitation energy.

(iii) Interesting features have been revealed in the excitation-energy dependences of P_f and σ_M^2. The fission probabilities P_f as calculated on the basis of the finite-range-interaction model are less than those

obtained within the liquid-drop model, although the fission barriers for a compound nucleus are lower within the former than within the latter model. Not only does the mass-distribution variance cease to grow at high excitation energies, but it even begins to decrease. These effects are both due to the emission of charged particles.

(iv) The fission probabilities calculated on the basis of the liquid-drop model for the reaction $^{19}F + ^{181}Ta \longrightarrow ^{200}Pb$ fall significantly short of the corresponding experimental values; at the same time, the results of the relevant calculations within the finite-range-interaction model are close to these experimental values.

(v) For the same reaction, the data on the mean multiplicities of prescission neutrons, $\langle n_{pre} \rangle$, are much better described within the liquid-drop model than within the finite-range-interaction model. The same conclusion follows from a comparison of the multiplicities computed for many other reactions with those that were obtained on the basis of experimental systematics [13, 21, 48].

(vi) Experimental data on the variances of the mass distributions of fission fragments [13] are described fairly well both within the liquid-drop model and within the finite-range-interaction model. In the latter case, however, the computed variances are systematically in excess of the experimental values, partly because of underestimated mean multiplicities of prescission neutrons.

REFERENCES

1. N. Bohr and J. A. Wheeler, Phys. Rev. **56**, 426 (1939).

2. H. A. Kramers, Physica (Amsterdam) **7**, 284 (1940).

3. G. D. Adeev, I. I. Gonchar, V. V. Pashkevich, *et al.*, Fiz. Élem. Chastits At. Yadra **19**, 1229 (1988) [Sov. J. Part. Nucl. **19**, 529 (1988)].

4. I. I. Gonchar, Fiz. Élem. Chastits At. Yadra **26**, 932 (1995) [Phys. Part. Nucl. **26**, 394 (1995)].

5. Y. Abe, S. Ayk, P.-G. Reinhard, *et al.*, Phys. Rep. **275**, 49 (1996).

6. P. Fröbrich and I. I. Gontchar, Phys. Rep. **292**, 131 (1998).

7. P. Fröbrich and R. Lipperheide, *Oxford Studies in Nuclear Physics, Vol. 18: Theory of Nuclear Reactions* (Oxford Univ. Press, Oxford, 1996).

8. T. Wada, Y. Abe, and N. Carjan, Phys. Rev. Lett. **70**, 3538 (1993).

9. P. Fröbrich, I. I. Gontchar, and N. D. Mavlitov, Nucl. Phys. A **556**, 281 (1993).

10. D. V. Vanin, G. I. Kosenko, and G. D. Adeev, Phys. Rev. C **59**, 2114 (1999).

11. I. I. Gontchar, L. A. Litnevsky, and P. Fröbrich, Comput. Phys. Commun. **107**, 223 (1997).

12. T. Wada, in *Proceedings of Tours Symposium on Nuclear Physics II, 1994*, p. 470.

13. A. Ya. Rusanov, M. G. Itkis, and V. M. Okolovich, Yad. Fiz. **60**, 773 (1997) [Phys. At. Nucl. **60**, 683 (1997)].

14. A. Ya. Rusanov, V. V. Pashkevich, and M. G. Itkis, Yad. Fiz. **62**, 595 (1999) [Phys. At. Nucl. **62**, 547 (1999)].

15. M. Brack, J. Damgaard, A. S. Jensen, *et al.*, Rev. Mod. Phys. **44**, 320 (1972).

16. R. W. Hasse and W. D. Myers, in *Geometrical Relationships of Macroscopic Nuclear Physics* (Springer-Verlag, Berlin, 1988).

17. W. D. Myers and W. J. Swiatecki, Nucl. Phys. **81**, 1 (1966); Ark. Fys. **36**, 343 (1967).

18. H. J. Krappe, J. R. Nix, and A. J. Sierk, Phys. Rev. C **20**, 992 (1979).

19. P. Möller, J. R. Nix, W. D. Myers, *et al.*, At. Data Nucl. Data Tables **59**, 185 (1995).

20. A. J. Sierk, Phys. Rev. C **33**, 2039 (1986).

21. M. G. Itkis, Yu. A. Muzychka, Yu. Ts. Oganessian, *et al.*, Yad. Fiz. **58**, 2140 (1995) [Phys. At. Nucl. **58**, 2026 (1995)].

22. L. D. Landau and E. M. Lifshitz, *Statistical Physics* (Nauka, Moscow, 1976; Pergamon, Oxford, 1980).

23. G. D. Adeev and I. I. Gontchar, Z. Phys. A **320**, 451 (1985).

24. R. Balian and C. Bloch, Ann. Phys. (N.Y.) **60**, 401 (1970).

25. A. V. Ignatyuk, M. G. Itkis, V. N. Okolovich, *et al.*, Yad. Fiz. **21**, 1185 (1975) [Sov. J. Nucl. Phys. **21**, 612 (1975)].

26. E. M. Rastopchin, Yu. B. Ostapenko, M. I. Svirin, and G. N. Smirenkin, Yad. Fiz. **49**, 24 (1989) [Sov. J. Nucl. Phys. **49**, 15 (1989)].

27. J. Toke and W. J. Swiatecki, Nucl. Phys. A **372**, 141 (1981).

28. H. J. Krappe, Phys. Rev. C **59**, 2640 (1999).

29. N. D. Mavlitov, P. Fröbrich, and I. I. Gontchar, Z. Phys. A **342**, 195 (1992).

30. H. A. Weidenmüller and Zhang Jing-Shang, J. Stat. Phys. **34**, 191 (1984).

31. K. T. R. Davies, A. J. Sierk, and J. R. Nix, Phys. Rev. C **13**, 2385 (1976).

32. J. Blocki, Y. Boneh, J. R. Nix, *et al.*, Ann. Phys. (N.Y.) **113**, 330 (1978).

33. J. Randrup and W. J. Swiatecki, Nucl. Phys. A **429**, 105 (1984).

34. J. P. Blocki, H. Feldmeier, and W. J. Swiatecki, Nucl. Phys. A **459**, 145 (1986).

35. G. I. Kosenko, I. I. Gonchar, O. I. Serdyuk, and N. I. Pischasov, Yad. Fiz. **55**, 920 (1992) [Sov. J. Nucl. Phys. **55**, 514 (1992)].

36. G. D. Adeev and I. I. Gonchar, Z. Phys. A **322**, 479 (1985).

37. I. I. Gontchar, Yu. A. Lazarev, and N. D. Mavlitov, *Heavy Ion Physics*, Scientific Report (1989–1990) No. E7-91-75 (JINR, Dubna, 1991), p. 70; p. 72.

38. G. D. Adeev, I. I. Gonchar, L. A. Marchenko, and N. I. Pischasov, Yad. Fiz. **43**, 1137 (1986) [Sov. J. Nucl. Phys. **43**, 727 (1986)].

39. J. Marten and P. Fröbrich, Nucl. Phys. A **545**, 854 (1992).

40. V. S. Stavinskiĭ, N. S. Rabotnov, and A. A. Seregin, Yad. Fiz. **7**, 1051 (1968) [Sov. J. Nucl. Phys. **7**, 631 (1968)].

41. V. V. Pashkevich, Nucl. Phys. A **169**, 275 (1971).

42. H.-G. Ortlepp, W. Wagner, P. Gippner, *et al.*, Nucl. Phys. A **642**, 407 (1998).

43. Yu. A. Lazarev, I. I. Gontchar, and N. D. Mavlitov, Phys. Rev. Lett. **70**, 1220 (1993).

44. R. J. Charity, J. R. Leigh, J. J. M. Bokhorst, *et al.*, Nucl. Phys. A **457**, 441 (1986).

45. J. S. Forster, L. V. Mitchell, J. U. Andersen, *et al.*, Nucl. Phys. A **464**, 497 (1987).

46. J. O. Newton, D. J. Hinde, R. J. Charity, *et al.*, Nucl. Phys. A **483**, 126 (1988).

47. D. J. Hinde, H. Ogata, M. Tanaka, *et al.*, Phys. Rev. C **39**, 2268 (1989).

48. É. M. Kozulin, A. Ya. Rusanov, and G. N. Smirenkin, Yad. Fiz. **56** (2), 37 (1993) [Phys. At. Nucl. **56**, 166 (1993)].

49. K. Siwek-Wilczynska, J. Wilczynski, and R. H. Siemssen, Phys. Rev. C **51**, 2054 (1995).

50. J. Wilczynski, K. Siwek-Wilczynska, and H. W. Wilschut, Phys. Rev. C **54**, 325 (1996).

Translated by A. Isaakyan

=========== NUCLEI ===========
Theory
==============================

Description of the Low-Energy Doublet Neutron–Deuteron Scattering in Terms of Parameters Characterizing Bound and Virtual Triton States

V. A. Babenko and N. M. Petrov

Bogolyubov Institute for Theoretical Physics, National Academy of Sciences of Ukraine,
Metrologicheskaya ul. 14b, Kiev, 252143 Ukraine
Received June 24, 1999; in final form, November 29, 1999

Abstract—Low-energy doublet neutron–deuteron scattering is described in terms of the energies of the bound and virtual triton states and the nuclear vertex constants for these states. For the first time, the van Oers–Seagrave formula is derived from the Bargmann representation of the S matrix for a system having two states. The presence of a pole in this formula is shown to be a direct corollary of the existence of a low-energy virtual triton state. Simple explicit expressions for the nd scattering length and for the pole of the function $k \cot \delta$ are obtained in terms of the parameters of the bound and virtual triton states. The low-energy parameters of nd scattering are calculated numerically, whereby it is shown that these parameters are highly sensitive to variations in the asymptotic normalization constant C_v^2 for the virtual state. The C_v^2 value fitted in our model to the experimental result for the nd scattering length is 0.0592. © *2000 MAIK "Nauka/Interperiodica".*

1. INTRODUCTION

The low-energy characteristics of three-body systems were studied previously [1, 2] on the basis of the two-body model with the Hulthén potential; in particular, a correlation between the binding energy of three hadrons and the hadron–deuteron scattering length was analyzed over a wide region of three-body parameters. An important role of the virtual triton state was revealed in studying this dependence (Phillips lines) in the region of the experimental values of the triton binding energy E_T and the doublet nd scattering length $^2a_{nd}$. The characteristics associated with the $T \longrightarrow d + n$ decay vertex were also calculated for the bound (T) and virtual (v) triton states. The results of the calculations for the position of the virtual triton level, B_v, as reckoned from the threshold of the elastic nd channel and for nuclear vertex constants G_T^2 and G_v^2 characterizing the ground and the virtual triton state, respectively, agree with the relevant results of three-body calculations and with experimental data. The results from [1, 2] evince a clear-cut correlation between the low-energy characteristics of two- and three-hadron systems.

It was established in [3–6] that the effective-range expansion of the doublet S-wave phase shift for nd scattering involves a pole situated in the nonphysical region near the threshold. For the function $k \cot \delta$, the corresponding four-parameter representation involving a pole is referred to as the van Oers–Seagrave formula. It should be noted that this formula was found in a purely empirical way without any theoretical justification.

In order to analyze two- and three-hadron systems, we propose here an approach based on the S matrix corresponding to so-called Bargmann potentials [7, 8]. We will consider the relation between the S-matrix representation introduced by Bargmann [7, 8] and the effective-range approximation and demonstrate that, on the basis of this representation, the effective-range approximation can be obtained for the case where the system in question has one state, bound or virtual. An example of such a situation is provided by neutron–proton scattering. We will then generalize this analysis to systems having two states, as in the case of doublet neutron–deuteron scattering. It will be shown that the van Oers–Seagrave formula for the function $k \cot \delta$ involving a pole follows directly from the Bargmann representation of the S matrix for a system having two states. This analysis makes it possible to relate the parameters of the effective-range expansion to the characteristics of the bound and virtual states of the system.

We assume that any state of the system is specified by two parameters, the energy corresponding to the pole of the S matrix on the imaginary axis in the complex plane of the wave number k and the nuclear vertex constant, which is directly expressed in terms of the residue of the S matrix at this pole [9]. Nuclear vertex constants are fundamental physical characteristics of nuclei like more conventional quantities, including mass, spin, and parity. Kinematical factors apart, nuclear vertex constants are related to the on-shell amplitude for the virtual or real decay (or fusion) of a nucleus into two fragments. The properties of vertex constants, their values for a number of nuclei, and

methods for determining them experimentally and theoretically were surveyed elsewhere [9].

2. DERIVATION OF THE EFFECTIVE-RANGE APPROXIMATION FROM THE BARGMANN REPRESENTATION OF THE S MATRIX INVOLVING ONE STATE: NEUTRON–PROTON SYSTEM

Bargmann [7] proposed taking the Jost function $f(k)$ entering into the well-known S-matrix expression [8]

$$S(k) = \frac{f(-k)}{f(k)} \tag{1}$$

in the form of a rational function having some simple poles and zeros and exhibiting a correct asymptotic behavior at high energies—that is, approaching unity at infinity:

$$\lim_{k \to \infty} f(k) = 1. \tag{2}$$

In the simplest case of only one state in the system, the Jost function has the form

$$f(k) = \frac{k - i\alpha}{k + i\lambda}, \tag{3}$$

where the parameter λ is always positive, whereas the parameter α is positive for a bound state and negative for a virtual state. Upon the substitution of (3) into (1), the S matrix for the system having one state assumes the form

$$S(k) = \frac{k + i\alpha}{k - i\alpha}\frac{k + i\lambda}{k - i\lambda}. \tag{4}$$

This state has the energy

$$E_0 = -\frac{\hbar^2\alpha^2}{2m}, \tag{5}$$

where m is the reduced mass of the system and $\hbar$ is the Planck constant. The first pole factor in expression (4) for the S matrix corresponds to a physical bound or a virtual state of the system. The second factor in the S matrix (4) includes the well-known superfluous pole [8, 10], which is associated with no bound state of the system. The superfluous pole ensures the correct asymptotic behavior (2) of the Jost function. The nuclear vertex constant G^2 for the state being considered is directly expressed in terms of the residue of the S matrix at the pole $k = i\alpha$ as

$$G^2 = i\pi\lambdabar^2 \operatorname*{Res}_{k = i\alpha} S(k), \tag{6}$$

where $\lambdabar \equiv \hbar/mc$ is the reduced Compton wavelength of the system. Calculating the residue on the basis of (6) and (4), we express the vertex constant in terms of the parameters α and λ as

$$G^2 = -2\pi\lambdabar^2\alpha\frac{\alpha + \lambda}{\alpha - \lambda}. \tag{7}$$

Using (4) and considering that the S matrix is expressed in terms of the phase shift $\delta(k)$ as

$$S(k) = e^{2i\delta(k)} = \frac{\cot\delta + i}{\cot\delta - i}, \tag{8}$$

we represent the function $k\cot\delta$ in the form

$$k\cot\delta = -\frac{1}{a} + \frac{1}{2}r_ek^2. \tag{9}$$

This is the expression in the effective-range approximation, with the scattering length a and the effective range r_e being given by

$$a = \frac{1}{\alpha} + \frac{1}{\lambda}, \tag{10}$$

$$r_e = \frac{2}{\alpha + \lambda}. \tag{11}$$

Thus, the effective-range approximation (9) immediately follows from the Bargmann representation (4) of the S matrix for a system having one state. Formulas (10) and (11) relate the parameters of the effective-range approximation to the S-matrix parameters and, together with (5) and (7), the parameters of low-energy scattering to the binding energy E_0 and the nuclear vertex constant G^2 (parameters of the bound state of the system).

As a specific example, we will now consider neutron–proton scattering in the triplet spin state. In this case, the system features one bound state, the deuteron, with the binding energy being $\varepsilon_d = 2.225$ MeV. The nuclear vertex constant G_d^2 for the deuteron corresponds to the $d \rightleftharpoons n + p$ vertex and takes the value of $G_d^2 = 0.43$ fm [9]. It should be recalled that the nuclear vertex constants are directly related to the asymptotic normalization factors for the bound-state wave functions. The latter factors are often introduced in the analysis along with the nuclear vertex constants. In the case under consideration, the constant G_d^2 is expressed in terms of the dimensionless asymptotic normalization factors C_d for the deuteron wave function as

$$G_d^2 = 2\pi\lambdabar^2\alpha C_d^2, \tag{12}$$

where $\lambdabar = 2\lambdabar_N$, with $\lambdabar_N = \hbar/m_Nc$ being the nucleon Compton wavelength (m_N is the nucleon mass). The relevant numerical value is $C_d^2 = 1.673$. With the aid of (7) and (12), we can easily express the S-matrix parameter λ in terms of the deuteron normalization factor as

$$\lambda = \alpha\frac{C_d^2 + 1}{C_d^2 - 1}. \tag{13}$$

Substituting (13) into (10) and (11), we obtain

$$a = \frac{2}{\alpha}\frac{C_d^2}{C_d^2 + 1} \tag{14}$$

and

$$r_e = \frac{1}{\alpha}\left(1 - \frac{1}{C_d^2}\right), \tag{15}$$

respectively. Formulas (14) and (15) yield explicit expressions for the parameters of low-energy np scattering in terms of the bound-state parameters, the deuteron binding energy ε_d and the deuteron nuclear vertex constant G_d^2. For the scattering length and the effective range, the substitution of the above experimental values of ε_d and G_d^2 into expressions (14) and (15) yields

$$a = 5.41 \text{ fm}, \tag{16}$$

$$r_e = 1.74 \text{ fm}. \tag{17}$$

These values are very close to the experimental values [11]

$$a^{\text{expt}} = 5.42 \text{ fm}, \tag{18}$$

$$r_e^{\text{expt}} = 1.76 \text{ fm}. \tag{19}$$

This corresponds to the well-known fact that low-energy neutron–proton scattering can be very well interpreted by using the effective-range approximation (9). Thus, low-energy neutron–proton scattering in the triplet spin state can be accurately described on the basis of data on the deuteron bound state.

3. DERIVATION OF THE VAN OERS–SEAGRAVE FORMULA FROM THE BARGMANN REPRESENTATION OF THE S MATRIX INVOLVING TWO STATES: NEUTRON–DEUTERON SYSTEM

Let us now consider elastic neutron–deuteron scattering in the doublet spin state at energies below the threshold for deuteron breakup. In this case, there are two states in the system, the triton ground state and its virtual state. The existence of the latter has been firmly established [12]. For the case where the system has two states, we take the Jost function in the form of the rational function

$$f(k) = \frac{k - i\alpha}{k + i\lambda}\frac{k - i\beta}{k + i\mu}, \tag{20}$$

which has the correct asymptotic behavior given by (2). The parameters α, λ, and μ, which appear on the right-hand side of (20), are positive, while the parameter β, which corresponds to the virtual state, is negative. Substituting (20) into (1), we obtain the S matrix for the system having two states in the form

$$S(k) = \frac{k + i\alpha}{k - i\alpha}\frac{k + i\beta}{k - i\beta}\frac{k + i\lambda}{k - i\lambda}\frac{k + i\mu}{k - i\mu}. \tag{21}$$

The energies of the bound and the virtual state are given by

$$E_0 = -\frac{\hbar^2\alpha^2}{2m}, \tag{22}$$

$$E_v = -\frac{\hbar^2\beta^2}{2m}, \tag{23}$$

where the reduced mass m is $(2/3)m_N$. The first and the second pole factor in expression (21) for the S matrix correspond to, respectively, the bound and the virtual triton state. The third and the fourth factor involve superfluous poles of the S matrix. The nuclear vertex constants G_T^2 and G_v^2 for, respectively, the bound and the virtual state are directly expressed in terms of the residues of the S matrix at the respective poles $k = i\alpha$ and $k = i\beta$ as

$$G_T^2 = i\pi\lambdabar^2 \operatorname*{Res}_{k=i\alpha} S(k), \tag{24}$$

$$G_v^2 = i\pi\lambdabar^2 \operatorname*{Res}_{k=i\beta} S(k), \tag{25}$$

where $\lambdabar = \frac{3}{2}\lambdabar_N$. Calculating the residues and using (24), (25), and (21), we find that the vertex constants are expressed in terms of the S-matrix parameters as

$$G_T^2 = -2\pi\lambdabar^2\alpha\frac{\alpha+\beta}{\alpha-\beta}\frac{\alpha+\lambda}{\alpha-\lambda}\frac{\alpha+\mu}{\alpha-\mu}, \tag{26}$$

$$G_v^2 = 2\pi\lambdabar^2\beta\frac{\alpha+\beta}{\alpha-\beta}\frac{\beta+\lambda}{\beta-\lambda}\frac{\beta+\mu}{\beta-\mu}. \tag{27}$$

For a further analysis, it is worthwhile to introduce the following combinations of the S-matrix parameters:

$$p \equiv \alpha + \beta, \tag{28}$$

$$q \equiv \alpha\beta, \tag{29}$$

$$u \equiv \lambda + \mu, \tag{30}$$

$$v \equiv \lambda\mu. \tag{31}$$

Multiplying the corresponding factors in the numerator and the denominator of (21), we can represent the S matrix in the form

$$S(k) \tag{32}$$
$$= \frac{k^4 - (q+v+pu)k^2 + qv + ik[(p+u)k^2 - pv - qu]}{k^4 - (q+v+pu)k^2 + qv - ik[(p+u)k^2 - pv - qu]}.$$

Comparing (32) with the representation in (8), we recast the expression for $k\cot\delta$ into the form

$$k\cot\delta = \frac{qv - (q+v+pu)k^2 + k^4}{-pv - qu + (p+u)k^2}. \tag{33}$$

Upon dividing the polynomial in the numerator by the polynomial in the denominator, we arrive at

$$k\cot\delta = -A + Bk^2 - \frac{C}{1+Dk^2}. \tag{34}$$

This expression is nothing but the well-known empirical van Oers–Seagrave formula [4], which describes well low-energy neutron–deuteron scattering in the doublet spin state. The parameters in expansion (34)

were obtained in [4] by fitting low-energy experimental data. Comparing (34) and (33), we express the van Oers–Seagrave parameters in terms of the S-matrix parameters (28)–(31) as

$$A = \frac{pq + uv + pu(p+u)}{(p+u)^2}, \tag{35}$$

$$B = \frac{1}{p+u}, \tag{36}$$

$$C = \frac{qv}{pv+qu} - \frac{pq+uv+pu(p+u)}{(p+u)^2}, \tag{37}$$

$$D = -\frac{p+u}{pv+qu}. \tag{38}$$

Thus, the van Oers–Seagrave formula (34) immediately follows from the Bargmann representation (21) of the S matrix for the system having two states. The same two states in the system are responsible for the pole in the expression for the function $k\cot\delta$. We note that, in the S matrix, it is necessary to take into account, along with two poles corresponding to the bound and the virtual state, two superfluous poles, which ensure the correct asymptotic behavior of the Jost function. For the case of potentials leading to a finite number of poles in the S matrix, it follows from the Levinson theorem that the number of superfluous poles is determined by the total number of bound, virtual, and quasistationary states. If we use an interaction leading to two states in the system, a ground and a virtual one, the S matrix will therefore have two superfluous poles.

Since the neutron–proton system considered above has a single state, a bound state in the triplet channel or a virtual one in the singlet channel, the S matrix for a system having one state and the corresponding effective-range approximation for the function $k\cot\delta$ provide a good approximation for the np interaction. The limiting transition from the van Oers–Seagrave formula to the effective-range approximation can easily be obtained by recasting formula (33) into the form

$$k\cot\delta = \frac{-1/a + c_2 k^2 + c_4 k^4}{1+Dk^2}. \tag{39}$$

The two-state S matrix (21) reduces to the one-state S matrix (4) if the second state goes to infinity; that is, $\beta \longrightarrow \infty$ and $\mu \longrightarrow \infty$. It can easily be seen that, in this case, the coefficients c_4 and D in (39) vanish, so that expression (39) reduces to the effective-range approximation (9). Thus, we can see that the van Oers–Seagrave formula is a direct generalization of the effective-range approximation to the case of a system having two states.

The nuclear vertex constants G_T^2 and G_v^2 for, respectively, the bound and the virtual triton state are expressed in terms of the corresponding dimensionless asymptotic constants C_T^2 and C_v^2 as

$$G_T^2 = 3\pi\lambda^2 \alpha C_T^2, \tag{40}$$

$$G_v^2 = 3\pi\lambda^2 \beta C_v^2. \tag{41}$$

Using (26), (27), (40), and (41) and taking into account (30) and (31), we obtain

$$u = -(\alpha+\beta) \tag{42}$$
$$\times \frac{4(\alpha+\beta)^2 + 6(\alpha^2-\beta^2)(C_T^2-C_v^2) - 9(\alpha-\beta)^2 C_T^2 C_v^2}{4(\alpha+\beta)^2 - 6(\alpha+\beta)^2(C_T^2+C_v^2) + 9(\alpha-\beta)^2 C_T^2 C_v^2},$$

$$v = \alpha\beta \tag{43}$$
$$\times \frac{4(\alpha+\beta)^2 + 6(\alpha+\beta)^2(C_T^2+C_v^2) + 9(\alpha-\beta)^2 C_T^2 C_v^2}{4(\alpha+\beta)^2 - 6(\alpha+\beta)^2(C_T^2+C_v^2) + 9(\alpha-\beta)^2 C_T^2 C_v^2}.$$

Formulas (35)–(38), together with (28), (29), (42), and (43), provide explicit expressions for the van Oers–Seagrave parameters in terms of the parameters of the bound and the virtual triton state (their energies and nuclear vertex constants). Since these general expressions are very cumbersome, we consider here only the expressions for the scattering length and for the pole of the function $k\cot\delta$.

4. EXPRESSIONS FOR THE nd SCATTERING LENGTH AND FOR THE POLE OF THE FUNCTION $k\cot\delta$ IN TERMS OF THE PARAMETERS OF THE BOUND AND THE VIRTUAL TRITON STATE

As can be seen from (34), the doublet nd scattering length $a \equiv {}^2a_{nd}$ is expressed in terms of the van Oers–Seagrave parameters as

$$a = \frac{1}{A+C} \tag{44}$$

or in terms of the S-matrix parameters as

$$a = \frac{p}{q} + \frac{u}{v} = \frac{1}{\alpha} + \frac{1}{\beta} + \frac{1}{\lambda} + \frac{1}{\mu}. \tag{45}$$

Substituting (28), (29), (42), and (43) into (45), we obtain

$$a = 6\left(\frac{1}{\alpha} + \frac{1}{\beta}\right) \tag{46}$$
$$\times \frac{2(\alpha+\beta)(\beta C_T^2 + \alpha C_v^2) + 3(\alpha-\beta)^2 C_T^2 C_v^2}{2(\alpha+\beta)^2[2 + 3(C_T^2+C_v^2)] + 9(\alpha-\beta)^2 C_T^2 C_v^2}.$$

This formula expresses the doublet nd scattering length in terms of the parameters of the bound and the virtual

triton state. From (38), we similarly find that the pole $k_0^2 \equiv 1/D$ of the function $k \cot \delta$ is given by

$$k_0^2$$

$$= \alpha\beta \frac{2(\alpha + \beta)(\beta C_T^2 + \alpha C_v^2) + 3(\alpha - \beta)^2 C_T^2 C_v^2}{2(\alpha + \beta)(\alpha C_T^2 + \beta C_v^2) - 3(\alpha - \beta)^2 C_T^2 C_v^2}. \quad (47)$$

We note that the effective range for nd scattering can be expressed in terms of the van Oers–Seagrave parameters as

$$r_e = 2(B + CD). \quad (48)$$

Along with the effective range, which is anomalously large, $r_e \sim 500$ fm, for doublet nd scattering, the so-called amplitude slope parameter [6], given by the dimensionless quantity $\frac{1}{2}\alpha_d^3 a^2 r_e$ with wave number $\alpha_d = 0.2316$ fm^{-1} corresponding to the deuteron, is often used in the literature.

5. NUMERICAL CALCULATION OF PARAMETERS OF LOW-ENERGY nd SCATTERING AND THE CONSTANT C_v^2

With the parameters specifying the bound and the virtual triton state, we have calculated numerically the low-energy nd scattering parameters a, $\varepsilon_0 = -\dfrac{\hbar^2 k_0^2}{2m}$, and $\frac{1}{2}\alpha_d^3 a^2 r_e$ for low-energy nd scattering by formulas (46)–(48). The calculation has revealed that these parameters of nd scattering are weakly sensitive to variations in the energies E_0 and E_v of the ground and the virtual state, respectively, and to the asymptotic normalization factor C_T^2 for the bound state. At the same time, these parameters greatly depend on the asymptotic normalization factor C_v^2 for the virtual state. The results of the calculations for the parameters of low-energy nd scattering are quoted in the table for various values of the constant C_v^2. In the calculations, the parameters of the triton were set to the values of $E_T = 8.48$ MeV [13] ($E_T = |E_0| + \varepsilon_d$), $B_v = |E_v| = 0.482$ MeV [12], and $C_T^2 = 3.5$ [1, 2, 6], which follow from a direct analysis of experimental data. From the results quoted in the table, it can be seen that the parameters of nd scattering are highly sensitive to variations in the constant C_v^2. The experimental value of $C_v^2 = 0.0504$ [12] adopted at present leads to the nd scattering length $a = 1.03$ fm, which differs considerably from its experi-
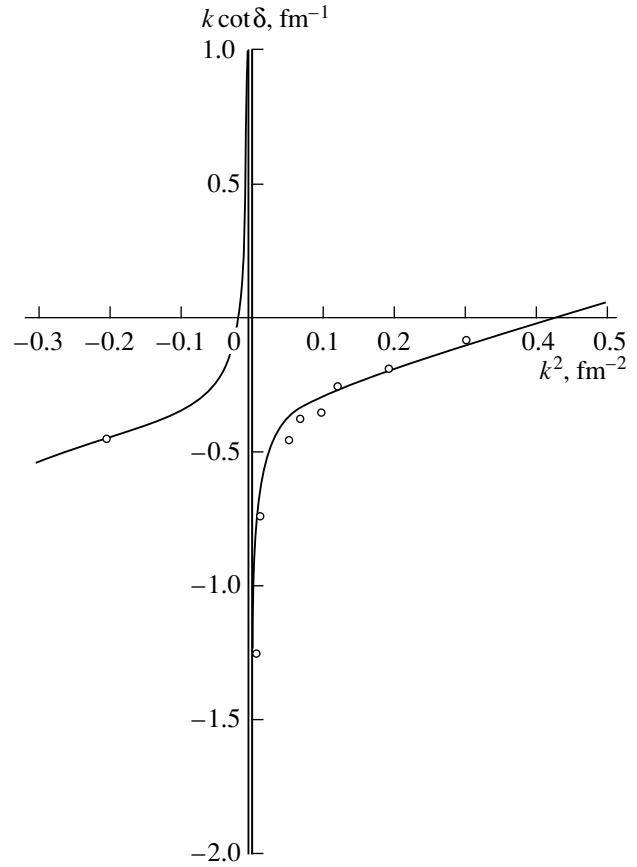
Function $k \cot \delta$ calculated for doublet nd scattering in the van Oers–Seagrave approximation with the parameter values (53)–(56) versus the energy k^2. The experimental data were taken from [4].

mental value now established to a high precision. The experimental value of the nd scattering length [14],

$$a^{\text{expt}} = 0.65 \text{ fm [14]}, \quad (49)$$

can be fitted with the asymptotic-constant value

$$C_v^2 = 0.0592, \quad (50)$$

which agrees well with the value of $C_v^2 = 0.06$ calculated in the two-body model of nd interaction simulated by the Hulthén potential [2]. Thus, the numerical value in (50) for the asymptotic normalization factor C_v^2 for the virtual state must be treated as the result of the theoretical calculation on the basis of our model. The high sensitivity of the scattering parameters to this quantity and a deviation of the theoretical results from its available experimental value indicate that a refinement of the experimental value of C_v^2 is necessary. The above highlights the crucial importance of in factor C_v^2 for exploring the properties of nd scattering in the doublet spin state. The experimental value in (49) for the nd

Parameters of low-energy *nd* scattering versus C_v^2

C_v^2	a, fm	ε_0, MeV	$\frac{1}{2}\alpha_d^3 a^2 r_e$
0.01	3.12	−0.43	0.51
0.02	2.54	−0.38	0.80
0.03	2.01	−0.32	1.04
0.04	1.51	−0.26	1.24
0.05	1.05	−0.20	1.40
0.06	0.62	−0.13	1.53
0.07	0.21	−0.05	1.63
0.08	−0.17	0.04	1.72
0.09	−0.52	0.13	1.79

scattering length and, accordingly, the value in (50) for C_v^2 correspond to the following values for the pole of the function $k\cot\delta$ and the amplitude slope parameter:

$$\varepsilon_0 = -0.1313 \text{ MeV}, \tag{51}$$

$$\frac{1}{2}\alpha_d^3 a^2 r_e = 1.52. \tag{52}$$

The value calculated for the pole position ε_0 and presented in (51) agrees well with $\varepsilon_0 = -0.15$ MeV quoted in [15] as an experimental value. The slope parameter (52) complies fairly well with the value of $\frac{1}{2}\alpha_d^3 a^2 r_e = 1.35$ [6] calculated theoretically from the Faddeev equations with separable nucleon–nucleon potentials.

For the van Oers–Seagrave parameters, a numerical calculation with C_v^2 from (50) yields

$$A = 0.3198 \text{ fm}^{-1}, \tag{53}$$
$$B = 0.7698 \text{ fm}, \tag{54}$$
$$C = 1.2190 \text{ fm}^{-1}, \tag{55}$$
$$D = 236.927 \text{ fm}^2. \tag{56}$$

The function $k\cot\delta$ calculated in the van Oers–Seagrave approximation with the parameter values (53)–(56) is shown in the figure versus the energy k^2. It can be seen that the theoretical curve faithfully reproduces experimental data from [4]. In summary, we have obtained a complete description of low-energy doublet *nd* scattering in terms of the parameters of the bound and the virtual triton state and demonstrated that this description is consistent with experimental data.

6. CONCLUSION

It has been shown that the van Oers–Seagrave formula for doublet *nd* scattering—it was originally deduced from a purely empirical consideration—immediately follows from the Bargmann *S*-matrix representation corresponding to the presence of two triton states, a bound and a virtual one, in the system. That the pole term proves to be necessary in the function $k\cot\delta$ is also due to the presence of two states in the system. Our analysis has given simple expressions relating the van Oers–Seagrave parameters to the *S*-matrix parameters. It has been shown that the van Oers–Seagrave formula is a direct generalization of the effective-range approximation to the case where the system being considered has two states; when one of these states goes to infinity, the former reduces to the latter.

For the doublet *nd* scattering length and the pole of the function $k\cot\delta$, we have obtained simple explicit expressions in terms of the energies of the bound and the virtual triton state and the nuclear vertex constants for these states. The resulting formulas make it possible to perform numerical calculations and to analyze the parameters of low-energy *nd* scattering versus the parameters of the triton. In particular, the calculations have revealed that the parameters of *nd* scattering are highly sensitive to variations in the asymptotic normalization factor C_v^2 for the virtual triton state. The experimental value of the *nd* scattering length is fitted at the value of $C_v^2 = 0.0592$, which differs from the experimental value presently accepted for this constant. Therefore, the constant C_v^2 is of paramount importance for studying the properties of the *nd* system and needs further experimental refinement.

REFERENCES

1. N. M. Petrov, Yad. Fiz. **48**, 50 (1988) [Sov. J. Nucl. Phys. **48**, 31 (1988)].
2. Yu. V. Orlov, N. M. Petrov, and G. N. Teneva, Yad. Fiz. **55**, 38 (1992) [Sov. J. Nucl. Phys. **55**, 23 (1992)].
3. L. M. Delves, Phys. Rev. **118**, 1318 (1960).
4. W. T. H. van Oers and J. D. Seagrave, Phys. Lett. **24B**, 562 (1967).
5. J. S. Whiting and M. G. Fuda, Phys. Rev. C **14**, 18 (1976).
6. I. V. Simenog, A. I. Sitnichenko, and D. V. Shapoval, Yad. Fiz. **45**, 60 (1987) [Sov. J. Nucl. Phys. **45**, 37 (1987)].
7. V. Bargmann, Rev. Mod. Phys. **21**, 488 (1949).

8. R. G. Newton, *Scattering Theory of Waves and Particles*, 2nd ed. (Springer-Verlag, New York, 1982; Russ. transl. of 1st ed., Mir, Moscow, 1969).

9. L. D. Blokhintsev, I. Borbeĭ, and É. I. Dolinskiĭ, Fiz. Élem. Chastits At. Yadra **8**, 1189 (1977) [Sov. J. Part. Nucl. **8**, 485 (1977)].

10. A. G. Sitenko, *Scattering Theory* (Springer-Verlag, Berlin, 1991).

11. O. Dumbrajs, R. Koch, H. Pilkuhn, *et al.*, Nucl. Phys. B **216**, 277 (1983).

12. B. A. Girard and M. G. Fuda, Phys. Rev. C **19**, 579 (1979).

13. D. R. Tilley, H. R. Weller, and H. H. Hasan, Nucl. Phys. A **474**, 1 (1987).

14. W. Dilg, L. Koester, and W. Nistler, Phys. Lett. **36B**, 208 (1971).

15. Yu. V. Orlov, Yu. P. Orevkov, and L. I. Nikitina, Izv. Akad. Nauk, Ser. Fiz. **60** (11), 152 (1996).

Translated by R. Tyapaev

Clustering Aspects of Nuclei in Highly Deformed States*

**T. M. Shneidman[1), 2)], G. G. Adamian[1), 2), 3)], N. V. Antonenko[1), 2)],
S. P. Ivanova[1), 2)], and W. Scheid[2)]**

Abstract—The potential energies, the moments of inertia, and the quadrupole and octupole moments of dinuclear systems are compared with corresponding values for the highly deformed nuclear states. The idea is advocated that hyperdeformed states of nuclei are close to near-symmetric dinuclear systems. The superdeformed states are considered as asymmetric dinuclear systems. The cluster superdeformed and hyperdeformed states have quite a large octupole deformation. Measurement of octupole deformations of highly deformed nuclei can answer the question of whether these nuclei exist in cluster configurations. © *2000 MAIK "Nauka/Interperiodica"*.

1. INTRODUCTION

One of the most important developments in the physics of nuclear structure was the prediction and observation of superdeformed (SD) [1] and hyperdeformed (HD) [2] nuclear shapes. The idea that nuclei could have highly deformed prolate shapes at low temperature originated from the discovery of deformed isomers in the actinide region [3, 4]. Another group of superdeformed states having the ratio 3 : 2 of the major to the minor axis was discovered near the ground state in the $A \approx 76$ mass region (^{72}Se, $^{74, 76}$Kr) [5, 6] and in the $A \approx 100$ mass region ($^{98, 100}$Sr, ^{100}Zr) [7, 8]. In these nuclei, there is strong mixing between the SD ground state and the excited states near the spherical band which coexist at a low spin [9]. While, in the rare-earth nuclei, highly deformed shapes are stabilized by collective rotation, highly deformed nuclei, which were mentioned above, exist even at zero spin. High-spin states are populated in heavy-ion-fusion reactions. In the study of rotational bands, one can determine the moment of inertia of a highly deformed nucleus. On the basis on the experimental values of the moment of inertia, it was found that SD and HD states are related to the shapes with axis ratio 2 : 1 and 3 : 1, respectively. Since the intensity of γ transitions drastically decreases with decreasing angular momentum L, an experimental determination of the excitation energy of the SD band becomes difficult. In actinides, the third minimum (HD state) is elucidated from a microstructure in the resonances found in the (n, f), (t, pf), and (d, pf) reactions

[10]. Another piece of evidence supporting the existence of the third minimum is the observation of an asymmetric angular distribution of light fission fragments of nuclei around ^{232}Th [11]. Transitions of odd multipole orders indicate a reflection-asymmetric shape of a nucleus.

An interesting observation in the shell-model calculations is that the nucleus in the third minimum corresponds to a dinuclear-system (DNS) configuration [12]. In this model, however, clusters deeply penetrate each other because the relative distance between the centers of clusters, R, is smaller than the sum of the cluster radii, $R_1 + R_2$. As was shown in [13, 14], there is a large energy hindrance for the overlap of nuclei at smaller relative distances R. Therefore, we treat here SD and HD states as the DNS with $R \approx R_1 + R_2$, which corresponds to the minimum of the nucleus–nucleus potential [15]. In addition to theoretical studies, there are many pieces of experimental evidence for the existence of cluster-type configurations in fissile nuclei [16]. In light α-particle nuclei, the similarity of a hyperdeformed and a cluster-type state was already mentioned in [17]. In the present study, we find the relationship between the DNS-type cluster configurations [18] and highly deformed states of heavy nuclei. The consequences of considering HD and SD states as cluster-type states are discussed.

2. INTRINSIC MULTIPOLE MOMENTS OF DNS

The mass ($k = m$) and charge ($k = c$) intrinsic multipole moments of the DNS are calculated by the formula

$$Q_{\lambda\mu}^{(k)} = \sqrt{\frac{16\pi}{2\lambda + 1}} \int \rho^{(k)}(\mathbf{r}) r^\lambda Y_{\lambda\mu}(\Omega) d\tau. \qquad (1)$$

For a small overlap of nuclei in the DNS ($R \geq R_1 + R_2$, where R_1 and R_2 are the radii of the nuclei and R is dis-

---

tance between the centers of the nuclei), the mass and charge densities $\rho^{(k)}$ in the DNS can be written as the sum of corresponding densities in each nucleus:

$$\rho^{(k)}(\mathbf{r}) = \rho_1^{(k)}(\mathbf{r}) + \rho_2^{(k)}(\mathbf{r}). \tag{2}$$

Using Eq. (2) and assuming the axial symmetry of nuclear shapes, we can represent the multipole moments of the DNS in the c.m. frame as

$$Q_{\lambda 0}^{(k)} = Q_\lambda^{(k)} = \sum_{\substack{\lambda_1 = 0 \\ \lambda_1 + \lambda_2 = \lambda}}^{\lambda} (-1)^\lambda \frac{\lambda}{\lambda_1! \lambda_2!}$$

$$\times [(-1)^{\lambda_1} A_2^{\lambda_1} Q_{\lambda_2}^{(k)}(1) + A_1^{\lambda_1} Q_{\lambda_2}^{(k)}(2)] \frac{R^{\lambda_1}}{A^{\lambda_1}}, \tag{3}$$

where the multipole moments of the DNS nuclei, $Q_{\lambda_2}^{(k)}(i)$ ($i = 1, 2$), are calculated in their centers of mass. By way of example, we indicate that, up to $\lambda = 3$, the values of $Q_\lambda^{(k)}$ are

$$Q_1^{(m)} = 0,$$

$$Q_1^{(c)} = 2e \frac{A_2 Z_1 - A_1 Z_2}{A} R,$$

$$Q_2^{(m)} = 2m_0 \frac{A_1 A_2}{A} R^2 + Q_2^{(m)}(1) + Q_2^{(m)}(2),$$

$$Q_2^{(c)} = 2e \frac{A_2^2 Z_1 + A_1^2 Z_2}{A^2} R^2 + Q_2^{(c)}(1) + Q_2^{(c)}(2), \tag{4}$$

$$Q_3^{(m)} = 2m_0 \frac{A_1 A_2}{A} \frac{A_2 - A_1}{A} R^3$$
$$+ 3 \frac{A_2 Q_2^{(m)}(1) - A_1 Q_2^{(m)}(2)}{A} R,$$

$$Q_3^{(c)} = 2e \frac{A_2^3 Z_1 - A_1^3 Z_2}{A^3} R^3 + 3 \frac{A_2 Q_2^{(c)}(1) - A_1 Q_2^{(c)}(2)}{A} R,$$

where $A = A_1 + A_2$; A_i, Z_i ($i = 1, 2$) are the mass and charge numbers of the DNS nuclei, respectively; and m_0 is the nucleon mass. The experimental values of the quadrupole moments of the DNS nuclei are used in the calculations. We consider nuclei in the pole–pole orientation, which corresponds to the potential-energy minimum. Since allowances made for the diffuseness in $\rho_i^{(k)}(\mathbf{r})$ have virtually no effect on the results for R considered here, we disregard it in the present study.

The shape of an axially-deformed nucleus can be described by using the multipole expansion

$$R = R_0(1 + \beta_0 Y_{00} + \beta_1 Y_{10} + \beta_2 Y_{20} + \beta_3 Y_{30}), \tag{5}$$

where R_0 is the spherical equivalent radius of the nucleus, while β_0, β_1, β_2, and β_3 are deformation parameters with respect to the center of mass [19]. In Eq. (5), we take only the quadrupole and octupole deformations into consideration to find the parameters β_i corresponding to Q_i calculated for the DNS. Despite the existence of a better shape parametrization [20] than that in (5), the parameters β_i are widely used to characterize experimental spectroscopic information. The parameter β_0 is responsible for invariability of the system volume. The parameter β_1 provides the vanishing dipole moment $Q_{10}^{(m)} = 0$. With Eq. (5), one can well describe the DNS shape for small mass asymmetry $\eta = |(A_2 - A_1)/A| < 0.5$. For larger η, equation (5) leads to a shape smoother than that of a DNS. However, even asymmetric configurations can be effectively characterized by the parameters β_i. With Eqs. (1) and (5), the intrinsic mass multipole moments of the system are expressed in terms the deformation parameters β_λ ($\lambda = 0, 1, 2, 3$) as

$$\tilde{Q}_\lambda^{(m)} = \frac{3}{\lambda + 3} A m_0 R_0^\lambda$$

$$\times \sum_{k_0 = 0}^{\lambda + 3} \sum_{k_1 = 0}^{k_0} \sum_{k_2 = 0}^{k_1} \sum_{k_3 = 0}^{k_2} G_{k_0 k_1 k_2 k_3}^\lambda \beta_0^{k_0 - k_1} \beta_1^{k_1 - k_2} \beta_2^{k_2 - k_3} \beta_3^{k_3}, \tag{6}$$

where

$$G_{k_0 k_1 k_2 k_3}^\lambda = \frac{1}{2^{\lambda + k_2} \lambda!} \sqrt{\frac{3^{k_1 - k_2} 5^{k_2 - k_3} 7^{k_3}}{(4\pi)^{k_0}}} \binom{\lambda + 3}{k_0} \binom{k_0}{k_1}$$

$$\times \binom{k_1}{k_2} \binom{k_2}{k_3}^{k_2 - k_3} \sum_{i = 0}^{k_3} \sum_{j = 0}^{} (-1)^{i + j} 3^{k_2 - k_3 - i + j} 5^{k_3 - j}$$

$$\times \binom{k_2 - k_3}{i} \binom{k_3}{j} I_{ij},$$

$$I_{ij} = \sum_{k = 0}^{\left[\frac{\lambda}{2}\right]} (-1)^k \binom{\lambda}{k} \frac{(2\lambda - 2k)!}{(\lambda - 2k)!}$$

$$\times \frac{2\delta_{k_1 + k_2 + k_3 + \lambda + 1, \text{ odd}}}{(k_1 + k_2 + k_3 + \lambda + 1 - 2i - 2j - 2k)}.$$

Here, $\binom{n}{k} = n!/(k!(n - k)!)$.

Using the mass quadrupole and octupole moments, experimentalists derive the deformation parameters β_λ ($\lambda = 2, 3$) with the aid of expressions similar to (6). We repeat the same procedure but exploit the DNS multipole moments $Q_\lambda^{(m)}$ from (4) instead of the moments
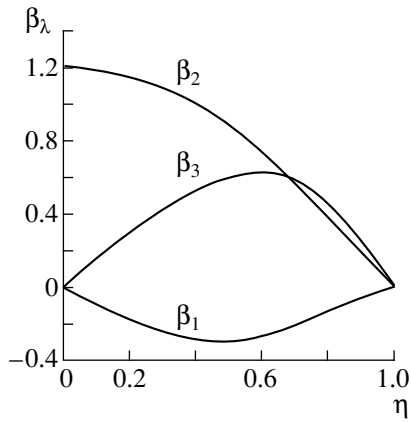
Fig. 1. Deformation parameters β_1, β_2, and β_3 as functions of mass asymmetry η. The calculations were performed for spherical nuclei of the DNS. The results do not depend on the total charge and mass numbers of the DNS.

extracted from experimental data. From a numerical solution of the set of equations

$$\tilde{Q}_\lambda^{(m)} = Q_\lambda^{(m)}, \tag{7}$$

we find the dependences of β_λ on the mass (charge) asymmetry $\eta = (A_2 - A_1)/A$ ($\eta_Z = (Z_2 - Z_1)/Z$) (see Fig. 1) and the relative distance between the centers of nuclei. It can be seen from Fig. 1 that the values of quadrupole- and octupole-deformation parameters become close to each other at a large mass asymmetry. For a very asymmetric DNS consisting of spherical nuclei, we can use some simple analytic expressions for β_2 and β_3:

$$\beta_2 = \sqrt{\frac{5}{4\pi}} \frac{4\pi}{3} \frac{A_1 A_2}{A^2} \frac{R^2}{R_0^2},$$

$$\beta_3 = \sqrt{\frac{7}{4\pi}} \frac{4\pi}{3} \frac{A_1 A_2}{A^2} \frac{A_2 - A_1}{A} \frac{R^3}{R_0^3}. \tag{8}$$

In this case, β_2 and β_3 do not depend on the total charge and mass numbers of the DNS. This can be demonstrated straightforwardly if we take $A_1 = A(1 - \eta)/2$ and $A_2 = A(1 + \eta)/2$. For the case where the DNS nuclei are spherical, the values of β_2 and β_3 and their dependence on η are universal (Fig. 1).

3. MOMENT OF INERTIA OF DNS

The DNS moment of inertia is defined [15] as

$$\Im = \Im_1 + \Im_2 + m_0 \frac{A_1 A_2}{A} R^2. \tag{9}$$

For large angular momenta, the moments of inertia $\Im_i$ ($i = 1, 2$) of the DNS components can be calculated in the rigid-body approximation as

$$\Im_i = \frac{1}{5} m_0 A_i (a_i^2 + b_i^2),$$

$$a_i = R_{0i}\left(1 - \frac{\alpha_i^2}{4\pi}\right)\left(1 + \sqrt{\frac{5}{4\pi}}\alpha_i\right), \tag{10}$$

$$b_i = R_{0i}\left(1 - \frac{\alpha_i^2}{4\pi}\right)\left(1 - \sqrt{\frac{5}{16\pi}}\alpha_i\right),$$

where R_{0i} and α_i ($i = 1, 2$) are the spherical equivalent radii and the parameters of quadrupole deformation of the DNS nuclei. For small angular momenta, we should use the experimental values of $\Im_i$ found in studying low-lying rotational nuclear states. The moment of inertia is a unique well-measurable quantity for the SD and HD states. Therefore, a comparison of the calculated and experimental values of the moment of inertia is necessary for checking our interpretation of the shapes of highly deformed nuclei.

4. POTENTIAL ENERGY OF DNS

In order to check the possibility of the DNS formation from the excited compound nucleus, the potential energy of the DNS is calculated as

$$U(R, \eta, L) = B_1 + B_2$$
$$+ V(R, \eta, L) - B_{12}. \tag{11}$$

Here, B_1, B_2, and B_{12} are the realistic binding energies of the fragments and the compound nucleus [15], respectively. The shell effects are included in these binding energies. The isotopic composition of the nuclei forming the DNS is chosen under the condition of N/Z equilibrium in the system. The value of $U(R, \eta, L)$ is normalized to the energy of the compound nucleus by B_{12}. The nucleus–nucleus potential $V(R, \eta, L)$ in (11) is calculated by a method of [15]. The nuclear parts of the $V(R, \eta, L)$ were calculated within the double-folding formalism with a nuclear radius parameter $r_0 = (1.12–1.15)$ fm and a diffuseness parameter $a = (0.54–0.56)$ fm depending on the mass number of the isotope. Deformation effects are taken into account in the calculation of the potential-energy surface [15]. For the heavy nuclei in the DNS, which are deformed in the ground state, the parameters of quadrupole deformation are taken from [21, 22]. The light nuclei of the DNS are assumed to be deformed only if the energies of their first 2^+ states do not exceed 1.5 MeV. As is known from experiments on subbarrier fusion, these states are easily populated. As follows from our calculations [23] within the two-center shell model, the polarization effects in the DNS lead to the deformations of the nuclei which are close to ones for the first 2^+ state. The relative orientation of the deformed nuclei in the DNS follows the minimum of the potential energy which corresponds to the pole–pole orientation. The DNSs are localized in the pocket of the nucleus–nucleus potential at the relative

distance $R \approx R_{01}\left(1 + \sqrt{\frac{5}{4\pi}}\alpha_1\right) + R_{02}\left(1 + \sqrt{\frac{5}{4\pi}}\alpha_2\right)$.

All potentials were calculated with the same set of the parameters and assumptions. We found that the final results are not crucial to reasonable variation of the parameters in the calculation of potential energy. Since we deal mainly with sufficiently small excitation energies, the calculation of the DNS potential energy immediately shows which DNS can be related to the SD or HD nuclear states.

5. RESULTS AND DISCUSSIONS

The dependences of β_2, β_3, Q_2 ($Q_2 = Q_2^{(c)}$), and Q_3 ($Q_3 = Q_3^{(c)}$) on the mass asymmetry η are presented in Fig. 2 for the DNS corresponding to the ^{152}Dy compound nucleus. Since the deformations of the DNS nuclei are functions of η, these dependences have some oscillations. While Q_2 and β_2 decrease with increasing η, the dependences of Q_3 and β_3 on η have maxima. The positions of these maxima approximately correspond to the maxima of the DNS potential energy as a function of η (see Fig. 3). The value of β_3 steeply increases with η from zero. For highly asymmetric DNS, β_3 again becomes small enough. Therefore, a single value of β_3 can correspond to a pair of DNSs with different mass asymmetry. For the symmetric DNS with spherical nuclei, the difference by factor $\sqrt{2}$ between our values of β_2 and β_2 obtained in [24] is due to different definitions of β_2.

The DNS potential energy as a function of mass asymmetry is presented in Fig. 3 in the cases of spherical and deformed nuclei in the DNS forming ^{152}Dy. For the deformed nuclei, the minima of potential energy appear at $\eta = 0.026(^{74}$Ge $+ ^{78}$Se), $\eta = 0.16(^{64}$Ni $+ ^{88}$Sr), and $\eta = 0.34(^{50}$Ti $+ ^{102}$Ru). For zero angular momentum, the potential energy of combination ^{50}Ti $+ ^{102}$Ru is about 20 MeV, which is close to the value estimated in [25] for the HD state. For this DNS, the calculated moment of inertia $\Im = 134\hbar^2$ MeV^{-1} is close to the experimental one $\Im = 130\hbar^2$ MeV^{-1} [2]. For the DNS, the obtained value $\beta_2 = 1.3$ is in agreement with the experimental estimate $\beta_2 \geq 0.9$. Therefore, the shape of the DNS ^{50}Ti $+ ^{102}$Ru is compatible with the shape of ^{152}Dy nucleus in the HD state.

We found that in the asymmetric DNS, for example, ^{22}Ne $+ ^{130}$Ba and ^{26}Mg $+ ^{126}$Xe (where the driving potential has minima), the moments of inertia and quadrupole moments are close to the experimental values known for the SD state $\Im = (85 \pm 3)\hbar^2$ MeV^{-1} and $Q_2 = (18 \pm 3)$ e b. For the system ^{22}Ne $+ ^{130}$Ba, we have $\Im = 96\hbar^2$ MeV^{-1}, $Q_2 = 20$ e b, and $\beta_2 = 0.8$. In the system ^{26}Mg $+ ^{126}$Xe, we obtained $\Im = 104\hbar^2$ MeV^{-1}, $Q_2 = 24$ e b, and $\beta_2 = 0.9$. These DNSs correspond to nearly zero temperature if they are formed in the reaction ^{48}Ca(205 MeV)(^{108}Pd, $4n$)^{152}Dy. At $L = 0$, the potential energies of these DNSs with respect to the ground state
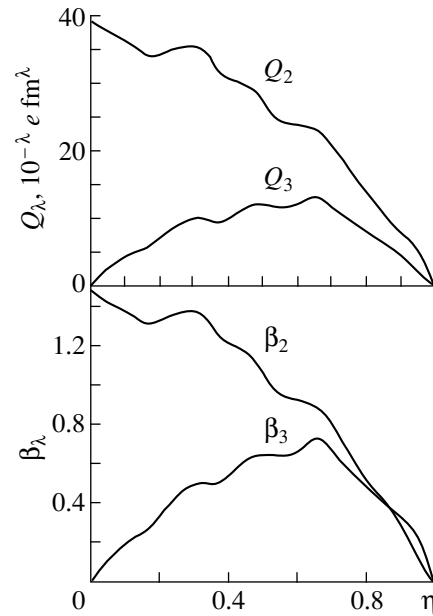
Fig. 2. Q_2 (10^{-2} e fm^2), Q_3 (10^{-3} e fm^3) (upper part), and β_2, β_3 (lower part) as functions of the mass asymmetry η of the DNS corresponding to the compound nucleus ^{152}Dy. The deformation of the DNS nuclei was taken into account.
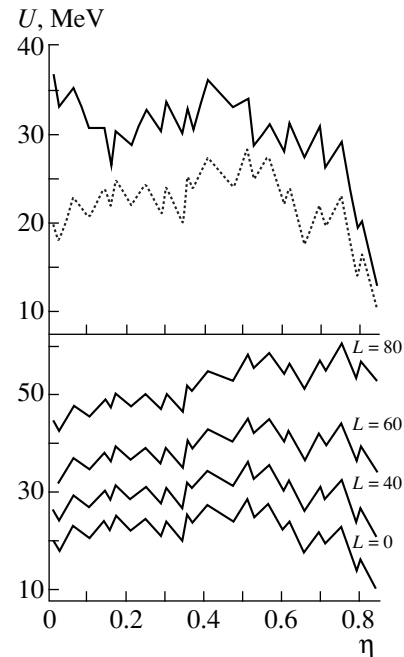
Fig. 3. Potential energy U of the DNS as a function of the mass asymmetry η for the compound nucleus ^{152}Dy. At $L = 0$, the results calculated with and without a deformation of the DNS nuclei are presented by, respectively, dotted and solid lines (upper part). The results calculated with the deformations of the DNS nuclei are shown for various values of the angular momentum (lower part).

of ^{152}Dy are about 8 MeV larger than ones estimated for the SD shapes in [25]. The energies of these two systems with respect to the energy of compound nucleus as functions of angular momentum L are presented in Fig. 4.
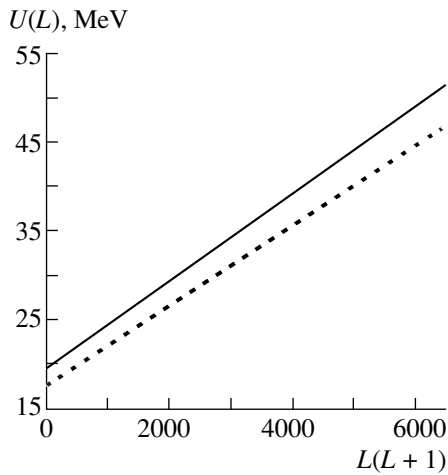
Fig. 4. Energies of (solid line) ^{22}Ne + ^{130}Ba and (dotted line) ^{26}Mg + ^{126}Xe as functions of $L(L + 1)$. The energy is normalized to the energy of a rotating compound nucleus.

Fig. 5. Potential energy U of the DNS as a function of η for the compound nuclei (upper part) ^{232}Th, (middle part) ^{76}Kr, and (lower part) ^{240}Pu at $L = 0$. The deformation of the DNS nuclei was taken into account.

The SD bands in the mass region $A \approx 150$ are populated up to an anomalously high intensity around $55\hbar$ spin. There is no significant population of these states for L below $(45–50)\hbar$ [26]. This fact can be explained by the DNS interpretation of the SD states. The DNS potential energy as dependent on η becomes flat with decreasing angular momentum, and the DNS can evolve to a larger η. This takes place because the potential barrier in the direction of larger mass asymmetries decreases with L (Fig. 3). Due to the distribution among a variety of configurations at small L and motion to a compound nucleus with increasing η, the transition from the SD state to the ground state is not observable.

Analyzing the potential energy of the DNS as a function of η for the ^{232}Th compound nucleus (Fig. 5), we found well-distinct minima corresponding to the systems ^{100}Zr + ^{132}Sn ($\eta = 0.138$) and ^{82}Ge + ^{150}Ce ($\eta = 0.293$). In Fig. 6, one can see that the dependences of β_2 and $\mathcal{T}$ on η are weak for small mass asymmetries. In these systems, β_2 is about 1.5, $\beta_3 \approx 0.40$, and $\mathfrak{I}$ is about $290\hbar^2$ MeV^{-1}, and the energies are near the energy of the ground state of ^{232}Th at $L = 0$. Except for the values of β_2, the values in the table are close to the corresponding ones calculated for the third minimum in [12]. In our calculation, β_2 is larger in comparison to $\beta_2 = 0.85$ in [12] due to the negligible overlap of nuclei in the DNS and, thus, larger elongation of the system.

The SD rotational bands in ^{232}Th could be interpreted as the DNS states ^{28}Mg + ^{204}Pt and ^{26}Ne + ^{206}Hg (see table). For the ^{234}U nucleus, we also have the SD and HD cluster configurations (see table): ^{26}Ne + ^{208}Pb, ^{28}Mg + ^{206}Hg, ^{82}Ge + ^{152}Nd, ^{100}Zr + ^{134}Te, and ^{104}Mo + ^{130}Sn. The depth of the third well derived experimentally (which corresponds to the HD state) is found to be (3.6 ± 0.3) MeV for the ^{234}U nucleus [27]. For the DNS configurations, this value is in agreement with the value
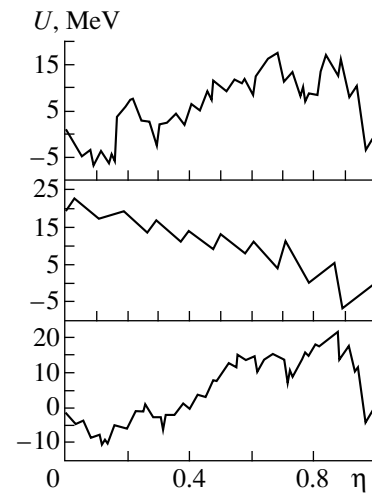
of the depth of the pocket in the nucleus–nucleus potential. For example, for the ^{100}Zr + ^{134}Te and ^{104}Mo + ^{130}Sn configurations, the depth of the pocket is about 3.4 MeV. The "driving" potential is shown in Fig. 5 for the ^{240}Pu compound nucleus, where in the resonance subbarrier fission experiment the SD bands were observed [27]. These SD states could be treated as the DNS-type state: ^{32}Mg + ^{208}Pb and ^{34}Si + ^{206}Hg (see table). From the results presented in the table, one can predict some HD cluster states for the ^{240}Pu nucleus.
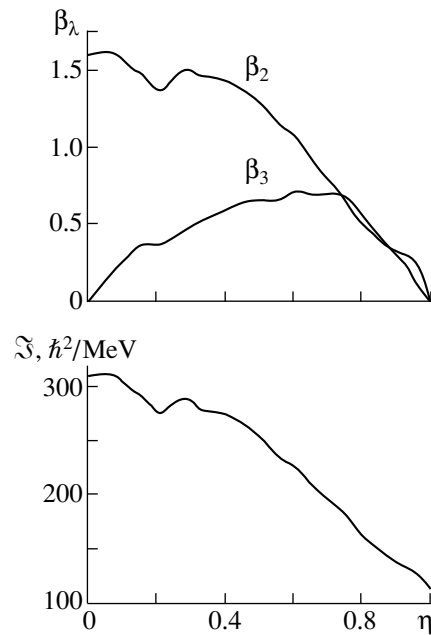
Fig. 6. Deformation parameters β_2 and β_3 (upper part) and moments of inertia $\mathfrak{I}$ (lower part) as functions of the mass asymmetry η of the DNS corresponding to the compound nucleus ^{232}Th.

Calculated values of the moment of inertia, $\Im$; the charge quadrupole and octupole moments, Q_2 and Q_3, respectively; and quadrupole and octupole deformation parameters, β_2 and β_3, for various DNSs corresponding to the compound nuclei ^{232}Th, ^{234}U, and ^{240}Pu (see main body of the text)

| Cluster configurations	$\Im$, $\hbar^2$/MeV	$Q_2 \times 10^{-2}$, e fm^2	$Q_3 \times 10^{-3}$, e fm^3	β_2	β_3
^{26}Ne + ^{206}Hg $\longrightarrow$ ^{232}Th	171	24.9	18.8	0.57	0.63
^{28}Mg + ^{204}Pt $\longrightarrow$ ^{232}Th	180	31.0	23.9	0.65	0.68
^{82}Ge + ^{150}Ce $\longrightarrow$ ^{232}Th	292	70.9	19.8	1.53	0.47
^{100}Zr + ^{132}Sn $\longrightarrow$ ^{232}Th	292	70.1	16.2	1.48	0.34
^{29}Ne + ^{208}Pb $\longrightarrow$ ^{234}U	169	20.9	18.0	0.47	0.61
^{28}Mg + ^{206}Hg $\longrightarrow$ ^{234}U	179	29.9	23.7	0.61	0.68
^{82}Ge + ^{152}Nd $\longrightarrow$ ^{234}U	291	70.4	20.5	1.49	0.49
^{100}Zr + ^{134}Te $\longrightarrow$ ^{234}U	326	71.8	14.0	1.73	0.27
^{104}Mo + ^{130}Sn $\longrightarrow$ ^{234}U	296	71.8	14.0	1.48	0.28
^{32}Mg + ^{208}Pb $\longrightarrow$ ^{240}Pu	191	28.7	23.2	0.57	0.71
^{34}Si + ^{206}Hg $\longrightarrow$ ^{240}Pu	197	33.9	25.4	0.69	0.70
^{82}Ge + ^{158}Sm $\longrightarrow$ ^{240}Pu	307	75.3	22.1	1.53	0.50
^{104}Zr + ^{136}Xe $\longrightarrow$ ^{240}Pu	305	74.1	14.8	1.49	0.33
^{106}Mo + ^{134}Te $\longrightarrow$ ^{240}Pu	314	76.4	16.0	1.52	0.32
^{110}Ru + ^{130}Sn $\longrightarrow$ ^{240}Pu	311	75.3	12.4	1.49	0.23

The potential energy of the DNS corresponding to the ^{76}Kr compound nucleus is shown in Fig. 5. It is seen that there is a deep minimum with energy on the level of compound nucleus energy corresponding to the cluster configuration ^{8}Be + ^{68}Ge. For this cluster state, we have $Q_2 = 4.9$ e b, $Q_3 = 2.0 \times 10^3$ e fm^3, and $\Im = 26\hbar^2$/MeV. A similar picture is observed for other nuclei in $A \approx 76$ mass region, such as for ^{74}Kr and ^{72}Se. In the DNS configuration with light cluster ^{8}Be, we found $Q_2 = 4.7$ e b and $Q_3 = 1.9 \times 10^3$ e fm^3 for the ^{72}Se compound nucleus. For the nuclei in mass region $A \approx 100$, the energies of such cluster configurations are between 5 and 6 MeV above the energies of the corresponding compound nuclei.

Taking N/Z equilibrium into consideration, in the nuclei ^{72}Se and ^{74,76}Kr we obtained the minima of the DNS potential energy for the configurations with α-particle nuclei (multiples of α clusters) at large η. The potential energies of these DNSs are small because the light nuclei in them are most stable. Such behavior of the DNS potential energy is not observed for the asymmetric configurations with light clusters in the $A \approx 100$ mass region.

If very asymmetric DNSs are energetically favorable, the wave function of compound nucleus has components corresponding to the cluster-type configurations. For example, in many cases, the cluster configuration

$$^A Z \longrightarrow {}^{(A-4)}(Z-2) + {}^4\text{He} \qquad (12)$$
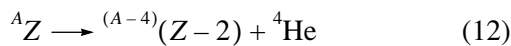
corresponds to an energy that is close to or even less than the energy of the ground state of compound nucleus. As a result, the nucleus can acquire the octupole deformation in the ground state. Since the shape of the nucleus

is no more symmetric under space inversion, the spectra of the nucleus must contain states with different parity. This fact was found experimentally in a variety of nuclei with $Z \approx 88$–90 ($N \approx 86$–90), for different isotopes of nuclei Ra, Th, and U, and with $Z \approx 60$, for isotopes of Ba, Ce, Nd, Sm, and Gd [28]. Another result of reflection asymmetric shape is appearance of $E1$ and $E3$ transitions. These transitions were found in ^{226}Ra with $Q_2 = 750$ e fm^2 and $Q_3 = 3100$ e fm^3 [29] and in ^{148}Nd with $Q_2 = 400$ e fm^2 and $Q_3 = 1500$ e fm^3 [30]. The experimental dipole moments of these nuclei are found to be 0.16 e fm for ^{226}Ra [29] and 0.32 e fm for ^{148}Nd [30]. Here, the intrinsic multipole moments are considered. On the assumption that the cluster configuration (12) mainly contributes to the ground state with static octupole deformation, we can derive the values of multipole moments for these nuclei. For ^{226}Ra, we found $Q_1 = Q_1^{(c)} = 4$ e fm, $Q_2 = 776$ e fm^2, and $Q_3 = 2662$ e fm^3. For ^{148}Nd, we obtained $Q_1 = 3$ e fm, $Q_2 = 486$ e fm^2, and $Q_3 = 1844$ e fm^3. The calculated values of Q_2 and Q_3 are close to the experimental ones. However, the values of Q_1 are at least an order of magnitude too high. The same problem was observed in the cluster model [31]. These deviations of the theoretical results from experimental ones are due to the use of the simplified consideration of the N_1/Z_1 ratios in the DNS nuclei. The value of Q_1 strongly depends on these ratios and $Q_1 = 0$ in the limit of the same N/Z ratio in the DNS nuclei. For such overly asymmetric DNS, in the light nucleus, N/Z ratios are enhanced effectively against a unit N/Z ratio in the α particle because the heavy nucleus of the DNS strongly overlaps the α particle and there is at least one valence neutron supplying the coupling α particle with
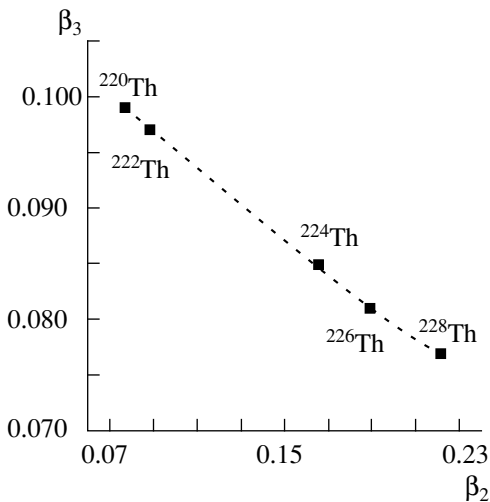
Fig. 7. β_2 vs. β_3 plot for isotopes of ^{A}Th in the cluster state $^{(A-4)}$Ra + ^{4}He.

the heavy nucleus. If we take the (^{4}He + $1n$) cluster instead of ^{4}He in the DNS or slightly increase the N/Z ratio in the contact region of two nuclei of the DNS, then the theoretical Q_1 values for ^{226}Ra and ^{148}Nd become consistent with the experimental data and the Q_2 and Q_3 values are virtually unchanged.

As is seen in Fig. 7, the octupole (quadrupole) deformation is reduced (enhanced) with increasing atomic number of Th isotopes. This is because the quadrupole deformation of the DNS heavy cluster is enlarged when we pass through this mass region. Such behaviors of β_2 and β_3 are in an agreement with ones obtained in [32].

6. SUMMARY

The DNS potential energy as a function of mass asymmetry has a few global minima. Most of them lie above the energy corresponding to the compound nucleus. It is possible, however, to populate these states in heavy ion induced reactions by choosing the appropriate reaction partners and bombarding energy of the projectile. At high spin, these cluster states remain cold and long-lived. It was established that the energies, the moments of inertia, and the quadrupole deformation of certain DNSs are close to the ones experimentally found for the SD and HD nuclei. Since many DNS states exhibit appreciable octupole deformation, the experimental measurement of octupole deformation for highly deformed nuclei can answer whether these nuclei exist in cluster configurations. One piece of evidence that SD nuclei can have octupole deformation comes from observation of an excited SD band in ^{190}Hg which decays to the lowest energy (yrast) SD band by transitions of odd multipole order [33]. The $E1$ rate observed in [33] is three order of magnitude larger than those typically observed in heavily deformed nuclei

and is similar to those observed in the octupole-unstable normally deformed actinide nuclei [34].

In some nuclei with $A \approx 230$ or $A \approx 76$, the potential energy of the DNS has minima which lie on the same level as the energy of the compound nucleus. This means that such cluster states can exist at low spin. We attempted to describe the nuclei with static octupole deformation in the ground state as the DNS where the α cluster is the lighter cluster. It was found that calculated quadrupole and octupole deformations are close to the experimental ones and such DNSs are energetically favorable.

ACKNOWLEDGMENTS

REFERENCES

1. P. J. Twin *et al.*, Phys. Rev. Lett. **57**, 811 (1986).
2. A. Galindo-Uribarri *et al.*, Phys. Rev. Lett. **71**, 231 (1993).
3. S. M. Polikanov, Zh. Éksp. Teor. Fiz. **42**, 1464 (1962) [JETP **15**, 1016 (1962)].
4. H. J. Specht, Phys. Lett. **41B**, 43 (1972).
5. J. H. Hamilton *et al.*, Phys. Rev. Lett. **32**, 239 (1974).
6. R. B. Piercey *et al.*, Phys. Rev. Lett. **47**, 1514 (1981).
7. T. A. Kahn *et al.*, Z. Phys. A **283**, 103 (1977).
8. R. F. Azuma *et al.*, Phys. Lett. **86B**, 5 (1979).
9. J. H. Hamilton, Prog. Part. Nucl. Phys. **28**, 87 (1992).
10. B. B. Brick *et al.*, Phys. Rev. Lett. **28**, 1707 (1972).
11. K. Th. Brinkmann *et al.*, Nucl. Phys. A **502**, 271 (1989).
12. S. Cwiok *et al.*, Phys. Lett. B **322**, 304 (1994).
13. Yu. F. Smirnov and Yu. M. Tchuvil'sky, Phys. Lett. **134B**, 25 (1984).
14. G. G. Adamian *et al.*, Phys. Lett. B **451**, 289 (1999).
15. G. G. Adamian *et al.*, Int. J. Mod. Phys. E **5**, 191 (1996).
16. Yu. V. Pyatkov *et al.*, Nucl. Phys. A **624**, 140 (1997).
17. N. Cindro, J. Phys. G **4**, L23 (1978); N. Cindro and W. Greiner, J. Phys. G **9**, L175 (1983).
18. V. V. Volkov, *Nuclear Reactions of Deep Inelastic Transfers* (Énergoizdat, Moscow, 1982).
19. F. A. Gareev, S. P. Ivanova, and V. V. Pashkevich, Yad. Fiz. **11**, 1200 (1970) [Sov. J. Nucl. Phys. **11**, 667 (1970)].
20. V. V. Pashkevich, Nucl. Phys. A **169**, 275 (1971).
21. S. Raman *et al.*, At. Data Nucl. Data Tables **36**, 1 (1987).

22. P. Möller and R. Nix, At. Data Nucl. Data Tables **39**, 213 (1988); http://t2.lanl.gov/data/atro/molnix96/massd.html

23. G. G. Adamian *et al.*, Nucl. Phys. A **646**, 29 (1999).

24. S. Royer, J. Phys. G **21**, 339 (1995).

25. S. Aberg, Nucl. Phys. A **557**, 17 (1993).

26. M. A. Bentley *et al.*, J. Phys. G **17**, 481 (1991).

27. D. Gassmann *et al.*, in *Abstract of Frühjahrstagung der Deutschen Physikalischen Gesellschaft, Freiburg, 1999.*

28. P. A. Butler and W. Nazarewicz, Rev. Mod. Phys. **68**, 349 (1996).

29. H. J. Wollersheim, Nucl. Phys. A **556**, 261 (1993).

30. R. Ibbotson, Phys. Rev. Lett. **71**, 1990 (1993).

31. B. Buck, A. C. Merchant, and S. M. Perez, Phys. Rev. C **59**, 750 (1999).

32. W. Nazarewitcz *et al.*, Nucl. Phys. A **467**, 437 (1987).

33. B. Crowell *et al.*, Phys. Lett. B **333**, 320 (1994).

34. I. Ahmad and P. A. Butler, Annu. Rev. Nucl. Part. Sci. **43**, 71 (1993).

======================= **NUCLEI** =======================
Theory
===

Dineutron Configurations in Neutron-Excess Nuclei from the Viewpoint of the Diffraction Model

M. V. Evlanov, A. M. Sokolov, and V. K. Tartakovsky

National Center Institute for Nuclear Research, National Academy of Sciences of Ukraine,
pr. Nauki 47, UA-252028 Kiev, Ukraine

Received February 3, 1999; in final form, June 23, 1999

Abstract—Cross sections measured for the interactions of incident neutron-excess nuclei ^{6}He and ^{11}Li with other nuclei are analyzed in terms of expressions obtained for relevant integrated cross sections within the diffraction approximation. The results of this analysis suggest that there exists a dineutron configuration in the ^{6}He nucleus and that there is no such configuration in the ^{11}Li nucleus. On the basis of calculations performed for various observables, some new specific experiments are proposed for discovering dineutrons more reliably in nuclei having a neutron halo. © *2000 MAIK "Nauka/Interperiodica".*

1. INTRODUCTION

General theoretical considerations prove—and an analysis of numerous relevant experiments confirms this—that there does not exist a bound state of two neutrons [1]. Such a state could emerge, primarily in the singlet S state, upon a certain modification to the description of nucleon–nucleon forces. By convention, a bound state of two neutrons in this state is referred to as a dineutron. In principle, a dineutron can exist in some neutron-excess nuclei, where conditions necessary for this can be realized [2, 3].

In recent years, there have appeared a great number of experimental and theoretical studies that discuss the problem of the existence of a dineutron in peripheral regions of unstable nuclei having a sizable neutron halo [4–23]. It is obvious that there is much controversy about this problem: the relevant conclusions are frequently ambiguous and even sometimes contradictory. At present, it is hardly possible to indicate at least one nucleus where the presence of a dineutron has been established conclusively. In this connection, it is of interest to perform a theoretical analysis of relevant experimental data and to make predictions for dineutron configurations in nuclei within various approaches.

In the present study, we perform a theoretical analysis of some integrated observables of the fragmentation of two exotic nuclear species, ^{6}He and ^{11}Li, on nuclei within the diffraction model. Relying on this model, we compute the integrated reaction cross section σ_R and the cross section σ_{-2n} for the removal of two neutrons from the above two neutron-excess nuclear species and then conduct a comparison with relevant experimental data obtained in recent years [20, 21] and a discussion of the possible existence of a dineutron in the unstable nuclear species ^{6}He and ^{11}Li. In our analysis, we treat the exotic nuclei ^{6}He and ^{11}Li on the basis

of a two-cluster model (^{6}He $\longrightarrow$ $2n + {}^4$He, ^{11}Li $\longrightarrow$ $2n + {}^9$Li) where a hypothesized dineutron ($2n$) appears as one of the clusters. It is assumed here that the range of the interaction between this dineutron and the target nucleus, R_1, differs from the ranges R_2 of the interaction between the same target nucleus and the second clusters of the ^{6}He and ^{11}Li nuclei. Target nuclei are taken to be strongly absorbing objects, so that the profile function $\omega_j(\rho)$ for the jth cluster of the projectile nucleus ($j = 1, 2$) is taken in the form

$$\omega_j(\rho) = \begin{cases} 1, & \rho \le R_j \\ 0, & \rho > R_j, \end{cases} \qquad (1)$$

where ρ is the impact parameter and

$$R_j = r_0(A_j^{1/3} + A^{1/3}) \qquad (2)$$

is the range of the interaction between jth cluster containing A_j nucleons and the target nucleus whose mass number is A.

In the concluding section of the present article, we quote the results of our calculations for various integrated cross sections characterizing the diffractive and the Coulomb interaction between the incident ^{6}He nuclei and various target nuclei; discuss the dependences of these cross section (including the cross sections σ_R and σ_{-2n}) on the structure of the ^{6}He nucleus, on the mass number of the target nucleus, and on Coulomb interaction effects; and put forth some proposals for new experiments.

2. EXPRESSIONS FOR INTEGRATED CROSS SECTIONS IN THE DIFFRACTION APPROXIMATION

We begin by expressing the integrated reaction cross section σ_R and the cross section σ_{-2n} for the removal of

two neutrons from the projectile nucleus in terms of the known partial integrated cross sections for the diffractive interaction between a target nucleus and a projectile neutron-excess two-cluster nucleus [24–26] containing a hypothesized dineutron ($2n$) as one of the clusters. Each of the aforementioned two measurable cross sections can be broken down into the nuclear and Coulomb component as

$$\sigma_R = \sigma_R^N + \sigma_R^{\mathrm{Coul}}, \quad \sigma_{-2n} = \sigma_{-2n}^N + \sigma_{-2n}^{\mathrm{Coul}}. \quad (3)$$

Below, we present expressions for these individual components of either cross section, simultaneously describing physical processes contributing to the integrated cross sections σ_R and σ_{-2n}.

As a matter of fact, the nuclear component of the integrated reaction cross section, σ_R^N, is equal to the sum of the integrated cross sections for all inelastic processes within the two-cluster model being considered: the cross section σ_d^N for the diffractive breakup of the projectile nucleus into two fragments (clusters), one of these being a dineutron ($2n$); the cross section $\sigma_s^{(1)} = \sigma_s^{(2n)}$ for the stripping of the first cluster (dineutron) further absorbed by the target nucleus; the cross section $\sigma_s^{(2)}$ for the stripping of the second cluster further absorbed by the target nucleus; and the cross section σ_a for the full absorption of the projectile nucleus as a discrete unit. The cross section σ_R^N can also be represented as the difference between the total reaction cross section σ_{tot} and the integrated cross section σ_{el} for the elastic scattering of the projectile nucleus, so that, for a strongly absorbing target nucleus, the expression for σ_R^N has the form

$$\sigma_R^N = \sigma_{\mathrm{tot}} - 2\pi \int_0^\infty dq\, q$$

$$\times \left| \frac{R_1 J_1(qR_1)}{q} \Phi(-\beta_2 q) + \frac{R_2 J_1(qR_2)}{q} \Phi(\beta_1 q) \right. \quad (4)$$

$$\left. - \frac{R_1 R_2}{2\pi} \int d^{(2)}\mathbf{q}' \Phi(q') \frac{J_1(|\beta_1\mathbf{q} - \mathbf{q}'|R_1)}{|\beta_1\mathbf{q} - \mathbf{q}'|} \frac{J_1(|\beta_2\mathbf{q} + \mathbf{q}'|R_2)}{|\beta_2\mathbf{q} + \mathbf{q}'|} \right|^2$$

with

$$\sigma_{\mathrm{tot}} = 2\pi(R_1^2 + R_2^2)$$

$$- 4\pi R_1 R_2 \int_0^\infty \frac{dq}{q} \Phi(q) J_1(qR_1) J_1(qR_2). \quad (5)$$

Here, $\Phi(q)$ is the form factor associated with the projectile structure and given by

$$\Phi(q) = \int d\mathbf{r} \cdot \exp(-i\mathbf{q} \cdot \mathbf{r}) \varphi^2(r), \quad \Phi(0) = 1, \quad (6)$$

$\varphi(r)$ being the wave function of the bound state for the relative motion of the two clusters, and $\beta_1 = 1 - \beta_2 = \dfrac{M_1}{M_1 + M_2}$, M_1 and M_2 being the cluster masses.

The nuclear component of the cross section for the removal of the first cluster (dineutron) from the projectile nucleus is $\sigma_{-2n}^N = \sigma_d^N + \sigma_s^{(1)} = \sigma_R^N - (\sigma_a + \sigma_s^{(2)})$, where, for a strongly absorbing target nucleus, we have

$$\sigma_s^{(j)} = \pi R_j^2 - 2\pi R_1 R_2 \int_0^\infty \frac{dq}{q} \Phi(q) J_1(qR_1) J_1(qR_2)$$

$$\quad (7)$$

$$= \frac{1}{2}\sigma_{\mathrm{tot}} - \pi(R_1^2 + R_2^2 - R_j^2), \quad j = 1, 2.$$

Considering that, for a strongly absorbing target nucleus, $\sigma_a = \dfrac{1}{2}\sigma_{\mathrm{tot}} - \sigma_s^{(1)} - \sigma_s^{(2)}$, we eventually find that the cross section σ_{-2n}^N can be represented as

$$\sigma_{-2n}^N = \sigma_R^N - \left(\frac{1}{2}\sigma_{\mathrm{tot}} - \sigma_s^{(1)}\right) = \sigma_R^N - \pi R_2^2. \quad (8)$$

It is obvious that the Coulomb component of the integrated reaction cross section, σ_R^{Coul}, is equal to the Coulomb component of the cross section for the removal of two neutrons, $\sigma_{-2n}^{\mathrm{Coul}}$, each being equal to the sum of the integrated cross section for the Coulomb dissociation of the projectile nucleus into two fragments (clusters), σ_d^{Coul}, and the correcting term associated with the interference of the Coulomb and the nuclear dissociation of the projectile nucleus into two clusters. Considering that the first cluster (dineutron) is not charged, we find that, within the model that we use here—a strongly absorbing projectile nucleus—the Coulomb components σ_R^{Coul} and $\sigma_{-2n}^{\mathrm{Coul}}$ of the cross sections σ_R and σ_{-2n}, respectively, can be expressed as

$$\sigma_R^{\mathrm{C}} = \sigma_{-2n}^{\mathrm{C}} = \sigma_d^{\mathrm{C}} + \sigma_{\mathrm{int}} = \sigma_d^{\mathrm{C}} - 8\pi n \int_0^\infty \frac{dq}{q^2} \left\{ R_2 J_1(qR_2) \right.$$

$$\times [1 - \Phi^2(\beta_1 q)] + R_1 J_1(qR_1)[\Phi(q) - \Phi(\beta_1 q)\Phi(\beta_2 q)]$$

$$- \frac{qR_1 R_2}{2\pi} \int d^{(2)}\mathbf{q}' \frac{J_1(|\beta_1\mathbf{q} - \mathbf{q}'|R_1)}{|\beta_1\mathbf{q} - \mathbf{q}'|} \frac{J_1(|\beta_2\mathbf{q} + \mathbf{q}'|R_2)}{|\beta_2\mathbf{q} + \mathbf{q}'|} \quad (9)$$

$$\left. \times [\Phi(|\beta_1\mathbf{q} - \mathbf{q}'|) - \Phi(q')\Phi(\beta_1 q)] \right\}$$

$$\times \mathrm{Im}\left[\left(\frac{2}{qR_2}\right)^{2in} \frac{\Gamma(1 + in)}{\Gamma(1 - in)} - qR_2 \int_0^1 d\varsigma\, J_1(qR_2\varsigma)\varsigma^{2in} \right],$$

$$\sigma_d^C = 8\pi n^2 R_2^2 \int\limits_{q_{min}}^{\infty} \frac{dq}{q} [1 - \Phi^2(\beta_1 q)]$$

$$\times \left| \int\limits_{1}^{\infty} d\varsigma J_1(qR_2\varsigma)\varsigma^{2in} \right|^2, \qquad (10)$$

where $n = \dfrac{Z'Ze^2}{\hbar v}$, v being the relative velocity of the projectile nucleus having a charge $Z'e$ and the target nucleus having a charge Ze, and $q_{min} = \dfrac{\varepsilon}{\hbar v}\left(1 - \dfrac{v^2}{c^2}\right)^{1/2} \max(1, 4n)$ is the minimal momentum transfer [27, 28], ε being the binding energy of the projectile nucleus with respect to disintegration into two fragments (clusters)—in other words, the energy of dineutron removal from the projectile neutron-excess nucleus. Bringing together the individual terms (4), (8), and (9) and using the representations in (3), we obtain expressions for the cross sections σ_R and σ_{-2n} in the diffraction approximation within the model of a strongly absorbing target nucleus.

3. CALCULATION OF THE CROSS SECTIONS σ_R AND σ_{-2n} FOR THE PROJECTILE NUCLEUS ^{6}He AND ANALYSIS OF RELEVANT EXPERIMENTAL DATA

On the basis of the diffraction model being considered, we have calculated the cross sections σ_R and σ_{-2n} for the interaction of projectile nuclei ^{6}He with target nuclei ^{28}Si in the energy range between 13.7 and 55.6 MeV per projectile nucleon. This corresponds to the conditions of the experiments reported in [20, 21]. In the calculations, we used the Hulthén wave function $\varphi(r)$ for describing the relative motion of two neutrons and the alpha particle in the ^{6}He nucleus. In this function,

$$\varphi(r) = \sqrt{\frac{\alpha\beta(\alpha+\beta)}{2\pi(\beta-\alpha)^2}} \frac{\exp(-\alpha r) - \exp(-\beta r)}{r},$$

$$\alpha = \sqrt{\frac{2M_1M_2\varepsilon}{\hbar^2(M_1+M_2)}}, \qquad (11)$$

the binding energy ε of the ^{6}He nucleus with respect to disintegration into two clusters ($2n$ and α) was taken to be $\varepsilon = 0.975 \pm 0.040$ MeV in accordance with data reported in [29], while the parameter β was assumed to be $\beta = 7\alpha$ (in just the same way as for the deuteron), which reduces to $\beta \approx 1.75$ fm in our case. The parameter r_0 in (2) was set to $r_0 = 1.3$ fm.

According to (4), (5), (7), and (8), the cross sections for the diffractive nuclear interaction of two-cluster nuclei with strongly absorbing target nuclei are inde-

pendent of the projectile energy, and so are the nuclear components σ_R^N and σ_{-2n}^N of the cross sections σ_R and σ_{-2n}. It follows that, over the entire range of energies E indicated above, the cross sections that we computed for ^{6}He nuclei incident on ^{28}Si nuclei take the same values, which are the following:

$$\sigma_{tot} = 2.629 \text{ b}, \quad \sigma_e = 1.158 \text{ b},$$

$$\sigma_d^N = 0.157 \text{ b}, \quad \sigma_s^{(1)} \equiv \sigma_s^{(2n)} = 0.179 \text{ b}, \qquad (12)$$

$$\sigma_s^{(2)} \equiv \sigma_s^{(\alpha)} = 0.335 \text{ b}, \quad \sigma_a = 0.801 \text{ b};$$

$$\sigma_R^N = \sigma_d^N + \sigma_s^{(1)} + \sigma_s^{(2)} + \sigma_a$$

$$= \sigma_{tot} - \sigma_e = 1.472 \text{ b}; \qquad (13)$$

$$\sigma_{-2n}^N = \sigma_d^N + \sigma_s^{(1)} = 0.336 \text{ b}. \qquad (14)$$

From (9) and (10), it can be seen, however, that the Coulomb components σ_R^{Coul} and σ_{-2n}^{Coul} depend on the projectile energy E through the Coulomb parameter n and through q_{min}. Therefore, the theoretical cross sections $\sigma_R = \sigma_R^N + \sigma_R^C$ and $\sigma_{-2n} = \sigma_{-2n}^N + \sigma_{-2n}^C$ depend on the energy E through their Coulomb components σ_R^{Coul} and σ_{-2n}^{Coul}, which are equal to each other according to (9).

In the experiments reported in [20, 21], the cross sections σ_R and σ_{-2n} were measured as energy-averaged quantities in four finite intervals $\Delta E_k = E_2^k - E_1^k$, where E_1^k and E_2^k are, respectively, the minimal and the maximal energy for each of the intervals. Accordingly, the theoretical values of the cross sections $\sigma_R^C = \sigma_{-2n}^C$, σ_R, and σ_{-2n} were computed for four energy values equal to $\bar{E}_k = 1/2(E_1^k + E_2^k)$. The resulting theoretical values of σ_R and σ_{-2n} are quoted in Table 1, along with the measured cross sections σ_R^{expt} and σ_{-2n}^{expt} and errors in them.

By comparing the theoretical values found for the cross sections σ_R and σ_{-2n} with the corresponding experimental values σ_R^{expt} and σ_{-2n}^{expt}, we find that these are in good agreement for all four energy values $\bar{E}_k$. That the experimental energy dependences of the integrated reaction cross section and the cross section for the removal of two neutrons from the ^{6}He nucleus could be simultaneously described on the basis of the two-cluster (dineutron) model for the ^{6}He nucleus with a unified set of parameter values can be considered as strong evidence for the existence of a dineutron in the ground state of the ^{6}He nucleus. This conjecture is in accord with the conclusion drawn by Ter-Akopian *et al.* in [22], where experimental data obtained by those authors for the interaction of a secondary beam of ^{6}He ions with ordinary nuclei at an energy of 25 MeV per projectile nucleon were analyzed by other methods—

Table 1. Integrated cross sections σ_R and σ_{-2n} calculated on the basis of the dineutron model for the projectile nucleus ^{6}He along with experimental data for this nucleus from [20, 21]

k	E_1^k	E_2^k	$\bar{E}_k$, MeV/nucleon	σ_R, b	σ_R^{expt}, b	σ_{-2n}, b	$\sigma_{-2n}^{\text{expt}}$, b
1	13.7	29.0	21.35	1.63	1.59 ± 0.06	0.49	0.47 ± 0.06
2	29.0	39.5	34.25	1.60	1.62 ± 0.06	0.46	0.47 ± 0.05
3	39.5	48.1	43.80	1.58	1.54 ± 0.06	0.44	0.40 ± 0.04
4	48.1	55.6	51.85	1.57	1.67 ± 0.10	0.43	0.35 ± 0.15

namely, on the basis of the optical model and within the approximation of distorted waves.

Our analysis that was performed along similar lines and which dealt with the measured cross section $\sigma_{-2n}^{\text{expt}}$ for the removal of two neutrons from the ^{6}He nucleus in its interaction with a ^{12}C nucleus at the much higher (relativistic) energy of $E = 800$ MeV per projectile nucleon [30] also confirms the existence of a dineutron configuration in the ^{6}He nucleus. The integrated cross sections that we calculated for nuclear interaction at $r_0 = 1.15$ fm in (2) and at $\beta = \infty$ in (11) then assume the values

$$\sigma_{\text{tot}} = 1.427 \text{ b}, \quad \sigma_e = 0.611 \text{ b}, \quad \sigma_d^N = 0.103 \text{ b},$$

$$\sigma_s^{(1)} \equiv \sigma_s^{(2n)} = 0.089 \text{ b}, \quad \sigma_s^{(2)} \equiv \sigma_s^{(\alpha)} = 0.190 \text{ b}, \quad (15)$$

$$\sigma_a = 0.434 \text{ b}, \quad \sigma_{-2n}^N = \sigma_d^N + \sigma_s^{(2n)} = 0.192 \text{ b}.$$

The cross sections associated with Coulomb interaction proved to be quite small:

$$\sigma_d^C = 3.51 \times 10^{-3} \text{ b}, \quad \sigma_{\text{int}} = 2.07 \times 10^{-4} \text{ b},$$
$$\sigma_{-2n}^C = \sigma_d^C + \sigma_{\text{int}} = 3.72 \times 10^{-3} \text{ b}. \quad (16)$$

Thus, the theoretical value of the cross section $\sigma_{-2n} = \sigma_{-2n}^N + \sigma_{-2n}^N$ becomes (here, it nearly coincides with σ_{-2n}^N)

$$\sigma_{-2n} = 0.196 \text{ b}, \quad (17)$$

which complies well with the corresponding experimental value

$$\sigma_{-2n}^{\text{expt}} = 0.189 \pm 0.014 \text{ b}. \quad (18)$$

It should be noted that the parameter values used in calculating the cross sections in (15)–(17) are somewhat smaller than those in calculating the cross sections in (12)–(14) and in Table 1, where $E \sim 30$ MeV/nucleon. The value of the parameter r_0 in (2) and the wave function of the relative motion of the two clusters in the ^{6}He nucleus for zero-range nuclear forces ($\beta^{-1} = 0$) between the clusters are qualitatively justified because, at $E = 800$ MeV/nucleon, the linear dimensions of the region of nuclear interaction in the direction of the projectile momentum undergo a considerable FitzGerald–Lorentz contraction. The agreement between the calculated cross section σ_{-2n} and the corresponding experimental value $\sigma_{-2n}^{\text{expt}}$ is improved

considerably even upon taking this effect qualitatively into account, whereas there is not so good an agreement with experimental data [see (17) and (18)] at $r_0 = 1.3$ fm in (2) and $\beta = 7\alpha$ in (11).

4. CALCULATION OF THE CROSS SECTIONS σ_R AND σ_{-2n} FOR THE PROJECTILE NUCLEUS ^{11}Li AND COMPARISON WITH EXPERIMENTAL DATA

We have also performed here similar calculations of the cross sections σ_R and σ_{-2n} and of the partial contributions to them for neutron-excess nuclei ^{11}Li incident on target nuclei ^{28}Si at projectile energies E of 22.7 to 57.1 MeV per nucleon, which correspond to the experiment reported in [20]. In just the same way as for ^{6}He nuclei, the cross sections for ^{11}Li nuclei were measured as energy-averaged quantities in three finite intervals of energies E: (i) $22.7 \leq E \leq 37.1$ MeV/nucleon, (ii) $37.1 \leq E \leq 47.9$ MeV/nucleon, and (iii) $47.9 \leq E \leq 57.1$ MeV/nucleon. The cross sections were calculated for three midpoints of energies in these intervals. As for the ^{6}He nucleus, the Hulthén function (11) was used here to describe the relative motion of two neutrons and the ^{9}Li cluster in the projectile nucleus ^{11}Li, but the binding energy of the two neutrons and the ^{9}Li cluster ($2n + {}^9$Li) was set to the different value of $\varepsilon = 0.25 \pm 0.08$ MeV [31, 32] (naturally, the mass M_2 of the second cluster ^{9}Li was also different).

The cross sections σ_R and σ_{-2n} calculated for the case being discussed are displayed in Table 2 both for the structural-parameter value of $\beta = 7\alpha$ in (11) (lower row for each energy $\bar{E}_k$ in the table) and for $\beta = \infty$ (upper row for each $\bar{E}_k$), the latter corresponding to zero range of nuclear forces between the clusters ($2n$) and ^{9}Li. Without presenting numerical values calculated for the partial integrated cross sections, we only note a much more considerable weight of the Coulomb contribution $\sigma_d^{\text{Coul}} + \sigma_{\text{int}}$ to the cross sections σ_R and σ_{-2n} for projectile nuclei ^{11}Li in relation to the analogous contribution for projectile nuclei ^{6}He at nonrelativistic energies.

The cross sections quoted in Table 2 were calculated for the most popular binding-energy and r_0 values of $\varepsilon = 0.25$ MeV and $r_0 = 1.3$ fm, respectively, for which

Table 2. Integrated cross sections σ_R and σ_{-2n} calculated on the basis of the dineutron model for the projectile nucleus [11]Li along with experimental data for this nucleus from [20]

$\overline{E}_k$, MeV/nucleon	σ_R, b	σ_R^{expt}, b	σ_{-2n}, b	$\sigma_{-2n}^{\text{expt}}$, b
29.9	2.14	2.55 ± 0.10	0.74	0.47 ± 0.04
	2.45		1.06	
42.5	2.06	2.37 ± 0.10	0.67	0.39 ± 0.04
	2.34		0.95	
52.5	2.02	1.97 ± 0.10	0.63	0.38 ± 0.06
	2.28		0.89	

the theoretical values of the cross section σ_R at $\beta = 7\alpha$ in (11) provide the best fit to the corresponding experimental values σ_R^{expt} at all three (nonrelativistic) energies $\overline{E}_k$. From Table 2, it can be seen, however, that at none of the above three energy values do we have agreement between the computed cross section σ_{-2n} and the experimental cross section $\sigma_{-2n}^{\text{expt}}$ (they differ nearly by a factor of two). These cross sections were also calculated at the smaller r_0 value of $r_0 = 1.2$ fm but at the same binding energy of $\varepsilon = 0.25$. This leads to a decrease in the cross sections σ_R and σ_{-2n} with the result that the agreement of σ_R with σ_R^{expt} becomes poorer, σ_{-2n} still remaining much larger than $\sigma_{-2n}^{\text{expt}}$.

Since the binding energy ε of the [11]Li nucleus with respect to breakup into two fragments ($2n$ system and [9]Li nucleus) is known at present with large uncertainties ($0.17 \le \varepsilon \le 0.33$ MeV), we have also performed calculations here for the boundary values constraining the experimental binding energy (namely, for $\varepsilon = 0.17$ and 0.33 MeV) and for two values of the parameter r_0, 1.3 and 1.2 fm; as before, we considered the cases of $\beta = 7\alpha$ and $\beta = \infty$. At these values of the parameters ε, r_0, and β, the general pattern of deviations of the calculated cross sections from those that are observed shows no improvements in relation to data in Table 2. With increasing r_0, the cross sections σ_R and σ_{-2n} become larger over the entire range of the uncertainty in ε for all three energy values. With increasing ε, the cross sections σ_R and σ_{-2n} decrease, and so do they when we go over from $\beta = 7\alpha$ to $\beta = \infty$, irrespective of r_0 and $\overline{E}_k$. At the extreme right (maximum) value of the uncertainty interval for ε ($\varepsilon = 0.33$ MeV) and $r_0 = 1.2$ fm, the calculated cross section σ_{-2n} approaches the observed cross section $\sigma_{-2n}^{\text{expt}}$, but the former still considerably exceeds the latter. If a dineutron were present in the composition of the [11]Li nucleus, we could conclude that the binding energy ε is closer to the maximal value of $\varepsilon = 0.33$ MeV.

In all the preceding cases, the parameter β in the wave function (11) of the [11]Li nucleus was set to 7α or ∞. In order to visualize better the effect exerted by the details of the structure of the [11]Li nucleus on the behavior of the cross sections σ_R and σ_{-2n}, we have calculated these cross sections for $\beta < 7\alpha$ as well. As the parameter β was reduced to $\beta \approx \alpha$, the cross sections σ_R and σ_{-2n} increased with the result that the deviations from experimental data became more pronounced than in the data from Table 2.

Thus, the observed cross sections σ_R^{expt} and $\sigma_{-2n}^{\text{expt}}$ for projectile [11]Li nuclei could not be simultaneously described within the two-cluster dineutron model of the [11]Li nucleus if the structural and interaction parameters are allowed to vary only within reasonable limits. This seems to suggest the absence (or a very low probability) of a dineutron configuration in the [11]Li nucleus, in accord with the conclusions drawn in [12, 13, 16, 17] and with a somewhat naive qualitative consideration according to which the lower probability for the emergence of a dineutron cluster in the [11]Li nucleus than in the [6]He nucleus is due to the much lower binding energy ε of two neutrons in [11]Li than in [6]He—that is, the $2n$ system in [11]Li is nearly free and cannot be bound [1, 33].

We note that, for more reliably studying the problem of whether a dineutron is absent or present in the [11]Li nucleus, as well as in other nuclei having a neutron halo, it would be desirable to measure and analyze the cross sections for the elastic scattering and the diffractive disintegration of exotic [11]Li nuclei on nuclei, as well to explore polarizations in such processes. A theoretical consideration of allied problems within the diffraction approximation was given in our earlier study [34].

5. DEPENDENCE OF INTEGRATED CROSS SECTIONS ON THE PROPERTIES OF TARGET NUCLEI AND THEIR STRUCTURE

In order to draw more reliable conclusions on the existence of dineutron configurations in neutron-excess nuclei, it is important to have experimental information about the interaction of beams of such nuclei with various target nuclei, both light and heavy ones. In this connection, we deemed it worthwhile to analyze, in the diffraction approximation, the cross sections σ_R and σ_{-2n} and the partial integrated cross sections for the interaction between $E = 30$ MeV/nucleon projectile nuclei [6]He treated on the basis of the two-cluster ($2n + \alpha$) model and various target nuclei from carbon to uranium, thereby tracing, in particular, the dependence of the cross sections on the mass number A and the charge number Z of the target nucleus.

The results of our calculations underlying such an analysis are displayed in Tables 3 and 4. The calculations were performed by using the wave function (11) both with $\beta = 7\alpha$ and with $\beta = \infty$ (respectively, the sec-

Table 3. Cross sections for the interaction of 30-MeV/nucleon projectile nuclei with various target nuclei (for each target-nucleus species, the results in the first and in the second row were obtained with the zero-range potential and the Hulthén potential, respectively)

Nucleus	σ_d^N, b	$\sigma_s^{(2n)}$, b	$\sigma_s^{(\alpha)}$, b	σ_a, b	σ_R, b	σ_{-2n}, b
$^{12}_{6}$C	0.1195	0.0982	0.2273	0.5706	1.0382	0.2403
	0.1387	0.1467	0.2758	0.5222	1.1174	0.3194
$^{28}_{14}$Si	0.1334	0.1201	0.2752	0.860	1.4771	0.3419
	0.1570	0.1795	0.3346	0.8006	1.6046	0.4694
$^{64}_{29}$Cu	0.1660	0.1479	0.3365	1.3210	2.2693	0.6118
	0.1917	0.2211	0.4097	1.2478	2.5175	0.860
$^{112}_{48}$Cd	0.1833	0.1712	0.3884	1.7916	3.2180	1.0380
	0.2140	0.2562	0.4733	1.7066	3.6718	1.4919
$^{181}_{73}$Ta	0.2128	0.1951	0.4413	2.3449	4.4759	1.6897
	0.2441	0.2917	0.5379	2.2482	5.2282	2.4421
$^{208}_{82}$Pb	0.2175	0.2026	0.4581	2.5382	4.9408	1.9445
	0.2502	0.3031	0.5586	2.4377	5.8102	2.8139
$^{238}_{92}$U	0.2241	0.2103	0.4753	2.7421	5.5403	2.3229
	0.2577	0.3146	0.5796	2.6378	6.5714	3.3540

Table 4. Nuclear and Coulomb components of the cross sections σ_{-2n} and σ_R for the interaction of 30-MeV/nucleon projectile nuclei ^{6}He with various target nuclei (for each target-nucleus species, the results in the first and in the second row were obtained with the delta-function potential and the Hulthén potential, respectively)

Nucleus	σ_R^N, b	σ_{-2n}^N, b	$\sigma_R^C = \sigma_{-2n}^C$, b
$^{12}_{6}$C	1.0156	0.2177	0.0226
	1.0834	0.2854	0.0340
$^{28}_{14}$Si	1.3887	0.2535	0.0884
	1.4717	0.3365	0.1329
$^{64}_{29}$Cu	1.9713	0.3138	0.2980
	2.0703	0.4128	0.4472
$^{112}_{48}$Cd	2.5344	0.3544	0.6836
	2.650	0.4701	1.0218
$^{181}_{73}$Ta	3.1940	0.4078	1.2819
	3.3220	0.5359	1.9062
$^{208}_{82}$Pb	3.4164	0.4201	1.5244
	3.5497	0.5534	2.2605
$^{238}_{92}$U	3.3652	0.4344	1.8885
	3.7898	0.5724	2.7816

ond and the first row for each target-nucleus species). The choice of the wave function $\varphi(r)$ has a much stronger effect on the cross section σ_{-2n} for all target nuclei than on the cross section σ_R. Changes in the parameter β appearing in (11) affect σ_R much more pronouncedly for heavy target nuclei than for light ones. The cross sections σ_R and σ_{-2n} both increase monotonically with increasing A and Z. However, this increase is much slower than the corresponding growth of the cross section σ_d^{Coul} for the Coulomb dissociation of a ^{6}He nucleus into a hypothesized dineutron and an alpha particle: in the mass-number range $12 \leq A \leq 238$, the cross section σ_d^{Coul} grows by more than two orders of magnitude, while the σ_d^N grows only by a factor of 2, σ_R and σ_{-2n} concurrently growing by a factor of 6.5 and by a factor of 14, respectively. In just the same way as σ_{-2n}, the partial cross sections σ_d^{Coul} and $\sigma_s^{(2n)}$ reveal the highest sensitivity to the internal structure [that is, to the choice of the function $\varphi(r)$]; by separately measuring the last two cross sections, it would therefore be possible to obtain deeper insights into the structure of the ^{6}He nucleus and into the problem of the existence of a dineutron in the ^{6}He nucleus (as well as in other nuclei having a neutron halo).

The individual contributions of the nuclear and Coulomb components to the cross sections are quoted in Table 4. We can see that the nuclear-component contribution σ_R^N to the cross section σ_R exceeds noticeably the Coulomb contribution σ_R^{Coul} for all target-nucleus species, but that the nuclear-component contribution σ_{-2n}^N to the cross section σ_{-2n} is dominant only for light target nuclei; from $Z \approx 30$ nuclei—and especially for heavy nuclei—the Coulomb component σ_{-2n}^C is everywhere much larger than the nuclear component σ_{-2n}^N.

It should be noted that, in the study of Warner [21], who calculated the cross section σ_{-2n} for the removal of two neutrons from nonrelativistic ^{6}He nuclei (of energy 30 MeV per projectile nucleon) interacting with various target nuclei and who relied, in that calculation, on a method different from ours, the contribution of the nuclear component to σ_{-2n} proved to be larger than our results in Table 4. It was concluded in [21] that, even for the heaviest target nuclei, the nuclear component in the cross section σ_{-2n} is sizable, if not dominant, whereas, in our calculations, the Coulomb contribution to the cross section σ_{-2n} is much larger than the nuclear contribution for heavy target nuclei. Only at sufficiently high energies can the nuclear contribution dominate the

cross section σ_{-2n}—and not only for heavy target nuclei [as can be seen from (15)–(17)]—and this is quite natural. In all probability, only experiments will be able to give an unambiguous answer to the question of which component—the Coulomb or the nuclear one—makes the main contribution to the cross section σ_{-2n} for heavy target nuclei.

6. SUMMARY AND CONCLUDING COMMENTS

Within the diffraction nuclear model, we have proposed general expressions describing the integrated reaction cross section σ_R and the cross section σ_{-2n} for the removal of two neutrons from two-cluster neutron-excess nuclei featuring a hypothesized dineutron as one of the clusters. It is assumed in this approach that the range of dineutron interaction with a strongly absorbing target nucleus, R_1, differs from the range R_2 of the interaction between the second cluster with the same nucleus. Within the diffraction approximation, the integrated reaction cross section σ_R and the cross section σ_{-2n} for the removal of two neutrons from the ^{6}He nucleus have been calculated for the interaction of intermediate- and high-energy ^{6}He nuclei with ^{28}Si and ^{12}C nuclei. That the results of these calculations has proved to comply well with experimental data suggests the two-cluster structure of the ^{6}He nucleus and, possibly, the existence of a dineutron in it.

A similar analysis of the measured cross sections σ_R^{expt} and $\sigma_{-2n}^{\text{expt}}$ for exotic nuclei ^{11}Li incident on ^{28}Si nuclei seems to indicate that there is no dineutron configuration in the neutron-excess nucleus ^{11}Li.

Our conclusions on the structure of the neutron halo in the ^{6}He and in the ^{11}Li nucleus are consistent with the results of some experimental and theoretical studies recently performed on the subject.

The present calculations of the cross sections σ_R and σ_{-2n} and of the partial integrated cross sections for diffractive interactions of ^{6}He nuclei with various target nuclei from carbon to uranium have revealed the dependence of these cross sections on the mass number and on the charge number of target nuclei; a strong effect of the structure of the ^{6}He nucleus on the cross section σ_{-2n} and on the partial cross sections for Coulomb dissociation, σ_d^{Coul} and for the stripping of a hypothesized dineutron, $\sigma_s^{(2n)}$; and a dominance of the Coulomb component $\sigma_{-2n}^{\text{Coul}}$ in the cross section σ_{-2n} for heavy target nuclei at nonrelativistic energies of projectile nuclei ^{6}He.

To conclude, we emphasize once again that the simple model used here cannot provide an unambiguous answer to the question of whether a dineutron is present or absent in the exotic nuclei ^{6}He and ^{11}Li. Within one model of the nucleus or another, we can only evaluate the probability of finding a dineutron configuration—

or, more specifically, its weight in the total wave function of the nucleus being studied. In order to arrive at a firmer (possibly, unambiguous) solution to the problem of the existence of dineutrons (more precisely, to assess the numerical value of a noticeable or even a dominant probability of their existence) in some neutron-excess nuclei, it is therefore necessary to perform a detailed analysis of a wider set of both available and future experiments, including correlation measurements, by invoking better substantiated models of nuclear structure and interactions. In this respect, models used in [14, 19], for example, may be of considerable interest. It is worth noting that new pieces of evidence for a dominant probability of the dineutron configuration in the ^{6}He nucleus appeared [35, 36] when the present article was submitted for publication.

REFERENCES

1. A. I. Baz', V. I. Gol'danskiĭ, V. Z. Gol'dberg, and Ya. B. Zel'dovich, *Light and Medium-Mass Nuclei near the Nucleon Drip Line* (Nauka, Moscow, 1972).
2. A. B. Migdal, Yad. Fiz. **16**, 427 (1972) [Sov. J. Nucl. Phys. **16**, 238 (1972)].
3. P. G. Hansen and B. Jonson, Europhys. Lett. **4**, 409 (1987).
4. I. Tanihata, Nucl. Phys. A **488**, 113 (1988).
5. C. A. Bertulani and G. Baur, Phys. Rep. **163**, 299 (1988).
6. T. Kobayashi *et al.*, Phys. Lett. B **232**, 51 (1989).
7. I. Tanihata, Nucl. Phys. A **522**, 275 (1991).
8. C. A. Bertulani *et al.*, Nucl. Phys. A **526**, 751 (1991).
9. A. S. Jensen and K. Riisager, Nucl. Phys. A **537**, 45 (1992).
10. H. Esbensen and G. F. Bertsch, Phys. Rev. C **46**, 1552 (1992).
11. W. Mittig, Nucl. Phys. A **538**, 609 (1992).
12. D. Sackett *et al.*, Phys. Rev. C **48**, 118 (1993).
13. K. Ieki *et al.*, Phys. Rev. Lett. **70**, 730 (1993).
14. M. V. Zhukov *et al.*, Phys. Rep. **231**, 151 (1993).
15. S. Shimoura *et al.*, Phys. Lett. B **348**, 29 (1995).
16. B. G. Harvey, Phys. Rev. C **54**, 1520 (1996).
17. K. Ieki *et al.*, Phys. Rev. C **54**, 1589 (1996).
18. M. V. Evlanov, A. M. Sokolov, and V. K. Tartakovsky, Yad. Fiz. **59**, 679 (1996).
19. B. V. Danilin *et al.*, Izv. Akad. Nauk, Ser. Fiz. **60** (1), 28 (1996).
20. R. E. Warner *et al.*, Phys. Rev. C **54**, 1700 (1996).
21. R. E. Warner, Phys. Rev. C **55**, 298 (1997).
22. G. M. Ter-Akopian *et al.*, in *Proceedings of the International Conference on Nuclear Physics, Moscow, June 16–19, 1998*, p. 203; Phys. Lett. B **426**, 251 (1998).
23. D. V. Aleksandrov *et al.*, in *Abstracts of Papers Presented at the 48th Conference on Nuclear Spectroscopy and Nuclear Structure, Moscow, June 16–19, 1998*, p. 230.
24. A. G. Sitenko, *Theory of Nuclear Reactions* (World Sci. Singapore, 1990).

25. M. V. Evlanov, in *Proceedings of the 3rd International School on Nuclear Physics, Kiev, 1992*, Vol. 1, p. 183.

26. M. V. Evlanov and A. M. Sokolov, Yad. Fiz. **56** (10), 88 (1993) [Phys. At. Nucl. **56**, 1351 (1993)].

27. M. V. Evlanov, A. M. Sokolov, and V. K. Tartakovsky, JINR Rapid Commun., No. 4-78, 33 (1996).

28. M. V. Evlanov, A. M. Sokolov, and V. K. Tartakovsky, Yad. Fiz. **60**, 444 (1997) [Phys. At. Nucl. **60**, 373 (1997)].

29. F. Ajzenberg-Selove, Nucl. Phys. A **490**, 1 (1988).

30. T. Kobayashi *et al.*, Phys. Rev. Lett. **60**, 2599 (1988).

31. C. Thibault *et al.*, Phys. Rev. C **12**, 644 (1975).

32. J. M. Wouters *et al.*, Z. Phys. A **331**, 229 (1988).

33. L. D. Landau and E. M. Lifshitz, *Quantum Mechanics: Non-Relativistic Theory* (Fizmatgiz, Moscow, 1963; Pergamon, Oxford, 1977, 3rd ed.).

34. M. V. Evlanov, A. M. Sokolov, and V. K. Tartakovskii, Yad. Fiz. **58**, 1010 (1995) [Phys. At. Nucl. **58**, 937 (1995)].

35. R. Wolsky *et al.*, in *Abstracts of Papers Presented at the 49th Conference on Nuclear Spectroscopy and Nuclear Structure, Dubna, April 21–24, 1999*, p. 274.

36. Yu. Ts. Oganessian *et al.*, in *Proceedings of the International Conference on Nuclear Physics, Dubna, April 21–24, 1999*, p. 275; Yu. Ts. Oganessian, V. I. Zagrebaev, and J. S. Vaagen, Phys. Rev. C **60**, 044605 (1999).

Translated by A. Isaakyan

<center>

NUCLEI
Theory

</center>

Collective Excitations in Neutron-Rich Nuclei within the Model of a Fermi Liquid Drop*

V. M. Kolomietz and A. G. Magner**

Institute for Nuclear Research, National Academy of Sciences of Ukraine, pr. Nauki 47, Kiev, 252028 Ukraine
Received June 23, 1999; August 10, 1999

Abstract—We discuss a new mechanism of splitting of giant multipole resonances (GMR) in spherical neutron-rich nuclei. This mechanism is associated with the basic properties of an asymmetric drop of nuclear Fermi liquid. In addition to well-known isospin shell-model predictions, our approach can be used to describe the GMR splitting phenomenon in the wide nuclear-mass region $A \sim 40$–240. For the dipole isovector modes, the splitting energy, the relative strength of resonance peaks, and the contribution to the energy-weighted sum rules are in agreement with experimental data for the integrated cross sections for photonuclear (γ, n) and (γ, p) reactions. © 2000 MAIK "Nauka/Interperiodica".

1. INTRODUCTION

Giant-dipole-resonance (GDR) splitting observed in isospin-conjugated photonuclear (γ, n) and (γ, p) reactions is often explained as a phenomenon of nuclear asymmetry within the isospin shell model (ISM) [1–4]. The ISM predicts a shift of the main peak in the (γ, xp) cross section with respect to the (γ, xn) cross section to higher energies. The ISM estimates of the GDR splitting and the relative strengths of the two resonances are confirmed quite well by experimental data in a wide region of light and medium-mass spherical nuclei (see [3, 5–10]). Another deformation splitting leads to the double-bump GDR structure in deformed heavy nuclei like rare earth and actinide nuclei with approximately identical strengths of the two peaks. It was intensively studied in the photonuclear and inelastic-electron-scattering reactions (see [4, 7, 9, 11]) and can be explained theoretically within the dynamical collective model (DCM) [12].

However, the splitting of giant resonances into two or more peaks is a very general effect observed for each kind of above reactions. We encounter such GDR splittings in many nearly spherical neutron-rich nuclei like ^{48}Ca, ^{58}Ni, and several Sn isotopes [2, 4], irrespective of their masses and of the reaction type. Sometimes, the splitting or the double-resonance structure is not so pronounced as in the classical example of the deformed nuclei $^{152, 154}$Sm, but it can be seen through the asymmetry of the GDR maximum with an enhancement of the cross section on the right slope of the main peak. As an example, we can mention the excitation of the GDR in the spherical-like isotopes $^{146, 148, 150}$Sm [11] or the exactly spherical nucleus ^{208}Pb [4]. Even for these cases, the splitting of the GDR can be established on the basis of a fit of the cross section in terms of two Lorentzian (or Breit–Wigner) peaks with a much smaller relative strength of

the right maximum in contrast to the DCM prediction for deformed nuclei. Thus, there is a general phenomenon of a satellite near the main peak in the GDR strength, irrespective of the deformation, the nuclear mass, or the reaction type. In particular, a similar splitting was recently found in a random-phase-approximation (RPA) calculation of the GDR (see, for instance, [13]).

In the present study, we propose a much more general explanation of the splitting of both the isoscalar and the isovector modes in spherical neutron-rich nuclei within the model of a Fermi liquid drop (FLD model, also referred to as FLDM) [14, 15]. This model, based on Landau kinetic theory [16], was extended to two-component asymmetric nuclei in [17]. In our semiclassical approach, RPA or time-depend Hartree–Fock (TDHF) theories for small amplitudes are simplified significantly by using the linearized Landau–Vlasov equation within the nucleus and simple macroscopic boundary conditions on its surface [18, 19]. Although our approach is quite general, we restrict ourselves to applying it to the collision-free and zero-temperature case, using GDR splitting as an example to represent a final result.

2. ASYMMETRIC MODEL OF A NUCLEAR FERMI LIQUID DROP

2.1. Equations of Motion inside the Nucleus

The linearized collision-free Landau–Vlasov equation for a two-component (neutron–proton) Fermi liquid has the form

$$\frac{\partial}{\partial t}\delta f_{\tau}(\mathbf{r}, \mathbf{p}, t) + \frac{\mathbf{p}}{m}\nabla_r \left[\delta f_{\tau}(\mathbf{r}, \mathbf{p}, t) \right.$$

$$\left. + \delta(\varepsilon - \varepsilon_{\mathrm{F}}^{\tau})\left(\frac{\pi^2 \hbar^3}{2m}\sum_{\tau'}\frac{F_{\tau\tau'}}{p_{\mathrm{F}}^{\tau'}}\delta\rho_{\tau'} + V_{\mathrm{ext}}^{\tau} \right) \right] = 0, \quad (1)$$

where $\delta f_\tau(\mathbf{r}, \mathbf{p}, t)$ is a deviation from the equilibrium Fermi distribution; m the nucleon mass; τ the isotopic index, $\tau = \left\{ \begin{array}{c} p \\ n \end{array} \right\}$; and $\delta\rho(\mathbf{r}, t)$ is the dynamical particle-density component. The external field V_{ext}^τ will be specified below. For the sake of simplicity, the Landau scattering amplitudes $F_{\tau\tau'}$ in equation (1) are assumed to be isotropic, although the main results will be presented below for a more general case.

We will first consider the eigenvibration problem without an external field V_{ext}. The main idea is to take into account the difference between the proton and neutron Fermi energies ε_F^τ, $\varepsilon_F^\tau = (p_F^\tau)^2/2m = \varepsilon_F(1 \mp \Delta)$, where $\Delta = (4/3)(1 + F')X$, $X = (N - Z)/A$, in the linear approximation in parameter Δ [20]. We use the following notation: $F = (F_{pp} + F_{pn})/2$, $F' = (F_{pp} - F_{pn})/2$, and $A = N + Z$ ($F = 2f$ and $F' = 2f'$ in the notation used in [20]) We seek solutions to equations (1) with a given multipole order L of the vibrations in $\mathbf{r}$ space in the form [14, 15, 21]

$$\delta f_\tau(\mathbf{r}, \mathbf{p}, t) = \delta(\varepsilon - (p_F^\tau)^2/2m)\int d\Omega_\mathbf{q} \nu_\tau Y_{L0}(\hat{q})e^{i(\mathbf{q}\cdot\mathbf{r} - \omega t)},$$
$$\hat{q} = \mathbf{q}/q \tag{2}$$

with frequency $\omega = v_F^\tau s_\tau q = v_F s q$, where $v_F^\tau = p_F^\tau/m$, $s_\tau = s(1 \pm \Delta/2)$, and s is the dimensionless speed of sound (see below).

Substituting Eq. (2) into (1), we perform integration with respect to the angles Ω of the momentum $\mathbf{p}$ and neglect all nonlinear terms in Δ. For the sound-velocity eigenvalues s, one finally obtains the dispersion relation $(Q_1(s) - 1/F)(Q_1(s) - 1/F') = 0$ and then the ratio $\delta\rho_p/\delta\rho_n$ of the densities $\delta\rho_\tau$ defined in terms of the zero $\mathbf{p}$ moments of the distribution-function amplitudes ν_τ, $\delta\rho_\tau \propto \int d\Omega\,\nu_\tau$. The solution to the dispersion equation for s is split into two branches of the sound-wave propagation with speeds s_1 and s_2 given by[1]

$$Q_1(s) = \frac{1}{F}\left(1 + \frac{F_1 s^2}{FG_1}\right)^{-1} \quad \text{for } s_1,$$
$$Q_1(s) = \frac{1}{F'} \quad \text{for } s_2, \tag{3}$$

where $Q_1(s)$ is the Legendre function of the second kind. For each root s_n of Eqs. (3), it is convenient to transform the ratio of the above particle densities $\delta\rho_\tau$ to

those for the isoscalar (+) and isovector (–) modes $\delta\rho_\pm = \delta\rho_p \pm \delta\rho_n$. In this way, we obtain

$$\frac{\delta\rho_-}{\delta\rho_+} = \frac{2F'[s_1^2(1 + F) - 1]}{(F' - F)(s_1^2 - 1)}\Delta,$$
$$\frac{\delta\rho_+}{\delta\rho_-} = \frac{2F[s_2^2(1 + F') - 1]}{(F - F')(s_2^2 - 1)}\Delta \tag{4}$$

for s_1 and s_2, respectively. We note that the expansion in the small parameter Δ used here can be justified for sufficiently large $F - F'$, as can be seen from Eqs. (4), where such differences appear in the denominators. However, our approach is applied to nuclear matter for which the quantity F is in fact much smaller than F'. As can be seen from Eqs. (4), the solution s_1 leads to a purely isoscalar mode with $\delta\rho_- = 0$ and $\delta\rho_+ \neq 0$ in the limit of the symmetric nuclei with $N = Z$—that is, $\Delta = 0$; at the same time, s_2 gives a purely isovector mode with $\delta\rho_+ = 0$ and $\delta\rho_- \neq 0$ (at $N = Z$). In the asymmetrical case ($\Delta \neq 0$), each sound wave with a certain velocity s_n obtained from Eqs. (3) is associated both with isoscalar and with isovector density excitations $\delta\rho_\pm$, according to Eqs. (4). We emphasize that, in this case, the isovector vibrations described by the density $\delta\rho_- \neq 0$, for instance, include the both s_1 and s_2 sound waves and that the same is true for the isoscalar modes with $\delta\rho_+ \neq 0$. However, Eqs. (4) show that the isovector density variation $\delta\rho_-$ for the s_1 velocity branch is much smaller than that for the s_2 one for a small Δ, in contrast to the isoscalar density $\delta\rho_+$, for which the s_1 solution is dominant.

2.2. Boundary Conditions

Collective dynamics near the nuclear edge is much more complicated because of a sharp change in the mean potential, so that the simple semiclassical Landau–Vlasov equations (1) cannot be applied there. Instead, we will augment the volume equation of motion (1) by the boundary conditions at the sharp nuclear surface. Following [18, 19], we define the time-dependent proton and neutron surfaces as the density gradient maxima at $r = R_\tau \equiv R_0 + \delta R_\tau(\hat{r}, t)$, where $\delta R_\tau(\hat{r}, t) = R_0 \alpha_s^\tau(t)Y_{L0}(\hat{r})$ describes the local displacement of the surface from its equilibrium position, $r = R_0$, and $\alpha_s^\tau(t)$ is a small amplitude of the surface vibrations. Using the effective surface approximation $a/R_\tau \approx A^{-1/3} \ll 1$ (a is the diffuseness parameter of the particle density profile) and integrating the equations of motion through the relatively small surface region, the boundary condition can be derived in the following form (see details in [18, 19]):

$$u_r^\pm|_{r = R_0} = R_0\dot{\alpha}_s^\pm Y_{L0}(\hat{r}), \quad \delta\Pi_{rr}^\pm|_{r = R_0} = \alpha_s^\pm\overline{\mathscr{P}}_s^\pm Y_{L0}(\hat{r}), \tag{5}$$

___

[1]For the sake of completeness, we recovered here the scattering-amplitude anisotropy in terms of the Landau constant F_1 for the simplest case of the effective mass m_τ^* independent of the isotopic index τ, $m^* = m_\tau^* = mG_1$, $G_1 = 1 + F_1/3$.

where the velocity field $\mathbf{u}^\pm(\mathbf{r}, t)$ and the momentum flux tensor $\delta\Pi^\pm_{\nu\mu}$ are determined in terms of the first and second $\mathbf{p}$ moments of the distribution function $\delta f^\pm(\mathbf{r}, \mathbf{p}, t)$ (see [14, 17]). The surface pressure tensor $\overline{\mathcal{P}}^\pm_s$ in equation (5) is given by

$$\overline{\mathcal{P}}^+_s = \frac{b^+_s \bar{\rho}}{3A^{1/3}}(L-1)(L+2), \quad \overline{\mathcal{P}}^-_s = \frac{1}{3}b^-_s \bar{\rho} A^{1/3}, \quad (6)$$

where $\bar{\rho} = 3/4\pi r_0^3$, $R_0 = r_0 A^{1/3}$, and $b^\pm_s$ are the surface-energy interaction constants, ($b^+_s = 4\pi r_0^2 \sigma^+_s$ and $b^-_s = 4\pi r_0^4 \sigma^-_s$), which are related to the diagonal elements of the surface tension coefficient 2×2 matrix, while $\sigma_\pm \approx 2\beta_\pm \int_0^\infty dr (\partial\rho_\pm/\partial r)^2$ as in the one-component case [22]. The constants $\beta_\pm$ related to the particle-density gradient terms of the energy density in the nuclear equation of state [17] will be considered here as free parameters. We neglect here small nondiagonal components of the surface tension matrix which are proportional to the asymmetry parameter $(N - Z)/A$.

3. SPLITTING OF GIANT MULTIPOLE RESONANCES

3.1. Secular Equations

Substituting the $\mathbf{p}$ moments of the distribution function $\delta f_\tau(\mathbf{r}, \mathbf{p}, t)$ (2) into the boundary conditions (5), one gets the isoscalar solution (+) which satisfies equations (5) at $\alpha^-_s = 0$, $\alpha^+_s \neq 0$, and the isovector one (–) for $\alpha^-_s \neq 0$, $\alpha^+_s = 0$. As noted above, each kind of vibrations are obtained in terms of the two eigenmodes with the eigenfrequencies $\omega^{(1)}_{L,+}$ and $\omega^{(2)}_{L,+}$ for the isoscalar excitation and $\omega^{(1)}_{L,-}$ and $\omega^{(2)}_{L,-}$ for the isovector one.

For brevity, we shall show our basic results for the isovector vibrations only. For the eigenfrequencies $\omega^{(n)}_{L,-}$ ($n = 1, 2$), we arrive at the secular equations:

$$\mathcal{D}^{(n)}_L(\omega) \equiv j'_L(qR_0)$$
$$- \frac{3}{2}\xi qR_0[c^{(n)}_1 j''_L(qR_0) + c^{(n)}_2 j_L(qR_0)] = 0, \quad (7)$$

where j_L and j'_L are the spherical Bessel functions and their derivatives, $\xi = \varepsilon_F/(b^-_s A^{1/3})$ and $\omega^{(n)}_{L,-} = v_F s_n q^{(n)}_L$. The coefficients $c^{(n)}_i$ in Eqs. (7) read

$$c^{(1)}_1 = \{\mathcal{R}[1 - F'(3s_1^2/Q_1 - 1)]$$
$$+ (Q_1 - F')[3s_1^2(Q_1 - \Delta_s)$$
$$+ [3s_1^2 F/Q_1 - 3(Q_1 + 1) + Q_1 - F]\Delta_s\}/c,$$

$$c^{(1)}_2 = \{\mathcal{R}[1 - F'(s_1^2/Q_1 + 1/3)] \quad (8)$$
$$+ (Q_1 - F')[s_1^2(Q_1 - \Delta_s)$$
$$- [2Fs_1^2/Q_1 + 3(Q_1/3 - \Delta_s)$$
$$+ (Q_1 - F)(3s_1^2/Q_1 - 1/3) - 2F]\Delta_s\}/c,$$
$$c^{(2)}_1 = 1 - 3s_2^2 + F', \quad c^{(2)}_2 = 1 - s_2^2 + F',$$

where $c = G_1\{F'\mathcal{R} + [Q_1\Delta_s(1 + 1/G_1) + \mathcal{R}](Q_1 - F')\}/Q_1$, $\mathcal{R} = (2Q_1 - F)\Delta_s - Q_1^2$, and $\Delta_s = s_1^2 - 1$.

In the case of the dipole isovector excitations, $L = 1$, the energy splitting $\hbar(\omega^{(1)} - \omega^{(2)})$ can be roughly estimated from the secular Eqs. (7) expanding the spherical Bessel functions in power series (we omit the low indices L, – or some of them for simplicity). For realistic interaction parameters F and F', we can take approximately $s_1 \approx s_2 \approx 1$ and obtain finally,

$$\hbar\omega^{(1)} \approx \hbar\Omega\sqrt{\frac{10}{3(1 + 2\xi(9 - 7F')/3G_1)}},$$
$$\hbar\omega^{(2)} \approx \hbar\Omega\sqrt{\frac{10}{3(1 + 2\xi(3 + F'))}}, \quad (9)$$

where $\Omega = v_F/R_0 \approx \varepsilon_F/A^{1/3}\hbar$. The resonance energies $\hbar\omega^{(n)}$ (9) are proportional mainly to $A^{-1/3}$ through $\hbar\Omega$, but the quantity $\hbar\omega^{(1)} \times A^{1/3}$ increases slowly with A because of the additional $A^{-1/3}$ dependence of ξ in equations (9). We point out that such kind of A dependence of the isovector GDR energies agrees with the experimental data (see Fig. 1). Using the expansion in ξ in Eqs. (9) for large atomic number A and $G_1 = 1$, one obtains from Eqs. (9) a simpler estimate for the energy splitting, $\hbar(\omega^{(1)} - \omega^{(2)}) \approx (10/3)^{3/2}\varepsilon_F^2 F'/b^-_s A^{2/3}$. The latter diminishes with the atomic number A and the surface tension parameter b^-_s or with a decrease in the Landau interaction constant F'. This means that the splitting effect in our FLDM depends significantly on the effective volume (F') and surface (b^-_s) isovector interactions and does not depend on the neutron excess $N - Z$. These results show a new GDR splitting effect compared to the traditional ISM explanation. Notice also that the isoscalar giant resonances (ISGR) are split in our FLDM too. However, the energy of ISGR splitting is much larger than the one for the isovector giant resonances (IVGR) and is roughly estimated as $\hbar(\omega^{(1)}_+ - \omega^{(2)}_+) \sim \hbar\Omega \propto A^{-1/3}$, in contrast to the IVGR case where $\hbar(\omega^{(1)}_- - \omega^{(2)}_-) \propto A^{-2/3}$.
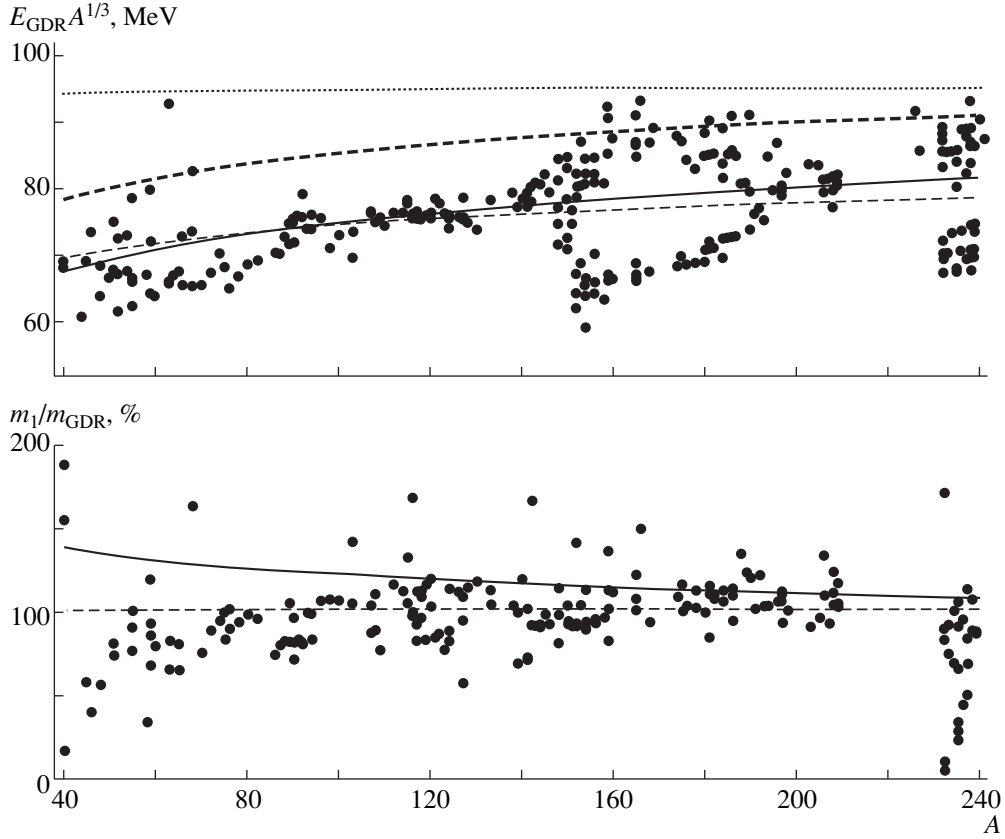
Fig. 1. Giant-dipole-resonance energies E_{GDR} multiplied by $A^{1/3}$ (upper panel) and depletion m_1 of the model-independent EWSR m_{GDR} in percent (bottom panel) for main isotopes versus the atomic number A: (full circles) experimental data from [26–28]; (solid and thick dashed lines) main GDR resonances and their satellites, respectively, found from Eqs. (7) for $F' = 1.2$, $F = 0.34$, $F_1 = 1.0$, $b_s^- = 110$ MeV, $\varepsilon_F = 40$ MeV, and $r_0 = 1.1$ fm; and (dotted and thin dashed lines) estimates in (9).

3.2. Nuclear Response

Let us consider a response of a nucleus to the external perturbation

$$V_{ext}^\tau(\mathbf{r}, t) = \lambda_\tau^\omega(t)\hat{Q}(\mathbf{r}),$$

$$\lambda_\tau^\omega(t) = \lambda_\tau^\omega \exp[-i(\omega + i\eta)t], \quad \hat{Q}(\mathbf{r}) = r^L Y_{L0} \quad (10)$$

for $L \geq 1$ and $\eta \longrightarrow +0$. The linear response function $\chi_\pm(\omega)$ can be derived through the Fourier transform $\delta\rho_\pm^\omega(\mathbf{r})$ of the dynamical particle-density component $\delta\rho_\pm \equiv \delta\rho_\pm(\mathbf{r}, t)$ [15],

$$\chi_\pm(\omega) = -\frac{1}{\lambda_\pm^\omega}\int d\mathbf{r}\,\hat{Q}(\mathbf{r})\delta\rho_\pm^\omega(\mathbf{r}). \quad (11)$$

The density variation $\delta\rho_\pm(\mathbf{r}, t)$ is a sum of the "volume" part discussed in Subsection 2.1 and the "surface" one due to the nuclear surface motion (see also [23]).

Using Eqs. (1), (2), (4), and (5) and applying the method of [23] for the two-component system, one obtains the response function $\chi_{L,\pm}^{(n)}(\omega)$ for a given multipole order L and the vibration mode $n = 1, 2$. In par-

ticular, for the isovector vibrations, one gets [we omit the subindex (−) as above]

$$\chi_L^{(n)}(\omega) = \frac{\mathscr{A}_L^{(n)(q)}}{\mathscr{D}_L^{(n)}(\omega - i\Gamma/2)}, \quad \omega = v_F s_n q. \quad (12)$$

For the main solution $n = 2$, $s = s_2$ [see Eqs. (3), (4)], one has

$$\mathscr{A}_L^{(2)}(q) = -L^2\left[1 + \frac{12\xi(L-1)}{5(L+2)}\right]\frac{\bar{\rho}R_0^{2L+1}}{m\omega^2} \quad (13)$$

$$\times j_L(qR_0)(1 + O(\Delta)),$$

where $\omega = v_F s_2 q$, i.e., the same result as obtained earlier for the symmetric nuclei [24]. We also have another isovector response for the solution $s = s_1$ which is proportional to the Δ and exists only in the asymmetric nuclei,

$$\mathscr{A}_L^{(1)}(q) = -\frac{3\bar{\rho}R_0^{L+4}\xi\Delta}{5\varepsilon_F qR_0 c} \quad (14)$$

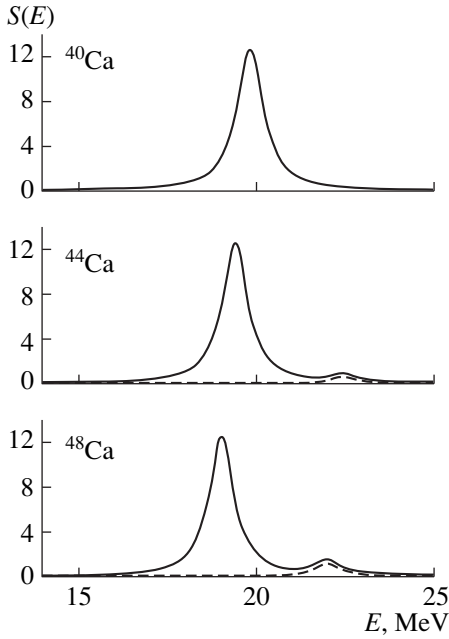$$\times [c_3 j_L(qR_0) - qR_0(c_3 + c)j_L'(qR_0)],$$

Fig. 2. Strength functions for several Ca isotopes versus the energy E. Solid and dashed lines represent, respectively, the total $[S(E) = S^{(1)}(E) + S^{(2)}(E)]$ and satellite $[S^{(2)}(E)]$ strength functions ($\Gamma = 0.03\hbar\Omega \approx 0.5$ MeV; other parameters are identical to those in Fig. 1).

where $c_3 = (F - F' - Q_1)\Delta_s - Q_1^2$. We introduced a small imaginary part $i\Gamma/2$ in Eq. (12) for illustrative convenience to show the strength function as a result of some smoothing procedure. More consequent Fermi-liquid theory which relates Γ with the collision integral in the kinetic equation (1) will be discussed in the succeeding publication.

For small Γ compared to the resonance energies $\hbar\omega_L^{(n)}$, we obtain the strength function $S_L^{(n)}(\omega) = -\mathrm{Im}\,\chi_L^{(n)}(\omega)/\pi$ in terms of the imaginary part of the response function and then its moments,

$$m_{L,k}^{(n)} = \hbar^{k+1}\int d\omega\,\omega^k S_L^{(n)}(\omega)$$

$$\approx \left(\frac{\hbar v_F s_n}{R_0}\right)^{k+1} \frac{(q_L^{(n)} R_0)^k \mathcal{A}_L^{(n)}(q_L^{(n)})}{\mathcal{D}_L^{(n)\prime}(\omega_L^{(n)})}. \tag{15}$$

Here, we restricted the sum over eigenfrequencies to the main lowest solutions $q_L^{(n)}$ of the secular equation (7). The main dipole resonance ($n = 2, L = 1$) of the zero order in Δ (15), (13) depletes mainly the energy weighted sum rule, $m_{1,1}^{(2)}/m_{\mathrm{GDR}} \approx 1$, where $m_{\mathrm{GDR}} = (3/4\pi)(\hbar^2/2m)N$ {see Eqs. (6.176) of [25] adopted for the transition density with the normalization to the atomic number A instead of the nuclear charge eZ; the weight factor 3 was omitted because of our choice of

the multipole operator $\hat{Q}(\mathbf{r})$ (10)}. The strength of the other (satellite) resonance ($n = 1$) is linear in Δ and is relatively small as compared to the main peak, $m_{1,1}^{(1)}/m_{\mathrm{GDR}} \approx 16\varepsilon_F(1 + F')X/5b_s^- A^{1/3}$. Note that the relative strength of a such satellite increases with the asymmetry parameter X and decreases with growing atomic number A. It also depends on the surface (b_s^-) and volume (F') isovector constants.

4. DISCUSSION

Figure 1 shows the GDR energies E_{GDR} and their depletion of the sum rule m_{GDR} independent of the model [25] versus the mass number [26–28] for the main isotopes near the β-stability line. In addition to the well-known deformation splitting of the GDR energies in the rare earth ($A \approx 140$–190) and actinide (220–240) elements discussed earlier in [4, 7, 9, 11], the rest of the full points represent the GDR characteristics of the main peaks obtained by different experimental groups cited in [26–28]. These points for spherical-like nuclei are in a good agreement with our FLDM results for the main GDR energies $E_{\mathrm{GDR}} = \hbar\omega^{(2)}$ and the EWSR Eqs. (15), (13) for $k = 1, L = 1$ (the low index $L = 1$ is omitted again within this section). They were obtained by solving the secular ($n = 2$) equation (7) for $\omega^{(2)}$ with the sound velocity s_2 from Eqs. (3) for the particular choice of the interaction parameters $F' = 1.2$ and $b_s^- = 110$ MeV. The energies $E_{\mathrm{GDR}}A^{1/3}$ of the main resonances approach the A-independent constant of the Steinwendel–Jensen model (SJM) for large atomic numbers A and become a slightly decreasing function of A for lighter nuclei similarly to the Goldhaber–Teller model (GTM). It is shown analytically from a comparison of the corresponding asymptotic limits of Eqs. (7) for $\omega^{(2)}$ with the well-known secular equations in both SJM and GTM [12]. In the top panel of Fig. 1, we also plot the satellite energy $\hbar\omega^{(1)}$ calculated from the secular equation in (7) for $n = 1$. As seen from Fig. 1, the satellites appear for higher energies near the main peaks, and our GDR splitting, which is independent of the asymmetry parameter X in the lowest order in Δ, is almost independent of the atomic number A. The simple estimates for the energies $\hbar\omega^{(2)}$ and $\hbar\omega^{(1)}$ [see (9)] shown in Fig. 1 are in a good agreement with the exact solutions of the secular equations (7). The value of m_1 (15) for the main ($s = s_2$) GDR (see the bottom of Fig. 1) depletes more than in 50% the dipole sum-rule value m_{GDR}. Moreover, they are close enough to their analytic estimate $\approx 100\%$. Thus, our FLDM predicts that the main isovector GDR is related to the Fermi-liquid vibrations with the sound velocity s_2.

A resonance splitting into the main peak which exhausts approximately the EWSR and its satellite with smaller strength is shown more clearly in Figs. 2 and 3
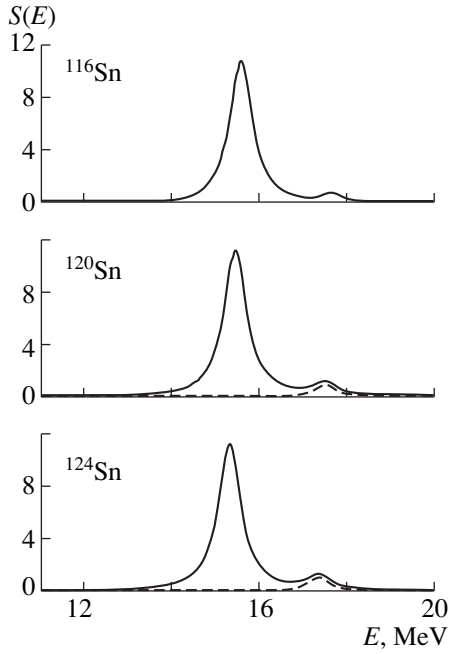
Fig. 3. As in Fig. 2, but for Sn isotopes ($\Gamma \approx 0.3$ MeV).

where the strength functions $S(\omega + i\Gamma/2)$ are plotted versus the excitation energy variable $E = \hbar\omega$ for some Ca and Sn isotopes. For convenience, we show the strength functions with Lorentz-like smoothing with the width $\Gamma = 0.03\hbar\Omega \approx 0.03\varepsilon_F/A^{1/3}$. The satellite appears on the right of the main resonance for $N > Z$ and achieves about 10% of the main peak height in accordance with Eqs. (9) and evaluations of the strength Eqs. (15) [see also (14), (13)].

The asymmetry-parameter dependence of the GDR characteristics for several Ca and Sn isotopes is presented in Figs. 4 and 5. The main ($\hbar\omega^{(2)}$) and satellite ($\hbar\omega^{(1)}$) GDR energies, their relative strength $m_0^{(1)}/m_0^{(2)}$ {i.e., the ratio of the transition probabilities $B(E1)$ [see (15) for $k = 0$]} and the depletion of the EWSR versus the asymmetry parameter X are compared with the experimental data and ISM estimates. The joined points which represent the mean GDR energies ignoring fine structure are taken from [26–28].

The squares in Figs. 4 and 5 and triangles in Fig. 4 were found, respectively, from the energy dependence of the cross section for the photoneutron (γ, xn) and photoproton (γ, xp) reactions for Ca isotopes [5, 8–10] and for Sn ones [2, 4]. They show the parameters of two Lorentzian fitting of the cross sections mentioned above. The energy interval for the mean-square fitting includes the main peak and the first growing values on its right-hand side which are interpreted as the satellites discussed here. For the neutron cross sections with the deformed targets $^{42, 44}$Ca [8, 9], our fitting procedure is applied for the second broader maximum, which we interpret as a sum of the main peak and its satellite. As
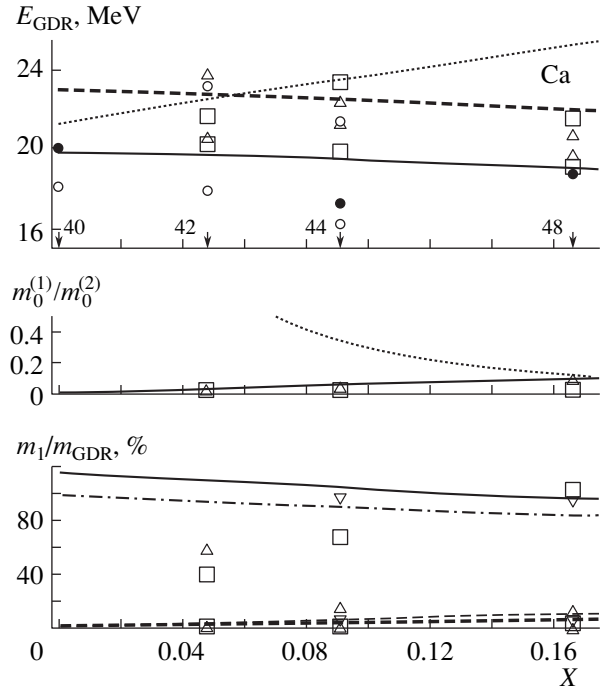
Fig. 4. Energies E_{GDR} (top panel), EWSR depletion m_1/m_{GDR} in percent (bottom panel), and satellite strength $m_0^{(1)}$ divided by the main peak $m_0^{(2)}$ (middle panel) for the Ca isotopes versus the asymmetry parameter $X = (N - Z)/A$: (closed and open circles) experimental data from [26–28] and [7], respectively; (squares, triangles, and inverted triangles) results obtained from the cross sections for the corresponding (γ, xn) and (γ, xp) reactions [5, 8–10] (see the main body of the text); (dotted curves in the top and middle panels) ISM; [solid (dash-dotted) and thick dashed (thin dashed) in the bottom panel] analytic (exact integral) EWSR depletion (15) for the main GDR and satellites (see Subsection 2.2; the parameter values are identical to those in Fig. 1).

seen from the upper panels of Figs. 4 and 5, the splitting magnitude in our FLDM does not depend on the neutron exceed $N - Z$ and there is good agreement with our presentation of the experimental data (squares and triangles). Its slow decrease with the asymmetry parameter X is explained in our case by the A dependence in equations (9). This is in contrast to another splitting effect predicted by the ISM which shows an increase in the energy splitting of the GDR with the isospin quantum number $T_z = (N - Z)/2$. The latter can be obtained from the above-mentioned experimental data by comparing the main (γ, xp) peak of the cross section with the dominating (γ, xn) one in lighter nuclei like Ca isotopes, [3, 5–10].

The satellite strength ratio $m_0^{(1)}/m_0^{(2)}$ in the middle of Figs. 4 and 5 is small and increases linearly with the asymmetry parameter X in contrast to both the opposite ISM behavior $m_0^{(1)}/m_0^{(2)} \approx 1/T_z$ and the case of the deformation DCM effect with $m_0^{(1)}/m_0^{(2)} \approx 1$. Figures 4

Fig. 5. As in Fig. 4, but for the Sn isotopes. Closed joined circles show experimental data from [26–28] (see also references therein) of various groups; data represented by squares and triangles were obtained from Fig. 49 in [2] and from Fig. 1.1 (middle) in [4].

and 5 are completed by the EWSR depletion (see bottom panels), which are about constant for the main GDR and are proportional to the asymmetry parameter X for much smaller satellite con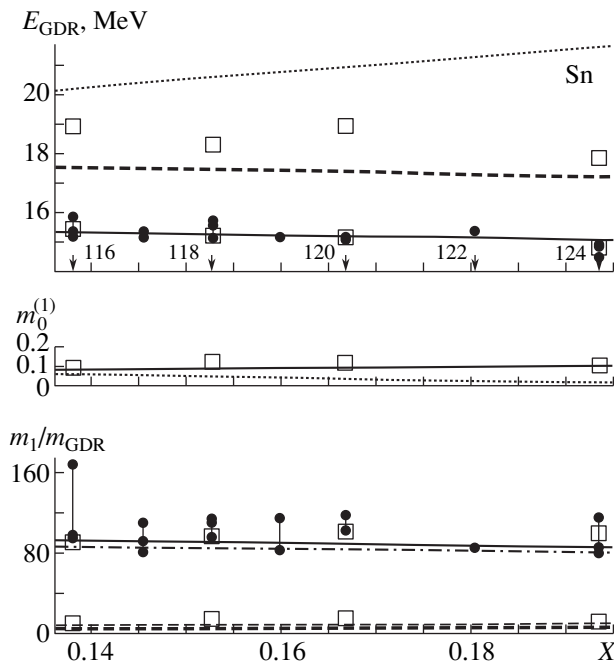tributions. The relative strengths and the depletion of the EWSR for all satellites go to zero, and they vanish in the symmetric limit $X \longrightarrow 0$. The strength ratios for both peaks and their depletion of the EWSR are also in good agreement with the experimental results presented by squares (in Figs. 4 and 5) and triangles (in Fig. 4). Small values of both main and satellite EWSR depletion for the (γ, p) reactions with $^{44,\,48}$Ca targets (triangles in bottom panel of Fig. 4) are explained by small total EWSR (about 0.1) compared to the m_{GDR} estimate. Note that this is not a typical of the GDR that should exhaust mainly the model-independent dipole sum rule. We might again get the relative EWSR for the cross sections of these reactions in close agreement with our results assuming approximately 100% for the total EWSR depletion (see the back triangles in this figure). Finally, the open circles in Fig. 4 found in the inelastic (e, e') reactions with the $^{42,\,44}$Ca targets (see [7]), can also be explained by the FLDM splitting of the GDR, at least its magnitude and approximate independence of the asymmetry parameter X.

5. CONCLUSIONS

As a conclusion, the FLDM is extended to the neutron-rich nuclei within the linear approximation in the asymmetry parameter X. The FLDM predicts existence of two kinds of isovector (or isoscalar) vibrations related to two zero-sound velocities s_1 and s_2. The latter are determined by the isoscalar and isovector Landau interaction amplitudes in the Fermi liquid. We showed that the isospin and the asymmetry Fermi liquid effect coexist and they complete the interpretation of the experimental data. The asymmetrical FLDM is better for larger atomic number A, whereas the precision of the ISM is not sufficient for heavy elements like Sn. Such an asymmetry Fermi liquid effect exists even in spherical nuclei in contrast to the double GDR structure due to the nuclear deformation in the DCM.

The FLDM shows the satellite structure of the isovector and isoscalar resonances. We pointed out that the energy splitting of the isovector GDR does not depend on the neutron excess in the lowest order in X. Moreover, the satellite structure of the isovector GDR does not depend on the type of these reactions (γ, xn), (γ, xp) or inelastic electron scattering and can be found for each reaction and for spherical targets in contrast to the ISM and DCM predictions. The isovector splitting appears essentially due to the asymmetry effect in the collective FLDM dynamics and is determined by the isovector volume (F') and surface (b_s^-) interactions. The lowest peak depletes mainly the EWSR, and another one, localized at higher energy, is the satellite with the significantly smaller contribution to the EWSR proportional to the asymmetry parameter X.

Our results can be helpful in a further understanding of experimental data like photonuclear reactions and inelastic electron scattering in a wide region of the nuclear isotope targets near the β-stability line within a small asymmetry parameter Δ which, however, corresponds to a large enough neutron (or proton) excess.

REFERENCES

1. B. S. Ishkhanov and I. M. Kapitonov, *Electromagnetic Radiation Interaction with Atomic Nuclei* (Mosk. Gos. Univ., Moscow, 1970).
2. B. L. Berman and S. C. Fultz, Rev. Mod. Phys. **47**, 713 (1975).
3. I. Bergqvist, *Neutron Radiative Capture* (Pergamon, Oxford, 1985), Vol. 3, p. 33.
4. A. van der Woude, Prog. Part. Nucl. Phys. **18**, 217 (1987).

5. S. Oifawa and K. Shoda, Nucl. Phys. A **277**, 301 (1977).

6. S. C. Fultz, R. A. Álvarez, B. L. Berman, and P. Meyer, Phys. Rev. C **10**, 608 (1974).

7. K. Itoh, Y. M. Shin, T. Saito, and Y. Torizuka, Phys. Rev. C **24**, 1969 (1981).

8. Y. I. Assafiri and M. N. Thompson, Nucl. Phys. A **357**, 429 (1981).

9. P. D. Harty and M. N. Thompson, Aust. J. Phys. **34**, 505 (1981).

10. G. J. O'Keefe, M. N. Thompson, Y. I. Assafiri, and R. E. Pywell, Nucl. Phys. A **469**, 239 (1987).

11. P. Carlos *et al.*, Nucl. Phys. A **225**, 171 (1974).

12. J. M. Eisenberg and W. Greiner, *Nuclear Models* (North-Holland, Amsterdam, 1970), Vol. 1.

13. I. Hamamoto, H. Sagawa, and X. Z. Zhang, Phys. Rev. C **56**, 3121 (1997); Nucl. Phys. A **626**, 669 (1997).

14. V. M. Kolomietz, A. G. Magner, and V. A. Plujko, Z. Phys. A **345**, 131, 137 (1993).

15. A. G. Magner, V. M. Kolomietz, H. Hofmann, and S. Shlomo, Phys. Rev. C **51**, 2457 (1995).

16. A. A. Abrikosov and I. M. Khalatnikov, Rep. Prog. Phys. **22**, 329 (1959).

17. V. M. Kolomietz, *Local-Density Approximation in Atomic and Nuclear Physics* (Naukova Dumka, Kiev, 1990).

18. V. M. Strutinsky, A. G. Magner, and M. Brack, Z. Phys. A **319**, 205 (1984).

19. A. G. Magner and V. M. Strutinsky, Z. Phys. A **322**, 633 (1985); Yad. Fiz. **44**, 916 (1986) [Sov. J. Nucl. Phys. **44**, 591 (1986)].

20. A. B. Migdal, *Theory of Finite Fermi Systems and Applications to Atomic Nuclei* (Nauka, Moscow, 1983; Interscience, New York, 1967).

21. V. M. Strutinsky, A. G. Magner, and V. Yu. Denisov, Z. Phys. A **315**, 301 (1984).

22. V. M. Strutinsky, A. G. Magner, and V. Yu. Denisov, Z. Phys. A **322**, 149 (1985).

23. A. G. Magner, V. Yu. Denisov, and V. M. Strutinsky, Izv. Akad. Nauk SSSR, Ser. Fiz. **50**, 196 (1986).

24. V. Yu. Denisov, Yad. Fiz. **43**, 46 (1986) [Sov. J. Nucl. Phys. **43**, 28 (1986)].

25. A. Bohr and B. R. Mottelson, *Nuclear Structure* (Benjamin, New York, 1975; Mir, Moscow, 1977), Vol. 2.

26. V. V. Varlamov, V. V. Sapunenko, and M. E. Stepanov, *Index: Photonuclear Data 1976–1995* (Mosk. Gos. Univ., Moscow, 1996).

27. V. V. Varlamov, B. S. Ishkhanov, and M. E. Stepanov, Preprint No. 96-32/439, MGU (Moscow State University, Moscow, 1996).

28. S. S. Dietrich and B. L. Berman, At. Data Nucl. Data Tables **38**, 199 (1988).

Mass-Surface Predictions near the Doubly Magic Nuclide ^{78}Ni

V. I. Isakov, K. A. Mezilev, Yu. N. Novikov, K. I. Erokhina[1], B. Fogelberg[2], and H. Mach[2]

Petersburg Nuclear Physics Institute, Russian Academy of Sciences, Gatchina, 188350 Russia
Received April 24, 1999; in final form, November 26, 1999

Abstract—The mass surface of nuclei close to the doubly magic nuclide ^{78}Ni is calculated by two methods. The first relies on the multiparticle shell model based on an effective interaction and a mean nuclear potential. The second employs the concept of so-called "magic crosses" and enables us to determine the masses of odd–odd nuclei close to ^{78}Ni by using similarity of the shell structure and neutron–proton interaction in the region of nuclei under consideration and in the region of heavy magic nuclides. The energies of the separation of one and two neutrons from nuclei close to ^{78}Ni and the energies of the β decay of these nuclei—recall that these quantities of astrophysical interest—are presented. © *2000 MAIK "Nauka/Interperiodica".*

1. INTRODUCTION

In recent years, much attention has been given to investigating the structure of neutron-excess nuclei close to the doubly magic nuclide ^{78}Ni. Information about the mass surface (mass relief) in this region of nuclei and about their properties is of crucial importance both for nuclear physics and for astrophysics.

What is of prime interest from the standpoint of nuclear physics is that a new magic region is studied here. The number of such regions within the entire nuclide chart is very limited. At the same time, magic nuclei, together with their nearest neighbors, are unique objects for testing the applicability of various theoretical approaches to describing heavy nuclei—the farther the relevant nuclide region from the β-stability valley, the more important and intriguing the results of investigations performed there. If the combination $Z = 28$ and $N = 50$ of the numbers of protons and neutrons, respectively, does indeed render the ^{78}Ni nucleus doubly magic, it is worthwhile to establish whether the neutron-excess nuclei from this extremely far region have the same properties as other near-magic nuclei [1–3].

Astrophysically, interest in the nuclei under consideration is motivated by the fact that, according to theoretical predictions, the ^{78}Ni nuclide is involved in the astrophysical process of the fast capture of neutrons, so-called *r* process, whose region of the origin is close to the nuclide in question [4]. This first stage of the *r* process is virtually insensitive to its multiple repetitions because the yields of the nuclei of interest in neutron-induced fission, which stops the *r* process in the region of heavy nuclei, are relatively small. Investigation of nuclei from the magic region in question would also make it possible to test various models of nucleo-synthesis. It should be noted however, that, since the peak in the abundances of $A \sim 80$ nuclei is not very pronounced, such a test is more ambiguous than that in the case of heavier nuclei [5, 6].

In view of a special role of the ^{78}Ni nuclide, theoretical and semiempirical predictions for the properties of nuclei from this, as-yet-unexplored, magic region are of value, the more so as various projects for their experimental investigation with ionic beams of exotic nuclei are still in their infancy.

Various semiempirical approaches to describing nuclear masses (see, for example, [7]) can obviously be used in constructing the mass surface near the ^{78}Ni nuclide. However, the application of the relevant mass formulas to nuclei featuring extremely large neutron excess can yield only rough predictions, since this requires extrapolations to far regions.

In the present study, an approach based on the multiparticle spherical shell model is developed for determining the mass surface. Here, there arises the key question of whether the ^{78}Ni nuclide is indeed a doubly magic nucleus. The comprehensive analysis of shell effects in nuclei close to the neutron drip line in [8]—this analysis was performed within relativistic mean-field theory—revealed that shell effects are quite sizable in the nuclei being discussed. At the same time, an opposite result was obtained in [9] (see also [10] and reference therein), where it was indicated that the shell effects in light and medium-mass nuclei near the neutron drip line can be suppressed by the interaction of bound orbitals with a continuum.

By comparing the results obtained from shell-model calculations for the $N = 50$ isotopes ^{82}Ge and ^{83}As having four and five protons, respectively, in excess of the $Z = 28$ shell with experimental data, it was concluded in [11] that the region around ^{78}Ni can be considered to be doubly magic. A similar conclusion follows from the study of Hoff and Fogelberg [12], who analyzed the properties of the excited states of the Ge and As nuclei

---

[1] Ioffe Institute for Physics and Technology, Russian Academy of Sciences, Politekhnicheskaya ul. 26, St. Petersburg, 194021 Russia.
[2] Department of Neutron Research, Uppsala University, S-61182 Nyköping, Sweden.

where the numbers of neutrons are close to $N = 50$. On the basis of shell-model calculations, the β-decay properties of the ^{80}Zn nucleus were reproduced in [13], where it was assumed that this nucleus consists of the doubly magic core ^{78}Ni and a pair of protons. Finally, we would also like to mention the study of Khatz [14], who was able to reproduce the half-lives of some nuclei from the Co–Ga region on the basis of calculations within the random-phase approximation (RPA) and who also used the mass predictions of relevant mass formulas.

As a rule, predictions for the r process are based on the semiempirical mass formulas that are more or less global, taking no account of local features of individual nuclei or small regions of nuclei.

In contrast to the aforementioned approaches, we will rely here on the assumption that the ^{78}Ni nuclide is magic, which is justified by the calculation of the single-particle spectrum. That this assumption is realistic is confirmed by the known effect of the "mutual support" of magic numbers [15] in doubly magic nuclides. This opens the possibility for appropriately and precisely calculating the properties of near-magic nuclei close to ^{78}Ni (in particular, the mass relief for them) and for further determining the β-decay energies and the neutron- separation energies, the latter being of astrophysical interest.

Specific calculations of the decay energies and of the separation energies were performed here by the method based on the multiparticle shell model [16] and by the method using the concept of the magic crosses, which was developed in [3] (see also [1, 2]).

2. SHELL-MODEL CALCULATIONS

Shell-model calculations presented here are based on the concepts of a mean nuclear field and a residual interaction. The parameters of the Woods–Saxon mean-field potential were chosen by fitting experimental data on single-particle energies in odd nuclei close to ^{208}Pb and ^{132}Sn. A finite-range effective interaction is used here in the form that was employed in [17–21] to describe two-quasiparticle nuclei close to the above magic cores.

Another idea consists in using the ground state of the ^{78}Ni nuclide as a vacuum with respect to which all near-magic nuclei under study can be treated in terms of a few quasiparticles. This approach makes it possible to cover all 25 nuclides where the numbers of protons and neutrons fall within the intervals $26 \le Z \le 30$ and $48 \le N \le 52$, respectively.

In the representation of the eigenfunctions of the Hartree–Fock method, the Hamiltonian has the form

$$H = E_0 + \sum_{\alpha} \varepsilon_{\alpha} N(a_{\alpha}^{+} a_{\alpha})$$

$$+ \frac{1}{4} \sum_{\alpha, \beta, \gamma, \delta} {}_a\langle \alpha\beta | \vartheta | \gamma\delta \rangle_a N(a_{\alpha}^{+} a_{\beta}^{+} a_{\delta} a_{\gamma}), \quad (1)$$

where the single-particle orbitals $|\alpha\rangle$ are formally determined from the self-consistent Hartree–Fock procedure for the core nucleus; E_0 is the vacuum energy (that is, the sign-inverted binding energy of the ^{78}Ni nucleus), which is immaterial in determining the decay and separation energies; ϑ is the effective residual interaction; and $N(…)$ stands for a normally ordered operator product with respect to the chosen vacuum.

In order to generate single-particle orbitals, we actually used, as was said above, the Woods–Saxon potential (instead of the Hartree–Fock potential)

$$U(r, \hat{\sigma}) = \frac{V}{1 + \exp[(r - R)/a]}$$

$$+ V_{ls}r_0^2 \frac{1}{r}\frac{d}{dr}\left[\frac{1}{1 + \exp[(r - R)/a]}\right]\hat{\mathbf{l}} \cdot \hat{\mathbf{s}}, \quad (2)$$

where $V = -V_0\left(1 - \beta\frac{N - Z}{A}t_z\right)$; $R = r_0 A^{1/3}$; and $t_z = -1/2$ and $1/2$ for protons and neutrons, respectively. In the case of protons, we added the potential of a uniformly charged sphere of radius $R_c = r_c A^{1/3}$. For the parameters appearing in formula (2), we used the values of $V_0 = 51.5$ MeV, $r_0 = 1.27$ fm, $\beta = 1.39$, $V_{ls} = -0.43V$, and $r_c = 1.25$ fm. The diffuseness parameters were taken to be $a_{\pi} = 0.67$ fm and $a_{\nu} = 0.55$ fm for protons and neutrons, respectively. The effective interaction was taken in the form

$$\vartheta = (V + V_{\sigma}\boldsymbol{\sigma}_1 \cdot \boldsymbol{\sigma}_2 + V_T S_{12} + V_{\tau}\boldsymbol{\tau}_1 \cdot \boldsymbol{\tau}_2$$

$$+ V_{\sigma\tau}(\boldsymbol{\sigma}_1 \cdot \boldsymbol{\sigma}_2)(\boldsymbol{\tau}_1 \cdot \boldsymbol{\tau}_2) + V_{\tau T}S_{12}\boldsymbol{\tau}_1 \cdot \boldsymbol{\tau}_2)\exp\left(-\frac{r^2}{r_{00}^2}\right), \quad (3)$$

where $V = -9.95$ MeV, $V_{\sigma} = 2.88$ MeV, $V_T = -1.47$ MeV, $V_{\tau} = 5.90$ MeV, $V_{\sigma\tau} = 4.91$ MeV, $V_{\tau T} = 1.51$ MeV, and $r_{00} = 1.8$ fm.

The single-particle energies in the potential (2) are used to determine the binding energies of the four odd nuclei appearing to be neighbors of ^{78}Ni and to generate the entire single-particle spectrum. The latter is necessary for calculating the binding energies of nuclei having more than one valence quasiparticle, in which case the residual interaction and the mixing of configurations both contribute.

Considered below are individual cases separately.

2.1. Nuclei of the "^{78}Ni Core Plus Two Quasiparticles" Type

The binding energies of the ground states were calculated within the RPA, where the eigenfrequencies and the amplitudes of the states $f_{\alpha\beta} = \begin{pmatrix} X \\ Y \end{pmatrix}$ are determined by the set of matrix equations

$$\left\| \begin{matrix} A & M \\ M & C \end{matrix} \right\| \begin{pmatrix} X \\ Y \end{pmatrix} = \omega_k \begin{pmatrix} X \\ -Y \end{pmatrix}, \quad (4)$$

with the normalization condition being given by

$$\left| \sum_{a,\beta} X_{\alpha,\beta}(\omega_k) X_{\alpha\beta}(\omega_{k'}) - \sum_{\alpha,\beta} Y_{\alpha\beta}(\omega_k) Y_{\alpha\beta}(\omega_{k'}) \right| \tag{5}$$
$$= \delta(kk'),$$

where $f_{\alpha\beta} = \begin{pmatrix} X_{ab} \\ Y_{a'b'} \end{pmatrix}$ for particle–particle channels

(nuclei of the "core plus $(\pm 2\pi)$, $(\pm 2\nu)$, $(\pm\pi \pm \nu)$" types)

and $f_{\alpha\beta} = \begin{pmatrix} X_{ab'} \\ Y_{a'b} \end{pmatrix}$ for particle–hole channels (nuclei of

the "core $\pm\pi \mp \nu$" types). The primed and unprimed Latin subscripts correspond to single-particle levels below and above the Fermi level, respectively.

The quantities appearing in Eq. (4) are given by

$$A_{\alpha\beta;\,\mu\nu} = E_{\alpha\beta}\delta_{\alpha\mu}\delta_{\beta\nu} + M^J_{\alpha\beta;\,\mu\nu}, \tag{6}$$

$$C_{\alpha\beta;\,\mu\nu} = -E_{\alpha\beta}\delta_{\alpha\mu}\delta_{\beta\nu} + M^J_{\alpha\beta;\,\mu\nu}. \tag{7}$$

For the particle–particle channel, $E_{\alpha\beta} = \varepsilon_\alpha + \varepsilon_\beta$, where $\alpha = a$ and $\beta = b$ (or $\alpha = a'$ and $\beta = b'$), while $M^J_{\alpha\beta;\,\mu\nu}$ is the appropriately antisymmetrized particle–particle matrix element between the states $|\alpha\beta; J\rangle$ and $|\mu\nu; J\rangle$ for given values of the angular momentum. In the case of the particle–hole channel, $E_{\alpha\beta} = \varepsilon_a - \varepsilon_b$, where $\alpha = a$ and $\beta = b'$ (or $\alpha = a'$ and $\beta = b$), while $M^J_{\alpha\beta;\,\mu\nu}$ is the particle–hole matrix element. The formulas for the particle–particle and the particle–hole matrix elements $M^J_{\alpha\beta;\,\mu\nu}$ are presented elsewhere [17, 18]. The "upper" solutions to the set of equations (4) with $\omega_n \simeq \varepsilon_a + \varepsilon_b$ for the particle–particle channel correspond to the $(A + 2)$ nucleus, while the "lower" solutions with $\omega_m \simeq \varepsilon'_a + \varepsilon'_b$ correspond to the $(A - 2)$ nucleus. In this case, the solutions to the set of equations (4) are related to the excitation energies of the relevant nuclei as

$$E_n(A + 2) = \omega_n + B(A + 2) - B(A), \tag{8}$$

$$E_m(A - 2) = -\omega_m + B(A - 2) - B(A), \tag{9}$$

where B stands for the binding energies of the ground states and A denotes the core $[B(A) \equiv -E_0]$. For the charged particle–hole channel, $\omega_n \simeq \varepsilon_a - \varepsilon'_b$ and $\omega_m \simeq \varepsilon'_a - \varepsilon_b$ correspond to, respectively, the "core $+\pi - \nu$" and the "core $-\pi + \mu$" nucleus. In this case, we have

$$\begin{aligned} E_n&(Z + 1, N - 1) \\ &= \omega_n + B(Z + 1, N - 1) - B(Z, N), \end{aligned} \tag{10}$$

$$\begin{aligned} E_m&(Z - 1, N + 1) \\ &= -\omega_m + B(Z - 1, N + 1) - B(Z, N), \end{aligned} \tag{11}$$

where (Z, N) refers to the core. The differences $B(A \pm 2) - B(A)$ and $B(Z \pm 1, N \mp 1) - B(A)$ of the binding energies of the two-quasiparticle nucleus and the core were determined by varying the values $B(A \pm 2)$ and $B(Z \pm 1, N \mp 1)$ unless the excitation energies E_n and E_m associated with the lowest states and given by expressions (8)–(11) were fitted to zero.

2.2. Nuclei of the "⁷⁸Ni Core Plus Three Quasiparticles" Type

In this subsection, we consider nuclei having the "core plus $(\pm 2\pi \pm \nu)$, $(\pm 2\pi \mp \nu)$, $(\pm 2\nu \pm \pi)$, $(\pm 2\nu \mp \pi)$" structures. For all these cases, the calculations were performed within the three-quasiparticle shell model with the wave functions in the form

$$\Psi_{IM} = \sum_{\alpha,\beta,\mu,J} X^I_{\alpha\mu(J)\beta} \big| [\xi^+_{j\alpha}\xi^+_{j\mu}]^J, \xi^+_{j\beta}; IM|0\rangle, \tag{12}$$

where

$$[\xi^+_{j\alpha}\xi^+_{j\mu}]^{JM} = \frac{1}{\sqrt{1 + \delta_{j_\alpha j_\mu}}} \sum_{m_\alpha,m_\mu} C^{JM}_{j_\alpha m_\alpha j_\mu m_\mu} \xi^+_{j_\alpha m_\alpha} \xi^+_{j_\mu m_\mu}, \tag{13}$$

$$\xi^+_{j_a m_a} = a^+_{j_a m_a}; \quad \xi^+_{j_{a'} m_{a'}} = (-1)^{l_{a'} + j_{a'} - m_{a'}} a_{j_{a'} - m_{a'}}. \tag{14}$$

In expression (12), α and μ correspond to protons (both particles and holes), while β corresponds to neutrons, or vice versa; $|0\rangle$ is the ground state of the ⁷⁸Ni nucleus.

The eigenvectors X and the corresponding eigenvalues were found by solving the secular equation

$$\|D\|(X) = \omega_k(X), \tag{15}$$

where

$$\begin{aligned} D^{J_2 J_1(I)}_{\alpha_2\mu_2\beta_2,\,\alpha_1\mu_1\beta_1} &= (\bar{\varepsilon}_{\alpha_1} + \bar{\varepsilon}_{\mu_1} + \bar{\varepsilon}_{\beta_1})\delta_{\alpha_2\alpha_1}\delta_{\mu_2\mu_1}\delta_{\beta_2\beta_1}\delta_{J_2 J_1} \\ &+ \langle\alpha_2\mu_2(J_2)\beta_2; I|H_{int}|\alpha_1\mu_1(J_1)\beta_1; I\rangle. \end{aligned} \tag{16}$$

Here, the relations $\bar{\varepsilon}_a = \varepsilon_a$, $\bar{\varepsilon}_{a'} = -\varepsilon_{a'}$, etc., hold. The excitation energies E_k are related to the solutions ω_k to Eq. (15) as

$$E_k = \omega_k + B(A + 3qp) - B(A). \tag{17}$$

The three-quasiparticle matrix element of the interaction entering into (16) can be expressed in terms of the quantities M^J as

$$\langle\alpha_2\mu_2(J_2)\beta_2; I|H_{int}|\alpha_1\mu_1(J_1)\beta_1; I\rangle$$
$$= \delta_{\beta_2\beta_1}\delta_{J_2 J_1} M^{J_1}_{\alpha_2\mu_2;\,\alpha_1\mu_1} + \left[\frac{(2J_2 + 1)(2J_1 + 1)}{(1 + \delta_{\alpha_2\mu_2})(1 + \delta_{\alpha_1\mu_1})} \right]^{1/2}$$

$$\times \left\{ \delta_{\mu_2\mu_1} \sum_L (2L+1) W[j_{\beta_2} L J_2 j_{\mu_2}; j_{\alpha_2} I] \right.$$

$$\times W[j_{\beta_1} L J_1 j_{\mu_2}; j_{a_1} I] M^L_{\alpha_2\beta_2;\,\alpha_1\beta_1}$$

$$+ (-1)^{j_{\alpha_1}+j_{\mu_1}+J_1+1} \delta_{\mu_2\alpha_1}$$

$$\times \sum_L (2L+1) W[j_{\beta_2} L J_2 j_{\mu_2}; j_{\alpha_2} I] W[j_{\beta_1} L J_1 j_{\mu_2}; j_{\mu_1} I]$$

$$\times M^L_{\alpha_2\beta_2;\,\mu_1\beta_1} + (-1)^{j_{\alpha_2}+j_{\mu_2}+J_2+1} \delta_{\alpha_2\mu_1} \qquad (18)$$

$$\times \sum_L (2L+1) W[j_{\beta_2} L J_2 j_{\alpha_2}; j_{\mu_2} I] W[j_{\beta_1} L J_1 j_{\alpha_2}; j_{\alpha_1} I]$$

$$\times M^L_{\mu_2\beta_2;\,\alpha_1\beta_1} + (-1)^{j_{\alpha_2}+j_{\mu_2}+J_2+j_{\alpha_1}+j_{\mu_1}+J_1} \delta_{\alpha_2\alpha_1}$$

$$\times \sum_L (2L+1) W[j_{\beta_2} L J_2 j_{\alpha_2}; j_{\mu_2} I]$$

$$\left. \times W[j_{\beta_1} L J_1 j_{\alpha_2}; j_{\mu_1} I] M^L_{\mu_2\beta_2;\,\mu_1\beta_1} \right\}.$$

In expression (18) and below, $M^J_{ab;\,cd}$ and $M^J_{a'b';\,c'd'}$ refer to the particle–particle channel, while $M^J_{ab';\,cd'}$ and $M^J_{a'b;\,c'd}$ refer to the particle–hole channel.

The values of $B(A + 3qp)$ were determined from the condition requiring that the energy E_k of the lowest state vanish.

2.3. Nuclei of the "^{78}Ni Core Plus Four Quasiparticles" Type

In this subsection, we consider nuclei having the "core plus $(\pm 2\pi \pm 2\nu)$, $(\pm 2\pi \mp 2\nu)$" structures. In this case, the wave function can be represented as

$$\Psi_{IM} \qquad (19)$$
$$= \sum_{\alpha,\,\mu,\,\beta,\,\eta,\,J_1,\,J_2} X^I_{\alpha\mu(J_1)\beta\eta(J_2)} \big| [\xi^+_{j\alpha}\xi^+_{j\mu}]^{J_1}, [\xi^+_{j\beta}\xi^+_{j\eta}]^{J_2}; IM|0\rangle,$$

where α and μ correspond to protons, while β and η correspond to neutrons, or vice versa; α and μ or β and η refer simultaneously to particles or holes. In specific calculations, we restricted the basis to the $J_1 = J_2 = 0$ states yielding the greatest overlap matrix elements within the $I = 0$ state. In this case, $\alpha = \mu$ and $\beta = \eta$, and the relevant secular equation can also be formally represented in form (15) with

$$D_{\alpha_2\beta_2,\,\alpha_1\beta_1} = (2\bar{\varepsilon}_{\alpha_2} + 2\bar{\varepsilon}_{\beta_2}) \delta_{\alpha_2\alpha_1} \delta_{\beta_2\beta_1}$$

$$+ \delta_{\beta_2\beta_1} M^0_{\alpha_2\alpha_2,\,\alpha_1\alpha_1} + \delta_{\alpha_2\alpha_1} M^0_{\beta_2\beta_2,\,\beta_1\beta_1} \qquad (20)$$
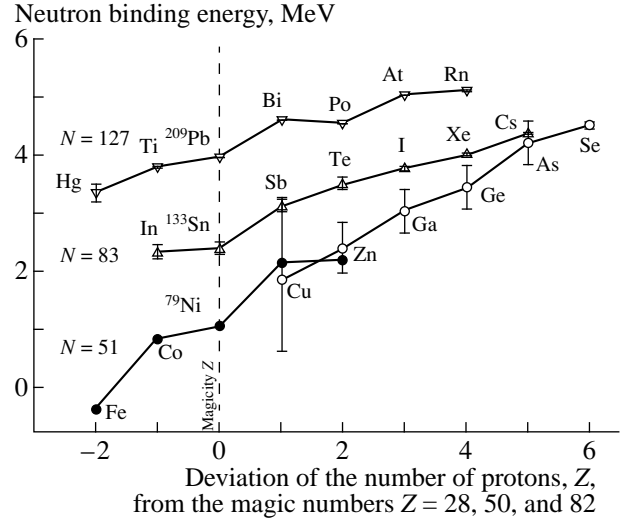
Fig. 1. Neutron binding energies obtained in (closed circles) this study and in (open symbols) [22] as functions of the deviation of the proton number Z from the magic numbers of $Z = 28$, 50, and 82 for (closed and open circles) the $N = 51$ isotopes, (triangles) the $N = 83$ isotopes, and (inverted triangles) the $N = 127$ isotopes, respectively.
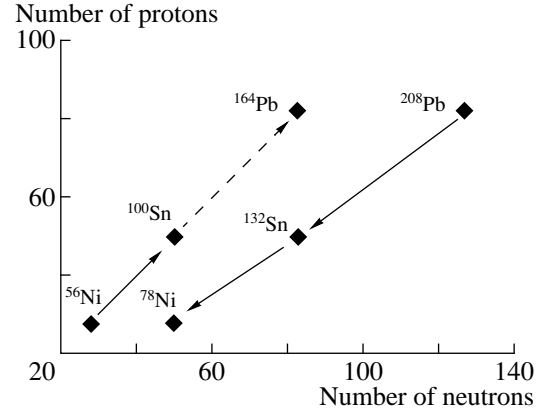
Fig. 2. Two common lines for allied magic regions.

$$+ \delta_{\alpha_2\alpha_1} \delta_{\beta_2\beta_1} \frac{4}{(2j_{\alpha_1}+1)(2j_{\beta_1}+1)} \sum_L (2L+1) M^L_{\alpha_1\beta_1,\,\alpha_1\beta_1}.$$

In all cases of two-, three-, and four-quasiparticle nuclei considered here, the single-particle basis including one shell above and one shell below the Fermi surface is used in the calculations for each particle species.

Table 1 displays the spins predicted for the ground states and the difference $B(A) - B(^{78}\text{Ni})$ of their binding energies as obtained (rows a) in this study and (rows b, c, d) from available compilations. Table 2 quotes our results for the energies of the separation of one or two neutrons and for the β-decay energies. Figure 1 shows the neutron binding energies calculated for the $N = 51$ isotopes close to the ^{78}Ni nucleus and the relevant sys-

Table 1. Part of the nuclide chart near the ^{78}Ni nucleus

	^{78}Zn; 0$^+$	^{79}Zn; 9/2$^+$	^{80}Zn; 0$^+$	^{81}Zn; 5/2$^+$	^{82}Zn; 0$^+$
a	20.12	25.04	31.33	33.56	37.32
b	21.93(1.11)	26.18(1.13)	32.63(1.11)	35.05(1.17)	39.06(1.17)
c	21.15(1.04)	25.16(1.10)	31.75(1.11)	34.00(1.19)	37.90(1.30)
d	21.46	25.23	31.65	33.68	37.27
	^{77}Cu; 3/2$^-$	^{78}Cu; 5$^-$	^{79}Cu; 3/2$^-$	^{80}Cu; 4$^-$(1$^-$)	^{81}Cu; 3/2$^-$
a	5.31	9.52	14.86	17.03	20.15
b	5.91(1.30)	9.45(1.36)	15.23(1.42)	–	–
c	5.49(1.12)	9.42(1.16)	15.17(1.19)	17.16(1.26)	20.33(1.32)
d	5.79	9.56	15.08	16.78	19.64
	^{76}Ni; 0$^+$	^{77}Ni; 9/2$^+$	^{78}Ni; 0$^+$	^{79}Ni; 5/2$^+$	^{80}Ni; 0$^+$
a	−8.29	−5.11	0.00	1.07	3.91
b	−8.71(1.43)	−5.61(1.48)	0.00(1.10)	–	–
c	−8.68(1.19)	−5.67(1.25)	0.00(0.90)	1.15(1.35)	4.05(1.41)
d	−8.09	−5.35	0.00	0.79	3.32
	^{75}Co; 7/2$^-$	^{76}Co; 8$^-$(1$^-$)	^{77}Co; 7/2$^-$	^{78}Co; 5$^-$	^{79}Co; 7/2$^-$
a	−26.94	−23.58	−20.08	−19.25	−17.11
b	–	–	–	–	–
c	−28.32(1.30)	−25.19(1.37)	−20.43(1.41)	−19.37(1.48)	−17.29(1.55)
d	−27.67	−25.02	−20.52	−19.91	−18.27
	^{74}Fe; 0$^+$	^{75}Fe; 9/2$^+$	^{76}Fe; 0$^+$	^{77}Fe; 5/2$^+$	^{78}Fe; 0$^+$
a	−45.06	−42.08	−38.35	−38.72	−37.22
b	–	–	–	–	–
c	−45.72(1.47)	−43.69(1.53)	−38.82(1.57)	−38.65(1.66)	−36.67(1.73)
d	−45.10	−43.46	−39.06	−39.25	−37.83

Note: The differences $B(Z, N) - B(^{78}\text{Ni})$ calculated here are presented in row a, while the relevant data from [22–24] are given in rows b, c, and d. For the ^{80}Cu and ^{76}Co nuclei, the spins of the first low-lying excited levels are presented in addition to the spin of the ground states. The numbers in parentheses are the rms errors associated with the errors in the binding energies of the nucleus under study and the core nucleus.

tematics of experimental data for the $N = 51$, 83, and 127 isotopes.

3. CALCULATION OF THE SEPARATION ENERGIES ON THE BASIS OF THE SIMILARITY OF THE ^{78}Ni AND ^{132}Sn SHELL STRUCTURES

The concept of the magic crosses [3], which is based on the assumption of Blomqvist [1] that the shell structures in the two magic regions close to ^{132}Sn and ^{208}Pb are similar, provides yet another possibility for predicting the properties of near-magic nuclei far from the stability valley. This similarity is due to the fact that the single-particle shells in these two nuclides have analogous structures such that the quantum numbers of the orbitals of the next shell can be obtained from those for the preceding shell by means of the substitutions $n \longrightarrow$

n, $l \longrightarrow l + 1$, and $j \longrightarrow j + 1$. This concept was extended to other regions of nuclear masses (^{56}Ni and ^{100}Sn) and was analyzed within various theoretical approaches [2]. An extrapolation of the Blomqvist concept leads to a more general pattern of similarity of the shell structures of magic nuclei where similar magic regions occur on a common line connecting doubly magic nuclei on the nuclide chart that differ from each other by one filled proton and one filled neutron shell. Figure 2 shows that there exist two such lines, one leading to proton-deficient nuclei and the other leading to neutron-deficient nuclei.

Experimental data favoring this idea were obtained in [3], where nuclear masses were determined for the so-called magic cross near the ^{132}Sn nucleus and where it was shown that, within two standard deviations, the

Table 2. Energies of the separation of one and two neutrons (S_ν and $S_{2\nu}$, respectively) and β-decay energies (Q_β) as determined from shell-model calculations

Nucleus	S_ν, MeV	$S_{2\nu}$, MeV	Q_β, MeV	Nucleus	S_ν, MeV	$S_{2\nu}$, MeV	Q_β, MeV
^{75}Fe	2.98	–	15.92	^{79}Ni	1.07	6.18	14.57
^{76}Fe	3.73	6.71	15.55	^{80}Ni	2.84	3.91	13.90
^{77}Fe	−0.37	3.36	19.42	^{78}Cu	4.21	–	11.38
^{78}Fe	1.50	1.13	18.75	^{79}Cu	5.34	9.55	10.96
^{76}Co	3.36	–	16.07	^{80}Cu	2.17	7.51	15.08
^{77}Co	3.50	6.86	15.75	^{81}Cu	3.12	5.29	14.19
^{78}Co	0.83	4.33	20.03	^{79}Zn	4.92	–	–
^{79}Co	2.14	2.97	18.96	^{80}Zn	6.29	11.21	–
^{77}Ni	3.18	–	11.20	^{81}Zn	2.23	8.52	–
^{78}Ni	5.11	8.29	10.30	^{82}Zn	3.76	5.99	–

Table 3. Neutron-separation energies (in MeV) for the $N = 51$ isotopes as obtained in various approaches

Nucleus	MN	CKZ	Tach.	JM	AW(1995)	a	b
^{78}Co	1.07	1.06	1.35	0.61	–	0.83	1.11
^{79}Ni	1.72	1.15	1.44	0.79	–	1.07	1.20
^{80}Cu	2.16	1.99	2.30	1.70	–	2.17	2.03
^{81}Zn	2.17	2.25	2.55	2.03	2.42(44)	2.23	–

Note: Mass differences were calculated in the present study and were taken from [7, 22]. The following notation is used in this table: (MN) Möller–Nix, (CKZ) Comay–Kelson–Zidon, (Tach.) Tachibana *et al.*, (JM) Jänecke–Masson, (AW) Audi–Wapstra; columns a and b quote the results of the present calculations performed on the basis of the shell model and the magic-cross concept, respectively.

energies of the neutron–proton interactions in the respective states of nuclei close to tin and lead are equal. In the context of this experimental fact, we can extend the concept of magic crosses to nuclei close to ^{78}Ni and determine, in this way, the masses of the odd–odd nuclei forming the magic cross near ^{78}Ni and having two or less particles or holes in excess the doubly filled shell (see Fig. 2). Thus, we use the following correspondence both for proton and for neutron orbitals in three magic regions:

$$^{78}\text{Ni}(l-1, j-1) \Leftrightarrow {}^{132}\text{Sn}(l, j) \Leftrightarrow {}^{208}\text{Pb}(l+1, j+1).$$

Among the nuclei being considered, ^{78}Co, ^{79}Ni, ^{80}Cu, and ^{81}Zn are of special interest for astrophysics, because the energies of neutron separation from them determine the waiting points in the *r* process. Using the definition of the energies of the πν interaction in the form [3]

$$\Delta_{\pm\pi\pm\nu} = ME(\pm\pi, \pm\nu) + ME(0, 0) \\ - ME(\pm\pi, 0) - ME(0, \pm\nu), \quad (21)$$

where the plus and minus signs correspond to particles and holes, respectively, and where $ME(0, 0)$ is the mass excess for the core ^{78}Ni nuclide, we can obtain

$$S_\nu(^{78}\text{Co}) = S_\nu(^{79}\text{Ni}) - \Delta_{\pi\nu}(^{78}\text{Co}), \quad (22)$$

$$S_\nu(^{80}\text{Cu}) = S_\nu(^{79}\text{Ni}) - \Delta_{\pi\nu}(^{80}\text{Cu}), \quad (23)$$

where $S_\nu(^{79}\text{Ni}) \equiv -\varepsilon_\nu(2d_{5/2})$ is the energy of neutron separation from the $2d_{5/2}$ valence orbit. The values of $\Delta_{\pi\nu}$ for ^{78}Co and ^{80}Cu in (22) and (23) can be obtained from data for nuclei forming the magic cross near ^{132}Sn:

$$\Delta_{\pi\nu}(^{78}\text{Co}, \pi 1f_{7/2}^{-1}\nu 2d_{5/2})$$
$$= \Delta_{\pi\nu}(^{132}\text{In}, \pi 1g_{9/2}^{-1}\nu 2f_{7/2}) = 0.091_{87} \text{ MeV},$$

$$\Delta_{\pi\nu}(^{80}\text{Cu}, \pi 2p_{3/2}\nu 2d_{5/2})$$
$$= \Delta_{\pi\nu}(^{134}\text{Sb}, \pi 2d_{5/2}\nu 2f_{7/2}) = -0.834_{70} \text{ MeV}.$$

Here, we have used the most accurate values of the mass excess from [25].

Using expressions (22) and (23) and the mean value of S_ν for ^{79}Ni, we arrive at

$$S_\nu(^{78}\text{Co}) = 1.11 \text{ MeV},$$

$$S_\nu(^{79}\text{Ni}) = 1.20 \text{ MeV},$$

$$S_\nu(^{80}\text{Cu}) = 2.03 \text{ MeV}.$$

The resulting values of the separation energies are quoted in Table 3, along with the predictions of various semiempirical mass formulas.

4. CONCLUSION

Our results for the neutron-separation energies clearly demonstrate that the nuclei of ^{76}Fe, ^{77}Co, ^{78}Ni, and possibly ^{79}Cu can be considered as the waiting points on the path of the *r* process. However, the disposition of this path in the mass region around $A = 78$ depends on whether the shell effect is weakened for the magic number $N = 50$ near the neutron drip line [10]. This weakening can destroy the nuclear structure inherent in the spherical shell model used in our calculations. Fortunately, this destructive effect of excess neutrons in the region around ^{78}Ni seems weak owing to the mutual support of the magic numbers that is observed everywhere on the nuclide chart [15].

In conclusion, we emphasize that our mass-surface predictions are based on the assumption of the pronounced filling of the shells in the regions of the neutron-excess nuclei under consideration and on the obvious similarity of the shell structures of the nuclei in these regions. We used methods that differ considerably from the approaches underlying the majority of the mass formulas and employing extrapolations of the parameters fitted in the regions of nuclei far from the drip line. Our results are valid, provided that our basic assumption, magicity of the ^{78}Ni nuclide, is true.

ACKNOWLEDGMENTS

REFERENCES

1. J. Blomqvist, in *Proceedings of the 4th International Conference on Nuclei Far from Stability, Helsingor, 1981*; CERN Report 81-09 (Geneva, 1981), p. 536.
2. G. A. Leander *et al.*, Phys. Rev. C **30**, 416 (1984).
3. K. A. Mezilev *et al.*, Phys. Scr. **56**, 272 (1995).
4. F.-K. Thielemann *et al.*, Phys. Rep. **227**, 269 (1993).
5. K.-L. Kratz *et al.*, Astrophys. J. **403**, 216 (1993).
6. B. Pfeiffer, K.-L. Kratz, and F.-K. Thielemann, Z. Phys. A **357**, 235 (1997).
7. P. E. Haustein, At. Data Nucl. Data Tables **39**, 185 (1988).
8. M. M. Sharma *et al.*, Phys. Rev. Lett. **72**, 1431 (1994).
9. J. Dobaczewski *et al.*, Phys. Rev. Lett. **72**, 981 (1994).
10. W. Nazarewicz, Nucl. Phys. A **630**, 239 (1998).
11. J. A. Winger *et al.*, in *NFFS-5 International Conference, Rosseau Lake, 1987* (AIP, 1988), p. 375; Phys. Rev. C **38**, 285 (1988).
12. P. Hoff and B. Fogelberg, Nucl. Phys. A **368**, 210 (1981).
13. K.-L. Kratz *et al.*, Phys. Rev. C **38**, 278 (1988).
14. K.-L. Kratz *et al.*, J. Phys. G (Suppl.) **14**, 331 (1988).
15. K. H. Schmidt and D. Vermeulen, AMCO-6, 1979, p. 119.
16. A. Shalit and I. Talmi, *Nuclear Shell Theory* (Academic, New York, 1963).
17. K. I. Erokhina and V. I. Isakov, Izv. Akad. Nauk, Ser. Fiz. **56** (11), 78 (1992).
18. K. I. Erokhina and V. I. Isakov, Yad. Fiz. **57**, 212 (1994) [Phys. At. Nucl. **57**, 198 (1994)].
19. V. I. Isakov, S. A. Artamonov, and L. A. Sliv, Izv. Akad. Nauk SSSR, Ser. Fiz. **41**, 2074 (1977).
20. H. Mach *et al.*, Phys. Rev. C **51**, 500 (1995).
21. K. I. Erokhina and V. I. Isakov, Yad. Fiz. **59**, 621 (1996) [Phys. At. Nucl. **59**, 589 (1996)].
22. G. Audi and A. H. Wapstra, Nucl. Phys. A **595**, 409 (1995).
23. E. Comay, I. Kelson, and A. Zidon, At. Data Nucl. Data Tables **39**, 235 (1988).
24. J. Janecke and P. I. Masson, At. Data Nucl. Data Tables **39**, 265 (1988).
25. B. Fogelberg *et al.*, Phys. Rev. Lett. **82**, 1823 (1999).

Translated by R. Tyapaev

NUCLEI
Theory

Effect of the Interference between Orbital and Spin Currents on Form Factors for Nuclear Electroexcitation

N. G. Goncharova, A. A. Dzhioev, and V. V. Shershakov

Institute of Nuclear Physics, Moscow State University, Vorob'evy gory, Moscow, 119899 Russia
Received November 5, 1999; in final form, January 24, 2000

Abstract—The momentum-transfer dependence of the transverse and longitudinal form factors is considered for all transitions forming electric multipole resonances in cross sections for nuclear electroexcitation. The contributions of the matrix elements of orbital and spin currents to transverse *EJ* form factors are analyzed. The special features of the form factors due to interference between nucleon current are revealed. A universal character of the destructive interference between currents is proven for transitions dominant in the wave function for the giant photonuclear dipole resonance. © 2000 MAIK "Nauka/Interperiodica".

Investigation of nuclei in inelastic electron scattering appears to be the most informative method for exploring giant multipole resonances in cross sections for nuclear excitation. In contrast to photonuclear reactions, which furnish predominantly information about dipole resonances, electroexcitation enables us to study—by varying the momentum transfer to a nucleus—resonances of higher multipole orders, both of the vibrational and of the rotational type, in nuclear-excitation cross sections. By investigating giant dipole resonances (GDR) in cross sections for inelastic electron scattering, it is possible to reveal those features of GDR that could not be observed in the cross sections for photonuclear reactions. In particular, photonuclear reactions make it possible to investigate only the effect of electron interaction with the intranuclear orbital current, whereas electronuclear reactions open a window on spin magnetization currents as well. By analyzing electric modes of giant-multipole-resonance excitation in inelastic electron scattering, we can study in detail the wave function of the relevant resonance. This is because electric modes are excited in (*e*, *e'*) reactions owing to electron interaction both with the nuclear charge density and with the intranuclear current. The response of a nucleus to interactions of the first type is expressed in terms of longitudinal (Coulomb) *CJ* form factors; interactions of the second type are associated with transverse *EJ* form factors. For electric-type multipole resonances, (*e*, *e'*) cross sections for small and large scattering angles can therefore be markedly different, which reflects the difference between the momentum-transfer dependences of the longitudinal and the transverse form factor associated with the same resonance. In the present article, we focus on the problem of revealing the configuration structure of the resonance peak on the basis of a comparative analysis of its longitudinal and transverse form factors.

The differential cross section for electron–nucleus scattering depends on the features of the nuclear structure via the longitudinal and transverse form factors [1],

$$\frac{d\sigma}{d\Omega d\omega} = \frac{4\pi\sigma_M}{\eta_R}\left[F_L^2(q, \omega) + \left(\frac{1}{2} + \tan^2\frac{\theta}{2}\right)F_T^2(q, \omega)\right]. \quad (1)$$

Longitudinal and transverse form factors appear to be the sums of the multipole form factors, each being a function of the momentum transfer *q* to the nucleus and of the nuclear excitation energy ω,

$$F_L^2(q, \omega) = \sum_{J=0}^{\infty} F_{CJ}^2(q, \omega),$$

$$F_T^2(q, \omega) = \sum_{J=1}^{\infty} \{F_{EJ}^2(q, \omega) + F_{MJ}^2(q, \omega)\}. \quad (2)$$

Longitudinal form factors dominate in inelastic electron scattering into the forward hemisphere. Purely backward scattering reveals only transverse form factors. By analyzing the features of the peaks corresponding to individual resonance excitations (that is, at a fixed excitation energy ω) against the momentum transfer to the nucleus, we can identify the multipole order of a resonance.

However, a comparison of the momentum-transfer dependences of the longitudinal and transverse form factors for a resonance peak makes it possible, in principle, to make a further step in studying the nature of giant multipole resonances. Our microscopic analysis of the effect of the structure of excited-state wave functions on the behavior of the form factors for electric resonances enables us to conclude that a comparison of the momentum-transfer dependences of transverse and longitudinal form factors reveals those giant multipole resonances whose wave functions are dominated by the $1l_{l+1/2} \longrightarrow 1(l+1)_{l+3/2}$ single-particle transitions. Spe-

cial features induced in the transverse electric form factors for $E1$ and $E3$ excitations of $1p$- and $1d2s$-shell nuclei owing to the destructive interference between orbital and spin nucleon currents were studied in [2, 3]. The calculation presented below for the positions of the first minima of the transverse form factor on the momentum-transfer axis enables us to conclude that the destructive interference between orbital and spin currents occurs for all $1\hbar\omega\ 1l_{l+1/2} \longrightarrow 1(l+1)_{l+3/2}$ transitions, irrespective of the shell and of the multipole order.

The transverse form factor for all single-particle transitions forming electric multipole resonances can be represented as the sum of contributions from spin and orbital currents,

$$F_{EJ}(y) = A_J(y) + B_{J-1}(y) + B_{J+1}(y), \qquad (3)$$

where $y = (qb/2)^2$, b being the oscillator parameter (the actual calculation of the matrix elements for single-particle transitions was performed with harmonic-oscillator wave functions). Hereafter, $A_J(y)$ and $B_J(y)$ correspond to matrix elements involving the spin-current operator $[Y_J \times \hat{\sigma}]$ and the orbital-current operator $[Y_J \times \hat{\nabla}]$, respectively. The calculations show that the momentum-transfer dependence of the spin- and orbital-current contributions to the transverse form factor for the $1l_j \longrightarrow 1(l+1)_{j'}$ transition can be represented as

$$A_J(y) \sim y^{\frac{J+1}{2}} F\left(-l + \frac{J+1}{2}; \frac{2J+3}{2}; y\right), \qquad (4)$$

$$B_{J-1}(y) + B_{J+1}(y)$$
$$\sim \frac{d}{dy} y^{\frac{J+1}{2}} F\left(-l + \frac{J+1}{2}; \frac{2J+3}{2}; y\right), \qquad (5)$$

where $F(\alpha, \gamma, y)$ is a confluent hypergeometric function. We now present expressions for the transverse form factors for the $1l_{l+1/2} \longrightarrow 1(l+1)_{l+3/2}$ and $1l_{l+1/2} \longrightarrow 1(l+1)_{l+1/2}$ transitions [expressions (6) and (7) below for the former and the latter, respectively]:

$$F_{EJ}(y) = K(J, l)e^{-y}$$
$$\times \left[\mu_T y^{\frac{J+1}{2}} F\left(-l + \frac{J-1}{2}; \frac{2J+3}{2}; y\right) \qquad (6)\right.$$
$$\left. - e_T \frac{d}{dy} y^{\frac{J+1}{2}} F\left(-l + \frac{J-1}{2}; \frac{2J+3}{2}; y\right)\right],$$

$$F_{EJ}(y) = N(J, l)e^{-y}$$
$$\times \left[\mu_T(2l+2) y^{\frac{J+1}{2}} F\left(-l + \frac{J-1}{2}; \frac{2J+3}{2}; y\right)\right. \qquad (7)$$

$$\left. + e_T \frac{d}{dy} y^{\frac{J+1}{2}} F\left(-l + \frac{J-1}{2}; \frac{2J+3}{2}; y\right)\right].$$

Here, e_T and μ_T are the isospin-representation matrix elements of the charge operator and the magnetic-moment operator, respectively, while $K(J, l)$ and $N(J, l)$ are constants depending on the resonance multipole order and on the orbital quantum number. Since we have $\mu_V/\mu_S \approx 4.71/0.88$ for the ratio of the unrenormalized isovector and isoscalar magnetic moments, nuclear electroexcitation is dominated by isovector multipole resonances, and it is these resonances that are considered in the present study. From (6) and (7), we can see that the ratio of the spin-current contribution to the orbital-current contribution is larger for the spin-flip $1l_{l+1/2} \longrightarrow 1(l+1)_{l+1/2}$ transition than for the $1l_{l+1/2} \longrightarrow 1(l+1)_{l+3/2}$ transition.

The longitudinal form factor for single-particle $1l_j \longrightarrow 1(l+1)_{j'}$ transitions can be represented in the form

$$F_{CJ}(y) = D(J, l, j, j') \exp(-y) e_T y^{\frac{J}{2}}$$
$$\times F\left(-l + \frac{J-1}{2}; \frac{2J+3}{2}; y\right). \qquad (8)$$

Therefore, the longitudinal form factors exhibit the same momentum-transfer dependence for all single-particle $1l_j \longrightarrow 1(l+1)_{j'}$ transitions of the same multipole order, but they differ in magnitude. In addition, the expression for the spin current and the expression for the longitudinal form factor involve the same confluent hypergeometric function. Hence, $F_{CJ}^2(y)$ and $A_J^2(y)$ reach a minimum at the same q value (the positions of the maxima are close). As a result, the longitudinal and the transverse form factor behave similarly in the momentum-transfer regions dominated by the spin current.

We now apply our results to analyzing the behavior of the cross section for dipole electroexcitation. The transverse form factor for dipole isovector single-particle $1\hbar\omega$ transitions is the sum of the contributions of the spin current $A_1(y)$ and the orbital currents $B_0(y)$ and $B_2(y)$,

$$F_{E1}(y) = A_1(y) + B_0(y) + B_2(y). \qquad (9)$$

In the photoabsorption cross section, the GDR is formed exclusively by the contribution of the element $B_0(y)$ at $q = \omega$. Substituting $J = 1$ into (6) and (8), we find that the transverse and the longitudinal form factor for the dipole $1l_{l+1/2} \longrightarrow 1l_{l+3/2}$ transition are given by

$$F_{E1}(y) = -\frac{1}{Mb} \frac{1}{\sqrt{6\pi}} \sqrt{(l+2)(l+1)}\, e^{-y}$$
$$\times \left[\mu_V y F\left(-l; \frac{5}{2}; y\right) - e_V \frac{d}{dy} y F\left(-l; \frac{5}{2}; y\right)\right], \qquad (10)$$
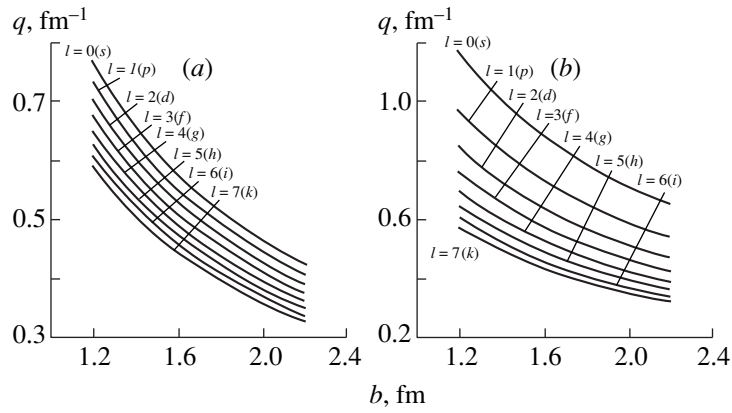
Fig. 1. (*a*) Position of the first interference minimum of the transverse *E*1 form factor and (*b*) position of the first interference maximum of the longitudinal *C*1 form factor for the $1l_{l+1/2} \longrightarrow 1(l+1)_{l+3/2}$ dipole transition versus the oscillator parameter *b* for various values of *l*.

$$F_{C1}(y) = \frac{e_V}{\sqrt{3\pi}}\sqrt{(l+2)(l+1)}\,e^{-y}y^{\frac{1}{2}}F\left(-l;\frac{5}{2};y\right). \quad (11)$$

At low momentum transfers, the main contribution to the resonance comes from the orbital component $B_0(y)$ of the intranuclear current, the contribution of the spin current being small. With increasing momentum transfer, the orbital current decreases, while the spin current increases; as a result, the transverse form factor vanishes. Solutions to Eq. (10) determine the positions of the zeros of the *E*1 form factor that correspond to the destructive interference between the spin current and the orbital current. The curves in Fig. 1*a* show the positions of the first zeros of the *E*1 form factors for all $1l_{l+1/2} \longrightarrow 1(l+1)_{l+3/2}$ transitions corresponding to various values of the orbital angular momentum and of the oscillator parameter. We can see that, for all 1*p*-shell nuclei, up to the heaviest ones, the first zero of the transverse *E*1 form factor occurs between 0.4 and 0.7 fm^{-1}. At these momentum-transfer values, the *C*1 form factor (11) is close to its peak for all single-particle transitions under consideration; the results of the calculations for the position of the maximum in this form factor are presented in Fig. 1*b*.

The destructive interference between the spin current and the orbital currents results in that the cross sections for electron scattering at small and at large angles behave very differently for all dipole-resonance excitations whose wave functions are dominated by the $1l_{l+1/2} \longrightarrow 1(l+1)_{l+3/2}$ transition. For light nuclei, these single-particle transitions make the main contribution to the wave functions for the photonuclear GDR [4]. An analysis of available experimental data for a number of nuclei demonstrates that the cross sections for forward and backward (*e, e'*) scattering behave very differently in the region where the GDR is localized.

Electric dipole transitions make a very small contribution to the cross section for the electronuclear reaction that occurs on ^{12}C nuclei and which was studied in [5] in backward electron scattering at a momentum transfer of 0.5 fm^{-1} within the excitation-energy range between 21 and 22 MeV. This cross section is dominated by the peaks of the *M*2 and *E*2 resonances.

A detailed investigation of the contributions from the longitudinal and the transverse form factor to the electroexcitation cross section was performed at the MAMI A accelerator [6] for ^{12}C and ^{16}O nuclei. In accordance with the above destructive-interference effects in the transverse form factor for the $1p_{3/2} \longrightarrow 1d_{5/2}$ transition, its contribution to the electroexcitation cross section is minimal at momentum transfers of about 0.5–0.6 fm^{-1}. This experimental fact reflects the dominant role of the $1p_{3/2} \longrightarrow 1d_{5/2}$ transition in the formation of the GDRs in these nuclei. Unfortunately, the longitudinal and the transverse form factor have not yet been separated in the electroexcitation cross sections for heavier nuclei. Nevertheless, the measurements of (*e, e'*) scattering on ^{208}Pb nuclei [7] in the energy region of GDR excitation in this nuclear species at large scattering angles indicate that the contribution of the *E*1 form factor to the electroexcitation cross section is very small at a momentum transfer of 0.56 fm^{-1}. This corresponds qualitatively to the vanishing of the *E*1 form factor for the single-particle $1h_{11/2} \longrightarrow 1i_{13/2}$ and $1i_{13/2} \longrightarrow 1k_{15/2}$ transitions, which are dominant in the GDR of this nucleus.

For electric-dipole resonances of the so-called spin–isospin (transverse) type, which are dominated by the spin-flip $1l_{l+1/2} \longrightarrow 1(l+1)_{l+1/2}$ transitions, the interference between the orbital and the spin current in the *E*1 form factor, in contrast to the case considered above, does not lead to the emergence of nondiffraction zeros. For all spin-flip transitions, the transverse *E*1
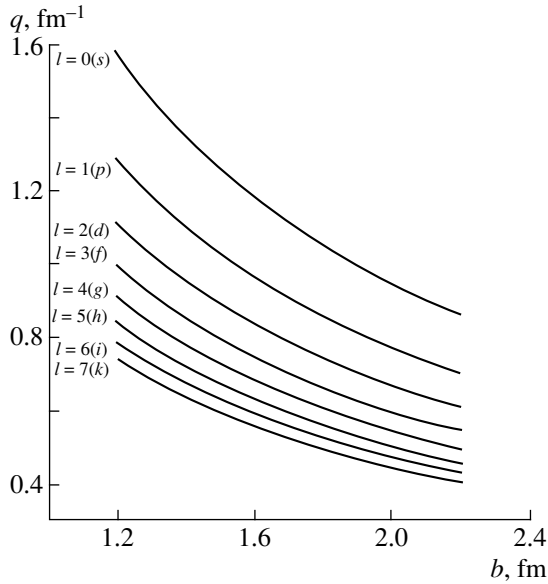
Fig. 2. Position of the first interference maximum of the transverse $E1$ form factor for the spin-flip $1l_{l+1/2} \longrightarrow 1(l+1)_{l+1/2}$ dipole transition versus the oscillator parameter b for various values of l.

form factors are given by

$$
F_{E1}(y) = -\frac{1}{Mb} \frac{1}{\sqrt{6\pi}} \sqrt{\frac{l+1}{2l+1}} e^{-y}
$$

$$
\times \left[\mu_V (2l+2) y F\left(-l; \frac{5}{2}; y\right) + e_v \frac{d}{dy} y F\left(-l; \frac{5}{2}; y\right) \right]. \tag{12}
$$

The results obtained by numerically solving Eq. (12) for extremal points are displayed in Fig. 2. The positions of the first maxima of these $E1$ form factors are close to the positions of the maxima of the corresponding longitudinal form factors. Apart from a constant factor, the latter are given by the expression coinci-

dent—as was pointed out above—with expression (11) for the $1l_{l+1/2} \longrightarrow 1(l+1)_{l+3/2}$ longitudinal form factor. Therefore, an increase in the momentum transfer results in that the transverse $E1$ form factors of the dipole resonances whose wave functions feature a considerable contribution from the spin-flip one-particle components begin to exceed the transverse form factors for the photonuclear resonance. Since spin-flip transitions are excited, owing to spin–orbit splitting, at higher energies than non-spin-flip transitions, the increase in the momentum transfer to the nucleus from $q = \omega$ to $q = 1$ fm^{-1} shifts the center of gravity of the dipole resonances toward higher excitation energies. Thus, the effect of the destructive interference between the spin and orbital currents for transitions that are dominant in the formation of the GDR also changes the localization of the dipole $E1$ contributions to cross sections for nuclear electroexcitation.

In the case of $1l_{l+1/2} \longrightarrow 1(l+1)_{l+3/2}$ transitions, the destructive interference occurs for $E3$ transitions as well. For such a transition, the expressions for the $E3$ and $C3$ form factors with allowance for the spin- and the orbital-current contribution are given by

$$
F_{E3}(y) = K(3, l) e^{-y}
$$

$$
\times \left[\mu_V y^2 F\left(-l+1; \frac{9}{2}; y\right) - e_v \frac{d}{dy} y^2 F\left(-l+1; \frac{9}{2}; y\right) \right], \tag{13}
$$

$$
F_{C3}(y) = D(3, l) e^{-y} y^{\frac{3}{2}} F\left(-l+1; \frac{9}{2}; y\right). \tag{14}
$$

The position of the first solution to the equation $F_{E3}(y) = 0$ as a function of the orbital angular momentum l and of the oscillator parameter b is shown in Fig. 3a. The maximum of the longitudinal $C3$ form factor for these transitions occurs at higher momentum transfers (see Fig. 3b). Near the first zero of the $E3$ form factor (or near the first minimum on a more conven-
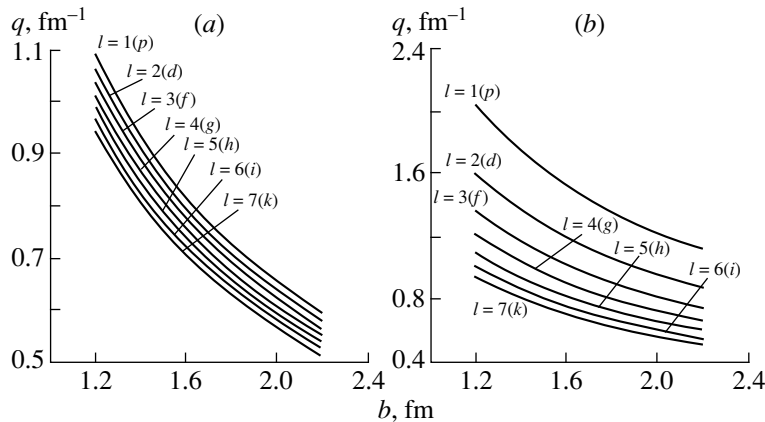

Fig. 3. (*a*) Position of the first interference minimum of the transverse $E3$ form factor and (*b*) position of the first interference maximum of the longitudinal $C3$ form factor for the $1l_{l+1/2} \longrightarrow 1(l+1)_{l+3/2}$ dipole transition versus the oscillator parameter b for various values of l.
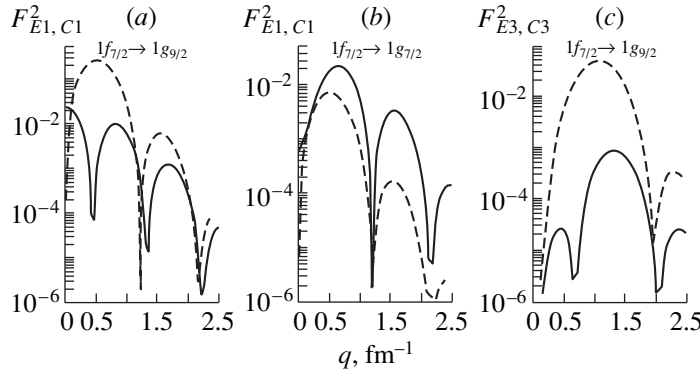
Fig. 4. (*a*) Longitudinal *C*1 form factor (dashed curve) and (*b*) transverse *E*1 form factor (solid curve) for the $1f_{7/2} \longrightarrow 1g_{9/2}$ and $1f_{7/2} \longrightarrow 1g_{7/2}$ transitions; (*c*) longitudinal *C*3 form factor (dashed curve) and transverse *E*3 form factor (solid curve) for the $1f_{7/2} \longrightarrow 1g_{9/2}$ transition.
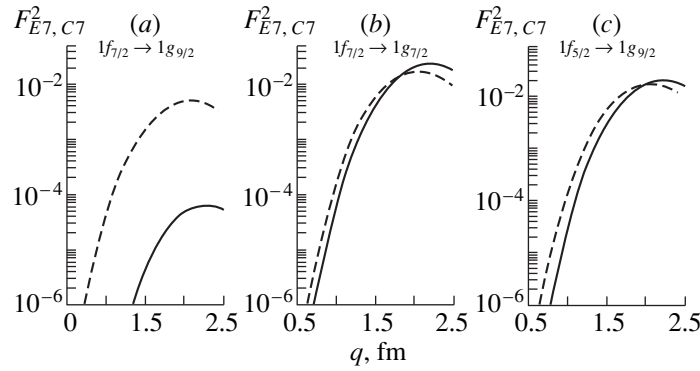
Fig. 5. Longitudinal *C*7 form factor (dashed curve) and transverse *E*7 form factor (solid curve) for single-particle transitions from $1f$ subshell that are involved in the formation of the *E*7 resonance.

tional logarithmic scale), however, the *C*3 form factor is sufficiently large for the octupole resonance to be observed experimentally in electron scattering into the forward hemisphere.

For 1*p*- and 1*d*2*s*-shell nuclei, the behavior of the dipole and octupole form factors for the transitions being discussed was illustrated in [2, 3]. Figure 4 shows (on a logarithmic scale) the form factors for the transitions from the $1f_{7/2}$ subshell. Figure 4*a* illustrates the sharply different types of behavior of the *E*1 and *C*1 form factors for the $1f_{7/2} \longrightarrow 1g_{9/2}$ transition. The *E*1 and *C*1 form factors for the spin-flip $1f_{7/2} \longrightarrow 1g_{7/2}$ transition are displayed in Fig. 4*b*. Figure 4*c* depicts the behavior of the octupole form factors for the first transition.

Of particular interest is the behavior of the form factors for electric multipole resonances whose multipole order is one unit less than the maximum multipole order of $1\hbar\omega$ transitions. States of highest spin (J_{max}) are excited only by the $1l_{l+1/2} \longrightarrow 1(l+1)_{l+3/2}$ transitions ($J_{max} = 2l + 2$) and are associated exclusively with the spin component of the intranuclear nucleon current, $A_{J_{max}-1}(y)$. Intensive investigations into these resonances (see, for example, [8–10]) have revealed an

important heuristic role of these states both for studying the interaction of test hadronic particles with a nucleus and for exploring the mechanism of fragmentation of multipole-transition strengths. In (*e*, *e'*) processes, the highest-spin magnetic resonances are excited only in backward electron scattering, the relevant transverse form factor being maximal at momentum transfers in the range $q = 1.5$–2.5 fm^{-1}. Electric resonances $E(J_{max} - 1)$ formed by three single-particle transitions are also pronounced in this momentum-transfer region. However, it is quite difficult to separate unambiguously these two types of excitations by considering the momentum-transfer dependence of the transverse form factor since, for $q > 1$ fm^{-1}, the $E(J_{max} - 1)$ resonances are dominated by the contribution of the matrix elements of the same spin-current operator $[Y_{J_{max}-1} \times \hat{\sigma}]$ as that which is operative for the highest-spin states. As a result, the transverse form factors behave similarly. The separation would become possible upon simultaneously measuring the form factors for scattering into the backward and into the forward hemisphere, where only the longitudinal form factor for the electric resonance is operative. In addition, it is possible to determine the configuration of the $E(J_{max} - 1)$ res-

onance. Figure 5 displays the form factors for all three single-particle transitions that proceed from the $1f$ subshell and which are involved in the formation of the $E7$ resonance. From Fig. 5a, we can see that the $E7$ and the $C7$ form factor for the $1f_{7/2} \longrightarrow 1g_{9/2}$ transition differ by more than one order of magnitude; at the same time, these form factors are nearly identical for the $1f_{7/2} \longrightarrow 1g_{7/2}$ and $1f_{5/2} \longrightarrow 1g_{9/2}$ transitions (see Figs. 5b, 5c). As a result, a comparison of the longitudinal and transverse form factors would enable us to reveal the configuration structure in question.

The basic results obtained here from our analysis of the form factors for single-particle transitions forming electric $1\hbar\omega$ multipole resonances can be summarized as follows:

(i) It has been proven that the destructive interference between the orbital and the spin nucleon current in a nucleus results in the emergence of a nondiffraction minimum in the transverse form factor within the momentum-transfer region $q < 1$ fm^{-1}. This effect occurs for all $1l_{l+1/2} \longrightarrow 1(l + 1)_{l+3/2}$ electric transitions, irrespective of the shell number and of the resonance multipole order.

(ii) For all $1l_{l+1/2} \longrightarrow 1(l + 1)_{l+1/2}$ electric transitions (that is, spin-flip transitions) the interference of the currents is not destructive for $q < 1$ fm^{-1}; therefore, the longitudinal and the transverse form factors peak at close momentum-transfer values.

(iii) A comparison of the momentum-transfer dependences of the longitudinal and the transverse form factor for electric transitions can be used to reveal the configuration structure of the wave function of an electric multipole resonance.

REFERENCES

1. T. W. Donnelly and J. D. Walecka, Annu. Rev. Nucl. Sci. **225**, 329 (1975).

2. N. G. Goncharova and A. A. Dzhioev, Vestn. Mosk. Univ., Ser. Fiz. **5**, 30 (1997).

3. N. G. Goncharova, Fiz. Élem. Chastits At. Yadra **29**, 789 (1998) [Phys. Part. Nucl. **29**, 319 (1998)].

4. B. S. Ishkhanov, I. M. Kapitonov, V. G. Neudachin, *et al.*, Usp. Fiz. Nauk **160** (3), 57 (1990) [Sov. Phys. Usp. **33**, 204 (1990)].

5. R. S. Hicks, J. B. Flanz, R. A. Lindgren, *et al.*, Phys. Rev. C **30**, 1 (1984).

6. N. Zimmermann, H. G. Weyand, *et al.*, Physics with MAMI A (Inst. für Kernphysik, Mainz, 1988), SFB 201, p. 159.

7. A. Richter, in *Proceedings of the 4th Seminar on Electromagnetic Interactions of Nuclei, Moscow, 1977*, p. 258.

8. B. L. Clausen, R. A. Lindgren, *et al.*, Phys. Rev. Lett. **65**, 547 (1990).

9. B. L. Clausen, R. J. Peterson, *et al.*, Phys. Rev. C **48**, 1632 (1993).

10. N. G. Goncharova, Fiz. Élem. Chastits At. Yadra **23**, 1715 (1992) [Sov. J. Part. Nucl. **23**, 748 (1992)].

Translated by O. Chernavskaya

Theory of Doorway States for One-Nucleon-Transfer Reactions*

B. L. Birbrair** and V. I. Ryazanov

Petersburg Nuclear Physics Institute, Russian Academy of Sciences, Gatchina, 188350 Russia
Received July 23, 1999; in final form, October 14, 1999

Abstract—Doorway states considered in the present study are eigenstates of the Hamiltonian defined as the sum of the kinetic energy and the infinite-energy limit of the single-particle mass operator. Only Hartree diagrams with free-space nucleon–nucleon forces contribute in this limit; therefore, the observed doorway-state energies carry important information about both the nuclear structure and the free-space nucleon–nucleon interaction. © 2000 MAIK "Nauka/Interperiodica".

1. INTRODUCTION

Experimental data on quasielastic knockout reactions $(p, 2p)$, (p, pn), $(e, e'p)$, etc., leading to deeply bound hole states of complex nuclei carry important information about both the nuclear structure and the free-space nucleon–nucleon forces. Of course, such information is contained in all nuclear data, but it is extracted from the data in question by simple, highly reliable means. The reasons are as follows.

(i) As was shown by Baranger [1], doorway states for one-nucleon-transfer reactions are eigenstates of a nucleon in a static nuclear field (see Section 2), thus being solutions of particle motion in a central potential well. This is one of the simplest problems in quantum mechanics.

(ii) As a consequence of contemporary ideas about the *NN*-interaction mechanism (see Section 3), the only contribution to the static field of a nucleus comes from Hartree diagrams with free-space nucleon–nucleon forces: the two-particle, Fig. 1a; three-particle, Fig. 1b; four-particle, Fig. 1c; etc.

(iii) The two-particle contribution of the diagram in Fig. 1a is the convolution of the free-space two-particle *NN* interaction with the one-nucleon density in the nucleus; therefore, it can be found from experiments. Indeed, two-particle forces are determined by the properties of the deuteron and elastic *NN* phase shifts below the pion-production threshold, whereas one-nucleon densities are deduced from a combined analysis of data on elastic electron–nucleus [2] and proton–nucleus scattering [3].

Information about many-particle contributions to the static nuclear field (hence, about free-space many-particle *NN* forces) can be obtained by comparing the observed doorway-state energies with the results of calculations that include only the two-particle contribution. In this way, we found that the free-space many-

particle interaction includes at least three-particle repulsion and four-particle attraction (see Section 4).

2. BARANGER THEOREM

Evolution of a state initiated by a sudden creation of a particle or a hole above the ground state of the A nucleus is described by the single-particle propagator [4]

$$S(x, x'; \tau) = -i\langle A_0|T\psi(x, \tau)\psi^+(x', 0)|A_0\rangle$$

$$= i\theta(-\tau)\sum_j \Psi_j(x)\Psi_j^+(x')e^{-iE_j\tau} \qquad (1)$$

$$- i\theta(\tau)\sum_k \Psi_k(x)\Psi_k^+(x')e^{-iE_k\tau},$$

where

$$\begin{aligned}
\Psi_j(x) &= \langle(A-1)_j|\psi(x)|A_0\rangle, \\
E_j &= \mathscr{E}_0(A) - \mathscr{E}_j(A-1), \\
\Psi_k(x) &= \langle A_0|\psi(x)|(A+1)_k\rangle, \\
E_k &= \mathscr{E}_k(A+1) - \mathscr{E}_0(A).
\end{aligned} \qquad (2)$$

Thus, the propagator describes the evolution of a hole (particle) state at negative (positive) τ values. According to (2), the excitation-energy region for the $A-1$ nucleus is

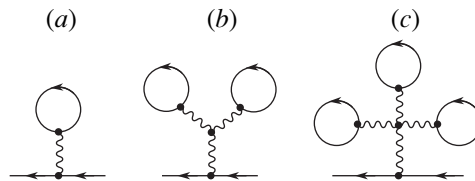$$-\infty < E_j \leq \mathscr{E}_0(A) - \mathscr{E}_g(A-1), \qquad (3)$$

(a)   (b)   (c)

Fig. 1. Hartree diagrams for the static field of a nucleus.

---

where $\mathcal{E}_g(A-1)$ and $\mathcal{E}_0(A)$ are the ground-state energies of the $A-1$ and the A nucleus, respectively, while that for the $A+1$ nucleus is

$$\mathcal{E}_g(A+1) - \mathcal{E}_0(A) \le E_k < \infty. \tag{4}$$

This energy scale is convenient for us because the two regions do not overlap in stable nuclei.

The Fourier component of the propagator,

$$G(x, x'; \varepsilon) = \int_{-\infty}^{+\infty} S(x, x'; \tau) e^{i\varepsilon\tau} d\tau$$

$$= \sum_j \frac{\Psi_j(x)\Psi_j^+(x')}{\varepsilon - E_j - i\delta} + \sum_k \frac{\Psi_k(x)\Psi_k^+(x')}{\varepsilon - E_k + i\delta}, \tag{5}$$

which is referred to as the single-particle Green's function, obeys the Dyson equation

$$\varepsilon G(x, x'; \varepsilon) = \delta(x-x') + \hat{k}_x G(x, x'; \varepsilon)$$

$$+ \int M(x, x_1; \varepsilon) G(x_1, x'; \varepsilon) dx_1, \tag{6}$$

where $\hat{k}_x$ is the kinetic term and $M(x, x'; \varepsilon)$ is the mass operator. The latter has the following general form:

$$M(x, x'; \varepsilon) = U(x, x') + \Sigma(x, x'; \varepsilon), \tag{7}$$

where the energy-independent part $U(x, x')$ is the static field of a nucleus, and the energy-dependent part $\Sigma(x, x'; \varepsilon)$ includes all kinds of correlation effects (including Pauli, particle–particle, particle–hole, ground-state, long-range, and short-range correlations). Its high-energy asymptotic behavior is [5, 6]

$$\sum_{\varepsilon \to \infty}(x, x'; \varepsilon) = \frac{\Pi(x, x')}{\varepsilon} + \ldots, \tag{8}$$

where the ellipsis on the right-hand side stands for terms of higher order in ε^{-1}. As a result, the static nuclear field appears to be the high-energy limit of the mass operator,

$$U(x, x') = \lim_{\varepsilon \to \infty} M(x, x'; \varepsilon), \tag{9}$$

the decomposition (7) thus being unambiguous.

Let us now introduce the single-particle Hamiltonian

$$\mathcal{H}_{sp}(x, x') = \hat{k}_x \delta(x-x') + U(x, x') \tag{10}$$

and its eigenstates

$$\varepsilon_\lambda \psi_\lambda(x) = \int \mathcal{H}_{sp}(x, x') \psi_\lambda(x') dx', \tag{11}$$

which are those of a nucleon in the static field of a nucleus. They are not directly measurable because they are described by only a part of the total nuclear Hamiltonian. However, their physical origin is clarified on the basis of the Heisenberg relation, according to which the large value of ε is equivalent to the short period τ.

Hence, the eigenstates of $\mathcal{H}_{sp}$ (10) describe the initial step of the process under consideration, thus being the doorway states for one-nucleon-transfer reactions.

In order to demonstrate this more explicitly, we use the asymptotic expression for the Green's function (5) at high-energies,

$$G(x, x'; \varepsilon)_{\varepsilon \to \infty}$$

$$= \frac{I_0(x, x')}{\varepsilon} + \frac{I_1(x, x')}{\varepsilon^2} + \frac{I_2(x, x')}{\varepsilon^3} + \ldots, \tag{12}$$

where

$$I_0(x, x') = \sum_j \Psi_j(x)\Psi_j^+(x') + \sum_k \Psi_k(x)\Psi_k^+(x'), \tag{13}$$

$$I_1(x, x') = \sum_j E_j \Psi_j(x)\Psi_j^+(x') + \sum_k E_k \Psi_k(x)\Psi_k^+(x'), \tag{14}$$

$$I_2(x, x') = \sum_j E_j^2 \Psi_j(x)\Psi_j^+(x') + \sum_k E_k^2 \Psi_k(x)\Psi_k^+(x'). \tag{15}$$

From the spectral representation of the propagator (1), it follows that

$$I_0(x, x') = i(S(x, x'; +0) - S(x, x'; -0)), \tag{13a}$$

$$I_1(x, x') = -(\dot{S}(x, x'; +0) - \dot{S}(x, x'; -0)), \tag{14a}$$

$$I_2(x, x') = -i(\ddot{S}(x, x'; +0) - \ddot{S}(x, x'; -0)). \tag{15a}$$

Therefore, the above sums describe the initial step of the evolution process $\left(\dot{S} = \dfrac{\partial S}{\partial \tau}\right), \left(\ddot{S} = \dfrac{\partial^2 S}{\partial \tau^2}\right)$. Using the definition in (10) and the asymptotic expression (8), we can recast the Dyson equation (6) into the form

$$\varepsilon G(x, x'; \varepsilon) = \delta(x-x')$$

$$+ \int \left(\mathcal{H}_{sp}(x, x_1) + \frac{\Pi(x, x_1)}{\varepsilon} + \ldots\right) G(x_1, x'; \varepsilon) dx_1. \tag{16}$$

Substituting (12) into (16) and equating the coefficients at the same powers of ε^{-1}, we obtain

$$\sum_j \Psi_j(x)\Psi_j^+(x') + \sum_k \Psi_k(x)\Psi_k^+(x') = \delta(x-x'), \tag{13b}$$

$$\sum_j E_j \Psi_j(x)\Psi_j^+(x') + \sum_k E_k \Psi_k(x)\Psi_k^+(x')$$

$$= \mathcal{H}_{sp}(x, x'), \tag{14b}$$

$$\sum_j E_j^2 \Psi_j(x)\Psi_j^+(x') + \sum_k E_k^2 \Psi_k(x)\Psi_k^+(x')$$

$$= \mathcal{H}_{sp}^2(x, x') + \Pi(x, x'). \tag{15b}$$

From (14a) and (14b), it follows that

$$\mathcal{H}_{sp}(x, x') = -(\dot{S}(x, x'; +0) - \dot{S}(x, x'; -0)). \tag{17}$$

Thus, the evolution of a hole (particle) state begins as the formation of nucleon eigenstates in the static field of a nucleus, the Baranger theorem thus being proved.

Let us now discuss the way to extract the doorway energies ε_λ (11) from the experimental data. The weights of the doorway component in the actual nuclear states are

$$s_{j,k}^{(\lambda)} = \left| \int \psi_\lambda^+(x) \Psi_{j,k}(x) dx \right|^2. \tag{18}$$

Multiplying (13b)–(15b) by $\psi_\lambda^+(x)\psi_\lambda(x')$ and performing integration with respect to x and x' (x stands for the total set of space and spin variables), we obtain

$$\sum_j s_j^{(\lambda)} + \sum_k s_k^{(\lambda)} = 1, \tag{13c}$$

$$\sum_j E_j s_j^{(\lambda)} + \sum_k E_k s_k^{(\lambda)} = \varepsilon_\lambda, \tag{14c}$$

$$\sum_j E_j^2 s_j^{(\lambda)} + \sum_k E_k^2 s_k^{(\lambda)} = \varepsilon_\lambda^2 + \sigma_\lambda^2, \tag{15c}$$

$$\sigma_\lambda^2 = \int \psi_\lambda^+(x)\Pi(x,x')\psi_\lambda(x') dx dx'. \tag{19}$$

It is remarkable that, in contrast to the widths of Landau–Migdal quasiparticles [5], the variance σ_λ (19) depends on the wave function $\psi_\lambda(x)$ rather than on the energy ε_λ, thus taking nearly identical values for all doorway states. In such a position, it is reasonable to identify σ with the largest observed width value. The latter is the widths of the peaks in the cross sections for quasielastic knockout reactions $(p, 2p)$ and (p, pn) [7, 8] leading to the $1s_{1/2}$ hole states. According to the above references, it is about 20 MeV in all nuclei.

As can be seen from (14c), the doorway-state energies ε_λ depend on the energies and s factors of the actual nuclear states. In the general case, the latter ones belong both to the $A - 1$ and to the $A + 1$ nuclei; therefore, the s factors from two different reactions, pickup and stripping, are required. The absolute values of the s factors are, however, measured with too poor an accuracy because of both the experimental errors and theoretical uncertainties. For this reason, the energies of weakly bound states with $|\varepsilon_\lambda| < \sigma$ are yet unknown (one should bear in mind that the low-lying states of $A \mp 1$ nuclei are Landau–Migdal quasiparticles [5] rather than the states of a nucleon in a static nuclear field).

The situation is more favorable for the states with $|\varepsilon_\lambda| > \sigma$. In this case [see (3) and (4)], the actual nuclear states, over which the doorway states are distributed, belong mainly to either the $A - 1$ nucleus or the $A + 1$ one, only one term on the left-hand side (the first for hole states and the second for particle ones) of (13c)–(15c) thus being active. This is just the case for deeply bound hole states which are excited in the quasielastic
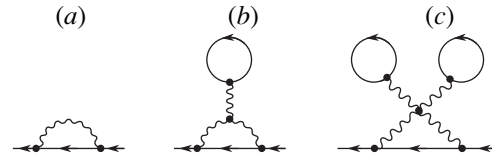
Fig. 2. First-order exchange contributions to the mass operator.

knockout reactions $(p, 2p)$ and (p, pn) [7, 8]. For this reason, the average energies of the peaks in the cross sections may be chosen as the doorway-state energies within the experimental accuracy between 2 and 3 MeV. We use the facts that, for the quasielastic knockout reaction leading to the fixed nuclear state, the cross section is proportional to the s factor of this state, and the absolute values of the s factors are not needed if the energy range of the doorway state belongs to the same nucleus entirely (in this case, the relative values are sufficient).

The experimental data of [7, 8], which are used in the present work, are not free of some possible ambiguity: the energy of the knocked-out nucleon is only about 100 MeV in the experiments. This value is not high enough to neglect the final-state inelastic interactions leading to additional excitation of the final nucleus. As a result of such excitations, the average positions of the peaks may be shifted away from the doorway ones because there is not a pure quasielastic knockout in this case. For a greater confidence, the additional quasielastic knockout experiments $(p, p'N)$ or $(e, e'N)$ are desired, in which the energy of the knock-out nucleon would be on the order of 0.5–1 GeV. We hope that our work will stimulate such experiments.

3. THE STATIC FIELD OF NUCLEUS

Let us consider the high-energy asymptotic behavior of the Feynman diagrams involving the mass operator. Let us begin with those of the first order about the free-space NN interaction. The Hartree diagrams of Fig. 1 are obviously energy-independent. But this is not the case for the corresponding Fock diagrams resulting from the two-particle (Fig. 2a), three-particle (Fig. 2b), four-particle (Fig. 2c), etc., forces. Indeed, according to the contemporary ideas, the NN interaction proceeds via the exchange by either mesons in the Yukawa-like models (OBE [9], Paris [10], Bonn [11], OSBEP [12]) or quarks and gluons in more sophisticated ones. In any case, the interaction includes both the momentum and the energy transfer. As a result of the latter, the Fock diagrams have the ε^{-1} asymptotic behavior. Let us display this result for the diagram of Fig. 2a,

$$M_{\rm F}(x, x'; \varepsilon)$$

$$= \int \frac{i d\omega d^3\mathbf{q}}{(2\pi)^4} e^{i\mathbf{q} \cdot (\mathbf{r} - \mathbf{r}')} v(q, \omega) G(x, x'; \varepsilon + \omega), \tag{20}$$
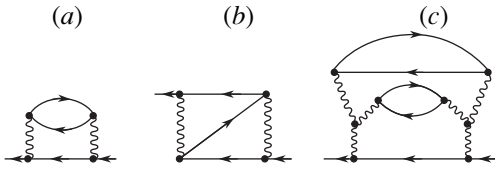
Fig. 3. Some second-order diagrams for the mass operator.

using the Bonn B potential [11] for the two-particle NN forces. It is a sum of the terms in the four-momentum space,

$$v_i(q, \omega) = g_i^2 \left(\frac{\Lambda_i^2 - \mu_i^2}{\Lambda_i^2 + q^2 - \omega^2} \right)^{2\alpha} \frac{1}{\mu_i^2 + q^2 - \omega^2}, \quad (21)$$

$$i = \pi, \eta, \rho, \omega, \sigma 1, \sigma 0, \delta,$$

the form of the meson–nucleon vertices and the sign being specified by the Lorentz symmetry of the mesons. Both the sign and the Lorentz structure are disregarded here because they are irrelevant for the energy dependence. Confining ourselves to the monopole form factor, $\alpha = 1$, we get

$$M_F(x, x'; \varepsilon) = g^2 \int \frac{d^3 \mathbf{q}}{(2\pi)^3} e^{i\mathbf{q} \cdot (\mathbf{r} - \mathbf{r}')} \left\{ \frac{1}{2\omega_\mu(q)} \right.$$

$$\times \left[\sum_j \frac{\Psi_j(x)\Psi_j^+(x')}{\varepsilon - E_j + \omega_\mu(q)} + \sum_k \frac{\Psi_k(x)\Psi_k^+(x')}{\varepsilon - E_k - \omega_\mu(q)} \right]$$

$$\left. - \left[1 - (\Lambda^2 - \mu^2) \frac{\partial}{\partial \Lambda^2} \right] \frac{1}{2\omega_\Lambda(q)} \right\} \quad (22)$$

$$\times \left[\sum_j \frac{\Psi_j(x)\Psi_j^+(x')}{\varepsilon - E_j + \omega_\Lambda(q)} + \sum_k \frac{\Psi_k(x)\Psi_k^+(x')}{\varepsilon - E_k - \omega_\Lambda(q)} \right] \right\},$$

$$\omega_\mu(q) = \sqrt{\mu^2 + q^2}, \quad \omega_\Lambda(q) = \sqrt{\Lambda^2 + q^2}.$$

In the $\varepsilon \longrightarrow \infty$ limit, this gives

$$M_F(x, x'; \varepsilon) = \frac{g^2}{4\pi^2} \frac{\delta(x - x')}{\varepsilon}$$

$$\times \int q^2 \left[\omega_\mu^{-1}(q) - \omega_\Lambda^{-1}(q) - \frac{\Lambda^2 - \mu^2}{2} \omega_\Lambda^{-3}(q) \right] dq. \quad (23)$$

The second-order diagrams of Fig. 3, as well as the higher order ones, contain the propagators of intermediate states, and therefore they all have at least the ε^{-1} asymptotic behavior. Thus, the only contribution to the nuclear static field (9) is provided by the Hartree diagrams.

The two-particle contribution to the static field of the nucleus (Fig. 1a) is calculated with two different models for the free-space two-particle NN interaction, both being of clear physical meaning and containing a small number of adjustable parameters. The first, the Bonn [11], is the sum of the OBE potentials with the vertex form factors, (21). The parameters are adjusted to reproduce the results of the full form of the Bonn potential, which has only one adjustable parameter: see [13] for details. In the second, the OSBEP [12], mesons are treated as objects of nonlinear theory. The mesons are the same as those in the Bonn B, but the form of the momentum space potentials is different. It is (we have taken into account that there is no energy transfer in the Hartree diagrams, i.e., $\omega = 0$)

$$v_i(q) = g_i^2 \sum_{n=0}^{\infty} \frac{(2pn+1)^{2pn-2}[1 + 2(1-p)n]^2 (S+1)^n \alpha_\pi^{2n} \mu_\pi^{2pn}}{\left\{ 1 + [4(p+1)\alpha_\pi]^{-\frac{2}{p}} (S+1)^{-\frac{1}{p}} \times \frac{q^2 + (2pn+1)^2 \mu_i^2}{4\mu_\pi^2 (2pn+1)^2} \right\}^{(S+1)(2pn+1)}} \frac{1}{q^2 + (2pn+1)^2 \mu_i^2}, \quad (24)$$

where $p = 1/2$ for scalar mesons and $p = 1$ for pseudoscalar and vector ones, S is the spin of the meson, and the sum over n is virtually convergent at $n = 4$ [12].

Both these approaches permit one to check the status of the Walecka model [14] by calculating the values of the vector and scalar fields in nuclear matter. For the case of charge-symmetric matter

$$V = v_\omega(0)\rho, \quad S = -\left[\frac{3}{4} v_{\sigma 1}(0) + \frac{1}{4} v_{\sigma 0}(0) \right] \rho_s, \quad (25)$$

where the scalar density ρ_s is

$$\rho_s = \rho - \frac{2\tau}{(2m + S - V)^2}, \quad \tau = \frac{3}{5} k_F^2 \rho, \quad (26)$$

k_F is the Fermi momentum, and m is the free nucleon mass. Using the conventional equilibrium value of the nuclear matter density, $\rho = 0.17$ fm^{-3}, and the parameters of Table 5 of [11] and Table 1 of [12], we get

$$V = +284 \text{ MeV}, \quad S = -367 \text{ MeV} \quad (27)$$

for the Bonn B potential and

$$V = +322 \text{ MeV}, \quad S = -404 \text{ MeV} \quad (28)$$

for the OSBEP, both being close to those provided by the Dirac phenomenology [15]. So the contemporary NN interaction potentials lead to nuclear relativity, the latter thus being really existing phenomenon rather than the suggestion of Walecka.

For this reason, the doorway-state wave functions $\psi_\lambda(x)$ should be treated as bispinors obeying the Dirac equation with

$$\mathcal{H}_{sp} = -i\gamma_0\boldsymbol{\gamma}\cdot\boldsymbol{\nabla} + i\Phi(r)\boldsymbol{\gamma}\cdot\frac{\mathbf{r}}{r} + (\gamma_0 - 1)m \quad (29)$$
$$+ V(r) + \gamma_0 S(r).$$

The scalar S and vector V fields of the finite nuclei are the sums of the isoscalar and isovector parts, the vector field also including the Coulomb potential

$$S(r) = S_0(r) - \tau_3 S_1(r), \quad \tau_3 = \begin{cases} -1, & n \\ +1, & p \end{cases},$$

$$V(r) = V_\omega(r) - \tau_3 V_\rho(r) + \frac{1+\tau_3}{2}C(r),$$

$$S_0(r) = -\int\left[\frac{3}{4}v_{\sigma 1}(q) + \frac{1}{4}v_{\sigma 0}(q)\right]F_s(q)e^{i\mathbf{q}\cdot\mathbf{r}}\frac{d^3\mathbf{q}}{(2\pi)^3},$$

$$S_1(r) = -\int\left[v_\delta(q) + \frac{1}{4}v_{\sigma 1}(q) - \frac{1}{4}v_{\sigma 0}(q)\right]$$
$$\times F_s^-(q)e^{i\mathbf{q}\cdot\mathbf{r}}\frac{d^3\mathbf{q}}{(2\pi)^3}, \quad (30)$$

$$V_{\omega(r)} = \int v_\omega(q)F(q)e^{i\mathbf{q}\cdot\mathbf{r}}\frac{d^3\mathbf{q}}{(2\pi)^3},$$

$$V_\rho(r) = \int v_\rho(q)F^-(q)e^{i\mathbf{q}\cdot\mathbf{r}}\frac{d^3\mathbf{q}}{(2\pi)^3},$$

$$C(r) = e^2\int\frac{\rho_{ch}(r')}{|\mathbf{r}-\mathbf{r'}|}d^3\mathbf{r'}; \quad \Phi(r) = \tau_3\frac{\kappa}{2m}\frac{dV_\rho}{dr},$$

where

$$F_s(q) = \int\rho_s(r)e^{-\mathbf{q}\cdot\mathbf{r}}d^3\mathbf{r}, \quad F_s^-(q) = \int\rho_s^-(r)e^{-i\mathbf{q}\cdot\mathbf{r}}d^3\mathbf{r},$$

$$F(q) = \int\rho(r)e^{-i\mathbf{q}\cdot\mathbf{r}}d^3\mathbf{r},$$

$$F^-(q) = \int\left(\rho^-(r) + \frac{\kappa}{2mr^2}\frac{d}{dr}(r^2 w^-(r))\right)e^{-i\mathbf{q}\cdot\mathbf{r}}d^3\mathbf{r}, \quad (31)$$

$$\rho(r) = \rho_n(r) + \rho_p(r), \quad \rho^-(r) = \rho_n(r) - \rho_p(r),$$

$$\rho_s(r) = \rho_{sn}(r) + \rho_{sp}(r), \quad \rho_s^-(r) = \rho_{sn}(r) - \rho_{sp}(r),$$

$$w^-(r) = w_n(r) - w_p(r).$$

The scalar densities and the quantities $w(r)$ are

$$\rho_s(r) = \rho(r) - \frac{2(\tau(r) + \Phi(r)\rho'(r) + \Phi^2(r)\rho(r))}{(2m + S(r) - V(r))^2}, \quad (32)$$

$$w(r) = \frac{\rho'(r) + 2\Phi(r)\rho(r)}{2m + S(r) - V(r)}. \quad (33)$$

They are calculated separately for neutrons and protons. The quantity $\tau(r)$ is calculated in the local-density approximation using (26). The isovector quantity $\Phi(r)$, (29) and (30), arises from the tensor ρNN coupling, and $\kappa = f_\rho/g_\rho$ is the tensor-to-vector coupling ratio.

So the two-particle contributions may be determined from experiment by using a definite model for the two-particle NN interaction. Little is known, however, about the many-particle NN forces. Under such conditions, it is reasonable to look for the many-particle contribution as a power series expansion in the nucleon-density distribution,

$$U_m(r) = S_m(r) + V_m(r) = a_3\rho^2(r) + a_4\rho^3(r) + \dots, \quad (34)$$

the ρ^2 (ρ^3) term resulting from three-(four-particle) forces, etc. To elucidate the physical meaning of the coefficients, let us consider a general form of the three-particle term:

$$U_3(r)$$
$$= \int f_3(|\mathbf{r}-\mathbf{r}_1|, |\mathbf{r}-\mathbf{r}_2|)\rho(r_1)\rho(r_2)d^3\mathbf{r}_1 d^3\mathbf{r}_2. \quad (35)$$

In homogeneous nuclear matter, this gives

$$U_3 = \rho^2\int f_3(|\mathbf{r}\cdot\mathbf{r}_1|, |\mathbf{r}-\mathbf{r}_2|)d^3\mathbf{r}_1 d^3\mathbf{r}_2, \quad (36)$$

and therefore

$$a_3 = \int f_3(\eta, \xi)d^3\boldsymbol{\xi}d^3\boldsymbol{\eta}. \quad (37)$$

In the same way,

$$a_4 = \int f_4(\xi, \eta, \zeta)d^3\boldsymbol{\xi}d^3\boldsymbol{\eta}d^3\boldsymbol{\zeta}. \quad (38)$$

These volume integrals are the only parameters which do not require any specific model for the many-particle NN forces. Such model is, however, necessary to take into account the finite range of the forces. We did not try to do this since (a) the problem of the many-particle NN interaction mechanism is beyond the scope of our work and (b) the additional adjustable parameters describing the finite range cannot be safely determined because of the insufficient accuracy of the available experimental data.

The same reason forced us to introduce as few free parameters as possible and use all permissible simplifications. In particular, the many-particle terms are assumed to be equally distributed between the scalar and vector fields:

$$S_m(r) = V_m(r) = \frac{1}{2}U_m(r). \quad (39)$$

4. RESULTS

The observed and calculated spectra of the doorway-state energies in ^{40}Ca, ^{90}Zr, and ^{208}Pb nuclei are plotted in Figs. 4 and 5.
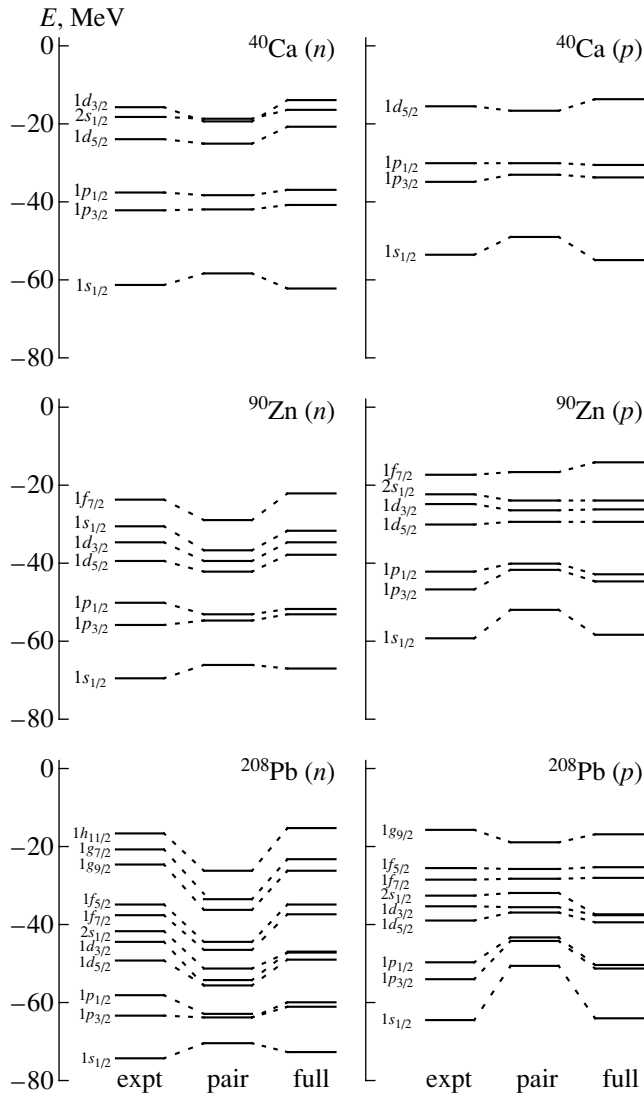
Fig. 4. Spectra of doorway-state energies in the case of the Bonn (*B*) potential for the two-particle forces.
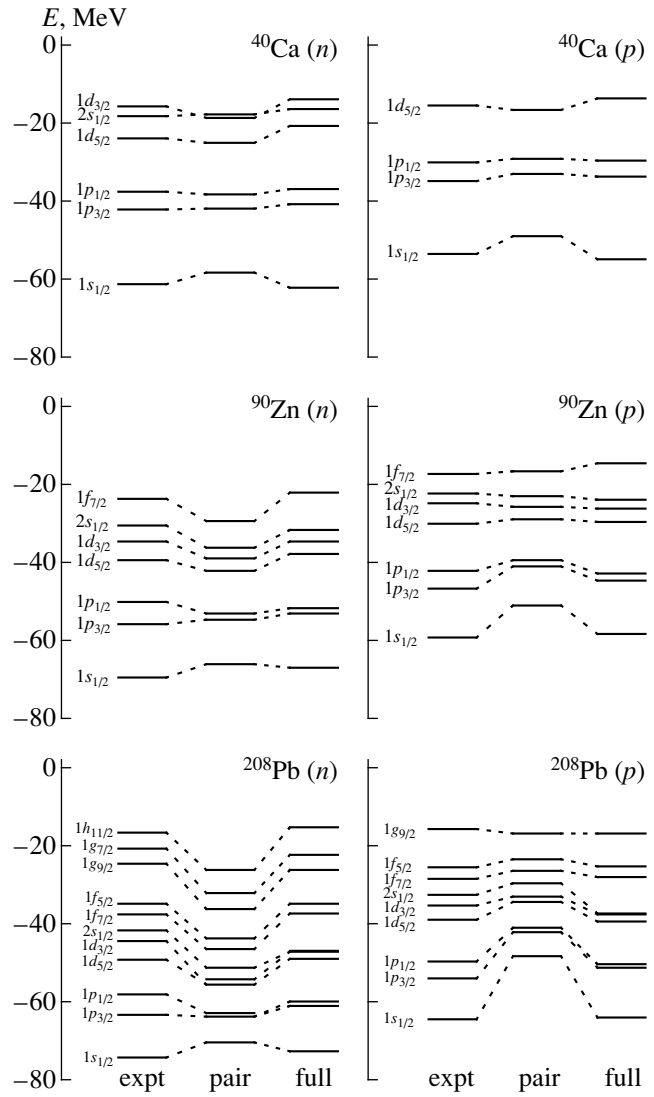
Fig. 5. As in Fig. 4, but for OSBEP.

The calculations are performed with two different two-particle potentials: the Bonn *B* (Fig. 4), and the OSBEP (Fig. 5).

The results for the two-particle forces only are labeled as "pair." As seen from the figures, the "pair" spectra are constricted compared to the observed ones, the lowest $1s_{1/2}$ states being significantly underbound. This means that the potential well resulting from the two-particle forces only is too wide but insufficiently deep, and so the actual well must be deeper and narrower as illustrated by Fig. 6.

Hence, the many-particle contribution (as discussed above, this is the only reason for the difference between the actual and "pair" wells) consists of attractive and repulsive parts, the radius of the former being less than that of the latter. The simplest form obeying this condition is provided by the sum of the first two terms of the expansion (34) with $a_3 > 0$ and $a_4 < 0$. In other words, the free-space many-particle *NN* interaction includes at least three-particle repulsion and four-particle attraction (of course, the presence of higher many-particle forces is not excluded).

Accounting for the fact that the many-particle forces contribute to both the isoscalar and isovector parts of the static nuclear field, the quantity $U_m(r)$ is chosen in the form

$$U_m(r) = a_3 \rho^2(r) + a_4 \rho^3(r)$$
$$- \tau_3 [\bar{a_3}\rho(r) + \bar{a_4}\rho^2(r)]\bar{\rho}(r), \qquad (40)$$

$$\rho(r) = \rho_n(r) + \rho_p(r), \quad \bar{\rho}(r) = \rho_n(r) - \rho_p(r).$$

The finite size of the nucleon is taken into account in the free-space *NN* forces, and therefore the static field of nucleus is expressed through the point nucleon den-

sities. The proton ones $\rho_p(r)$ are obtained from the charge-density distributions of [2] by a usual deconvolution procedure. They are shown in Fig. 7a. The point-neutron densities $\rho_n(r)$ are obtained from the folded densities of [3] in the same way.

The data of [2] are based on high precision measurements of elastic electron–nucleus scattering, thus providing the proton-density distributions in the whole nuclear region. The situation for the neutron densities is different since the elastic 1-GeV proton–nucleus scattering underlying the data of [3] is sensitive mainly to the surface region of the nucleus because of the absorption. For this reason, the neutron densities $\rho_n(r)$ may differ from the Woods–Saxon-like ones of [3] in the nuclear interior (as seen from Fig. 7a, the proton densities are indeed different from the Woods–Saxon-like ones). The latter is just the region to which the doorway-state energies are sensitive; therefore, they may be used to specify the data from [3] on the neutron densities. We looked for the latter ones in the form

$$\rho_n(r) = \rho_0[W_A(r) + \alpha W_A(0)\varphi_4(\beta r)], \qquad (41)$$

where $W_A(r)$ are the deconvoluted neutron densities of [3] and $\varphi_4(x)$ is the fourth Hermite function. The neutron density parameters α, β and the strength ones a_3, a_4, a_3^-, and a_4^- are determined from the best fit for both the doorway-state energies and the elastic 1-GeV proton-nucleus scattering, the latter being calculated within the Glauber theory [16].

The density parameters are shown in the table. They are different for the two choices of the two-particle forces, but the difference is rather small. For this reason, neither the resulting neutron-density distributions (Fig. 7b) nor the 1-GeV proton–nucleus elastic scattering cross sections (Fig. 8) are distinguishable in the figures. We also calculated the proton–nucleus cross sections with the original results of [3] for the density distributions. As seen from Fig. 8, the agreement with experiment is equally good for both the specified densities (41) and the original ones. The many-particle strength parameters are

$$a_3 = 16.9296 \text{ fm}^5, \quad a_4 = -107.6744 \text{ fm}^8,$$
$$a_3^- = 25.5873 \text{ fm}^5, \quad a_4^- = -128.5134 \text{ fm}^8 \qquad (42)$$

for the Bonn B two-particle forces and

$$a_3 = 17.0011 \text{ fm}^5, \quad a_4 = -110.3747 \text{ fm}^8,$$
$$a_3^- = 26.9036 \text{ fm}^5, \quad a_4^- = -130.1210 \text{ fm}^8 \qquad (43)$$

for the OSBEP ones. As seen from (42) and (43), the strength parameters of the free-space many-particle forces are almost the same for the two cases. This is not surprising because both the Bonn B and the OSBEP potentials provide an equally good description of the two-nucleon data (see the discussion in the Introduction).
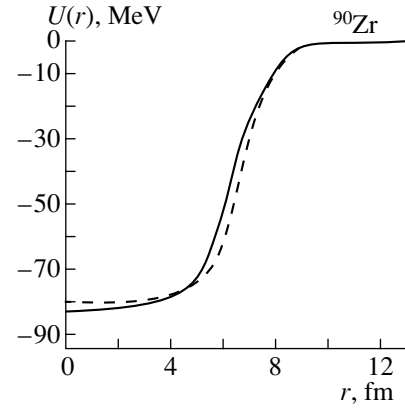
Fig. 6. Isoscalar part of the static field in ^{90}Zr. The dashed and full curves were plotted for the "pair" and actual wells, respectively. The calculations were performed with the Bonn (B) two-particle forces and original nucleon-density distributions of [3].
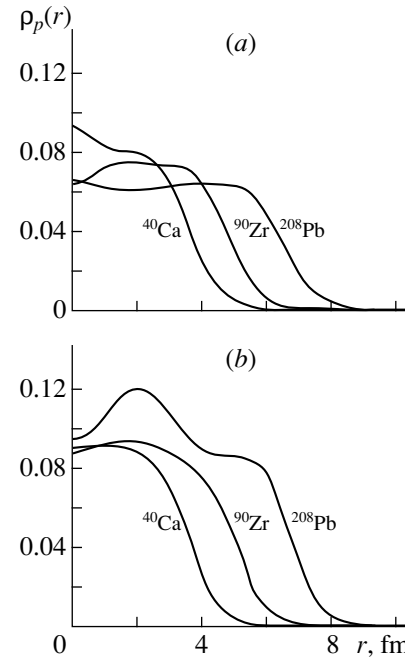
Fig. 7. Density distributions of (a) protons and (b) neutrons in the ^{40}Ca, ^{90}Zr, and ^{208}Pb nuclei.

The results including both the contribution from the many-particle forces and the specified neutron densities are labeled as "full" in Figs. 4 and 5. The "full" doorway-state energies agree with the observed ones (which are labeled as "expt") within the experimental error of 3 MeV. The exception is provided by the $2s_{1/2}$ states in ^{208}Pb: in this case the discrepancy is about 5 MeV. The reason is not clear yet, but the discrepancy does not exceed two experimental errors.

To estimate the relative importance of the two-particle and many-particle contributions to the static field of the nucleus, let us perform the calculations for nuclear
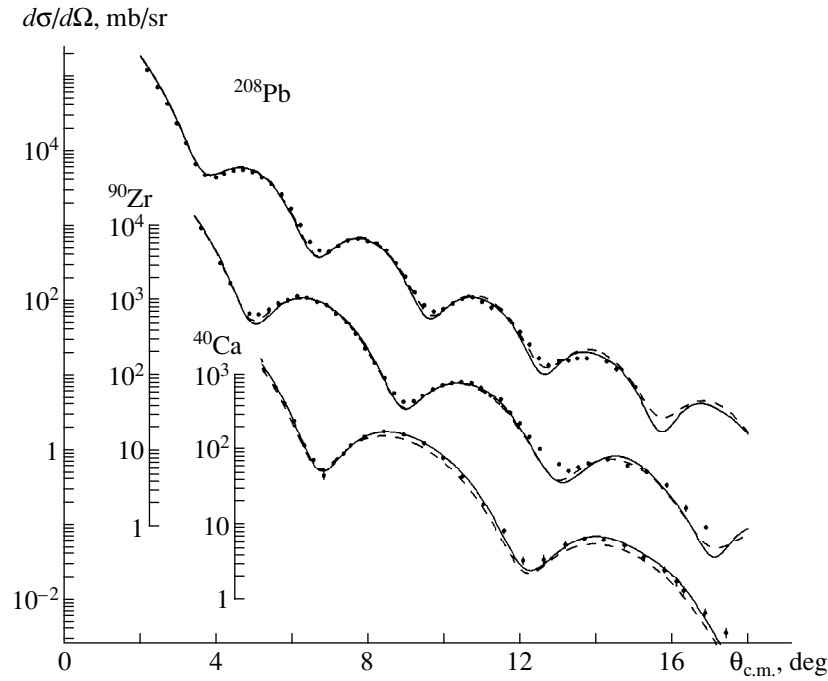
Fig. 8. Cross sections for elastic proton–nucleus scattering at 1 GeV. Dashed and solid curves were calculated with the original neutron density-distributions from [3] and the specified ones, respectively.

matter (see Section 3). First consider the isoscalar part. The two-particle contribution is

$$U_2 = V_2 + S_2 = \left\{ v_\omega(0)\rho - \left[\frac{3}{4}v_{\sigma 1}(0) + \frac{1}{4}v_{\sigma 0}(0)\right]\rho_s \right\} \tag{44}$$

$$= \begin{cases} -83 \text{ MeV}, & \text{Bonn } B \\ -82 \text{ MeV}, & \text{OSBEP}, \end{cases}$$

whereas those from three-particle and four-particle forces are

$$U_3 = a_3\rho^2 = \begin{cases} 96.5 \text{ MeV}, & \text{Bonn } B \\ 97 \text{ MeV}, & \text{OSBEP}, \end{cases}$$

$$U_4 = a_4\rho^3 = \begin{cases} -104 \text{ MeV}, & \text{Bonn } B \\ -107 \text{ MeV}, & \text{OSBEP}, \end{cases} \tag{45}$$

the many-particle contributions thus being as large as the two-particle one.

Neutron-density parameters

	Bonn B		OSBEP	
	α	β	α	β
^{40}Ca	-0.0295	0.5314	-0.0255	0.5230
^{90}Zr	-0.0758	0.5551	-0.0646	0.5442
^{208}Pb	-0.2645	0.5445	-0.2667	0.5389

The isovector part may be estimated by putting $\rho^- = \dfrac{N-Z}{A}\rho$ and $\rho_s^- = \dfrac{N-Z}{A}\rho_s$. The two-particle contribution is (see Section 3)

$$U_2^- = \left\{ v_\rho(0)\rho^- - \left[v_\delta(0) + \frac{1}{4}v_{\sigma 1}(0) - \frac{1}{4}v_{\sigma 0}(0)\right]\rho_s^- \right\} \tag{46}$$

$$= \begin{cases} 6\dfrac{N-Z}{A} \text{ MeV}, & \text{Bonn } B \\ 0.15\dfrac{N-Z}{A} \text{ MeV}, & \text{OSBEP}, \end{cases}$$

the many-particle one being

$$U_m^- = (a_3^-\rho + a_4^-\rho^2)\rho^-$$

$$= \begin{cases} (146 - 125 = 21)\dfrac{N-Z}{A} \text{ MeV}, & \text{Bonn } B \\ (153 - 126 = 27)\dfrac{N-Z}{A} \text{ MeV}, & \text{OSBEP}. \end{cases} \tag{47}$$

Thus, the many-particle forces provide the dominant part of the isovector nuclear potential. The reason is due to the fact that the two-particle contribution arises from the exchange by isovector mesons ρ and δ, which are weakly coupled to nucleons (see Table 5 of [11] and Table 1 of [12]).

5. SUMMARY

The above results can be summarized as follows:

(I) Our results for the many-particle forces are quite competitive with those from the few-nucleon systems [17]. Indeed, the properties of the latter ones (binding energies, sizes, form factors, etc.) are expressed through the interaction in all orders of the perturbation theory, and therefore the solution of a rather complicated quantum mechanical problem is necessary to get information on the many-particle forces. In contrast to few-nucleon systems, the doorway states for the one-nucleon transfer reactions in complex nuclei are solutions of a much simpler problem for one nucleon in a central field. In addition, the static nuclear field is expressed through the NN forces in first order of the perturbation theory, the results thus being very visual (see Figs. 1 and 6). Information from the doorway states is, however, restricted because it concerns only spin-independent terms of the many-particle forces (the spin-dependent ones do not contribute to the Hartree diagrams). Nevertheless, it is a useful addition to that from few-nucleon systems.

Two important points should be mentioned in this connection. (i) Only three-particle forces (in addition to the two-particle ones) are included in all available calculations for few-nucleon systems. Our results clearly show that this is insufficient. (ii) Calculating the nuclear correlation effects (binding energies and rms radii of finite nuclei, equation of state of nuclear matter, etc.) with the free-space NN interaction, we have no reason to neglect the many-particle forces because they are as strong as the two-particle ones (compare (44) and (45)).

(II) The effective three-particle and four-particle forces are also repulsive and attractive, respectively, in the recent calculations within the relativistic mean-field approximation [18, 19] (see the Appendix). Such forces include implicitly the correlation effects which are not taken into account explicitly within this framework. For this reason, the above signs of the forces might be treated as an artifact of the approximation. But our results for the free-space many-particle forces show that this is not an artifact.

APPENDIX

The potential energy of the σ mesons is [18, 19]

$$U(\sigma) = \frac{\mu^2}{2}\sigma^2 + \frac{\lambda_3}{3}\sigma^3 + \frac{\lambda_4}{4}\sigma^4 \qquad (A.1)$$

with $\lambda_3 < 0$ and $\lambda_4 < 0$, the scalar field $S = g\sigma$ thus obeying the equation

$$(\Delta - \mu^2)S = g^2\rho_s + \frac{\lambda_3}{g}S^2 + \frac{\lambda_4}{g^2}S^3. \qquad (A.2)$$

Let us use the following iteration procedure:

$$(\Delta - \mu^2)S_n = g_\sigma^2\rho_s + \frac{\lambda_3}{g}S_{n-1}^2 + \frac{\lambda_4}{g^2}S_{n-1}^3 \qquad (A.3)$$

with

$$(\Delta - \mu^2)S_0 = g_\sigma^2\rho_s \qquad (A.4)$$

for the initial iteration. The result is

$$S(r) = -g^2\int y(|\mathbf{r} - \mathbf{r}_1|)\rho_s^{(r)}(r_1)d^3\mathbf{r}_1$$
$$+ \int f_3(|\mathbf{r} - \mathbf{r}_1|, |\mathbf{r} - \mathbf{r}_2|)\rho_s(r_1)\rho_s(r_2)dr_1dr_2$$
$$+ \int f_4(|\mathbf{r} - \mathbf{r}_1|, |\mathbf{r} - \mathbf{r}_2|, |\mathbf{r} - \mathbf{r}_3|)$$
$$\times \rho_s(r_1)\rho_s(r_2)\rho_s(r_3)d^3\mathbf{r}_1d^3\mathbf{r}_2d^3\mathbf{r}_3 + \dots, \qquad (A.5)$$

where

$$y(|\mathbf{r} - \mathbf{r}'|) = \frac{\exp(-\mu|\mathbf{r} - \mathbf{r}'|)}{4\pi|\mathbf{r} - \mathbf{r}'|}, \qquad (A.6)$$

$$f_3(|\mathbf{r} - \mathbf{r}_1|, |\mathbf{r} - \mathbf{r}_2|)$$
$$= -\lambda_3 g^3\int y(|\mathbf{r} - \mathbf{r}'|)y(|\mathbf{r}_1 - \mathbf{r}'|)y(|\mathbf{r}_2 - \mathbf{r}'|)d^3\mathbf{r}', \qquad (A.7)$$

$$f_4(|\mathbf{r} - \mathbf{r}_1|, |\mathbf{r} - \mathbf{r}_2|, |\mathbf{r} - \mathbf{r}_3|)$$
$$= \lambda_4 g^4\int y(|\mathbf{r} - \mathbf{r}'|)y(|\mathbf{r}_1 - \mathbf{r}'|)y(|\mathbf{r}_2 - \mathbf{r}'|)y(|\mathbf{r}_3 - \mathbf{r}'|)d^3r'$$
$$- 2\lambda_3^2 g^4\int y(|\mathbf{r} - \mathbf{r}'|)y(|\mathbf{r}_1 - \mathbf{r}'|)y(|\mathbf{r}' - \mathbf{r}''|)$$
$$\times y(|\mathbf{r}_2 - \mathbf{r}''|)y(|\mathbf{r}_3 - \mathbf{r}''|)d^3\mathbf{r}'d^3\mathbf{r}''. \qquad (A.8)$$

The ellipsis on the right-hand side of (A.5) represents the higher power terms in respect of ρ_s resulting from the higher many-particle forces. As seen from (A.7), the three-particle force is repulsive because of the sign of λ_3 ($g > 0$ in [18, 19]). The four-particle one (A.8) consists of two terms. The first is of first order with respect to the λ_4 term of (A.1). It is attractive because of the sign of λ_4. The second is of second order with respect to the λ_3 term. It is attractive irrespective of the sign of λ_3.

The volume integrals of the forces (A.7) and (A.8), (37), and (38) are

$$a_3 = -g^3\lambda_3\mu^{-6}, \quad a_4 = g^4(\lambda_4 - 2\lambda_3^2\mu^{-2})\mu^{-8}. \quad (A.9)$$

The least values of these quantities correspond to the NL–SH parameter set of [18, Table 2]. They are

$$a_3 = 21.9 \text{ fm}^5, \quad a_4 = -136.5 \text{ fm}^8, \qquad (A.10)$$

thus being rather close to the free-space values, (42) and (43).

REFERENCES

1. M. Baranger, Nucl. Phys. A **149**, 225 (1970).
2. H. de Vries *et al.*, At. Data Nucl. Data Tables **36**, 495 (1987).
3. G. D. Alkhazov *et al.*, Nucl. Phys. A **381**, 430 (1982).
4. A. A. Abrikosov, L. P. Gor'kov, and I. E. Dzyaloshinskiĭ, *Methods of Quantum Field Theory in Statistical Physics*

(Fizmatgiz, Moscow, 1962; Prentice-Hall, Englewood Cliffs, 1963).

5. A. B. Migdal, *Theory of Finite Fermi Systems and Applications to Atomic Nuclei* (Nauka, Moscow, 1983; Interscience, New York, 1967).

6. S. G. Kadmenskiǐ and P. A. Lukyanovich, Yad. Fiz. **49**, 1285 (1989) [Sov. J. Nucl. Phys. **49**, 800 (1989)].

7. S. S. Volkov *et al.*, Yad. Fiz. **52**, 1339 (1990) [Sov. J. Nucl. Phys. **52**, 848 (1990)].

8. A. A. Vorob'ev *et al.*, Yad. Fiz. **58**, 1923 (1995) [Phys. At. Nucl. **58**, 1817 (1995)].

9. K. Erkelenz, Phys. Rep. **13**, 191 (1974).

10. M. Lacombe, Phys. Rev. C **21**, 861 (1980).

11. R. Machleidt, K. Holinde, and Ch. Elster, Phys. Rep. **149**, 1 (1987).

12. L. Jäde and H. V. von Geramb, Phys. Rev. C **57**, 496 (1998).

13. R. Machleidt, Adv. Nucl. Phys. **19**, 189 (1989).

14. J. D. Walecka, Ann. Phys. (N.Y.) **83**, 491 (1974).

15. S. J. Wallace, Comments Nucl. Part. Phys. **13**, 27 (1984).

16. R. J. Glauber, *Lectures on Theoretical Physics*, Ed. by W. E. Brittin *et al.* (New York, 1959), Vol. 1.

17. R. Schiavilla, V. R. Pandharipande, and R. B. Wiringa, Nucl. Phys. A **449**, 219 (1986).

18. G. A. Lalazissis, J. König, and P. Ring, Phys. Rev. C **55**, 540 (1997).

19. M. L. Cescato and P. Ring, Phys. Rev. C **57**, 134 (1998).

NUCLEI
Theory

Proton-Separation Vertex Constants for *sd*-Shell Nuclei from an Analysis of Peripheral Transfer Reactions

S. V. Artemov, É. A. Zaparov, M. A. Kayumov, and G. K. Nie

Institute of Nuclear Physics, Uzbek Academy of Sciences, pos. Ulughbek, UZ-702132 Tashkent, Republic of Uzbekistan
Received October 22, 1998; in final form, November 1, 1999

Abstract—The differential cross sections for the (^{3}He, *d*) reactions on ^{16}O nuclei at $E_{3_{He}}$ = 42 MeV and on ^{19}F and ^{26}Mg nuclei at $E_{3_{He}}$ = 22.3 MeV are measured for angles from the forward hemisphere. These data and those from the literature are analyzed by using a procedure that combines the method of distorted waves and the elements of the dispersion approach. It is established that the reactions in question are peripheral. Phenomenological values of nuclear vertex constants for proton separation are obtained both for the ground state and for low-lying excited states of the final nucleus, and the corresponding spectroscopic factors are evaluated. It is indicated that these data can be used for nuclear astrophysics. © *2000 MAIK "Nauka/Interperiodica".*

1. INTRODUCTION

The investigations reported here were initiated by the development of the approach that is aimed at solving the problem of correctly extracting spectroscopic information from an analysis of nucleon-transfer reactions and which introduces elements of dispersion reaction theory [1, 2] in the distorted-wave method (abbreviated as DWM in indices and in Table 2). Although a great number of phenomenological spectroscopic factors have been obtained for stable nuclear states over the last 30 years, there remains the problem of a large scatter of their values. This may be due to the illegitimate use of the distorted-wave method in some specific cases of nuclear-transfer reactions, but ambiguities in choosing model-parameter values also contribute to the above scatter. By way of example, we indicate that, in describing a bound nuclear state, the single-particle approximation implies the dominance of the stripping (pickup) pole diagram, but this is not always so in nucleon-transfer reactions. Moreover, only peripheral processes can be analyzed by the method with some degree of reliability because, in other regions, results are affected more strongly by ambiguities in the parameters of distorted waves. A wide scatter of spectroscopic-factor values also stems from variations in values of geometric parameters like the radius r_0 and the diffuseness a of the Woods–Saxon potential for a nucleon bound state.

To a considerable extent, these difficulties are removed within the aforementioned combined method for purely peripheral processes, in which case the differential cross sections for processes dominated by the pole mechanism are parametrized not in terms of spectroscopic factors but in terms of the square of the vertex constant, which has the meaning of an asymptotic normalization factor for the overlap integral [2]. Here, criteria formulated within the combined approach make it

possible to select reliably the aforementioned cases. It should be noted that, in such an analysis, vertex constants are independent of the geometric features of the transferred particle. The approach in question is convenient, on one hand, as a method for deriving phenomenological values of nuclear vertex constants and, on the other hand, as a method for computing cross sections for peripheral processes—in particular, astrophysical nuclear reactions of radiative capture [3].

From this point of view, data on neutron-transfer reactions and data on proton-transfer reactions involving 1*p*-shell nuclei were analyzed in [4] and [5], respectively. The objective of the present study is to assess the possibility of correctly deducing the phenomenological values of proton-separation vertex constants for the ground states and low-lying excited states of the *sd*-shell nuclei ^{17}F, ^{20}Ne, and ^{27}Al, which have various degrees of deformation. On the basis of the combined method, we have performed a global analysis of the entire body of available data on peripheral (^{3}He, *d*) and (*d*, ^{3}He) reactions over the region of energies and angles where the reactions in question proceed predominantly via a mere stripping (capture) of a proton. In order to extend the set of data subjected to analysis, we have measured the differential cross sections for the (^{3}He, *d*) reactions on ^{16}O, ^{19}F, and ^{26}Mg nuclei for angles in the forward hemisphere. Special measures were taken to ensure precision measurements in the region of small angles, where the main peak of the angular distribution occurs.

2. BASIC RELATIONS OF THE COMBINED METHOD

Since the method was described in detail elsewhere [2, 5], we present here only basic relations used in our
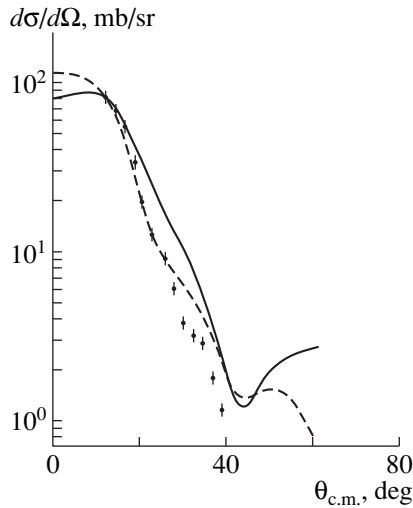
$d\sigma/d\Omega$, mb/sr

Fig. 1. Angular distributions of deuterons from the reaction
$^{16}O(^{3}He, d)^{17}F$ populating the ground state of the final
nucleus ($E^* = 0$ MeV) and occurring at $E_{^{3}He} = 42.0$ MeV:
(points) experimental values, (solid curve) results of the cal-
culation on the basis of the DWUCK5 code at $r_{cut} = 0$ fm,
and (dashed curve) results of the calculation on the basis of
the DWUCK5 code at $r_{cut} = 4.0$ fm.

analysis. For the sake of definiteness, we will analyze
proton-stripping reactions of the type $A(x, y)B$, where
$B = A + p$ and $x = y + p$. Specifically, we will consider
the behavior of the quantity

$$R(b) = \left(\frac{d\sigma^{DWM}}{d\Omega}\right)\Bigg|_{max} /b^2 \qquad (1)$$

as a function of b for various values of the parameters
r_0 and a of the potential for the bound state. Here, b is
the asymptotic normalization factor for the shell-model
wave function of the proton bound state in nucleus B.
The condition $R(b) = $ const must be satisfied for a
peripheral reaction; in addition, the computed value of
$d\sigma^{DWM}/d\Omega|_{max}$ must be independent of the radius r_{cut} of
cutoff at the lower integration limit within the nuclear
interior. The diffraction structure of the experimental
differential cross section must be well described within
the distorted-wave method at least in the region of the
main peak of the angular distribution. If these three
conditions are satisfied, the reaction being investigated
can be considered as a peripheral one. For reactions
dominated by the pole mechanism, the phenomenolog-
ical value of vertex constant is given by

$$\left[\frac{d\sigma^{expt}}{d\Omega}\right] = |G|^2 \left[\frac{\mu c}{\pi^{1/2}\hbar}\right]^2 R(b), \qquad (2)$$

where G is the $B \longrightarrow A + p$ vertex constant, while μ is
the reduced mass of A and p. For a peripheral reaction,
the vertex constant is independent of the choice of val-
ues for the model parameters of the potential for the

bound nucleon state [see Eq. (2)]. The agreement
between the vertex-constant values extracted at differ-
ent incident-particle energies, as well as the agreement
between such values for peripheral reactions that are
induced by different projectile species, but which are
described by amplitude involving the same vertex, may
be considered as an indication of pole-mechanism
dominance. The spectroscopic factor and the vertex
constant are related by the equation

$$Sb^2 = \left(\frac{\mu c}{\pi^{1/2}\hbar}\right)^2 |G|^2. \qquad (3)$$

It should be emphasized that, without fixing the geo-
metric parameters r_0 and a (that is, the quantity b) on
the basis of one physical argument or another, the phe-
nomenological spectroscopic factor cannot be deter-
mined from (3) for a peripheral reaction.

For stripping reactions ($^{3}He, d$), the differential
cross section was computed by the formula

$$\frac{d\sigma^{DWM}}{d\Omega} = S_{^{3}He}(2J_B + 1)/(2J_A + 1)$$
$$\times [10 \text{ mb/fm}^2]\frac{d\sigma^{DWUCK5}}{d\Omega}, \qquad (4)$$

where $d\sigma^{DWUCK5}/d\Omega$ is the differential cross section cal-
culated in the "post" approximation on the basis of the
DWUCK5 code [6]; the proton spectroscopic factor in
the ^{3}He nucleus, $S_{^{3}He} = 1.35$, was computed on the
basis of (3) at $|G_{^{3}He}|^2 \approx |G_t|^2 = 1.34$ fm [4], with G_t
being the vertex constant for proton separation from a
triton as calculated at $r_0 = 1.25$ fm and $a = 0.65$ fm. For
pickup reactions ($d, ^{3}He$), we used the relation

$$\frac{d\sigma^{DWM}}{d\Omega} = S_{^{3}He}[10 \text{ mb/fm}^2]\frac{d\sigma^{DWUCK5}}{d\Omega}. \qquad (5)$$

3. EXPERIMENTAL PROCEDURE

The measurements at 22.3 MeV and those at
42.0 MeV were performed at, respectively, the 120-cm
cyclotron installed at the Institute of Nuclear Physics
(Moscow State University, Moscow) and the 150-cm
isochronous cyclotron of the National Nuclear Center
of the Republic of Kazakhstan (Almaty). Secondary
deuterons were recorded by ΔE–E telescopes of semi-
conductor detectors. The total energy resolution was
between 1 and 1.5%.

The differential cross sections for the reaction
$^{16}O(^{3}He, d)^{17}F$ at 42 MeV were measured for laboratory
angles in range 10°–34° scanned with a step of 2°
(Fig. 1). For targets, we used Mylar films of thickness
about 1 mg/cm². The target thicknesses in the region
traversed by the beam were determined from the alpha-
particle energy losses prior to and after the measure-
ments, this being accomplished at the target device

Table 1. Parameters of the optical potentials (OP) used in the present calculations within the distorted-wave method

OP	E_{lab}, MeV	V, MeV	R_V, fm	A_V, fm	W, MeV	R_W, fm	A_W, fm	V_{so}, MeV	R_c, fm	References
$o\tau2$	29.0	190.0	1.14	0.675	11.2V	2.17	0.426		1.27	[7]
$o\tau3$	44.0	126.9	1.0	0.88	8.6V	2.10	0.62		1.3	[8]
$o\tau4$	44.0	122.1	1.1	0.84	13.1D	1.65	0.57		1.3	[8]
$o\tau5$	18.0	130.0	1.07	0.79	9.17D	1.67	0.72	4.0	1.3	[7]
$o\tau6$	17.3	159.7	1.302	0.615	19.76V	1.383	0.929	4.10	1.3	[7]
$fd1$	22.3^{16}O	104.4	1.05	0.80	19.0D	1.37	0.77		1.3	[9]
$fd2$	16.3^{16}O	70.6	1.318	0.586	9.6D	1.523	0.577	9.22	1.3	[7]
$fd3$	34.4^{16}O	92.94	1.036	0.787	8.91D	1.355	0.727		1.3	[7]
$f\tau1^*$	22.3	177.0	1.08	0.73	17.4V	1.73	0.80		1.40	[10]
$ned1^{**}$	22.3	100.0	1.00	0.90	10.0D	1.50	0.80		1.3	[11]
$m\tau2$	17.85	155.0	1.08	0.80	15.0V	1.78	0.60	9.4	1.4	[12]
$m\tau3$	20.2	159.3	1.149	0.683	17.86V	1.567	0.878		1.25	[13]
$m\tau1$	22.3	105.8	1.028	0.911	15.9V	1.794	0.830		1.40	[7]
$ad1$	23.4	103.6	1.02	0.85	11.82D	1.413	0.695	8.19	1.25	[7]
$ad2$	17.85	90.0	1.15	0.81	22.5D	1.34	0.68	12.0	1.3	[12]
$ad3$	20.2	120.0	1.00	0.90	100D	1.50	0.50		1.3	[13]

Note: The potential labeled with an asterisk (two asterisks) was taken with the deformation parameter(s) $\beta_2 = 0.45$ ($\beta_2 = 0.45$ and $\beta_4 = 0.15$).

directly. In processing the collected spectra, we performed a test normalization to the differential cross sections for deuteron groups originating from the reaction ^{12}C(^{3}He, d)^{13}N. For this, we invoked the differential cross sections measured for the last reaction in the same experiment by using a carbon foil.

The differential cross sections for the reaction ^{19}F(^{3}He, d)^{20}Ne at 22.3 MeV were measured in the angular interval 8°–60° (in the laboratory frame) with a step between 2° and 5° (the resulting data are displayed in Fig. 2). In these measurements, we used a set of targets made from a fluoroplastic film of thickness about 0.9 to 1.0 mg/cm^2. A considerable depletion of the targets during the measurements was taken into account via a normalization to the elastic-scattering peak from a monitoring detector. In the process of experimenting, the targets were replaced at regular time intervals, and each such replacement was followed by a test measurement of the deuteron spectrum at an angle of 13°, which corresponded to the main peak of the angular distribution.

At an energy of 22.3 MeV, we have also measured the differential cross sections for the reaction ^{26}Mg(^{3}He, d)^{27}Al in the region of the main peak. The target used in this measurement was manufactured by sputtering a magnesium layer enriched in the ^{26}Mg isotope to 87.3% onto a nickel substrate 0.16 mg/cm^2 thick.

For all differential cross sections subjected to analysis, we accumulated statistics with a precision not poorer than 3% in the region around the main peak. As to the total error in the measurement of the differential cross sections, it did not exceed 8%.

4. ANALYSIS OF THE DIFFERENTIAL CROSS SECTIONS FOR (^{3}He, d) AND (d, ^{3}He) REACTIONS

In performing our calculations on the basis of the distorted-wave method, we assumed a finite interaction range. The parameters of the optical potentials used in an analysis of our present data and in a reanalysis of data from the literature are listed in Table 1. In the cases where the proton-transfer process proved to be peripheral according to the above criteria, we determined the phenomenological values of the vertex constants on the basis of Eq. (2). The results are displayed in Table 2. These values are virtually independent of the choice of the geometric parameters of the potential for the bound state. For convenience of comparison also presented in this table are the spectroscopic-factor values that we obtained from a reanalysis of data from the literature by using everywhere the standard geometric parameters of the potential for the bound state ($r_0 = 1.25$ fm and $a = 0.65$ fm) and the Thomas spin–orbit term with $\lambda = 25$. In those cases where the spectroscopic factors were found in the literature at different values of r_0 and a, they are quoted as well.

4.1. Reaction ^{16}O(^{3}He, d)^{17}F

Previously, this reaction was investigated at 18 MeV [16, 17], 25 MeV [18], and 33 MeV [19]; we studied it at 34 MeV in [5], but we used there a shallow potential in the input channel. Since this does not seem justifiable physically, the analysis in the present study is performed with the $o\tau2$ deep potentials; as a result, the vertex-constant and spectroscopic-factor values became

ARTEMOV *et al.*

Table 2. Phenomenological vertex-constant and spectroscopic-factor values for the reactions $^{17}F \longrightarrow ^{16}O + p$, $^{20}Ne \longrightarrow ^{19}F + p$, and $^{27}Al \longrightarrow ^{26}Mg + p$

Reaction, E_{lab}, MeV	OP_{in}, OP_{out}	$|G|^2$, fm	Parameters of the potential for the bound state r_0, a (fm)	c^2S	References
			$^{17}F \longrightarrow ^{16}O + p$, $E^* = 0.0$ MeV, $J^\pi = 5/2^+$, $nlj = 1d_{3/2}$		
(d, n), 8.0	OP from [14]	0.121 ± 0.024	SS*	0.84 ± 0.17	[14]
(d, n), 9.3	OP from [14]	0.111 ± 0.022	SS*	0.77 ± 0.15	[14]
(d, n), 7.73	OP from [15]	0.151 ± 0.038	SS*	1.05 ± 0.26	[15]
(d, n), 11.0	OP from [15]	0.130 ± 0.032	SS*	0.90 ± 0.22	[15]
(d, n), 12.0	OP from [15]	0.122 ± 0.030	SS**	0.85 ± 0.21	[15]
(τ, d), 18.0	OP from [16]	0.121 ± 0.025	1.26, 0.60 ($V_{so} = 6.0$)	0.93 ± 0.19	[16]
		0.121 ± 0.025	SS*	0.85 ± 0.17	
(τ, d), 18.0	OP from [17]	0.12	SS*	0.83	[17]
(τ, d), 20.0	OP from [17]	0.14	SS*	0.98	[17]
(τ, d), 25.0	OP from [18]	0.145 ± 0.013	SS*	1.0 ± 0.09	[18]
(τ, d), 33.3	OP from [19]	0.09		0.6	[19]
(τ, d), 34.0	$o\tau2, fd1$	0.129 ± 0.013	SS*	0.90 ± 0.09	[5]
(τ, d), 42.0	$o\tau2, fd3$	0.14 ± 0.008	SS*	0.97 ± 0.06	
(τ, d), 42.0	$o\tau3, fd3$	0.131 ± 0.008	SS*	0.91 ± 0.06	
(τ, d), 42.0	$o\tau4, fd3$	0.136 ± 0.008	SS*	0.96 ± 0.06	
(τ, d), 42.0	$o\tau5, fd2$	0.139 ± 0.008	SS*	0.96 ± 0.06	
(τ, d), 42.0	$o\tau6, fd2$	0.130 ± 0.008	SS*	0.90 ± 0.06	
			$^{17}F \longrightarrow ^{16}O + p$, $E^* = 0.495$ MeV, $J^\pi = 1/2^+$, $nlj = 2s_{1/2}$		
(d, n), 8.0	OP from [14]	1031 ± 206	SS*	0.93 ± 0.19	[14]
(d, n), 9.3	OP from [14]	1065 ± 213	SS*	0.96 ± 0.19	[14]
(d, n), 7.7	OP from [15]	1276 ± 319	SS*	1.15 ± 0.29	[15]
(d, n), 11.0	OP from [15]	1054 ± 263	SS*	0.95 ± 0.24	[15]
(d, n), 12.0	OP from [15]	1054 ± 263	SS*	0.95 ± 0.24	[15]
(τ, d), 18.0	OP from [16]	854 ± 170	1.26, 0.6 ($V_{so} = 6.0$)	0.84 ± 0.17	[16]
		854 ± 170	SS*	0.79 ± 0.16	
(τ, d), 25.0	OP from [18]	911 ± 82	SS*	0.82 ± 0.08	[18]
(τ, d), 34.0	$o\tau2, fd1$	816 ± 103	SS*	0.97 ± 0.09	[5]
		819 ± 101	1.3; 0.7	0.80 ± 0.08	
			$^{20}Ne \longrightarrow ^{19}F + p$, $E^* = 0$ MeV, $J^\pi = 0^+$, $nlj = 2s_{1/2}$		
(τ, d), 10.0	OP from [20]	40.9 ± 8.0	SS*	0.31 ± 0.06	[20]
(τ, d), 16.0	OP from [21]	36.9	SS*	0.27 DWM	[21]
				0.30 CCM	
(τ, d), 21.0, 23.0	OP from [10]	39.6	SS*	0.30 DWM	[10]
				0.43 CCM	
(τ, d), 22.3	$f\tau1, ned1$	32.8 ± 5.5	SS*	0.24 ± 0.04 DWM	[22]
		30.1 ± 5.2		0.22 ± 0.04 CCM	
(τ, d), 25.0	OP from [18]	79.5	SS*	0.54	[18]
	$f\tau1, ned1$	75.3	SS*	0.51	
(d, τ), 52.0	OP from [23]	112.2	SS*	0.76 DWM	[23]
		56.1		0.38 CCM	
			$^{20}Ne \longrightarrow ^{19}F + p$, $E^* = 1.63$ MeV, $J^\pi = 2^+$, $nlj = 1d_{5/2}$		
(τ, d), 10.0	OP from [20]	8.2 ± 1.2	SS*	0.62 ± 0.12	[20]
(τ, d), 16.0	OP from [21]	5.9	SS*	0.43 DWM	[21]

Table 2. (Contd.)

Reaction, E_{lab}, MeV	OP_{in}, OP_{out}	$|G|^2$, fm	Parameters of the potential for the bound state r_0, a (fm)	$c^2 S$	Refe-rences
				0.29 CCM	
(τ, d), 16.0	OP from [11]	4.38	SS*	0.32	[11]
(τ, d), 21.0, 23.0	OP from [10]	5.76	SS*	0.42 DWM	[10]
				0.38 CCM	
(τ, d), 22.3	$f\tau 1$, $ned1$	4.12 ± 0.65	SS*	0.31 ± 0.04 DWM	[22]
				0.49 ± 0.06 CCM	
(τ, d), 25.0	OP from [18]	6.6 ± 0.6	SS*	0.48	[18]
^{27}Al $\longrightarrow$ ^{26}Mg $+ p$, $E^* = 0.0$ MeV, $J^\pi = 5/2^+$, $nlj = 1d_{5/2}$					
(τ, d), 11.0	OP from [24]	5.41 ± 1.08	SS*	0.28 ± 0.056	[24]
(τ, d), 14.0	OP from [25]	5.18	1.2, 0.65	0.32	[25]
		4.85	SS*	0.27	
(τ, d), 17.9	$m\tau 2$, $ad2$	4.04	1.2, 0.6	0.25	[12]
		4.04	SS*	0.22	
(τ, d), 20.2	$m\tau 3$, $ad3$	5.61	SS*	0.29	[13]
(τ, d), 22.3	$m\tau 1$, $ad1$	4.82 ± 1.0	SS*	0.26 ± 0.05	
(τ, d), 25.0	OP from [18]	4.25	SS*	0.22	[18]
(d, τ), 29.0	OP from [26]	5.55	SS*	0.30	[26]
(d, τ), 34.5	OP from [27]	4.63	1.2, 0.65	0.30	[27]
		4.63	SS*	0.26	
(d, τ), 52.0	OP from [28]	4.98 ± 0.75	SS*	0.27 ± 0.04	[28]
(d, τ), 80.0	OP from [29]	4.93		0.26	[29]
^{27}Al $\longrightarrow$ ^{26}Mg $+ p$, $E^* = 0.84$ MeV, $J^\pi = 1/2^+$, $nlj = 2s_{1/2}$					
(τ, d), 11.0	OP from [24]	58.66 ± 11.7	SS*	0.44 ± 0.09	[24]
(τ, d), 14.0	OP from [25]	49.16	1.2, 0.65	0.42	[25]
		49.16	SS*	0.37	
(τ, d), 17.9	$m\tau 2$, $ad2$	58.5	1.2, 0.65	0.50	[12]
		58.5	SS*	0.43	
(τ, d), 20.2	$m\tau 3$, $ad3$	57.3	SS*	0.43	[13]
(τ, d), 22.3	$m\tau 1$, $ad1$	70.5 ± 14.1	SS*	0.58 ± 0.12	
(τ, d), 25.0	$m\tau 1$, $ad1$	42.5 ± 8.5	SS*	0.35 ± 0.07	[18]
(τ, d), 25.0	OP from [18]	57.3 ± 5.16	SS*	0.43 ± 0.04	[18]
^{27}Al $\longrightarrow$ ^{26}Mg $+ p$, $E^* = 2.98$ MeV, $J^\pi = 3/2^+$, $nlj = 1d_{3/2}$					
(τ, d), 11.0	OP from [24]	2.60 ± 0.52	SS*	0.44 ± 0.09	[24]
(τ, d), 14.0	OP from [25]	2.61	1.2, 0.65	0.52	[25]
		2.61	SS*	0.45	
(τ, d), 17.9	$m\tau 2$, $ad2$	3.16	1.2, 0.65	0.63	[12]
		3.16	SS*	0.54	
(τ, d), 20.2	$m\tau 3$, $ad3$	3.07	SS*	0.52	[13]
(τ, d), 22.3	$m\tau 1$, $ad1$	2.84 ± 0.42	SS*	0.48 ± 0.07	
(τ, d), 25.0	OP from [18]	2.66	SS*	0.45	[18]

Note: The abbreviation SS* stands for the standard set of values for the parameters of the potential for the proton bound state ($r_0 = 1.25$ fm, $a = 0.65$ fm, and $r_c = 1.3$ fm; V_{so} is taken with $\lambda = 25$).

smaller by about 25% at an energy of 18 MeV and by about 19% at an energy of 34 MeV. We have performed an analysis of data from the literature that were taken at 25 and 33 MeV and of the differential cross sections that we measured at 42 MeV. In analyzing data at 25 MeV from [18] and 33 MeV from [19] by the combined method, we employed the values of the optical-potential parameters from those studies.
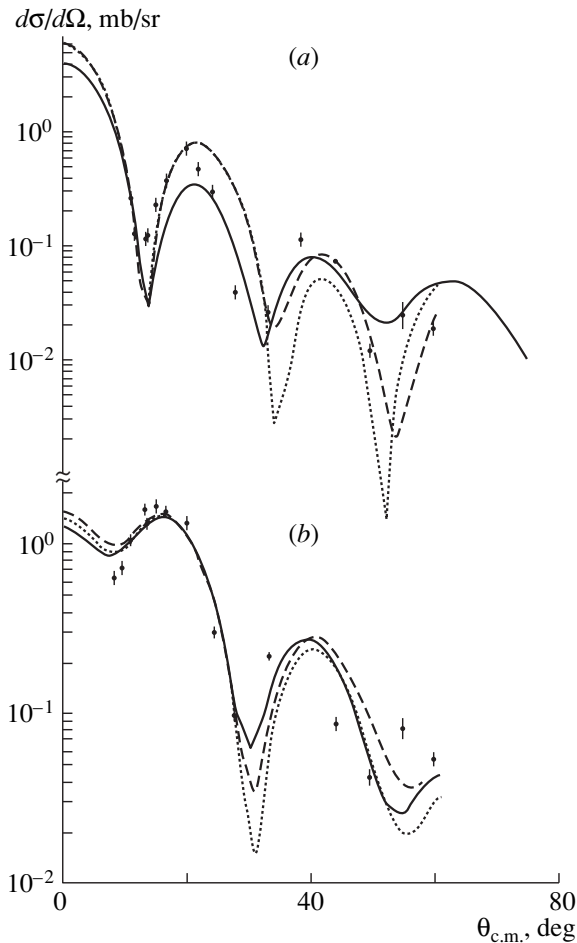
$d\sigma/d\Omega$, mb/sr

Fig. 2. Angular distributions of deuterons from the reaction $^{19}F(^3He, d)^{20}Ne$ populating the final-nucleus states at $E^* =$ (*a*) 0 MeV (ground state) and (*b*) 1.63 MeV and occurring at $E_{3_{He}} = 22.3$ MeV: (solid curve) results of the calculations on the basis of the CHUCK3 code, (dashed curve) results of the calculation on the basis of the DWUCK5 code at $r_{cut} = 0$ fm, and (dotted curve) results of the calculation on the basis of the DWUCK5 code at $r_{cut} = 4.0$ fm.
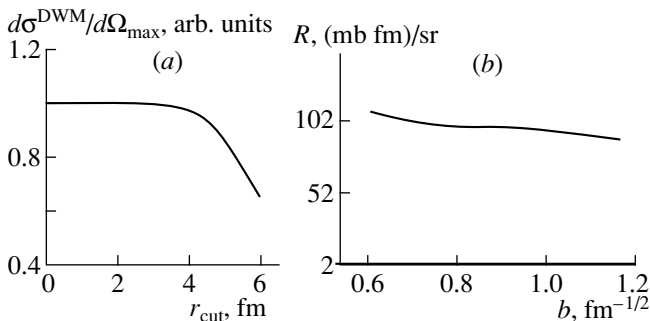

Fig. 3. (*a*) Differential cross section $d\sigma^{DWM}/d\Omega|_{max}$ at the main peak of the angular distribution as a function of the cutoff radius and (*b*) function $R(b)$ for the transition to the final-nucleus ground state ($E^* = 0$ MeV) in the reaction $^{16}O(^3He, d)^{17}F$ at $E_{3_{He}} = 42$ MeV.

The angular distribution of deuterons that was calculated for proton transfer to the ground state of the ^{17}F nucleus at $E_{3_{He}} = 42$ MeV is displayed in Fig. 1, along with the experimental distribution. In our analysis, we used five sets of the optical-potential parameters for the input channel from [7, 8], $o\tau 2$–$o\tau 6$, in conjunction with the sets *fd*2 and *fd*3 [7, 8] for the output channel. Figure 1 shows the calculated differential cross sections that were obtained with the cutoff-radius values of $r_{cut} = 0$ and 4.0 fm and which are typical of these potentials. From this figure, we can see that the description of the experimental angular distributions is improved upon introducing the cutoff radius of $r_{cut} = 4.0$ fm; at the same time, this does not change the values of the differential cross sections in the region around the maximum. The dependence of the cross section in the region of the main peak on the cutoff radius suggests that the dominant contribution to this observable comes from the region $r \geq 4.0$ fm (Fig. 3*a*). By investigating the *b* dependence of *R* (Fig. 3*b*), we can see that this quantity is weakly sensitive to variations in the geometric parameters r_0 and *a* within reasonable limits, in accord with our conjecture that the reaction in question is peripheral.

The empirical values obtained with aid of (2) for the squared absolute values of the vertex constants for the virtual decay $^{17}F \longrightarrow {}^{16}O + p$ are quoted in Table 2 for each of the two bound states. In order to test the correctness of our determination of the experimental differential-cross-section values from other studies quoted in the literature, the relevant vertex constants were also found on the basis of (3) by using the spectroscopic factors presented in those studies and by calculating the corresponding values of *b*. The errors indicated in Table 2, are determined by the experimental uncertainties in the measured differential cross sections, by the scatter of the cross sections computed on the basis of the distorted-wave method with different optical potentials, and by the weak dependence of *R* on the geometric parameters r_0 and *a* of the potential for the proton bound state.

4.2. Reaction $^{19}F(^3He, d)^{20}Ne$ and Reaction Inverse to It

We have analyzed the differential cross sections for the reaction that results in the production of final nuclei ^{20}Ne in the ground ($J^\pi = 0^+$) state and in the $J^\pi = 2^+$ excited state at $E^* = 1.63$ MeV and which was explored in our experiment at 22.3 MeV. Since it is not obvious that the one-step proton-transfer mechanism is dominant at mass numbers of $A = 19$ and 20, the angular distributions of deuterons were calculated within the standard distorted-wave method (DWUCK5 code) and within the coupled-channel method (CHUCK3 code). The resulting curves are shown in Fig. 2, along with the experimental differential cross sections. In the calculations based on the CHUCK3 code, we used the defor-

mation parameter of $\beta_2 = 0.45$ for the input channel and the deformation parameters of $\beta_2 = 0.45$ and $\beta_4 = 0.15$ for the deuteron channels. In the coupled-channel method, we took into account couplings according to the scheme presented in Fig. 4. The spectroscopic-factor values used in our calculations were borrowed from [10]. From the figures, it can be seen that, in the region of small angles, the inclusion of channel coupling does not improve the description of experimental angular distributions in relation to that achieved in the distorted-wave method. The spectroscopic factors as obtained within the coupled-channel method, $c^2S = 0.22$ ($E^* = 0$ MeV) and $c^2S = 0.49$ ($E^* = 1.65$ MeV), are also close to the values calculated on the basis of the distorted-wave method under the assumption of direct stripping (see Table 2). This suggests that, in the region of angles being considered, the dominant channels are 2–1 for the ground state and 4–1 for $E^* = 1.63$ MeV. At large scattering angles, the application of CHUCK3 leads to a considerable improvement of the description of the experimental distribution. For the ground state of ^{20}Ne, the description of the main peak in the angular distribution of deuterons is satisfactory. In the case of $E^* = 1.63$ MeV, the description in the region of small angles is improved by introducing the cutoff radius of $r_{\text{cut}} = 4.0$ fm for the overlap integral at the lower limit (see Fig. 2). At the same time, the cutoff-radius dependence of the calculated differential cross section at the maximum of the angular distribution for stripping into the lowest two states indicates that the great bulk of the contribution to this cross section comes from the region $r \geq 4.0$ fm. The peripheral character of the processes being discussed is also suggested by the fact that R is independent of b over a wide range of b ($r_0 = 1.1$– 1.4 fm, $a = 0.5$–0.7 fm). We have performed a similar analysis of the differential cross sections available for this reaction at $E_{^3\text{He}} = 10$ [20], 16 [11], and 21 and 23 [10] MeV and showed that both processes are peripheral for $E_{^3\text{He}} \geq 16$ MeV.

Data from the literature on the inverse reaction ^{20}Ne(d, ^{3}He)^{19}F involving proton pickup to the ground state of ^{20}Ne and occurring at an energy of 52 MeV [23] have also been considered here. The squared absolute values of the vertex constant, $|G|^2$, that were calculated on the basis of (2) are quoted in Table 2, which also displays the spectroscopic factors obtained at the geometric-parameter values of $r_0 = 1.25$ fm and $a = 0.6$ fm.

4.3. Reaction ^{26}Mg(^{3}He, d)^{27}Al and Reaction Inverse to It

We have analyzed the differential cross sections that we measured for the reaction ^{26}Mg(^{3}He, d)^{27}Al occurring at $E_{^3\text{He}} = 22.3$ MeV and leading to the production of ^{27}Al final states at $E^* = 0$, 0.84, and 2.98 MeV, their spin–parities being $(5/2)^+$, $(1/2)^+$, and $(3/2)^+$, respec-
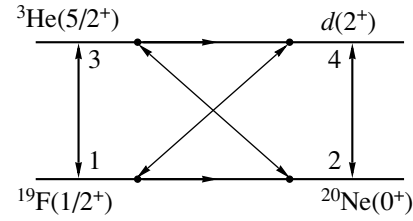
Fig. 4. Scheme of channel coupling in the calculations on the basis of the CHUCK3 code.

tively. The behavior of the function $R(b)$ suggests a peripheral character of these processes. Assuming a peripheral character and the pole mechanism of proton transfer, we obtained the relevant values of the vertex constant for proton separation, which are listed in Table 2. Previously, the reaction being discussed was studied at lower energies between 11 and 20 MeV [12, 13, 24, 25]. The spectroscopic factors obtained in those studies are also quoted in Table 2. For those cases where the spectroscopic factors were obtained by their authors at nonstandard values of the geometric parameters of the potential for the bound state, we have calculated the relevant values of the spectroscopic factors and of the vertex constants.

5. DISCUSSION OF THE ENTIRE SET OF VALUES OBTAINED FOR VERTEX CONSTANTS

In the case where a proton is transferred to the ground and to the first excited state of the final nucleus ^{17}F, a comparison of phenomenological values obtained for $|G|^2$ from processing experimental data taken at various energy values leads to the conclusion that the (^{3}He, d) reaction being discussed is dominated by the pole mechanism. This result justifies the use of the standard distorted-wave method for deducing reliable spectroscopic information about the ^{17}F nucleus. This is also confirmed by the results of Fortune et al. [16], who studied the role of multistep processes in the above reaction and showed that such processes are immaterial for transfers to the ground and to the first excited state. The values that we obtained for the vertex constants and the values that the authors of [14, 15] present for the spectroscopic factors are in fairly good agreement (see Table 2) with the array of data on (^{3}He, d) reactions, with the exception of the vertex-constant value from an analysis of data on the (d, n) reaction at $E_d = 7.7$ MeV [15] for the 0.495-MeV state of the ^{17}F nucleus. This discrepancy may reflect the significant role of the compound-nucleus mechanism at so low an energy value.

The spectroscopic-factor values from the study of Lui et al. [19], who employed a polarized beam of energy $E_{^3\text{He}} = 33.3$ MeV, also differ considerably from what would correspond to the vertex constant calcu-

Table 3. Mean phenomenological values of vertex constants and spectroscopic factors

$B \longrightarrow A + p$ E^*, MeV	nlj	$\|G\|^2$, fm	c^2S
^{17}F $\longrightarrow$ ^{16}O $+ p$			
0.00	$1d_{5/2}$	0.130 ± 0.021	0.90 ± 0.15
0.495	$2s_{1/2}$	976 ± 122	0.89 ± 0.10
^{20}Ne $\longrightarrow$ ^{19}F $+ p$			
0.00	$2s_{1/2}$	37.6 ± 4.8	0.28 ± 0.04
1.63	$1d_{5/2}$	5.35 ± 1.23	0.39 ± 0.09
^{27}Al $\longrightarrow$ ^{26}Mg $+ p$			
0.00	$1d_{5/2}$	4.94 ± 0.71	0.275 ± 0.055
0.84	$2s_{1/2}$	56.3 ± 14.2	0.45 ± 0.13
2.98	$1d_{3/2}$	2.82 ± 0.34	0.51 ± 0.12

lated here at the standard values of the geometric parameters of the potential for the bound state (see Table 2). One of the reasons behind these distinctions may be associated with errors in the normalization to the experimental data, since the latter were obtained for $\theta_{\text{c.m.}} > 20°$; that is, at the slope of the angular distribution. It is because of this that we performed our measurements of the differential cross sections for the reaction ^{16}O(^{3}He, d)^{17}F at $E_{3_{\text{He}}} = 34$ MeV; the analysis of these cross sections has been given above. The authors of [14, 15] studied the reaction ^{16}O(d, n)^{17}F at $E_{3_{\text{He}}}$ in the energy range 8–12 MeV. Our estimates revealed that, under such conditions, the quantity $R(b)$ changes within 20% in response to variations of the geometric parameters of the potential for bound state within reasonable limits, whence we deduce that the reaction (d, n) being considered can be treated as a peripheral one.

In order to obtain phenomenological vertex-constant values quoted in Table 3, we performed averaging over the results deduced from the analysis of data on proton-transfer reactions (see Table 2). From this analysis, we excluded data reported in [15, 19]. For the error, the table indicates the maximum deviation from the mean value over the entire set of the data used.

In the reaction ^{19}F(^{3}He, d)^{20}Ne, one-step proton transfer is not obvious even for a transition into the strongly populated ground ($j = 1/2$) state at $E^* = 1.63$ MeV ($j = 5/2$ transition), since nuclei in the mass region around $A \sim 20$ are strongly deformed, as a rule. In order that the empirical values of $\|G\|^2$ that are obtained in various proton-stripping processes could be identified with the ^{20}Ne $\longrightarrow$ ^{19}F $+ p$ vertex constants, we have compared the results of the data analyses for peripheral reactions within the distorted-wave method and within the coupled-channel method (see Table 2, where the latter method is abbreviated as CCM). In the case of proton transfer to the ground state of the ^{20}Ne

nucleus, the agreement (within 25%) between the $\|G\|^2$ values obtained from the above two analyses that is achieved for a major part of data for $E_{3_{\text{He}}} < 25$ MeV can be considered as the indication that channel coupling is insignificant here. At the same time, the values determined within the distorted-wave method grow with energy in the region $E_{3_{\text{He}}} \geq 25$ MeV, whereas the analogous values obtained with allowance for channel coupling remain close to the relevant mean values. This seems to suggest that the role of channel coupling becomes more pronounced with increasing projectile energy.

For the case where a proton is transferred to the state at $E^* = 1.63$ MeV, a major part of available data covers the angular region of the main peak ($l = 2$ in that case). Variations in the empirical values of $\|G\|^2$ with projectile energy are quite irregular. From Table 2, it can be seen, however, that the inclusion of channel coupling does not lead to any significant systematic changes in the extracted values of the spectroscopic factors. This suggests that the role of channel coupling is modest for the (^{3}He, d) reaction that leads to the formation of the 2^+ ^{20}Ne state at 1.63 MeV.

For the reasons discussed above, data from [18] at $E_{3_{\text{He}}} = 33$ MeV and from [23] at $E_d = 52$ MeV were excluded from the calculation of the averaged vertex constants and spectroscopic factors for the ground state of the ^{20}Ne nucleus. For the state of the same nucleus at $E^* = 1.63$ MeV in Table 3, we did not take into account the results from [20] at $E_{3_{\text{He}}} = 10$ MeV because these results could feature a considerable contribution from the compound-nucleus mechanism.

In earlier studies (see, for example, [18]), the reaction ^{26}Mg(^{3}He, d)^{27}Al was treated, as a rule, without taking into account channel coupling for the ground state of the ^{27}Al nucleus and for its two low-lying states at $E^* = 0.912$ and 2.78 MeV, which are populated quite intensely, but this did not have a sizable effect on the results because, in fact, the contribution of this coupling is insignificant. The resulting sets of vertex-constant and spectroscopic-factor values from the selected peripheral reactions, including (d, ^{3}He) and (d, n), show but a small scatter (see Table 2), thereby lending support to the conjecture that proton transfer is of a one-step pole character.

It should be recalled that the results obtained here for the vertex constants and for the spectroscopic factors were computed with the value of $\|G\|^2 = 1.34$ fm for ^{3}He $\longrightarrow$ $d + p$, and this can in principle be a source of systematic errors.

It is worthy of note that reliable values of spectroscopic factors could be found in terms of vertex constants upon invoking additional information about the geometric parameters of the bound states of the particle that is transferred in a given process. At the same time,

reliable data on vertex constants are also of paramount importance since, in terms of these, one can parametrize the cross sections for nuclear astrophysical processes occurring at inaccessibly low energies—in particular, cross sections for radiative proton capture in stellar cycles of hydrogen burning.

6. CONCLUSION

A combined analysis of (^{3}He, d) reactions and reactions inverse to these for angles from the forward hemisphere makes it possible to establish, under the conditions of precision measurements in the region around the main peak of angular distributions, a peripheral character of the reactions being discussed and the degree to which the pole mechanism of proton transfer is dominant; to extract vertex-constant values; and to assess the reliability of the resulting spectroscopic-factor values for various regions of the sd shell. For the ground and low-lying excited states of the ^{17}F, ^{20}Ne, and ^{27}Al nuclei, we have obtained here the phenomenological values of nuclear vertex constants for proton separation from a set of available data appropriate for a combined analysis. As was indicated in [3, 5], these data can be used not only in the theory of the nucleus and of nuclear reactions [30] but also in the calculation of the cross sections for direct radiative capture in astrophysical processes whose experimental investigation is hardly possible.

REFERENCES

1. S. A. Goncharov *et al.*, Yad. Fiz. **35**, 662 (1982) [Sov. J. Nucl. Phys. **35**, 383 (1982)].
2. L. D. Blokhintsev *et al.*, Fiz. Élem. Chastits At. Yadra **8**, 1189 (1977) [Sov. J. Part. Nucl. **8**, 485 (1977)].
3. A. M. Mukhamedzhanov *et al.*, Phys. Rev. C **56**, 1302 (1997).
4. I. R. Gulamov, A. M. Mukhamedzhanov, and G. K. Nie, Yad. Fiz. **58**, 1789 (1995) [Phys. At. Nucl. **58**, 1689 (1995)].
5. S. V. Artemov *et al.*, Yad. Fiz. **59**, 454 (1996) [Phys. At. Nucl. **59**, 428 (1996)].
6. J. Rapoport and A. V. Kerman, Nucl. Phys. A **119**, 641 (1968).
7. C. M. Perey and F. G. Perey, At. Data Nucl. Data Tables **17**, 1 (1976).
8. R. Gorgen *et al.*, Nucl. Phys. A **320**, 296 (1979).
9. S. Cotach and R. J. Philpott, Phys. Rev. Lett. **31**, 559 (1973).
10. A. W. Obst and K. W. Kemper, Phys. Rev. C **8**, 1682 (1973).
11. T. Vertse *et al.*, Nucl. Phys. A **223**, 207 (1974).
12. H. F. Lutz *et al.*, Phys. Rev. C **2**, 981 (1970).
13. A. J. Howard *et al.*, Nucl. Phys. A **528**, 298 (1991).
14. S. T. Thornton, Nucl. Phys. A **137**, 531 (1969).
15. C. J. Oliver *et al.*, Nucl. Phys. A **127**, 567 (1969).
16. H. T. Fortune *et al.*, Phys. Rev. C **12**, 1723 (1975).
17. B. Mertens *et al.*, Nucl. Phys. A **158**, 97 (1970).
18. J. Vernotte *et al.*, Nucl. Phys. A **571**, 1 (1994).
19. Y.-W. Lui *et al.*, Nucl. Phys. A **333**, 221 (1980).
20. R. H. Siemssen, L. L. Lee, and D. Cline, Phys. Rev. B **140**, 1258 (1965).
21. H. M. Sen Gupta, T. A. Belote, and D. Roaf, Nucl. Phys. A **267**, 205 (1976).
22. S. V. Artemov *et al.*, Izv. Akad. Nauk, Ser. Fiz. **60** (11), 192 (1996).
23. G. Th. Kashl *et al.*, Nucl. Phys. A **155**, 417 (1970).
24. W. Bohne *et al.*, Nucl. Phys. A **131**, 273 (1969).
25. W. P. Alford *et al.*, Nucl. Phys. A **130**, 119 (1969).
26. J. Vernotte *et al.*, Phys. Rev. C **48**, 205 (1993).
27. B. H. Wildenthal and E. Newman, Phys. Rev. **175**, 1431 (1968).
28. G. J. Wagner *et al.*, Nucl. Phys. A **125**, 80 (1969).
29. M. Arditi *et al.*, Nucl. Phys. A **165**, 129 (1971).
30. A. M. Mukhamedzhanov and N. K. Timofeyuk, Yad. Fiz. **51**, 679 (1990) [Sov. J. Nucl. Phys. **51**, 431 (1990)].

Translated by A. Isaakyan

NUCLEI
Theory

Photonuclear Reaction ^{7}Li$(\gamma, t)\alpha$ and Light-Cluster-Interaction Models

I. V. Kopytin[1], *, A. V. Sinyakov[2], A. A. Khuskivadze[1], and Yu. M. Tchuvil'ski[2]

Received December 2, 1999; in final form, February 8, 2000

Abstract—On the basis of various versions of the αt cluster model, the observables of the photonuclear reaction ^{7}Li$(\gamma, t)\alpha$ were calculated by using two purely attractive αt potentials and their two supersymmetric partners that involve a repulsive core each and which lead to the spectra and the phase shifts identical to those quantities for the above attractive potentials. Use is made of either the simple two-cluster model or the model relying on the Saito orthogonality conditions. The reaction amplitude is calculated in the coordinate representation either on the basis of the multipole expansions of the wave functions and of the transition operator or on the basis of the exact solutions to the Schrödinger equation for radial wave functions for both the discrete and the continuous spectrum. The sensitivity of reaction observables to the choice of model and potential type is revealed, and it is found that a somewhat better description of experimental data is attained within the Saito model and with the potential featuring no repulsive core. © *2000 MAIK "Nauka/Interperiodica"*.

1. INTRODUCTION

The disintegration of ^{6}Li and ^{7}Li nuclei into two fragments that is induced by incident photons with energies up to 90 MeV (in particular, by linearly polarized photons) was studied in [1], both experimentally and theoretically. Among other things, it was shown there that, within a simple model that treats the ^{7}Li nucleus as a system of two clusters (α and t) bound by a deep attractive potential and which takes into account final-state αt interaction, it is possible to obtain a fairly good description of experimental data on the asymmetry factor in reaction ^{7}Li$(\vec{\gamma}, t)\alpha$. At the same time, this model yields a much poorer description of the energy dependence of the differential cross section for the reaction induced by unpolarized photons of energy in excess of 40 MeV.

The experimental data from [1] on the reactions ^{7}Li$(\gamma, t)\alpha$ and ^{7}Li$(\vec{\gamma}, t)\alpha$ were used in [2] to probe the structure of the cluster potential also within a simple two-cluster model. On the basis of the energy dependence of the differential cross sections for the above two reactions and the energy dependence of the asymmetry factors in these reactions, an attempt was made to establish the form of the interaction of nuclear particles at small distances—that is, to resolve the important question of whether this interaction is purely attractive in accord with [3] or it involves a repulsive core, whose parameters can be adjusted empirically. This problem was already addressed in [4, 5] in analyzing the

bremsstrahlung spectra for pp and $\alpha\alpha$ scattering. For want of experimental data on the yield of hard bremsstrahlung from these interactions, however, the question remained open, although the answer to it could in principle be obtained from such investigations.

It was shown in [2] that the experimental data obtained in [1] for the observables of ^{7}Li photodisintegration over a wide range of photon energies also provide a firm ground for testing cluster potentials. Indeed, it was deduced from a theoretical analysis that the energy dependences of the cross section for the reaction ^{7}Li$(\gamma, t)\alpha$ and especially of the asymmetry factor for this reaction in the case of irradiation with linearly polarized photons favor a deep attractive αt potential featuring no attractive core. Although the conclusions drawn in [2] seem quite compelling, the fundamental importance of the problem at hand still requires a further in-depth investigation with a greater emphasis on the sensitivity of the observables of ^{7}Li disintegration to the structure of the cluster-interaction potential.

In the present article, this will be one of the lines of our investigation. Only one of the known attractive αt potentials whose radial dependence was taken in the form of a Gaussian function and its supersymmetric (SUSY) partner (see [6]) that leads to equivalent phase shifts (phase-equivalent SUSY partner) and which involves a repulsive core at small distances were used for analysis in [2]. There naturally arises the question as to the degree of generality of the result obtained in [2]. In order to lift this question, we also investigate here the attractive potential that was proposed in [7] and which features the Woods–Saxon radial dependence and its phase-equivalent SUSY analog involving a repulsive core. We hope that the use of αt potentials whose radial dependences have different forms will make our conclusions more convincing.

---
[1] Voronezh State University, Universitetskaya pl. 1, Voronezh, 394693 Russia.
[2] Moscow State University, Vorob'evy gory, Moscow, 119899 Russia.
* e-mail: kiv@kryl.vsu.ru

Yet another question of fundamental importance is the following: Is the simple two-cluster model is appropriate for describing processes highly sensitive to the details of nuclear structure, such as reactions involving photon emission and absorption (see also [8])? This question generates another line of the present investigation—an analysis aimed at refining the validation of the cluster model as such. The point is that the optical-potential model used in [2] to obtain the wave functions of relative motion in a two-cluster system is approximate. In constructing the wave function of the ^{7}Li nucleus, antisymmetrization in the coordinates of the nucleons entering into the composition of different clusters (α and t in the present case) was not performed within this method. The importance of this effect for solving the problem at hand can hardly be assessed on the basis of some a priori considerations. By using the scheme of the resonating-group method [9]—or, more precisely, the model of the Saito orthogonal conditions, which was proposed in [10]—antisymmetrization effects coming into play as the two nuclear particles approach each other can be, however, taken into account to such an extent as to estimate their contribution to the computed observables of ^{7}Li photodisintegration. In our opinion, it is of crucial importance to clarify these two questions, since they have a direct bearing on the principles underlying the theory of composite-particle interactions.

2. CLUSTER MODEL OF THE PHOTODISINTEGRATION PROCESS ^{7}Li(γ, t)α

It was shown in [11] that the use of the simple αt cluster model for the ground state of the ^{7}Li nucleus makes it possible to describe fairly well both its static features and the cross sections for processes induced by photons of moderate energies (up to 20 MeV). Within this model, which we use as a basis, the ground state of ^{7}Li is classified as $P_{3/2}$. The wave function of this state can be represented as

$$|i\rangle \equiv |^7\text{Li}; 3/2, m_i\rangle$$

(1)

$$= r^{-1} R_{P_{3/2}}(r) \sum_m C_{1m_i - m \frac{1}{2} m}^{\frac{3}{2} m_i} Y_{1m_i - m}(\mathbf{r}^{(0)}) \chi_m \prod_\lambda |\xi^{(\lambda)}; \beta_i^{(\lambda)}\rangle,$$

where $R_{P_{3/2}}(r)$ is the radial wave function for relative motion in the bound state of the αt system; $C_{j_1 m_1 j_2 m_2}^{jm}$ is the relevant Clebsch–Gordan coefficient; $\mathbf{r}^{(0)} = \mathbf{r}/|\mathbf{r}|$; χ_m is the spin wave function; $\xi^{(\lambda)} \equiv (\xi_1^{(\lambda)}, \ldots, \xi_{A_\lambda}^{(\lambda)})$, $\xi_j^{(\lambda)}$ being the coordinate specifying the position of the jth nucleon of the cluster λ with respect to the center of mass of this cluster [the superscript λ corresponds to the particles t ($\lambda = 1$) or α ($\lambda = 2$), A_λ being the mass number of the cluster λ]; and $\beta_s^{(\lambda)}$ is the set of quantum

numbers specifying the sth internal state of the particle λ [the subscript s labels quantities referring to the initial ($s = i$) or the final state ($s = f$) state].

For the final state of the αt system, the wave function that has the required asymptotic behavior and which belongs to the continuous spectrum can be represented as [12]

$$|f\rangle = \Psi_{\mathbf{k}, m_f}^{(-)}(\mathbf{r}) \prod_\lambda |\xi^{(\lambda)}; \beta_f^{(\lambda)}\rangle,$$

$$\Psi_{\mathbf{k}, m_f}^{(-)} = (2\pi)^{3/2} (kr)^{-1} \sum_{l, j} i^l e^{-i\eta_{lj}} R_{lj}^{(f)}(r) \qquad (2)$$

$$\times \sum_{m_j, m'} C_{lm_j - m_f \frac{1}{2} m_f}^{jm_j} C_{lm_j - m' \frac{1}{2} m'}^{jm_j} Y_{lm_j - m'}(\mathbf{r}^{(0)}) Y_{lm_j - m_f}^*(\mathbf{k}^{(0)}) \chi_{m'},$$

where $\hbar \mathbf{k}$ is the relative momentum in the αt system, $\mathbf{k}^{(0)} = \mathbf{k}/|\mathbf{k}|$, and η_{lj} is the sum of the Coulomb and nuclear phase shifts. In either case, the radial functions $R_{lj}^{(s)}(r)$ were determined from the equation

$$\left\{ \frac{d^2}{dr^2} - \frac{l(l+1)}{r^2} + k_s^2 - \frac{2m_N A_{12}}{\hbar^2} [U(r) + a_j U_{ls}(r)] \right\} \qquad (3)$$

$$\times R_{lj}^{(s)}(r) = 0,$$

where m_N is the nucleon mass; $A_{12} = A_1 A_2 (A_1 + A_2)^{-1}$; $k_i^2 = -2m_N A_{12} |E_0|/\hbar^2$, E_0 being the energy of the bound state of the αt system; $k_f^2 \equiv k^2 = 2m_N A_{12} \varepsilon_f /\hbar^2$, ε_f being the energy of the final state of the αt system; $U(r)$ and $U_{ls}(r)$ are, respectively, the central and the spin–orbit potential; and

$$a_j = \begin{cases} l/2, & \text{for } j = l + 1/2 \\ -(l+1)/2, & \text{for } j = l - 1/2. \end{cases}$$

It is assumed that the functions $R_{lj}^{(f)}(r) \equiv R_{lj}(k, r)$ are normalized by the condition

$$\int_0^\infty R_{lj}^*(k, r) R_{lj}(k', r) dr = \delta(k - k')$$

and that their asymptotic behavior is given by

$$R_{lj}(k, r) \xrightarrow[r \to \infty]{} \left(\frac{2}{\pi}\right)^{1/2}$$

$$\times \sin\left(kr - \frac{l\pi}{2} - \frac{2m_N A_{12} c \alpha_e}{\hbar k} \ln kr + \eta_{lj}\right),$$

where $\alpha_e = e^2/\hbar c$ is the fine-structure constant.

In the Hamiltonian describing the interaction of the αt system with an electromagnetic field, we retain, as in

[2], only the electric component (this is quite legitimate at photon energies not exceeding 90 MeV, which were studied in the experiment reported in [1]). We then have

$$\hat{H}_\gamma \approx \alpha_e^{1/2}(\hbar/m_N)(2\pi\hbar c/E_\gamma)^{1/2} \sum_{\lambda=1,2} (-1)^\lambda A_\lambda^{-1}$$

$$\times \sum_j e_j \exp(i\mathbf{k}_\gamma \cdot \boldsymbol{\xi}_j^{(\lambda)})(\mathbf{u} \cdot \hat{\mathbf{p}}) \qquad (4)$$

$$\times \exp\{(-1)^{\lambda+1}(A_{12}/A_\lambda)i\mathbf{k}_\gamma \cdot \mathbf{r}\},$$

where $\mathbf{k}_\gamma$, $\mathbf{u}$, and E_γ are the photon momentum, polarization (unit) vector, and energy, respectively; e_j is the nucleon charge number equal to zero for the neutron and to unity for the proton; and $\hat{\mathbf{p}} = -i\hbar\partial/\partial\mathbf{r}$. The differential cross section has the standard form

$$\frac{d\sigma}{d\Omega} = \frac{m_N A_{12} k}{16\pi^2\hbar^3 c} \sum_{m_i, m_f} |\langle f|\hat{H}_\gamma|i\rangle|^2, \qquad (5)$$

where $\Omega = (\theta, \varphi)$, θ and φ being angles determining the direction of the vector $\mathbf{k}$. This cross section can be calculated by using expressions (1) and (2) and the multipole expansion of $\hat{H}_\gamma$. In order to avoid encumbering the presentation, we do not quote here the corresponding exact expressions from [2] for the differential photodisintegration cross section averaged over photon polarizations, $\overline{d\sigma/d\Omega}$, or for the asymmetry factor at a fixed photon polarization, $\Sigma(\theta)$. In the ensuing analysis, we will need only their simplified forms at $\theta = \pi/2$ (this value was fixed in the experiment) in the dipole approximation without spin–orbit interaction. These are

$$\overline{\left[\frac{d\sigma}{d\Omega}(\theta=\pi/2)\right]}_{\text{dip}} = \frac{\alpha_e\pi\hbar^2 A_{12}}{9m_N E_\gamma k}\left(\frac{Z_1}{A_1} - \frac{Z_2}{A_2}\right)^2$$

$$\times\left[R_0^2 + \frac{5}{2}R_2^2 - \cos(\eta_0 - \eta_2)R_0 R_2\right], \qquad (6)$$

$$\Sigma(\theta=\pi/2) = 3[R_2^2 - 2R_0 R_2\cos(\eta_0 - \eta_2)]$$

$$\times\left\{2P_\gamma\left[R_0^2 + \frac{5}{2}R_2^2 - \cos(\eta_0 - \eta_2)R_0 R_2\right]\right\}^{-1}, \qquad (7)$$

where P_γ is the degree of photon-beam polarization and

$$R_l = \int_0^\infty R_l(k, r)\left(\frac{d}{dr} + \frac{2l^2 - l - 2}{2r}\right)R_{P_{3/2}}^{(i)}(r)dr, \qquad (8)$$

$$l = 0, 2.$$

Formulas (6) and (7) are also appropriate when use is made of the Siegert theorem—that is when the matrix elements of the momentum operator are replaced by the matrix elements of the coordinate operator. In this case,

it is necessary to make the substitution

$$R_l \longrightarrow \frac{m_N E_\gamma A_{12}}{\hbar}\int_0^\infty R_l(k, r)rR_{P_{3/2}}^{(i)}(r)dr. \qquad (9)$$

It should be recalled that the theoretical analysis of experimental data that was performed in [1] relied precisely on expressions (6) and (7) with the substitution in (9).

3. ^{7}Li PHOTODISINTEGRATION IN THE SAITO MODEL

From the viewpoint of the modern theory of nuclear structure, the optical-potential method used in the cluster model (see Section 2) is approximate. Indeed, this method treats the nuclear system in question as a two-body one; moreover, effects associated with antisymmetrization in the nucleon coordinates are disregarded in determining the wave function of the relative motion of the clusters, and no account is taken of the contribution of exchange amplitudes in calculating the relevant matrix elements [10]. However, the computational scheme can be modified on the basis of the resonating-group method [9] or its approximation in terms of the Saito orthogonality conditions [see Eq. (5)].

The physical meaning of this modification can be briefly clarified as follows. Let us represent the wave function of the ^{7}Li nucleus in the symbolic form

$$|^7\text{Li}\rangle = |\hat{A}\{\Psi_\alpha\Psi_t\Phi\}\rangle, \qquad (10)$$

where $\Psi_{t(\alpha)}$ is the wave function of the triton cluster (alpha-particle cluster) antisymmetrized in the permutations of nucleons entering into its composition, Φ is the wave function of the relative motion of the clusters, and $\hat{A}$ is the operator of antisymmetrization with respect to permutations of the coordinates of nucleons entering into the composition of the different clusters. The Schrödinger equation for the wave function $|^7\text{Li}\rangle$ then has the form

$$\hat{H}_0|\hat{A}\{\Psi_\alpha\Psi_t\Phi\}\rangle = E|\hat{A}\{\Psi_\alpha\Psi_t\Phi\}\rangle, \qquad (11)$$

where $\hat{H}_0$ is the Hamiltonian of the system consisting of seven nucleons in the absence of external fields.

Projecting Eq. (11) onto the space of the functions $|\hat{A}\{\Psi_\alpha\Psi_t\}\rangle$, we arrive at

$$\langle\hat{A}\{\Psi_\alpha\Psi_t\}|\hat{H}_0|\hat{A}\{\Psi_\alpha\Psi_t\Phi\}\rangle$$
$$= E\langle\hat{A}\{\Psi_\alpha\Psi_t\}|\hat{A}\{\Psi_\alpha\Psi_t\Phi\}\rangle. \qquad (12)$$

This is the equation of the resonating-group method for the ^{7}Li nucleus. Let us represent it in the form

$$\hat{H}'\Phi = E\hat{N}\Phi, \qquad (13)$$

where

$$\hat{N}\Phi = \int \langle \hat{A}\{\Psi_\alpha \Psi_t \delta(\mathbf{r} - \mathbf{r'})\} | \hat{A}\{\Psi_\alpha \Psi_t \delta(\mathbf{r} - \mathbf{r''})\} \rangle \Phi d^3 r,$$

$$\hat{H}'\Phi = \int \langle \hat{A}\{\Psi_\alpha \Psi_t \delta(\mathbf{r} - \mathbf{r'})\} | \hat{H}_0 | \hat{A}\{\Psi_\alpha \Psi_t \delta(\mathbf{r} - \mathbf{r''})\} \rangle \Phi d^3 r.$$

Equation (13) can be formally reduced to the form of the Schrödinger equation with a Hermitian pseudo-Hamiltonian. For this, it is necessary to apply the operator $\hat{N}^{-1/2}$ to equation (13):

$$\hat{N}^{-1/2}\hat{H}'\hat{N}^{-1/2} \cdot \hat{N}^{1/2}\Phi = E\hat{N}^{1/2}\Phi.$$

Let us introduce the notation

$$\hat{H} \equiv \hat{N}^{-1/2}\hat{H}'\hat{N}^{-1/2}, \quad \varphi \equiv \hat{N}^{1/2}\Phi.$$

Instead of (13), we then obtain

$$\hat{H}\varphi = E\varphi. \tag{14}$$

From (14), it follows that, by using the optical-potential method, we find the function $\varphi = \hat{N}^{1/2}\Phi$ rather than the wave function Φ of the relative motion of the clusters. In order to obtain the wave function Φ, which appears in (10), it is therefore necessary to apply the operator $\hat{N}^{-1/2}$ to the function φ appearing to be a solution to the Schrödinger equation with an optical potential. This transformation preserves normalization in going over from the two-body wave functions of the cluster model to the functions in (10). Other ways of renormalization, including renormalization in terms of a constant factor, change the asymptotic behavior of the relevant functions at large distances. As a matter of fact, the above device forms the conceptual framework of the Saito orthogonal-condition model, which is valid at least for processes not accompanied by the excitation of clusters, as well as under the additional condition that at least one of the clusters contains a magic number of nucleons.

The result of applying the operator $\hat{N}^{-1/2}$ to the function φ can be found within the shell model of the nucleus. The results of such calculations are quite accurate, provided that the intrinsic wave functions of the clusters and the wave function of their relative motion are taken in the form of oscillator functions with the same oscillator parameter $\hbar\omega$. We denote the wave function of the relative motion of the clusters by $R_{nl}(\mathbf{r}/r_0)$, where $n = 2\nu + 1$, ν being the number of nodes of the wave function, and r_0 is the oscillator radius. This wave function is an eigenfunction of the operator $\hat{N}$, the corresponding eigenvalue being independent of orbital angular momenta; that is,

$$\hat{N}R_{nl} = \varepsilon_n R_{nl}. \tag{15}$$

We then have

$$\hat{N}^{-1/2}\varphi = \hat{N}^{-1/2}\sum_n C_n R_{nl} = \sum_n \varepsilon_n^{-1/2} C_n R_{nl}, \tag{16}$$

where $C_n = \langle \varphi | R_{nl} \rangle$. We note that, in (16), summation is performed only over $n \geq 3$, since $n = 0, 1, 2$ states are forbidden by the Pauli exclusion principle—in other words, the antisymmetrized components of the seven-nucleon wave function that correspond to these values of n vanish identically:

$$\hat{A}\{\Psi_\alpha \Psi_t R_{nl}\} \equiv 0.$$

Presented immediately below is the scheme for computing ε_n on the basis of the method developed in [13]. By using equation (15) and taking into account the explicit form of the operator $\hat{N}$, we can represent ε_n as

$$\varepsilon_n = \langle \hat{A}\{\Psi_\alpha \Psi_t R_{nl}\} | \hat{A}\{\Psi_\alpha \Psi_t R_{nl}\} \rangle, \tag{17}$$

but it is more convenient to calculate the quantity

$$\varepsilon_n^{\text{shell}} = \langle \hat{A}\{\Psi_\alpha \Phi_\alpha(00)\Psi_t \Phi_t(n0)l\} | \hat{A}\{\Psi_\alpha \Phi_\alpha(00)\Psi_t \Phi_t(n0)l\} \rangle, \tag{18}$$

where Φ_α and Φ_t are the wave functions describing the motion of the centers of mass of the alpha-particle cluster and the triton cluster, respectively. A transition from one representation to the other is accomplished with the aid of the Talmi transformation

$$|\Psi_\alpha \Phi_\alpha(00)\Psi_t \Phi_t(n0)l\rangle$$

$$= \sum_{\substack{n_{\text{rel}}, N \\ n_{\text{rel}} + N = n}} \langle (00)(n0) : (n0)l | 4 : 3 | (N0)(n_{\text{rel}}0) : (n0)l\rangle$$

$$\times |\Psi_\alpha \Psi_t R_{n_{\text{rel}}} \Phi_N\rangle, \tag{19}$$

where $\langle (00)(n0)(n0)l | 4 : 3 | (N0)(n_{\text{rel}}0)(n0)l\rangle$ is the Talmi coefficients for the αt system.

Substituting (19) into (18) and taking into account (17), we find that, in the $SU(3)$ representation, the quantity introduced in (18) can be written as

$$\varepsilon_n^{\text{shell}} = \sum_{n_{\text{rel}}} \langle (00)(n0):(n0)l | 4 : 3 | (N0)(n_{\text{rel}}0):(n0)l\rangle^2 \varepsilon_{n_{\text{rel}}}.$$

By using the explicit expressions for the Talmi coefficients in the $SU(3)$ scheme and solving the triangle set of linear equations for ε_n, we obtain

$$\varepsilon_n = \sum_{\nu=0}^{n} (-1)^{\nu-n} \frac{n!}{\nu!(n-\nu)!} \frac{A_t^{n-\nu}(A_t + A_\alpha)^\nu}{A_\alpha^n} \varepsilon_\nu^{\text{shell}},$$

where A_α and A_t are the mass numbers of the alpha-particle cluster and the triton cluster, respectively.

Evaluating the overlap integrals of the shell functions and performing relevant summations, we eventually obtain

$$\varepsilon_n = 1 - 3\left(\frac{5}{12}\right)^n + 3\left(-\frac{1}{6}\right)^n - \left(-\frac{3}{4}\right)^n. \quad (20)$$

Since $\varepsilon_n \longrightarrow 1$ for $n \longrightarrow \infty$, the calculations become more convenient if we make use of the representation

$$\Phi = \hat{N}^{-1/2}\varphi = \varphi + \sum_n (\varepsilon_n^{-1/2} - 1)C_n R_{nl}.$$

Thus, a transition to the wave functions of the Saito model amounts to quite a simple renormalization. In principle, this model makes it possible to perform an exact calculation of the matrix elements of the electromagnetic-interaction Hamiltonian (4) within the microscopic seven-nucleon formalism—that is, to take into account, in addition to the matrix elements calculated in the two-cluster model, exchange matrix elements. It was shown in [14], however, that, in the electric components of electromagnetic transitions, exchange effects are strongly suppressed, whence we conclude that the approximation where exchange effects are disregarded is reasonable. In this approximation, the only modification that must be introduced in the computational scheme in order to go over from the cluster model to the Saito model consists in the renormalization of the wave functions describing relative motions in the initial and in the final state. It is precisely this scheme that is used in the present study.

4. RESULTS OF THE CALCULATIONS AND THEIR DISCUSSIONS

The results obtained by calculating the differential cross section $\overline{d\sigma/d\Omega}$ and the asymmetry factor Σ for the reaction $^7\text{Li}(\vec{\gamma}, t)\alpha$ {either on the basis of the exact expressions from [2] or on the basis of expressions (6) and (7)} are contrasted here against experimental data from [1] in order to test the models of αt interaction. We borrowed two purely attractive potentials involving forbidden states from [7, 11]. In [7], the radial dependence of the potential was taken in the Woods–Saxon form and was parametrized as

$$U_M(r) = V(r) + V_{\text{Coul}}(r), \quad (21)$$

where

$$V(r) = -[V_0 + (-1)^{l+1}\Delta V] \times \{1 + \exp[(r - R_0)/a]\}^{-1} \quad (22)$$

with $V_0 = 97.04$ MeV, $\Delta V = 11.5$ MeV, $R_0 = 1.8$ fm, and $a = 0.7$ fm. We somewhat reduced the value of V_0 in relation to that in [7] (where it was 98.5 MeV) in order to fit the binding energy of the ^7Li nucleus to the experimental value (this change in V_0 has only a small effect on phase shifts). The Coulomb potential was taken in the form

$$V_{\text{Coul}}(r) = \begin{cases} (\alpha_e \hbar c/R_{\text{Coul}})(3 - r^2/R_{\text{Coul}}^2), & r < R_{\text{Coul}} \\ 2\alpha_e \hbar c/r, & r > R_{\text{Coul}}, \end{cases} \quad (23)$$

where R_{Coul} is a preset parameter (in the case being considered, it was chosen to be R_0). The form of the spin–orbit potential $U_{ls}(r)$ was

$$U_{ls}(r) = \kappa_l \lambda_\pi^2 r^{-1} dV/dr \quad (24)$$

with $\lambda_\pi^2 = 2$ fm^2 and $\kappa_l = 0.0015[3 + (-1)^{l+1}]$.

In [11], the radial dependence of the potential had a Gaussian form. The spin–orbit interaction was not singled out as a separate term; therefore, the potential parameters depended not only on the orbital angular momentum l but also on the total angular momentum j:

$$U_D(r) = -V_0(l, j)e^{-\beta r^2} + V_{\text{Coul}}(r). \quad (25)$$

Here, $\beta = 0.15747$ fm^{-2} and $R_{\text{Coul}} = 3.095$ fm; for the $S_{1/2}$, $P_{1/2}$, $P_{3/2}$, $D_{3/2}$, $D_{5/2}$, $F_{5/2}$, and $F_{7/2}$ states, the parameter $V_0(l, j)$ took the values of 67.47, 81.92, 83.83, 66.0, 69.0, 75.89, and 84.80 MeV, respectively.

The attractive potentials (21) and (25) were used as a basis for constructing their exact SUSY partners $U^{(\text{SUSY})}(r)$, which are, by definition, spectrally equivalent and phase-equivalent to the original potential, but which do not involve states forbidden by the Pauli exclusion principle. The latter circumstance renders the original potential shallower and leads to the emergence of a repulsive core. The procedure used to eliminate forbidden states was described in detail elsewhere [6]; for this reason, we will not consider it here (see also [2]). We denote by $U_M^{(\text{SUSY})}(r)$ and $U_D^{(\text{SUSY})}(r)$ the potentials that feature a repulsive core and which were obtained from the potentials $U_M(r)$ and $U_D(r)$.

The radial functions $R_{P_{3/2}}(r)$ and $R_{S_{1/2}}(k, r)$ calculated for, respectively, the discrete and the continuous spectrum on the basis of Eq. (3) are displayed in Fig. 1, along with the corresponding normalized functions $\hat{N}^{-1/2}R_{P_{3/2}}(r)$ and $\hat{N}^{-1/2}R_{S_{1/2}}(k, r)$. To avoid encumbering the figure, the behavior of the functions is shown only for the potentials $U_M(r)$ and $U_M^{(\text{SUSY})}(r)$, since the calculations with the potentials $U_D(r)$ and $U_D^{(\text{SUSY})}(r)$ yield results differing only slightly from those that are presented. As we learn from Fig. 1, the radial wave functions can behave quite differently at relatively small distances. Their behavior depends, on one hand,
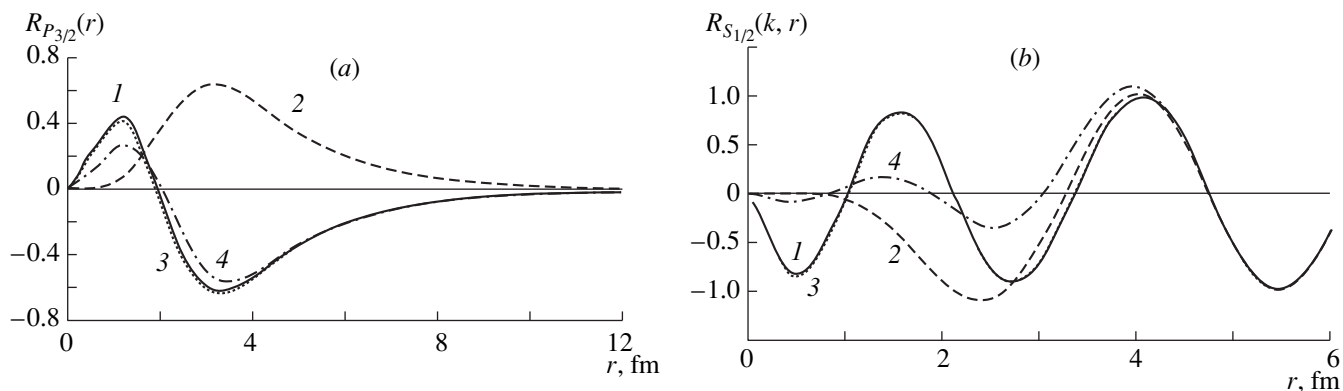
Fig. 1. (*a*) Wave function $R_{P_{3/2}}(r)$ for the bound state and (*b*) wave function $R_{S_{1/2}}(k, r)$ for the continuous spectrum (the relative-motion energy is 60 MeV) versus radius for the αt system. The curves represent the results of the calculations with the potentials (*1, 3*) $U_M(r)$ [7] and (*2, 4*) $U_M^{(SUSY)}(r)$. Curves *3* and *4* correspond to the renormalized wave functions.

on whether the wave function describing the relative motion of the clusters is renormalized (according to the procedure from Section 3) or is not renormalized and, on the other hand, on whether there is a repulsive core in the αt potential or there is no such core.

The differential cross section $\overline{d\sigma/d\Omega}$ calculated as a function of the photon energy E_γ at $\theta = 90°$ [according to expression (6)] is presented in Fig. 2 ($5 \leq E_\gamma \leq 30$ MeV) and in Fig. 3 ($E_\gamma \geq 30$ MeV). It should be noted that the values along the ordinate in Fig. 3 are plotted on a logarithmic scale. As in [2], the charge form factors for the ^3H and for the ^4He nucleus were taken in the form [11]

$$f_\lambda(\mathbf{k}_\gamma) = [1 - (a_\lambda k_\gamma^2)^{n_\lambda}]\exp(-b_\lambda k_\gamma^2), \qquad (26)$$

where $a_1 = 0.0793$ fm^2, $b_1 = 0.40425$ fm^2, and $n_1 = 5.14$ for ^3H and $a_2 = 0.009986$ fm^2, $b_2 = 0.46376$ fm^2, and $n_2 = 6$ for ^4He.

From Figs. 2 and 3, it can be seen that the attractive potential (21) provides a better description of experimental data (curves *1, 3*) than the potential featuring a repulsive core (curves *2, 4*). It is worth noting that the cross sections $\overline{d\sigma/d\Omega}$ as calculated here with the potentials $U_M(r)$ and $U_M^{(SUSY)}(r)$ are 1.5–2 times smaller than the values of these cross sections obtained in [2] (see the analogous Fig. 1 from [2]) by using the potentials $U_D(r)$ and $U_D^{(SUSY)}(r)$. These distinctions do not stem from the replacements of the potentials $U_D(r)$ by $U_M(r)$—the results of the calculations for the cross section $\overline{d\sigma/d\Omega}$ with the above potentials differ insignificantly, as in the case of the wave functions. Unfortunately, a numerical factor was overlooked in the calculations from [2] with the result that the value of $\overline{d\sigma/d\Omega}$
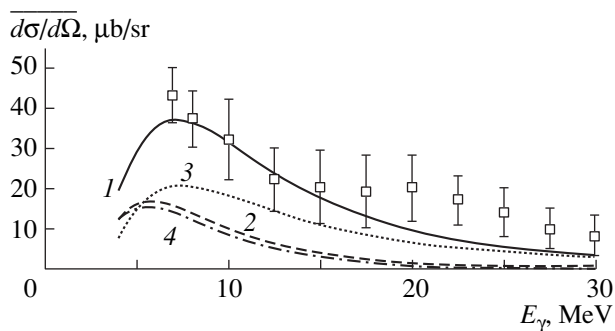
Fig. 2. Photon-polarization-averaged differential cross section $\overline{d\sigma/d\Omega}$ for the reaction $^7Li(\gamma, t)\alpha$ as a function of the photon energy E_γ in the region between 5 and 30 MeV in the c.m. frame. The curves represent the results of the calculations with the potentials (*1, 3*) $U_M(r)$ [7] and (*2, 4*) $U_M^{(SUSY)}(r)$. Curves *3* and *4* correspond to the renormalized wave functions. Experimental data were borrowed from [15–17] (only the total error is indicated because of a large scatter of data).
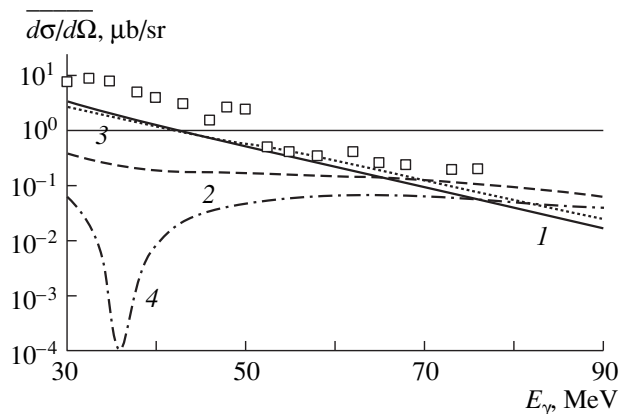
Fig. 3. As in Fig. 2, but for $E_\gamma = 30$–90 MeV. Experimental data were borrowed from [1].
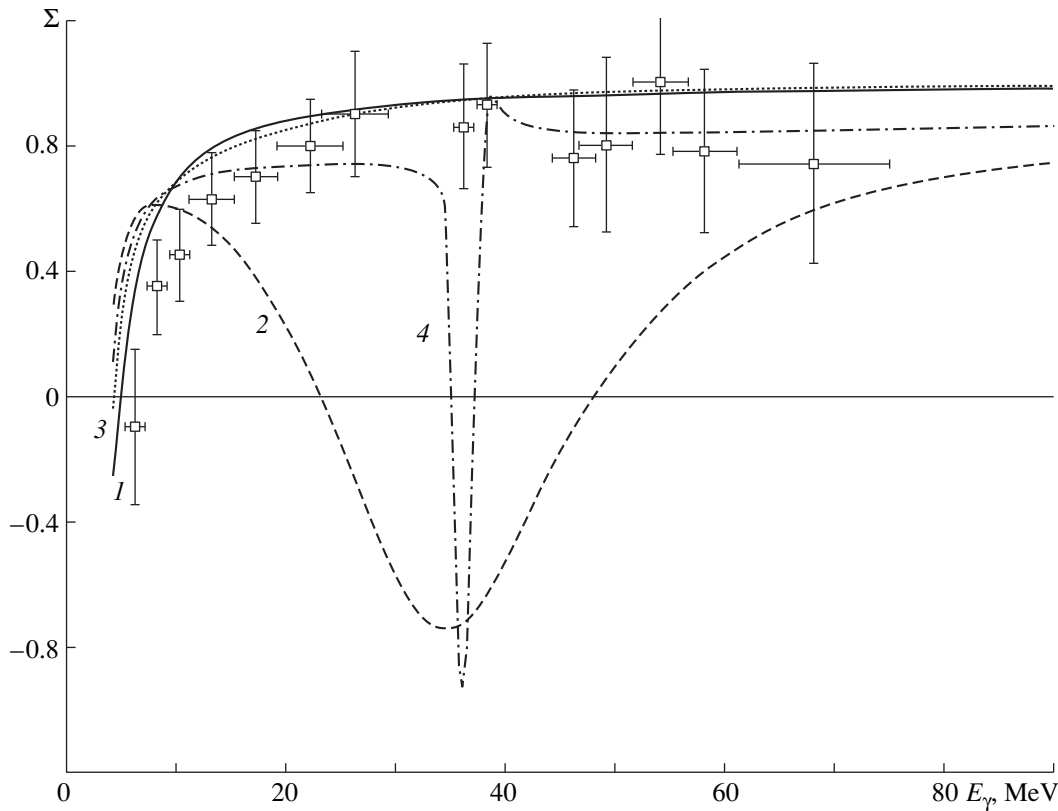
Fig. 4. Asymmetry factor Σ for the reaction $^7\text{Li}(\vec{\gamma}, t)\alpha$ as a function of the photon energy E_γ at $\theta = 90°$ in the c.m. frame. The notation for the curves is identical to that in Fig. 2. Experimental data were borrowed from [1].

was strongly biased in region being discussed. This error was corrected in [18].

A transition to the Saito model—this transition is necessary for refining the cluster model of ^7Li photodisintegration—also affects sizably the results of the calculations. In particular, this leads to the growth of the reaction yield in the region $E_\gamma > 70$ MeV, improving the agreement with experimental data. Concurrently, the maximum observed at the low-energy end of the spectrum becomes less pronounced. Here, the details of the structure of the ^7Li nucleus that are associated with the asymptotic behavior of its wave function at large distances may come into play. In order to take these details into account, it is necessary to go beyond the two-cluster model in constructing the ground state of the ^7Li nucleus.

For the reaction asymmetry factor Σ at $\theta = \pi/2$ (the results of the calculations for this quantity are displayed in Fig. 4), the situation is much less certain. As in [2], the behavior of the asymmetry Σ computed with the potential $U_{\text{M}}^{(\text{SUSY})}(r)$ featuring a repulsive core and with the unrenormalized wave functions (curve 2) differs dramatically over a wide range of photon energies E_γ from what is seen experimentally. When we use, however, renormalized wave functions, the quantity Σ still takes negative values (curve 4), in sharp contrast

with experimental data, but, now, this occurs in a much narrower interval of E_γ values. We can see that, while the theoretical behavior of the asymmetry factor Σ as determined by using the unrenormalized wave functions definitively favors the purely attractive potential—it is precisely on this basis that preference was given to it in [2] without any qualifications—our present results cast some doubt on the validity of that statement. Since the dip in the energy dependence of the above asymmetry factor became very narrow in the calculations with the renormalized wave functions, there are no strong reasons to be positive about the existence of this discrepancy in actual fact—the dip could have been merely missed in studying the experimental dependence of Σ on E_γ. Indeed, it can be seen from Fig. 5 in [1] that there are no data on Σ in the range $25 \le E_\gamma \le 35$ MeV, but this is precisely the range where the theoretical calculations with potentials featuring a repulsive core predict a dip. On the other hand, a further refinement of the computational scheme may smooth out the theoretical dependence of Σ on the photon energy.

By analyzing, on the basis of exact expressions from [2], various approximations used in calculating the differential cross section $\overline{d\sigma/d\Omega}$ and the asymmetry Σ, it was found that the results are barely affected either by

taking into account spin–orbit interaction or by going beyond the long-wave approximation. However, the use of the Siegert theorem [19], according to which the matrix element of the momentum operator is replaced by the matrix element of the coordinate operator, changes strongly the behavior of the asymmetry factor Σ. It was the approximation in which Burkova *et al.* [1] performed their theoretical analysis [see equations (6) and (7) above with the substitution in (9) for the radial integrals]. In that case, the asymmetry factor Σ behaves very similarly for the potentials featuring a repulsive core and for the purely attractive potentials. The reason for this similarity is that, for photon energies in the region $E_\gamma \geq 10$ MeV, the matrix elements of the coordinate r at various l take very close values for the different potentials, because the region of small r, where the radial functions differ significantly (see Fig. 1), makes virtually no contribution to relevant integrals in view of the presence of the operator $\hat{r}$ in the integrands. From the approximate equality of the radial matrix elements, it follows that $\Sigma \approx 1$ for all types of the potentials considered here. If, however, the gradient formula is used for the momentum operator, the radial matrix elements depend greatly on the orbital angular momentum l with the result that the asymmetry factor behaves differently for potentials having a repulsive core and for potentials having no such core.

In our opinion, the use of the Siegert theorem cannot be justified in the problem being considered, since the optical potentials (21) and (25) and their SUSY partners are nonlocal; therefore, the conditions of the theorem are not satisfied. This is reason why we preferred to calculate directly the matrix elements of the momentum operator, whereby we obtained the above results. This approach disregards, however, changes in the nuclear-current density that are induced by mesonic degrees of freedom. Therefore, the effect that such a renormalization of the current density may exert on eventual results in the presence of an electromagnetic field is not clear. At present, there is no simple solution to the problem of taking into account mesonic degrees of freedom in constructing the current-density operator; anyway, analysis of this problem is beyond the scope of the present investigation. In view of this, we only state that, within the conceptual framework adopted here, the asymmetry factor Σ is sensitive to the structure of the αt potential and highlight circumstances that prevent us from drawing definitive conclusions.

5. SUMMARY

We have investigated the disintegration of ^{7}Li nuclei within various versions of the αt cluster model. The results of this investigation can be summarized as follows:

(i) The Saito model, which is more justified from the theoretical point of view, constrains considerably the

scatter of the observables of ^{7}Li photodisintegration that are calculated with various interaction potentials. This is because the wave functions for potentials featuring a repulsive core change in this model, taking a form similar to that of the wave functions for deep attractive potentials. However, the latter potentials have a more reliable theoretical basis and provide a better description of experimental data.

(ii) The differential cross section $\overline{d\sigma/d\Omega}$ for the disintegration process induced by unpolarized gamma radiation is sensitive to the structure of the αt potential. In particular, this observable has been much better reproduced with purely attractive potentials than with potentials involving a repulsive core. At the same time, the yield from this reaction is underestimated at low energies when effects that stem from antisymmetrization of the wave functions are taken into account.

(iii) The asymmetry factor Σ shows strongly different energy dependences for the different potential types. By way of example, we indicate that, for the potentials involving a repulsive core at small distances, there exists a photon-energy range where $\Sigma < 0$; at the same time, the experimental values of Σ are positive and are close to unity over a wide energy range. Upon the inclusion of antisymmetrization effects, the region of negative values of Σ for potentials featuring a repulsive core shrinks considerably, but it does not disappear completely. The experimental behavior of the asymmetry factor is faithfully reproduced with the purely attractive potentials.

(iv) The conclusions listed in item (iii) cannot be considered to be ultimate for the following reasons. First, the energy region where the theoretical values of the asymmetry factor Σ are negative has not yet received adequate experimental study. Second, it would be desirable to take into account the effect of meson-exchange currents on the structure of the current-density operator in the computational scheme making no use of the Siegert theorem. We cannot rule out the possibility that the appearance of the region where the asymmetry factor takes negative values is due to the disregard of this effect in the model employed in the present article.

ACKNOWLEDGMENTS

REFERENCES

1. N. A. Burkova, V. V. Dehyak, R. A. Eramzhyan, *et al.*, Nucl. Phys. A **586**, 293 (1995).

2. I. V. Kopytin, A. A. Khuskivadze, and V. N. Pomerantsev, Yad. Fiz. **61**, 641 (1998) [Phys. At. Nucl. **61**, 569 (1998)].

3. V. I. Kukulin, V. G. Neudachin, and Yu. F. Smirnov, Fiz. Élem. Chastits At. Yadra **10**, 1236 (1979) [Sov. J. Part. Nucl. **10**, 492 (1979)].

4. V. G. Neudatchin, N. A. Khokhlov, A. M. Shirokov, and V. A. Knyr, Yad. Fiz. **60**, 1086 (1997) [Phys. At. Nucl. **60**, 971 (1997)].

5. I. V. Kopytin, M. A. Dolgopolov, and A. A. Khuskivadze, Yad. Fiz. **61**, 630 (1998) [Phys. At. Nucl. **61**, 558 (1998)].

6. D. Baye, Phys. Rev. Lett. **58**, 2738 (1987).

7. V. G. Neudatchin, A. N. Boyarkina, V. P. Korennoy, and V. I. Kukulin, Lett. Nuovo Cimento **5**, 834 (1972).

8. D. Baye and P. Descouvemont, Ann. Phys. (N.Y.) **165**, 115 (1985).

9. J. A. Wheeler, Phys. Rev. **52**, 1107 (1937).

10. S. Saito, Prog. Theor. Phys. **41**, 705 (1969).

11. S. B. Dubovichenko and A. V. Dzhazairov-Kakhramanov, Yad. Fiz. **56** (2), 87 (1993) [Phys. At. Nucl. **56**, 195 (1993)]; Yad. Fiz. **58**, 635 (1995) [Phys. At. Nucl. **58**, 579 (1995)].

12. M. L. Goldberger and K. M. Watson, *Collision Theory* (Wiley, New York, 1964; Mir, Moscow, 1967).

13. S. D. Kurgalin and Yu. M. Tchuvil'sky, Ukr. Fiz. Zh. (Russ. Ed.) **35**, 829 (1990).

14. R. A. Eramzhyan, G. G. Ryzhikh, and Yu. M. Tchuvil'sky, Yad. Fiz. **62**, 42 (1999) [Phys. At. Nucl. **62**, 37 (1999)].

15. D. M. Skopik, J. Asai, E. L. Tomusiak, and J. J. Murphy, Phys. Rev. C **20**, 2025 (1979).

16. G. Junghans, K. Bangert, U. E. P. Berg, *et al.*, Z. Phys. A **291**, 353 (1979).

17. V. P. Denisov and I. Ya. Chubukov, Yad. Fiz. **35**, 11 (1982) [Sov. J. Nucl. Phys. **35**, 6 (1982)].

18. I. V. Kopytin, A. S. Kornev, and A. A. Khuskivadze, Izv. Akad. Nauk, Ser. Fiz. **63**, 1005 (1999).

19. M. E. Rose, *Multipole Fields* (Wiley, New York, 1955; Inostrannaya Literatura, 1957).

Translated by A. Isaakyan

Subthreshold and Near-Threshold K^+-Meson Photoproduction on Nuclei*

É. Ya. Paryev

Institute for Nuclear Research, Russian Academy of Sciences, pr. Shestidesyatiletiya Oktyabrya 7a, Moscow, 117312 Russia
Received January 25, 1999; in final form, August 9, 1999

Abstract—The inclusive K^+-meson production in photon-induced reactions in the near-threshold and sub-threshold energy regimes is analyzed for the one-step ($\gamma N \longrightarrow K^+ Y$, $Y = \Lambda, \Sigma$) incoherent production processes on the basis of an appropriate new folding model that takes properly into account the struck-target nucleon-removal energy and the internal momentum distribution (nucleon spectral function), extracted from recent quasielastic-electron-scattering experiments and from many-body calculations based on realistic models of NN interaction. Simple parametrizations of the total and differential cross sections for K^+ production in photon–nucleon collisions are presented. A comparison of the model calculations of the K^+ differential cross sections for γ^{12}C interactions in the threshold region with existing experimental data is given, which displays the contributions to K^+ production at considered incident energies from the use of the single-particle part, as well as high momentum and high removal energy part, of the nucleon spectral function. Detailed predictions for the K^+ total and differential cross sections for γ^2H, γ^{12}C, and γ^{208}Pb interactions at subthreshold and near-threshold energies are provided. The effect of the uncertainties in the elementary K^+-production cross sections on the K^+ yield is explored. © 2000 MAIK "Nauka/Interperiodica".

1. INTRODUCTION

Extensive investigations of the production of K^+ mesons in proton–nucleus collisions [1–15] at incident energies lower than the free nucleon–nucleon threshold have been carried out over the past years. Because of rather weak K^+ rescattering in the surrounding medium in relation to pions, etas, antiprotons, and antikaons, one hopes to extract from these studies information about both the intrinsic properties of target nuclei (such as Fermi motion, high-momentum components of the nuclear wave function, clusters of nucleons or quarks) and reaction mechanism, in-medium properties of hadrons. Investigations of inclusive subthreshold kaon production in pion–nucleus reactions were much less extensive [16, 17]. Finally, the electromagnetic production of K^+ mesons on nuclei in the threshold region has so far received very little consideration [18], probably, because of a lack of suitable facilities and associated detectors. Since the cross sections for (γ, K^+) reactions at subthreshold and near-threshold energies are expected to be extremely small [about one hundred times smaller than those for (π^+, K^+) reactions under the same kinematical conditions], a high duty cycle and high-intensity electron beams are needed to allow accurate inclusive (γ, K^+) measurements on nuclear targets in the threshold region. Such measurements are planned to be conducted in the near future at the Continuous Electron Beam Accelerator Facility (CEBAF) [19, 20] using a tagged photon beam in the CLAS (the

CEBAF Large Acceptance Spectrometer) detector system. New data from CEBAF [19, 20] will hopefully permit improving our understanding of the phenomenon of the near-threshold and subthreshold kaon production in composite hadronic systems, since here we can take advantage of much cleaner electromagnetic probes compared to hadronic ones. It is clear that, in order to analyze such data, a relevant formalism has to be developed.

The main goal of the present study is to extend the spectral-function approach [10], which was employed previously to describe the measured total [1] and differential [8] kaon-production cross sections for p^{12}C collisions in the near-threshold and subthreshold energy regimes to K^+-producing electromagnetic processes. It is evident that the use of a single model to describe simultaneously K^+ production on nuclei in the threshold region from hadronic and electromagnetic probes will enable us to disentangle reliably the underlying reaction mechanism. In this study, predictions for the K^+ total and differential cross sections are presented for $\gamma + {}^2$H, $\gamma + {}^{12}$C, and $\gamma + {}^{208}$Pb interactions in the threshold energy region. Part of these predictions, which were obtained within the first-collision model [10] based on nucleon spectral function, is then compared with available data.

2. FIRST-COLLISION MODEL

An incident photon can produce a K^+ meson directly in the first inelastic γN collision owing to nucleon

---

* This article was submitted by the author in English.

Fermi motion. Since we are interested in the photon energy region up to approximately 1.4 GeV, we have taken into account the elementary processes

$$\gamma + p \longrightarrow K^+ + \Lambda, \qquad (1)$$

$$\gamma + p \longrightarrow K^+ + \Sigma^0, \qquad (2)$$

$$\gamma + n \longrightarrow K^+ + \Sigma^-, \qquad (3)$$

which have the lowest free-production thresholds (respectively, 0.911, 1.046, and 1.052 GeV).[1]

Because the mean free paths of both γ and K^+ in a nuclear medium are relatively long in relation to those of p, $\pi^\pm$, and K^- because of small photon–nucleon and kaon–nucleon cross sections, we will neglect the photon initial- and kaon final-state interactions in the present study. Moreover, we will also ignore here the medium modification of hadron masses, since the kaon mass in a medium is barely affected by medium effects [21], as well as in view of substantial uncertainties in model hyperon self-energies [22–24]. We can then represent the invariant inclusive cross section for K^+ production on nuclei by an initial photon with momentum $\mathbf{p}_\gamma$ as [10]

$$E_{K^+}\frac{d\sigma_{\gamma A \rightarrow K^+ X}^{(\mathrm{prim})}(\mathbf{p}_\gamma)}{d\mathbf{p}_{K^+}} = Z\Bigg[\Bigg\langle E_{K^+}\frac{d\sigma_{\gamma p \rightarrow K^+ \Lambda}(\mathbf{p}_\gamma, \mathbf{p}_{K^+})}{d\mathbf{p}_{K^+}}\Bigg\rangle$$

$$+ \Bigg\langle E_{K^+}\frac{d\sigma_{\gamma p \rightarrow K^+ \Sigma^0}(\mathbf{p}_\gamma, \mathbf{p}_{K^+})}{d\mathbf{p}_{K^+}}\Bigg\rangle\Bigg] \qquad (4)$$

$$+ N\Bigg\langle E_{K^+}\frac{d\sigma_{\gamma n \rightarrow K^+ \Sigma^-}(\mathbf{p}_\gamma, \mathbf{p}_{K^+})}{d\mathbf{p}_{K^+}}\Bigg\rangle,$$

where

$$\Bigg\langle E_{K^+}\frac{d\sigma_{\gamma N \rightarrow K^+ Y}(\mathbf{p}_\gamma, \mathbf{p}_{K^+})}{d\mathbf{p}_{K^+}}\Bigg\rangle = \iint P(\mathbf{p}_t, E)d\mathbf{p}_t dE$$

$$\times \Bigg[E_{K^+}\frac{d\sigma_{\gamma N \rightarrow K^+ Y}(\sqrt{s}, \mathbf{p}_{K^+})}{d\mathbf{p}_{K^+}}\Bigg]. \qquad (5)$$

Here, $E_{K^+}d\sigma_{\gamma N \rightarrow K^+ Y}(\sqrt{s}, \mathbf{p}_{K^+})/d\mathbf{p}_{K^+}$ stands for the free invariant inclusive cross sections for K^+ production in reactions (1)–(3); $P(\mathbf{p}_t, E)$ is the nucleon spectral function normalized to unity; $\mathbf{p}_t$ and E are, respectively, the internal momentum and the removal energy of the struck target nucleon just before the collision; Z and N are the numbers of protons and neutrons in the target nucleus ($A = N + Z$); $\mathbf{p}_{K^+}$ and E_{K^+} are the K^+-meson momentum and total energy, respectively; $E_{K^+} =$

---

[1]In the energy domain of our interest, we can neglect the K^+-production processes featuring higher kaon [$K^+(892)$] and hyperon [$\Lambda(1405)$, $\Lambda(1520)$, $\Sigma^0(1385)$] resonances in the final states because of their larger production thresholds in γN collisions. For example, the threshold for free $\Sigma^0(1385)$ excitation is 1.412 GeV.

$\sqrt{p_{K^+}^2 + m_K^2}$ (m_K is the rest mass of a kaon in free space); and s is the γN c.m. energy squared. The expression for s is

$$s = (E_\gamma + E_t)^2 - (\mathbf{p}_\gamma + \mathbf{p}_t)^2, \qquad (6)$$

where E_γ and E_t are the projectile total energy given by $E_\gamma = p_\gamma$ and the struck-target-nucleon total energy, respectively. Taking into account the recoil and excitation energies of the residual ($A - 1$) system, one has [10, 25]

$$E_t = M_A - \sqrt{(-\mathbf{p}_t)^2 + (M_A - m_N + E)^2}, \qquad (7)$$

where M_A is the rest masses of the initial target nucleus and m_N is the nucleon mass. It can easily be seen that, in this case, the struck target nucleon is off-shell. In (4), any difference between the proton and the neutron spectral functions is disregarded [10].

Taking into consideration the two-body kinematics of the elementary processes (1)–(3), we can readily obtain the Lorentz invariant inclusive cross sections for these processes in the form

$$E_{K^+}\frac{d\sigma_{\gamma N \rightarrow K^+ Y}(\sqrt{s}, \mathbf{p}_{K^+})}{d\mathbf{p}_{K^+}} = \frac{\pi}{I_2(s, m_Y, m_K)}\frac{d\sigma_{\gamma N \rightarrow K^+ Y}(s)}{d\overset{*}{\mathbf{\Omega}}}$$

$$\times \frac{1}{(\omega + E_t)}\delta[\omega + E_t - \sqrt{m_Y^2 + (\mathbf{Q} + \mathbf{p}_t)^2}], \qquad (8)$$

where

$$I_2(s, m_Y, m_K) = \frac{\pi}{2}\frac{\lambda(s, m_Y^2, m_K^2)}{s}, \qquad (9)$$

$$\lambda(x, y, z) = \sqrt{[x - (\sqrt{y} + \sqrt{z})^2][x - (\sqrt{y} - \sqrt{z})^2]}, \qquad (10)$$

$$\omega = E_\gamma - E_{K^+}, \qquad \mathbf{Q} = \mathbf{p}_\gamma - \mathbf{p}_{K^+}. \qquad (11)$$

Here, $d\sigma_{\gamma N \rightarrow K^+ Y}(s)/d\overset{*}{\mathbf{\Omega}}$ stands for the K^+ differential cross sections in the γN c.m. frame normalized to the corresponding total experimental cross sections $\sigma_{\gamma N \rightarrow K^+ Y}$, while m_Y is the mass of a Y hyperon (Λ or Σ) in free space. The existing experimental data (see Figs. 1–3) on the total cross sections $\sigma_{\gamma N \rightarrow K^+ Y}$ were fitted (see also Figs. 1–3) in terms of the simple expressions

$$\sigma_{\gamma N \rightarrow K^+ Y}(\sqrt{s}) = \frac{A_Y(\sqrt{s} - \sqrt{s_0})}{B_Y + (\sqrt{s} - \sqrt{s_0})^2}, \qquad (12)$$

$$\sigma_{\gamma p \to K^+ \Sigma^0}(\sqrt{s})$$

$$= \begin{cases} 8.67 \left(\dfrac{\sqrt{s} - \sqrt{s_0}}{\text{GeV}} \right)^{0.7907} \ [\mu b] \\[4pt] \text{for} \ \ \sqrt{s_0} < \sqrt{s} \leq 1.873 \ \text{GeV} \\[8pt] 0.3665 \left(\dfrac{\text{GeV}}{\sqrt{s} - \sqrt{s_0}} \right)^{1.0956} \ [\mu b] \\[4pt] \text{for} \ \ \sqrt{s} > 1.873 \ \text{GeV}, \end{cases} \qquad (13)$$

where the parameters A_Y, B_Y, and $\sqrt{s_0}$ are given in Table 1 and $\sqrt{s_0} = 1.6861$ GeV.

The currently available experimental information (see Fig. 4) concerning the angular distribution of outgoing kaons in the reaction $\gamma p \longrightarrow K^+ \Lambda$ in the photon energy range of interest can be fitted as

$$\frac{d\sigma_{\gamma p \to K^+ \Lambda}(s)}{d\overset{*}{\Omega}} = [1 + A_1(\sqrt{s}) \cos \Theta_{K^+}] \frac{\sigma_{\gamma p \to K^+ \Lambda}(\sqrt{s})}{4\pi}. \quad (14)$$

Here, Θ_{K^+} is the K^+-production angle in the c.m. frame, the quantity $\sigma_{\gamma p \to K^+ \Lambda}$ is defined above by (12), and the parameter A_1 is given by

$$A_1(\sqrt{s}) = \begin{cases} 0.928 \left(\dfrac{\sqrt{s} - \sqrt{s_0}}{\text{GeV}} \right)^{0.137} \\[4pt] \text{for} \ \sqrt{s_0} < \sqrt{s} \leq 1.7372 \ \text{GeV} \\[8pt] 2.485 \left(\dfrac{\sqrt{s} - \sqrt{s_0}}{\text{GeV}} \right)^{0.616} \\[4pt] \text{for} \ 1.7372 < \sqrt{s} \leq 1.8375 \ \text{GeV} \\[8pt] 1 \ \ \text{for} \ \ \sqrt{s} > 1.8375 \ \text{GeV}. \end{cases} \quad (15)$$

In our calculations, the angular distributions $d\sigma_{\gamma p \to K^+ \Sigma^0}/d\overset{*}{\Omega}$ and $d\sigma_{\gamma n \to K^+ \Sigma^-}/d\overset{*}{\Omega}$ were assumed to be isotropic [26].

To examine the influence of the uncertainties in the total cross section $\sigma_{\gamma p \to K^+ \Lambda}$ for K^+ production via the dominant elementary process $\gamma p \longrightarrow K^+ \Lambda$ at subthreshold incident energies on the K^+ yield from nuclear targets, we will also use in our calculations the following parametrization of $\sigma_{\gamma p \to K^+ \Lambda}$:

$$\sigma_{\gamma p \to K^+ \Lambda}(\sqrt{s}) = \begin{cases} 3.60 \left(\dfrac{\sqrt{s} - \sqrt{s_0}}{\text{GeV}} \right)^{0.2275} \ [\mu b] \\[4pt] \text{for} \ \sqrt{s_0} < \sqrt{s} \leq 1.6204 \ \text{GeV} \\[8pt] 1.29 \ [\mu b] \ \text{for} \ \sqrt{s} > 1.6204 \ \text{GeV}. \end{cases} \quad (16)$$
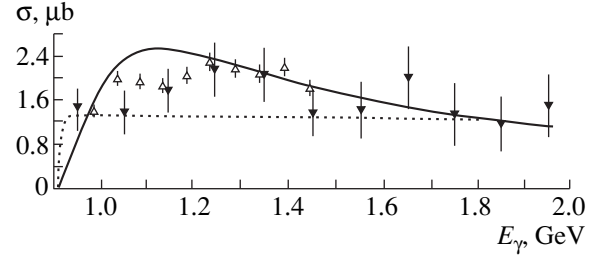
Fig. 1. Total cross section for the reaction $\gamma p \longrightarrow K^+ \Lambda$ as a function of photon energy. The solid and dotted lines represent the results of the calculations based on (12) and (16), respectively. Experimental data were borrowed from (open triangles) [26] and (full triangles) [27].
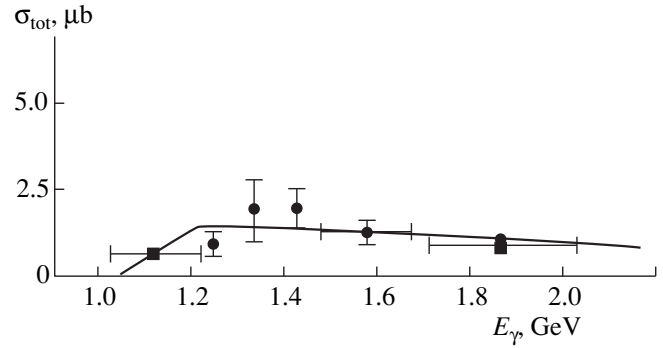
Fig. 2. Total cross section for the reaction $\gamma n \longrightarrow K^+ \Sigma^-$ as a function of photon energy. The solid line represents the results of the calculation based on (12). Experimental data were borrowed from [28].
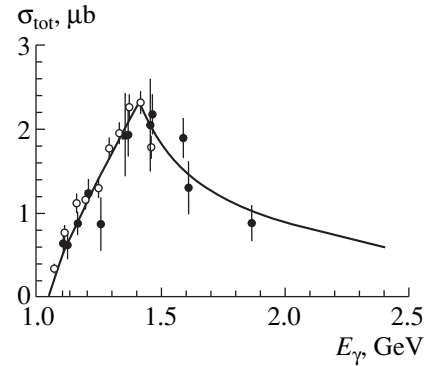
Fig. 3. Total cross section for the reaction $\gamma p \longrightarrow K^+ \Sigma^0$ as a function of photon energy. The solid line represents the results of the calculation based on (13). Experimental data were borrowed from (open circles) [26] and (full circles) [29].

It is shown by the dotted line in Fig. 1. The choice of the approximation of the total cross section $\sigma_{\gamma p \to K^+ \Lambda}$ in the form (16) has been motivated by the fact that in the threshold energy region ($E_\gamma < 0.93$ GeV) it virtually coincides with the prediction for this cross section obtained within the pseudovector coupling description of the $KN\Lambda$ interaction [30] for the coupling constant

$d\sigma/d\Omega$, μb/sr
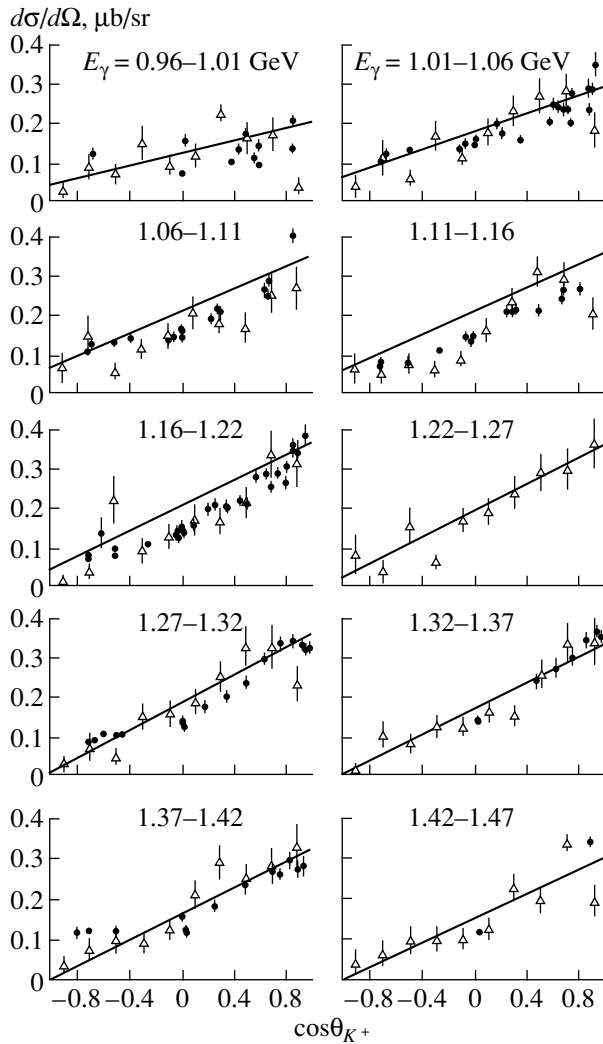
Fig. 4. Differential cross section for the reaction $\gamma p \longrightarrow K^+\Lambda$. The solid line represents the results of the calculation based on (14) and (15). Experimental data were borrowed from [26].

$g_{K N \Lambda}/\sqrt{4\pi} = -2.0$ settled close to the value calculated in [31] using the QCD sum-rule method. At higher beam energies ($E_\gamma > 0.93$ GeV), it also reproduces the available data reasonably well.

Before going to the next step, we discuss now the nucleon spectral function needed for our calculations. The nucleon spectral function, $P(\mathbf{p}_t, E)$, which repre-

Table 1. Parameters in the approximation of the partial cross sections for the production of K^+ mesons in γN collisions

Reaction	A_Y, μb GeV	B_Y, GeV^2	$\sqrt{s_0}$, GeV
$\gamma + p \longrightarrow K^+ + \Lambda$	0.6343	0.0151	1.6093
$\gamma + n \longrightarrow K^+ + \Sigma^-$	0.4562	0.0236	1.6909

sents the probability of finding a nucleon with momentum $\mathbf{p}_t$ and removal (binding) energy E in the nucleus, is a crucial point in the evaluation of the subthreshold production of any particles on a nuclear target. In what follows, we consider the ground-state NN correlations, which are generated by the short-range and tensor parts of realistic NN interaction. Then, the spectral function $P(\mathbf{p}_t, E)$ can be represented in the following form [32, 33]:

$$P(\mathbf{p}_t, E) = P_0(\mathbf{p}_t, E) + P_1(\mathbf{p}_t, E), \qquad (17)$$

where P_0 includes the ground and one-hole states of the residual $(A - 1)$ nucleon system and P_1 includes more complex configurations (mainly $1p$–$2h$ states) that arise from the $2p$–$2h$ excited states generated in the ground state of the target nucleus by NN correlations. Before considering the specific expressions for the functions P_0 and P_1, let us recall a few important quantities that are related to the nucleon spectral function [32, 33]:

$$n(\mathbf{p}_t) = \int P(\mathbf{p}_t, E) dE$$
$$= \int P_0(\mathbf{p}_t, E) dE + \int P_1(\mathbf{p}_t, E) dE = n_0(\mathbf{p}_t) + n_1(\mathbf{p}_t), \qquad (18)$$

the internal nucleon momentum distribution;

$$\langle T \rangle = \iint \frac{p_t^2}{2m_N} P(\mathbf{p}_t, E) d\mathbf{p}_t dE = \int \frac{p_t^2}{2m_N} n(\mathbf{p}_t) d\mathbf{p}_t, \qquad (19)$$

the mean nucleon kinetic energy; and

$$\langle E \rangle = \iint E P(\mathbf{p}_t, E) d\mathbf{p}_t dE, \qquad (20)$$

the mean nucleon removal energy.

The last two quantities are related to the total binding energy per nucleon ϵ_A by the following energy sum rule (the Koltun sum rule [34]):

$$\epsilon_A = \frac{1}{2}\left(\frac{A-2}{A-1}\langle T \rangle - \langle E \rangle\right) \qquad (21)$$

if the nuclear Hamiltonian contains only two-body density-independent forces. The quantities ϵ_A and $n(\mathbf{p}_t)$ have been calculated [32, 33] for different nuclear systems ranging from light nuclei to infinite nuclear matter within the framework of many-body approaches with realistic NN interactions, so that the theoretical values of $\langle T \rangle$ and $\langle E \rangle$ for various nuclei are known presently [32, 33].

In calculating the cross sections for kaon production in γ^2H interactions, we have used for the nucleon spectral function $P(\mathbf{p}_t, E)$ the following expression [33]:

$$P(\mathbf{p}_t, E) = n_d(\mathbf{p}_t)\delta(E - |\epsilon_d|), \qquad (22)$$

where $n_d(\mathbf{p}_t)$ is the nucleon momentum distribution in the deuteron and $|\epsilon_d| = 2.226$ MeV is the deuteron binding energy. The momentum distribution $n_d(\mathbf{p}_t)$ has been calculated in [33] using the Paris potential [35, 36], and

the results of calculations have been parametrized as follows:

$$n_d(\mathbf{p}_t) = \frac{1}{4\pi}\sum_{i=1}^{3} A_i \frac{\exp(-B_i p_t^2)}{\left(1 + C_i p_t^2\right)^2}. \quad (23)$$

The values of the parameters appearing in (23) are given in Table 2.

It can be easily obtained that in the case of the deuteron the off-shell energy E_t of the struck-target nucleon given by (7) has the following simple form:

$$E_t = M_d - \sqrt{(-\mathbf{p}_t)^2 + m_N^2}. \quad (24)$$

Consider now the quantity $P(\mathbf{p}_t, E)$ for ^{12}C and ^{208}Pb target nuclei. For K^+ production calculations in the case of ^{12}C and ^{208}Pb target nuclei reported here, we have employed for the single-particle (uncorrelated) part $P_0(\mathbf{p}_t, E)$ of the nucleon spectral function the following relation [10]:

$$P_0(\mathbf{p}_t, E) = \begin{cases} S_0 P^{(\text{SM})}(\mathbf{p}_t, E) & \text{for } ^{12}\text{C} \\ S_0 P^{(\text{FG})}(\mathbf{p}_t, E) & \text{for } ^{208}\text{Pb}. \end{cases} \quad (25)$$

Here, $P^{(\text{SM})}(\mathbf{p}_t, E)$ and $P^{(\text{FG})}(\mathbf{p}_t, E)$ are the harmonic-oscillator and Fermi gas model spectral functions; the parameter $S_0 = 0.8$ [32, 33] takes into account the depletion of states below the Fermi sea due to the NN correlations. According to [10], one has[2]

$$P^{(\text{SM})}(\mathbf{p}_t, E) = \frac{4}{A} n_{1s}(\mathbf{p}_t)\delta(E - |\epsilon_{1s}|)$$
$$+ \left(\frac{A-4}{A}\right) n_{1p}(\mathbf{p}_t)\delta(E - |\epsilon_{1p}|), \quad (26)$$

where the s- and p-shell nucleon momentum distributions $n_{1s}(\mathbf{p}_t)$ and $n_{1p}(\mathbf{p}_t)$ are

$$n_{1s}(\mathbf{p}_t) = (b_0/\pi)^{3/2}\exp(-b_0 p_t^2),$$
$$n_{1p}(\mathbf{p}_t) = \frac{2}{3}(b_0/\pi)^{3/2}b_0 p_t^2 \exp(-b_0 p_t^2) \quad (27)$$

[$b_0 = 68.5$ (GeV/c)$^{-2}$] and binding energies of $|\epsilon_{1s}| = 34$ MeV and $|\epsilon_{1p}| = 16$ MeV for the s and p shells, respectively, were used. The expression for $P^{(\text{FG})}(\mathbf{p}_t, E)$ [38] is

$$P^{(\text{FG})}(\mathbf{p}_t, E) = \frac{1}{(4/3)\pi p_F^3}\theta(p_F - p_t)\delta(E - |\epsilon_{p_t}|), \quad (28)$$

where $\theta(x) = (x + |x|)/2|x|$, $\epsilon_{p_t} = (p_t^2/2m_N) + U_0$ (m_N is the nucleon mass), and the constants p_F and U_0 ($p_F^2/2m_N = 30.5$ MeV, $U_0 = -50.7$ MeV) for ^{208}Pb were fixed requiring $\langle T \rangle = 38.2$ MeV, $\langle E \rangle = 53.7$ MeV [33].

---

[2] It should be pointed out that, as our calculations showed, the use of Gaussian functions for the s- and p-shell nucleon removal energy distributions for ^{12}C target nuclei in line with [37] in calculating the inclusive cross sections we are interested in leads to results that are sufficiently close to those obtained with the spectral function in the δ-function form (26).

Table 2. Values of the parameters A_i, B_i, and C_i appearing in the parametrization (23) of the nucleon momentum distribution in the deuteron

i	A_i, fm^3	B_i, fm^2	C_i, fm^2
1	157.4	1.24	18.3
2	0.234	1.27	
3	0.00623	0.22	

Here, the mean kinetic $\langle T \rangle$ and removal $\langle E \rangle$ energies were calculated [see (17)–(20), (25), (28)] according to the following expressions:

$$\langle T \rangle = S_0\langle T \rangle_{\text{FG}} + \langle T \rangle_1,$$
$$\langle E \rangle = S_0\langle E \rangle_{\text{FG}} + \langle E \rangle_1, \quad (29)$$

where

$$\langle T \rangle_{\text{FG}} = \frac{3}{5}\frac{p_F^2}{2m_N}, \quad \langle E \rangle_{\text{FG}} = -(U_0 + \langle T \rangle_{\text{FG}}); \quad (30)$$

$$\langle T \rangle_1 = \int \frac{p_t^2}{2m_N} n_1(\mathbf{p}_t)d\mathbf{p}_t, \quad \langle E \rangle_1 = \iint E P_1(\mathbf{p}_t, E)d\mathbf{p}_t dE;$$

and the spectral function $P_1(\mathbf{p}_t, E)$ is given below.

Let us concentrate now on the high momentum and high removal energy part (correlated part) $P_1(\mathbf{p}_t, E)$ of the nucleon spectral function. As was shown in [33], function $P_1(\mathbf{p}_t, E)$ can be expressed as a convolution integral of the momentum distributions describing the relative and c.m. motions of a correlated NN pair in the nuclear medium. Inspection of the convolution formula (53) from [33] for the spectral function $P_1(\mathbf{p}_t, E)$ leads to the following simple analytic expression for the $P_1(\mathbf{p}_t, E)$ (see, also, [10]):

$$P_1(\mathbf{p}_t, E) = a_1 n_1(\mathbf{p}_t)\exp\{-3[(A-2)/(A-1)]$$
$$\times m_N[\sqrt{E - E_{\text{thr}}} - \sqrt{E_1(p_t) - E_{\text{thr}}}]^2/\langle p_{\text{c.m.}}^2 \rangle\}, \quad (31)$$

where

$$a_1 = \frac{3[(A-2)/(A-1)]m_N}{\left\{e^{-\alpha_0^2} + \alpha_0\sqrt{\pi}[1 + \text{erf}(\alpha_0)]\right\}\langle p_{\text{c.m.}}^2 \rangle}, \quad (32)$$

$$\alpha_0 = \frac{p_t}{(\langle p_{\text{c.m.}}^2 \rangle)^{1/2}}\sqrt{\frac{3}{2}\left(\frac{A-2}{A-1}\right)^2\left[1 - \left(\frac{A-1}{A-2}\right)\gamma\right]}, \quad (33)$$

$$\text{erf}(x) = \frac{2}{\sqrt{\pi}}\int_0^x e^{-t^2}dt,$$

$$E_1(p_t) = E_{\text{thr}} + \left(\frac{A-2}{A-1}\right)\frac{p_t^2}{2m_N}\left[1 - \left(\frac{A-1}{A-2}\right)\gamma\right], \quad (34)$$

$$\gamma = \frac{\langle p_{\text{c.m.}}^2 \rangle}{\langle p_{\text{rel}}^2 \rangle}.$$

Here, a_1 is a proper normalization constant [such that $\int_{E_{thr}}^{\infty} P_1(\mathbf{p}_t, E)dE = n_1(\mathbf{p}_t)$]; $E_{thr} = M_{A-2} + 2m_N - M_A$ is the two-particle breakup threshold (E_{thr} is equal to 14 and 25 MeV for ^{208}Pb and ^{12}C target nuclei, respectively); $\langle p_{c.m.}^2 \rangle$ and $\langle p_{rel}^2 \rangle$ are the mean-square momenta associated with the low and high momentum parts of the momentum distribution for c.m. motion of a correlated NN pair and the momentum distribution for the relative motion of this pair, respectively. In our calculations of the K^+-production cross sections on the ^{12}C and ^{208}Pb target nuclei, we have used the values $\langle p_{c.m.}^2 \rangle = 1.5$ fm^{-2} for ^{12}C, $\langle p_{c.m.}^2 \rangle = 1.8$ fm^{-2} for ^{208}Pb, and $\langle p_{rel}^2 \rangle = 7.5$ fm^{-2} [33] both for ^{12}C and for ^{208}Pb. The many-body momentum distribution $n_1(\mathbf{p}_t)$ for ^{12}C has been presented in [32]. Taking into account the corresponding normalization of $n_1(\mathbf{p}_t)$ ($\int n_1(\mathbf{p}_t)d\mathbf{p}_t = S_1 = 1 - S_0 = 0.2$), it can be parametrized as follows [10]:

$$n_1(\mathbf{p}_t) = \frac{S_1}{(2\pi)^{3/2}(1 + \alpha_1)}$$
$$\times \left[\frac{1}{\sigma_1^3}\exp(-p_t^2/2\sigma_1^2) + \frac{\alpha_1}{\sigma_2^3}\exp(-p_t^2/2\sigma_2^2) \right], \tag{35}$$

where $\sigma_1^2 = 0.162$ fm^{-2}, $\sigma_2^2 = 2.50$ fm^{-2}, and $\alpha_1 = 2.78$. This momentum distribution has also been employed in the case of a ^{208}Pb target nucleus [33].

Now let us perform an averaging of the $\gamma N \longrightarrow K^+ Y$ inclusive invariant differential cross section (8) over the Fermi motion of the nucleons in the nucleus using the properties of the energy-conserving Dirac δ function. The integration in (5) over the polar angle ϑ between $\mathbf{p}_t$ and $\mathbf{Q}$ yields (see also [39, 40])

$$\left\langle E_{K^+}\frac{d\sigma_{\gamma N \to K^+ Y}(\mathbf{p}_\gamma, \mathbf{p}_{K^+})}{d\mathbf{p}_{K^+}} \right\rangle$$

$$= \frac{\pi}{Q} \int_{E_{min}}^{E_{max}(Q, \omega)} dE \int_{p_t^{min}(Q, \omega, E)}^{p_t^{max}(Q, \omega, E)} p_t dp_t P(\mathbf{p}_t, E) \tag{36}$$

$$\times \int_0^{2\pi} d\varphi \frac{1}{I_2[s(x_0, \varphi, E), m_Y, m_K]} \frac{d\sigma_{\gamma N \to K^+ Y}[s(x_0, \varphi, E)]}{d\mathbf{\Omega}^*},$$

where

$$E_{min} = M_{A-1} + m_N - M_A, \quad E_{max} = E_{min} + \Delta_x;$$
$$\Delta_x = M_x - (M_{A-1} + m_Y), \tag{37}$$
$$M_x = [(\omega + M_A)^2 - Q^2]^{1/2}.$$

The values of $p_t^{min}(Q, \omega, E)$ and $p_t^{max}(Q, \omega, E)$ are determined by the constraint $-1 \leq \cos\vartheta \leq 1$, with $\cos\vartheta$ given by the energy conservation

$$\omega + M_A = \sqrt{m_Y^2 + Q^2 + p_t^2 + 2Qp_t\cos\vartheta}$$
$$+ \sqrt{(M_A - m_N + E)^2 + p_t^2}, \tag{38}$$

and can be expressed as

$$p_t^{min}(Q, \omega, E) = \alpha |p_t^{c.m.} - \beta E_{A-1}^{c.m.}|, \tag{39}$$

$$p_t^{max}(Q, \omega, E) = \alpha(p_t^{c.m.} + \beta E_{A-1}^{c.m.}), \tag{40}$$

where

$$E_{A-1}^{c.m.} = \sqrt{M_{A-1}^{*2} + (p_t^{c.m.})^2},$$
$$p_t^{c.m.} = \frac{1}{2M_x}\lambda(M_x^2, M_{A-1}^{*2}, m_Y^2), \tag{41}$$
$$M_{A-1}^* = M_A - m_N + E,$$

and

$$\beta = Q/(\omega + M_A),$$
$$\alpha = (1 - \beta^2)^{-1/2} = (\omega + M_A)/M_x. \tag{42}$$

In equation (36)

$$s(x, \varphi, E) = (E_\gamma + E_t)^2 - p_\gamma^2 - p_t^2$$
$$- 2p_\gamma p_t(\cos\vartheta_{\mathbf{Q}} \times x + \sin\vartheta_{\mathbf{Q}} \times \sqrt{1 - x^2}\cos\varphi), \tag{43}$$

$$x_0 = [(\omega + E_t)^2 - m_Y^2 - Q^2 - p_t^2]/(2Qp_t), \tag{44}$$

where

$$\cos\vartheta_{\mathbf{Q}} = \mathbf{p}_\gamma \cdot \mathbf{Q}/(p_\gamma Q). \tag{45}$$

Because the nucleon spectral function $P(p_t, E)$ is a rapidly decreasing function of p_t and E, even for the moderate momentum transfer Q the quantities E_{max} and p_t^{max} can be safely replaced, as our calculations showed, by infinity. Therefore, the Q dependence of the momentum-energy-averaged differential cross section (36) will be essentially governed by the Q dependence of p_t^{min} (39). The latter is determined from the energy conservation [cf. (38)]

$$\omega + M_A = \sqrt{m_Y^2 + (Q \pm p_t^{min})^2} + \sqrt{M_{A-1}^{*2} + (p_t^{min})^2}. \tag{46}$$

The positive and negative signs before p_t^{min} in (46) correspond to $\omega > \omega_0$ and to $\omega < \omega_0$, respectively, with $\omega_0 = (m_Y^2 + Q^2)^{1/2} + M_{A-1}^* - M_A$. The foregoing leads, as is easy to see, to the conclusion that $x_0|_{p_t = p_t^{min}} = +1$ for $\omega > \omega_0$ and $x_0|_{p_t = p_t^{min}} = -1$ for $\omega < \omega_0$.

Let us discuss now the results of our calculations in the framework of the approach outlined above.

3. RESULTS

Figure 5 shows a comparison of the calculated differential cross sections for the production of K^+ mesons at the laboratory angles of $10° \leq \theta_{K^+} \leq 40°$ from primary $\gamma N \longrightarrow K^+ Y$ channels with the experimental data [18] for $\gamma + {}^{12}C \longrightarrow K^+ + X$ reaction at the various photon energies. The differential cross sections under consideration have been calculated according to the following expression:

$$\frac{d\sigma_{\gamma A \to K^+ X}^{(prim)}(\mathbf{p}_\gamma)}{d\mathbf{\Omega}_{K^+}} = \frac{1}{\cos(10°) - \cos(40°)} \times \int_{10°}^{40°} \sin\theta_{K^+} d\theta_{K^+} \int_0^{p_{K^+}^{lim}(\theta_{K^+})} dp_{K^+} \frac{d^2\sigma_{\gamma A \to K^+ X}^{(prim)}(\mathbf{p}_\gamma)}{dp_{K^+} d\mathbf{\Omega}_{K^+}}, \quad (47)$$

where

$$p_{K^+}^{lim}(\theta_{K^+}) = \frac{[\beta_A p_\gamma \cos\theta_{K^+} + (E_\gamma + M_A)\sqrt{\beta_A^2 - 4m_K^2(s_A + p_\gamma^2 \sin^2\theta_{K^+})}]}{2(s_A + p_\gamma^2 \sin^2\theta_{K^+})}; \quad (48)$$

$$\beta_A = s_A + m_K^2 - (M_{A-1} + m_Y)^2,$$
$$s_A = (E_\gamma + M_A)^2 - p_\gamma^2. \quad (49)$$

Here, $p_{K^+}^{lim}(\theta_{K^+})$ is the kinematical limit for kaon production at the laboratory angle θ_{K^+} from photon–nucleus interactions. The double differential cross section $d^2\sigma_{\gamma A \to K^+ X}^{(prim)}(\mathbf{p}_\gamma)/dp_{K^+} d\mathbf{\Omega}_{K^+}$ entering into (47) is defined above by (4), (5), and (36). The minimum value of the removal energy E_{min} [see (37)] in the calculations was taken to be 15.5 MeV for ${}^{12}C$ [41]. One can see the following:

(i) The contributions to the K^+ production from the primary reaction channels (1), (2), and (3) with Λ and Σ particles in the final states are comparable at the photon energies $E_\gamma \geq 1.2$ GeV, whereas at lower photon energies the primary production process (1) is significantly more important than (2) and (3).

(ii) The kaon yield from the one-step K^+-production mechanism is entirely governed by the single-particle part $P_0(\mathbf{p}_t, E)$ of the nucleon spectral function at all considered beam energies ($0.8 \leq E_\gamma \leq 1.3$ GeV), which makes it difficult to extract information about the high momentum and high removal energy components within the ${}^{12}C$ target nucleus from the first kaon photoproduction experiment [18].

(iii) Our calculations for the one-step reaction channels (1)–(3) carried out under two assumptions about the total cross section of the subprocess (1) following from formulas (12) (solid line) and (16) (dotted line) reproduce reasonably well the experimental data [18] in the energy region $E_\gamma \leq 1.0$ GeV, but overestimate the data by a factor of 2.5 at higher photon energies, which might be due to possible in-medium modifications of

the elementary $\gamma N \longrightarrow K^+ Y$ reactions which have not been considered in the present work.

(iv) The experimental data are reproduced better by our first-chance collision model when the parametrization (16) for the total cross section of the elementary process $\gamma p \longrightarrow K^+ \Lambda$ has been employed, which indicates the need for high quality kaon-photoproduction data on both the proton and the nuclear targets at considered beam energies from future experiments [19, 20, 42] to reliably test the spectral function approach presented in this study as well as to deeply elucidate the underlying mechanism of subthreshold and near-threshold kaon photoproduction and the possible modifications of the elementary photon–nucleon interaction in the nuclear medium.

It is clear that the data from coincidence and polarization experiments are also needed to improve our understanding of the basic kaon-photoproduction mechanism at subthreshold incident energies. Therefore, the predictions for some photoproduction coincidence and polarization observables would be useful to plan these experiments as well as to pin down the reaction mechanism. But calculation of these observables is beyond the scope of the present work.

In Fig. 6, we show the above model predictions for the differential cross sections for the production of K^+ mesons from primary $\gamma N \longrightarrow K^+ Y$ reaction channels at the laboratory angles of $10° \leq \theta_{K^+} \leq 40°$ in the interaction of different energy photons with the deuterons. Inspection of Figs. 5 and 6 tells us that the K^+ differential cross sections on ${}^{12}C$ and ${}^2H$ show charge number dependence approximately proportional to Z in the threshold region. This simply indicates that the results under consideration are insensitive to the details of the low-momentum portion of the internal nucleon momentum distribution.
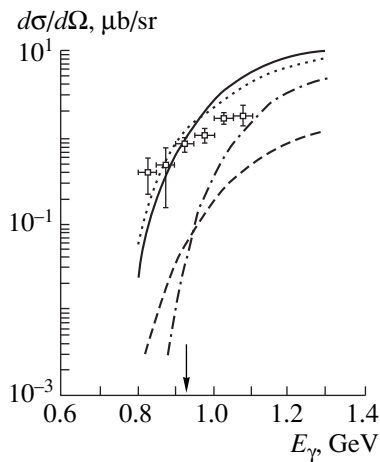
$d\sigma/d\Omega$, μb/sr

Fig. 5. Differential cross sections for K^+ production in $\gamma +$ ^{12}C interactions in the angular range $10° \leq \theta_{K^+} \leq 40°$ of the laboratory frame as functions of laboratory photon energy. Experimental data (open squares) were borrowed from [18]. The curves represent the results of our calculation: (solid and dash-dotted curves) results obtained on the basis of (47) with the total nucleon spectral function for primary production processes as given by, respectively, (1)–(3) and by (2) and (3) [the parametrizations (12) and (13) of the total cross sections for subprocesses (1)–(3) were used here]; (dashed curve) results obtained along the same lines as those represented by the solid curve, but the total nucleon spectral function given by (17), (25), and (31) is replaced here by its correlated part (31); and (dotted curve) results obtained along the same lines as those represented by the solid curve, but the total cross section (12) for subprocess (1) is replaced by the parametrization in (16). The arrow indicates the threshold for the reaction $\gamma p \longrightarrow K^+\Lambda$ occurring on a free proton.

Figure 7 presents the results of our calculations by (4), (5), and (36) for the double-differential cross sections for the production of K^+ mesons at an angle of $10°$ for the photon energies 0.8, 0.9, and 1.3 GeV with ^{12}C nuclei. We see the following:

(1) The calculated kaon momentum spectra reveal characteristic features of quasifree production (a singly peaked structure whose width reflects Fermi broadening, an asymmetric spectral shape) even at subthreshold photon energies.

(2) The main contribution to the K^+ production both at subthreshold and above the free γN threshold beam energies considered here comes from the use of the uncorrelated part[3] $P_0(\mathbf{p}_t, E)$ of the nucleon spectral function in the calculation of the proper momentum–energy-averaged differential cross sections for kaon production, which makes it highly difficult to extract the information on the correlated part of the nucleon spectral function even through analysis of the experimental double-differential cross sections for K^+ production at adopted photon energies ($E_\gamma \geq 0.8$ GeV).

---

[3]Compare to the analogous conclusion drawn from the analysis of the kaon differential cross sections presented in Fig. 5.

$d\sigma/d\Omega$, μb/sr
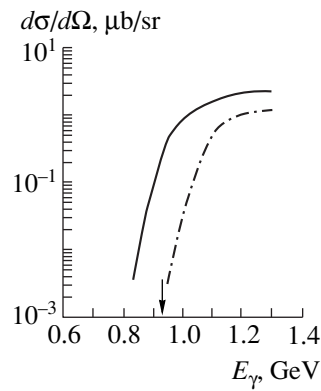
Fig. 6. Differential cross sections for K^+ production in $\gamma +$ ^{2}H interactions in the angular range $10° \leq \theta_{K^+} \leq 40°$ of the laboratory frame as functions of laboratory photon energy. The notation is similar to that in Fig. 5.

$d^2\sigma/(dp\,d\Omega)$, mb/(GeV/c) sr
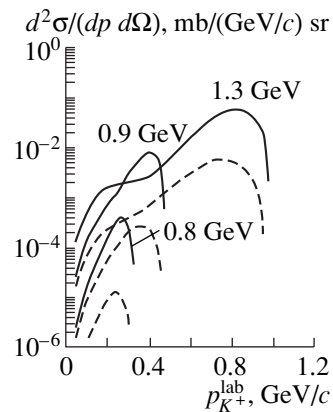
Fig. 7. Double differential cross sections for the production of K^+ mesons at an angle of $10°$ in the interaction of 0.8-, 0.9-, and 1.3-GeV photons with ^{12}C nuclei as functions of kaon momentum. The solid and dashed lines represent the results of our calculations on basis of (4), (5), and (36) for the primary production processes (1)–(3) with the total nucleon spectral function and its correlated part, respectively, and correspond, from top to bottom, to incident energies of 0.8, 0.9, and 1.3 GeV. The parametrizations (12) and (13) of the total cross sections for subprocesses (1)–(3) were used in the above calculations.

The total cross section for K^+ production in $\gamma + {}^2$H reactions calculated according to (4) is shown in Fig. 8 as a function of the laboratory photon energy E_γ. It is seen that the kaon yield from the direct K^+-production processes (1)–(3) is entirely governed by the low-momentum part ($p_t < 0.5$ GeV/c) of the deuteron momentum distribution at considered photon energies (at beam energies between the absolute reaction threshold and 1.4 GeV), which makes it difficult to test the high momentum tail of $n_d(\mathbf{p}_t)$ from the measurement of the primary-photon energy dependence of the total cross section for K^+ production in γ^2H collisions even in the far subthreshold region ($E_\gamma \sim 0.8$ GeV). One can also see that the contributions to the K^+ production from
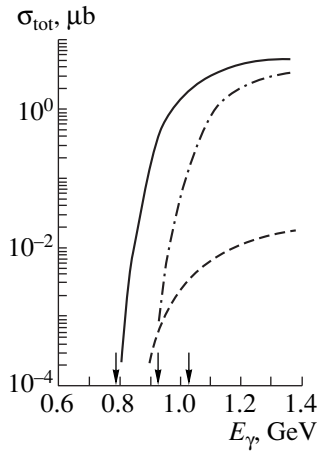
Fig. 8. Total cross section for K^+ production in $\gamma + {}^2H$ inter-actions as a function of laboratory photon energy: (solid and dash-dotted lines) results obtained with the "total" nucleon spectral function for the primary production processes (1)–(3) and (2), (3), respectively; (dashed line) results obtained on the same basis as those represented by solid line, but for the case where the "total" nucleon spectral function given by (22) and (23) is replaced by the "model" nucleon spectral function in which only the internal nucleon momenta greater than 0.5 GeV/c are taken into account. The parame-trizations (12) and (13) of the total cross sections for subpro-cesses (1)–(3) were used in the above calculations. The arrows indicate the thresholds for the reactions $\gamma p \longrightarrow K^+\Sigma^0$ and $\gamma p \longrightarrow K^+\Lambda$ occurring on a free proton and the absolute production threshold.

primary reaction channels (1), (2), and (3) with Λ and Σ particles in the final states are comparable at beam energies $E_\gamma \geq 1.2$ GeV, whereas at lower incident ener-gies the primary production process (1) is more impor-tant than those of (2) and (3). This is consistent with our previous findings of Figs. 5 and 6.

Figures 9 and 10 present the results of similar calcu-lations by (4) for the total cross sections for K^+ produc-tion in $\gamma + {}^{12}C$ and $\gamma + {}^{208}Pb$ reactions, respectively. It can be seen that in these cases the kaon yield from the one-step K^+-production mechanism is almost com-pletely determined by the correlated part $P_1(\mathbf{p}_t, E)$ of the nucleon spectral function only in the vicinities of the absolute reaction thresholds (at photon energies of $E_\gamma \leq 0.75$ GeV). This conclusion is in line with our find-ings inferred above (cf. Figs. 5 and 7) from the analysis of differential and double-differential kaon-production cross sections. The values of the total kaon-production cross sections in the far subthreshold region ($E_\gamma \leq 0.75$ GeV) are too small (in the range of 0.1–10 nb), but one should expect to measure these values on the updated experimental facilities such as the CEBAF [19, 20], Electron Stretcher Accelerator (ELSA) [26], and European Synchrotron Radiation Facility (ESRF) [29]. As in the preceding cases, the direct K^+-production pro-cesses (2), (3) play a minor role in kaon production in γA interactions at the energies $E_\gamma < 1.2$ GeV. It is also
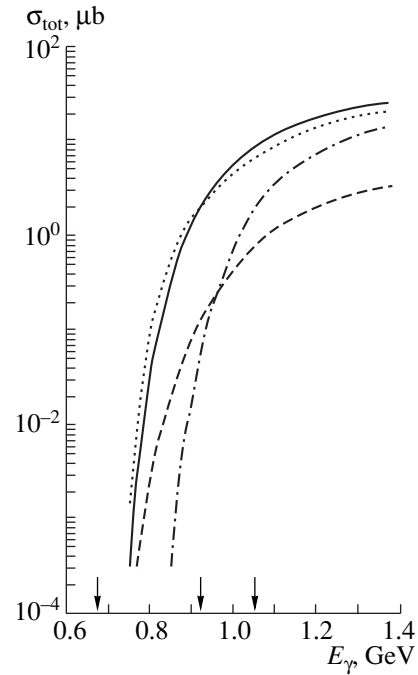
Fig. 9. Total cross section for K^+ production in $\gamma + {}^{12}C$ inter-actions as a function of laboratory photon energy: (solid and dash-dotted curves) results of the calculations with the total nucleon spectral function for primary production processes (1)–(3) for the former and (2) and (3) for the latter [the parametrizations (12) and (13) of the total cross sections for subprocesses (1)–(3) were used in these calculations]; (dashed curve) results obtained along the same lines as those represented by the solid curve, but the total nucleon spectral function given by (17), (25), and (31) is replaced here by its correlated part (31); and (dotted curve) results obtained along the same lines as those represented by the solid curve, but the total cross (12) section for subprocess (1) is replaced here by the parametrization in (16). The arrows indicate the thresholds for the reactions $\gamma p \longrightarrow K^+\Sigma^0$ and $\gamma p \longrightarrow K^+\Lambda$ occurring on a free proton and the absolute production threshold.

seen from Fig. 9 that the extrapolations (12) and (16) of the elementary cross section for $\gamma p \longrightarrow K^+\Lambda$ reaction to the threshold lead to different numerical predictions[4] for the respective kaon-production cross sections in $\gamma^{12}C$ collisions in the energy region far below the lowest threshold (at energies $E_\gamma \sim 0.75$ GeV). Thus, to achieve a better understanding of the phenomenon of the deep subthreshold K^+ production in γA interactions, it is important to measure the elementary cross section under consideration close to the threshold.

Kinematical considerations show that the two-step kaon-production processes of the type $\gamma N \longrightarrow MN$ and $MN \longrightarrow K^+Y$; $M = \{\pi, \eta\}$ may contribute to the (γ, K^+) reaction on nuclei at subthreshold incident energies. We have neglected in the present work the two-step kaon-creation processes mentioned above in calculating the K^+-production cross sections from γA reactions, since

---

[4])The difference between these predictions is of order five.
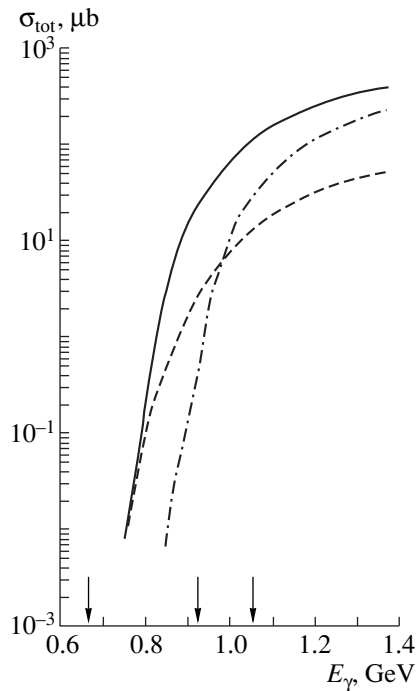
Fig. 10. Total cross section for K^+ production in $\gamma + {}^{208}$Pb interactions as a function of laboratory photon energy. The notation is identical to that in Fig. 9.

their contribution to the cross sections is expected to be small in the incident energy range of our main interest ($E_\gamma \leq 0.8$ GeV), where the intermediate pion and eta are produced (as shown our calculations) at energies where secondary $MN \longrightarrow K^+Y$ channels are suppressed energetically. Nevertheless, it would be interesting to carry out in the future a detailed study of subthreshold kaon production from the two-step processes under consideration.

Thus, our results demonstrate that measurements of the total and differential cross sections for K^+ production in γA reactions only in the far subthreshold region ($E_\gamma \leq 0.75$ GeV) will make it possible to get information on the high momentum and high removal energy part of the nucleon spectral function which is generated by ground-state two-nucleon short-range correlations inside the target nucleus.

4. CONCLUSIONS

In this paper, we have calculated the total and differential cross sections for K^+ production from $\gamma + {}^2$H, $\gamma + {}^{12}$C, and $\gamma + {}^{208}$Pb reactions in the near-threshold and subthreshold energy regimes by considering incoherent primary photon–nucleon production processes within the framework of the first-collision model based on free elementary cross sections for kaon production and on the nucleon spectral function. The comparison of the results of our calculations with the existing experimental data [18] was made. It was shown that in the case of

$\gamma + {}^{12}$C and $\gamma + {}^{208}$Pb reactions the calculated K^+-production cross sections are entirely governed by the correlated part of the nucleon spectral function only in the far subthreshold region, whereas for $\gamma + {}^2$H reaction they are completely determined by the low momentum part ($p_t < 0.5$ GeV/c) of the deuteron momentum distribution. It was obtained that at energies far below the lowest free K^+-production threshold ($E_\gamma \sim 0.75$ GeV) the expected total cross sections are in the measurable range at present experimental facilities (in the range of 0.1–10 nb).

Therefore, measurements in this region would make it possible to obtain information about the underlying mechanism of subthreshold kaon photoproduction and about the high momentum components in the momentum distribution of intranuclear nucleons.

REFERENCES

1. V. P. Koptev *et al.*, Zh. Éksp. Teor. Fiz. **94** (11), 1 (1988) [Sov. Phys. JETP **67**, 2177 (1988)].
2. A. Shor *et al.*, Nucl. Phys. A **514**, 717 (1990).
3. W. Cassing *et al.*, Phys. Lett. B **238**, 25 (1990).
4. A. A. Sibirtsev and M. Büscher, Z. Phys. A **347**, 191 (1994).
5. W. Cassing *et al.*, Z. Phys. A **349**, 77 (1994).
6. A. Sibirtsev, Phys. Lett. B **359**, 29 (1995).
7. H. Müller and K. Sistemich, Z. Phys. A **344**, 197 (1992).
8. M. Debowski *et al.*, Z. Phys. A **356**, 313 (1996).
9. A. Sibirtsev *et al.*, Z. Phys. A **358**, 357 (1997).
10. S. V. Efremov and E. Ya. Paryev, Yad. Fiz. **61**, 612 (1998) [Phys. At. Nucl. **61**, 541 (1998)].
11. A. V. Akindinov *et al.*, APH N.S., Heavy Ion Phys. **4**, 325 (1996).
12. Yu. T. Kiselev *et al.*, Preprint No. 56-96 (ITEP, Moscow, 1996).
13. B. Z. Kopeliovich and F. Niedermeier, Yad. Fiz. **44**, 517 (1986) [Sov. J. Nucl. Phys. **44**, 333 (1986)].
14. A. Badala *et al.*, Phys. Rev. Lett. **80**, 4863 (1998).
15. É. Ya. Paryev, Yad. Fiz. **63**, 348 (2000) [Phys. At. Nucl. **63**, 287 (2000)].
16. S. V. Efremov and E. Ya. Paryev, Yad. Fiz. **58**, 1796 (1995) [Phys. At. Nucl. **58**, 1696 (1995)].
17. S. V. Efremov and E. Ya. Paryev, Yad. Fiz. **59**, 2143 (1996) [Phys. At. Nucl. **59**, 2063 (1996)].
18. H. Yamazaki *et al.*, Phys. Rev. C **52**, R1157 (1995).
19. CEBAF experiment 91-014 (C. E. Hyde–Wright spokesman).
20. B. A. Mecking, Nucl. Phys. A **639**, 559 (1998).
21. D. B. Kaplan and A. E. Nelson, Phys. Lett. B **175**, 57 (1986); A. E. Nelson and D. B. Kaplan, Phys. Lett. B **192**, 193 (1987).

22. Y. Yamamoto and H. Bando, Phys. Lett. B **214**, 173 (1988).
23. M. Hjorth-Jensen *et al.*, Nucl. Phys. A **605**, 458 (1996).
24. G. Q. Li and C. M. Ko, Phys. Rev. C **54**, 1897 (1996).
25. C. Ciofi degli Atti and S. Simula, Phys. Lett. B **325**, 276 (1994).
26. M. Bockhorst *et al.*, Z. Phys. C **63**, 37 (1994).
27. ABBHHM Collab., Phys. Rev. **188**, 2060 (1969).
28. T. Mart *et al.*, Phys. Rev. C **51**, R1074 (1995).
29. J. C. David *et al.*, Phys. Rev. C **53**, 2613 (1996).
30. M. K. Cheoun *et al.*, Phys. Rev. C **54**, 1811 (1996).
31. S. Choe *et al.*, Phys. Rev. C **53**, 1363 (1996).
32. C. Ciofi degli Atti and S. Liuti, Phys. Lett. B **225**, 215 (1989).
33. C. Ciofi degli Atti and S. Simula, Phys. Rev. C **53**, 1689 (1996).
34. D. S. Koltun, Phys. Rev. C **9**, 484 (1974).
35. M. Lacombe *et al.*, Phys. Rev. C **21**, 861 (1980).
36. M. Lacombe *et al.*, Phys. Lett. **101B**, 139 (1981).
37. H. Hiramatsu *et al.*, Phys. Lett. **44B**, 50 (1973).
38. O. Benhar *et al.*, Phys. Lett. **410B**, 79 (1997).
39. E. Pace and G. Salme, Phys. Lett. **110B**, 411 (1982).
40. C. Ciofi degli Atti *et al.*, Phys. Rev. C **43**, 1155 (1991).
41. S. Frullani and J. Mougey, Adv. Nucl. Phys. **14**, 1 (1984).
42. M. Fujiwara, in *Abstracts of the APCTP Workshop on Strangeness Nuclear Physics, SNP'99, Seoul, Korea, 1999*, p. 83.

<center>

NUCLEI
Theory

</center>

Tensor Polarization of ^{6}Li(2.186 MeV, 3$^+$) States Produced in the Reaction ^{9}Be(p, α)^{6}Li* at 40 MeV

L. I. Galanina and N. S. Zelenskaya

Institute of Nuclear Physics, Moscow State University, Vorob'evy gory, Moscow, 119899 Russia
Received May 27, 1999; in final form, October 28, 1999

Abstract—A consistent theoretical analysis of polarization moments t_{kq} is performed for the ^{6}Li(2.186 MeV, 3$^+$) states produced in the reaction ^{9}Be(p, α)^{6}Li*. The analysis is based on the distorted-wave Born approximation implemented for finite-range forces with allowance for spin–orbit interaction. The calculated tensor moments are compared with relevant experimental data. Particle–particle angular-correlation functions and tensor moments are shown to provide radically new information about reaction mechanisms and about nuclear interactions. © 2000 MAIK "Nauka/Interperiodica".

1. INTRODUCTION

At the moment, much attention in nuclear physics is being given to investigations of oriented systems. However, customary experiments with polarized beams and targets are very complicated. An alternative method for deducing information about the properties of oriented systems is based on studying angular-correlation functions for reaction products (in this case, the final nucleus produced in the reaction under study and its polarization are not recorded). A method for reconstructing the spin density matrix for a nucleus was proposed in [1] on the basis of measurement of angular-correlation functions for reaction products in various detection planes with respect to the reaction plane. A number of experiments that relied on this method were performed [2], but the majority of these studied photon–particle angular correlations. The method being discussed was used in [3] to explore particle–particle angular correlations. Specifically, the angular correlations of alpha particles produced in the reaction

$$p + {}^9\text{Be} \longrightarrow \alpha + {}^6\text{Li*}$$
$$\underset{L=2}{\big\lfloor} \longrightarrow p + \alpha'$$

induced by 40-MeV protons were measured there for the ^{6}Li(2.186 MeV, $J = 3^+$) state. The spin–tensor components t_{kq} ($k_{max} = 2L = 4$) of the spin density matrix for the ^{6}Li(2.186 MeV, 3$^+$) state were reconstructed by using the measured angular-correlation function. All measurements were performed in the transverse coordinate frame where the x (z) axis is parallel (orthogonal) to $\mathbf{k}_{^6\text{Li*}}$ ($\mathbf{k}_p \times \mathbf{k}_\alpha$), with $\mathbf{k}_p$, $\mathbf{k}_\alpha$, and $\mathbf{k}_{^6\text{Li*}}$ being the momenta of the corresponding particles in the c.m. frame (that is, the reaction plane coincides with the xy plane).

The symmetry and Hermiticity requirements impose constraints on the spin–tensor components t_{kq}.

If projectiles (or target nuclei) are not polarized and if the polarization of the reaction products is not recorded, the entire system is invariant under reflections with respect to the reaction plane. In the chosen coordinate frame, this symmetry condition leads to the vanishing of the spin–tensor components t_{kq} with odd q. Combining this condition with the requirement that the density matrix be a Hermitian matrix, we arrive at $t_{kq}^* = t_{k-q}$, whence it follows that the components t_{k0} are real-valued. In other words, the spin features of the reaction ^{9}Be(p, α)^{6}Li* are determined by the components t_{kq} controlled by nine independent parameters: of these, three components (t_{00}, t_{20}, and t_{40}) are real-valued, while the remaining three (t_{22}, t_{42}, and t_{44}) are complex-valued.

The procedure for measuring the double differential cross section for the reaction ^{9}Be(p, α)^{6}Li* was described in detail elsewhere [3]. In that experiment, the angular-correlation function was measured in two planes; of these, one was coincident with the reaction plane, while the other was orthogonal to the reaction plane. It was shown in [1] that, for $L = 2$ transitions, measurements in two planes are insufficient for reconstructing all components t_{kq}, since such measurements provide only eight linear relations. In order to overcome this difficulty, use was made in [3] of an original system of ΔE–E ring detectors, whereby it became possible to transmit an incident beam directly and to measure the differential cross section, which coincides, apart from normalization, with the component t_{00}. As a result, one of the components t_{kq} was determined, and the above eight relations were sufficient for reconstructing the remaining eight quantities.

Eventually, the real and imaginary parts of the spin–tensor components t_{kq} at $k = 0, 2, 4$ and $q = 0, 2, 4$ were reconstructed in [3] for α-particle emission angles in the range between 10° and 100°. Within an appropriate

theoretical interpretation, these data might furnish information not only about the spin state of the final nucleus but also about the reaction mechanism and about the parameters of nuclear interactions. It is obvious that, in order to deduce such information, it is necessary to perform a consistent theoretical analysis of experimental spin–tensor components. In this study, the polarization tensors obtained for product nuclei from measurements of particle–particle angular-correlation functions are analyzed on the basis of the spin-density-matrix formalism [4] and the distorted-wave Born approximation implemented for finite-range forces with allowance for spin–orbit interaction [5].

2. CALCULATION OF THE SPIN–TENSOR COMPONENTS OF THE SPIN DENSITY MATRIX

Let us consider binary two-step processes of the type

$$x + A \longrightarrow y + B^*.$$
$$\longrightarrow D + d$$

We restrict our analysis to the case where $x \leq 4$ and $y \leq 4$. Hereafter, we denote by J_n and M_n ($n = x, A, y, B, D, d$) the total angular momenta of the nuclei and their projections on the z axis, respectively.

A detailed account of the general theory of angular correlations is given in [1, 4]. According to this theory, the spin density matrix $\rho_{J_B}(M_B, M'_B)$ for the final nucleus B can be expanded in a complete set of the irreducible tensor operators $T_{kq}(J)$ as

$$\rho_{J_B}(M_B, M'_B) = \sum_{k, q} \rho_{kq} \langle J_B M'_B | T_{kq}(J_B) | J_B M_B \rangle, \quad (1)$$

where the matrix elements of the tensor operator $T_{kq}(J)$ between the states $|J_B M_B\rangle$ and $|J_B M'_B\rangle$ are given by

$$\langle J_B M'_B | T_{kq}(J_B) | J_B M_B \rangle$$
$$= \frac{1}{\sqrt{2J_B + 1}} (-1)^{J_B - M_B} \langle J_B M_B J_B M'_B | kq \rangle. \quad (2)$$

From (1) and (2), it follows that

$$\rho_{kq} = \sqrt{2J_B + 1}$$
$$\times \sum_{M_B M'_B} (-1)^{J_B - M_B} \langle J_B M_B J_B M'_B | kq \rangle \rho_{J_B}(M_B, M'_B). \quad (3)$$

For unpolarized initial and final particles and an unpolarized target, the density matrix has the form

$$\rho_{J_B}(M_B, M'_B)$$
$$= \frac{\text{NORM}}{(2J_x + 1)(2J_A + 1)} \sum_{M_x M_A M_y} \mathbf{M}_{if}(M_B) \mathbf{M}^*_{if}(M'_B), \quad (4)$$

where $\mathbf{M}_{if}(M_B)$ is the matrix element for the reaction $x + A \longrightarrow y + B^*$; the normalization factor NORM was chosen in such a way that the density matrix was normalized to the differential cross section:

$$\text{tr} \, \rho_{J_B}(M_B, M'_B) = \rho_{00} = \frac{d\sigma}{d\Omega},$$

$$\text{NORM} = \frac{\mu_{xA} \mu_{yB} k_y}{4\pi^2 \hbar^4 k_x}.$$

Here, μ_{xA} and μ_{yB} are the reduced masses of the particles in the initial and the final state, respectively, and k_x and k_y are the corresponding c.m. momenta.

The y–d angular-correlation function (that is, the probability of simultaneously detecting particle y in the direction Ω_y and particle d in the direction Ω_d) is given by

$$W(\Omega_y, \Omega_d) = \sum_{kq} \rho_{kq} \varepsilon^*_{kq}, \quad (5)$$

where

$$\varepsilon_{kq} = \frac{2J_B + 1}{(2J_D + 1)(2J_d + 1)} Y_{kq}(\Omega_z)$$
$$\times \sum_{SLL'} (-1)^{S + L'} \sqrt{\frac{(2L+1)(2L'+1)}{2k+1}} \quad (6)$$
$$\times \langle L0L'0 | k0 \rangle W(LJ_B L'J_B : Sk)$$

is the detector efficiency tensor.

In (6), $\mathbf{S} = \mathbf{J}_d + \mathbf{J}_D$, $\mathbf{L} = \mathbf{S} + \mathbf{J}_B$, and Ω_z is the angle between the momenta of the emitted particles d and D in the rest frame of the ^{6}Li* nucleus.

For the decay process ^{6}Li*(3^+) $\longrightarrow d(J_d = 1) + \alpha'(J_D = 0)$, the main contribution comes from the $L = 2$, $S = J_d = 1$ component [3], whence it follows that the factor $\langle L0L'0 | k0 \rangle$ vanishes at odd k and that only at even k do the tensors ε_{kq} take nonzero values.

In calculating the reaction matrix element $\mathbf{M}_{if}$, we relied on the distorted-wave Born approximation implemented for finite-range forces and allowed for spin–orbit interaction both in the initial and in the final state [5]. Within this approach, we considered separately the contributions of direct and exchange processes (associated with the partition of the participant nuclei into clusters). For exchange processes, the reaction matrix element was calculated by the formula

$$\mathbf{M}_{if} = \sqrt{(2J_A + 1)(2J_B + 1)}$$
$$\times \sum_{S_i S_f} \langle J_x M_x J_A M_A | S_i M_i \rangle \langle J_y M_y J_B M_B | S_f M_f \rangle \mathbf{B}_{S_i S_f}, \quad (7)$$

where the partial-wave amplitudes $\mathbf{B}_{S_i S_f}$ corresponding

to specified spins of the channels are given by

$$\mathbf{B}_{S_i S_f} = \frac{4\pi\sqrt{2}}{k_x k_y} \sum_{l_x l_y \mu_y} (-1)^{2S_i + J_1 + S_f} i^{l_x - l_y} (2l + 1)$$

$$\times \langle l_x 0 S_i M_i | J_1 M_1 \rangle \langle l_y \mu_y S_f M_f | J_1 M_1 \rangle \begin{Bmatrix} J_1 & l_x & S_i \\ l & S_f & l_y \end{Bmatrix} \quad (8)$$

$$\times P_{l_y \mu_y}(\theta_y) \sum_{\Lambda_1 \Lambda_2 l} (-1)^{\Lambda_1 + \Lambda_2} \Theta_{\Lambda_1 \Lambda_2 l}^{S_i S_f} I_{l_x l_y J_1}^{\Lambda_1 \Lambda_2 l}.$$

Here, $P_{l_y \mu_y}(\theta_y)$ is an associated Legendre polynomial; Λ_1 and Λ_2 are the angular-momentum transfers in the decay vertices; l_x and l_y are the summation indices in the partial-wave expansion of the distorted waves in the initial and in the final states, respectively; and $\Theta_{\Lambda_1 \Lambda_2 l}^{S_i S_f}$ is a structural factor that is peculiar to the method used with allowance for spin–orbit interaction and which has the form

$$\Theta_{\Lambda_1 \Lambda_2 l}^{S_i S_f} = \sum_{sj} \sqrt{\frac{(2s+1)(2j+1)}{2J_A + 1}} (-1)^{s+j+J_A} \theta_{sj}^{\Lambda_1 \Lambda_2 l}$$

$$\times \begin{Bmatrix} J_y & J_x & s \\ J_A & j & S_i \end{Bmatrix} \begin{Bmatrix} S_i & J_y & j \\ J_B & l & S_f \end{Bmatrix},$$

where $\theta_{sj}^{\Lambda_1 \Lambda_2 l}$ is the structural factor that is peculiar to the ordinary distorted-wave Born approximation [6] and which is related to the reduced widths in the decay vertices. The quantity $I_{l_x l_y J_1}^{\Lambda_1 \Lambda_2 l}$ in (8) is the kinematical integral that depends on the form factor $F_{\Lambda_1 \Lambda_2 l}^{l_x l_y}(r_x r_y)$ and on the distorted waves $\chi_{l_x J_1}^{S_i(+)}(k_x r_x)$ and $\chi_{l_y J_2}^{S_f(-)}(k_y r_y)$ in the initial and in the final state and which has the form

$$I_{l_x l_y J_1}^{\Lambda_1 \Lambda_2 l}$$

$$= \int \chi_{l_x J_1}^{S_i(+)}(k_x r_x) F_{\Lambda_1 \Lambda_2 l}^{l_x l_y}(r_x r_y) \chi_{l_y J_2}^{S_f(-)}(k_y r_y) r_x r_y dr_x dr_y.$$

Taking into account expression (7), we eventually find that the spin–tensor components of the density matrix can be represented as

$$\rho_{kq} = \frac{(2J_B + 1)^{3/2}}{2J_x + 1} \mathrm{NORM} \sum_{M_f M_f'} (-1)^{-S_f' - J_y - k - J_B}$$

$$(9)$$

$$\times \langle S_f' M_f' k - q | S_f M_f \rangle \begin{Bmatrix} S_f' & J_B & J_y \\ J_B & S_f & k \end{Bmatrix} \mathbf{B}_{S_i S_f} \mathbf{B}_{S_i' S_f'}^*.$$

It is precisely the expression that was used in our calculations.

3. THEORETICAL ANALYSIS OF THE SPIN FEATURES OF THE REACTION $^9\mathrm{Be}(p, \alpha)^6\mathrm{Li}^*$

In the three-body-problem approximation corresponding to the method used, we consider the following mechanisms of the reaction $^9\mathrm{Be}(p, \alpha)^6\mathrm{Li}^*$:

(1) $p + {}^9\mathrm{Be} = p + (\alpha + {}^5\mathrm{He}) = \alpha + (p + {}^5\mathrm{He}) = \alpha + {}^6\mathrm{Li}^*$. In our approach, this partition corresponds to the exchange process, and the relevant matrix element and the spin–tensor components for the final nucleus were calculated directly according to the above expressions.

(2) $p + {}^9\mathrm{Be} = p + (t + {}^6\mathrm{Li}) = (p + t) + {}^6\mathrm{Li} = \alpha + {}^6\mathrm{Li}^*$. All expressions within our method were obtained under the conditions $x \le 4$ and $y \le 4$, which are invalid for the case under consideration: $y = {}^6\mathrm{Li} > 4$. Therefore, a direct application of the method to estimating the direct-mechanism contribution is not legitimate. Therefore, we used the method to calculate the matrix element for the inverse reaction $\alpha + {}^6\mathrm{Li}^* = (p + t) + {}^6\mathrm{Li} = p + (t + {}^6\mathrm{Li}) = p + {}^9\mathrm{Be}$ and determined the matrix element for the process being considered according to the detailed-balance principle [7]:

$$\mathbf{M}_{if}(x + A \longrightarrow y + B^*) = \mathbf{M}_{f^* i^*}(y + B^* \longrightarrow x + A).$$

Here, f^* and i^* are the states corresponding to opposite directions of the particle momenta and spin projections. The spin–tensor components of the density matrix for the $^6\mathrm{Li}$ nucleus were calculated directly by formulas (3) and (4).

Within our method, all the expressions were obtained in the longitudinal coordinate frame, with the z' (y') axis being parallel (orthogonal) to $\mathbf{k}_x$ ($\mathbf{k}_x \times \mathbf{k}_y$). It is the coordinate frame where we have calculated the components ρ_{kq}. At the same time, experimental data refer to the transverse coordinate frame xyz, related to the $x'y'z'$ frame by a rotation determined by the Euler angles $\alpha = \pi/2$, $\beta = \pi/2$, and $\gamma = \theta_y$. In order to compare the results of the calculations with experimental data, the results obtained for the components ρ_{kq} were transformed into the transverse coordinate frame and were normalized to the zero component:

$$t_{kq}(\theta_y) = \frac{1}{t_{00}} \sum_{q'} \rho_{kq'}(\theta_y) D_{q'q}^k(\pi/2, \pi/2, \theta_y).$$

Here, $D_{q'q}^k(\pi/2, \pi/2, \theta_y)$ are the conventional rotation D matrices [7].

4. RESULTS OF THE CALCULATIONS

By using the above formulas, we have calculated the spin–tensor components of the density matrix for the $^6\mathrm{Li}(2.186 \text{ MeV}, 3^+)$ state produced in the reaction $^9\mathrm{Be}(p, \alpha)^6\mathrm{Li}^*$ at $E_p = 40$ MeV. In our calculations, we took into account four one-step mechanisms. Of these,

two were direct mechanisms (stripping and heavy-particle stripping) and two were exchange ones (capture and exchange of a heavy cluster).

The spectroscopic factors $\theta_{sj}^{\Lambda_1\Lambda_2 l}$ for the direct and exchange processes were computed on the basis of the shell model. We allowed for all possible values of the orbital angular momenta in the decay vertices and of the total spin of the reaction. These are quoted in Table 1.

The wave functions describing the relative motion of the clusters in the bound state were determined by numerically solving the Schrödinger equation with the aid of the well-depth-prescription procedure. The distorted waves in the initial and in the final state of the reaction with allowance for spin–orbit interaction were determined by numerically solving the Schrödinger equation by the Runge–Kutta method with the optical potential

$$V(r) = -V_0 f_v(r) - i\left(W_0 f_W(r) + W_D \frac{d}{dr} f_W(r)\right)$$

$$+ \frac{1}{2m_\pi^2 c^2 r} V_{sl} \frac{d}{dr} f_{sl}(r),$$

$$f_n(r) = \frac{1}{1 + \exp\left(\dfrac{r - r_{0n} A^{1/3}}{a_n}\right)}, \quad n = V, W, sl,$$

where m_π is the pion mass. The parameters of the bound-state potentials and of the optical potentials used in our calculations are presented in Tables 2 and 3.

Figure 1 displays the differential cross section for the reaction being considered. As might have been expected, the main contribution to the cross section for final-particle emission angles below 70° comes from the direct processes. The exchange processes are dominant in the backward hemisphere. Both for the direct and for the exchange processes, the pole mechanisms play a leading role, while the contribution of the triangle mechanisms—the replacement and the exchange of a heavy cluster—is negligible. It is worth noting that the results are rather stable to variations in the optical-potentials parameters. The theoretical cross sections exhibit the highest sensitivity to changes in the radii of the bound-state potentials in the decay vertices. At the chosen parameter values, the calculated cross section complies quite well with the experimental cross section both in shape and in magnitude without absolute normalization.

Figures 2 and 3 show the polarization spin–tensor components

$$t_{kq}(\theta_y) = \frac{t_{kq}^{dir}(\theta_y)\sigma^{dir} + t_{kq}^{ex}(\theta_y)\sigma^{ex}}{\sigma^{dir} + \sigma^{ex}}$$

at $k = 2$ and 4. From the figures, we can see that, for all eight components, the agreement is good both in shape and in magnitude. In the interval of angles correspond-

Table 1. Quantum numbers and spectroscopic factors

j	l	Λ_1	Λ_2	$\theta_{sj}^{\Lambda_1\Lambda_2 l}$
Direct processes				
5/2	1	0	1	0.237
5/2	3	0	3	−0.252
7/2	3	0	3	−0.026
Exchange processes				
1	2	2	1	0.128
1	3	2	1	−0.363
1	3	4	1	0
1	4	4	1	0
2	1	0	1	−0.651
2	1	2	1	0.099
2	3	2	1	0.487

ing to experimental data, the polarization tensors are determined by the direct mechanism. The polarization-tensor components are more sensitive to the model
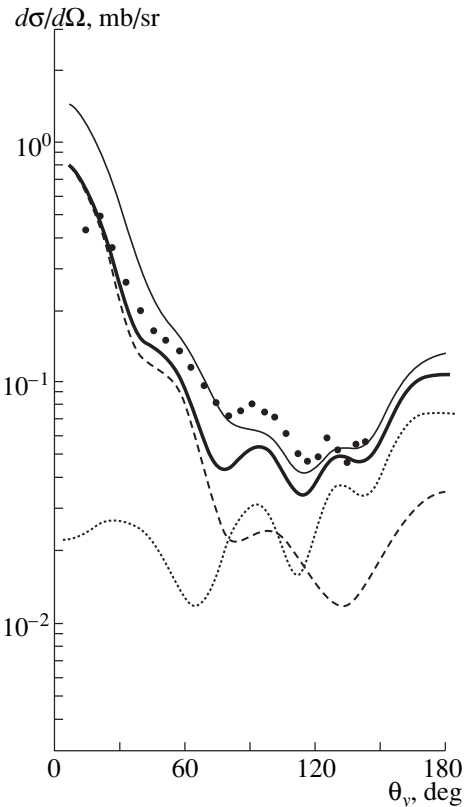
Fig. 1. Differential cross section for the reaction ^{9}Be(p, α)^{6}Li* at 40 MeV: (points) experiment data from [3], (dotted curve) contribution of exchange processes, (dashed curves) contribution of direct processes, (thick solid curve) cross sections allowing for both mechanisms and for spin–orbit interaction, and (thin solid curve) contribution of the two mechanisms without allowance for spin–orbit interaction.
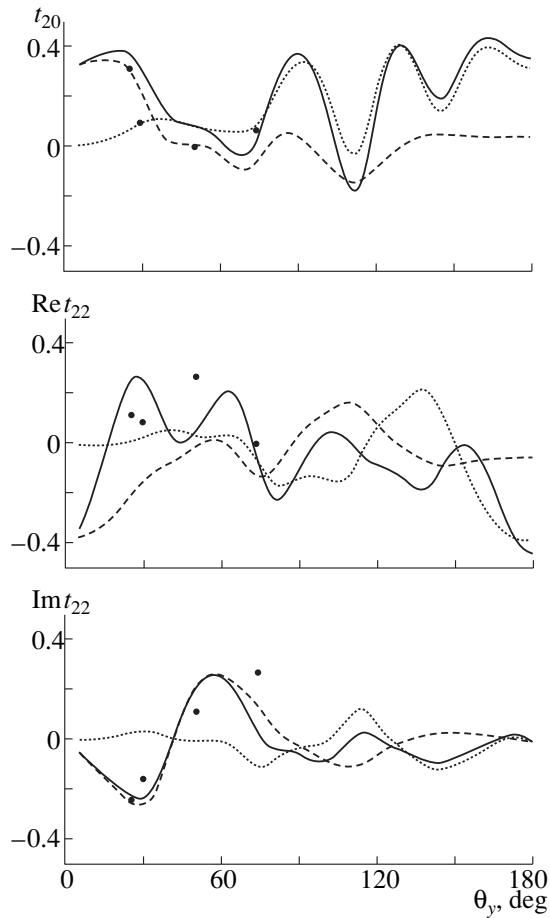
Fig. 2. Spin–tensor components t_{kq} of the density matrix for a ^{6}Li* nucleus at $k = 2$: (points) experimental data from [3], (dotted curve) contribution of exchange processes, (dashed curve) contribution of direct processes, and (solid curve) total contribution of the two mechanisms with allowance for spin–orbit interaction. Here and in Figs. 3–5, the spin–tensor components are given in relative units.

Fig. 3. Spin–tensor components t_{kq} of the density matrix for ^{6}Li* at $k = 4$. The notation is identical to that in Fig. 2.

parameters than the differential cross section; from the agreement between the calculated values and the data, we can therefore conclude that the model and its

parameters describe adequately the features of the reaction ^{9}Be$(p, \alpha)^6$Li*.

It is important to note that the reaction in question is superficial. The agreement between the calculated and experimental components is achieved only upon introducing, in the interaction potentials for the $p + {}^9$Be input channel, a soft core in the internal region of the nucleus with a radius of about 1 fm. As a matter of fact,

Table 2. Parameters of the optical potentials for distorted waves

Reaction channel	V_0, MeV	r_{0V}, fm	a_V, fm	W, MeV	W_D, MeV	r_{0W}, fm	a_W, fm	r_c, fm	V_{sl}, MeV	r_{sl}, fm	a_{sl}, fm
$p + {}^9$Be	38.30	1.18	0.62	3.59	1.00	1.69	0.69	1.20	5.60	1.10	0.58
$\alpha + {}^6$Li*	150.00	1.28	0.57	20.00	0	1.70	0.57	1.20	15.00	1.29	0.57

Table 3. Parameters of the rearrangement potentials and of the bound-state potentials

Decay vertex	V_0, MeV	r_0, fm	a, fm	Decay vertex	V_0, MeV	r_0, fm	a, fm
^{9}Be $= {}^5$He $+ \alpha$	40.4	1.90	0.8	^{6}Li* $= {}^5$He $+ p$	30.0	2.20	0.8
$\alpha = p + t$	58.0	0.94	0.6	^{6}Li* $\otimes p$	71.0	1.06	0.6
^{9}Be $= {}^6$Li* $+ t$	105.0	1.20	0.6	$\alpha \otimes p$	93.0	1.50	0.7
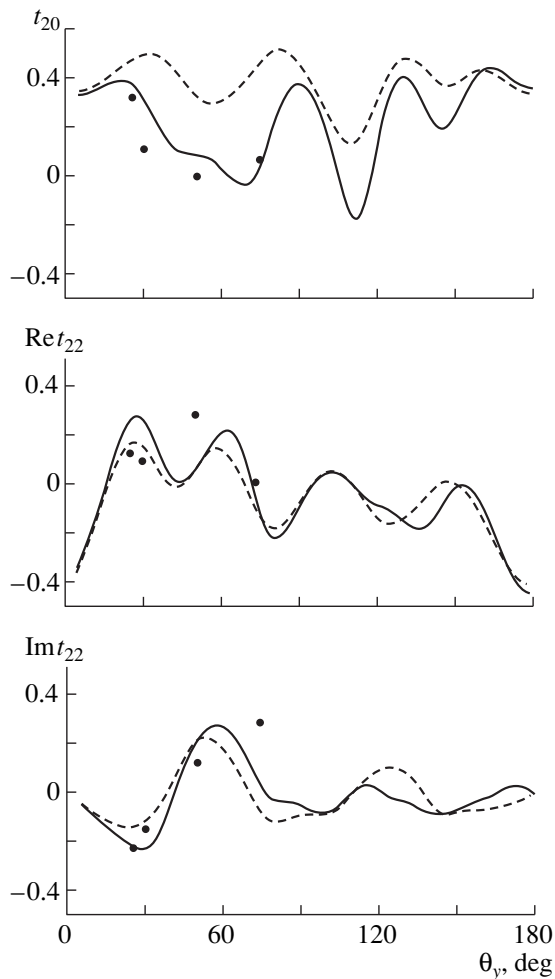
Fig. 4. Spin–tensor components t_{kq} of the density matrix for a ^{6}Li* nucleus at $k = 2$ (solid curve) with and (dashed curve) without allowance for spin–orbit interaction. Points represent experimental data from [3].

the introduction of the core is equivalent to discarding the first four partial waves in the expansion of the distorted wave in the input channel. A constraint on the internal interaction region in the output channel is insignificant, which is probably associated with the a low energy of the emitted alpha particles in the c.m. frame.

We have also investigated the effect of spin–orbit interaction on the spin properties of the final nucleus. According to the calculations, the inclusion of the spin–orbit interaction has virtually no effect on the differential cross section for the reaction (thin curve in Fig. 1). At the same time, the shapes of the spin–tensor components t_{kq} at $k = 2, 4$ calculated with and without allowing for spin–orbit interaction differ significantly (see Figs. 4 and 5 for $k = 2$ and 4, respectively). For experimental spin–tensor components to be described correctly, it is necessary to introduce a spin–orbit potential, especially for $k = 4$.

5. CONCLUSION

For the first time, all nine components of the spin density matrix for a ^{6}Li* nucleus that have been reconstructed on the basis of the measured particle–particle angular-correlation function have been described satisfactorily within a consistent theoretical model. The calculations have revealed that triton stripping (alpha-particle exchange) is the dominant reaction mechanism in the forward (backward) hemisphere. These mechanisms correspond to the reaction schemes

$$p + {}^9\text{Be} = p + (\alpha + {}^5\text{He}) = \alpha + (p + {}^5\text{He}) = \alpha + {}^6\text{Li*},$$

$$p + {}^9\text{Be} = p + (t + {}^6\text{Li}) = (p + t) + {}^6\text{Li} = \alpha + {}^6\text{Li*}.$$
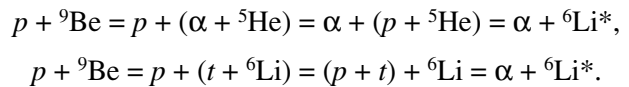
The calculation of the polarization tensors has confirmed the validity of these model schemes, which take
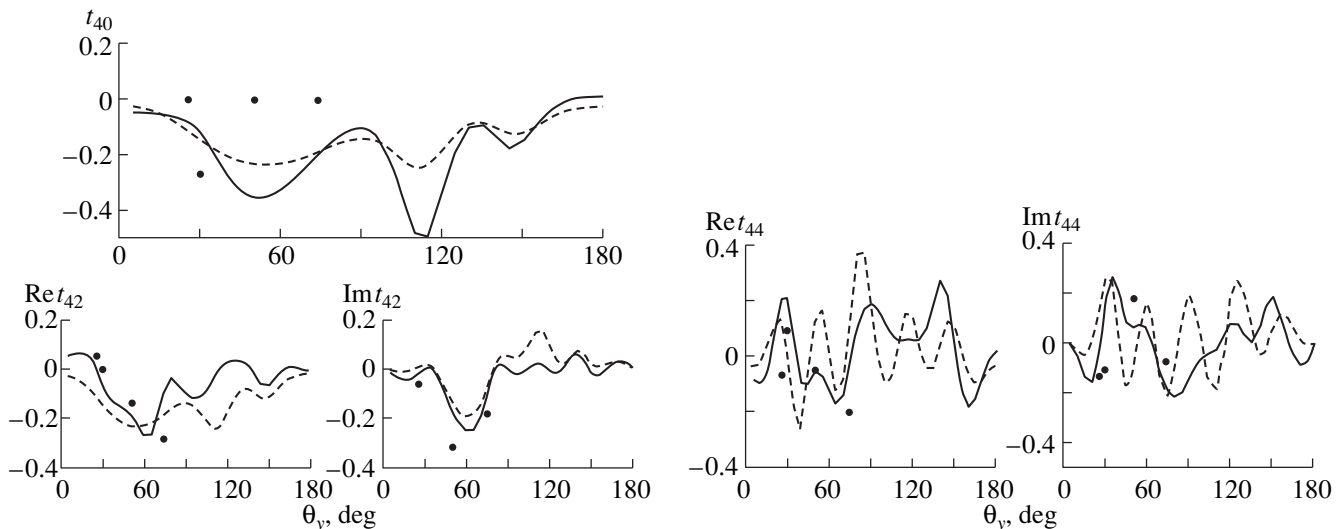
Fig. 5. Spin–tensor components t_{kq} of the density matrix for a ^{6}Li* nucleus at $k = 4$ (solid curve) with and (dashed curve) without allowance for spin–orbit interaction. Points represent experimental data from [3].

into account the fact that the input and the output channel are not equivalent in the kinetic energies of the proton and the alpha particle in the c.m. frame. It is because of this nonequivalence that the interaction in the input channel is peripheral, so that it becomes necessary to introduce a soft core of radius about 1 fm. The calculations have confirmed that the proposed model approach to analyzing polarization tensors is quite viable: it has provided quite a satisfactory description of all nine spin–tensor components $t_{kq}(\theta_y)$, including $t_{00}(\theta_y)$—the differential cross section for the reaction—without additional absolute normalization. This in turn has enabled us to refine the parameters of the interaction potentials and to confirm a correct determination of the structural factors for various clusters in the virtual decay vertices for the relevant nuclei.

ACKNOWLEDGMENTS

REFERENCES

1. N. S. Zelenskaya and I. B. Teplov, Nucl. Phys. A **406**, 306 (1983); *Features of Excited Nuclear States and Angular Correlations in Nuclear Reactions* (Énergoatomizdat, Moscow, 1995); T. L. Belyaeva and N. S. Zelenskaya, Fiz. Élem. Chastits At. Yadra **29**, 261 (1998) [Phys. Part. Nucl. **29**, 107 (1998)].

2. V. M. Lebedev, N. V. Orlova, and A. V. Spassky, Yad. Fiz. **61**, 1604 (1998) [Phys. At. Nucl. **61**, 1493 (1998)].

3. T. L. Belyaeva, N. S. Zelenskaya, W. R. Falk, *et al.*, Nucl. Phys. A **624**, 370 (1997).

4. K. Blum, *Density Matrix Theory and Its Applications* (Plenum, New York, 1981; Mir, Moscow, 1983).

5. L. I. Galanina and N. S. Zelenskaya, Yad. Fiz. **61**, 2188 (1998) [Phys. At. Nucl. **61**, 2077 (1998)].

6. T. L. Belyaeva, N. S. Zelenskaya, *et al*., *OLYMP Code for Calculating Cross Sections for Reactions Involving Complex Particles by the Distorted-Wave Method for Finite-Range-Interaction Forces* (Mosk. Gos. Univ., Moscow, 1981).

7. L. D. Landau and E. M. Lifshitz, *Quantum Mechanics: Non-Relativistic Theory* (Pergamon, Oxford, 1977, 3rd ed.; Nauka, Moscow, 1989, 4th ed.).

Translated by M. Kobrinsky

Cosmic Rays of Energies in the Range 10^3–10^5 TeV and Higher

S. I. Nikolsky and V. A. Romachin

Lebedev Institute of Physics, Russian Academy of Sciences, Leninskiĭ pr. 53, Moscow, 117924 Russia
Received August 13, 1999; in final form, December 21, 1999

Abstract—Over a period of more than 30 years, the knee in the spectrum of extensive air showers (EAS) generated by cosmic radiation has been explained in two ways: as a consequence of a cusp in the energy spectrum of primary cosmic rays or as a consequence of a change undergone by the process of multiparticle hadron production in the interactions of primary protons with nuclei of air atoms. Investigations at the Tien Shan EAS array confirm a change in the properties of showers generated by protons near the upper boundary of the atmosphere and evince the invariability of the energy spectrum of protons in the energy range 10^3–10^5 TeV. © *2000 MAIK "Nauka/Interperiodica".*

1. INTRODUCTION

Results obtained from investigations into the physics of cosmic rays with energies in excess of 10^3 TeV are often very uncertain. By way of example, we indicate that conclusions concerning the energy spectrum and the composition of primary cosmic rays at energies higher than 10^4 TeV depend explicitly and implicitly on the assumptions about multiparticle hadron production in the collisions of cosmic-ray protons and nuclei with nuclei of air atoms and about the subsequent development of hadronic cascades in the Earth's atmosphere, since information about multiparticle hadron production in nucleon–nucleon collisions at accelerators and colliders was obtained at incident-proton energies not higher than some 2×10^3 TeV. Experimental data from accelerators for hadron–nucleus and nucleus–nucleus collisions correspond to still lower energies. Measurement of parameters characterizing multiparticle production processes in primary cosmic rays is complicated by an a priori uncertainty in the energy of the primary particle and by a low intensity of high-energy primary particles: the flux of particles with energies in excess of 10^3 TeV is about 2.5×10^{-3} m^{-2} h^{-1} sr^{-1}.

That experimental studies of cosmic rays in the "superaccelerator" energy region are heavily dependent on the adopted conventions stems from a virtually unavoidable interplay of two aspects in one experiment: astrophysical investigations of ultrahigh-energy cosmic rays and analysis of the properties of inelastic hadron–hadron collisions in this energy region. This inevitably leads to quite arbitrary extrapolations of theoretical models to energies in excess of some 2×10^3 TeV (in the rest frame of the target proton), below which experiments validating these models were performed.

The disregard of the fact that results on cosmic rays and their properties at ultrahigh energies are heavily affected by the adopted conventions sometimes leads to mutually excluding conclusions from the same experi-

ment. Figure 1 shows data on the altitude of the maximum of the development of an electron–photon cascade for extensive air showers (EAS) of various energies according to the interpretation where it is assumed that cosmic rays change their composition with increasing energy of primary particles [1]. By comparing data with the results of calculations based on extrapolating the model of hadron interactions to the energy range 10^{12}–10^{15} eV, the altitude of the maximum of EAS development in the primary-energy interval 10^5–3×10^5 TeV and its increase at energies in the range 3×10^5–10^7 TeV were treated as phenomena associated with the predominance of heavy nuclei in the total flux of primary cosmic radiation at an energy of about 10^5 TeV and as a decrease in the fraction of heavy
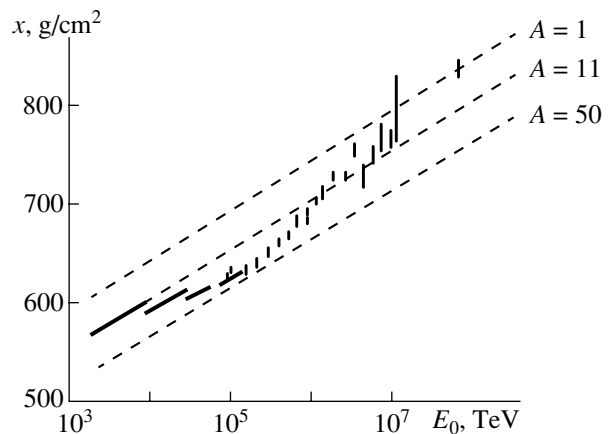
Fig. 1. Mean altitude of the maximum of EAS development according to observations of ionization luminosity of the atmosphere: (vertical dashes) experimental data and (dashed lines) calculated altitude for the cases of primary protons and nuclei containing 11 or 50 nucleons [1]. Thick inclined dashes represent the expected mean altitude of the maximum according to our calculations under the assumption of the enhanced multiplicity of secondary hadrons.
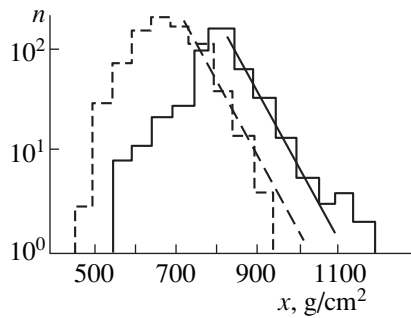
Fig. 2. Distribution of altitudes of the maxima of EAS development according to data of the spatial distribution of Cherenkov light for showers corresponding to the primary energies of (dashed line) $E_0 = 5 \times 10^5$ TeV and (solid line) $E_0 \simeq 5 \times 10^6$ TeV.
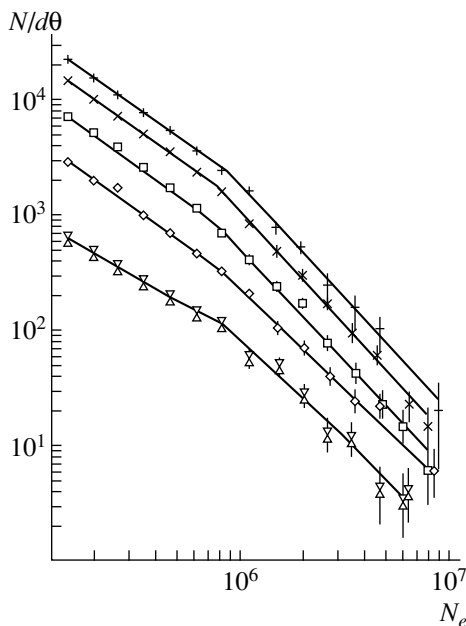

Fig. 3. Integrated spectra of EASs with respect to the number of electrons in a shower at an altitude of 3330 m above sea level according to observations in various zenith-angle intervals corresponding to the atmosphere depths of 724, 770, 850, 990, and 1220 g/cm² (from top to bottom).

correspond to the effective cross section of $\sigma \simeq 0.33 \times 10^{-24}$ cm^{-2} for inelastic collisions of protons with nuclei of air atoms. That this estimate proved to be feasible implies that, in the energy range 10^5–10^6 TeV, protons constitute a considerable fraction of the total flux of primary cosmic rays and that the conclusion of Bird *et al.* [1] that the fraction of protons in cosmic rays of energies 10^{17}–3×10^{17} eV is small only highlights inapplicability of the extrapolation from accelerator energies to much higher energies that was used in [1] to obtain theoretical results compared there with the observed mean altitude of the maximum of the development of the electron–photon shower component in order to assess the above fraction of protons.

The knee in the spectrum of EASs with respect to the number of electrons [3] at an electron flux of 5×10^5–10^6 in a shower was interpreted by the majority of researchers as an effect that is due to a change in the energy spectrum of primary cosmic radiation. This explanation was suggested by limitations existent in some hypotheses concerning the acceleration and confinement of cosmic rays in the Milky Way Galaxy. From the results of observations at the EAS array of the Tien Shan station of the Lebedev Institute of Physics, it follows, however, that the position of the knee in the spectrum of EASs with respect to the number of electrons is independent of the zenith angle of the observed EASs and, hence, on the depth of the atmosphere (see Fig. 3) and that the exponent of the spectrum in question changes quite sharply rather than gradually. It is obvious that these conclusions can hardly be reconciled with the multicomponent composition of cosmic radiation, as well as with a random character of its acceleration and propagation. The question of whether models capable of describing multiparticle hadron production in inelastic nucleon–nucleus collisions at energies studied in accelerator experiments can be extrapolated to the region where incident nucleons have energies above 10^4 TeV must be verified, especially as a change in the process of multiparticle hadron production near the quoted energy may be the reason behind the observed knee at $N_e \simeq 10^6$ in the spectrum of EASs with respect to the number of electrons at an invariable energy spectrum of primary cosmic rays.

nuclei when the primary energy increases up to 10^7 TeV. It is worth noting, however, that, on the basis of data from the same experiment on the distribution of the altitudes of the maximum of shower development, the range for inelastic collisions of primary protons with nuclei of air atoms at energies above 10^5 TeV could be estimated at about 60 g/cm². Such an analysis is possible only if a considerable number of protons is present in primary cosmic rays, as can be seen from Fig. 2, which illustrates experimental investigations of EASs generated by cosmic rays of energies in the range 10^{17}–10^{19} eV [2]. The distributions of the altitudes of the maxima of EAS development for two energy intervals show similar shapes of their right-hand sections and

2. EXPERIMENTAL INVESTIGATIONS OF EXTENSIVE ATMOSPHERIC SHOWERS AT THE TIEN SHAN STATION OF THE LEBEDEV INSTITUTE OF PHYSICS

Observation of extensive air showers representing hadron–lepton cascades that are generated by protons and nuclei of primary cosmic radiation and which traverse the atmosphere, forming a wide flux of photons, electrons, and muons, appears to be a basic means for studying cosmic rays of energies above 10^3 TeV. A wide lateral distribution of the electrons and muons of a shower around its core makes it possible to study EASs quite efficiently with an array of spatially spaced

charged-particle detectors. The results of such experiments aimed at probing the generation and development of hadronic and electron–photon cascades in the atmosphere form a basis for an analysis of data and their subsequent comparison with the results of calculations relying on models chosen to simulate these cascade processes.

Over a period of more than 30 years, EASs generated by primary particles of energies 10^2–10^5 TeV have been studied at the high-altitude station of the Lebedev Institute of Physics [4, 5]. An important feature peculiar to these experiments was that the measurements of basic parameters of EASs were combined there with a consistent step-by-step analysis of experimental data from known to unknown facts. The spectrum of EASs with respect to the number of electrons at various observation levels is the first and, presently, the main source of experimental information about the energy spectrum of primary cosmic radiation in the energy region above 10^3 TeV. Accordingly, the total number of electrons in a shower at the observation level was a reference parameter in an analysis of measurements associated with the energy of primary particles and their origin. All data on the composition of showers and on the properties of various EAS components were rescaled to a specific interval of showers with respect to the number of electrons, N_e. If, instead of N_e, the reports on the Tien Shan series of experiments quote the primary energy E_0 without indicating the relation between E_0 and N_e, the rescaling is performed according to the standard relation $E_0 = 4.7 \times 10^{-3} N_e^{0.926}$ TeV, which takes account neither of various model concepts of shower formation and evolution nor of possible changes in the nuclear composition of primary cosmic radiation, which is accessible to experiments beyond the atmosphere only in the energy range 1–10^3 TeV. From the results of the observations (see below), it follows that the use of the above relation leads to an underestimation of the primary-particle energy in the region of ultrahigh energies, since the model of inelastic hadron collisions that is based on investigations performed at energies below 10^3 TeV cannot be extrapolated to energies in excess of 10^4 TeV.

A transition from known to unknown facts in analyzing experimental data on cosmic rays is accomplished side by side with accumulation of relevant statistics; if changes in the parameters of a shower cease to be monotonic at some number of electrons in a shower and, hence, at some primary energy and if there are no violations of monotonicity of variations in primary cosmic radiation, this effect, if it has been established reliably, suggests some variations in the features of inelastic collisions between primary protons and nuclei of air atoms, since the subsequent development of the cascade includes only processes observed at lower energies of primary particles. The abruptness of any variations (such as that which is observed in the

spectrum of EASs with respect to the number of electrons) would indicate that the hypothesis of changes in the character of shower production and subsequent shower evolution is more probable than the hypothesis of changes in the composition of primary cosmic radiation, since the latter changes are averaged over various regions of its acceleration and are smeared by a diffuse propagation in intergalactic space. No effect of the position of the Solar System in the Milky Way Galaxy on the observed isotropy of high-energy primary cosmic rays has been revealed so far.

Figure 4 shows the layout of the array featuring ionization calorimeters used as a spectrometer for the flux of energy in the central part of a shower and for the energy of local cascades formed in the lead of the calorimeter [5]. Included in the basic analysis of experimental data were showers that traversed a 12×12 m^2 square above the ionization calorimeter. The zenith and azimuthal coordinates of the shower axes were determined from the relative delays in scintillation detectors arranged crosswise at distances of 20 m from the array center. The error with which this system measured zenith angles was less than 7° and was due to instrumental factors and to the smearing of the depth of the shower front.

The energy carried by the fluxes of high-energy hadrons, electrons, and photons was determined with the aid of an ionization calorimeter featuring a lead absorber. The total calorimeter area of 36 m^2 was sectioned by ionization chambers with a 300×25 cm^2 area of individual detection channels. In order to reduce the cell of the spatial calorimeter resolution, the ionization chambers in neighboring rows were arranged to be orthogonal to one another. Accordingly, individual electron–photon cascades could be resolved in the structure of EAS cores only if the distances between individual cascades were not less than 50 cm [6]. In analyzing the entire body of experimental data on EAS cores, the energy of the shower core was determined as the flux of energy as measured over the whole calorimeter area, provided that the shower axis traversed the calorimeter at a distance from its side faces that is not less than 1m. Our analysis of the experimental data and a simulation of the experiment revealed that, under this condition, the total energy in shower cores did not depend on the place where a shower traversed the calorimeter.

That use was made of the total energy of electrons and hadrons that was carried by a shower through the whole calorimeter area when it was possible to resolve individual cascades separated by a distance of 50 cm might seem an unreasonable roughening of experimental data. It should be borne in mind, however, that, in the problem at hand, the characteristics of the generation of hadron–lepton cascades by protons and nuclei of cosmic rays with energies not yet studied at accelerators were analyzed on the basis of data taken in the lower atmosphere; for this, in turn, it was important to
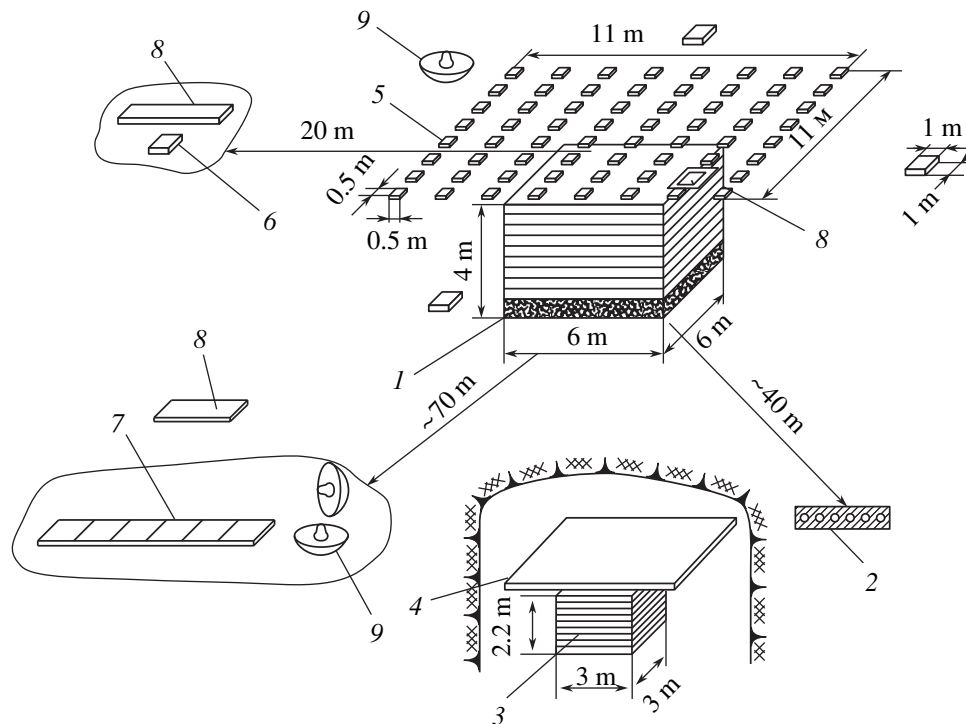
Fig. 4. Central part of the array for experimentally studying EASs at the high-altitude Tien Shan scientific station of the Lebedev Institute of Physics (1965–1986): (*1*) ionization calorimeter, (*2*) neutron monitor, (*3*) ionization calorimeter at a depth of 11 m in rock, (*4*) hodoscopic counters, (*5*) scintillation detectors of area 0.25 m^2 each, (*6*) scintillation detectors capable of measuring the relative time of signal passage in four detectors arranged crosswise at a distance of 20 m from the array center, (*7*) scintillation detectors of total area 12 m^2, (*8*) hodoscope of gas-discharge counters, and (*9*) detectors of Cherenkov light in the atmosphere.

know the energy balance between the energy lost by a shower in the atmosphere and the total energy of high-energy particles in the central region of the shower without recourse to any ad hoc assumptions on the parameters of primary events of cascade generation, including the assumption that the transverse momenta of secondary hadrons may depend on the energy of colliding particles.

In order to measure the energies of individual particles with the highest energy in a shower, the ionization calorimeter was equipped with an x-ray-emulsion chamber having a spatial resolution of about 0.1 mm for cascades characterized by energies in excess of 1 TeV and generated in the lead layer above the x-ray film used. In order to compare photographic data that have been accumulated, over a long time, in the form of spots having various degrees of darkening with relevant data in the ionization chamber that were recorded in real time, one of the two adjacent films was displaced at regular intervals. Because of flaws in the construction of the system ensuring such displacements of one of the films with respect to the other, observations with this chamber lasted for a short period of time, so that the results were of an episodic character [7].

The Hadron experiment [8] that commenced in 1987 differed from the experiment with the ionization calorimeter in that the calorimeter of area 36 m^2 was replaced by an x-ray-emulsion chamber of area 160 m^2. In addition, the arrangement of scintillation detectors that measured the electron flux density in EASs was changed, whereby the area over which the shower core could be sought with an error not greater than 1 m was considerably increased.

When a family of photons with energy in excess of 2 TeV was identified with the symmetry axis of the shower whose coordinates correspond to the symmetry axis of this family, the x-ray-emulsion chamber made it possible to obtain the energy spectrum of electrons and photons in EAS cores with a known number of electrons in a shower at the observation level and, hence, with a known primary-particle energy. In Fig. 5, the relative energy of electron and photon families, E_γ/E_0, in the cores of EASs whose primary energies are estimated at $E_0 = 4.7 \times 10^{-3} N_e^{0.926}$ TeV by using the numbers of electrons, N_e, is plotted along the abscissa. That attempts at finding cases where the energy spectra of electrons and photons from the cores of showers generated by primary particles whose energies exceeded 1.8×10^4 TeV would be similar to the spectra observed in showers generated by protons of primary energies not greater than 10^4 TeV proved to be futile confirmed that, at proton energies higher than 10^4 TeV, the model of quark–gluon strings or any other model for multiparti-

cle hadron generation in inelastic nucleon–nucleon collisions is inapplicable if the energy spectrum of secondary hadrons involves particles of energies comparable with the primary-particle energy [8, 9].

Owing to an increase in the area over which it was possible to determine the coordinates of the shower axis to within 1 m and to estimate the age parameter S for each observed shower,[1] the spectrum of EASs with respect to the number of electrons could be obtained in the range from 10^6 to 3×10^9 electrons in a shower at the observation level [10]. As a result, it was found that the exponent of the spectrum decreases by $\Delta\kappa = 0.2$–0.3, which complies with the inverse knee discovered much earlier by an experimental group headed by Khristiansen [11].

The methodological facet of the observation of EASs that have not yet reached the maximum of their development depends on the accuracy to which the EAS core is determined. The shower-age parameter $S < 1$ can be determined on the basis of the relationship between the electron-flux densities at distances from the axis in the range 20–40 m, on one hand, and 2–4 m (or 80–150 m), on the other hand. In the first case, the error in determining the shower axis must be less than 2–4 m. This is equivalent to positioning the detectors at distances of 4–8 m from one another over the area where the experiment seeks the points of arrival of the showers under analysis. In the second case, the requirements on the accuracy in determining the shower axis can be considerably relaxed, but the area of the detectors deployed for measuring the electron-flux density at distances of 80–150 m from the shower axis must ensure a high accuracy in measuring the electron-flux density, so that it is necessary to have a large total area of scintillation detectors (more than 100 m²).

The aforementioned array for studying EAS spectra [4, 5, 8] met the first of these requirements. A method that determines the number of electrons in a shower with the aid of equipment not ensuring sufficient accuracy in locating the shower axis may underestimate the electron flux in those showers for which the electron–photon cascade has not yet reached the maximum of its development; if the number of such showers is small, they can be lost completely. In Fig. 6, the data from the Hadron experiment [10] for the spectrum of EASs with respect to the number of electrons, N_e, are displayed along with the results obtained experimentally in [12] by separating the total N_e spectrum into groups of showers characterized by various values of the parameter S. As can be seen from this figure, the inverse knee appears to be a continuation of the spectrum of young showers (those for which $S \leq 0.75$). For a long time, no experiment that employed widely spaced detectors of electron-flux densities in showers could observe the
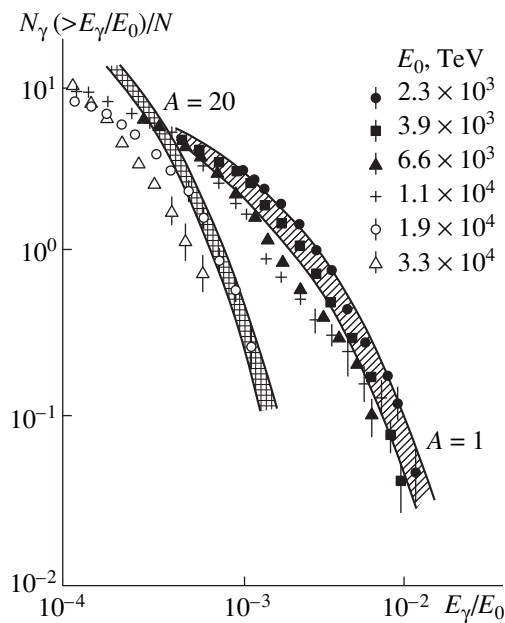
Fig. 5. Integrated energy spectra of electrons and photons in the cores of showers corresponding to the primary energy E_0 (N stands for the number of showers subjected to analysis in the corresponding group of E_0 values; the notation for these is given in the right upper corner of the figure). Shaded bands represent the results of the calculations for primary protons and primary nuclei containing 20 nucleons.
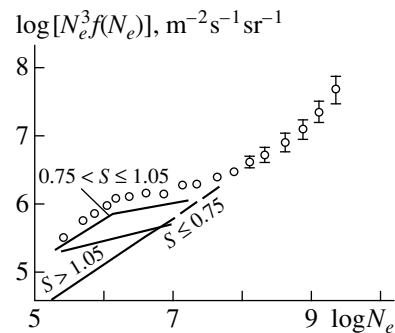

Fig. 6. Differential spectrum of EAS (open circles) from [9] (the ordinates of the spectrum are multiplied by the factor N_e^3 corresponding to the abscissa, N_e being the number of electrons in a shower). Solid lines represent the result obtained by decomposing the total spectrum of EASs in the interval $N_e = 2 \times 10^5$–2×10^7 into three components corresponding to showers generated predominantly by primary nuclei in the upper atmosphere ($S > 1.05$), showers generated by protons in the depth of the atmosphere ($S \leq 0.75$), and the most numerous showers generated by primary protons and helium nuclei in the upper atmosphere (at a depth less than 200 g/cm²).

above inverse knee in the spectrum of EASs with respect to the number of electrons (Fig. 6). In the region of primary-particle energies around 10^7 TeV, where the fraction of young showers in the total flux may be as large as 90%, such showers cannot be lost completely, which leads to a decrease in the observed exponent of
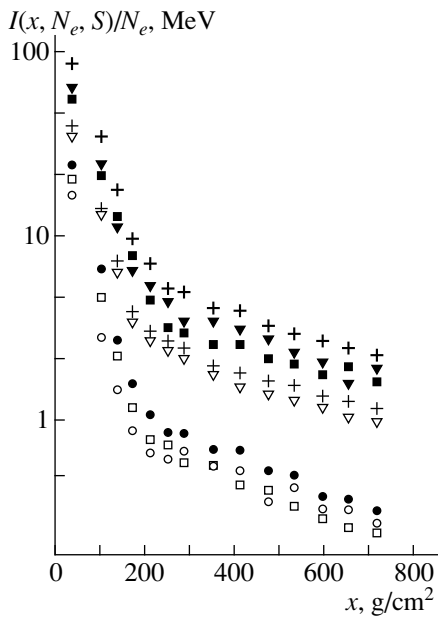
$I(x, N_e, S)/N_e$, MeV

Fig. 7. Absorption of the electron–photon and hadronic components of the EAS cores in the lead of ionization calorimeter. The data are presented for (closed symbols) $S > \bar{S}$ and (open symbols) $S < \bar{S}$ at various numbers of electrons in a shower: (+, +) $(1–3) \times 10^5$, (▼, ▽) $(3–10) \times 10^5$, (■, □) $(1–3) \times 10^6$, and (●, ○) $(3–10) \times 10^6$.

the spectrum of EASs with respect to the number of electrons at energies not higher than 10^7 TeV.

3. FLUX OF ENERGY CARRIED BY THE HADRON COMPONENT OF THE EAS CORE

In Fig. 7, experimental data on the cascade curves for electron absorption in lead are shown for the case where the EAS cores traverse the ionization calorimeter of area 36 m² in such a way that the showers are separated from the nearest calorimeter face by a distance not less than 1 m [13]. Extensive atmospheric showers subjected to analysis were grouped according to the number of electrons in a shower at the observation level and according to the age-parameter values, for which two cases are considered: $S < \bar{S}$ and $S > \bar{S}$, where $\bar{S}$ is mean number of the parameter S for a shower group specified by a given number of electrons. Grouping EASs according to the age parameter singles out showers generated by protons in the depth of the atmosphere ($S < \bar{S}$) and showers generated predominantly by nuclei (in the interval of primary-particle energies that was studied with the aid of the ionization calorimeter, no more than one-half of showers from this group that were subjected to analysis are due to primary protons).

What stands out above all in the data displayed in Fig. 7 is that the flux of energy in showers generated by

protons is different from that in $S > \bar{S}$ showers, whose major fraction is generated by primary nuclei. For the number of electrons in a shower below 10^6, the hadronic component of the latter[2] carries energy one-half as large as that concentrated in the hadronic component of EASs generated by primary protons ($S < \bar{S}$). This distinction is quite consistent with the distinction between showers that are generated by nuclei in the upper atmosphere and which are roughly averaged in their further development over the number of nucleons in nuclei and showers generated by protons, in which case energy can be transported into the depth of the atmosphere both by primary protons directly and by hadrons leading in the energy spectrum of secondary hadrons. It should be noted that such large fluctuations of the energy flux in shower cores are also obtained from a calculation relying on a standard model and taking into account a complex composition of primary cosmic radiation. Kalmykov *et al.* [14] calculated the fluctuations of the flux of energy carried by hadrons within 3.5 m from the shower core. It is worth noting that the above twofold distinction between the energy fluxes in EAS cores, which was observed in the calorimeter upon breaking down the total flux of showers with a given number N_e of electrons into the $S < \bar{S}$ and the $S > \bar{S}$ group, is quite consistent with the distribution obtained by those authors. As a development of the calculations performed in [14], it would be of interest to clarify the question of what nuclear composition of primary cosmic radiation or what change in the multiparticle-generation event must be assumed in the calculation in order to describe the experiment under discussion, which recorded a fivefold decrease in the energy flux in the cores of $N_e \simeq 6 \times 10^6$ EASs that was normalized to the number of electrons, and to obtain simultaneously the absence of above-type distinctions for $S < \bar{S}$ and $S > \bar{S}$ in $N_e \geq 6 \times 10^6$ showers (see Fig. 7).

It should be emphasized that the same experiment recorded a knee in the EAS spectrum at $N_e \simeq 10^6$ and a sharp decrease in the energy in EAS cores for $N_e > 5 \times 10^6$. If we had adopted the popular explanation of the knee in the spectrum of EASs with respect to the number of electrons as a phenomenon that is due to a change in the exponent of the energy spectrum of primary protons, the cusp in the spectrum of hadrons and of the electron–photon component of the EAS core would have had the same position as the knee in the spectrum of EASs with respect to the number of electrons, the more so at the same array and in the same series of measurements. That the number of electrons in a shower at the point where the knee appears in the

---

[2] Here, we discuss the hadronic shower component, despite the fact that no difference can be seen in Fig. 7 between the hadronic and the electron–photon component in what is concerned with their dependences on the number of electrons in a shower or on the parameter S.

EAS spectrum differs from that at the point where the energy flux in EAS cores decreases sharply by a factor of 4 to 6 can be associated with the same factor if we assume that, at primary-proton energies not less than 5×10^3 TeV, the multiplicity of secondary hadrons increases sharply in the first events of multiparticle generation process owing to disappearance of secondary hadrons from the spectrum that have energies commensurate with the energy of primary protons. An increase in the multiplicity leads to the enhanced development of EASs in the upper atmosphere upon the first interactions and, accordingly, to a considerable decrease in the number of electrons, as is indeed observed in such showers in the lower atmosphere. Concurrently, fluctuations of the flux of energy carried by such showers to the depth of the atmosphere are reduced significantly with the result that they become similar to levels generated by primary nuclei.

With the aim of confirming the interpretation of calorimetric measurements and to extend them with special emphasis on finer details, the energy spectrum of electrons and photons near the EAS axis was investigated with the aid of an x-ray-emulsion chamber of area 160 m^2 [8, 9]. Experimental data on the relative energies of electrons and photons in EAS showers with respect to the energy of primary particles that have generated a given shower are displayed in Fig. 5, along with the results of calculations relying on the model describing the development of EASs in accordance with data from accelerator studies and on an extrapolation of this model to the region of cosmic-ray energies. The experimental data coming from x-ray-emulsion chambers were subjected to the conditions requiring that the x-ray film show at least one electron or photon (dark spot) with energy $E_\gamma \geq 2$ TeV and that the total energy of the family of such spots not be less than 10 TeV. These conditions made it possible to obtain unambiguous results in establishing correspondence between an EAS observed in real time with specific spatial coordinates of the shower axis and one of numerous families of dark spots accumulated in the x-ray-emulsion chamber over a one-year exposure. Shaded bands in Fig. 5 represent the expected energy spectra of electrons and photons for primary radiation containing 70% protons and 30% helium nuclei and for the case where protons generate EASs whose development in the atmosphere is similar to the development of showers induced by 20-nucleon nuclei (double shading). The calculations were performed under the assumption that secondary particles from inelastic hadron–nucleus collisions have scale-invariant energy spectra.

By imposing specific selections on showers containing high-energy electrons and photons, an attempt was made in the more recent analysis reported in [15] to find EASs where the number of electrons was not less than 10^7 and where the energy spectra of secondary hadrons were similar to those in showers that involved not more than 10^6 electrons and which were generated by primary protons. These selections singled out showers

where the total energy of electrons and photons in the core was higher than the mean energy for the group of showers under analysis and where the energy of one of the electrons or of one of the photons in the shower core exceeded $8 \times 10^{-4} E_0$. Each of these two conditions separated almost independently about one-half of all showers analyzed in this way. About 23% of all showers that correspond to primary energies $E_0 \geq 2 \times 10^4$ TeV and which were recorded experimentally satisfy the two conditions simultaneously. This value is smaller than the fraction of primary-proton-induced showers that is expected in the case that would have been realized if the knee in the spectrum of EASs with respect to the number of electrons had been due to the cusp in the primary energy spectrum of cosmic rays at a magnetic rigidity of about 5×10^3 TeV. These showers were similar, in energy spectrum of electrons and photons, to showers generated by helium nuclei and corresponded to their fraction in the primary flux of cosmic rays that does not contain any protons for one reason or another. Thus, it can be concluded that, if we do not assume sharp, threshold, changes in the multiplicities and energy spectra of secondary hadrons from multiparticle-production events, searches for cases where showers having primary energies not less than 5×10^3 TeV are generated by primary protons in events characterized by an energy spectrum of secondary hadrons that is similar to the spectra observed at lower energies have given a negative result. The statistical significance of the experiment admits not more than 5% showers that are generated by protons of energies not less than 10^4 TeV in inelastic collisions and which correspond to models extrapolating accelerator data on multiparticle hadron production in inelastic hadron–nucleus collisions.

To conclude the exposition of the results obtained by studying the fluxes of energies carried the electron–photon and the hadronic component in the shower cores, we would like to highlight once again the basic conclusion drawn from these measurements: the knee in the spectrum of EASs with respect to the number of electrons and an approximately fivefold decrease in the flux of energy in the EAS cores occur at substantially different values of the number of electrons in a shower in the same experiment ($N_e \simeq 10^6$ and $N_e > 4 \times 10^6$, respectively). Moreover, measurements with an x-ray-emulsion chamber confirmed that the energies of electrons and photons in the EASs cores decrease considerably at $N_e \geq 4 \times 10^6$. Not only do all these observations indicate that the features of multiparticle-hadron-generation events change substantially at the c.m. energy of colliding nucleons about 6 TeV, but they also suggests that the relationship between the energy of primary protons for $E_0 > 10^{16}$ eV and the number of electrons in the showers observed in the lower part of the atmosphere undergoes significant changes (by a factor of 4 to 6).

4. INVESTIGATION OF THE KNEE IN THE SPECTRUM OF EXTENSIVE AIR SHOWERS

That the set of EASs having primary energies in excess of 10^4 TeV (this value corresponds to a reduction of energy in the EAS cores if rescaling from the number of electrons in a shower to the mean energy of primary particles is performed in a conventional way) features no showers such that the energy spectra of electrons and photons in their cores would confirm their generation by primary protons is reflected in the development and absorption of the above-type showers in the atmosphere. In the preceding section, it has already been noted that the absence of such protonic showers in the depth of the atmosphere does not inevitably mean that there are no protons in the composition of primary cosmic radiation. On the basis of the properties exhibited by showers in the lower part of the atmosphere, it is hardly possible to distinguish between the generation of a six to ten times as great number of secondary hadrons by a proton in a first inelastic collision with an air atom and interactions of lithium or beryllium nuclei of the same energy; this is so almost always, with the exception of rare, albeit statistically significant, cases in which primary protons penetrate the atmosphere to a depth greater than 200 g/cm^2.

The development of a shower toward the observation level is characterized by the cascade parameter S. In the electron–photon cascade, this parameter relates the spatial distribution and the energy spectrum of electrons and photons in a shower at the observation level to the amount of matter traversed by this shower in the atmosphere. The hadronic cascade, which appears to be a source of energy, is coupled to the electron–photon cascade by the total flux of energy transferred to the electron–photon component of the shower. If the transverse momenta of product hadrons are bounded, as is the case in inelastic collisions up to c.m. energies of colliding nucleons about 10^3 TeV, the production of neutral pions is concentrated near the EAS core. Upon the formation of a shower, the role of the hadronic EAS component reduces to additionally supplying energy to the electron–photon cascade in the depth of the atmosphere, since the critical energies of the particles involved in the development of the electron–photon and the hadronic cascade differ by a factor greater than 300.

Another feature of EAS development in a medium where the range with respect to nucleon interactions is only about twice as great as the cascade length unit for the development of the electron–photon cascade is associated with the distinctions between the development and the absorption of the hadronic and of the electron–photon cascade. The hadronic cascade develops quickly, transferring more than 70% of primary energy to the electron–photon cascade up to the depth of its maximal development, this depth becoming greater with increasing primary-particle energy. This is followed by a delayed absorption of the electron–photon cascade as long as the cascade parameter S is less than
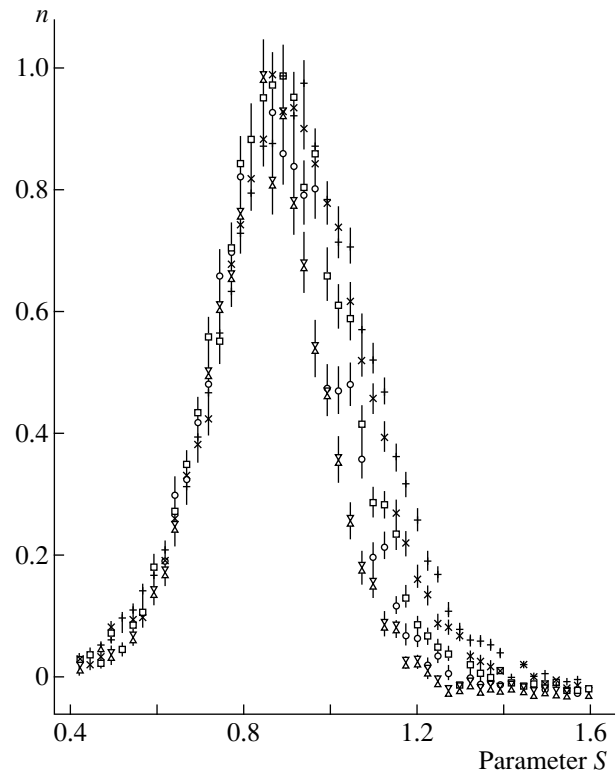
Fig. 8. Frequency of observation of EASs as a function of the parameter S for showers containing various numbers $\bar{N}_e$ of electrons: (+) 1.5×10^5, (×) 2.04×10^5, (□) 2.72×10^5, (○) 3.63×10^5, and ($\boxtimes$) 4.83×10^5.

1.3. Because of all the above, EASs generated by protons and those generated by nuclei develop and are absorbed quite differently.

At the EAS array of the high-altitude Tien Shan station [4], the parameter s was determined for showers whose axis traversed a square housing 64 scintillation shower-electron detectors uniformly arranged over its area. For each shower with an age parameter S determined in a conventional way, the lateral distribution of electrons up to distances of about 70 m could be found upon bounding, in this way, the location of the shower axis in the plane. The error in determining the age parameter was $\Delta S < 0.05$. Figure 8 illustrates the distributions with respect to the parameter S for EASs where the number of electrons at the observation level ranges between some 10^5 and 10^6. The distributions for the groups of EASs featuring different numbers of electrons were normalized by using the number of showers at the maximum of these distributions. As can be seen from the figure, the distributions are virtually coincident on the left of the maximum—that is, for $S < \bar{S}$—and are shifted with increasing number of electrons toward smaller values of S for $S \geq \bar{S}$.

Figure 9 displays the total spectrum of EASs with respect to the number of electrons and four components of this spectrum that correspond to shower groups characterized by different values of S [16]. Even at the highest primary energies quoted in Fig. 9, EASs corresponding to $S \leq 0.75$ must have been generated at a depth greater than 250 g/cm^2 in the atmosphere. Since only primary protons can reach this depth without undergoing interaction, the absence of a knee in the spectrum of EASs characterized by age-parameter values of $S \leq 0.75$ implies that, in the energy range 10^3–10^5 TeV, there is no cusp in the energy spectrum of primary protons.

All showers contributing to the knee at $N_e \simeq 10^6$ in the spectrum of EASs with respect to the number of electrons are concentrated in the EAS group corresponding to S values in the range 0.75–1.05. Showers belonging to this group have been generated predominantly by primary protons and partly by light nuclei in the upper part of the atmosphere at depths less than 250 g/cm^2. Up to $N_e \simeq 10^6$, the exponent of the spectrum of showers characterized by S values between 0.75 and 1.05 agrees, within the errors of its determination, with the exponent of the spectrum of showers that correspond to $S \leq 0.75$ and which have been generated by protons in the depth of the atmosphere. After the knee in the EAS spectrum at the number of electrons about 10^6, the spectrum of showers characterized by S values in the range $0.75 < S \leq 1.05$ appears to be close in exponent value to the spectrum of showers generated by primary nuclei in shower groups corresponding to $S > 1.05$. Thus, the knee in the EAS spectrum is associated with showers observed at the maximum of their development. Showers before the knee could be interpreted as EASs generated by protons. At a greater number of electrons, this group of levels is generated either by primary nuclei or by primary protons if showers generated by protons of energies in the region $E_0 \geq 5 \times 10^3$ TeV are similar to showers generated by nuclei heavier than helium nuclei. The difference in the generation and development of hadron–lepton cascades in the atmosphere that are induced by protons and by nuclei at cosmic-radiation energies E_0 below 10^4 TeV are due predominantly to lower energies of secondary hadrons in the second case and to an averaged development of the hadronic cascade because of primary-nucleus fragmentation in the first collision with nuclei of air atoms rather than to the distinction between the effective cross section for the first collision.

Showers observed after the maximum of their development in the interval $S = 1.05$–1.35, which were generated predominantly by nuclei, so that the development of their hadronic cascades has been averaged in the upper layers of the atmosphere, do not exhibit any features at $N_e \simeq 10^6$ in their spectra with respect to the number of electrons. There is a slight increase in exponent of the spectrum from $\kappa \leq 1.7$ to $\kappa \simeq 2.1$ in the interval of the numbers of electrons between 3×10^5 and 5×10^5. If this cusp is taken seriously, its position on the
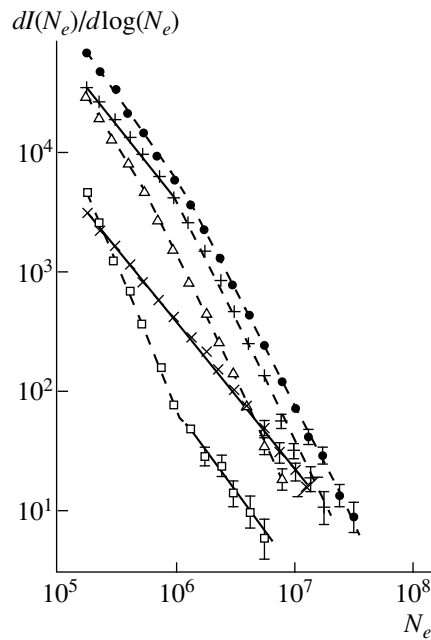

Fig. 9. (●) Total spectrum of EASs containing $N_e = 2 \times 10^5$– 3×10^7 electrons at the atmosphere depth of 760 g/cm^2 and four components of the spectrum that correspond to S values falling within the ranges (+) 0.75–1.05, (△) 1.05–1.35, (×) 0.35–0.75, and (□) 1.35–1.95.

scale of N_e can be attributed to a transition of showers generated by primary protons and helium nuclei from the above group to the group characterized by a smaller value of S.

Problems that arise in connection with the use of the age parameter S for analysis of experimental data on EASs were critically revisited in the theoretical study of Kalmykov *et al.* [14]. In particular, those authors showed that it is necessary to determine the parameter S to a high precision and that the flux of showers generated by primary nuclei depends on their energy and on this precision. An improvement of accuracy in determining the parameter S renders the dependence of an $S \geq 1.05$ EAS sample on the primary-particle energy more pronounced. A comparison of our experimental data with the results of the calculations from [14] validates the estimate of the accuracy in determining the parameter S in the experiment being discussed ($\Delta S \simeq 0.05$): the small fraction of the selected $S < 0.75$ EASs and the weak dependence of the $S < 0.75$ sample on the number of electrons in a shower are both consistent with the results of the theoretical simulation from [14]. Because of this weak dependence, the curves in the region $S < 1$ coincide in Fig. 8, provided that these curves are normalized to the same number of $S = 1$ showers; the shift in the right-hand section of the graph reflects the dependence of the $S > 1$ sample on the primary-particle energy.

The last and the smallest group of EASs in Fig. 9 contains $S > 1.35$ showers, whose integrated spectrum
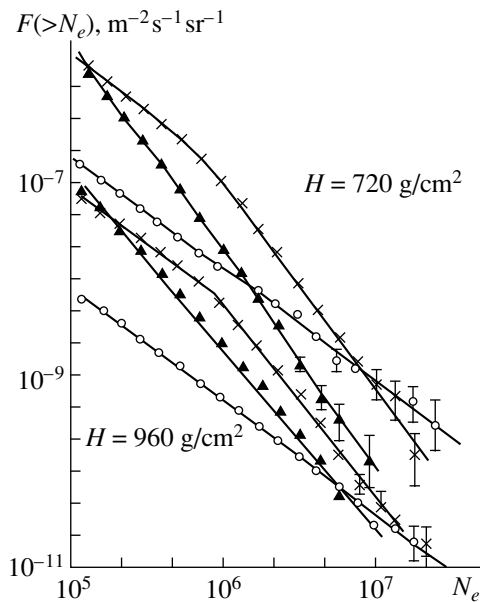
$F(>N_e)$, m^{-2}s^{-1}sr^{-1}

Fig. 10. Three components of the total flux of EASs involving N_e electrons at various values of the parameter S at the observation levels of 720 g/cm^2 ($\theta < 25°$) and 960 g/cm^2 ($\theta \geq 25°$): (○) $S \leq 0.75$, (×) $0.75 < S \leq 1.05$, and (▲) $S > 1.05$.

exhibits a cusp, where the exponent of the spectrum changes from $\kappa \simeq 2.3$ to a smaller value of $\kappa \simeq 1.2$. That the spectrum of $S > 1.35$ showers at greater values of N_e is similar in exponent of the spectrum with respect to the number of electrons in a shower and in absorption in the atmosphere to the spectrum of the group of showers generated by primary protons ($S < 0.75$) gives sufficient ground to treat the former as EASs generated by primary protons in events where the multiplicity of secondary hadrons in enhanced. A comparison of $S > 1.35$ and $S \leq 0.7$ EASs in the calculations weakly dependent on specific assumptions concerning changes in the parameters of the production event at primary-proton energies of about 10^4 TeV has revealed that, when the energy of primary protons increases from 8×10^3 to 1.5×10^4 TeV, we need at least a sixfold increase in the multiplicity of secondary protons or a considerable decrease in energy transferred to the electron–photon cascade in the first inelastic collisions of protons with nuclei of air atoms, because of decay processes featuring high momenta of product particles, including muons and neutrinos.

The viability of the above EAS classification in terms of the parameter S and the possibility of experimentally revealing showers generated by protons and nuclei of primary cosmic rays high above the observation level are confirmed by the analysis of the absorption of showers corresponding to different S values in comparing the spectral distributions of showers observed in different intervals of zenith angles, $\theta < 25°$ and $\theta \geq 25°$ (Fig. 10). Thus, the absorption of the electron flux is determined by considering the changes in the number of electrons in showers observed with the same frequency at the depths in the atmosphere of 720 and 960 g/cm^2.

For $S \leq 0.75$ showers, the range of electrons in the atmosphere with respect to absorption is $\lambda_a = 87 \pm 3$ g/cm^2, which does not of course imply the absorption of electrons in a developing shower ($S < 1$), but which rather corresponds to the absorption of protons in the atmosphere that generate these showers, their range being $\Lambda = 73 \pm 3$ g/cm^2. Not only does the difference of the ranges of 87 ± 3 and 73 ± 3 g/cm^2 reflect the observed spectrum of EASs with respect to the number of electrons in a shower [$F(>N_e) \sim N_e^{-1.2}$], but it is also affected by the parameters of the energy spectrum of primary protons and by the increase in the depth at which the electron–photon cascade reaches a given value of S in the atmosphere in response to the growth of the primary-proton energy.

The absorption of electrons in $S > 1.05$ showers in the atmosphere is such that the absorption range $\lambda_a = 170–280$ g/cm^2 increases with increasing primary-particle energy. This growth of the absorption range reflects the increase in the depth of the maximum of the cascade development with increasing primary-particle energy. If we assume that this change in λ_a corresponds to a decrease in $\bar{S}$ in the $S > 1.05$ group, then $\bar{S}$ decreases from 1.3 down to 1.1 in those groups. The absorption range for showers from the $S > 1.05$ group, which contains the smallest number of electrons, is $\lambda_a \simeq 135$ g/cm^2. This corresponds to the value of $S \simeq 1.5$ in electron–photon showers and, possibly, reflects the inefficiency of the detection of EASs generated by iron nuclei at such energies of primary particles.

The shower group that is characterized by S values in the range 0.75–1.05 and which is the most representative in the flux includes all showers contributing to the knee in the spectrum with respect to the number of electrons. Before the knee in the spectrum at $N_e \simeq 10^6$, this group of showers does not differ from the $S < 0.75$ EAS group and corresponds to the reduction of the number of electrons in the atmosphere that are generated by primary protons with the absorption range $\lambda_a = 89 \pm 3$ g/cm^2. Near the knee in the spectrum of showers in the range $N_e = 6 \times 10^5–2.0 \times 10^6$, the absorption range of these showers increases to values not less than 160 g/cm^2.

Thus, our analysis of EAS absorption in the atmosphere has revealed that, by the absorption ranges of electrons in a shower, all EASs can be partitioned quite unambiguously into two groups characterized by values of these absorption ranges in significantly different regions, $\lambda_a < 90$ g/cm^2 and $\bar{\lambda}_a > 160$ g/cm^2. The absorption range of electrons in $S < 1$ showers is meaningless, since such electron–photon cascades occur in the stage of development, so that the decrease in the number of electrons with increasing depth in the atmosphere for
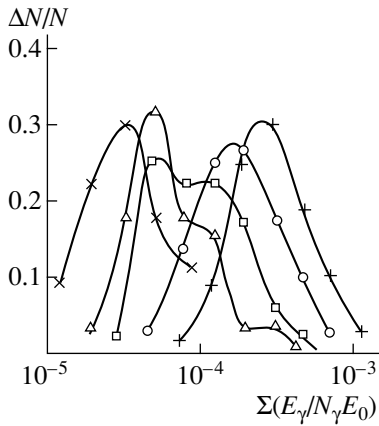
Fig. 11. Mean energy of electrons and photons in the cores of EASs corresponding to the following values of the primary-particle energy as estimated on the basis of the number of electrons at the observation level: (+) 2.2×10^3, (○) 3.2×10^3, (□) 6.2×10^3, (△) 10^6, and (×) 1.8×10^4 TeV.
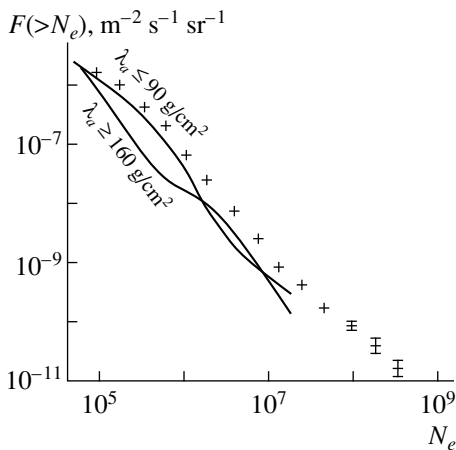

Fig. 12. Integrated spectrum of EASs with respect to the number of electrons in a shower at the observation level and its two components having different absorption lengths in the atmosphere: $\lambda_a \leq 90$ g/cm^2, which corresponds to the absorption of primary protons generating these showers, and $\lambda_a > 160$ g/cm^2, which corresponds to the absorption of electrons and photons that are in equilibrium with a hadronic cascade in the atmosphere [17].

an EAS observed at a given frequency reflects the absorption of primary protons in the atmosphere that generate such showers in the depth of the atmosphere. Extensive air showers characterized by the electron-flux absorption range in a shower above 160 g/cm^2 include hadron–lepton cascades after the maximum of their development, where the absorption of electrons depends on the relationship between the energy lost by the electron–photon cascade and the energy derived from the hadronic cascade via neutral pions.

To conclude our detailed analysis of the structure, spectrum, development, and absorption of EASs considered as hadron–lepton cascades generated by protons and nuclei of cosmic rays with energies in the

range 10^3–10^5 TeV, it should be emphasized that we were unable to find any experimental fact supporting the popular interpretation that treats the knee in the EAS spectrum at the number of electrons in a shower, N_e, about 10^6 as a phenomenon associated with the cusp in the energy spectrum of primary cosmic radiation. Neither the spectrum of old showers that are characterized by cascade-parameter values in excess of 1.05 and which represent hadron–lepton cascades generated by nuclei of primary cosmic radiation in the upper layers of the atmosphere nor the spectrum of EASs generated by primary protons in the depth of the atmosphere (at depths greater than 200 g/cm^2) exhibits a feature that would correspond to the knee in the total flux of EASs. This is demonstrated quite clearly by the experimental data presented in Figs. 9 and 10.

All showers contributing to the knee in the spectrum of EASs with respect to the number of electrons are generated by primary protons in the upper atmosphere. These are the same showers where the flux of energy in the cores decreases sharply at the number of electrons in the range $(4$–$7) \times 10^6$ both according to the measurements in the ionization calorimeter (Fig. 7) and according to the measurements in the x-ray-emulsion chamber (Figs. 5, 11).

5. ENERGY SPECTRUM OF PRIMARY COSMIC RADIATION IN THE RANGE 10^4–10^8 TeV

The above analysis of the spectra of EASs with respect to the number of electrons in a shower (see the preceding section) at various stages of EAS development and absorption in the lower third of the atmosphere at the number of electrons in a shower between 5×10^5 and 5×10^7 makes it possible to represent the total flux of EASs as the sum of two components appearing to be showers generated by protons in the depth of the atmosphere and showers generated by protons and nuclei in the upper atmosphere at depths less than three ranges of primary protons from cosmic radiation with respect to their inelastic collisions with nuclei of air atoms. Figure 12 shows a strange interplay of the two components of the total EAS flux with the different absorption ranges of electrons in EASs: $\lambda_a \leq 90$ g/cm^2—that is, the absorption range of primary protons generating these showers in the depth of the atmosphere—and $\lambda_a > 160$ g/cm^2—that is, the absorption range of electrons in hadron–electron cascades induced by nuclei and protons near the upper boundary of the atmosphere. As a matter of fact, this interplay of the EAS spectra observed in the lower atmosphere versus the number of electrons in showers resolves the question of choosing between the two version of explanation of the knees in the spectrum of EASs with respect to the number of electrons in the lower part of the atmosphere. In an attempt at explaining the interplay of the spectra in Fig. 12 by a transition from the dominance of primary protons to the dominance of nuclei, we must not only increase the exponent of the primary-proton

spectrum but also reduce, as can be seen from Fig. 12, the exponent of the spectrum of primary nuclei containing 6–10 nucleons. These two opposite assumptions concerning changes in the conditions of the acceleration of protons and nuclei in a narrow interval of primary-particle energies must be repeated in the inverse order at the energies of primary cosmic radiation that correspond to the inverted knee. It is a pity that, for want of relevant data, the authors who discovered the two knees in the spectrum [11] could not perform an angular analysis of the flux of EASs, because this would have made it possible to study their absorption in the atmosphere by comparing the intensities of showers in different intervals of zenith angles.

The discovery of a sharp decrease (by a factor of 4 to 5) in the flux of energy in the EAS cores became the basic experimental result that enabled one to make a definitive choice between the different reasons behind the knee in the spectrum of EASs with respect to the number of electrons observed at the level of measurements, a phenomenon that has been the subject of much controversy for more than 30 years. This decrease is observed at primary-proton energies that are four to five times as high as the primary-proton energy corresponding to the region of the knee at $N_e \simeq 10^6$ in the spectrum of EASs with respect to the number of electrons. That the number of electrons in showers that corresponds to the knee in the spectrum of EAS with respect to N_e differs considerably from that at which we observe a sharp decrease in the relative energy of hadrons, electrons, and photons in the EAS cores rules out the interpretation associating the knee in the EAS spectrum with the cusp in the energy spectrum of primary cosmic radiation. It should be emphasized that the narrow interval $(3 \times 10^6–10^7)$ of the EAS spectrum with respect to the number of electrons around a sharp decrease in the relative flux of energy in the cores of EASs generated by primary protons (Figs. 7, 11) coincides with the interval in which showers whose absorption range in the atmosphere is peculiar to the hadron–lepton cascade ($\lambda_a > 160$ g/cm^2) prevail over EASs that are in the equilibrium with the absorption of primary cosmic-ray protons in the atmosphere (Fig. 12).

If we consider implications of the interpretation of the knee in the EAS spectrum as a manifestation of changes in the multiparticle production of secondary hadrons in the first events of inelastic collisions of cosmic-ray protons with nuclei of air atoms and take into account experimental data on the absorption of showers in the atmosphere, we can establish some features of multiparticle hadron production in an inelastic collision of two nucleons at c.m. collision energies not less than 6 TeV.

(i) If the multiplicity of secondary hadrons increases considerably, a multiparticle-generation event cannot produce hadrons whose energy is commensurate with the energies of primary nucleons, because energy required for increasing the multiplicity of secondary

hadrons can come only from leveling the energies of secondary hadrons by their reduction. This is independent of whether secondary hadrons originate from decays of new (hadronic) bosons with a mass not less than 0.5 TeV/c^2 or they emerge from the divergence of excited quark matter.

(ii) A considerable increase in the multiplicity of secondary hadrons from inelastic collisions in the upper atmosphere is accompanied by at least a commensurate increase in the energy dissipated by the electron–photon cascade in the upper atmosphere, whereby the energy transferred by the hadronic and the electron–photon component of the shower core to the lower atmosphere is decreased accordingly. This leads to a reduction of the number of electrons per shower that is observed in the lower atmosphere and which represents the main parameter used to estimate the primary-particle energy. The energy threshold above which the processes of multiparticle hadron production undergo changes must be estimated with allowance for these changes in the relationship between the observed number of electrons and the energy of primary cosmic-ray protons.

(iii) Extensive air showers generated by protons at energies in excess of 5.4×10^3 TeV in events characterized by an enhanced multiplicity and by the secondary-hadron spectrum that exhibits a behavior very dissimilar to the quasiscaling behavior and which is closer in shape to the spectra of hadrons produced in fireball models that are quite forgotten at present reach the observation level with a number of electrons less than 10^6. This is a 30% supplement to the flux of showers generated by primary protons in events characteristic of primary energies E_0 below 5.4×10^3 TeV; formally, it must manifest itself in the region of the knee at $N_e \simeq 10^6$ in the EAS spectrum if the integrated spectra in Figs. 3 and 9 are rescaled into differential spectra, but no narrow intervals of the number of electrons in a shower have revealed so far this excess in experimental data. Fluctuations in the development of showers have smeared the excess of EAS over the region below the knee at about 10^6 electrons in the EAS spectrum with respect to the number of electrons. The smearing of the threshold is inevitable both physically and methodologically: a random number of quarks is involved in the first interaction of a primary proton with the nucleus of an air atom. The altitude of this interaction is also random and cannot be determined for each observed level without upgrading the experiment substantially.

In the review article of Gaisser and Stanev [18], data on the spectrum of primary cosmic radiation that were obtained in some studies by rescaling the observed spectra of EASs with the respect to the number of electrons in a shower (also, of muons and Cherenkov photons in the atmosphere) were confirmed up to energies of about 10^3 TeV by investigations into the spectrum of primary cosmic radiation beyond the atmosphere [19] (see Fig. 13). Needless to say, the use of conventional

methods for rescaling, (that is, of those that take no account of changes in the multiparticle-production process) observed data on the components of EASs into the energies of primary cosmic rays generating these showers reduces the observed knee in the spectrum of EASs with respect to the number of electrons to a cusp in the spectrum of primary protons and nuclei, underestimating their energy. This inevitably results from extrapolating the model of shower formation and absorption from the accelerator energy region without allowing for the observed changes in the energy balance between the fluxes of energy in the shower core and in the entire flow of electrons and photons at the observation level. Experimental data on the spectrum of primary protons generating EASs in the depth of the atmosphere (see Figs. 9 and 10) and data from [10] on the inverse knee disprove completely the energy spectrum of primary cosmic rays that was obtained in the way outlined immediately above (see Fig. 13).

In Sections 3 and 4 of the present article, we have already discussed in detail the results that were obtained from investigations of EASs and which are at odds with the assumptions underlying the interpretation of the spectrum in [18] (see Fig. 12). In particular, it was shown that the observed knee in the spectrum of EASs with respect to the number of electrons can be explained by changes in the generation of secondary particles in the first inelastic collisions between primary protons and nuclei of air atoms at proton energies higher than some 10^4 TeV and by a subsequent development of EASs and their absorption in the atmosphere. Theoretical models not allowing for these changes in the development of showers in the upper atmosphere underestimate considerably (by a factor of six or more) the energy of primary particles generating EASs containing more than 3×10^6 electrons in the lower half of the atmosphere.

This underestimation of the energy of primary particles that produce EASs involving more than 10^8 electrons has already been seen in experiments performed previously. Figure 2 [2] shows that the protonic part of the histograms representing the distribution of the altitudes of the maxima of the EAS development in the atmosphere complies quite well with the effective cross sections for inelastic collisions of protons with nuclei of air atoms both in the energy range 10^5–10^6 TeV and in the energy range 10^6–10^7 TeV. However, the left-hand parts of these histograms—they represent showers generated by primary nuclei—are quite different. If we plot the distribution in Fig. 2 on a linear scale, normalizing areas on the basis of the right-hand, protonic, part, showers generated by primary nuclei prove to be virtually absent from the distribution of the altitudes of the maxima of showers corresponding to primary energies in the range 10^6–10^7 TeV (see Fig. 14). The disintegration of nuclei by relic photons at energies corresponding to a giant resonance for the photodisintegration of nuclei in their rest frame may be the reason for the disappearance of nuclei from primary cosmic radiation. However, the energy at which the disappearance
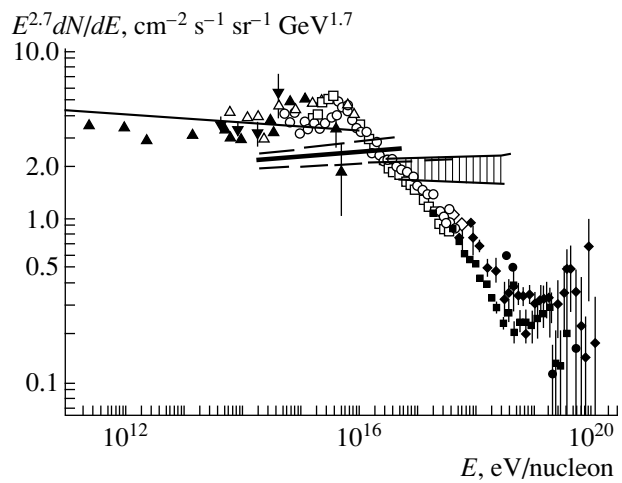

Fig. 13. Energy spectrum of primary cosmic rays from the review article of Gaisser and Stanev [18]. The straight line in the interval 10^{11}–10^{16} eV represents a generalization of experimental data on the energy spectrum of cosmic rays according to the studies beyond the atmosphere that are reported in [19]. The energy spectra of primary protons according to data on $S < 0.75$ EASs and to observations of the inverse knee in the spectrum are shown within the error corridors.
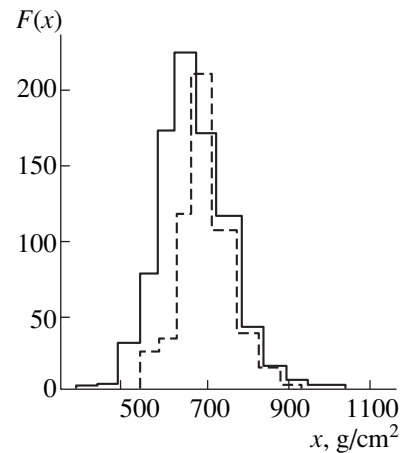

Fig. 14. Distributions of the altitudes of the maxima of EAS development for the primary-particle-energy intervals (solid histogram) 10^5–10^6 and (dashed histogram) 10^6–10^7 TeV. The areas of the histograms are superimposed and normalized by using the right-hand (protonic) part of the histogram.

of nuclei could be attributed to their disintegration by relic photons must be eight to ten times as great as the energy estimated on the basis of the number of electrons in EASs at the level of observation. There can be no doubt about the experimentally observed decrease in the flux of nuclei in relation to the flux of protons of energy estimated at about 5×10^6 TeV. A similar decrease in the contribution of nuclei to the total flux of cosmic rays generated by primary particles of energies above 3×10^6 TeV can be seen in data that come from the experiment reported in [1] and which are displayed in

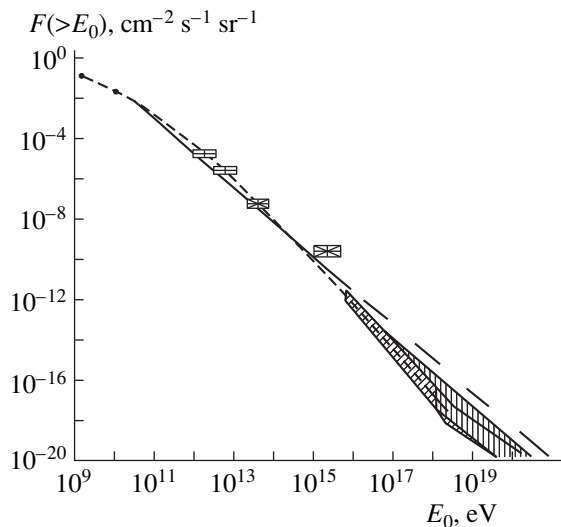$F(>E_0)$, cm^{-2} s^{-1} sr^{-1}

Fig. 15. Energy spectrum of primary cosmic radiation from [22] (short dashes). Boxes and the dashed band (left-hand part) illustrate experimental data quoted in [22]. The straight line represents the energy spectrum of primary cosmic radiation according to experimental data obtained beyond the atmosphere and generalized in the monograph [19]. The continuation of this straight line by dashes shows the extrapolation of the spectrum by the present authors to higher energies. The vertically shaded band corresponds to the experimental data from the review article of Gaisser and Stanev [18] (Fig. 13).

Fig. 1. It should be recalled that, over more than 40 years, there has been no experimental observation supporting the hypothesis of the cusp in the energy spectrum of cosmic radiation; therefore, it is hardly reasonable to seek, for the sake of preserving this hypothesis, factors—other than relic radiation—that could be responsible for the disappearance of nuclei from primary cosmic rays.

There is, however, the question of whether it is possible that observations of EASs show a relic "cutoff" for nuclei in the composition of primary cosmic radiation, but that they do not show this cutoff in the spectrum of primary protons [20, 21]. The distinctions between the masses of primary nuclei and the proton mass nearly compensate for the distinctions between the energies that relic photons must have in the rest frame of these nuclei in order to induce their photodisintegration and the energy that relic photons must have in the proton rest frame for pion photoproduction to be possible. However, the effective cross section for the photodisintegration of a nucleus is much larger than that for pion photoproduction on a proton. What is of still greater importance is that, after a collision event, a proton remains a proton (becomes a neutron) and can increase its energy while traveling in the metagalaxy. The photodisintegration of a nucleus by a photon has fateful consequences: the nucleus that has suffered a collision with a photon exists no longer, whereas the fragments of the former, which contribute to the energy spectrum of protons and the energy spectrum of cosmic-ray nuclei of lower energies, may escape observation in the total flux of cosmic rays.

Thus, the relic cutoff observed in the energy spectrum of nuclei of primary cosmic radiation at energies estimated according to EAS data at about 5×10^6 TeV, instead of an expected value of about 5×10^7 TeV, suggests that the hypothesized—but not yet confirmed experimentally—cusp in the energy spectrum of primary cosmic radiation, together with the assumption that it is possible to extrapolate the traditional description of the multiparticle production of secondary hadrons in inelastic nucleon–nucleon collisions from the explored energy region to the unexplored one, leads to a considerable underestimation of the primary energy of the EASs with $N_e > 10^6$ that are observed in the lower part of the atmosphere.

In Fig. 13, the existence of the knee is compellingly demonstrated by choosing different scales along the axes; what also catches the eye in this presentation of data relevant to the knee is that, owing to the factor $E^{2.7}$ relating the quantities plotted along the coordinate axes, the spectrum deviates from the horizontal line in the region of the knee. It is reasonable to return to a simple illustration of the energy spectrum of primary cosmic radiation by relying on the energy spectrum that Rossi presented at the Moscow International Cosmic Ray Conference in 1959 [22]. It should be recalled that experimental data on the knees in the EAS spectra at the number of electrons about 10^6 were also first discussed at that conference [23, 24].

Figure 15 reproduces experimental data on the energy spectrum of primary cosmic radiation from [22]. The straight solid line going to the energy range 10^3–10^4 TeV represents the results of investigations that were performed beyond the atmosphere and which were summarized in the monograph [19]. An extrapolation of this spectrum, $F(E) \sim E^{-2.75}$, to the region of higher energies is depicted by long dashes. In the energy region above 10^6 TeV, the spectrum was supplemented with up-to-date experimental data from Fig. 13. As can be seen from Fig. 15, the representation of the spectrum in the form of a smooth curve without a knee does not include the result of large-depth measurements of the flux of high-energy muons, whose production is associated theoretically with the intensity of primary cosmic-ray particles of energies 10^3–10^4 TeV.[3]

[3]The position of this point with respect to the curve representing the energy spectrum of primary cosmic rays is highly ambiguous. The intensity of high-energy muons is rescaled theoretically to the intensity of primary cosmic radiation, with the result of this rescaling at energies of 10–10^2 TeV being in agreement with the general spectrum of cosmic rays. As can be seen from Fig. 15, however, the result in question deviates from the smooth curve in the energy range 10^3–10^4 TeV, but this is the region of primary-cosmic-radiation energy where the first data on the knee in the spectrum of EASs with respect to the number of electrons at the observation level were presented at the same conference by the authors of [23, 24]. In addition to those circumstances, measurements of the flux of muons that correspond to the energy range 10^3–10^4 TeV recorded a muon-pair excess that could not be explained by the dominant muon-production-process via pion decays. Thus, we can see that, even at that time, it was necessary to resolve a dilemma in interpreting those data: the question was whether it was more appropriate to attribute this feature to a structure in the energy spectrum or to associate it with some new processes in inelastic collisions of primary protons with nuclei of air atoms.

Short dashes represent the results of rescaling the EAS spectrum with respect to the number of electrons into the energy of primary-cosmic-radiation particles in the range 10^2–10^6 TeV by using the Landau hydrodynamic model, which features no sharp variations in the multiparticle-production process. From Fig. 15, it follows that, if the possibility of significant changes in the multiparticle-hadron-production event is ruled out, the N_e spectrum of EASs that has a knee at about 10^6 [22, 23] and a gradual variation of this spectrum in accordance with the assumption from [22] lead to an underestimation of the cosmic-ray energy.

In the above analysis of the experiments performed at the Tien Shan station, the knee near $N_e \simeq 10^6$ in the spectrum of EASs with respect to the number of electrons was confirmed and studied in greater detail: the knee was observed in the spectrum of showers generated by primary protons at a depth in the atmosphere less than 200 g/cm^2. At primary-proton energies in excess of 5×10^3 TeV, such showers dissipate their energy in the upper half of the atmosphere. The most spectacular manifestation of this is that the relative energy in shower cores exhibits a fivefold decrease. Extensive atmospheric showers generated by primary protons in the depth of the atmosphere do not show a knee in their spectrum, as is demonstrated by the absence of cusps in the energy spectrum of primary protons below some 10^5 TeV.

Presently, nothing contradicts the assumption that protons and nuclei that have energies above some 10^2 TeV and which are observed near the Earth belong to the general spectrum of the Universe. They are accelerated in various processes occurring in widely separated active regions of the metagalaxy, ever increasing their energy in collisions with magnetic clouds. It is hardly reasonable to seek objects close to the Solar System that are capable of accelerating cosmic rays up to energies of 10^2–10^3 TeV. Such processes would not be favorable for the emergence of the Earth's biosphere. Even the first observations [25] of the sources of gamma rays with energies from 10^{12} eV support the hypothesis of the extragalactic origin of cosmic rays. In the Milky Way Galaxy, the Crab Nebula, which occurs near the Solar System, is the only source of gamma rays with energies higher than 10^{12} eV that has been reliably established so far. However, a few metagalactic sources occurring farther from the Earth by a factor of 10^4 are presently known to produce similar fluxes of gamma rays near the Earth. That the emissitivities of these metagalactic sources differ from those of galactic sources emitting photons of energies higher than 10^{12} eV by more than eight orders of magnitude demonstrates that their powers are incommensurate. The periods of the activity of galaxy cores and of supernova remnants differ considerably. Finally, the very fact that active galaxy cores emit photons of energies above 10^{12} eV appears to be evidence for the acceleration of protons and nuclei by such active objects of the metagalaxy at least to energies of 10^3–10^4 TeV.

6. CONCLUSION

Long-term investigations of extensive atmospheric showers generated by primary cosmic radiation of energies 5×10^2–10^5 TeV at the Tien Shan EAS array have not revealed any experimental fact supporting the interpretation in which the knee at $N_e \simeq 10^6$ in the EAS spectrum with respect to the number of electrons is associated with the cusp in the energy spectrum of primary cosmic radiation. We are unaware of any experimental data confirming unambiguously this interpretation of the above knee at $N_e \simeq 10^6$ in the spectrum of EASs with respect to the number of electrons.

For the first time, the investigations at the Tien Shan EAS array provided data that disprove the above interpretation of the knee at $N_e \simeq 10^6$ in the EAS spectra: neither spectra with respect to the number of electrons in showers generated by primary nuclei in the upper atmosphere, nor EASs generated in the depth of the atmosphere by primary-cosmic-ray protons exhibit a cusp in the interval of their spectra that corresponds to 10^5–10^7 electrons in a shower.

The knee in the spectrum of EASs with respect to the number of electrons is due to showers generated by primary protons in the upper third of the atmosphere. These are the same showers in which the relative energy in the EASs cores was found to decrease by a factor of five at $N_e \geq 3.5 \times 10^6$. Owing to this decrease in the energy in the cores of showers generated by primary protons, such EASs become similar to those generated by primary nuclei. In particular, the spectrum of showers with respect to the number of electrons approaches the spectrum of showers generated by primary nuclei; concurrently, the absorption range of electrons in such nuclei increases from $\lambda_a < 90$ g/cm^2 to $\lambda_a > 160$ g/cm^2.

Attempts at explaining all this by changes in the spectrum and composition of primary cosmic radiation would require, in addition to the assumption of the softening of the energy spectrum of primary protons, the assumption of the hardening of the energy spectrum of primary nuclei consisting of 6–10 nucleons.

If the knee in the spectrum of EASs with respect to the number of electrons is associated with changes in the multiparticle-hadron-production process at primary-proton energies of about 10^4 TeV [26], the difference between the number of electrons in showers that corresponds to the knee in the spectrum of EASs with respect to the number of electrons and the number of electrons that corresponds to a sharp decrease (by a factor of about 5) in the energy of particles in the EAS cores is explained by the same reason.

In analyzing experimental data, we adopted the model—simple by assumption and simple indeed in simulating EASs—that relies on the hypothesis that the multiplicity of secondary hadrons from the first event of inelastic collisions between primary protons and nuclei of air atoms increases by a factor of 6 to 10, but this is highly improbable in a narrow interval of pri-

mary-proton energies. A more probable reason for the energy threshold at which multiparticle-production processes undergo changes may be associated with real and virtual (having decay times less 10^{-24} s) heavy bosons with masses from 500 GeV/c^2. The existence of a family of such bosons with close masses could be manifested in their resonance production with an effective cross section not larger than $(1/3)\sigma_{inel}$ for nucleon–nucleon collisions and a subsequent decay into unstable baryons, or, alternatively, into W and Z bosons. It is important that this can serve as a good substitute for the assumption of the enormous increase in the multiplicity of secondary pions. New experimental information about the processes of EAS development in the upper atmosphere can be expected above all from a detailed analysis studying spatial, energy, and time characteristics of muons and the interplay of these properties on the basis of data on extensive air showers generated by primary protons and nuclei of known energies.

ACKNOWLEDGMENTS

REFERENCES

1. D. J. Bird, S. C. Corbato, *et al.*, in *Proceedings of the 23rd International Cosmic Ray Conference, Calgary, 1993*, Vol. 2, p. 38.

2. M. N. Dyakonov, V. P. Egorova, *et al.*, in *Proceedings of the 21st International Cosmic Ray Conference, Adelaide, 1990*, Vol. 9, p. 252.

3. G. B. Khristiansen, G. B. Kulikov, *et al.*, Pis'ma Zh. Éksp. Teor. Fiz. **18**, 353 (1973).

4. S. I. Nikolsky, in *Proceedings of the Seminar on Cosmic Ray Extensive Air Showers, Lodz, 1965*, p. 140.

5. T. P. Amineva, V. S. Aseĭkin, *et al.*, Tr. Fiz. Inst. Akad. Nauk SSSR **46**, 157 (1970).

6. V. A. Romakhin, N. M. Nesterova, *et al.*, Tr. Fiz. Inst. Akad. Nauk SSSR **109**, 77 (1979).

7. K. V. Cherdyntseva, I. V. Rakobol'skaya, and S. I. Nikol'skiĭ, Yad. Fiz. **9**, 152 (1969) [Sov. J. Nucl. Phys. **9**, 92 (1969)].

8. D. S. Adamov, B. N. Afanasjev, *et al.*, in *Proceedings of the 20th International Cosmic Ray Conference, Moscow, 1987*, Vol. 5, p. 460.

9. S. I. Nikolsky, in *Proceedings of the 23rd International Cosmic Ray Conference, Calgary, 1993*, Vol. 4, p. 243.

10. L. I. Vil'danova, P. A. Dyatlov, *et al.*, Izv. Akad. Nauk, Ser. Fiz. **58** (12), 79 (1994).

11. G. B. Khristiansen, in *Problems in Cosmic Ray Physics* (Nauka, Moscow, 1987), p. 226.

12. S. I. Nikolsky, Nucl. Phys. (Proc. Suppl.) **A75**, 217 (1999).

13. E. V. Danilova, N. B. Kabanova, *et al.*, in *Proceedings of the 24th International Cosmic Ray Conference, Roma, 1995*, Vol. 1, p. 285.

14. N. N. Kalmykov, G. B. Khristiansen, *et al.*, in *Proceedings of the 25th International Cosmic Ray Conference, South Africa, 1997*, Vol. 6, p. 277.

15. D. S. Adamov, V. V. Arabkin, *et al.*, Kratk. Soobshch. Fiz. **3/4**, 57, 63 (1993).

16. S. I. Nikolsky, Nucl. Phys. B (Proc. Suppl.) **60**, 144 (1998).

17. S. I. Nikolsky, in *Proceedings of the 25th International Cosmic Ray Conference, South Africa, 1997*, Vol. 6, p. 105.

18. T. K. Gaisser and T. Stanev, Phys. Rev. D **54**, 22 (1996).

19. V. S. Murzin, *Introduction to the Physics of Cosmic Rays* (Atomizdat, Moscow, 1979).

20. G. T. Zatsepin and V. A. Kuz'min, Pis'ma Zh. Éksp. Teor. Fiz. **4**, 114 (1966) [JETP Lett. **4**, 78 (1966)].

21. K. Greisen, Phys. Rev. Lett. **16**, 748 (1966).

22. B. Rossi, in *Proceedings of the International Cosmic Ray Conference, 1960*, Vol. 2, p. 33.

23. G. V. Kulikov and N. M. Nesterova, in *Proceedings of the International Cosmic Ray Conference, 1960*, Vol. 2, p. 87.

24. T. Kameda and T. Maeda, in *Proceedings of the International Cosmic Ray Conference, 1960*, Vol. 2, p. 56.

25. V. G. Sinitsyna and A. Y. Alaverdian, in *Proceedings of the 25th International Cosmic Rays Conference, South Africa, 1997*, Vol. 3, p. 273.

26. S. I. Nikol'skiĭ and A. Pomanskiĭ, Zh. Éksp. Teor. Fiz. **35**, 618 (1958) [Sov. Phys. JETP **8**, 430 (1958)].

Translated by A. Isaakyan

ELEMENTARY PARTICLES AND FIELDS
Theory

Exotic States $X^{\pm}(1600, I^G (J^{PC}) = 2^+ (2^{++}))$ in Photoproduction Reactions

N. N. Achasov and G. N. Shestakov

Laboratory of Theoretical Physics, Sobolev Institute for Mathematics, Siberian Division, Russian Academy of Sciences,
*Novosibirsk, 630090 Russia*
Received May 11, 1999

Abstract—It is shown that the list of unusual mesons that are planned to be studied in photoproduction reactions can be supplemented with $I^G (J^{PC}) = 2^+ (2^{++})$ exotic states $X^{\pm}(1600)$, which are natural to seek as manifestations of the $\rho^{\pm}\rho^0$ decay channels in the reactions $\gamma N \longrightarrow \rho^{\pm}\rho^0 N$ and $\gamma N \longrightarrow \rho^{\pm}\rho^0 \Delta$. A classification of the $\rho^{\pm}\rho^0$ states according to their quantum numbers is presented. A model for the spin structure of the amplitudes for the reactions $\gamma p \longrightarrow f_2(1270)p$, $\gamma p \longrightarrow a_2^0(1320)p$, and $\gamma N \longrightarrow X^{\pm}(N, \Delta)$ is proposed, and estimates are obtained for the corresponding cross sections. At $E_\gamma \approx 6$ GeV, it is found that $\sigma(\gamma p \longrightarrow f_2(1270)p) \approx 0.12$ μb, $\sigma(\gamma p \longrightarrow a_2^0(1320)p) \approx 0.25$ μb, $\sigma(\gamma N \longrightarrow X^{\pm}N \longrightarrow \rho^{\pm}\rho^0 N) \approx 0.018$ μb, and $\sigma(\gamma p \longrightarrow X^-\Delta^{++} \longrightarrow \rho^-\rho^0\Delta^{++}) \approx 0.031$ μb. The problem of isolating signals from $X^{\pm}$ states against the natural background that is associated with other channels of $\pi^{\pm}\pi^0\pi^+\pi^-$ production is discussed. It is deduced that searches for exotic states $X^{\pm}(2^+ (2^{++}))$ in experiments at JLAB will be quite efficient—for example, the yield of about 2.8×10^6 events per month is expected to correspond to the estimated cross sections for the reactions $\gamma N \longrightarrow X^{\pm}N \longrightarrow \rho^{\pm}\rho^0 N$. © 2000 MAIK "Nauka/Interperiodica".

1. INTRODUCTION

In the present study, we will show that the list of exotic mesons that are planned to be studied with an intense beam of 6-GeV photons at the Jefferson Laboratory (JLAB) [1–4] and at other centers using similar facilities can be supplemented with the $J^{PC} = 2^{++}$ tensor states $X^{\pm}(1600)$, which are members of the $I = 2$ isotopic multiplet. It is natural to seek these states by pursuing the $\rho^{\pm}\rho^0$ decay channels in the reactions $\gamma p \longrightarrow \rho^+\rho^0(n, \Delta^0)$, $\gamma n \longrightarrow \rho^-\rho^0(p, \Delta^+)$, $\gamma p \longrightarrow \rho^-\rho^0\Delta^{++}$, and $\gamma n \longrightarrow \rho^+\rho^0\Delta^-$. It is well known that their partner—the neutral isotensor–tensor state $X^0(1600, I^G(J^{PC}) = 2^+ (2^{++}))$ [5]—was observed near the threshold in the reactions $\gamma\gamma \longrightarrow \rho^0\rho^0$ [6, 7] and $\gamma\gamma \longrightarrow \rho^+\rho^-$ [8, 9] (for an overview, see [10, 11]; see also the figure, which displays data that were obtained by the Argus collaboration and which illustrate the situation in $\gamma\gamma$ collisions). Phenomena that it generates in the above processes were predicted in [12, 13] on the basis of the $q^2\bar{q}^2$ model [14]. Physically, the resonance interpretation of data on the transition $\gamma\gamma \longrightarrow \rho\rho$ seems most plausible, but it is not yet definitive and commonly accepted. Like other candidates for exotic states [15], $X^0(1600, 2^+ (2^{++}))$ calls for additional confirmations; probably, it will be reactions leading to the photoproduction of its charged partners $X^{\pm}$ that will provide a crucial test in this respect. It should be noted that cross sections for processes that are governed by strong interactions and

which can exhibit doubly charged partners of $X^0(1600, 2^+ (2^{++}))$ were estimated in [16].

The ensuing exposition is organized as follows. In Section 2, we present a full classification of the states of the $\rho^{\pm}\rho^0$ systems according to their quantum numbers. In Section 3, we establish the spin structure of the amplitudes for the reactions $\gamma p \longrightarrow f_2(1270)p$, $\gamma p \longrightarrow a_2^0(1320)p$, and $\gamma N \longrightarrow X^{\pm}(N, \Delta)$, employing available information about the processes $\gamma\gamma \longrightarrow f_2(1270) \longrightarrow \pi\pi$; $\gamma\gamma \longrightarrow a_2^0(1320) \longrightarrow \pi^+\pi^-\pi^0$, $\pi^0\eta$; and $\gamma\gamma \longrightarrow \rho\rho$ and relying on the vector-dominance model (VDM) and on the factorization property of pole Regge exchanges; we also estimate there relevant cross sections at a laboratory photon energy of $E_\gamma \approx 6$ GeV. In Section 4, the problem of isolating signals from $X^{\pm}$ states against the natural background associated with other channels of $\pi^{\pm}\pi^0\pi^+\pi^-$ production is discussed by considering predominantly the example of $\gamma N \longrightarrow \pi^{\pm}\pi^0\pi^+\pi^- N$ reactions. Based on information about planned statistics in recording rare ϕ-meson decays in the reaction $\gamma p \longrightarrow \phi p$ [1, 2], we conclude that searches for exotic states $X^{\pm}(2^+ (2^{++}))$ with a photon beam at JLAB will be quite efficient. New information about the world of hadrons to be obtained from such measurements may prove to be of paramount importance.

$\sigma(\gamma\gamma \to \rho\rho)$, nb
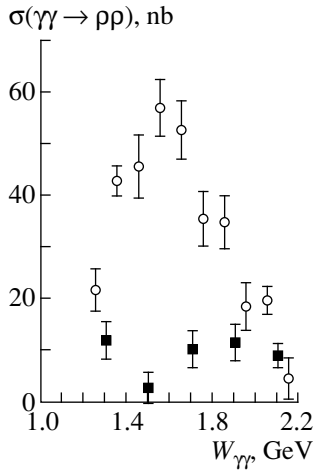
Data of the ARGUS group for the $(J^P, |J_z|) = (2^+, 2)$ partial-wave cross sections for the reactions (open circles) $\gamma\gamma \longrightarrow \rho^0\rho^0$ [7] and (closed boxes) $\gamma\gamma \longrightarrow \rho^+\rho^-$ [9] as functions of the total c.m. energy $W_{\gamma\gamma}$ of $\gamma\gamma$. For the conventional $I = 0$ resonance (pure $I = 2$ resonance), it is expected that $\sigma(\gamma\gamma \longrightarrow \rho^+\rho^-)/\sigma(\gamma\gamma \longrightarrow \rho^0\rho^0) = 2$ (1/2). The experimental value of this ratio is less than 1/2. A resonance interpretation of this result in terms of $q^2\bar{q}^2$ states requires the presence of an $I = 2$ tensor exotic state interfering with isoscalar contributions [5, 11, 12].

2. POSSIBLE STATES OF $\rho^\pm\rho^0$ SYSTEMS

The $\rho^\pm\rho^0$ states have a positive G parity. With allowance for constraints imposed by Bose statistics, their classification in terms of the total isospin I, the total angular momentum J, conventional parity, charge-conjugation symmetry of neutral components of isotopic multiplets, the total spin S, and the total orbital angular momentum L is displayed in Table 1. The table shows that, of eight series of the $\rho^\pm\rho^0$ states, five are exotic—they are forbidden in the $q\bar{q}$ system—and that only in the first, the second, and the last series have specific examples of possible resonance states been found so far. From this table, we can also see that, among even-J states, only $I^G (J^{PC}) = 2^+ (0^{++})$ and $I^G (J^{PC}) = 2^+ (2^{++})$ exotic states possess $L = 0$ $^{2S+1}L_J$ configurations and can therefore (in principle) manifest themselves efficiently near the true $\rho\rho$ threshold ($2m_\rho \approx 1540$ MeV). It should be noted that only for the $\rho_3(1690)$ and $X(1600, 2^+ (2^{++}))$ states can we be confident of the existence of coupling to the $\rho\rho$ system [17]. As to the $b_1(1235)$ resonance, it lies deeply below the $\rho\rho$ threshold; in the four-pion decay channel, this resonance is observed in the $\omega\pi$ mode [17]. For the hypothesized ρ_2 state, which is indicated in Table 1, the reader is referred to [18]. As to the decay process $\rho(1700) \longrightarrow 4\pi$, data available for it are compatible with the hypothesis that this process features no $\rho\rho$ component [17]. It should be emphasized that, to some extent, the notation $\rho(1700)$ is used tentatively in our context [19]. By $\rho(1700)$, we mean

the entire amount of the enhancement that is characterized by the quantum numbers $I^G (J^{PC}) = 1^+ (1^{--})$ and which was observed in the four-pion channels in the reactions $\gamma p \longrightarrow \pi^+\pi^-\pi^+\pi^- p$ and $\gamma p \longrightarrow \pi^+\pi^-\pi^0\pi^0 p$ [probably, however, with an admixture of $\rho_3(1690)$]—that is, the "old" ρ' [or $\rho(1600)$] resonance [20]; according to available data [17, 21–26], it is not necessary to partition it into the $\rho(1700)$ and $\rho(1450)$ components [27] in photoproduction reactions, at least for our purposes.

3. ESTIMATES OF THE CROSS SECTIONS FOR THE PHOTOPRODUCTION OF $f_2(1270)$, $a_2^0(1320)$, AND $X^\pm(1600, 2^+ (2^{++}))$ RESONANCES

We assume that, at high energies, the cross sections for the reactions $\gamma p \longrightarrow f_2 p$, $\gamma p \longrightarrow a_2^0 p$, and $\gamma N \longrightarrow X^\pm(N, \Delta)$ are determined primarily by natural-parity pole Regge exchanges—that is, exchanges of ρ^0 and ω Regge poles in the case of the production of f_2 and a_2 resonances and exchanges of $\rho^\pm$ Regge poles in the case of the production of isotensor $X^\pm$ states.[1] We note that one-pion exchange is forbidden in these reactions and that we disregard unnatural-parity b_1, h_1, ρ_2, and ω_2 exchanges. In order to establish the spin structure of the amplitudes for the reactions $\gamma p \longrightarrow f_2 p$, $\gamma p \longrightarrow a_2^0 p$, and $\gamma N \longrightarrow X^\pm(N, \Delta)$ in the Regge region and to estimate the corresponding cross sections, we note that, in the c.m. frame of the reactions $\gamma\gamma \longrightarrow f_2 \longrightarrow \pi\pi$ [28], $\gamma\gamma \longrightarrow a_2^0 \longrightarrow (\pi^+\pi^-\pi^0, \pi^0\eta)$ [29], and $\gamma\gamma \longrightarrow \rho\rho$ near the threshold [7, 9] (see figure), the production of tensor ($J^P = 2^+$) resonances occurs predominantly in states where the projections of their spins are $J_z = \lambda_1 - \lambda_2 = \pm 2$, λ_1 and λ_2 being the helicities of the primary photons, and where the quantization axis (z axis) is directed along the momentum of one of them. It is well known that the production of $J_z = \pm 2$, 2^+ resonances is described by the amplitude $g_{2^+\gamma\gamma} T_{\mu\nu}^{\lambda*} F_{\mu\tau}^{\gamma_1} F_{\nu\tau}^{\gamma_2}$ [12, 30], where $T_{\mu\nu}^{\lambda*}$ is the zero-trace symmetric polarization tensor of the final 2^+ resonance with helicity λ, $F_{\mu\nu}^{\gamma_i} = k_{i\mu}\epsilon_\nu^{\lambda_i}(k_i) - k_{i\nu}\epsilon_\mu^{\lambda_i}(k_i)$, and $\epsilon_\mu^{\lambda_i}(k_i)$ is the polarization vector of the photon γ_i with 4-momentum k_i and helicity $\lambda_i = \pm 1$ ($i = 1, 2$). Following the ideology of the VDM, we assume that the amplitudes of $\gamma V \longrightarrow 2^+$ transitions have the form $g_{2^+\gamma V} T_{\mu\nu}^{\lambda*} F_{\mu\tau}^{\gamma} F_{\nu\tau}^{V}$ [where $V = \rho$, ω and where $F_{\nu\tau}^V = k_{V\nu}\epsilon_\tau^{\lambda_V}(k_V) - k_{V\tau}\epsilon_\nu^{\lambda_V}(k_V)$, $\epsilon_\tau^{\lambda_V}(k_V)$ being the polarization 4-vector of the V meson with 4-momentum

---

[1]When it is clear what resonances are implied, we do not indicate their masses—for example, we write f_2 instead of $f_2(1270)$.

Table 1. Classification of $\rho^{\pm}\rho^0$ states

$I^G(J^{PC})$ series, $k = 0, 1, 2, ...$	Possible resonance states	$^{2S+1}L_J$ configurations for states lower in J
$1^+ ((2k+1)^{--})$	$\rho(1700)$, $\rho_3(1690)$	$(^1P_1, {}^5P_1, {}^5F_1); ({}^5P_3, {}^1F_3, {}^5F_3, {}^5H_3)$
$1^+ ((2k+1)^{+-})$	$b_1(1235)$	$^3S_1, {}^3D_1$
$1^+ ((2k+2)^{--})$	$\rho_2(?)$ [17, 18]	$^5P_2, {}^5F_2$
$1^+ ((2k+2)^{+-})$	Absent in the $q\bar{q}$ system	$^3D_2$
$2^+ ((2k+1)^{-+})$	$q^2\bar{q}^2$	$^3P_1, {}^3F_1$
$2^+ ((2k+1)^{++})$	$q^2\bar{q}^2$	$^5D_1$
$2^+ ((2k)^{-+})$	$q^2\bar{q}^2$	$(^3P_0); ({}^3P_2)$
$2^+ ((2k)^{++})$	$q^2\bar{q}^2$, $X(1600, 2^+ (2^{++}))$	$(^1S_0, {}^5D_0); ({}^5S_2, {}^1D_2, {}^5D_2, {}^5G_2)$

k_V and helicity λ_V] and that, for the coupling constants $g_{2^+\gamma V}$ and $g_{2^+\gamma\gamma}$, the following relations hold:

$$g_{f_2\gamma\rho} = 3g_{f_2\gamma\omega} = 3g_{a_2\gamma\omega} = 3g_{a_2\gamma\rho} = \frac{9}{10}g_{f_2\gamma\gamma}\left(\frac{f_\rho}{e}\right)$$
$$= \frac{1}{2}g_{a_2\gamma\gamma}\left(\frac{f_\omega}{e}\right) = \frac{1}{2}g_{a_2\gamma\gamma}\left(\frac{3f_\rho}{e}\right). \tag{1}$$

That there are slight deviations from these predictions of the naive quark model is immaterial for the further estimates. By using Eq. (1) and data from [17] on the widths with respect to the decay processes $f_2 \longrightarrow \gamma\gamma$ and $\rho^0 \longrightarrow e^+e^-$, we obtain $f_\rho^2/4\pi \approx 2.02$,

$$\frac{g_{f_2\gamma\rho}^2}{4\pi} \approx 0.0212 \text{ GeV}^{-2},$$
$$\Gamma_{f_2\gamma\rho} = \frac{g_{f_2\gamma\rho}^2|\mathbf{k}_\gamma|^3}{4\pi}\frac{1}{5}\left[1 + \frac{1}{2}r + \frac{1}{6}r^2\right] \approx 340 \text{ keV}, \tag{2}$$

where $r = m_\rho^2/m_{f_2}^2$ and $|\mathbf{k}_\gamma| = m_{f_2}(1-r)/2$.

Let us now construct the s-channel helicity amplitudes for the reaction $\gamma p \longrightarrow f_2 p$ in its c.m. frame that correspond to elementary ρ exchange at high energies and fixed momentum transfers. In just the same way as pole Regge amplitudes, the helicity amplitudes in question are characterized by the factorization of the spin structures of meson and baryon vertices (recall that this is one of the basic properties of Regge pole amplitudes); that is,

$$M^{(\rho)}_{\lambda_{f_2}\lambda'_p\lambda_\gamma\lambda_p} = V^{(\rho)}_{\lambda_{f_2}\lambda_\gamma}(t)\left(\frac{-2s}{t-m_\rho^2}\right)V^{(\rho)}_{\lambda'_p\lambda_p}(t), \tag{3}$$

where $s = (k+p)^2$; $t = (q-k)^2$; $k+p = q+p'$; $k, q, p,$ and p' are the 4-momenta of the photon, the f_2 meson, the initial proton, and the final proton, respectively; and λ_γ, λ_{f_2}, λ_p, and λ'_p are their helicities. According to the

model proposed above for $\gamma\rho f_2$ interaction, the vertex functions $V^{(\rho)}_{\lambda_{f_2}\lambda_\gamma}(t)$ in Eq. (3) are given by

$$V^{(\rho)}_{\pm2\pm1}(t) = \pm\frac{g_{f_2\gamma\rho}\sqrt{-t}}{2\sqrt{2}}, \quad V^{(\rho)}_{\pm1\pm1}(t) = \frac{g_{f_2\gamma\rho}t}{2\sqrt{2}m_{f_2}},$$
$$V^{(\rho)}_{0\pm1}(t) = \mp\frac{g_{f_2\gamma\rho}t\sqrt{-t}}{4\sqrt{3}m_{f_2}^2}. \tag{4}$$

It should be noted that we everywhere disregard the quantity $t_{\min} \approx -m_p^2 m_{f_2}^4/s^2$ and that we will not need explicit expressions for the vertex functions $V^{(\rho)}_{\lambda'_p\lambda_p}(t)$. From (4), it follows that, for $-t < 1$ GeV^2, the contributions to the differential cross section from the $\lambda_{f_2} = \pm1$ and $\lambda_{f_2} = 0$ amplitudes are suppressed in relation to the contributions from the $\lambda_{f_2} = \pm2$ amplitudes, the suppression factors being $-t/m_{f_2}^2$ and $t^2/6m_{f_2}^4$, respectively. Thus, our model predicts that the $\lambda_{f_2} = \pm2$ amplitudes for the production of the f_2 resonance are dominant in the region $-t < 1$ GeV^2. Going over to real physical amplitudes associated with the exchange of the ρ Regge pole, $\hat{M}^{(\rho)}_{\lambda_{f_2}\lambda'_p\lambda_\gamma\lambda_p}$, we adopt this prediction as a natural assumption and will henceforth take into account two independent pole amplitudes $\hat{M}^{(\rho)}_{2\frac{1}{2}1\frac{1}{2}}$ and $\hat{M}^{(\rho)}_{2\frac{1}{2}1-\frac{1}{2}}$. We denote by $\hat{V}^{(\rho)}_{\lambda_{f_2}\lambda_\gamma}(t)$ and $\hat{V}^{(\rho)}_{\lambda'_p\lambda_p}(t)$ the Regge vertex functions appearing in $\hat{M}^{(\rho)}_{\lambda_{f_2}\lambda'_p\lambda_\gamma\lambda_p}$. The contribution of the amplitude $\hat{M}^{(\rho)}_{2\frac{1}{2}1\frac{1}{2}}$ to the cross section for the reaction $\gamma p \longrightarrow f_2 p$ is quadrupled upon taking into account the exchange of the ω Regge pole. Assuming that the trajectories of the ρ and ω poles are identical,

$\alpha_\omega(t) = \alpha_\rho(t)$, and that, as in the naive quark model, $\hat{V}^{(\omega)}_{\lambda_{f_2}\lambda_\gamma}(t) = \hat{V}^{(\rho)}_{\lambda_{f_2}\lambda_\gamma}(t)/3$ [see also (1)] and $\hat{V}^{(\omega)}_{\lambda'_p = \frac{1}{2},\, \lambda_p = \frac{1}{2}}(t) = 3\hat{V}^{(\rho)}_{\lambda'_p = \frac{1}{2},\, \lambda_p = \frac{1}{2}}(t)$, we do indeed obtain $\hat{M}^{(\omega)}_{2\frac{1}{2}1\frac{1}{2}} = \hat{M}^{(\rho)}_{2\frac{1}{2}1\frac{1}{2}}$. At the same time, we can disregard the amplitude of ω exchange accompanied by helicity flip in the nucleon vertex, since $\hat{V}^{(\omega)}_{1\frac{1}{2}-\frac{1}{2}}(t) \ll \hat{V}^{(\rho)}_{1\frac{1}{2}-\frac{1}{2}}(t)$ and $\hat{V}^{(\omega)}_{1\frac{1}{2}-\frac{1}{2}}(t)/\sqrt{-t/1\ \mathrm{GeV}^2} \ll \hat{V}^{(\omega)}_{1\frac{1}{2}\frac{1}{2}}(t)$ (see, for example, [31–34]). For the reaction $\gamma p \longrightarrow f_2 p$, we eventually find that

$$\sigma(\gamma p \longrightarrow f_2 p) = \frac{1}{16\pi s^2}\int\left[4\left|\hat{M}^{(\rho)}_{2\frac{1}{2}1\frac{1}{2}}\right|^2 + \left|\hat{M}^{(\rho)}_{2\frac{1}{2}1-\frac{1}{2}}\right|^2\right]dt$$

$$= 4\sigma^{(\rho)}_{nf}\left(1 + \frac{1}{4}R\right), \tag{5}$$

where integration is performed over the region $0 < -t < 1\ \mathrm{GeV}^2$, which makes the leading contribution to the cross section; $\sigma^{(\rho)}_{nf}$ is the cross section associated with the amplitude of ρ exchange not accompanied by helicity flip in the nucleon vertex; and $R = \sigma^{(\rho)}_f/\sigma^{(\rho)}_{nf}$ is the ratio of the cross section $\sigma^{(\rho)}_f$ associated with the amplitude of ρ exchange accompanied by helicity flip in the nucleon vertex to $\sigma^{(\rho)}_{nf}$. In order to estimate the quantity R, we invoke data on the cross section for the reaction $\pi^- p \longrightarrow \pi^0 n$, which are well described in terms of the exchange of the ρ Regge pole [35]. Assuming, along with the factorization of the residues, approximate equality of the slopes, Λ, for the Regge amplitudes of interest[2] and using the results presented in [35], we arrive at $R \approx \sigma^{(\rho)}_f(\pi^- p \longrightarrow \pi^0 n)/\sigma^{(\rho)}_{nf}(\pi^- p \longrightarrow \pi^0 n) \approx 1.5$. We note that this value of R can be treated as a lower bound since R is proportional to $1/2\Lambda$ and since, for the reaction of $\pi^- p$ charge exchange at 6 GeV [35], $2\Lambda \approx 9\ \mathrm{GeV}^{-2}$, which is generally greater than the corresponding values in many other similar reactions.

According to quark-counting rules, the amplitudes of ρ exchange in the reaction $\gamma p \longrightarrow a_2^0 p$ is one-third as great as that in the reaction $\gamma p \longrightarrow f_2 p$, while the amplitude of ω exchange not accompanied by proton-helicity flip is three times as great [see also (1)]; that is, the reaction $\gamma p \longrightarrow a_2^0 p$ is dominated by ω exchanges.

---

[2]Here, we imply a conventional exponential parametrization, according to which any Regge amplitude is taken to be proportional to $e^{\Lambda t}$, with the slope being given by $\Lambda = \Lambda^0 + \alpha'\ln(s/s_0)$, where α' is the slope of the Regge pole trajectory, $s_0 = 1\ \mathrm{GeV}^2$, and Λ^0 is determined from a fit to data.

Considering also that, in the reaction $\gamma p \longrightarrow f_2 p$, $\hat{M}^{(\omega)}_{2\frac{1}{2}1\frac{1}{2}} = \hat{M}^{(\rho)}_{2\frac{1}{2}1\frac{1}{2}}$, we find that the cross section for the reaction $\gamma p \longrightarrow a_2^0 p$ is given by

$$\sigma(\gamma p \longrightarrow a_2^0 p)$$

$$= \frac{1}{16\pi s^2}\int\left[\frac{100}{9}\left|\hat{M}^{(\rho)}_{2\frac{1}{2}1\frac{1}{2}}\right|^2 + \frac{1}{9}\left|\hat{M}^{(\rho)}_{2\frac{1}{2}1-\frac{1}{2}}\right|^2\right]dt \tag{6}$$

$$= \frac{100}{9}\sigma^{(\rho)}_{nf}\left(1 + \frac{1}{100}R\right) \approx \frac{100}{9}\sigma^{(\rho)}_{nf}.$$

We further note that ω and ρ exchanges are precisely in the same ratio in the reaction $\gamma p \longrightarrow a_2^0 p$ as in the reaction $\gamma p \longrightarrow \pi^0 p$, these exchanges being dominant in the cross section for the latter reaction [32–34, 36–38]. Moreover, the helicities change by unity in the meson vertices both in the reaction $\gamma p \longrightarrow \pi^0 p$ and in our model for the reaction $\gamma p \longrightarrow a_2^0 p$ (and in the reaction $\gamma p \longrightarrow f_2 p$ as well), and all the corresponding vertices are proportional to $\sqrt{-t}$. Defining the amplitude for the decay $\omega \longrightarrow \pi^0\gamma$ in a conventional way, $g_{\omega\gamma\pi}\varepsilon_{\mu\nu\tau\kappa}\epsilon^{\lambda_\omega}_\mu(k_\omega)k_{\omega\nu}\epsilon^{\lambda^*_\gamma}_\tau(k_\gamma)k_{\gamma\kappa}$, we can easily verify that, in the case of elementary ω and ρ exchanges, we have $\sigma(\gamma p \longrightarrow a_2^0 p)/\sigma(\gamma p \longrightarrow \pi^0 p) = g^2_{a_2\gamma\omega}/g^2_{\omega\gamma\pi}$ without any numerical factors. In the actual case of Reggeized ρ and ω exchanges, it is therefore reasonable to assume fulfillment of the estimate

$$\frac{\sigma(\gamma p \longrightarrow a_2^0 p)}{\sigma(\gamma p \longrightarrow \pi^0 p)} = \frac{g^2_{a_2\gamma\omega}}{g^2_{\omega\gamma\pi}}\frac{\Lambda^2_\pi}{\Lambda^2_{a_2}}, \tag{7}$$

where Λ_π and Λ_{a_2} are the Regge slopes of the amplitudes for the photoproduction of π^0 and a_2^0, respectively. There is no information about Λ_{a_2}. For this reason, we tentatively set $\Lambda_{a_2} \approx \Lambda_\pi/1.225$ or $\Lambda^2_\pi/\Lambda^2_{a_2} \approx 1.5$. We also have $\sigma(\gamma p \longrightarrow \pi^0 p) \approx 0.32\ \mu\mathrm{b}$ at 6 GeV [36–38] and $g^2_{\omega\gamma\pi}/4\pi \approx 0.0394\ \mathrm{GeV}^{-2}$ [17]. Taking into account this and relations (1), (2), (5), and (6) and considering that $R \approx 1.5$ at $E_\gamma \approx 6$ GeV, we can expect that $\sigma(\gamma p \longrightarrow f_2 p) \approx 0.12\ \mu\mathrm{b}$ and $\sigma(\gamma p \longrightarrow a_2^0 p) \approx 0.25\ \mu\mathrm{b}$. Our estimates are compatible both with extremely scanty data existing at present and with constraints on the cross sections for the reactions $\gamma p \longrightarrow f_2 p$ and $\gamma p \longrightarrow a_2^0 p$ [39–41]. As a matter of fact, reliable measurements for the above two processes have not yet been performed.

Similar considerations for $\gamma N \longrightarrow X^\pm N \longrightarrow \rho^\pm \rho^0 N$ reactions lead to the estimate

$$\sigma(\gamma p \longrightarrow X^+ n \longrightarrow \rho^+ \rho^0 n)$$

$$= \sigma(\gamma n \longrightarrow X^- p \longrightarrow \rho^- \rho^0 p)$$

$$\approx \frac{9}{50}\sigma(\gamma p \longrightarrow a_2^0 p)(1 + R)\frac{g_{X^\pm \gamma \rho^\pm}^2 \mathrm{Br}(X^\pm \longrightarrow \rho^\pm \rho^0)}{g_{f_2 \gamma \rho}^2} \quad (8)$$

$$\approx 0.018 \ \mu b.$$

In order to avoid invoking additional model arguments, we estimated here the quantity $(g_{X^+ \gamma \rho^\pm}^2/4\pi)\mathrm{Br}(X^\pm \longrightarrow \rho^\pm \rho^0)$ on the basis of data on the cross section $\sigma(\gamma\gamma \longrightarrow \rho^0 \rho^0)$ [7], which are presented in the figure. In doing this, we made use of the following chain of equalities:

$$\frac{g_{X^\pm \gamma \rho^\pm}^2}{4\pi}\mathrm{Br}(X^\pm \longrightarrow \rho^\pm \rho^0) = \frac{9}{8}\frac{g_{X^0 \gamma \rho^0}^2}{4\pi}\mathrm{Br}(X^0 \longrightarrow \rho^0 \rho^0)$$

$$= \frac{9}{8}\left(\frac{f_\rho}{e}\right)^2 \frac{g_{X^0 \gamma\gamma}^2}{4\pi}\mathrm{Br}(X^0 \longrightarrow \rho^0 \rho^0) \quad (9)$$

$$\approx \frac{9}{8}\left(\frac{f_\rho}{e}\right)^2 \frac{4}{\pi^2 \bar{m}}\left(\frac{1}{2}\int_{1.2 \text{ GeV}}^{2.2 \text{ GeV}} \sigma(\gamma\gamma \longrightarrow \rho^0 \rho^0)dW_{\gamma\gamma}\right)$$

$$\approx 0.00336 \text{ GeV}^{-2}.$$

Here, $\bar{m} \approx 1.6$ GeV is the mean mass of the enhancement that is observed in the reaction $\gamma\gamma \longrightarrow \rho^0 \rho^0$; the integral of the cross section is about 33.2 nb GeV; and we assumed on the basis of experience gained in the previous analyses from [11, 12] that approximately half of this quantity is due to the contribution of the X^0 resonance.

The cross sections for the reactions $\gamma N \longrightarrow X^\pm \Delta \longrightarrow \rho^\pm \rho^0 \Delta$ can be estimated at $\sigma(\gamma p \longrightarrow X^- \Delta^{++} \longrightarrow \rho^- \rho^0 \Delta^{++}) = \sigma(\gamma n \longrightarrow X^+ \Delta^- \longrightarrow \rho^+ \rho^0 \Delta^-) = 3\sigma(\gamma p \longrightarrow X^+ \Delta^0 \longrightarrow \rho^+ \rho^0 \Delta^0) = 3\sigma(\gamma n \longrightarrow X^- \Delta^+ \longrightarrow \rho^- \rho^0 \Delta^+) \approx 0.031 \ \mu b$. This estimate was obtained by merely multiplying the estimate in (8) by 1.75. In doing this, we considered that, in the region around 6 GeV, the cross section for the reaction $\pi^+ p \longrightarrow \pi^0 \Delta^{++}$ featuring, in the t channel, the quantum numbers of the ρ Regge pole [42, 43] is 1.5–2 times as large as the cross section for the reaction $\pi^- p \longrightarrow \pi^0 n$ governed by a similar mechanism [35, 43]. Apart from one-pion-exchange contributions, the cross sections for the reactions $\gamma p \longrightarrow \rho^- \Delta^{++}$ and $\gamma N \longrightarrow \rho^\pm N$ are in the same proportion [44, 45].

At the JLAB facility, about 30 ϕ mesons per second must be produced in the reaction $\gamma p \longrightarrow \phi p$, whose cross section at $E_\gamma \approx 6$ GeV is $\sigma(\gamma p \longrightarrow \phi p) \approx 0.5 \ \mu b$ [1, 2]; that is, 77.8×10^6 events of the reaction $\gamma p \longrightarrow \phi p$ can be accumulated over one month of operation. According to the estimate in (8), we can then expect

approximately 2.8×10^6 events of the reaction $\gamma N \longrightarrow X^\pm N \longrightarrow \rho^\pm \rho^0 N$ over the same period of time. Of course, we mean here the number of $\gamma N \longrightarrow X^\pm N \longrightarrow \rho^\pm \rho^0 N \longrightarrow \pi^\pm \pi^0 \pi^+ \pi^- N$ events that can be accumulated at a 100% detection efficiency. In all probability, the actual detection efficiency of the JLAB facility will be about 10% [1, 2]. For the sake of comparison, we indicate that the total statistics for the reaction $\gamma\gamma \longrightarrow \pi^+ \pi^- \pi^+ \pi^-$ studied in the TASSO, CELLO, TPC/2γ, PLUTO, and ARGUS experiments includes 15242 events [11]. At JLAB, it is planned to obtain about 10^3, 10^4, and 10^5 events of ϕ-meson decays whose branching ratios are Br $\approx 10^{-4}$–10^{-2} [1, 2]. On this scale, the cross-section values indicated in (8) are large, and expected significant statistics corresponding to them must be of use. In order to obtain unambiguous signals from exotic states $X^\pm$ in the $\pi^\pm \pi^0 \pi^+ \pi^-$ channels, it is necessary to solve the important problem of isolating them among all possible $\pi^\pm \pi^0 \pi^+ \pi^-$ events, but this is a rather complicated problem. We proceed to discuss it immediately below.

4. SEPARATION OF SIGNALS FROM $X^\pm(1600, 2^+(2^{++}))$ STATES

Let us consider $\gamma N \longrightarrow \pi^\pm \pi^0 \pi^+ \pi^- N$ reactions. First of all, it is necessary to establish channels through which these processes proceed, to assess the relevant partial cross sections, and to devise the simplest means for separating the channels. We note that comprehensive discussions on special methods for isolating more than ten channels in the allied reactions $\gamma p \longrightarrow 4\pi p$ can be found in [21–26, 46]. In Table 2, we compiled available data on $\gamma N \longrightarrow \pi^\pm \pi^0 \pi^+ \pi^- N$ reactions at mean photon energies ranging from 3.9 to 8.9 GeV [47–53]. It can be seen that these data are rather scanty and need refinement.

Let us go over to phenomenological estimates. For the sake of definiteness and without mentioning this in the following, we will consider the reaction $\gamma p \longrightarrow \pi^+ \pi^0 \pi^+ \pi^- n$ and its channels at $E_\gamma \approx 6$ GeV (however, all our conclusions will apply to the reaction $\gamma n \longrightarrow \pi^- \pi^0 \pi^+ \pi^- p$ as well). Should the need arise, we will extrapolate data on the cross sections to $E_\gamma \approx 6$ GeV, assuming that $\sigma \sim E_\gamma^n$, where $n = -2$ and -1 for, respectively, the mechanism of one-pion exchange (OPE) and the mechanism of ρ, a_2, or ω exchanges. We begin by considering the channel $\gamma p \longrightarrow \omega \Delta^+ \longrightarrow \omega \pi^+ n$. Assuming the dominance of the OPE mechanism and approximate equality of the slopes of the Regge reaction amplitudes and using data from [43, 54], we obtain the estimate

$$\sigma(\gamma p \longrightarrow \omega \Delta^+ \longrightarrow \omega \pi^+ n)$$

$$\approx \sigma^{(\text{OPE})}(\gamma p \longrightarrow \omega p)\frac{4}{9}\frac{\sigma(\pi^+ p \longrightarrow \rho^0 \Delta^{++})}{\sigma(\pi^- p \longrightarrow \rho^0 n)} \quad (10)$$

$$\approx (0.6 \ \mu b)\frac{4}{9}2 \approx 0.53 \ \mu b.$$

Table 2. Total and partial cross sections for $\gamma N \longrightarrow \pi^{\pm}\pi^0\pi^+\pi^- N$ reactions

E_γ, GeV	Reaction [47]	Cross section, μb	E_γ, GeV	Reaction [48–53]	Cross section, μb
4.3	$\gamma n \longrightarrow \pi^-\pi^0\pi^+\pi^- p$	7.5 ± 1.0	6.9–8.1	$\gamma n \longrightarrow \pi^-\pi^0\pi^+\pi^- p$	4.85 ± 0.89
	$\gamma n \longrightarrow \omega\pi^- p$	1.4 ± 0.5	3.6–5.1	$\gamma n \longrightarrow \pi^-\pi^0\pi^+\pi^- p$	11.0 ± 2.2
	$\gamma n \longrightarrow \rho^-\pi^+\pi^- p$	1.1 ± 0.5	7.5	$\gamma n \longrightarrow \pi^-\pi^0\pi^+\pi^- p$	6.1 ± 0.8
	$\gamma n \longrightarrow \rho^0\pi^0\pi^- p$	1.8 ± 1.0	2.5–5.3	$\gamma n \longrightarrow \omega\pi^- p$	1.6 ± 0.5
	$\gamma n \longrightarrow \rho^+\pi^-\pi^- p$	0.5 ± 0.5	4.2–4.8	$\gamma p \longrightarrow \omega\Delta^+ \longrightarrow \omega\pi^+ n$	0.83 ± 0.10
	$\gamma n \longrightarrow \pi^+\pi^-\pi^0\Delta^0$	0.6 ± 0.6	8.9	$\gamma N \longrightarrow \omega\Delta \longrightarrow \omega\pi^{\pm} N$	0.24 ± 0.023

If we assume that the whole channel $\gamma p \longrightarrow \omega\pi^+ n$ is dominated by one-pion exchange between $\gamma\omega$ and $p\pi^+ n$ vertices, then the use of data on the reaction $\gamma n \longrightarrow \omega\pi^- p$ [47] from Table 2 yields $\sigma(\gamma p \longrightarrow \omega\pi^+ n) \approx (1.4 \pm 0.5)$ μb $\times (4.3/6)^2 \approx 0.72 \pm 0.26$ μb. Owing to the fact that the ω resonance is narrow, the $\omega\pi^+ n$ channel can be isolated quite straightforwardly by cutting an appropriate interval in the invariant-mass spectrum of the $\pi^+\pi^-\pi^0$ system.

The C-odd $\pi^+\pi^-\pi^0$ system can be produced in the reaction $\gamma p \longrightarrow \pi^+\pi^0\pi^+\pi^- n$ with a still larger cross section owing to the contribution of the $h_1(1170)$ resonance decaying into $\rho\pi$ [17]. Taking into account the contribution of the OPE mechanism, we do indeed have

$$\sigma(\gamma p \longrightarrow h_1\pi^+ n) \approx \sigma(\gamma p \longrightarrow \omega\pi^+ n)(\Gamma_{h_1\gamma\pi}/\Gamma_{\omega\gamma\pi}) \quad (11)$$
$$\approx (1.48\text{--}2) \text{ μb.}$$

Here, we have used the above estimates for $\sigma(\gamma p \longrightarrow \omega\pi^+ n)$ and the relation $\Gamma_{h_1\gamma\pi} \approx 9\Gamma_{b_1\gamma\pi} \approx 9 \times 0.23$ MeV ≈ 2 MeV [17], which is valid in the case of ideal mixing in the $J^{PC} = 1^{+-}$ nonet. Since each channel of the decay $h_1 \longrightarrow \rho\pi \longrightarrow 3\pi$ such that the corresponding two-pion mass spectra show a ρ^+, a ρ^-, or a ρ^0 resonance (with accompanying kinematical reflections) features 1/3 of the events, we have, for example, $\sigma(\gamma p \longrightarrow h_1\pi^+ n \longrightarrow \rho^-\pi^+\pi^+ n) \approx (0.49\text{--}0.67)$ μb. We note that, in the reaction $\gamma p \longrightarrow \rho^-\pi^+\pi^+ n$, there is naturally no channel involving a negative ρ meson, $\gamma p \longrightarrow X^+ n \longrightarrow \rho^+\rho^0 p$. Therefore, a thorough analysis of $\gamma p \longrightarrow \rho^-\pi^+\pi^+ n$ events [which may also appear as $\gamma p \longrightarrow \rho^+\pi^-\pi^+ n$ events from the decays of a_1^0, a_2^0, π_2^0, and $\pi^0(1300)$ resonances[3)] produced in association with the $\pi^+ n$ system owing to ω and ρ exchanges] must make it possible to isolate reliably the $\rho^{\mp}\pi^{\pm}\pi^+ n$ and $\rho^0\pi^0\pi^+ n$ channels, which are of the origin indicated above. As can be seen from (10) and (11), these channels, together with the ω-production channel, can contribute 2 to 2.5 μb to the cross section for the reaction $\gamma p \longrightarrow \pi^+\pi^0\pi^+\pi^- n$.

[3)]Estimates show that the cross sections for the production of these resonances in the reaction $\gamma p \longrightarrow \pi^+\pi^0\pi^+\pi^- n$ are small.

The above analysis has dealt with channels involving the peripheral production of a neutral three-pion system. We will now consider the peripheral production of the $\pi^+\pi^-\pi^+$ system, in which case the a_1^+, a_2^+, π_2^+, and $\pi^+(1300)$ resonances can manifest themselves; our attention will be focused primarily on the reaction $\gamma p \longrightarrow \pi^+\pi^-\pi^+\Delta^0 \longrightarrow \pi^+\pi^-\pi^+\pi^0 n$. By using data from [21–23, 40, 41, 46, 55] on the reaction $\gamma p \longrightarrow \pi^+\pi^-\pi^-\Delta^{++}$ at $E_\gamma < 10$ GeV and assuming a peripheral character of Δ^{++} production, we can obtain the tentative estimate

$$\sigma(\gamma p \longrightarrow \pi^+\pi^-\pi^+\Delta^0 \longrightarrow \pi^+\pi^-\pi^+\pi^0 n)$$
$$\approx (2/9)\sigma(\gamma p \longrightarrow \pi^+\pi^-\pi^-\Delta^{++}) \approx (0.37\text{--}0.61) \text{ μb.} \quad (12)$$

It is clear that there is at least one method for isolating such events, that employing the signatures of the Δ^0 resonance. The production of Δ^+ in γp collisions is accompanied by the formation of the $\pi^+\pi^-\pi^0$ system (see above). (For the analogous channel in γn collisions, $\gamma n \longrightarrow \pi^+\pi^-\pi^0\Delta^0$, the cross section can be found in Table 2.) The $\pi^+\pi^0\pi^+\Delta^-$ final state must also be studied thoroughly. A manifestation of the $\rho^+\pi^+\Delta^-$ channel, which may be responsible for the excessive production of ρ^+ in relation to ρ^-, is quite possible here. It is rather hard to estimate the possible cross section for the channel $\gamma p \longrightarrow \rho^+\pi^+\Delta^-$. The same can be said about the cross section for the production of the $a_2^+\pi^0 n$ system, where the $\pi^0 n$ subsystem has an isospin of 1/2, and about the cross section for the channel $\gamma p \longrightarrow \rho^0\pi^+\pi^0 n$ involving a diffractively produced ρ^0 resonance.

Let us finally proceed to consider the channels of the peripheral production of the four-pion system $\pi^+\pi^0\pi^+\pi^-$. Of greatest interest here is the contribution from the production of the intermediate state ρ'^+. Unfortunately, this contribution can be estimated only on the basis of more or less plausible assumptions eventually amounting to the conjecture that the relation between the cross sections for the quasielastic reactions $\gamma p \longrightarrow \rho^0 p$ and $\gamma p \longrightarrow \rho'^0 p$ is nearly identical to the relation between the cross sections for the charge-exchange reactions $\gamma p \longrightarrow \rho^+ n$ and $\gamma p \longrightarrow \rho'^+ n$. Suppose that this is indeed the case. At $E_\gamma \approx 6$ GeV, we rely on the values of $\sigma(\gamma p \longrightarrow \rho^0 p) \approx 15$ μb [56], $\sigma(\gamma N \longrightarrow \rho^{\pm} N) \approx 0.58$ μb

(this cross section is determined primarily by ρ exchange) [44, 45], and $\sigma(\gamma p \longrightarrow \rho'^0 p \longrightarrow \pi^+\pi^-\pi^+\pi^- p) \approx 1.5$ μb [21–23]. It follows that $\sigma(\gamma p \longrightarrow \rho'^0 p \longrightarrow \pi^+\pi^-\pi^+\pi^- p)/\sigma(\gamma p \longrightarrow \rho^0 p) \approx 1/10$; according to our assumption, we then have

$$\sigma(\gamma p \longrightarrow \rho'^+ n \longrightarrow \pi^+\pi^0\pi^+\pi^- n)$$

$$\approx \frac{1}{10}\sigma(\gamma p \longrightarrow \rho^+ n)\begin{cases}1\\3/2\end{cases} \approx (0.058\text{–}0.087)\ \mu\text{b}, \tag{13}$$

where the factor of 1 corresponds to the model of the decay $\rho' \longrightarrow 4\pi$ through the $\rho\sigma$ intermediate state (σ is the S wave of the $I = 0$ $\pi\pi$ system), while the factor of 3/2 corresponds to the model of the decay $\rho' \longrightarrow 4\pi$ through the $a_1\pi$ intermediate state. Let us discuss the assumptions that resulted in the approximate equality of the ratios $\sigma(\gamma p \longrightarrow \rho'^0 p)/\sigma(\gamma p \longrightarrow \rho^0 p)$ and $\sigma(\gamma p \longrightarrow \rho'^+ n)/\sigma(\gamma p \longrightarrow \rho^+ n)$. There are two of these: (i) validity of the diagonal VDM for the amplitudes of Regge exchanges, both with vacuum and with nonvacuum quantum numbers, in the reactions $\gamma N \longrightarrow \rho N$ and $\gamma N \longrightarrow \rho' N$ and (ii) universality of ρ-Reggeon coupling to hadrons. As applied to the reactions $\gamma p \longrightarrow \rho^0 p$ and $\gamma p \longrightarrow \rho'^0 p$, the diagonal VDM was discussed in [22, 24, 25, 56, 57], where it was actually demonstrated that, with allowance for some natural relations like $\sigma_{\text{tot}}(\rho N) \approx \sigma_{\text{tot}}(\rho' N) \approx \sigma_{\text{tot}}(\pi N)$, this model allows one to explain reasonably well the magnitude of the cross section for the process $\gamma p \longrightarrow \rho'^0 p$. On the other hand, the fact that there is no evidence for the decay $\rho' \longrightarrow \rho\rho$ also favors the choice of diagonal vector dominance as a mechanism that determines the $\gamma(\rho^+)\rho'^+$ vertex, where (ρ^+) is a Reggeon. Supplementing this with assumption (ii) on ρ universality—that is, with the assumption that the $\rho^0(\rho^+)\rho^+$ and $\rho'^0(\rho^+)\rho'^+$ vertices, where (ρ^+) is again a Reggeon, are approximately equal to each other—we arrive at the estimate in (13).

In passing, we note that the expected suppression of the cross section for the reaction $\gamma p \longrightarrow \rho'^+ n \longrightarrow \pi^+\pi^0\pi^+\pi^- n$ in relation to the channel $\gamma p \longrightarrow \rho'^0 p \longrightarrow \pi^+\pi^-\pi^+\pi^- p$ is one of the main reasons why we propose seeking, in photoproduction reactions, $X^\pm$ states rather than the X^0 state.[4]

Comparing the estimates in (8) and (13), we conclude that, if events featuring the peripheral production of the $\pi^\pm\pi^0\pi^+\pi^-$ systems can be singled out in the reaction $\gamma p \longrightarrow \pi^+\pi^0\pi^+\pi^- n$ or in the reaction $\gamma n \longrightarrow \pi^-\pi^0\pi^+\pi^- p$, then it is quite possible to separate the $\rho'^\pm$ and $X^\pm$ contributions in the case of expected large statistics. For this, it would be necessary to perform a comprehensive global analysis of all two-pion and

three-pion mass spectra—for example, of those for the $\pi^+\pi^0$, $\pi^+\pi^-$, $\pi^+\pi^+$, $\pi^0\pi^-$, $\pi^+\pi^+\pi^0$, $\pi^+\pi^+\pi^-$, and $\pi^+\pi^-\pi^0$ systems in the reactions $\gamma p \longrightarrow \pi^+\pi^0\pi^+\pi^- n$—and of all relevant angular distributions. We note that a simulation of the angular and mass distributions for the decays $X \longrightarrow \rho\rho \longrightarrow 4\pi$ is described in detail elsewhere [6–11]. The presence of incident-photon polarization, if any, will facilitate considerably the separation of the $\rho'^\pm$ and $X^\pm$ signals. It is well known that a polarized photon beam will be employed in the facility at JLAB [4].

In investigating the ρ'^0 resonance in the reactions $\gamma p \longrightarrow \pi^+\pi^-\pi^+\pi^- p$ and $\gamma p \longrightarrow \pi^+\pi^0\pi^-\pi^0 p$, no dedicated attempts have been made to single out the possible contribution of the $\rho_3^0(1690)$ state [27]. In principle, we can hope that $\sigma(\gamma p \longrightarrow \rho_3^+ n)$ will be approximately one order of magnitude smaller than $\sigma(\gamma p \longrightarrow \rho'^+ n)$ if there is a universal relation between the Pomeron contribution and the contribution of the f_2 Regge pole in the reactions $\gamma p \longrightarrow \rho^0 p$ and $\gamma p \longrightarrow \rho_3^0 p$ and if exchange degeneracy [33] and the naive quark-counting rules are valid for ρ, a_2, and f_2 exchanges in the transition $\gamma N \longrightarrow \rho_3 N$.

The data in Table 2 suggest that, at $E_\gamma \approx 6$ GeV, $\sigma(\gamma N \longrightarrow \pi^\pm\pi^0\pi^+\pi^- N) \approx 7$ μb. Our analysis reveals that a small number of processes characterized by sizable cross sections and governed by relatively simple mechanisms account here for approximately 3 μb. The rest of the total cross section probably receives contributions from a greater number of less significant channels, whose incomplete list has been given above. In this sense, the analysis presented here is only preliminary. Of course, advances in determining the cross sections for individual channels and in establishing their probable mechanisms will soon be made owing to high-statistics experiments at modern facilities employing intense photon beams.

Let us briefly dwell upon the reaction $\gamma p \longrightarrow \pi^-\pi^0\pi^+\pi^- \Delta^{++}$ as well. Data that we know for it at incident-photon energies below 10 GeV [40, 41, 58, 59] are compiled in Table 3. The most probable value determined on this basis for the cross section $\sigma(\gamma p \longrightarrow \pi^-\pi^0\pi^+\pi^- \Delta^{++})$ is 1.87 ± 0.38 μb. As can be seen from

---

[4] In this connection, we also note the relation $\sigma(\gamma N \longrightarrow X^0 N \longrightarrow \rho^0\rho^0 N)/\sigma(\gamma N \longrightarrow X^\pm N \longrightarrow \rho^\pm\rho^0 N) = 4/9$ and the possibility of an additional background in the channel $\rho^0\rho^0 \longrightarrow \pi^+\pi^-\pi^+\pi^-$ from $I = 0$ states.

Table 3. Total cross section for the reaction $\gamma p \longrightarrow \pi^-\pi^0\pi^+\pi^- \Delta^{++}$ and cross section for the channel $\gamma p \longrightarrow \omega\pi^-\Delta^{++}$

E_γ, GeV	$\sigma(\gamma p \longrightarrow \pi^-\pi^0\pi^+\pi^- \Delta^{++})$, μb	$\sigma(\gamma p \longrightarrow \omega\pi^-\Delta^{++})$, μb	References
4.3	2.4 ± 0.8	≈ 1	[41]
4–6	$1.3 \pm 0.3 \pm 0.2$	–	[58]
4.5–5.8	$\leq 2.4 \pm 1.1$	–	[59]
5.25	3.9 ± 1.5	0.5 ± 0.2	[40]

Table 3, the only partial channel $\gamma p \longrightarrow \omega \pi^- \Delta^{++}$ observed experimentally [40, 41] can contribute no more than 1 μb to $\sigma(\gamma p \longrightarrow \pi^- \pi^0 \pi^+ \pi^- \Delta^{++})$. The cross section for the channel $\gamma p \longrightarrow \rho'^- \Delta^{++} \longrightarrow \pi^- \pi^0 \pi^+ \pi^- \Delta^{++}$ can be estimated by multiplying the cross-section values from (13) by the coefficient 1.75, in just the same way as this was done in Section 3 in going over from the estimate in (8) to the case of $X^- \Delta^{++}$ production. In this way, we obtain $\sigma(\gamma p \longrightarrow \rho'^- \Delta^{++} \longrightarrow \pi^- \pi^0 \pi^+ \pi^- \Delta^{++}) \approx$ (0.1–0.15) μb. In what is concerned with background conditions, the reaction featuring the production of Δ^{++} can in principle prove to be convenient for recording the X^- state, since only a few channels contribute to this reaction.

REFERENCES

1. A. R. Dzierba, in *Proceedings of the Second Workshop on Physics and Detectors for DAΦNE'95, Frascati, 1995*, Ed. by R. Baldini, F. Bossi, G. Capon, and G. Pancheri, Frascati Phys. Ser. **4**, 99 (1996).

2. A. R. Dzierba, in *Proceedings of the First Workshop on Hadron Dynamics with the New DAΦNE and CEBAF Facilities, Frascati, 1996*, Ed. by R. Baldini, E. De Sanctis, G. Pancheri, and G. Ricco, Nucl. Phys. A **623**, 142 (1997); G. S. Adams, Nucl. Phys. A **623**, 158 (1997).

3. P. R. Page, Phys. Lett. B **415**, 205 (1997); A. Afanasev and P. R. Page, Phys. Rev. D **57**, 6771 (1998).

4. J. Napolitano, in *Proceedings of the Jefferson Lab/NCSU Workshop on Hybrids and Photoproduction Physics, JLAB, 1997*, p. 1; T. Barnes, in *Proceedings of the Jefferson Lab/NCSU Workshop on Hybrids and Photoproduction Physics, JLAB, 1997*, p. 37; G. Blackett *et al.*, in *Proceedings of the Jefferson Lab/NCSU Workshop on Hybrids and Photoproduction Physics, JLAB, 1997*, p. 287; R. T. Jones, in *Proceedings of the Jefferson Lab/NCSU Workshop on Hybrids and Photoproduction Physics, JLAB, 1997*, p. 369; V. D. Burkert and R. Ent, in *Proceedings of the Jefferson Lab/NCSU Workshop on Hybrids and Photoproduction Physics, JLAB, 1997*, p. 385; P. Page, in *Proceedings of the Jefferson Lab/NCSU Workshop on Hybrids and Photoproduction Physics, JLAB, 1997*, p. 589.

5. Particle Data Group (R. M. Barnett *et al.*), Phys. Rev. D **54**, 1 (1996).

6. R. Brandelik *et al.*, Phys. Lett. **97B**, 448 (1980); D. L. Burke *et al.*, Phys. Lett. **103B**, 153 (1981); M. Althoff *et al.*, Z. Phys. C **16**, 13 (1982); H.-J. Behrend *et al.*, Z. Phys. C **21**, 205 (1984); Ch. Berger *et al.*, Z. Phys. C **38**, 521 (1988); H. Aihara *et al.*, Phys. Rev. D **37**, 28 (1988).

7. H. Albrecht *et al.*, Z. Phys. C **50**, 1 (1991).

8. H. Kolanoski, in *Proceedings of the 5th International Workshop on Photon–Photon Collisions, Aachen, 1983*, Ed. by Ch. Berger, Lect. Notes Phys. **191**, 175 (1983); H. Albrecht *et al.*, Phys. Lett. B **217**, 205 (1989); H.-J. Behrend *et al.*, Phys. Lett. B **218**, 493 (1989).

9. H. Albrecht *et al.*, Phys. Lett. B **267**, 535 (1991).

10. M. Poppe, Int. J. Mod. Phys. A **1**, 545 (1986); Ch. Berger and W. Wagner, Phys. Rep. **146**, 1 (1987); J. Olsson, in *Proceedings of the International Symposium on Lepton and Photon Interactions at High Energies, Hamburg, 1987*, Ed. by W. Bartel and R. Rückl (North-Holland, Amsterdam, 1987), p. 613; A. Buijs, PhD Thesis (Utrecht, 1987); H. Kolanoski and P. Zerwas, *High Energy Electron–Positron Physics*, Ed. by A. Ali and P. Söding (World Sci., Singapore, 1988); H. Albrecht *et al.*, Phys. Rep. **276**, 223 (1996); S. Godfrey and J. Napolitano, hep-ph/9811410, 1998 (submitted for publication in Rev. Mod. Phys.).

11. N. N. Achasov and G. N. Shestakov, Usp. Fiz. Nauk **161** (6), 53 (1991) [Sov. Phys. Usp. **34**, 471 (1991)]; Phys. Rev. D **52**, 6291 (1995).

12. N. N. Achasov, S. A. Devyanin, and G. N. Shestakov, Phys. Lett. **108B**, 134 (1982); Z. Phys. C **16**, 55 (1982); **27**, 99 (1985).

13. B. A. Li and K. F. Liu, Phys. Lett. **118B**, 435 (1982); Erratum: **124B**, 550 (1983); Phys. Rev. Lett. **51**, 1510 (1983).

14. R. L. Jaffe, Phys. Rev. D **15**, 267, 281 (1977).

15. S.-U. Chung, in *Proceedings of the 6th International Conference on Hadron Spectroscopy, HADRON'95, Manchester, 1995*, Ed. by M. C. Birse, G. D. Lafferty, and J. A. McGovern (World Sci., Singapore, 1996), p. 19.

16. N. N. Achasov and G. N. Shestakov, Int. J. Mod. Phys. A **7**, 4313 (1992).

17. Particle Data Group (C. Caso *et al.*), Eur. Phys. J. C **3**, 1 (1998).

18. N. N. Achasov and G. N. Shestakov, Phys. Rev. D **56**, 212 (1997).

19. N. N. Achasov and A. A. Kozhevnikov, Phys. Rev. D **55**, 2663 (1997).

20. Particle Data Group (C. G. Wohl *et al.*), Rev. Mod. Phys. **56**, S1 (1984).

21. H. Bingham *et al.*, Phys. Lett. **41B**, 653 (1972).

22. M. Davier *et al.*, Nucl. Phys. B **58**, 31 (1973).

23. P. Schacht *et al.*, Nucl. Phys. B **81**, 205 (1974).

24. D. P. Barber *et al.*, Z. Phys. C **4**, 169 (1980).

25. D. Aston *et al.*, Nucl. Phys. B **189**, 15 (1981).

26. M. Atkinson *et al.*, Z. Phys. C **26**, 499 (1985); **30**, 531 (1986).

27. A. B. Clegg and A. Donnachie, Z. Phys. C **62**, 455 (1994); A. Donnachie, Nucl. Phys. A **623**, 135 (1997).

28. H.-J. Behrend *et al.*, Z. Phys. C **56**, 382 (1992).

29. M. Acciarri *et al.*, Phys. Lett. B **413**, 147 (1997); H. Albrecht *et al.*, Z. Phys. C **74**, 469 (1997); D. Antreasyan *et al.*, Phys. Rev. D **33**, 1847 (1986); T. Oest *et al.*, Z. Phys. C **47**, 343 (1990).

30. P. Singer, Phys. Rev. D **27**, 2223 (1983).

31. F. A. Berends, A. Donnachie, and D. L. Weaver, Nucl. Phys. B **4**, 103 (1968).

32. G. L. Kane *et al.*, Phys. Rev. Lett. **25**, 1519 (1970).

33. R. Worden, Nucl. Phys. B **37**, 253 (1972).

34. M. Guidal, J.-M. Laget, and M. Vanderhaeghen, Nucl. Phys. A **627**, 645 (1997).

35. A. V. Barnes *et al.*, Phys. Rev. Lett. **37**, 76 (1976).

36. K. Lübelsmeyer, in *Proceedings of the 4th International Symposium on Electron and Photon Interactions at High Energies, Liverpool, 1969*, Ed. by D. W. Braben and R. E. Rand (Daresbury Nucl. Phys. Lab., 1969), p. 45; in

Proceedings of the XV International Conference on High Energy Physics, Kiev, 1970, Ed. by V. Shelest, Yu. Budagov, L. Jenkovsky, *et al.* (Naukova Dumka, Kiev, 1972), p. 296.

37. R. Anderson *et al.*, Phys. Rev. D **1**, 27 (1970); M. Braunschweig *et al.*, Nucl. Phys. B **20**, 191 (1970).

38. D. W. G. S. Leith, in *Proceedings of the Eleventh Session of Scottish Universities Summer School in Physics on Hadronic Interactions of Electrons and Photons, Midlothian, 1970*, Ed. by J. Cumming and H. Osborn (Academic, London, 1971), p. 195.

39. R. Erbe *et al.*, Phys. Rev. **175**, 1669 (1968).

40. J. Ballam *et al.*, Phys. Lett. **30B**, 421 (1969).

41. Y. Eisenberg *et al.*, Phys. Rev. Lett. **22**, 669 (1969).

42. G. Gidal *et al.*, Phys. Rev. Lett. **23**, 994 (1969); D. R. O. Morrison, Rapporteur's talk given at XV International Conference on High Energy Physics, Kiev, 1970; Preprint No. CERN/D.Ph.11/PHYS.71-10 (Geneva, 1971); Preprint No. ITP-71-66E (Institute for Theoretical Physics, Kiev, 1971).

43. V. Flaminio *et al.*, CERN-HERA 83-01 (Geneva, 1983).

44. J. Abramson *et al.*, Phys. Rev. Lett. **36**, 1432 (1976).

45. H. G. Hilpert *et al.*, Nucl. Phys. B **21**, 93 (1970); P. Benz *et al.*, Nucl. Phys. B **79**, 10 (1974); D. P. Barber *et al.*, Z. Phys. C **2**, 1 (1979).

46. G. Alexander *et al.*, Phys. Rev. D **8**, 1965 (1973).

47. Y. Eisenberg *et al.*, Nucl. Phys. B **25**, 499 (1971).

48. G. Alexander *et al.*, Phys. Rev. Lett. **26**, 340 (1971).

49. R. Schiffer *et al.*, Nucl. Phys. B **38**, 628 (1972).

50. G. Alexander *et al.*, Nucl. Phys. B **68**, 1 (1974).

51. P. Benz *et al.*, Nucl. Phys. B **115**, 385 (1976).

52. D. P. Barber *et al.*, Z. Phys. C **26**, 343 (1984).

53. C. A. Nelson *et al.*, Phys. Rev. D **17**, 647 (1978).

54. J. Ballam *et al.*, Phys. Rev. D **7**, 3150 (1973).

55. M. Davier *et al.*, Phys. Rev. D **1**, 790 (1970).

56. T. H. Bauer *et al.*, Rev. Mod. Phys. **50**, 261 (1978).

57. G. Alexander *et al.*, Phys. Lett. **57B**, 487 (1975).

58. W. Struczinski *et al.*, Nucl. Phys. B **108**, 45 (1976).

59. R. Erbe *et al.*, Phys. Rev. **188**, 2060 (1969).

Translated by A. Isaakyan

ELEMENTARY PARTICLES AND FIELDS
Theory

Near-Threshold ω- and φ-Meson Production in $pn \to dM$ Reactions and OZI-Rule Violation*

V. Yu. Grishina[1]), L. A. Kondratyuk, and M. Büscher[2])

Institute of Theoretical and Experimental Physics, Bol'shaya Cheremushkinskaya ul. 25, Moscow, 117259 Russia
Received November 3, 1999

Abstract—The reactions $pn \to d\omega$ and $pn \to d\phi$ are investigated near the corresponding thresholds. The S-wave amplitudes are calculated within the two-step model described by a triangle graph with π, ρ, and ω mesons in the intermediate state. The cross sections for the reactions $pn \to d\omega$ and $pn \to d\phi$ are predicted to be significantly larger than the cross sections for the corresponding reactions $pp \to pp\omega$ and $pp \to pp\phi$ at the same values of the c.m. excess energy Q. The phi-to-omega yield ratio is found to be $(34 \pm 10) \times 10^{-3}$. © 2000 MAIK "Nauka/Interperiodica".

1. INTRODUCTION

It is well known (see, for example, [1–3]) that the phi-to-omega yield ratio

$$R = \frac{\sigma_{A+B \to \phi X}}{\sigma_{A+B \to \omega X}} \qquad (1)$$

is a particularly sensitive probe of the OZI rule [4]. Using the standard value of $\delta = \theta - \theta_i = 3.7°$ for the deviation from the ideal $SU(3)_f$ mixing angle of $\theta_i = 35.3°$, we have $R/f = 4.2 \times 10^{-3}$ [3], where f is the ratio of the phase-space factors. However, experimental data show an apparent excess of R/f above the standard value ranging from $(10–30) \times 10^{-3}$ in πN and NN collisions to $(100–250) \times 10^{-3}$ in $\bar{N}N$ annihilation at rest and in flight (see, for example, the relevant discussion in [3]). In [3], the large excess of R in pp and $\bar{p}p$ collisions over the OZI-rule prediction was treated in terms of the shakeout and rearrangement of an intrinsic $\bar{s}s$ component in the nucleon wave function. On the other hand, the explanation in [5, 6] that was given for the strong violation of the OZI rule in $\bar{p}p$ annihilation at rest attributed it to the presence of hadronic intermediate $K\bar{K}*$ states, which might create φ mesons.

Another argument in favor of a large admixture of hidden strangeness in nucleons relied on an apparently large contribution of the φ meson to the isoscalar spectral function, which defines the isoscalar nucleon form factor through the dispersion relation (see [7]). It was shown later (see [8] and references therein), however, that the main contribution to the isoscalar spectral function near 1 GeV comes from correlated πρ exchange, which does not involve strange quarks.

Therefore, the question of whether there is a large admixture of hidden strangeness in nucleons has yet to be clarified. Thus, it is important to investigate such reactions where uncertainties in the interpretation of ω and φ production in terms of intermediate hadronic states are comparatively small. In this study, we argue that a good opportunity in this respect is provided by the reaction

$$pn \to dM. \qquad (2)$$

Here and below, M stands for the vector mesons ω and φ. We analyze the contributions of hadronic intermediate states to the S-wave amplitudes of the reactions $pn \to d\phi$ and $pn \to d\omega$ within the two-step model (TSM) described by triangle graphs with π-, ρ-, and ω-meson exchanges. Previously, this model was used to describe of Pontecorvo reactions $\bar{p}d \to pM$ (see, for example, [9, 10]). It was demonstrated in [11] that the TSM can also describe the cross section for the reaction $pn \to d\eta$ near the threshold with a reasonable choice of the coupling constants and cutoff parameters for π-, ρ-, and ω-meson exchanges. In order to predict the cross sections for the reactions $pn \to d\omega$ and $pn \to d\phi$, we use a similar approach and the same set of parameters for the MNN coupling constants and cutoff parameters. Note that, if the φ and ω yields are measured in reaction (2) near the threshold (this can be done, for example, at COSY–Jülich), the results will be useful for obtaining deeper insights into the dynamics of OZI-rule violation. For example, any significant deviation from the relevant TSM prediction would be a piece of evidence for the aforementioned shakeout or rearrangement of an intrinsic $\bar{s}s$ component in the nucleon wave function.

---

* This article was submitted by the authors in English.

[1)] Institute for Nuclear Research, pr. Shestidesyatiletiya Oktyabrya 7a, Moscow, 117312 Russia.

[2)] Forschungszentrum Jülich, Institut für Kernphysik, D-52425 Jülich, Germany.

Note that recent measurements of the φ/ω ratio in the reaction $pd \longrightarrow {}^3\mathrm{He}X$ (at SATURNE II [12, 13]) yield

$$R/f = (63 \pm 5^{+27}_{-8}) \times 10^{-3}, \tag{3}$$

which is also clearly above the expected value of 4.2×10^{-3}. However, the dynamics of the reaction $pd \longrightarrow {}^3\mathrm{He}X$ has yet to be understood conclusively. According to [14], the TSM underestimates the SATURNE data by a factor of 2, while, according to [15], the discrepancy between the TSM and the data may even become larger upon taking into account spin effects.

Experiments devoted to studying ω and φ production in the reaction $pp \longrightarrow ppM$ near the threshold were performed by the SPES3 and DISTO collaborations at SATURNE [16, 17] (see also the calculations of ω production in [18]). According to the DISTO data, the φ/ω ratio of the production cross sections at 2.85 GeV is $\sigma_{\mathrm{tot}}(pp \longrightarrow pp\phi)/\sigma_{\mathrm{tot}}(pp \longrightarrow pp\omega) = (3.7 \pm 1.3) \times 10^{-3}$. Introducing corrections for phase-space effects, Hibou *et al.* [16] found that, in this case, the φ/ω ratio is $(49 \pm 26) \times 10^{-3}$. Note that, near the threshold the dynamics of the reactions $pp \longrightarrow ppM$, $pn \longrightarrow pnM$, and $pn \longrightarrow dM$ are different because the first one is constrained by the Pauli exclusion principle and the two protons in the final state should be in a ${}^1S_0$ state. In the third case, the final pn system is in the ${}^3S_1$ state, while, in the second case, it can be in either state. Therefore, possible violations of the OZI rule are expected to be different in all those cases.

Finally, another interesting point is that, within the line-reverse-invariance (LRI) assumption, the reaction $pn \longrightarrow dM$ can be related to the Pontecorvo reaction $\bar{p}d \longrightarrow MN$. The data from the OBELIX and Crystal-Barrel collaborations result in a φ/ω ratio of about $(230 \pm 60) \times 10^{-3}$ [19, 20]. If LRI is applicable, we therefore expect the amount of violation of the OZI rule in the reaction $pn \longrightarrow dM$ to be much larger than that which is predicted by the TSM assuming the dominance of the hadronic intermediate states.

The ensuing exposition is organized as follows. In Section 2, we derive the amplitudes for the reactions $pn \longrightarrow d\phi$ and $pn \longrightarrow d\omega$ near the threshold within the TSM. In Section 3, we discuss the choice of parameters and present the results of our calculations. Our conclusions are summarized in Section 4.

2. NONRELATIVISTIC TWO-STEP MODEL FOR THE REACTION $pn \longrightarrow dM$

The triangle diagrams describing the TSM are shown in Fig. 1. In addition to π exchange, we also take into account ρ and ω exchanges.

We begin by considering the π^0-exchange term. In order to preserve the correct structure of the amplitude under permutations of the initial nucleons (which should be symmetric in the isoscalar state), the ampli-
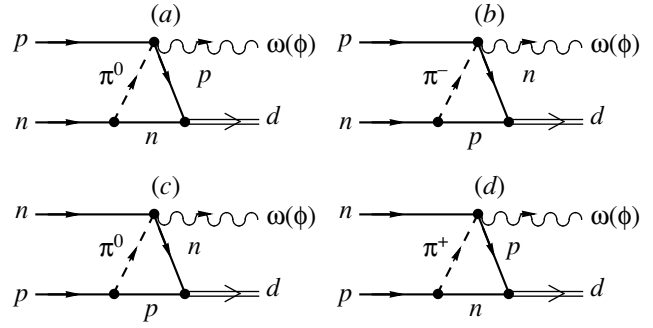
Fig. 1. Diagrams describing the two-step model (TSM). Note that, in addition to the π-exchange contribution, we also take into account diagrams involving the exchange of ρ and ω mesons.

tude is written as the sum of the *t*- and *u*-channel contributions in the form

$$T^\pi_{pn \to dM}(s, t, u) = A^\pi_{pn \to dM}(s, t) + A^\pi_{pn \to dM}(s, u). \tag{4}$$

Here, M is a vector meson, ω or φ; $s = (p_1 + p_2)^2$, $t = (p_3 - p_1)^2$, and $u = (p_3 - p_2)^2$, where p_1, p_2, p_3, and p_4 are the 4-momenta of the proton, the neutron, the meson M, and the deuteron, respectively. Since we are interested in the calculation of the cross section for reaction (2) near the threshold, where the momenta of the deuteron and the meson are comparatively small, we can use a nonrelativistic description of those particles by neglecting the fourth components of their polarization vectors. The relative motion of nucleons inside the deuteron is also treated nonrelativistically. The two terms on the right-hand side of (4) can then be represented as (see also [11])

$$A^\pi_{pn \to dM}(s, t) = \frac{f_\pi}{m_\pi} \varphi^T_{\lambda_2}(\mathbf{p}_2)(-i\sigma_2)\boldsymbol{\sigma} \cdot \mathbf{M}^\pi(\mathbf{p}_1)$$

$$\times \boldsymbol{\sigma} \cdot \boldsymbol{\epsilon}^{*(d)}\boldsymbol{\sigma} \cdot \boldsymbol{\epsilon}^{*(M)}\varphi_{\lambda_1}(\mathbf{p}_1)A_{\pi^0 N \to MN}(s_1, t), \tag{5}$$

$$A^\pi_{pn \to dM}(s, u) = \frac{f_\pi}{m_\pi} \varphi^T_{\lambda_1}(\mathbf{p}_1)(-i\sigma_2)\boldsymbol{\sigma} \cdot \mathbf{M}^\pi(-\mathbf{p}_1)$$

$$\times \boldsymbol{\sigma} \cdot \boldsymbol{\epsilon}^{*(d)}\boldsymbol{\sigma} \cdot \boldsymbol{\epsilon}^{*(M)}\varphi_{\lambda_2}(\mathbf{p}_2)A_{\pi^0 N \to MN}(s_1, u), \tag{6}$$

where $\boldsymbol{\epsilon}^{(d)}$ and $\boldsymbol{\epsilon}^{(M)}$ are, respectively, the deuteron and the meson polarization vector; φ_λ are the spinors of the nucleons in the initial state; and m_π and f_π are, respectively, the pion mass and the πNN coupling constant. The vector function $\mathbf{M}^\pi(\mathbf{p}_1)$ is defined by the integral

$$\mathbf{M}^\pi(\mathbf{p}_1) = \sqrt{2m}\int (\mathbf{k} + \mathbf{p}_1)\Phi_\pi(\mathbf{k}, \mathbf{p}_1)\Psi_d(\mathbf{k})\frac{d^3k}{(2\pi)^{3/2}}, \tag{7}$$

$$\Phi_\pi(\mathbf{k}, \mathbf{p}_1) = \frac{F_\pi(q^2)}{q^2 - m^2_\pi}, \tag{8}$$

which contains the deuteron wave function $\Psi_d(\mathbf{k})$ and the form factor $F_\pi(q^2)$ at the πNN vertex. Other kine-

matical quantities which are also dependent on the momenta $\mathbf{p}_1$ and $\mathbf{k}$ are defined as follows:

$$q^2 = m_\pi^2 - \delta_0(\mathbf{k}^2 + \beta(\mathbf{p}_1)) - 2\mathbf{p}_1 \cdot \mathbf{k}, \quad \mathbf{q} = \mathbf{k} + \mathbf{p}_1,$$

$$\beta(\mathbf{p}_1) = (\mathbf{p}_1^2 + m_\pi^2 - T_1^2)/\delta_0, \quad \delta_0 = 1 + T_1/m,$$

$$T_1 = \sqrt{\mathbf{p}_1^2 + m^2} - m,$$

with m being the nucleon mass.

Near threshold, we take into account only the S-wave part of the amplitude of the elementary reaction $\pi N \longrightarrow MN$. Deriving (5) and (6), we use the following spin structure of the $\pi^0 N \longrightarrow MN$ amplitude

$$\langle p_3'\lambda_3'; p_4'\lambda_4'|\hat{T}_{\pi^0 N \to NM}|p_1'; p_2'\lambda_2'\rangle$$

$$= \varphi_{\lambda_4'}^*(\mathbf{p}_4')\boldsymbol{\epsilon}_{\lambda_3'}^{*(M)} \cdot \boldsymbol{\sigma}\varphi_{\lambda_2'}(\mathbf{p}_2')A_{\pi^0 N \to NM}(s_1, t_1), \tag{9}$$

where p_1', p_2', p_3', and p_4' are the 4-momenta of the π meson, the initial nucleon, the final vector meson, and nucleon, respectively. The λ_i' are the spin projections of the particles, $\boldsymbol{\epsilon}^{(M)}$ is the polarization vector of the vector meson, and $s_1 = (p_1' + p_2')^2 = (p_3' + p_4')^2$, $t_1 = (p_1' - p_3')^2 = (p_2' - p_4')^2$.

The invariant amplitude is normalized to the total cross section as follows:

$$\left|A_{\pi^0 N \to MN}(s_1, t)\right|^2 = \left|A_{\pi^0 N \to MN}(s_1, u)\right|^2$$

$$= \frac{8}{3}\pi s_1 \frac{p_\pi^{\text{c.m.}}}{p_M^{\text{c.m.}}}\sigma_{\pi^- p \to Mn}, \tag{10}$$

where s_1 is the invariant mass squared of the Mn system.

It was shown in [11] that apart from the π-exchange contributions, heavier vector-meson exchanges—especially of ρ mesons—are important for the case of the reactions $pn \longrightarrow d\eta$ and $pn \longrightarrow d\eta'$. In our case, the amplitudes for the vector-meson exchanges can be written in the form

$$A_{pn \to dM}^V(s, t) = \frac{G_V}{2m}\varphi_{\lambda_2}^T(\mathbf{p}_2)(-i\sigma_2) \cdot A_{V^0 N \to MN}(s_1, t)$$

$$\times \{i[\mathbf{M}_2^V(\mathbf{p}_1) \times \boldsymbol{\epsilon}^{*(d)}] \cdot \boldsymbol{\epsilon}^{*(M)}$$

$$+ \mathbf{M}_1^V(\mathbf{p}_1) \cdot \boldsymbol{\epsilon}^{*(M)}\boldsymbol{\sigma} \cdot \boldsymbol{\epsilon}^{*(d)} \tag{11}$$

$$+ \mathbf{M}_2^V(\mathbf{p}_1) \cdot \boldsymbol{\epsilon}^{*(d)}\boldsymbol{\sigma} \cdot \boldsymbol{\epsilon}^{*(M)}$$

$$- \boldsymbol{\sigma} \cdot \mathbf{M}_2^V(\mathbf{p}_1)\boldsymbol{\epsilon}^{*(d)} \cdot \boldsymbol{\epsilon}^{*(M)}\}\varphi_{\lambda_1}(\mathbf{p}_1),$$

$$A_{pn \to dM}^V(s, u) = \frac{G_V}{2m}\varphi_{\lambda_1}^T(\mathbf{p}_1)(-i\sigma_2) \cdot A_{V^0 N \to MN}(s_1, u)$$

$$\times \{i[\mathbf{M}_2^V(-\mathbf{p}_1) \times \boldsymbol{\epsilon}^{*(d)}] \cdot \boldsymbol{\epsilon}^{*(M)}$$

$$+ \mathbf{M}_1^V(-\mathbf{p}_1) \cdot \boldsymbol{\epsilon}^{*(M)}\boldsymbol{\sigma} \cdot \boldsymbol{\epsilon}^{*(d)} \tag{12}$$

$$+ \mathbf{M}_2^V(-\mathbf{p}_1) \cdot \boldsymbol{\epsilon}^{*(d)}\boldsymbol{\sigma} \cdot \boldsymbol{\epsilon}^{*(M)}$$

$$- \boldsymbol{\sigma} \cdot \mathbf{M}_2^V(-\mathbf{p}_1)\boldsymbol{\epsilon}^{*(d)} \cdot \boldsymbol{\epsilon}^{*(M)}\}\varphi_{\lambda_2}(\mathbf{p}_2),$$

where

$$\mathbf{M}_1^V(\mathbf{p}_1) = \sqrt{2m}\int\frac{d^3k}{(2\pi)^{3/2}}(\mathbf{k} - \mathbf{p}_1)\Phi_V(\mathbf{k}, \mathbf{p}_1)\Psi_d^*(\mathbf{k}) \tag{13}$$

$$\mathbf{M}_2^V(\mathbf{p}_1) = \sqrt{2m}(1 + \kappa_V)$$

$$\times \int\frac{d^3k}{(2\pi)^{3/2}}(\mathbf{k} + \mathbf{p}_1)\Phi_V(\mathbf{k}, \mathbf{p}_1)\Psi_d^*(\mathbf{k}). \tag{14}$$

The function $\Phi_V(\mathbf{k}, \mathbf{p}_1)$ describes the product of the V-meson propagator $(q^2 - M_V^2)^{-1}$ and the form factor $F_V(q^2)$ at the VNN vertex. It is defined by (8), where m_π^2 should be replaced by m_V^2. The quantities G_V and $\kappa_V G_V$ are the vector and tensor coupling constants, respectively.

The general spin structure of the $VN \longrightarrow MN$ amplitude near threshold has the following form:

$$\langle p_3'\lambda_3'; p_4'\lambda_4'|\hat{T}_{V^0 N \to NM}|p_1'\lambda_1'; p_2'\lambda_2'\rangle = \varphi_{\lambda_4'}^*(\mathbf{p}_4')$$

$$\times (\boldsymbol{\epsilon}_{\lambda_3'}^{*(M)} \cdot \boldsymbol{\epsilon}_{\lambda_1'}^{(V)}A_{V^0 N \to NM}(s_1, t_1) \tag{15}$$

$$+ i[\boldsymbol{\epsilon}_{\lambda_3'}^{*(M)} \times \boldsymbol{\epsilon}_{\lambda_1'}^{(V)}] \cdot \boldsymbol{\sigma}B_{V^0 N \to NM}(s_1, t_1))\varphi_{\lambda_2'}(\mathbf{p}_2'),$$

where the notation is similar to that in (9). Two invariant amplitudes $A_{V^0 N \to NM}(s_1, t_1)$ and $B_{V^0 N \to NM}(s_1, t_1)$ are necessary to describe two possible transitions $\left(\frac{1}{2}\right)^- \longrightarrow \left(\frac{1}{2}\right)^-$ and $\left(\frac{3}{2}\right)^- \longrightarrow \left(\frac{3}{2}\right)^-$. It is known from the data on the Compton scattering (see, e.g., [21]) that the spin-flip amplitude $B_{\gamma N \to \gamma N}(s_1, t_1)$ is small as compared with the non-spin-flip amplitude $A_{\gamma N \to \gamma N}(s_1, t_1)$ except in the Δ-resonance region (see, e.g., [21]). Following the arguments of the vector-dominance model (VDM), we assume that this amplitude is also small in our case and take into account only the first non-spin-flip term in (15).

Note that the amplitudes A^π and A^ρ correspond to the exchange of neutral π and ρ mesons only (see the left diagrams in Fig. 1). To take into account also the charged π and ρ exchanges, we have to multiply amplitude (4) by a factor of 3. Of course, in the case of ω exchange such a factor is not necessary.

Therefore, the differential cross section of reaction (2) can be written as

$$\frac{d\sigma_{pn \to dM}}{dt} = \frac{1}{64\pi s}\frac{1}{(p_1^{\text{c.m.}})^2}$$

$$\times F(I)\overline{\left|A_{pn \to dM}(s, t) + A_{pn \to dM}(s, u)\right|^2}, \tag{16}$$

where the isospin factor $F(I)$ is equal to nine for isovector exchanges (ρ and π) and one for isoscalar exchange (ω).

3. CHOICE OF PARAMETERS AND RESULTS OF CALCULATIONS

We assume the form factors $F_\pi(q^2)$ and $F_V(q^2)$ to be of monopole type. Recent QCD lattice calculations [22] suggest that the cutoff in the pion form factor should be quite soft $\Lambda_\pi \simeq 0.8$ GeV/c (see also [23, 24]). Of course, such a soft-pion form factor suppresses pion exchange, and contributions of heavier meson exchanges become more important. This, for example, was demonstrated in [11], where it was found that the ρ-exchange contribution in the reactions $pn \longrightarrow d\eta$ and $pn \longrightarrow d\eta'$ is significant. Here, also, $\Lambda_\pi = 0.8$ GeV/c is used.

The coupling constants and vertex form factors for ρ and ω mesons are taken from the full Bonn NN potential [25]: $G_\rho^2/4\pi = 0.84$, $\kappa_\rho = 6.1$, $G_\omega^2/4\pi = 20$, $\kappa_\omega = 0$, and $\Lambda_\rho = 1.4$ GeV/c, $\Lambda_\omega = 1.5$ GeV/c.

For the deuteron wave function, we take the parametrization from [26] and neglect the D-wave part. As was demonstrated in [10] for the case of the reaction $\bar{p}d \longrightarrow Mn$ [where the same structure integrals (7) for π, ρ, and ω exchanges occur], the D-wave term of the deuteron wave function gives a negligibly small contribution compared to the S-wave term.

To define the amplitudes $\pi N \longrightarrow MN$, we use the following values of the S-wave cross sections (taken from [27]): $\sigma_{\pi^- p \to \omega n} = (8.3 \pm 0.07) p_{\mathrm{c.m.}}^M$ μb and $\sigma_{\pi^- p \to \phi n} = (0.29 \pm 0.06) p_{\mathrm{c.m.}}^M$ μb ($p_{\mathrm{c.m.}}^M$ in MeV/c). The experimental data show that the angular distribution in the reaction $\pi^- p \longrightarrow n\omega$ is isotropic and the S wave is dominant at least up to $k_V^{\mathrm{c.m.}}(s_1) = 260$ MeV/c (see the comment on p. 2805 in [27]). We ignore an apparent suppression of the S-wave amplitude very close to threshold ($k_V^{\mathrm{c.m.}}(s_1) \leq 80$–100 MeV/$c$), reported in [27], because according to [28] this effect has a kinematical origin.

To calculate the contributions of ρ and ω exchanges, we need the amplitudes $A_{\rho N \to \omega N}$, $A_{\omega N \to \omega N}$, $A_{\rho N \to \phi N}$, and $A_{\omega N \to \phi N}$. The elastic ωN scattering amplitude was assumed to be pure imaginary and corresponding to the cross section $\sigma_{\omega N \to \omega N} = 15$ mb, which is in agreement with the prediction of [29]. The amplitudes $A_{\rho N \to \omega N}$ and $A_{\rho N \to \phi N}$ were found using the VDM from the photoproduction cross sections $\sigma_{\gamma p \to \omega p} = 5.6$–7.8 μb at $E_\gamma = 1.3$ GeV and $\sigma_{\gamma p \to \phi p} = 0.2$–0.4 μb at $E_\gamma = 2$ GeV (see [30]). In the case of the $\rho N \longrightarrow \omega N$ reaction, our estimation corresponds to the cross section of about
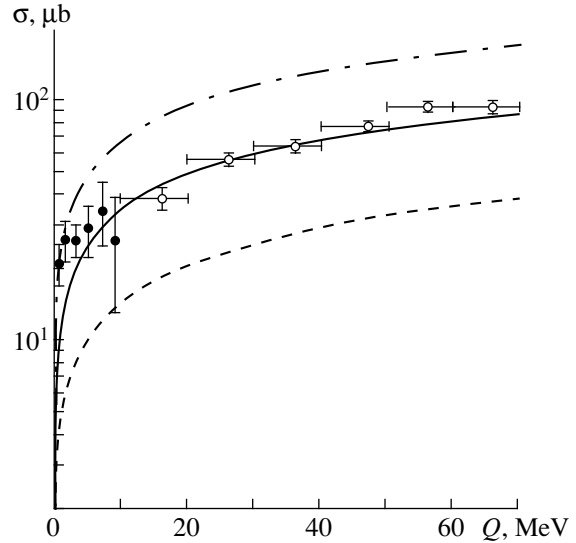

Fig. 2. Cross section for the reaction $pn \longrightarrow d\eta$ as a function of the c.m. excess energy (taken from [11]): (dashed curve) π-exchange contribution; (dash-dotted curve) sum of π, ρ, and ω exchanges; and (solid curve) all contributions (π, ρ, ω) multiplied by the normalization factor of $N = 0.52$ in order to take into account initial-state-interaction effects (see main body of the text). Experimental data were taken from (open circles) [31] and (closed circles) [32].

3.1 ± 0.5 mb at low energies. Finally we assumed that $\sigma_{\omega N \to \phi N} \simeq \sigma_{\rho N \to \phi N}$.

Since the relative phases of the different contributions are not known, we calculate the cross section of the reaction $pn \longrightarrow dM$ as the incoherent sum

$$\sigma_{pn \to dM} = N[\sigma^{(\pi)} + \sigma^{(\rho)} + \sigma^{(\omega)}]. \tag{17}$$

In Fig. 2 taken from [11], we show how the TSM (with the same coupling constants and cutoff parameters for π, ρ, and ω exchanges and the S-wave amplitudes $Vp \longrightarrow \eta p$ and $Vp \longrightarrow \eta' p$ estimated using VDM from the photoproduction data) describes the experimental data on the reaction $pn \longrightarrow d\eta$. The cross section of the reaction $pn \longrightarrow d\eta$ is presented as a function of the c.m. excess energy Q. The dashed curve shows the π-exchange contribution alone, whereas the dash-dotted curve describes the sum of π, ρ, and ω exchanges. The solid curve includes all contributions (π, ρ, ω) multiplied by a normalization factor $N = 0.52$ in order to take into account effects from the initial-state interaction (ISI). The data points are taken from [31] (open circles) and [32] (filled circles). The reduction factor appeared to be not very different from the prediction of the ISI effect within a simple model which assumes the dominant contribution from the on-shell rescattering [33] and gives $\lambda_{\mathrm{ISI}} \simeq 0.5$.

As we see from Fig. 2, pion exchange calculated with the soft cutoff parameter cannot describe the η-production data, and the contribution from heavier
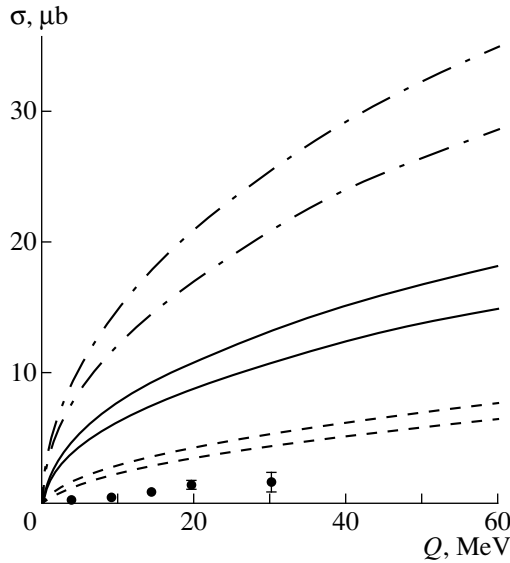
σ, μb

Fig. 3. Cross section for the reaction $pn \longrightarrow d\omega$ as a function of the c.m. excess energy: (dashed curves) π-exchange contribution alone; (dash-dotted curves) sums of π-, ρ-, and ω exchanges; and (solid curves) all contributions (π, ρ, ω) multiplied by the normalization factor of $N = 0.52$ in order to take into account initial-state-interaction effects. The upper and lower dashed, solid, and dash-dotted curves were calculated by using the maximal and minimal values of the elementary $\pi N \longrightarrow \omega N$ and $VN \longrightarrow \omega N$ S-wave amplitudes (see main body of the text). Points represent data on the reaction $pp \longrightarrow pp\omega$ from [16].

σ, μb
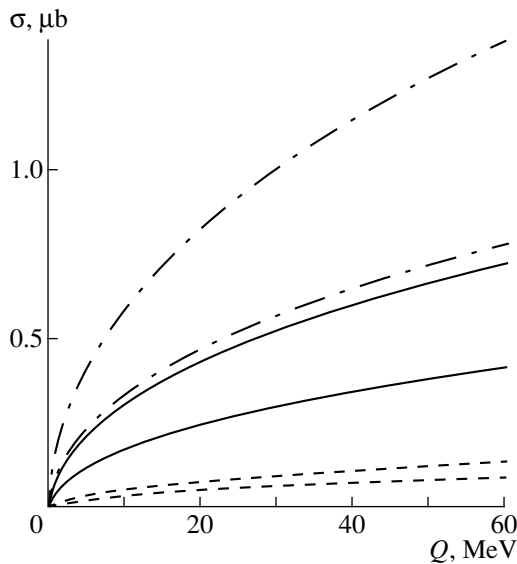
Fig. 4. Cross section for the reaction $pn \longrightarrow d\phi$ as a function of the c.m. excess energy. The notation for the curves is identical to that in Fig. 3.

meson exchanges (and especially of ρ [11]) is quite important.

In Figs. 3 and 4, we present the predictions of the TSM for the cross sections of the ω and ϕ production. The contribution of pion exchange is shown by the dashed curves. The lower and upper curves show the minimal and maximal values of the π-exchange contribution and demonstrate uncertainties which follow from the experimental errors of the elementary cross sections. The dash-dotted curves describe the sum of π-, ρ-, and ω-exchange contributions. The solid curves represent the results including all contributions (π, ρ, ω) multiplied by the same normalization factor $N = 0.52$ as in the case of η production in order to take into account effects from ISI. It can clearly be seen that, as in the case of η production, the ρ-exchange contribution to the cross sections for the reactions is very significant. The relative contribution of π exchange is about 20% in the case of ω production and is nearly one-half as great in the case of ϕ production. The ω exchange is more important in the case of ω production, where it gives about 18%; in the case of ϕ productions, its relative contribution is about 5%.

The cross sections of the reactions $pn \longrightarrow \omega d$ and $pn \longrightarrow \phi d$ can be parametrized as

$$\sigma_{pn \to dM} \approx D_M \sqrt{Q}, \qquad (18)$$

where $D_\omega = (2.2 \pm 0.2)$ μb/MeV$^{1/2}$ and $D_\phi = (0.08 \pm 0.02)$ μb/MeV$^{1/2}$. At very low Q that are on the order of the resonance width, each cross section might be a little larger because of the finite widths of the ω and ϕ [16].

In Fig. 3, we also show experimental data on the near-threshold production of ω mesons in the $pp \longrightarrow pp\omega$ reaction [16]. Near threshold, the predicted cross section of ω production with the deuteron in the final state is much higher than that of the reaction $pp \longrightarrow pp\omega$. This is very similar to the case of η production (see, e.g., [31, 32]) and is related to isospin and phase-space factors (see, e.g., [34]).

Let us discuss the relation between $\sigma(pp \longrightarrow pp\omega)$ and $\sigma(pn \longrightarrow d\omega)$ near threshold in more detail. Fäldt and Wilkin [35] proposed the following parametrization of the cross section of the reaction $pp \longrightarrow ppM$ near the threshold:

$$\sigma_{pp \to ppM} = C_M \left(\frac{Q}{\epsilon}\right)^2 (1 + \sqrt{1 + Q/\epsilon})^{-2}. \qquad (19)$$

This formula takes into account the strong final state interaction of two protons including also the Coulomb distortion with $\epsilon \approx 0.45$ MeV. For η and ω production, we have $C_\eta = (110 \pm 20)$ nb and $C_\omega = (37 \pm 8)$ nb [16]. At $Q = 15$ MeV, we have $\sigma(pp \longrightarrow pp\eta) \approx 2.6$ μb ($\sigma(pp \longrightarrow pp\omega) \approx 1$ μb), which is 15(8) times smaller than the cross section of the reaction $pn \longrightarrow d\eta$ ($pn \longrightarrow d\omega$). Note that in line with suggestions by Wilkin (see, e.g., [34]) the ratios $\sigma(pn \longrightarrow d\eta)/\sigma(pp \longrightarrow pp\eta)$ and $\sigma(pn \longrightarrow d\omega)/\sigma(pp \longrightarrow pp\omega)$ are, in fact, not very different.

The reaction $pp \longrightarrow pp\omega$ near the threshold was also analyzed within the framework of the meson-exchange model in [18]. Adjusting the cutoff parameter

of the form factor to the low-energy data, the authors of [18] calculated the cross section of the reaction $pp \longrightarrow pp\omega$ for proton-incident energies up to 2.2 GeV. This model predicts a cross section of about 15–20 μb at $Q \approx 100$ MeV, which is still not very different from parametrization (19). If parametrizations (18) and (19) were valid up to $Q = 1$ GeV, then the cross section of the reaction $\sigma(pp \longrightarrow pp\omega)$ would reach the same value as the cross section of the reaction $pn \longrightarrow d\omega$ only at 900 MeV. Of course, those formulas cannot be valid up to such large values of Q. Estimations within the framework of the Quark–Gluon String Model show that the cross section of the reaction $pn \longrightarrow d\omega$ can reach a maximum of about 30–50 μb at $Q = 100$–200 MeV and then will start to fall (see [36]). According to the parametrization of [37], the cross section of the reaction $\sigma(pp \longrightarrow pp\omega)$ reaches the value of 30 μb at $Q \approx 200$ MeV. Therefore, we can expect that in a rather broad interval of Q (at least up to about 100–150 MeV), the cross section of the reaction $pn \longrightarrow d\omega$ will be larger than the cross section of the reaction $\sigma(pp \longrightarrow pp\omega)$. This gives quite a good chance that the reaction $pn \longrightarrow d\omega$ can be detected using the missing-mass method at COSY by measuring the forward deuteron and spectator proton in the reaction $pd \longrightarrow d\omega p_{sp}$.

For the case of φ production, we also expect that near threshold the cross section of the reaction $pn \longrightarrow d\phi$ will be larger than that of the reaction $pp \longrightarrow pp\phi$. The latter was estimated using DISTO data in [34] and found to be equal to 0.28 ± 0.14 μb at $Q = 82$ MeV. Though there are uncertainties in extrapolating the prediction of the TSM (18) to such large Q, we would have $\sigma(pn \longrightarrow d\phi) \approx 0.6$–0.9 μb at this Q.

Let us discuss now the φ/ω ratio. TSM predicts the following value:

$$R_{pn \to dM} = D_\phi / D_\omega = (34 \pm 10) \times 10^{-3}. \qquad (20)$$

This is lower than the corresponding ratio in pp collisions [16]

$$R_{pp \to ppM} = C_\phi / C_\omega = (49 \pm 26) \times 10^{-3} \qquad (21)$$

and in the reaction $pd \longrightarrow {}^3\text{He}M$ [see (3)]. It is closer to the ratio of the φ-to-ω yields in $\pi^- p$ collisions (see, e.g., the discussion in [34])

$$R_{\pi^- p \to nM} = (37 \pm 8) \times 10^{-3}. \qquad (22)$$

Another estimate of R can be found if we assume the line-reverse invariance of the amplitudes, which correspond to the diagrams presented in Fig. 1. In this case, we have

$$\overline{\left| T^{\text{LRI}}_{pn \to dM}(s, t) \right|^2} = \overline{\left| A^{\text{LRI}}_{pn \to dM}(s, t) + A^{\text{LRI}}_{pn \to dM}(s, u) \right|^2}$$
$$= \overline{\left| A_{\bar{p}d \to nM}(s, t) + A_{\bar{p}d \to nM}(s, u) \right|^2} \qquad (23)$$

and we can define the ratio

$$R_{\text{LRI}} = \frac{\left| T^{\text{LRI}}_{pn \to d\phi} \right|^2}{\left| T^{\text{LRI}}_{pn \to d\omega} \right|^2} = \frac{\left| T_{\bar{p}d \to n\phi} \right|^2}{\left| T_{\bar{p}d \to n\omega} \right|^2}. \qquad (24)$$

Adopting the result of the OBELIX collaboration $Y(\bar{p}d \longrightarrow n\phi)/Y(\bar{p}d \longrightarrow n\omega) = (230 \pm 60) \times 10^{-3}$, we get

$$R_{\text{LRI}} = \frac{\left| T_{\bar{p}d \to n\phi} \right|^2}{\left| T_{\bar{p}d \to n\omega} \right|^2} \approx \frac{p^\omega_{\text{c.m.}}}{p^\phi_{\text{c.m.}}} \frac{Y(\bar{p}d \longrightarrow n\phi)}{Y(\bar{p}d \longrightarrow n\omega)} \qquad (25)$$
$$\simeq (250 \pm 60) \times 10^{-3},$$

which is one order of magnitude larger than the prediction of the TSM given by (20). If experimental studies should find an significant excess of $R(\phi/\omega)$ over the value predicted by the two-step model, it might be interpreted as a possible contribution of the intrinsic $s\bar{s}$ component to the nucleon wave function.

4. CONCLUSIONS

Using the two-step model which is described by triangle graphs with π-, ρ-, and ω-meson exchanges, we calculated the cross sections of the reactions $pn \longrightarrow dM$, where $M = \omega$ or φ, close to threshold. The predicted cross section for the reaction $pn \longrightarrow d\omega$ is found to be significantly larger than the cross section for the reaction $pp \longrightarrow pp\omega$. The same is expected to be the case for φ production. We find a φ/ω ratio of $R_{pn \to dM} = (34 \pm 10) \times 10^{-3}$. The measurement of the φ and ω yields in the reaction $pn \longrightarrow dM$ at the same energy release Q will be useful for a better understanding of the mechanism of the OZI-rule violation.

REFERENCES

1. H. J. Lipkin, Phys. Lett. **60B**, 371 (1976).
2. J. Ellis, E. Gabathuler, and M. Karliner, Phys. Lett. B **217**, 173 (1989).
3. J. Ellis, M. Karliner, D. E. Kharzeev, and M. G. Sapozhnikov, Phys. Lett. B **353**, 319 (1995).
4. S. Okubo, Phys. Lett. **5**, 165 (1963); G. Zweig, CERN Report 8419/TH 412, 1964; I. Iizuka, Prog. Theor. Phys. Suppl. **37/38**, 21 (1966).
5. M. P. Locher, Y. Lu, and B. S. Zou, Z. Phys. A **347**, 281 (1994).

6. D. Buzatu and F. Lev, Phys. Lett. B **329**, 143 (1994).

7. R. L. Jaffe, Phys. Lett. B **229**, 275 (1989).

8. U.-G. Meissner, V. Mull, J. Speth, and J. V. van Orden, Preprint KFA-IKP(TH)-1997-01 (Forschungszentrum Julich, 1997); Talk given at 6th Conference on the Intersection of Particle and Nuclear Physics, CIPAN'97, Big Sky, 1997.

9. L. A. Kondratyuk and M. G. Sapozhnikov, Phys. Lett. B **220**, 333 (1989); Few-Body Syst. Suppl. **5**, 201 (1992).

10. L. A. Kondratyuk *et al.*, Yad. Fiz. **61**, 1670 (1998) [Phys. At. Nucl. **61**, 1558 (1998)].

11. V. Yu. Grishina *et al.*, nucl-th/9905049, submitted for publication in Phys. Lett. B.

12. R. Wurzinger *et al.*, Phys. Rev. C **51**, R443 (1995).

13. R. Wurzinger *et al.*, Phys. Lett. B **374**, 283 (1996).

14. G. Fäldt and C. Wilkin, Nucl. Phys. A **587**, 769 (1995).

15. L. A. Kondratyuk and Yu. N. Uzikov, Yad. Fiz. **60**, 542 (1997) [Phys. At. Nucl. **60**, 468 (1997)].

16. F. Hibou *et al.*, nucl-ex/9903003.

17. F. Balestra *et al.*, Phys. Rev. Lett. **81**, 4572 (1998).

18. K. Nakayama *et al.*, Phys. Rev. C **57**, 1580 (1998).

19. OBELIX Collab. (A. Bertin *et al.*), Yad. Fiz. **59**, 1511 (1996) [Phys. At. Nucl. **59**, 1455 (1996)].

20. Crystal Barrel Collab., Z. Phys. A **351**, 325 (1995).

21. T. H. Bauer *et al.*, Rev. Mod. Phys. **50**, 261 (1978).

22. K. F. Liu *et al.*, Phys. Rev. Lett. **74**, 2172 (1995).

23. S. A. Coon and M. D. Scadron, Phys. Rev. C **23**, 1150 (1981).

24. G. Janssen, K. Holinde, and J. Speth, Phys. Rev. C **54**, 2218 (1996).

25. R. Machleidt, K. Holinde, and Ch. Elster, Phys. Rep. **149**, 1 (1987).

26. M. Lacomb *et al.*, Phys. Lett. **101B**, 139 (1981).

27. D. M. Binnie *et al.*, Phys. Rev. D **8**, 2789 (1973).

28. C. Hanhart and A. Kudryavtsev, nucl-th/9812022.

29. G. I. Lykasov, W. Cassing, A. Sibirtsev, and M. V. Rzjanin, Preprint No. UGI-98-37, 1998; nucl-th/9811019, submitted for publication in Eur. Phys. J.

30. R. Erbe *et al.*, Phys. Lett. **27B**, 54 (1968).

31. H. Calén *et al.*, Phys. Rev. Lett. **79**, 2642 (1997).

32. H. Calén *et al.*, Phys. Rev. Lett. **80**, 2069 (1998).

33. C. Hanhart and K. Nakayama, nucl-th/9809059; Phys. Lett. B (in press).

34. C. Wilkin, Invited talk at 8th International Conference on the Structure of Baryons, Baryon'98, Bonn, 1998; nucl-th/9810047.

35. G. Fäldt and C. Wilkin, Phys. Lett. B **382**, 209 (1996).

36. M. Büscher *et al.*, COSY Proposal No. 75, 1998.

37. A. Sibirtsev, Nucl. Phys. A **604**, 455 (1996).

ELEMENTARY PARTICLES AND FIELDS
Theory

Transverse-Momentum Dependence of Cumulative Pions*

M. A. Braun and V. V. Vechernin**

St. Petersburg State University, Petrodvorets, Russia
Received May 11, 1999; in final form, September 16, 1999

Abstract—The transverse-momentum dependence of the cumulative-pion-production rates is studied on the basis of the recently proposed QCD-based parton model for cumulative phenomena. The mean transverse-momentum value is found to grow with x in the cumulative region. The results are in agreement with available experimental data. © 2000 MAIK "Nauka/Interperiodica".

1. INTRODUCTION

A few years ago, we proposed a quark–parton model of cumulative phenomena in interactions with nuclei [1, 2]. This model is based on perturbative QCD calculations of the corresponding quark diagrams near the thresholds at which other quarks ("donors") in a nuclear flucton transfer all their longitudinal momenta to the distinguished active quark and become soft.

Let us consider the scattering of a hadronic projectile off a nucleus with a c.m. momentum P. At high energies, the momentum K of the product pion belongs to the cumulative region if $K_z > P_z/A$. For a reasonable first approximation, we treat the nucleus as a collection of $N = 3A$ valence quarks, which, on average, carry each longitudinal momentum $x_0 P_z/A$ with $x_0 = 1/3$. In our approach, the cumulative pion production proceeds in two steps. First, a valence quark with a scaling variable $x > 1$ is created. Afterward, it decays into the observed hadron with its scaling variable x close to the initial cumulative one of the quark. This second step is described by well-known quark fragmentation functions [3] and will not be discussed here.

The product cumulative ("active") quark acquires a momentum much greater than $x_0 P_z/A$ only if this quark has interacted by means of gluon exchanges with other p quarks of flucton ("donors") and has taken some of their longitudinal momenta (see Fig. 1). If this active quark accumulates the entire longitudinal momentum of these p quarks, then $K_z = (p + 1)x_0 P_z/A$ and the donors become soft. It is well known that interactions reducing the longitudinal momentum of one of the quarks to zero may be treated by perturbation theory [4]. This allows one to evaluate that part of Fig. 1 which is responsible for the creation of a cumulative quark explicitly. This was done in [1, 2], where the reader can find all details. As a result, we were able to explain the exponential falloff of the production rate in the cumulative region.

Since, with increasing x, the active quark has to interact with a greater number of donors, one expects that its mean transverse momentum also grows with x. This simple physical argument was used in [5] to predict a linear growth of $\langle K_\perp^2 \rangle$ with x. Moreover, in the quark picture, this mechanism also explains the observed rise of $\langle K_\perp^2 \rangle$ with x in the noncumulative region, since, at greater x, a greater number of quarks have to participate in particle production. We expect that this effect is present in our model as well. This point was not studied in [1, 2]: we limited ourselves to the inclusive cross section integrated over the transverse momenta, which leads to some simplifications. The objective of the present study is to find the transverse-momentum dependence of pion-production rate and the mean transverse-momentum value as a function of x in the cumulative region. This dependence and also the magnitude of $\langle K_\perp^2 \rangle$ were studied experimentally. By comparing our predictions with data, we will be able to obtain further support for our model and fix one of its two parameters (infrared cutoff).

2. $K_\perp$ DEPENDENCE

Repeating evaluation of the diagram in Fig. 1 as described in [1, 2], but not limiting ourselves to the inclusive cross section integrated with respect to the transverse momentum, we readily find that the dependence on the transverse momentum $K_\perp$ of the product particle is entirely concentrated in the factor

$$J(K_\perp) = \int \rho_A(\underbrace{r, ..., r}_{p+1} \mid \underbrace{\bar{r}, ..., \bar{r}}_{p+1})G(c_1, ..., c_p)$$
$$\times \prod_{i=1}^{p} \lambda(c_i - r)\lambda(c_i - \bar{r})d^2c_i e^{i(\bar{r}-r)K_\perp}d^2r d^2\bar{r}. \quad (1)$$

Here, ρ_A is the (translation-invariant) quark density matrix of the nucleus,

$$\rho_A(r_i | \bar{r}_i) \equiv \int \psi_{\perp A}(r_i, r_m)\psi_{\perp A}^*(\bar{r}_i, r_m)\prod_{m=p+2}^{N} d^2r_m, \quad (2)$$
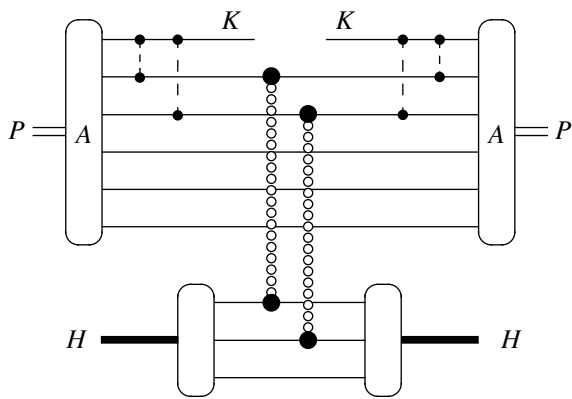
Fig. 1. Diagram for the production of a cumulative quark with a momentum K in the scattering of a projectile hadron with a momentum H off a nucleus A with a momentum P. Dashed and chain lines show gluon and Pomeron exchanges, respectively.

where $\psi_{\perp A}$ is the transverse part of the nuclear quark wave function. The propagation of soft donor quarks is described by

$$\lambda(c) = \frac{K_0(m|c|)}{2\pi}, \qquad (3)$$

where m is the constituent quark mass and K_0 is a modified Bessel function (Macdonald function). The interaction with the projectile contributes the factor

$$G(c_1, \ldots, c_p) = \int \prod_{i=1}^{p} \sigma_{qq}(c_i - b_i)\eta_H(b_1, \ldots, b_p)d^2b_i, \quad (4)$$

where $\sigma_{qq}(c)$ is the quark–quark cross section at a given value of the impact parameter c and

$$\eta_H(b_1, \ldots, b_p) = \sum_{L \geq p} \frac{L!}{(L-p)!} \int |\psi_{\perp H}(b_i)|^2$$
$$\times \delta^{(2)}\left(\frac{1}{L}\sum_{i=1}^{L} b_i\right)d^2b_{p+1}\ldots d^2b_L \qquad (5)$$

is a multiparton distribution in the projectile. This distribution is expressed in terms of the transverse part of its partonic wave function $\psi_{\perp H}$. If we integrate $J(K_\perp)$ with respect to $K_\perp$, we will return to our old result [(33) in [1]]:

$$\int J(K_\perp)\frac{d^2K_\perp}{(2\pi)^2} = \rho_A(\underbrace{0, \ldots, 0}_{p+1}|\underbrace{0, \ldots, 0}_{p+1})$$
$$\times \int G(c_1, \ldots, c_p)\prod_{i=1}^{p} \lambda^2(c_i - r)d^2c_i d^2r.$$

If one assumes factorization of the multiparton distribution $\eta_H(b_1, \ldots, b_p)$, then $G(c_1, \ldots, c_p)$ also factorizes:

$$G(c_1, \ldots, c_p) = \prod_{i=1}^{p} G_0(c_i). \qquad (6)$$

Following [2], we use the quasieikonal approximation for η_H:

$$\eta_H(b_1, \ldots, b_p) = \xi^{(p-1)/2}\nu_H^p\prod_{i=1}^{p}\eta_H(b_i).$$

Here, ξ is the quasieikonal diffraction factor, ν_H is the mean number of partons in the projectile hadron, and the single-parton distribution $\eta_H(b)$ is normalized to unity. In the Gaussian approximation for $\sigma(c)$ and $\eta_H(b)$, we obtain

$$G_0(c) = \xi^{\frac{1}{2}-\frac{1}{2p}} \cdot \frac{\nu_H\sigma_{qq}}{\pi r_{0H}^2}e^{-c^2/r_{0H}^2},$$

where σ_{qq} is the total quark–quark cross section; $r_{0H}^2 = r_0^2 + r_H^2$; and r_0 and r_H are the widths of $\sigma(c)$ and $\eta_H(b)$, respectively.

With the factorized $G(c_1, \ldots, c_p)$ (6), we have

$$J(K_\perp) = \int \rho_A(\underbrace{0, \ldots, 0}_{p+1}|\underbrace{\bar{r} - r, \ldots, \bar{r} - r}_{p+1})j^p(r, \bar{r})$$
$$\times e^{i(\bar{r}-r)K_\perp}d^2r d^2\bar{r},$$

where

$$j(r, \bar{r}) = \int d^2c\, G_0(c)\lambda(c - r)\lambda(c - \bar{r}).$$

We also have used the translation invariance of the matrix ρ. Note that, near the true threshold, we have no spectators and

$$\rho_A(\underbrace{0, \ldots, 0}_{p+1}|\underbrace{\bar{r} - r, \ldots, \bar{r} - r}_{p+1}) = \rho_A(\underbrace{0, \ldots, 0}_{p+1}|\underbrace{0, \ldots, 0}_{p+1}).$$

In any case, large $K_\perp$ corresponds to small $\bar{r} - r$, so that we factor ρ_A out of the integral sign at the zero point. In the remaining integral, we go over to the variables

$$B = \frac{r + \bar{r}}{2}, \quad b = \bar{r} - r$$

and shift the integration variable c. As a result, we obtain

$$J(K_\perp) = \rho_A(\underbrace{0, \ldots, 0}_{p+1}|\underbrace{0, \ldots, 0}_{p+1})$$
$$\times \int j^p(B, b)e^{ibK_\perp}d^2b d^2B, \qquad (7)$$

where

$$j(B, b) = \int G_0(B + c)\lambda\left(\frac{b}{2} - c\right)\lambda\left(\frac{b}{2} + c\right)d^2c. \quad (8)$$

3. CALCULATION OF $\langle|K_\perp|\rangle$

Now, we would like to find the width of the distribution with respect to $K_\perp$ as a function of p or—what is the same—of the cumulative number $x = (p + 1)/3$.

From the mathematical point of view, it is simpler to calculate the mean squared width of the distribution $\langle K_\perp^2 \rangle$. Unfortunately, this quantity is divergent logarithmically in our case at large $K_\perp$. This divergence results from the behavior of $j(B, b)$ at small b. This behavior is determined by the behavior of the $\lambda(b) = K_0(m|b|)(2\pi)$ (3), which has a logarithmic singularity at $|b| = 0$. Smooth $G_0(B + c)$ does not affect this behavior.

For this reason, we will rather calculate $\langle |K_\perp| \rangle$,

$$\langle |K_\perp| \rangle = \frac{1}{J_N} \int j^p(B, b)|K_\perp|e^{ibK_\perp}d^2bd^2B\frac{d^2K_\perp}{(2\pi)^2}, \quad (9)$$

where J_N is the same integral as in the numerator but without $|K_\perp|$. Representing $|K_\perp|$ as $K_\perp^2/|K_\perp|$ and $K_\perp^2$ as the Laplacian Δ_b applied to the exponent, we obtain

$$\langle |K_\perp| \rangle = -\frac{1}{J_N} \int j^p(B, b)\Delta_b e^{ibK_\perp}d^2bd^2B\frac{d^2K_\perp}{|K_\perp|(2\pi)^2}.$$

Twice integrating by parts and using the formula

$$\int \frac{d^2K_\perp}{|K_\perp|}e^{ibK_\perp} = \frac{2\pi}{|b|},$$

we arrive at

$$\langle |K_\perp| \rangle = -\frac{1}{2\pi J_N} \int \frac{1}{|b|}\Delta_b j^p(B, b)d^2bd^2B.$$

Now, we again integrate by parts once to find

$$\langle |K_\perp| \rangle = -\frac{1}{2\pi J_N} \int d^2B\frac{d^2b}{|b|^2}(n_b\nabla_b)j^p(B, b),$$

where $n_b = b/|b|$. This leads to our final formula

$$\langle |K_\perp| \rangle = -\frac{p}{2\pi J_N} \int d^2B\frac{d^2b}{|b|^2} \quad (10)$$
$$\times j^{p-1}(B, b)(n_b\nabla_b)j(B, b),$$

where $j(B, b)$ is given by (8), $\lambda(b)$ is given by (3), and

$$J_N = \int d^2B j^p(B, b = 0).$$

4. APPROXIMATIONS

In order to simplify numerical calculations, we make some additional approximations that are not very important, but which are well supported by a comparison with exact calculations at a few sample points.

As follows from the asymptotic behavior of $K_0(z)$ at large z,

$$K_0(z) \simeq \sqrt{\frac{\pi}{2z}}e^{-z},$$
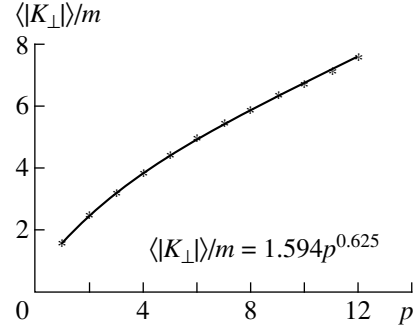
Fig. 2. $\langle |K_\perp| \rangle/m$ as a function of p. The points represent the results of calculations on the basis of (13). The line shows the best power-law fit.

the width of $\lambda(b)$ (3) is of order m^{-1}. The function G_0 is smooth in the vicinity of the origin, and its width $r_{0H} = \sqrt{r_0^2 + r_H^2}$ is significantly greater than the width of λ. For this reason, we factor $G_0(B + c)$ out of the integral in (8) with respect to c, taking it at the point B:

$$j(B, b) = G_0(B)\Lambda(b),$$
$$\Lambda(b) \equiv \int \lambda(c)\lambda(c - b)d^2c = \frac{|b|}{4\pi m}K_1(m|b|). \quad (11)$$

We then find that the integrals with respect to B and b decouple:

$$J(K_\perp) = \rho_A(\underbrace{0, \ldots, 0}_{p+1}|\underbrace{0, \ldots, 0}_{p+1})$$
$$\times \int G_0^p(B)d^2B\int \Lambda^p(b)e^{ibK_\perp}d^2b. \quad (12)$$

In this approximation, we find that $\langle |K_\perp| \rangle$ depends only on one parameter—the constituent quark mass m, which in our approach plays the role of an infrared cutoff:

$$\langle |K_\perp| \rangle = pm\int_0^\infty dzK_0(z)(zK_1(z))^{p-1}. \quad (13)$$

This allows us to relate m directly to the experimental data on the transverse-momentum dependence.

5. COMPARISON WITH THE DATA AND DISCUSSION

The integral in (13) can be easily calculated numerically. For values of $p = 1, \ldots, 12$, it is very well approximated by a power dependence (see Fig. 2), so that we obtain

$$\langle |K_\perp| \rangle/m = 1.594p^{0.625}. \quad (14)$$

As we observe, the rise of $\langle |K_\perp| \rangle$ turns out to be even faster than expected on naive physical grounds mentioned in the Introduction ($\sim\sqrt{p}$). The resulting plots
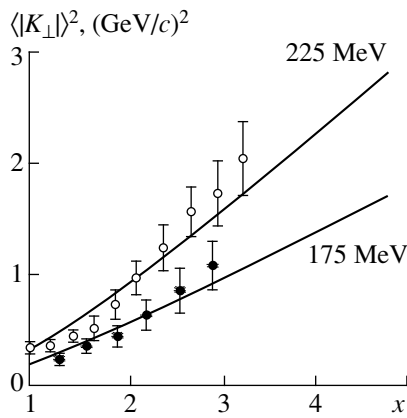
Fig. 3. $\langle |K_\perp| \rangle^2$ as a function of the cumulative number $x = (p + 1)/3$. The lines represent the results of the calculations on the basis of (13) at various values of parameter m. Closed circles correspond to experimental data from [6] on $\langle K_\perp^2 \rangle$ for pion production with a cutoff (see main body of the text) obtained in experiments where nuclei were bombarded by 10- and 9-GeV protons [6–10]. Open circles show data from earlier publications of the same group [7, 8] without a cutoff.

for $\langle |K_\perp| \rangle^2$ as a function of the cumulative number $x = (p + 1)/3$ at different values of parameter m are shown in Fig. 3 together with available experimental data from [6] on $\langle K_\perp^2 \rangle$ for pion production obtained in experiments [6–8] with 10-GeV protons and [9, 10] with 8.94-GeV, protons.

Note that earlier publications of the first group [7, 8] reported a much stronger increase of $\langle K_\perp^2 \rangle$ with x, up to a value of 2 (GeV/c)^2 at $x = 3$ for pion production. In our approach, such an increase would require the quark mass to be as high as $m \simeq 225$ MeV. In a recent publication [6], the rise of $\langle K_\perp^2 \rangle$ is substantially weaker (it corresponds to $m \simeq 175$ MeV in our approach). The authors of [6] explain this by new experimental data obtained and by a cutoff $K_{\perp\text{max}}$ introduced in calculations of $\langle K_\perp^2 \rangle$ in [6]. The introduction of this cutoff considerably (approximately two times) reduces the experimental value of $\langle K_\perp^2 \rangle$ at $x = 3$. In our opinion, this is a confirmation that the cumulative pion-production rate only weakly decreases with $K_\perp$ in the cumulative region, so that the integral over $K_\perp^2$, which enters the definition of $\langle K_\perp^2 \rangle$, is weakly convergent or even divergent, as in our approach. Undoubtedly, the presentation

of the experimental data in terms of the mean value $\langle |K_\perp| \rangle^2$ rather than $\langle K_\perp^2 \rangle$ should reduce the dependence on the cutoff $K_{\perp\text{max}}$ and make the results more informative.

One of the ideas behind the investigations of the cumulative phenomena is that they may be a manifestation of a cold quark–gluon plasma formed when several nucleons overlap in the nuclear matter. In [1], we pointed out that our model does not correspond to this picture. It implies coherent interactions of the active quark with donors and, as a result, strong correlations between the longitudinal and transverse motion. Predictions for the dependence of $\langle |K_\perp| \rangle$ on x are also different. From the cold quark–gluon plasma model, one expects $\langle |K_\perp| \rangle$ to behave as $x^{1/3}$ since the Fermi momentum of the quarks inside the overlap volume is proportional to the cubic root of the quark density. Our model predicts a much faster increase, with a power twice larger. The experimental data seem to support our predictions.

REFERENCES

1. M. Braun and V. Vechernin, Nucl. Phys. B **427**, 614 (1994).
2. M. Braun and V. Vechernin, Yad. Fiz. **60**, 506 (1997) [Phys. At. Nucl. **60**, 432 (1997)].
3. A. Capella and J. Tran Thanh Van, Z. Phys. C **10**, 249 (1981).
4. S. J. Brodsky, P. Hoyer, A. Mueller, and W.-K. Tang, Nucl. Phys. B **369**, 519 (1992).
5. A. B. Kaidalov, G. I. Lykasov, and N. V. Slavin, in *Proccedings of the IX International Seminar on High Energy Physics Problems, Joint Institute for Nuclear Research, Dubna, 1988*, p. 271.
6. S. V. Boyarinov *et al.*, Yad. Fiz. **57**, 1452 (1994) [Phys. At. Nucl. **57**, 1379 (1994)].
7. S. V. Boyarinov *et al.*, Yad. Fiz. **55**, 1675 (1992) [Sov. J. Nucl. Phys. **55**, 917 (1992)].
8. S. V. Boyarinov *et al.*, Yad. Fiz. **46**, 1472 (1987) [Sov. J. Nucl. Phys. **46**, 871 (1987)].
9. A. M. Baldin *et al.*, Preprint No. E-1-82-472, OIYaF (Joint Institute for Nuclear Research, Dubna, 1982).
10. A. M. Baldin *et al.*, Preprint No. R-1-83-432, OIYaF (Joint Institute for Nuclear Research, Dubna, 1983).

ELEMENTARY PARTICLES AND FIELDS
Theory

Radial Excitations of Scalar, η, and η' Mesons in a Chiral Quark Model*

M. K. Volkov** and V. L. Yudichev

Joint Institute for Nuclear Research, Dubna, Moscow oblast, 141980 Russia
Received May 28, 1999; in final form, October 19, 1999

Abstract—First radial excitations of the scalar-meson nonet and of the pseudoscalar mesons η and η' are described within a nonlocal chiral quark model of the Nambu–Jona-Lasinio type with 't Hooft interaction. In this model, simple form factors are used, which allows us to describe first radial excitations of the mesons and to retain the gap equations describing spontaneous breakdown of chiral symmetry in the standard form. The external parameters of form factors are fixed by the masses of excited pseudoscalar mesons, and the same form factors are used to predict the masses of excited scalar mesons. The strong decays of excited scalar mesons and of η and η' mesons are described in satisfactory agreement with experimental data. © *2000 MAIK "Nauka/Interperiodica".*

1. INTRODUCTION

A nonlocal chiral quark model of the Nambu–Jona-Lasinio (NJL) type was proposed in [1–4] for describing the first radial excitations of mesons. The nonlocality was introduced in the effective four-quark interaction through form factors represented by first-order polynomials in the quark momentum squared k^2. In [1], it was shown that such form factors can be rewritten in a relativistic form and that the internal parameters of these form factors (slope parameters) can be chosen in such a way that the quark condensates and gap equations appearing in the standard NJL model remain unchanged. With the form factors introduced in this way, all low-energy theorems hold in the chiral limit (see [1]).

In [2–4], this model was used to describe the mass spectrum of excited pions and kaons, and of the nonet of vector mesons. The main strong decays were also described therein.

Attempts at constructing a model for describing radially excited meson states were made, for example, by the authors of [5], who proposed a model involving quasilocal four-quark interaction in the polycritical regime. Various nonlocal models [6–8] were also proposed.

In the present work, we accomplish the investigation of the nonet of an excited pseudoscalar meson, considering the excited states of η and η' and studying the first radially excited states of the scalar meson nonet.

In order to describe correctly the masses of η and η' and of the isoscalar–scalar mesons, it is necessary to introduce, in addition to the standard four-quark inter-

action, six-quark 't Hooft interaction which breaks chiral symmetry and helps solve the so-called $U_A(1)$ problem. In contrast to the nonlocal four-quark interaction, 't Hooft vertices are purely local in accordance with their instantaneous origin.

The 't Hooft interaction gives rise to the mixing of four pseudoscalar states η, η', $\hat{η}$, and $\hat{η}'$ (the caret symbol labels radially excited meson states) and four scalar states σ, $\hat{σ}$, f_0, and $\hat{f}_0$. After diagonalization of the free meson Lagrangians, we obtain the mass spectrum of these meson states.

Each of the form factors used here depends on two arbitrary parameters, a slope parameter $d_α$ and an external parameter $c_α$. There are three slope parameters—d_{uu}, d_{us}, and d_{ss}. They are unambiguously defined by the condition requiring that excited mesons not contribute to the quark condensate (tadpoles including one form factor in the vertex equal to zero) and not therefore contribute to the gap equations. Meanwhile, the constituent quark masses remain constant. The external parameters $c_α$ affect the interaction of excited meson state with quarks or the corresponding four-quark interaction. For the pseudoscalar and vector mesons, we define these parameters, using the masses of excited meson states. For the scalar mesons, we use, however, the same form factors as for the pseudoscalar ones. Thus, we can predict the masses of excited scalar-meson states. They prove to be in satisfactory agreement with experimental data and allow us to identify the members of scalar-meson nonets and tell us which of them represent the ground states and which are radially excited states. This problem is discussed in the Conclusion.

After fitting the parameters $c_α$ and defining the basic model parameters [constituent quark masses m_u and m_s ($m_u ≈ m_d$), ultraviolet cutoff $Λ$, four-quark coupling

---

* This article was submitted by the authors in English.
** e-mail: volkov@tsun1.jinr.ru

constant G, and 't Hooft coupling constant K], we can describe all strong coupling constants of mesons and calculate their strong decay widths.

The ensuing exposition is organized as follows. In Section 2, we introduce the chiral quark Lagrangian involving nonlocal four-quark vertices and local 't Hooft interaction. In Section 3, we calculate the effective Lagrangian for isovector and strange mesons in the one-loop approximation. There, we renormalize meson fields, transform the free part of the Lagrangian to the diagonal form, and obtain meson mass formulas. Section 4 is devoted to isoscalar mesons, for which we find the masses and the mixing coefficients. The model parameters are discussed in Section 5. In Section 6, we calculate the widths with respect to the main strong decays of excited states of a_0, σ, f_0, and K_0^* mesons. In Section 7, we investigate the strong decays of the first radial excitations of η and η'. In Section 8, we analyze our results and compare them with experimental data. Some details of the calculations performed in Sections 4 and 6 are given in Appendix.

2. $U(3) \times U(3)$ CHIRAL LAGRANGIAN WITH EXCITED MESON STATES AND 't HOOFT INTERACTION

In the model that we use, a nonlocal separable four-quark interaction of a current–current form that admits nonlocal vertices (form factors) in the quark currents is supplemented with a purely local six-quark 't Hooft interaction [9, 10]:

$$\mathcal{L}(\bar{q}, q) = \int d^4 x \bar{q}(x)(i\partial\!\!\!/ - m^0)q(x) + \mathcal{L}_{int}^{(4)} + \mathcal{L}_{int}^{(6)}, \quad (1)$$

$$\mathcal{L}_{int}^{(4)} = \frac{G}{2}\int d^4 x \sum_{a=0}^{8} \sum_{i=1}^{N} [j_{S,i}^a(x)j_{S,i}^a(x) + j_{P,i}^a(x)j_{P,i}^a(x)], \quad (2)$$

$$\mathcal{L}_{int}^{(6)} = -K\{\det[\bar{q}(1+\gamma_5)q] + \det[\bar{q}(1-\gamma_5)q]\}. \quad (3)$$

Here, m^0 is the matrix of the current quark masses $(m_u^0 \approx m_d^0)$, while $j_{S(P),i}^a$ stands for the scalar (pseudo-scalar) quark currents

$$j_{S(P),i}^a(x) = \int d^4 x_1 d^4 x_2 \bar{q}(x_1) F_{S(P),i}^a(x; x_1, x_2)q(x_2), \quad (4)$$

where $F_{S(P),i}^a(x; x_1, x_2)$ are the scalar (pseudoscalar) nonlocal quark vertices. In order to describe the first radial excitations of mesons, we choose the form factors in the momentum space as (see [1–3])

$$F_{S,j}^a(\mathbf{k}) = \lambda^a f_j^a, \quad F_{P,j}^a = i\gamma_5\lambda^a f_j^a, \quad (5)$$

$$f_1^a \equiv 1, \quad f_2^a \equiv f_a(\mathbf{k}) = c_a(1 + d_a\mathbf{k}^2), \quad (6)$$

where λ^a are Gell-Mann matrices and $\lambda^0 = \sqrt{2/3} \cdot \mathbf{1}$, with $\mathbf{1}$ being an identity matrix. Here, we consider the

form factors in the meson rest frame.[1]

That part of the Lagrangian in (1) which describes the ground states and first radial excitations can be rewritten in the form (see [9, 10])

$$\mathcal{L} = \int d^4 x \left\{ \bar{q}(x)(i\partial\!\!\!/ - m^0)q(x) \right.$$

$$+ \frac{G}{2}\sum_{a=0}^{8} [(j_{S,2}^a(x))^2 + (j_{P,2}^a(x))^2]$$

$$+ \frac{1}{2}\sum_{a=1}^{9} [G_a^{(-)}(\bar{q}(x)\tau_a q(x))^2 + G_a^{(+)}(\bar{q}(x)i\gamma_5\tau_a q(x))^2]$$

$$+ G_{us}^{(-)}(\bar{q}(x)\lambda_u q(x))(\bar{q}(x)\lambda_s q(x))$$

$$\left. + G_{us}^{(+)}(\bar{q}(x)i\gamma_5\lambda_u q(x))(\bar{q}(x)i\gamma_5\lambda_s q(x)) \right\}, \quad (7)$$

where

$$\tau_i = \lambda_i \ (i = 1, \ldots, 7), \quad \tau_8 = \lambda_u = (\sqrt{2}\lambda_0 + \lambda_8)/\sqrt{3},$$

$$\tau_9 = \lambda_s = (-\lambda_0 + \sqrt{2}\lambda_8)/\sqrt{3},$$

$$G_1^{(\pm)} = G_2^{(\pm)} = G_3^{(\pm)} = G \pm 4Km_s I_1(m_s),$$

$$G_4^{(\pm)} = G_5^{(\pm)} = G_6^{(\pm)} = G_7^{(\pm)} = G \pm 4Km_u I_1(m_u), \quad (8)$$

$$G_u^{(\pm)} = G \mp 4Km_s I_1(m_s), \quad G_s^{(\pm)} = G,$$

$$G_{us}^{(\pm)} = \pm 4\sqrt{2}Km_u I_1(m_u).$$

Here, m_u and m_s are the constituent quark masses, and $I_1(m_q)$ is the integral that is defined for an arbitrary n as

$$I_n(m_q) = \frac{-iN_c}{(2\pi)^4}\int_{\Lambda_3} d^4 k \frac{1}{(m_q^2 - k^2)^n}. \quad (9)$$

The three-dimensional cutoff Λ_3 in (9) is implemented to regularize divergent integrals.[2]

---

[1] The form factors depend on the transverse parts of the relative momentum of quark–antiquark pairs $k_\perp = k - P(k \cdot P)/P^2$, where k and P are, respectively, the relative and the total momentum of a quark–antiquark pair. In the meson rest frame, $\mathbf{P}_{meson} = 0$, the transverse momentum is then $k_\perp = (0, \mathbf{k})$, and we can define the form factors in such a way that they depend only on the three-dimensional momentum $\mathbf{k}$.

[2] For instance, we have $I_1(m) = \dfrac{N_c m^2}{8\pi^2}[x\sqrt{x^2+1} - \ln(x + \sqrt{x^2+1})]|_{x=\Lambda_3/m}$.

3. MASSES OF ISOVECTOR AND STRANGE MESONS (GROUND AND EXCITED STATES)

After bosonization, that part of the Lagrangian in (7) that describes isovector and strange mesons takes the form

$$\mathscr{L}(a_{0,1}, K_{0,1}^*, \pi_1, K_1, a_{0,2}, K_{0,2}^*, \pi_2, K_2)$$

$$= -\frac{a_{0,1}^2}{2G_{a_0}} - \frac{(K_{0,1}^*)^2}{G_{K_0^*}} - \frac{\pi_1^2}{2G_\pi} - \frac{K_1^2}{G_K}$$

$$- \frac{1}{2G}(a_{0,2}^2 + 2(K_{0,2}^*)^2 + \pi_2^2 + 2K_2^2) \tag{10}$$

$$- iN_c \,\mathrm{tr}\ln\left[1 + \frac{1}{i\slashed{\partial} - m}\sum_{a=1}^{7}\sum_{j=1}^{2}\lambda_a(\sigma_j^a + i\gamma_5\varphi_j^a)f_j^a\right],$$

where $m = \mathrm{diag}(m_u, m_d, m_s)$ is the matrix of constituent quark masses ($m_u \approx m_d$), while σ_j^a and φ_j^a are the scalar and pseudoscalar fields: $\sum_{a=1}^{3}(\sigma_j^a)^2 \equiv a_{0,j}^2 = (a_{0,j}^0)^2 + 2a_{0,j}^+ a_{0,j}^-$, $\sum_{a=4}^{7}(\sigma_j^a)^2 \equiv 2(K_{0,j}^*)^2 = 2(\bar{K}_{0,j}^*)^0(K_{0,j}^*)^0 + 2(K_{0,j}^*)^+(K_{0,j}^*)^-$, $\sum_{a=1}^{3}(\varphi_j^a)^2 \equiv \pi_j^2 = (\pi_j^0)^2 + 2\pi_j^+\pi_j^-$, and $\sum_{a=4}^{7}(\varphi_j^a)^2 \equiv 2K_j^2 = 2\bar{K}_j^0 K_j^0 + 2K_j^+ K_j^-$. As to the coupling constants G_a, they will be defined later [see Section 5 and Eq. (8)].

The free part of the Lagrangian in (10) has the form

$$\mathscr{L}^{(2)}(\sigma, \varphi)$$

$$= \frac{1}{2}\sum_{i,j=1}^{2}\sum_{a=1}^{7}(\sigma_i^a K_{\sigma,ij}^a(P)\sigma_j^a + \varphi_i^a K_{\varphi,ij}^a(P)\varphi_j^a), \tag{11}$$

where the coefficients $K_{\sigma(\varphi),ij}^a(P)$ are given by

$$K_{\sigma(\varphi),ij}^a(P) = -\delta_{ij}\left[\frac{\delta_{i1}}{G_a^{(\mp)}} + \frac{\delta_{i2}}{G}\right]$$

$$- iN_c \,\mathrm{tr}\int_{\Lambda_3}\frac{d^4k}{(2\pi)^4}\frac{1}{\slashed{k} + \slashed{P}/2 - m_q^a}r^{\sigma(\varphi)}f_i^a \tag{12}$$

$$\times \frac{1}{\slashed{k} - \slashed{P}/2 - m_{q'}^a}r^{\sigma(\varphi)}f_j^a,$$

$$r^\sigma = 1, \quad r^\varphi = i\gamma_5, \tag{13}$$

$$m_q^a = m_u \ (a = 1, \ldots, 7), \quad m_{q'}^a = m_u \ (a = 1, \ldots, 3),$$
$$m_{q'}^a = m_s \ (a = 4, \ldots, 7), \tag{14}$$

with m_u and m_s being the constituent quark masses; the quantities f_j^a are defined in (6). The integral in (12) is

evaluated by means of an expansion in the meson field momentum P. To order P^2, one obtains

$$K_{\sigma(\varphi),11}^a(P) = Z_{\sigma(\varphi),1}^a(P^2 - (m_q^a \pm m_{q'}^a)^2 - M_{\sigma^a(\varphi^a),1}^2),$$

$$K_{\sigma(\varphi),22}^a(P) = Z_{\sigma(\varphi),2}^a(P^2 - (m_q^a \pm m_{q'}^a)^2 - M_{\sigma^a(\varphi^a),2}^2), \tag{15}$$

$$K_{\sigma(\varphi),12}^a(P) = K_{\sigma(\varphi),21}^a(P) = \gamma_{\sigma(\varphi)}^a(P^2 - (m_q^a \pm m_{q'}^a)^2),$$

where

$$Z_{\sigma,1}^a = 4I_2^a, \quad Z_{\sigma,2}^a = 4I_2^{f f_a}, \quad \gamma_\sigma^a = 4I_2^{f_a}, \tag{16}$$

$$Z_{\varphi,1}^a = ZZ_{\sigma,1}^a, \quad Z_{\varphi,2}^a = Z_{\sigma,2}^a, \quad \gamma_\varphi^a = Z^{1/2}\gamma_\sigma^a, \tag{17}$$

$$M_{\sigma^a(\varphi^a),1}^2 = (Z_{\sigma(\varphi),1}^a)^{-1}\left[\frac{1}{G_a^{(\mp)}} - 4(I_1(m_q^a) + I_1(m_{q'}^a))\right], \tag{18}$$

$$M_{\sigma^a(\varphi^a),2}^2 = (Z_{\sigma(\varphi),2}^a)^{-1}\left[\frac{1}{G} - 4(I_1^{f f_a}(m_q^a) + I_1^{f f_a}(m_{q'}^a))\right]. \tag{19}$$

The factor Z here appears owing to the inclusion of π–a_1 transitions [2, 11],

$$Z = 1 - \frac{6m_u^2}{M_{a_1}^2}, \tag{20}$$

and the integrals $I_2^{f\ldots f}$ contain form factors:

$$I_2^{f\ldots f_a}(m_q^a, m_{q'}^a)$$

$$= \frac{-iN_c}{(2\pi)^4}\int_{\Lambda_3}d^4k\frac{f_a(\mathbf{k})\ldots f_a(\mathbf{k})}{((m_q^a)^2 - k^2)((m_{q'}^a)^2 - k^2)}. \tag{21}$$

Further, we consider only the scalar–isovector and strange mesons because the masses of the pseudoscalar mesons have been already described in [2].

After renormalizing the scalar fields as

$$\sigma_i^{ar} = \sqrt{Z_{\sigma,i}^a}\,\sigma_i^a, \tag{22}$$

we can recast that part of the Lagrangian in (11) which describes the scalar mesons into the form

$$\mathscr{L}_{a_0}^{(2)} = \frac{1}{2}(P^2 - 4m_u^2 - M_{a_0,1}^2)a_{0,1}^2$$

$$+ \Gamma_{a_0}(P^2 - 4m_u^2)a_{0,1}a_{0,2} + \frac{1}{2}(P^2 - 4m_u^2 - M_{a_0,2}^2)a_{0,2}^2, \tag{23}$$

$$\mathscr{L}_{K_0^*}^{(2)} = \frac{1}{2}(P^2 - (m_u + m_s)^2 - M_{K_{0,1}^*}^2)(K_{0,1}^*)^2$$

$$+ \Gamma_{K_0^*}(P^2 - (m_u + m_s)^2)K_{0,1}^* K_{0,2}^* \tag{24}$$

$$+ \frac{1}{2}(P^2 - (m_u + m_s)^2 - M_{K_{0,2}^*}^2)(K_{0,2}^*)^2,$$

where

Table 1. Mixing coefficients for the ground and lowest radially excited states of scalar and pseudoscalar isovector and strange mesons (carets label excited states)

	a_0	$\hat{a}_0$		K_0^*	$\hat{K}_0^*$
$a_{0,1}$	0.87	0.82	$K_{0,1}^*$	0.83	0.89
$a_{0,2}$	0.22	−1.17	$K_{0,2}^*$	0.28	−1.11
	π	$\hat{\pi}$		K	$\hat{K}$
π_1	1.00	0.54	K_1	0.96	0.56
π_2	0.01	−1.14	K_2	0.09	−1.11

$$\Gamma_{\sigma^a} = \frac{I_2^{f_a}}{\sqrt{I_2 I_2^{ff_a}}}. \tag{25}$$

After the transformation of the meson fields, we have

$$\sigma^a = \cos(\theta_{\sigma,a} - \theta_{\sigma,a}^0)\sigma_1^{ar} - \cos(\theta_{\sigma,a} + \theta_{\sigma,a}^0)\sigma_2^{ar},$$
$$\hat{\sigma}^a = \sin(\theta_{\sigma,a} - \theta_{\sigma,a}^0)\sigma_1^{ar} - \sin(\theta_{\sigma,a} + \theta_{\sigma,a}^0)\sigma_2^{ar}. \tag{26}$$

The Lagrangians in (23) and (24) take the diagonal form

$$\mathscr{L}_{a_0}^{(2)} = \frac{1}{2}(P^2 - M_{a_0}^2)a_0^2 + \frac{1}{2}(P^2 - M_{\hat{a}_0}^2)\hat{a}_0^2, \tag{27}$$

$$\mathscr{L}_{K_0^*}^{(2)} = \frac{1}{2}(P^2 - M_{K_0^*}^2)(K_0^*)^2 + \frac{1}{2}(P^2 - M_{\hat{K}_0^*}^2)(\hat{K}_0^*)^2. \tag{28}$$

Here, we have

$$M_{(a_0,\hat{a}_0)}^2 = \frac{1}{2(1-\Gamma_{a_0}^2)}[M_{a_0,1}^2 + M_{a_0,2}^2$$
$$\pm \sqrt{(M_{a_0,1}^2 - M_{a_0,2}^2)^2 + (2M_{a_0,1}M_{a_0,2}\Gamma_{a_0})^2}] + 4m_u^2, \tag{29}$$

$$M_{(K_0^*,\hat{K}_0^*)}^2 = \frac{1}{2(1-\Gamma_{K_0^*}^2)}\Big[M_{K_0^*,1}^2 + M_{K_0^*,2}^2$$
$$\pm \sqrt{(M_{K_0^*,1}^2 - M_{K_0^*,2}^2)^2 + (2M_{K_0^*,1}M_{K_0^*,2}\Gamma_{K_0^*})^2}\Big]$$
$$+ (m_u + m_s)^2, \tag{30}$$

$$\tan 2\bar{\theta}_{\sigma,a} = \sqrt{\frac{1}{\Gamma_{\sigma^a}^2} - 1}\left[\frac{M_{\sigma^a,1}^2 - M_{\sigma^a,2}^2}{M_{\sigma^a,1}^2 + M_{\sigma^a,2}^2}\right], \tag{31}$$

$$2\theta_{\sigma,a} = 2\bar{\theta}_{\sigma,a} + \pi,$$

$$\sin\theta_{\sigma,a}^0 = \sqrt{\frac{1+\Gamma_{\sigma^a}}{2}}. \tag{32}$$

The caret symbol labels the first radial excitations of mesons. The transformations in (26) express the "physical" fields σ and $\hat{\sigma}$ in terms of the "bare" fields σ_i^{ar}, and these equations must be inverted for calculations. For practical use, we collect the values of the inverted equations for the scalar and pseudoscalar fields[3] in Table 1.

4. MASSES OF ISOSCALAR MESONS (GROUND AND EXCITED STATES)

The 't Hooft interaction effectively gives rise to additional four-quark vertices in the isoscalar part of the Lagrangian in (7):

$$\mathscr{L}_{\text{isosc}}$$
$$= \sum_{a,b=8}^{9}[(\bar{q}\tau_a q)T_{ab}^S(\bar{q}\tau_b q) + (\bar{q}i\gamma_5\tau_a q)T_{ab}^P(\bar{q}i\gamma_5\tau_b q)]. \tag{33}$$

Here $T^{S(P)}$ is a matrix whose elements are defined as [for the definition of $G_u^{(\mp)}$, $G_s^{(\mp)}$, and $G_{us}^{(\mp)}$, see (8)]

$$T_{88}^{S(P)} = G_u^{(\mp)}/2, \quad T_{89}^{S(P)} = G_{us}^{(\mp)}/2,$$
$$T_{98}^{S(P)} = G_{us}^{(\mp)}/2, \quad T_{99}^{S(P)} = G_s^{(\mp)}/2. \tag{34}$$

This leads to nondiagonal terms in the free part of the effective Lagrangian for isoscalar scalar and pseudoscalar mesons after bosonization,

$$\mathscr{L}_{\text{isosc}}(\sigma,\varphi) = -\frac{1}{4}\sum_{a,b=8}^{9}[\sigma_1^a(T^S)_{ab}^{-1}\sigma_1^b + \varphi_1^a(T^P)_{ab}^{-1}\varphi_1^b]$$
$$-\frac{1}{2G}\sum_{a=8}^{9}[(\sigma_2^a)^2 + (\varphi_2^a)^2] \tag{35}$$
$$-i\operatorname{tr}\ln\left\{1 + \frac{1}{i\slashed{\partial}-m}\sum_{a=8}^{9}\sum_{j=1}^{2}\tau^a[\sigma_j^a + i\gamma_5\varphi_j^a]f_j^a\right\},$$

where $(T^{S(P)})^{-1}$ is the inverse of $T^{S(P)}$:

$$(T^{S(P)})_{88}^{-1} = 2G_s^{(\mp)}/D^{(\mp)},$$
$$(T^{S(P)})_{89}^{-1} = (T^{S(P)})_{98}^{-1} = -2G_{us}^{(\mp)}/D^{(\mp)},$$
$$(T^{S(P)})_{99}^{-1} = 2G_u^{(\mp)}/D^{(\mp)}, \tag{36}$$
$$D^{(\mp)} = G_u^{(\mp)}G_s^{(\mp)} - (G_{us}^{(\mp)})^2.$$

From (35), in the one-loop approximation, one obtains the free part of the effective Lagrangian

---

[3]Although the formulas for the pseudoscalars are not displayed here (they have already been obtained in [2]), we need the values because we are going to calculate the decay widths with respect to processes where pions and kaons are secondary particles.

$$\mathscr{L}^{(2)}(\sigma, \varphi)$$

$$= \frac{1}{2} \sum_{i,j=1}^{2} \sum_{a,b=8}^{9} (\sigma_i^a K_{\sigma, ij}^{[a,b]}(P)\sigma_j^b + \varphi_i^a K_{\varphi, ij}^{[a,b]}(P)\varphi_j^b). \quad (37)$$

The definition of $K_{\sigma(\varphi), ij}^{[a,b]}$ is given in the Appendix.

After the renormalization of both the scalar and pseudoscalar fields, analogous to (22), we come to the Lagrangian which can be represented in a form slightly different from that of (37). It is convenient to introduce 4-vectors of "bare" fields

$$\Sigma = (\sigma_1^{8r}, \sigma_2^{8r}, \sigma_1^{9r}, \sigma_2^{9r}),$$
$$\Phi = (\varphi_1^{8r}, \varphi_2^{8r}, \varphi_1^{9r}, \varphi_2^{9r}). \quad (38)$$

Thus, we have

$$\mathscr{L}^{(2)}(\Sigma, \Phi)$$

$$= \frac{1}{2} \sum_{i,j=1}^{4} (\Sigma_i \mathscr{H}_{\Sigma, ij}(P)\Sigma_j + \Phi_i \mathscr{H}_{\Phi, ij}(P)\Phi_j), \quad (39)$$

where we introduced new functions $\mathscr{H}_{\Sigma(\Phi), ij}(P)$ (see Appendix).

Up to this moment, one has four pseudoscalar and four scalar meson states which are the octet and nonet singlets. The mesons of the same parity have the same quantum numbers; therefore, they are expected to be mixed. In our model, the mixing is represented by 4×4 matrices $R^{\sigma(\varphi)}$, which transform the "bare" fields σ_i^{8r}, σ_i^{9r}, φ_i^{8r}, and φ_i^{9r}, entering into the 4-vectors Σ and Φ, to the "physical" ones σ, $\hat{\sigma}$, f_0, $\hat{f}_0$, η, η', $\hat{\eta}$, and $\hat{\eta}'$, represented as components of vectors Σ_{ph} and Φ_{ph}:

$$\Sigma_{ph} = (\sigma, \hat{\sigma}, f_0, \hat{f}_0), \quad \Phi_{ph} = (\eta, \hat{\eta}, \eta', \hat{\eta}'), \quad (40)$$

where, let us recall once again, a caret over a meson field stands for the first radial excitation of the meson. The transformation $R^{\sigma(\varphi)}$ is linear and nonorthogonal:

$$\Sigma_{ph} = R^{\sigma}\Sigma, \quad \Phi_{ph} = R^{\varphi}\Phi. \quad (41)$$

In terms of "physical" fields, the free part of the effective Lagrangian is of the conventional form and the coefficients of matrices $R^{\sigma(\varphi)}$ give the mixing of the $\bar{u}u$ and $\bar{s}s$ components, with and without form factors.

Because of the complexity of the procedure of diagonalization for the matrices of dimensions greater than 2, there is no such simple formulas as, for example, in (26). Hence, we do not implement it analytically but use numerical methods to obtain matrix elements (see Table 2).

Table 2. Mixing coefficients for isoscalar meson states

	η	$\hat{\eta}$	η'	$\hat{\eta}'$
φ_1^8	0.71	0.62	−0.32	0.56
φ_2^8	0.11	−0.87	−0.48	−0.54
φ_1^9	0.62	0.19	0.56	−0.67
φ_2^9	0.06	−0.66	0.30	0.82
	σ	$\hat{\sigma}$	f_0	$\hat{f}_0$
σ_1^8	−0.98	−0.66	0.10	0.17
σ_2^8	0.02	1.15	0.26	−0.17
σ_1^9	0.27	−0.09	0.82	0.71
σ_2^9	−0.03	−0.21	0.22	−1.08

5. MODEL PARAMETERS AND MESON MASSES

In our model, we have five basic parameters: the masses of the constituent $u(d)$ and s quarks, $m_u = m_d$ and m_s, the cutoff parameter Λ_3, the four-quark coupling constant G, and the 't Hooft coupling constant K. We have fixed these parameters by means of input parameters: the pion decay constant $F_\pi = 93$ MeV, the ρ-meson decay constant $g_\rho = 6.14$ (decay $\rho \longrightarrow 2\pi$),[4] the masses of pion and kaon, and the mass difference of η and η' mesons (for details of these calculations, see [2, 3, 10]). Here, we give only numerical estimates of these parameters:

$$m_u = 280 \text{ MeV}, \quad m_s = 405 \text{ MeV}, \quad \Lambda_3 = 1.03 \text{ GeV},$$
$$G = 3.14 \text{ GeV}^{-2}, \quad K = 6.1 \text{ GeV}^{-5}. \quad (42)$$

We also have a set of additional parameters $c_{qq}^{\sigma^a(\varphi^a)}$ in form factors f_2^a. These parameters are defined by masses of excited pseudoscalar mesons, $c_{uu}^{\pi, a_0} = 1.44$, $c_{uu}^{\eta, \eta', \sigma, f_0} = 1.5$, $c_{us}^{K, K_0^*} = 1.59$, and $c_{ss}^{\eta, \eta', \sigma, f_0} = 1.66$. The slope parameters d_{qq} are fixed by special conditions satisfying the standard gap equation, $d_{uu} = -1.78$ GeV^{-2}, $d_{us} = -1.76$ GeV^{-2}, and $d_{ss} = -1.73$ GeV^{-2} (see [2]). Using these parameters, we obtain masses of pseudoscalar and scalar mesons which are listed in Table 3 together with experimental values.

From our calculations, we come to the following interpretation of $f_0(1370)$, $f_0(1710)$, and $a_0(1470)$

---

[4]Here, we do not consider vector and axial-vector mesons; however, we have used the relation $g_\rho = \sqrt{6} g_\sigma$ together with the Goldberger–Treiman relation $g_\pi = m/F_\pi = Z^{-1/2}g_\sigma$ to fix the parameters m_u and Λ_3 (see [2]).

Table 3. Model and experimental masses of mesons (in MeV)

	M_σ	M_{f_0}	M_{a_0}	$M_{K_0^*}$
GR	530	1070	830	960
EXC	1330	1600	1500	1500
GR (expt) [12]	400–1200	980 ± 10	983.4 ± 0.9	905 ± 50 [13]
EXC (expt) [12]	1200–1500	1712 ± 5	1474 ± 19	1429 ± 12
	M_π	M_K	M_η	$M_{\eta'}$
GR	140	490	520	910
EXC	1300	1300	1280	1470
GR (expt) [12]	139.56995 ± 0.00035	497.672 ± 0.031	547.30 ± 0.12	957.78 ± 0.14
EXC (expt) [12]	1300 ± 100	1460 (?)	1297.8 ± 2.8	1440–1470

mesons: we consider them as the first radial excitations of the ground states $f_0(400–1200)$, $f_0(980)$, and $a_0(980)$. Meanwhile, the meson $f_0(1500)$ is likely a glueball. However, this is just our supposition. Only consideration of a version of the NJL model with glueball states (or dilatons) will allow us to clarify the status of $f_0(1500)$ and $f_0(1710)$.

6. STRONG DECAYS OF THE SCALAR MESONS

The ground and excited states of scalar mesons f_0 and a_0 decay mostly into pairs of pseudoscalar mesons. In the framework of a quark model and in the leading order of $1/N_c$ expansion, the processes are described by triangle quark diagrams (see Fig. 1). Before we start to calculate the amplitudes corresponding to these diagrams, we introduce, for convenience, Yukawa coupling constants which naturally appear after the renormalization (22) of meson fields:

$$g_{\sigma_u} \equiv g_{\sigma^a}\big|_{a=1,2,3,8} = [4I_2(m_u)]^{-1/2},$$

$$g_{K_0^*} \equiv g_{\sigma^a}\big|_{a=4,5,6,7} = [4I_2(m_u, m_s)]^{-1/2},$$

$$g_{\sigma_s} \equiv g_{\sigma^9} = [4I_2(m_s)]^{-1/2}, \quad g_{\varphi^a} = Z^{-1/2}g_{\sigma^a}, \quad (43)$$

$$g_\pi \equiv g_{\varphi^a}\big|_{a=1,2,3}, \quad g_K \equiv g_{\varphi^a}\big|_{a=4,5,6,7},$$

$$g_{\varphi_u} \equiv g_{\varphi^8}, \quad g_{\varphi_s} \equiv g_{\varphi^9},$$

$$\hat{g}_{\sigma_u} \equiv \hat{g}_{\sigma^a}\big|_{a=1,2,3,8} = [4I_2^{ff}(m_u)]^{-1/2},$$

$$\hat{g}_{K_0^*} \equiv \hat{g}_{\sigma^a}\big|_{a=4,5,6,7} = [4I_2^{ff}(m_u, m_s)]^{-1/2},$$

$$\hat{g}_{\sigma_s} \equiv \hat{g}_{\sigma^9} = [4I_2^{ff}(m_s)]^{-1/2}, \quad \hat{g}_{\varphi^a} = \hat{g}_{\sigma^a}, \quad (44)$$

$$\hat{g}_\pi \equiv \hat{g}_{\varphi^a}\big|_{a=1,2,3}, \quad \hat{g}_K \equiv \hat{g}_{\varphi^a}\big|_{a=4,5,6,7},$$

$$\hat{g}_{\varphi_u} \equiv \hat{g}_{\varphi^8}, \quad \hat{g}_{\varphi_s} \equiv \hat{g}_{\varphi^9}.$$

They can easily be related to $Z^a_{\sigma(\varphi),i}$ introduced in the beginning of our paper. Thus, the one-loop contribution to the effective Lagrangian can be rewritten in terms of the renormalized fields:

$$\mathcal{L}_{1\text{-loop}}(\sigma, \varphi)$$

$$= -iN_c \,\text{tr}\ln\left[1 + \frac{1}{i\hat{\partial} - m}\sum_{a=1}^{9}\tau_a[g_{\sigma^a}\sigma_1^a + i\gamma_5 g_{\varphi^a}\varphi_1^a \right. \quad (45)$$

$$\left. + (\hat{g}_{\sigma^a}\sigma_2^a + i\gamma_5\hat{g}_{\varphi^a}\varphi_2^a)f_a\right].$$

All amplitudes that describe processes of the type $\sigma \longrightarrow \varphi_1\varphi_2$ can be divided into two parts:

$$T_{\sigma\to\varphi_1\varphi_2} = C\left(-\frac{iN_c}{(2\pi)^4}\right)\int_{\Lambda_3} d^4k$$

$$\times \frac{\text{tr}[(m + \not{k} + \not{p}_1)\gamma_5(m + \not{k})\gamma_5(m + \not{k} - \not{p}_2)]}{(m^2 - k^2)[m^2 - (k + p_1)^2][m^2 - (k - p_2)^2]}$$

$$= 4mC\left(-\frac{iN_c}{(2\pi)^4}\right)\int_{\Lambda_3} d^4k \quad (46)$$

$$\times \frac{1 - p_1\cdot p_2/(m^2 - k^2)}{[m^2 - (k + p_1)^2][m^2 - (k - p_2)^2]}$$

$$= 4mC[I_2(m, p_1, p_2) - p_1\cdot p_2 I_3(m, p_1, p_2)]$$

$$= T^{(1)} + T^{(2)}.$$

Here, $C = 4g_\sigma g_{\varphi_1}g_{\varphi_2}$ and p_1, p_2 are momenta of the pseudoscalar mesons. Using (43) and (44), we rewrite the amplitude $T_{\sigma\to\varphi_1\varphi_2}$ in another form

$$T_{\sigma\to\varphi_1\varphi_2} \approx 4mZ^{-1/2}g_{\varphi_1}\left[1 - p_1\cdot p_2\frac{I_3(m)}{I_2(m)}\right], \quad (47)$$

$$p_1 \cdot p_2 = \frac{1}{2}(M_\sigma^2 - M_{\varphi_1}^2 - M_{\varphi_2}^2). \qquad (48)$$

We assumed here that the ratio I_3/I_2 slowly changes with momentum in comparison with factor $p_1 \cdot p_2$. Therefore, we ignore its momentum dependence in (47). With this assumption we hope to obtain just a qualitative picture for decays of the excited scalar mesons.

In (46) and (47), we omitted the contributions from the diagrams which include form factors in vertices. The whole set of diagrams consists of those containing zero, one, two, and three form factors. To obtain the complete amplitude, one needs to sum up all contributions.

After these general comments, let us consider the decays of $a_0(1450)$, $f_0(1370)$, and $f_0(1710)$. First, we estimate the decay width of the process $\hat{a}_0 \longrightarrow \eta\pi$ taking the mixing coefficients from Tables 1 and 2 (see Appendix for the details). The result is

$$T^{(1)}_{\hat{a}_0 \to \eta\pi} \approx 0.2 \text{ GeV}, \qquad (49)$$

$$T^{(2)}_{\hat{a}_0 \to \eta\pi} \approx 3.5 \text{ GeV}, \qquad (50)$$

$$\Gamma_{\hat{a}_0 \to \eta\pi} \approx 160 \text{ MeV}. \qquad (51)$$

From this result, one can see that $T^{(1)} \ll T^{(2)}$ and the amplitude is dominated by its second part, $T^{(2)}$, which is momentum dependent. The first part is small because the diagrams with different numbers of form factors cancel each other. As a consequence, in all processes where an excited scalar meson decays into a pair of ground pseudoscalar states, the second part of the amplitude defines the rate of the process.

For the decay $\hat{a}_0 \longrightarrow \pi\eta'$, we obtain the values of amplitudes

$$T^{(1)}_{\hat{a}_0 \to \pi\eta'} \approx 0.8 \text{ GeV}, \qquad (52)$$

$$T^{(2)}_{\hat{a}_0 \to \pi\eta'} \approx 3 \text{ GeV}, \qquad (53)$$

and the decay width

$$\Gamma_{\hat{a}_0 \to \pi\eta'} \approx 36 \text{ MeV}. \qquad (54)$$

The decay of $\hat{a}_0$ into kaons is described by the amplitudes $T_{\hat{a}_0 \to K^+ K^-}$ and $T_{\hat{a}_0 \to \bar{K}^0 K^0}$, which, in accordance with our scheme, can again be divided into two parts: $T^{(1)}$ and $T^{(2)}$ (see Appendix for details):

$$T^{(1)}_{\hat{a}_0 \to K^+ K^-} \approx 0.2 \text{ GeV}, \qquad (55)$$

$$T^{(2)}_{\hat{a}_0 \to K^+ K^-} \approx 2.1 \text{ GeV}, \qquad (56)$$

and the decay width is

$$\Gamma_{\hat{a}_0 \to KK} = \Gamma_{\hat{a}_0 \to K^+ K^-} + \Gamma_{\hat{a}_0 \to \bar{K}^0 K^0} \approx 100 \text{ MeV}. \qquad (57)$$
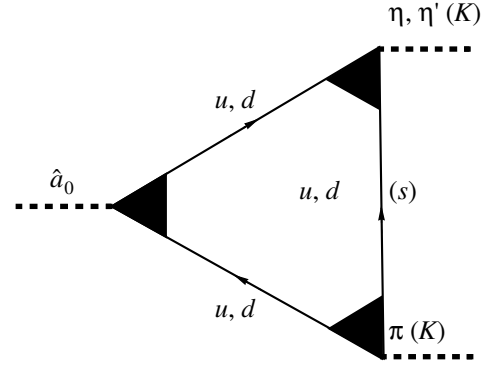

Fig. 1. Diagrams describing the decays of $\hat{a}_0$ into pseudoscalars.

Qualitatively, our results do not contradict the experimental data

$$\Gamma^{\text{tot}}_{\hat{a}_0} = 256 \pm 13 \text{ MeV},$$
$$\text{Br}(\hat{a}_0 \longrightarrow KK) : \text{Br}(\hat{a}_0 \longrightarrow \pi\eta) = 0.88 \pm 0.23. \qquad (58)$$

The decay widths of radial excitations of scalar–isoscalar mesons are estimated in the same way as was shown above. We obtain (Γ in MeV)

$$\Gamma_{\hat{\sigma} \to \pi\pi} = \begin{cases} 550 \ (M_{\hat{\sigma}} = 1.3 \text{ GeV}) \\ 460 \ (M_{\hat{\sigma}} = 1.25 \text{ GeV}), \end{cases} \qquad (59)$$

$$\Gamma_{\hat{\sigma} \to \eta\eta} = \begin{cases} 24 \ (M_{\hat{\sigma}} = 1.3 \text{ GeV}) \\ 15 \ (M_{\hat{\sigma}} = 1.25 \text{ GeV}), \end{cases} \qquad (60)$$

$$\Gamma_{\hat{\sigma} \to \sigma\sigma} = \begin{cases} 6 \ (M_{\hat{\sigma}} = 1.3 \text{ GeV}) \\ 5 \ (M_{\hat{\sigma}} = 1.25 \text{ GeV}), \end{cases} \qquad (61)$$

$$\Gamma_{\hat{\sigma} \to KK} \sim 5, \qquad (62)$$

$$\begin{array}{ll} \Gamma_{f_0(1710) \to 2\pi} \approx 3, & \Gamma_{f_0(1500) \to 2\pi} \approx 3, \\ \Gamma_{f_0(1710) \to 2\eta} \approx 40, & \Gamma_{f_0(1500) \to 2\eta} \approx 20, \\ \Gamma_{f_0(1710) \to \eta\eta'} \approx 42, & \Gamma_{f_0(1500) \to \eta\eta'} \approx 10, \\ \Gamma_{f_0(1710) \to KK} \approx 24, & \Gamma_{f_0(1500) \to KK} \approx 20. \end{array} \qquad (63)$$

The rates of $f_0(1500)$ and $f_0(1710)$ decays into $\sigma\sigma$ pairs are negligible, so we disregard them.

Here, we displayed our estimates for both $f_0(1710)$ and $f_0(1500)$ resonances. Comparing them one to another will allow us to decide which one to consider as the first radial excitation of $f_0(980)$ and which one as a glueball. From the experimental data

$$\Gamma^{\text{tot}}_{\sigma'} = 200\text{–}500 \text{ MeV}, \quad \Gamma^{\text{tot}}_{f_0(1710)} = 133 \pm 14 \text{ MeV},$$
$$\Gamma^{\text{tot}}_{f_0(1500)} = 112 \pm 10 \text{ MeV}, \qquad (64)$$

Table 4. $\eta(1295)$ and $\eta(1440)$ decay modes (Γ in MeV)

	$a_0\pi$	$\eta\sigma$	$\eta\pi\pi$	$K\bar{K}\pi$	KK^*	Γ_{tot}
$\eta(1295)$	3	30	4	5	–	48
$\eta(1440)$	10	3	6	26	0.07	45

we can see that in the case of $f_0(1500)$ being a $\bar{q}q$ state there is a deficit in the decay widths, whereas for $f_0(1710)$ the result is close to experiment. From this, we conclude that the meson $f_0(1710)$ is a radially excited partner for $f_0(980)$ and the meson state $f_0(1370)$ is the first radial excitation of $f_0(400-1200)$. As to the state $f_0(1500)$, we are inclined to consider it as a glueball which significantly contributes to the decay width.[5]

The first radially excited state of the strange scalar $\hat{K}_0^*$ decays mostly to $K\pi$ and is characterized by the width

$$\Gamma_{\hat{K}_0^* \to K\pi} \approx 300 \text{ MeV}. \tag{65}$$

This value is in agreement with experiment:

$$\Gamma_{K_0^*(1430) \to K\pi}^{\text{exp}} \approx 287 \pm 23 \text{ MeV}. \tag{66}$$

The strong decay widths of the ground states of scalar mesons were calculated in [10] in the framework of the standard NJL model with 't Hooft interaction. It was shown that a strange scalar meson state with mass about 960 MeV decays into $K\pi$ with the rate

$$\Gamma_{K_0^*(960) \to K\pi} = \frac{3}{Z\pi M_{K_0^*}}\left(\frac{m_u m_s}{2F_\pi}\right)^2$$

$$\times \sqrt{\frac{[M_{K_0^*}^2 - (M_K - M_\pi)^2][M_{K_0^*}^2 - (M_K + M_\pi)^2]}{M_{K_0^*}^4}} \tag{67}$$

$$\approx 360 \text{ MeV}.$$

From comparing this result with the analysis of phase shifts given in [13], where evidence for existence of a strange scalar meson with the mass equal to 905 ± 50 MeV and decay width 545 ± 170 MeV is shown, we identify the state $K_0^*(960)$ as a member of the ground scalar meson nonet. The state $K_0^*(1430)$ is thereby its first radial excitation.

7. STRONG DECAYS OF $\eta(1295)$ AND $\eta(1440)$

The mesons $\eta(1295)$ and $\eta(1440)$ have common decay modes: $a_0\pi$, $\eta\pi\pi$, $\eta(\pi\pi)_{S\text{-wave}}$, and $K\bar{K}\pi$. Moreover, the heavier pseudoscalar $\eta(1440)$ also decays into

---

[5]Let us emphasize again that it is only our preliminary conclusion. A more careful investigation of this problem will be done in our further works.

KK^*. For the processes with two secondary particles, the calculations of decay widths are done in the same way as shown in the previous section, by calculating triangle diagrams similar to that in Fig. 1.

Let us consider the decay $\hat{\eta} \longrightarrow a_0\pi$. The corresponding amplitude is of the same form as given in (46) for decays of the type $\sigma \longrightarrow \varphi_1\varphi_2$. It can also be divided into two parts $T^{(1)}$ and $T^{(2)}$ which in our approximation are constant and momentum-dependent in the sense explained in the previous section (see (47) and the text below):

$$T_{\hat{\eta} \to a_0\pi}^{(1)} \approx 0.3 \text{ GeV}, \tag{68}$$

$$T_{\hat{\eta} \to a_0\pi}^{(2)} \approx -1 \text{ GeV}. \tag{69}$$

Therefore, the decay width is

$$\Gamma_{\hat{\eta} \to a_0\pi} \approx 3 \text{ MeV}. \tag{70}$$

The decay $\hat{\eta} \longrightarrow \eta(\pi\pi)_{S\text{-wave}}$ is nothing else than the decay $\hat{\eta} \longrightarrow \eta\sigma \longrightarrow \eta(\pi\pi)_{S\text{-wave}}$ where we have the σ meson in the final state decaying then into pions in the S wave. We simply calculate $\hat{\eta} \longrightarrow \eta\sigma$, with σ as a decay product.

The calculation of decay widths for the rest of the decay modes with two particles in the final state is similar, and the result is given in Table 4.

The decay $\hat{\eta}' \longrightarrow KK^*$ differs from the other modes by a strange vector meson among the decay products. In this case, we have

$$T_{\hat{\eta}' \to KK^*}^\mu = 4(p_1 + p_2)^\mu\{[g_u g_K g_{K^*} I_2(m_u, m_s) + \ldots] - \sqrt{2}[g_s g_K g_{K^*} I_2(m_u, m_s) + \ldots]\}, \tag{71}$$

where p_1 is the momentum of $\hat{\eta}'$, p_2 is the momentum of K, and dots stand for the terms with form factors (not displayed here). These two parts are of the same order of magnitude and differ in sign and therefore cancel each other, which reduces the decay width up to tens of keV:

$$\Gamma_{\hat{\eta}' \to KK^*} \approx 70 \text{ keV}. \tag{72}$$

When there are three particles in the final state, poles appear in amplitudes, associated with intermediate scalar resonances. As is well known from $\pi\pi$ scattering, these diagrams can play a crucial role in the description of such processes. So, in addition to the "box" diagram, we take into account the diagrams with poles provided by σ, f_0, and a_0 resonances (see Fig. 2 for the decay $\hat{\eta} \longrightarrow \eta\pi\pi$). Here, we neglect the momentum dependence in the box diagram, approxi-

mating it by a constant. The amplitude is thereby

$$T_{\hat{\eta} \to \eta\pi\pi} = B + \frac{c_{\sigma\eta\hat{\eta}}c_{\sigma\pi\pi}}{M_\sigma - s - iM_\sigma\Gamma_\sigma} + \frac{c_{f_0\eta\hat{\eta}}c_{f_0\pi\pi}}{M_{f_0} - s - iM_{f_0}\Gamma_{f_0}}$$

$$+ \frac{c_{a_0\hat{\eta}\pi}c_{a_0\eta\pi}}{M_{a_0} - t - iM_{a_0}\Gamma_{a_0}} + \frac{c_{a_0\hat{\eta}\pi}c_{a_0\eta\pi}}{M_{a_0} - u - iM_{a_0}\Gamma_{a_0}} + \text{excited,} \quad (73)$$

where B is given by the "box" diagram:

$$B = 12\left(\frac{m_u}{F_\pi}\right)^2 Z^{-1}[R_{11}R_{12} + \ldots]. \quad (74)$$

The ellipsis in (74) stands for the contribution from diagrams with form factors, and R_{ij} are taken from Table 2 (for η and $\hat{\eta}$). The coefficients $c_{\sigma\varphi\varphi}$ represent the amplitudes describing decays of a scalar to a pair of pseudoscalars; the calculation of them is discussed in the preceding section. In general, they are momentum-dependent.

The kinematical invariants s, t, and u are Mandelstam variables: $s = (p_{\pi_1} + p_{\pi_2})^2$, $t = (p_\eta + p_{\pi_1})^2$, and $u = (p_\eta + p_{\pi_2})^2$.

The "excited" terms are the contributions from excited scalar resonances of a structure similar to that for the ground states. The decay widths of processes $\hat{\eta} \to \eta\pi\pi$ and $\hat{\eta}' \to \eta\pi\pi$ are thereby

$$\Gamma_{\hat{\eta} \to \eta\pi\pi} \approx 4 \text{ MeV}, \quad \Gamma_{\hat{\eta}' \to \eta\pi\pi} \approx 6 \text{ MeV}. \quad (75)$$

For the processes $\hat{\eta} \to K\overline{K}\pi$ and $\hat{\eta}' \to K\overline{K}\pi$, we approximate their decay widths by neglecting the pole-diagram contribution because it turns out that the "box" is dominant here. The result is given in Table 4.

Unfortunately, the branching ratios for different decay modes of $\eta(1295)$ and $\eta(1440)$ are not known well from experiment; so, one can only find their total decay widths

$$\Gamma_{\eta(1295)}^{\text{tot}} = 53 \pm 6 \text{ MeV}, \quad \Gamma_{\eta(1440)}^{\text{tot}} = 50\text{--}80 \text{ MeV}, \quad (76)$$

which is in satisfactory agreement with our results.

Strong and electromagnetic decays of the ground states of η and η' mesons were already investigated within framework of the standard NJL model in [11], and we do not consider them here.

8. DISCUSSION AND CONCLUSION

Let us briefly recall some problems concerning the interpretation of experimental data on scalar, η, and η' mesons. Several years ago, attempts were undertaken to consider the state $\eta'(1440)$ as a glueball [14]. There is an analogous problem with the interpretation of scalar states $f_0(1500)$ and $f_0(1710)$. Moreover, the experimental status of the lightest scalar–isoscalar singlet meson was unclear. In some papers, the resonance $f_0(1370)$ was considered as a member of the ground nonet [15],
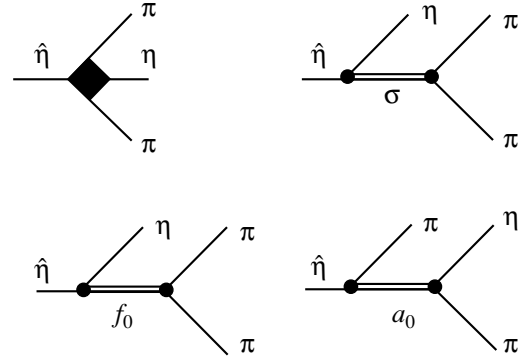

Fig. 2. Diagrams describing the decay $\hat{\eta} \to \eta\pi\pi$. The black box depicts the sum of "box" diagrams represented by one-loop quark graphs with four meson vertices. The rest of the diagrams are a set of pole graphs with the σ, f_0, and a_0 scalar resonances. The diagram featuring a_0 must be taken into account for two channels (due to exchange of the pion momenta). There are analogous contributions from radially excited resonances.

and it was not until 1998 that the resonance $f_0(400–1200)$ was included in the summary tables of PDG review[6] [12].

One will find a problem of the same sort in the case of K_0^*. The strange meson $K_0^*(1430)$ seems too heavy to be the ground state: 1 GeV is more characteristic of the ground meson states (see [13, 16]).

From our calculations we conclude that the states $\eta(1295)$ and $\eta(1440)$ can be treated as radial excitations of the ground states η and η'. The calculation of their strong decay widths also confirms our conclusion. Let us note that these meson states are significantly mixed.

In [14], the authors came to similar conclusions about $\eta(1295)$ and $\eta(1440)$, where the radial excitations of the mesons were investigated in the potential $^3P_0$ model.

Our calculations also showed that we can interpret the scalar states $f_0(1370)$, $a_0(1450)$, $f_0(1710)$, and $K_0^*(1430)$ as the lowest radial excitations of $f_0(400–1200)$, $a_0(980)$, $f_0(980)$, and $K_0^*(960)$. We estimated their masses and the widths of main decays in the framework of a nonlocal chiral quark model. We would like to emphasize that we did not use additional parameters except those necessary to fix the mass spectrum of pseudoscalar mesons. We used the same form factors for both scalar and pseudoscalar mesons, which is required by the global chiral symmetry.

We assumed that the state $f_0(1500)$ is a glueball, and its probable mixing with $f_0(980)$, $f_0(1370)$, and $f_0(1710)$ may provide us with a more correct description of the

---

[6]However, in earlier editions of PDG, the light σ state still could be found; it was excluded later.

masses of these states[7] (see Table 3 and [17]). We hope to consider this problem in a subsequent publication.

A more complicated situation takes place for the ground state $a_0(980)$. In the framework of our quark–antiquark model, we have a mass deficit for this meson, 830 MeV rather than 980 MeV. We suspect that this deficiency is due to a four-quark component in this state which we did not take into account [18].

In the future, we are going to consider glueball states [17] and to develop a model with quark confinement [19] to describe the momentum dependence of the meson amplitudes.

ACKNOWLEDGMENTS

APPENDIX

COEFFICIENTS OF THE FREE PART OF EFFECTIVE LAGRANGIAN FOR THE SCALAR–ISOSCALAR MESONS

The functions $K^{[a,a]}_{\sigma(\varphi),ij}$ introduced in Section 4 [Eq. (37)] are defined as follows:

$$K^{[a,a]}_{\sigma(\varphi),11}(P) = Z^a_{\sigma(\varphi),1}[P^2 - (m^a_q \pm m^a_{q'})^2 - M^2_{\sigma^a(\varphi^a),1}],$$

$$K^{[a,a]}_{\sigma(\varphi),22}(P) = Z^a_{\sigma(\varphi),2}[P^2 - (m^a_q \pm m^a_{q'})^2 - M^2_{\sigma^a(\varphi^a),2}],$$

$$K^{[a,a]}_{\sigma(\varphi),12}(P) = K^{[a,a]}_{\sigma(\varphi),21}(P) = \gamma^a_{\sigma(\varphi)}[P^2 - (m^a_q \pm m^a_{q'})^2],$$

$$K^{[8,9]}_{\sigma(\varphi),11}(P) = K^{[9,8]}_{\sigma(\varphi),11}(P) = \frac{1}{2}(T^{S(P)})^{-1}_{89}, \quad \text{(A.1)}$$

$$K^{[8,9]}_{\sigma(\varphi),12}(P) = K^{[9,8]}_{\sigma(\varphi),12}(P) = K^{[8,9]}_{\sigma(\varphi),21}(P) = 0,$$

$$K^{[9,8]}_{\sigma(\varphi),21}(P) = K^{[8,9]}_{\sigma(\varphi),22}(P) = 0, \quad K^{[9,8]}_{\sigma(\varphi),22}(P) = 0,$$

where the "bare" meson masses are

$$M^2_{\sigma^8(\varphi^8),1} = (Z^8_{\sigma(\varphi),1})^{-1}\left(\frac{1}{2}(T^{S(P)})^{-1}_{88} - 8I_1(m_u)\right),$$

$$M^2_{\sigma^9(\varphi^9),1} = (Z^9_{\sigma(\varphi),1})^{-1}\left(\frac{1}{2}(T^{S(P)})^{-1}_{99} - 8I_1(m_s)\right),$$

$$M^2_{\sigma^8(\varphi^8),2} = (Z^8_{\sigma(\varphi),2})^{-1}\left(\frac{1}{G} - 8I^{ff}_1(m_u)\right), \quad \text{(A.2)}$$

$$M^2_{\sigma^9(\varphi^9),2} = (Z^9_{\sigma(\varphi),2})^{-1}\left(\frac{1}{G} - 8I^{ff}_1(m_s)\right).$$

In the case of isoscalar mesons, it is convenient to combine the scalar and pseudoscalar fields into 4-vectors

$$\Sigma = (\sigma^{8r}_1, \sigma^{8r}_2, \sigma^{9r}_1, \sigma^{9r}_2),$$

$$\Phi = (\varphi^{8r}_1, \varphi^{8r}_2, \varphi^{9r}_1, \varphi^{9r}_2),$$

and introduce 4×4 matrix functions $\mathcal{K}_{\sigma(\varphi),ij}$ instead of $K^{[a,b]}_{\sigma(\varphi),ij}$, where indices i, j run from 1 to 4. This allows us to rewrite the free part of the effective Lagrangian, which then, with the meson fields renormalized, is written as

$$\mathcal{L}^{(2)}(\Sigma, \Phi)$$
$$= \frac{1}{2}\sum_{i,j=1}^{4}(\Sigma_i\mathcal{K}_{\sigma,ij}(P)\Sigma_j + \Phi_i\mathcal{K}_{\varphi,ij}(P)\Phi_j), \quad \text{(A.3)}$$

and the functions $\mathcal{K}_{\sigma(\varphi),ij}$ are

$$\mathcal{K}_{\sigma(\varphi),11}(P) = P^2 - (m_u \pm m_u)^2 - M^2_{\sigma^8(\varphi^8),1},$$

$$\mathcal{K}_{\sigma(\varphi),22}(P) = P^2 - (m_u \pm m_u)^2 - M^2_{\sigma^8(\varphi^8),2},$$

$$\mathcal{K}_{\sigma(\varphi),33}(P) = P^2 - (m_s \pm m_s)^2 - M^2_{\sigma^9(\varphi^9),1},$$

$$\mathcal{K}_{\sigma(\varphi),44}(P) = P^2 - (m_s \pm m_s)^2 - M^2_{\sigma^9(\varphi^9),2}, \quad \text{(A.4)}$$

$$\mathcal{K}_{\sigma(\varphi),12}(P) = \mathcal{K}_{\sigma(\varphi),21}(P) = \Gamma_{\sigma_u(\eta_u)}[P^2 - (m_u \pm m_u)^2],$$

$$\mathcal{K}_{\sigma(\varphi),34}(P) = \mathcal{K}_{\sigma(\varphi),43}(P) = \Gamma_{\sigma_s(\eta_s)}[P^2 - (m_s \pm m_s)^2],$$

$$\mathcal{K}_{\sigma(\varphi),13}(P) = \mathcal{K}_{\sigma(\varphi),31}(P) = (Z^8_{\sigma(\varphi),1}Z^9_{\sigma(\varphi),1})^{-1/2}(T^{S(P)})^{-1}_{89}.$$

Now, to transform (A.3) to conventional form, one should just diagonalize a four-dimensional matrix, which is better to do numerically.

THE CALCULATION OF THE AMPLITUDES FOR THE DECAYS OF THE EXCITED SCALAR MESON $\hat{a}_0$

Here, we collect some instructive formulas which display some of the details of the calculations made in this work. Let us demonstrate how the amplitude of the decay $\hat{a}_0 \longrightarrow \eta\pi$ is obtained. The mixing coefficients are taken from Table 1. Moreover, the diagrams where pion vertices contain form factors are neglected because, as one can see from Table 1, their contribution is significantly reduced:

$$T^{(1)}_{\hat{a}_0 \to \eta\pi} = 4\frac{m_u^2}{F_\pi}\left\{0.82 \cdot 0.71 Z^{-1/2}\frac{I_2(m_u)}{I_2(m_u)}\right.$$

$$-(1.17 \cdot 0.71 Z^{-1/2} - 0.82 \cdot 0.11)\frac{I_2^f(m_u)}{\sqrt{I_2(m_u)I_2^{ff}(m_u)}}$$

$$\left. -1.17 \cdot 0.11\frac{I_2^{ff}(m_u)}{I_2^{ff}(m_u)}\right\} \approx 0.2 \text{ GeV},$$

$$T^{(2)}_{\hat{a}_0 \to \eta\pi} = 2\frac{m_u^2}{F_\pi}(M_{a_0}^2 - M_\eta^2 - M_\pi^2)$$

$$\times \left\{0.82 \cdot 0.71 Z^{-1/2}\frac{I_3(m_u)}{I_2(m_u)}\right.$$

$$-(1.17 \cdot 0.71 Z^{-1/2} - 0.82 \cdot 0.11)\frac{I_3^f(m_u)}{\sqrt{I_2(m_u)I_2^{ff}(m)}}$$

$$\left. -1.17 \cdot 0.11\frac{I_3^{ff}(m_u)}{I_2^{ff}(m_u)}\right\} \approx 3.5 \text{ GeV}.$$

The appropriate decay width thereby is

$$\Gamma_{\hat{a}_0 \to \eta\pi} = \frac{\left|T_{\hat{a}_0 \to \eta\pi}\right|^2}{16\pi M_{\hat{a}_0}^3}$$

$$\times \sqrt{M_{\hat{a}_0}^4 + M_\eta^4 + M_\pi^4 - 2(M_{\hat{a}_0}^2 M_\eta^2 + M_{\hat{a}_0}^2 M_\pi^2 + M_\eta^2 M_\pi^2)}$$

$$\approx 160 \text{ MeV}.$$

Here, $I_2(m_u) = 0.04$, $I_2^f(m_u) = 0.014c$, $I_2^{ff}(m_u) = 0.015c^2$, $I_3(m_u) = 0.11$ GeV^{-2}, $I_3^f(m_u) = 0.07c$ GeV^{-2}, $I_3^{ff}(m_u) = 0.06c^2$ GeV^{-2}, and c is the external form factor parameter factored out and canceled in the ratios of the integrals.

For the decay into strange mesons, we obtain (see Fig. 1)

$$T_{\hat{a}_0 \to K^+ K^-} = C_K\left(-\frac{iN_c}{16\pi^2}\right)\int d^4 k$$

$$\times \frac{\text{tr}[(m_u + \slashed{k} + \slashed{p}_1)\gamma_5(m_s + \slashed{k})\gamma_5(m_u + \slashed{k} + \slashed{p}_2)]}{(m_s^2 - k^2)[m_u^2 - (k - p_1)^2][m_u^2 - (k - p_2)^2]}$$

$$\approx 2C_K\{(m_s + m_u)I_2(m_u) - \Delta I_2(m_u, m_s)$$

$$- [m_s(M_{\hat{a}_0}^2 - 2M_K^2) - 2\Delta^3]I_3(m_u, m_s)\},$$

where $\Delta = m_s - m_u$ and

$$I_3(m_u, m_s) = -i\frac{N_c}{(2\pi)^4}\int_{\Lambda_3} \frac{d^4 k}{(m_u^2 - k^2)^2(m_s^2 - k^2)}.$$

The coefficient C_K absorbs the Yukawa coupling constants and some structure coefficients. The integral $I_2(m_u, m_s)$ is defined by (21). This is only the part of the amplitude without form factors. The complete amplitude of this process is a sum of contributions which also contain the integrals $I_2^{f...f}$ and $I_3^{f...f}$ with form factors. Thus, the amplitude is

$$T_{\hat{a}_0 \to K^+ K^-} = T^{(1)} + T^{(2)},$$

$$T^{(1)} = \frac{m_u + m_s}{2F_K}\{(m_s + m_u) \cdot 0.13 - \Delta \cdot 0.21\}$$

$$\approx 0.2 \text{ GeV},$$

$$T^{(2)} = \frac{m_u + m_s}{2F_K}\{[m_s(M_{\hat{a}_0}^2 - 2M_K^2) - 2\Delta^3] \cdot 1 \text{ GeV}^{-2}\}$$

$$\approx 2.1 \text{ GeV},$$

$$F_K = 1.2 F_\pi.$$

The decay width therefore is evaluated to be

$$\Gamma_{\hat{a}_0 \to K^+ K^-} = \Gamma_{\hat{a}_0 \to \bar{K}^0 K^0} \approx 50 \text{ MeV}.$$

REFERENCES

1. M. K. Volkov and C. Weiss, Phys. Rev. D **56**, 221 (1997).

2. M. K. Volkov, Yad. Fiz. **60**, 2094 (1997) [Phys. At. Nucl. **60**, 1920 (1997)]; hep-ph/9612456.

3. M. K. Volkov, D. Ebert, and M. Nagy, Int. J. Mod. Phys. A **13**, 5443 (1998); hep-ph/9705334.

4. M. K. Volkov, D. Ebert, and V. L. Yudichev, JINR Rapid Commun., No. 6 (92)-98, 5 (1998); hep-ph/9810470; M. K. Volkov and V. L. Yudichev, Yad. Fiz. **63**, 527 (2000) [Phys. At. Nucl. **63**, 464 (2000)].

5. A. A. Andrianov and V. A. Andrianov, Nucl. Phys. B (Proc. Suppl.) **39C**, 257 (1995); A. A. Andrianov, V. A. Andrianov, and V. L. Yudichev, Theor. Math. Phys. **108**, 1069 (1996).

6. S. B. Gerasimov and A. B. Govorkov, Z. Phys. C **32**, 405 (1986).

7. L. S. Celenza, B. Huang, and C. M. Shakin, Phys. Rev. C **59**, 1041 (1999).

8. V. Ja. Burdanov, G. V. Efimov, S. N. Nedelko, and S. A. Solunin, Phys. Rev. D **54**, 4483 (1996).

9. H. Vogl and W. Weise, Prog. Part. Nucl. Phys. **27**, 195 (1991).

10. M. K. Volkov, M. Nagy, and V. L. Yudichev, Nuovo Cimento A **112** (1999) (in press); Preprint No. E2-982-101, JINR (Dubna, 1998); hep-ph/9804347.

11. M. K. Volkov, Ann. Phys. (N.Y.) **157**, 282 (1984); Fiz. Élem. Chastits At. Yadra **17**, 433 (1986) [Sov. J. Part. Nucl. **17**, 186 (1986)].

12. Particle Data Group, Eur. Phys. J. C **3**, 1 (1998).

13. S. Ishida, M. Ishida, T. Ishida, *et al.*, Prog. Theor. Phys. **98**, 621 (1997); M. Y. Ishida and S. Ishida, in *Proceedings of the 4th International Conference on Hadron Spectroscopy, HADRON'97, Upton, USA, 1997*; hep-ph/9712231.

14. S. B. Gerasimov and A. B. Govorkov, Z. Phys. C **29**, 61 (1985); **36**, 435 (1987).

15. N. Törnqvist, Phys. Rev. Lett. **49**, 624 (1982); J. Lanik, Phys. Lett. B **306**, 139 (1993); V. Dmitrašinovič, Phys. Rev. C **53**, 1383 (1996).

16. M. D. Scadron, Phys. Rev. D **26**, 239 (1982).

17. K. Kusaka, M. K. Volkov, and W. Weise, Phys. Lett. B **302**, 145 (1993); M. Jaminon and B. van den Bossche, Nucl. Phys. A **619**, 285 (1997).

18. R. L. Jaffe, Phys. Rev. D **15**, 267, 281 (1977); N. N. Achasov, S. A. Devyanin, and G. N. Shestakov, Usp. Fiz. Nauk **142**, 361 (1984) [Sov. Phys. Usp. **27**, 161 (1984)].

19. D. Blaschke, G. Burau, M. K. Volkov, and V. L. Yudichev, Preprint No. MPG-VT-UR 178/98 (Rostock University, Rostock, 1998); hep-ph/9812503; M. K. Volkov and V. L. Yudichev, Yad. Fiz. **62**, 1674 (1999) [Phys. At. Nucl. **62**, 1567 (1999)].

ELEMENTARY PARTICLES AND FIELDS
Theory

Production Rates for π^+K^-, pK^-, and $p\pi^-$ Atoms in Inclusive Processes*

O. E. Gorchakov**, A. V. Kuptsov, L. L. Nemenov, and D. Yu. Riabkov[1)]

Joint Institute for Nuclear Research, Dubna, Moscow oblast, 141980 Russia
Received May 26, 1999; in final form, September 15, 1999

Abstract—The yields of π^+K^-, pK^-, and $p\pi^-$ atoms in the reaction p +Al ⟶ atom + X at energies of 24, 70, 450 GeV and emission angles of $\theta_{lab} = 1°–6°$ are calculated from inclusive-production cross sections for p, π^+, π^-, and K^-. Estimates of these hadronic-atom yields for a Ta target are also given. The inclusive-production cross sections for p, π^+, π^-, and K^- are obtained within the Lund model of string fragmentation. The accuracy of the calculations is estimated by comparing single particle yields calculated by the Lund model and experimental yields of particles in proton–nucleus interactions. © 2000 MAIK "Nauka/Interperiodica".

1. INTRODUCTION

Measurement of the annihilation probabilities for hadronic atoms allow one to determine the threshold amplitudes for the transitions of the particles forming the atoms into all possible final states. The relation between the amplitude of the process [1]

$$\pi^- p \longrightarrow \pi^0 n \tag{1}$$

and the probability of the annihilation of the π^- meson and of the proton from a Coulomb bound state into $\pi^0 n$ were found. The binding energy of the $p\pi^-$ atom is 3.2 keV. At such a small energy, the amplitude of process (1) can be expressed [1] in terms of the S-wave πN scattering lengths in the isospin-1/2 and isospin-3/2 states.

Similar expressions were obtained for the probabilities of the annihilation of atoms formed by π^+ and π^- mesons ($A_{2\pi}$) [2, 3] and oppositely charged π and K mesons ($A_{\pi K}$) [3]. By measurement of the annihilation probabilities for the channels

$$A_{2\pi} \longrightarrow \pi^0 + \pi^0, \tag{2}$$

$$A_{\pi K} \longrightarrow \pi^0 + K^0, \tag{3}$$

it is possible to determine the amplitudes of the processes

$$\pi^+ + \pi^- \longrightarrow \pi^0 + \pi^0, \tag{4}$$

$$\pi^+ + K^- \longrightarrow \pi^0 + K^0 \tag{5}$$

by a model-independent method nearly at zero energy in the c.m. system of initial particles. Because, at low energies, the amplitudes of reactions (4) and (5) can be

expressed in terms of the differences of $\pi\pi$ and πK scattering lengths, measurement of the probabilities of processes (2) and (3) allows one to determine the quantities

$$a_0 - a_2, \tag{6}$$

$$b_{1/2} - b_{3/2} \tag{7}$$

by a model-independent method. Here, a_0 and a_2 ($b_{1/2}$ and $b_{3/2}$) are the $\pi\pi$ (πK) S-wave scattering lengths in the isospin-0, 2 (isospin-1/2, 3/2) states. In [4, 5], a_0 and a_2 were calculated on the basis of chiral perturbation theory (ChPT) to within 5%. In [6–8], the uncertainties were reduced to a level of 2 to 3%.

A model-independent measurement of the $\pi\pi$ scattering lengths to a precision of a few percent allows one to test ChPT predictions and, consequently, our understanding of chiral-symmetry breaking [9] as in the basis of the QCD Lagrangian, which describes interactions of quarks and gluons, and effective Lagrangians, which describe interactions of physical particles. Generalized ChPT allows one to determine the quark-condensate magnitude [7, 8] by using the value of $a_0 - a_2$ from precise measurement.

The πK-scattering lengths were also calculated within ChPT [10]. A model-independent measurement of these quantities allows one to test the concept of chiral-symmetry breaking in the processes involving strangeness.

Bernard *et al.* [11] obtained relations that allow one to calculate the production rates for $A_{2\pi}$, $A_{\pi K}$ and those for any other atoms if the inclusive-production cross sections for the particles forming these bound states are known. Those authors also proposed a method for observation and lifetime measurement of the atoms and presented estimates for the yields of $A_{2\pi}$, $A_{\pi K}$, and other atoms in pp collisions at a beam energy of 70 GeV and an atom emission angle of 8.4° in the laboratory frame.

---

* This article was submitted by the authors in English.
** e-mail: gorchakov@nusun.jinr.ru
[1)] University of Utah, Salt Lake City, UT 84112, USA.

The $A_{2\pi}$ process was studied experimentally at the U-70 accelerator [12]. Atoms produced in pTa collisions at $E_p = 70$ GeV were detected at a angle of 8.4° in the laboratory frame. Later, the $A_{2\pi}$ lifetime was estimated on the basis of experimental data [13]. Presently, the experiment proposed in [14] and aimed at measuring the $A_{2\pi}$ lifetime and at determining the difference of $\pi\pi$ scattering lengths to a precision of 5% is under preparation at PS CERN.

The yields of $A_{2\pi}$ in proton–nucleus collisions and the spectra of $A_{2\pi}$ were calculated in [15] at $E_p = 24$, 70, 450, and 1000 GeV for a set of angles from 1° to 6°. Here, we present the results of similar calculations for $A_{\pi K}$, $A_{p\pi}$ (atoms formed by p and π^-), and A_{pK} (atoms formed by p and K^-). The results of the calculations show that the intensities of $A_{\pi K}$, A_{pK}, and $A_{p\pi}$ production are sufficiently high for the lifetime of these atoms to be measured by the same method as that proposed for measuring the $A_{2\pi}$ lifetime.

Because the lifetime of $A_{p\pi}$ was measured [16] with a precision of ~1%, this kind of measurements allows one to check the precision of the method [11] and to measure the lifetime of almost any hadronic atom. The experiment aimed at measuring the energy of the $2P$–$1S$ transition and the widths of γ lines [17, 18] of A_{pK} is under preparation. However, it is reasonable to measure the A_{pK} lifetime by a different method as well [11].

2. BASIC RELATIONS

The rate of atom production is proportional to the double inclusive cross section for the production of the two particles that form this atom and which have low relative momenta. Calculating the atom-production cross sections, one should exclude the contribution to the double cross section from those constituents that arise from the decays of long-lived particles and which cannot form the atom. When one or both of the particles in the pair originate from these decays, the typical distance between them is much greater than the Bohr radius of the atom. Consequently, the probability of atom production is negligible. The main long-lived sources of pions are η, η', Λ, K_S^0, and $\Sigma^\pm$, while the main long-lived sources of protons are Λ and $\Sigma^\pm$. At the same time, the abundance of the long-lived sources of kaons is much smaller than that of their short-lived sources.

The differential inclusive cross section for atom production in the laboratory frame can be written in the form [11]

$$\frac{d\sigma_n^A}{d\mathbf{p}_A} = (2\pi)^3 \frac{E_A}{M_A} |\Psi_n(0)|^2 \frac{d\sigma_s^0}{d\mathbf{p}_1 d\mathbf{p}_2}\bigg|_{\mathbf{p}_1 = \frac{m_1}{m_2}\mathbf{p}_2 = \frac{m_1}{M_A}\mathbf{p}_A}, \quad (8)$$

where $\mathbf{p}_A$, E_A, and M_A are, respectively, the momentum, the energy, and the mass of the atom in this frame; $|\Psi_n(0)|^2 = p_B^3/\pi n^3$ (p_B is the Bohr momentum of the par-

ticles in the atom) is the square of the atomic wave function (taking no account of strong interactions between the particles forming the atom—that is, the pure Coulomb wave function) at the origin for the case of zero orbital angular momentum l, n being the principal quantum number; $d\sigma_s^0/d\mathbf{p}_1 d\mathbf{p}_2$ is the double inclusive cross section for the production of pairs from short-lived sources (hadronization processes, ρ, ω, Δ, K^*, Σ^*, etc.) without allowance for the $\pi^+\pi^-$ Coulomb interaction in the final state; and $\mathbf{p}_1$ and $\mathbf{p}_2$ are the momenta of the particles forming the atom in the laboratory frame. The momenta obey the relation $\mathbf{p}_1 = \frac{m_1}{m_2}\mathbf{p}_2 = \frac{m_1}{M_A}\mathbf{p}_A$ (m_1 and m_2 are the masses of the particles). The atoms are formed more easily with zero orbital angular momentum $l = 0$, because $|\Psi_{n,l}(0)|^2 = 0$ when $l \neq 0$. The product atoms are distributed with respect to n as n^{-3}: $W_1 = 83\%$, $W_2 = 10.4\%$, $W_3 = 3.1\%$, and $W_{n \geq 4} = 3.5\%$. Note that $\sum_{n=1}^{\infty} |\Psi_n(0)|^2 = 1.202|\Psi_1(0)|^2$.

The double inclusive cross section without allowance for the Coulomb interaction can be written in the form [19]

$$\frac{d\sigma^0}{d\mathbf{p}_1 d\mathbf{p}_2} = \frac{1}{\sigma_{in}} \frac{d\sigma}{d\mathbf{p}_1} \frac{d\sigma}{d\mathbf{p}_2} R(\mathbf{p}_1, \mathbf{p}_2), \quad (9)$$

where $d\sigma/d\mathbf{p}_1$ and $d\sigma/d\mathbf{p}_2$ are the single-particle inclusive cross sections, σ_{in} is the inelastic cross section for hadron production, and R is a correlation function due to strong interaction.

The rate of the particle production per interaction event (yield) can be expressed in terms of the differential cross section as

$$\frac{dN}{d\mathbf{p}} = \frac{d\sigma}{d\mathbf{p}} \frac{1}{\sigma_{in}}. \quad (10)$$

By using Eqs. (8)–(10) and the expression for $|\Psi_n(0)|^2$ and performing summation over n, one can express the inclusive yield of atoms in all S states in terms of the inclusive yields of positive and negative hadrons as

$$\frac{d^2 N_A}{d p_A d\Omega}$$
$$= 1.202 \cdot 8\pi^2 (\mu\alpha)^3 \frac{E_A}{M_A} \frac{p_A^2}{p_1^2 p_2^2} \frac{d^2 N_1}{d p_1 d\Omega} \frac{d^2 N_2}{d p_2 d\Omega} R, \quad (11)$$

where μ is the reduced mass of the atom $\left(\mu = \frac{m_1 m_2}{m_1 + m_2}\right)$; α is the QED fine-structure constant; p_1 and p_2 are the momenta of, respectively, positive and negative hadrons $\left(p_1 = \frac{m_1}{m_2} p_2\right)$; and Ω is a solid angle.

3. RESULTS OF THE CALCULATIONS

In order to obtain the yields of protons and of p, K^-, π^+-, and π^- mesons, we used the computer simulation codes FRITIOF 6.0 [20] and JETSET 7.3 [21] (CERN Program Library) based on the Lund string-fragmentation model. FRITIOF is a generator for hadron–hadron, hadron–nucleus, and nucleus–nucleus collisions, which makes use of JETSET for fragmentation.

In order to calculate particle yields, simulated events were accumulated in two-dimensional arrays depending on the emission angle and the momenta of the particles having an angular bin width of $0.3°$ and a momentum bin width of 0.1 GeV/c. At this stage, the selection of particles from long-lived and short-lived sources was performed. The particle yield distributions were parametrized by the linear combinations of elementary functions. Further, using yields only from the short-lived sources, we calculated the distributions of the atom yields with respect to the angle and momentum. The correlation coefficient due to strong interac-

tions was found to be $R = 1.65 \pm 0.05$ [19, 22] for the pairs of $\pi^+\pi^-$ mesons whose momenta satisfy the condition $\mathbf{p}_1 = \mathbf{p}_2$. Because R is not yet known for the pairs of π^+K^-, $p\pi^-$, and pK^-, we assume $R = 1$ through the calculations.

The results are presented in Figs. 1–3, where the yields of $A_{\pi K}$, $A_{p\pi}$, and A_{pK} for the reaction $p + \text{Al} \longrightarrow \text{atom} + X$ at the proton energies $E_p = 24$, 70, and 450 GeV and atom-emission angles $\theta_{\text{lab}} = 1°-6°$ are plotted versus the momentum of the atom. The probability of atom production in the momentum interval Δp_A and the solid angle range $\Delta\Omega$ at the emission angle θ can be estimated by multiplying the yields averaged over the given momentum interval by the values of this interval in GeV/c and the solid angle $\Delta\Omega$ in sr.

The yields of $A_{\pi K}$, $A_{p\pi}$, and A_{pK} integrated over the momentum are shown in Fig. 4 versus the emission angle.

Similar calculations for the reaction $p + \text{Ta} \longrightarrow \text{atom} + X$ were performed in order to obtain the scale of
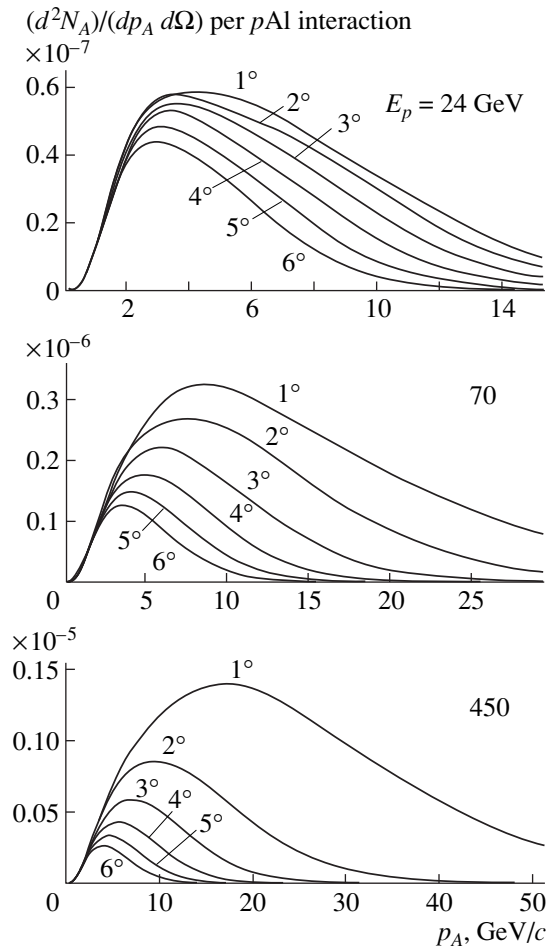

Fig. 1. Yields of $A_{\pi K}$ from the reaction $p\text{Al} \longrightarrow A_{\pi K}X$ (per $p\text{Al}$-interaction event) at the energies of $E_p = 24$, 70, and 450 GeV and the emission angles of $\theta_{\text{lab}} = 1°$, $2°$, $3°$, $4°$, $5°$, $6°$ as the functions of the atom momentum p_A.

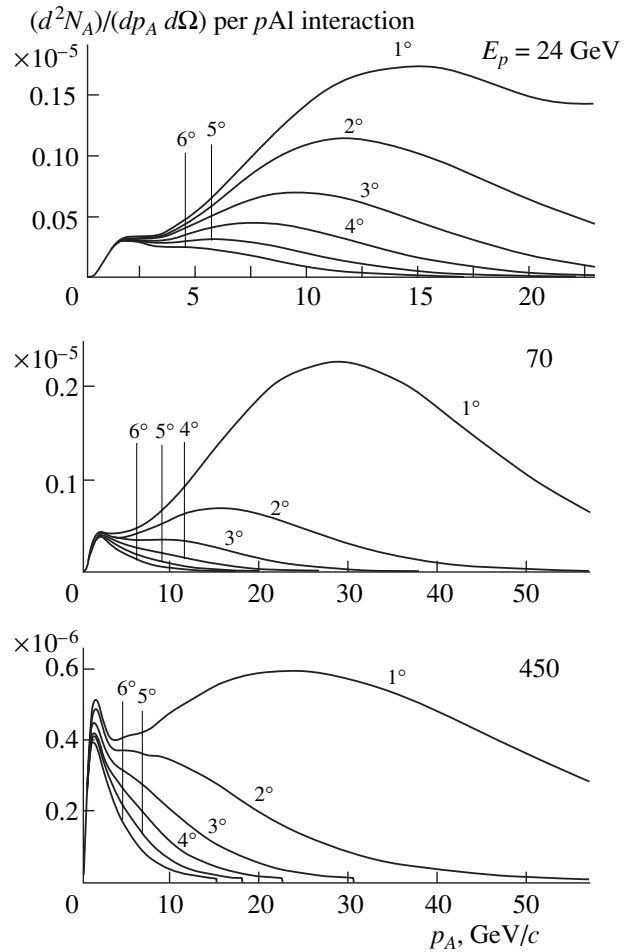**Fig. 2.** Yields of $A_{p\pi}$ from the reaction $p\text{Al} \longrightarrow A_{p\pi}X$; the other parameters are identical to those in Fig. 1.
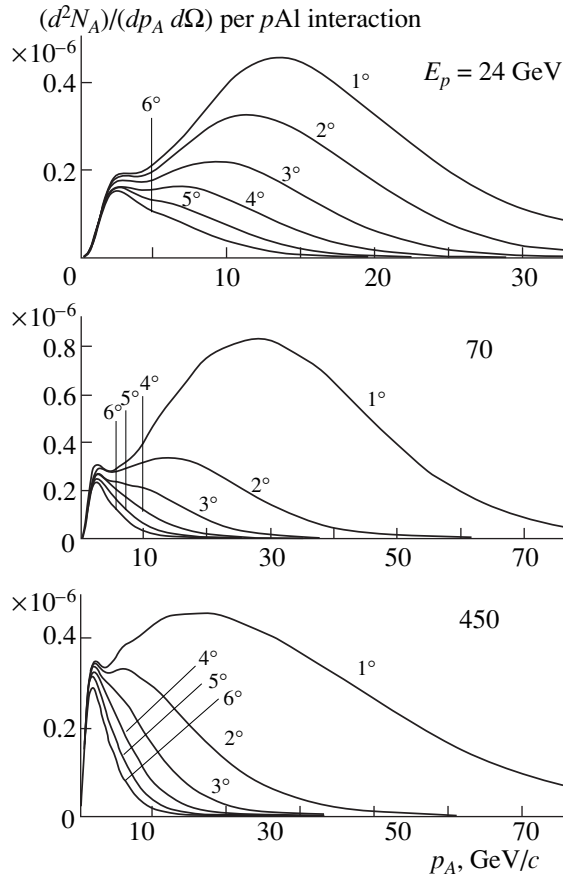
$(d^2N_A)/(dp_A \, d\Omega)$ per pAl interaction

Fig. 3. Yields of A_{pK} from the reaction pAl $\longrightarrow A_{pK}X$; the other parameters are identical to those in Fig. 1.
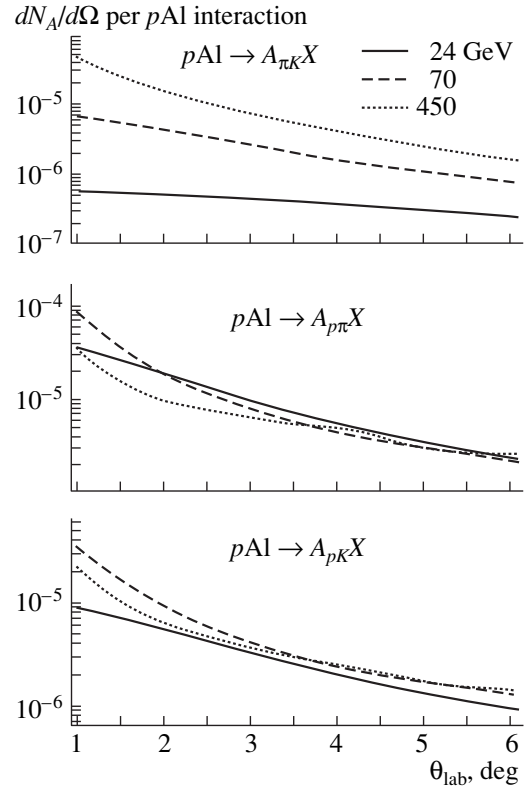
$dN_A/d\Omega$ per pAl interaction

Fig. 4. Momentum-integrated yields of $A_{\pi K}$, $A_{p\pi}$, and A_{pK} from the reaction pAl $\longrightarrow$ (atom)X (per pAl-interaction event) at the energies of $E_p = 24$, 70, 450 GeV versus atom emission angles.

the A dependence for the atom yields. In the table the ratios of the atom yields integrated over the momentum for pTa to those for pAl are given as a function of the emission angle.

Ratios of the atom yields integrated with respect to a momentum for a Ta target to those for an Al target at $E_p = 24$, 70, and 450 GeV versus the emission angles

	1°	2°	3°	4°	5°	6°
$E_p = 24$ GeV						
$A_{\pi K}$	1.10	1.16	1.19	1.20	1.25	1.30
$A_{p\pi}$	0.90	1.03	1.22	1.44	1.65	1.83
A_{pK}	0.82	0.98	1.14	1.37	1.53	1.69
$E_p = 70$ GeV						
$A_{\pi K}$	1.14	1.24	1.39	1.50	1.58	1.64
$A_{p\pi}$	1.13	1.68	2.06	2.27	2.36	2.39
A_{pK}	1.01	1.49	1.81	1.99	2.05	2.05
$E_p = 450$ GeV						
$A_{\pi K}$	1.67	1.92	2.07	2.17	2.25	2.31
$A_{p\pi}$	2.21	2.48	2.58	2.63	2.64	2.66
A_{pK}	2.19	2.51	2.63	2.68	2.70	2.74

A comparison of the FRITIOF 6.0 results with the experimental data was made. For the case $E_p = 24$ GeV, the most complete description of the yields of p, π^+, π^-, K^+, and K^- by the experimental data in the given range of emission angles and momenta is available in the paper [23]. The comparison with these data shows that the deviation of the calculated yields from the data does not exceed 20%. Thus, the precision of the calculated yields of $A_{\pi K}$, $A_{p\pi}$, and A_{pK} is better than 40%.

The description of the particle yields at 24 GeV for the same angles and momenta by FRITIOF 7.02, the latest version of FRITIOF, shows satisfactory agreement with the experimental data for π^+ and π^-, but appreciable differences for p, K^+, and K^-. A large deviation of the FRITIOF 7.02 results from the experimental data is observed for the proton yields. We noticed that the shapes of the calculated proton spectra did not correspond to the shapes of the experimental yields, in contrast to the proton yields calculated by FRITIOF 6.0. This difference in the behavior of these two codes can probably be explained by the fact that FRITIOF 7.02 was developed for higher energies and higher $p_\perp$ than under the conditions described. For this reason, we used FRITIOF 6.0 for our calculations.

We also compared the calculated particle yields with the experimental data [24] at an energy of 70 GeV. It was shown that agreement with the experimental data is satisfactory for the emission-angle range from 3° to 6°, but for the angle range of 1°–2.5° the simulated yields are higher by a factor of about 2 than the experimental yields.

For $E_p = 450$ GeV, we assume that the program provides reasonable results for the calculated hadron atom yields for $p_\perp > 400$ MeV/c because this code was worked out for this energy range.

The validity of the calculation by FRITIOF 6.0 for the single-particle yields was also considered in [15].

ACKNOWLEDGMENTS

REFERENCES

1. S. Deser *et al.*, Phys. Rev. **96**, 774 (1954).
2. J. Uretsky and J. Palfrey, Phys. Rev. **121**, 1798 (1961).
3. S. M. Bilenky *et al.*, Yad. Fiz. **10**, 812 (1969) [Sov. J. Nucl. Phys. **10**, 469 (1970)].
4. J. Gasser and H. Leutwyler, Phys. Lett. **125B**, 327 (1983).
5. J. Gasser and H. Leutwyler, Nucl. Phys. B **250**, 465, 517, 539 (1985).
6. J. Bijnens *et al.*, Phys. Lett. B **374**, 210 (1996).
7. J. Stern, H. Sazdjian, and N. H. Fuchs, Phys. Rev. D **47**, 3814 (1993).
8. M. Knecht *et al.*, Nucl. Phys. B **455**, 513 (1995).
9. H. Leutwyler, in *Proceedings of the XXVI International Conference on High Energy Physics, Dallas, 1992*, Ed. by J. R. Sanford, AIP Conf. Proc., No. 272, 185 (1992).
10. V. Bernard *et al.*, Nucl. Phys. B **357**, 129 (1991); Phys. Rev. D **43**, R2757 (1991).
11. L. Nemenov, Yad. Fiz. **41**, 980 (1985) [Sov. J. Nucl. Phys. **41**, 629 (1985)].
12. L. G. Afanasyev *et al.*, Phys. Lett. B **308**, 200 (1993).
13. L. G. Afanasyev *et al.*, Phys. Lett. B **338**, 478 (1994); Yad. Fiz. **60**, 1049 (1997) [Phys. At. Nucl. **60**, 938 (1997)].
14. B. Adeva *et al.*, *Lifetime Measurement of* $\pi^+\pi^-$ *Atoms to Test Low Energy QSD Predictions*, Proposal to the SPSLC, CERN/SPSLC 95-1, SPSLC/P 284 (Geneva, 1994).
15. O. E. Gorchakov *et al.*, Yad. Fiz. **59**, 2015 (1996) [Phys. At. Nucl. **59**, 1942 (1996)].
16. D. Sigg *et al.*, Nucl. Phys. A **609**, 269 (1996).
17. R. Baldini *et al.*, The DEAR Proposal (Laboratori Nazionali di Frascati, October 1995).
18. S. Bianco *et al.*, in *Proceedings of the International Workshop of Hadronic Atoms and Positronium in the Standard Model, Dubna, 1998*.
19. V. G. Grishin, *Inclusive Processes in Hadron Interactions at High Energy* (Énergoizdat, Moscow, 1982), p. 131.
20. B. Nilsson-Almquist and E. Stenlund, Comput. Phys. Commun. **43**, 387 (1987).
21. T. Sjöstrand and M. Bengtsson, Comput. Phys. Commun. **43**, 367 (1987).
22. J. Uribe *et al.*, Phys. Rev. D **49**, 4373 (1994).
23. T. Eichten *et al.*, Nucl. Phys. B **44**, 333 (1972).
24. N. I. Bozhko *et al.*, Preprint No. 79-78 (IHEP, Serpukhov, 1979).

ELEMENTARY PARTICLES AND FIELDS
Theory

Strangeness Photoproduction on a Deuteron and Hyperon–Nucleon Interaction*

B. O. Kerbikov

Institute of Theoretical and Experimental Physics, Bol'shaya Cheremushkinskaya ul. 25, Moscow, 117259 Russia
Received November 23, 1999

Abstract—Pronounced effects due to final-state hyperon–nucleon interaction are predicted in a strangeness photoproduction reaction on a deuteron. Use is made of the covariant reaction formalism and of the P-matrix approach to the hyperon–nucleon interaction. © 2000 MAIK "Nauka/Interperiodica".

The first measurement of kaon photoproduction on a deuteron is expected this year [1]. These data may open a new window on ΛN and ΣN forces since the final state YN interaction (FSI) plays an important role in the reaction $\gamma d \longrightarrow K^+YN$. This problem has been studied by several authors since the pioneering paper by F.M. Renard and Y. Renard [2] (see also [3]). From the previous work, the present study differs in two respects: (i) the use of the covariant formalism both for the reaction mechanism and for the deuteron wave function and (ii) FSI treatment within the P-matrix approach, which makes it possible to take into account subnuclear degrees of freedom and to disentangle dynamical singularities from kinematical threshold effects [4]. Our main result is a prediction of spectacular effects in the reaction cross section due to the YN FSI.

The reaction $\gamma d \longrightarrow K^+Yn$, $Y = \Lambda, \Sigma^0$ is a $2 \longrightarrow 3$ process. The corresponding double-differential cross section has the form

$$d^2\sigma \equiv \frac{d^2\sigma}{d|\mathbf{p}_K|d\Omega_K} = \frac{1}{2^{11}\pi^5}\frac{\mathbf{p}_K^2}{kM_dE_K}$$
$$\times \frac{\lambda^{1/2}(s_2, m_Y^2, m_n^2)}{s_2}\int d\Omega_{Yn}^*|T|^2, \quad (1)$$

where k, $\mathbf{p}_K^2$, E_K, and Ω_K correspond to the deuteron rest system with the z axis aligned with the incident-photon-beam direction $\mathbf{k}$. The solid angle Ω_{Yn}^* is defined in the Yn center-of-momentum frame. The quantity $\lambda(x, y, z)$ is the standard kinematical function $\lambda(x, y, z) = x^2 - 2(y + z)x + (y - z)^2$.

We will use the covariant relativistic approach to calculate the amplitude T for the process $\gamma d \longrightarrow K^+YN$. The amplitude will be approximated by two leading diagrams, the tree (pole, or plane waves) graph and the triangle graph featuring FSI. It will be demonstrated that, within the covariant approach, one easily retrieves

* This article was submitted by the authors in English.

the usual nonrelativistic impulse approximation and the Migdal–Watson approach to FSI. We start with the tree diagram. To calculate it, two blocks have to be specified: (i) the elementary amplitude $M^{\gamma K}$ for photoproduction on a proton and (ii) the deuteron vertex Γ_d. The elementary amplitude used in the present calculation was derived from the tree-level effective Lagrangian [5]. We took into account resonances with spin $\leq 5/2$ in the s channel, the spin-1/2 resonances in the u channel, and $K^*(892)$ and $K1(1270)$ resonances in the t channel. This amplitude is decomposed into invariant terms as [6]

$$M^{\gamma K} = \bar{u}_Y\sum_{j=1}^{6}\mathcal{A}_j\mathcal{M}_j(s', t', u')u_p, \quad (2)$$

where $s' = (k + p_p)^2$, $t' = (k - p_K)^2$, and $u' = (k - p_Y)^2$.

The decomposition of the deuteron vertex function Γ_d into independent Lorentz structures has the form [7]

$$\Gamma_d = \sqrt{m_N}[(p_p + p_n)^2 - M_d^2]$$
$$\times \left[\varphi_1(t_2)\frac{(p_p - p_n)_\mu}{2m_N^2} + \varphi_2(t_2)\frac{1}{m_N}\gamma_\mu\right]\mathcal{E}^\mu(p_d, \lambda), \quad (3)$$

where $t_2 = (p_d - p_n)^2$ and $\mathcal{E}^\mu(p_d, \lambda)$ is the polarization 4-vector of the deuteron with momentum p_d and polarization λ.

For the tree diagram, we can now write the expression

$$T^{(t)} = \bar{u}_Y\left\{\left(\sum_{j=1}^{6}\mathcal{A}_j\mathcal{M}_j(s', t', u')\right)S(p_p)\Gamma_d\right\}u_n^c, \quad (4)$$

where $S(p_p)$ is the proton propagator and u_n^c is the charge-conjugated neutron spinor.

Covariant equations (1) and (4) can easily be reduced to the standard impulse approximation. Neglecting the spin summation in the matrix element (4) (factorization hypothesis) and introducing the deuteron wave function as the product [8] $\psi_d = [2(2\pi)^3M_d]^{1/2}S(p_p)\Gamma_d$,

one retrieves the nonrelativistic impulse approximation,

$$\frac{d^2\sigma}{d|\mathbf{p}_K|d\Omega_K} = \frac{\mathbf{p}_K^2|\mathbf{p}_Y^*|}{64\pi^2 k E_K \sqrt{s_2}} \int d\Omega_{Yn}^* |M^{\gamma K}|^2 |\psi_d|^2, \quad (5)$$

where $\mathbf{p}_Y^*$ corresponds to the YN center-of-momentum frame. The main physical difference between the covariant deuteron vertex used in the present calculation and the nonrelativistic wave function entering into (5) is that the former contains singlet and triplet p-wave components absent in the latter [8].

We next consider the loop (triangle) diagram featuring YN FSI. The corresponding amplitude is given by

$$T^{(l)} = \int \frac{d^4 p_n}{(2\pi)^4} \bar{u}_Y(p_Y')$$

$$\times \left\{ \left(\sum_{j=1}^{6} \mathscr{A}_j \mathscr{M}_j \right) S(p_p) \Gamma_d C S(p_n) T_{Yn} S(p_Y) \right\} \bar{u}_n(p_n'), \quad (6)$$

where $C = \gamma^2 \gamma_0$ is the charge-conjugation matrix and T_{Yn} is the four-fermion hyperon–nucleon vertex; this vertex, being dressed by corresponding spinors, constitutes the hyperon–nucleon amplitude F_{YN}.

A comprehensive treatment of the loop diagram will be presented in the forthcoming detailed publication, while, here, we resort to a simple approximation with the aim of exposing FSI effects. Namely, only positive-frequency components are retained in all three propagators $S(p_j)$, $j = p, n, Y$; then, integration with respect to the time component dp_n^0 is performed, and the deuteron wave function is introduced in the same way as this was done in deriving equation (5). Thus, we obtain $T^{(l)}$ in the form

$$T^{(l)} = -\sqrt{(2\pi)^3 \cdot 2M_d} \int \frac{d\mathbf{p}^*}{(2\pi)^3} \frac{M^{\gamma K} \psi_d F_{YN}(E_{Yn}^*)}{(\mathbf{p}^*)^2 - (\mathbf{p}^{*\prime})^2 - i0}, \quad (7)$$

where $(\mathbf{p}^*)^2$ and $(\mathbf{p}^{*\prime})^2$ are the Yn momenta in the c.m. of the Yn system before and after rescattering, and $F_{Yn}(E_{Yn}^*)$ is the half-off-shell Yn scattering amplitude at the energy $E_{Yn}^* = (\mathbf{p}_{Yn}^*)^2/m_{Yn}$. The use of the nonrelativistic propagator in (7) is legitimate since FSI is important at low YN relative momenta. In the kinematical region where FSI is important, the amplitude $M^{\gamma K}$ and the deuteron wave function ψ_d are smoother functions of $\mathbf{p}^*$ than the scattering amplitude F_{Yn}. Therefore, one can set $\mathbf{p}^* = \mathbf{p}^{*\prime}$ in their arguments and factor them outside the integral sign. It should be recalled next that, as was shown above, the tree (plane waves) amplitude $T^{(t)}$ admits the representation

$$T^{(t)} \simeq \sqrt{(2\pi)^3 \times 2M_d} M^{\gamma K} \psi_d. \quad (8)$$

For the sum of the two diagrams, we can therefore write

$$T^{(t)} + T^{(l)} = T^{(t)} \int \frac{d\mathbf{p}^*}{(2\pi)^3} \Psi_{\mathbf{p}^{*\prime}}^{(-)*}(\mathbf{p}^*) \equiv T^{(t)}/D, \quad (9)$$

where

$$\Psi_{\mathbf{p}^{*\prime}}^{(-)}(\mathbf{p}^*) = (2\pi)^3 \delta(\mathbf{p}^* - \mathbf{p}^{*\prime})$$

$$- \frac{F_{YN}(E_{Yn}^*)}{(\mathbf{p}^*)^2 - (\mathbf{p}^{*\prime})^2 + i0}, \quad (10)$$

and $1/D$ denotes the enhancement factor, which will be calculated in the P-matrix approach. The P-matrix description of the YN interaction, including threshold phenomena and the resonance at 2.13 GeV close to the ΣN threshold, was presented in [9]. According to [9], the 2.13-GeV structure is not a genuine six-quark state, but the P-matrix partner of the deuteron (see also [10]). With the aid of the relation between S and P matrices [11], the enhancement factor can be represented as

$$D^{-1} = \frac{e^{-ip^{*\prime}b}}{2ip^{*\prime}b} \left\{ \frac{e^{-ip^{*\prime}b} R(-ip^{*\prime}) - e^{ip^{*\prime}b} R(+ip^{*\prime})}{R(+ip^{*\prime})} \right\}, \quad (11)$$

where

$$R(ip^{*\prime}) = (P_1^0 - ip^{*\prime})$$

$$\times \left(E - E_n + \frac{\lambda_1^2}{P_1^0 - ip^{*\prime}} + \frac{\lambda_2^2}{P_2^0 - ip_2^{*\prime}} \right), \quad (12)$$

and where the elements of the P matrix are given by [11]

$$P_{ij} = P_i^0 \delta_{ij} + \frac{\lambda_i \lambda_j}{E - E_n}, \quad (13)$$

the indices 1 and 2 correspond to the Λn and $\Sigma^0 n$ channels, and $p_2^{*\prime}$ is the momentum in the $\Sigma^0 n$ channel. The numerical values of the P-matrix parameters entering into (11)–(13) can be found in [9].

Finally, we present the results of the calculations based on equations (1), (4), (9), and (11). Here, use was made of the elementary photoproduction amplitude from [5] and of the deuteron vertex function taken from the relativistic Gross model [8]. The plane-wave diagram (4) with this input was calculated in [12]. In Fig. 1, the double-differential cross section (1) is shown as a function of the photon energy in the Λn invariant-mass region close to the Λn threshold (2.05 GeV $\leq \sqrt{s_{\Lambda n}} \leq$ 2.09 GeV). The pronounced peak typical of FSI is seen at the Λn threshold.

In Fig. 2, the same cross section is plotted under different kinematical conditions covering a wider region of the NY invariant mass (2.05 GeV $\leq \sqrt{s_{\Lambda n}} \leq$ 2.17 GeV), including the ΣN threshold. Apart from the structure at

$d^2\sigma/(dp_K \, d\Omega_K)$, nb/(MeV sr)

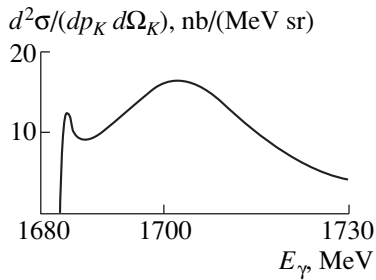**Fig. 1.** Double differential cross section as a function of the photon energy for $p_K = 1.4$ GeV and $\theta_{\gamma K} = 1$.

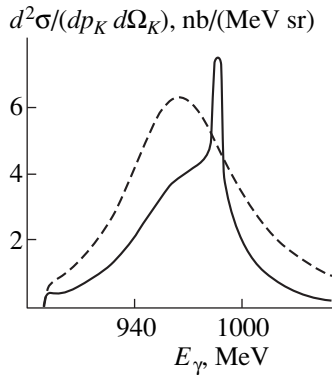$d^2\sigma/(dp_K \, d\Omega_K)$, nb/(MeV sr)

Fig. 2. Double differential cross section as a function of photon energy for $p_K = 0.426$ GeV and $\theta_{\gamma K} = 15$: (Full line) P-matrix result and (dashed line) Verma–Sural potential.

the Λn threshold, we can see a spectacular peak due to the 2.13-GeV resonance lying in the immediate vicinity of the $\Sigma^0 n$ threshold. Also shown are the results obtained with the Verma–Sural potential of the ΛN interaction [13]. The difference is quite distinct.

The main conclusion is that FSI effects in the reaction $\gamma_d \longrightarrow K^+\Lambda n$ are measurable and distinctly reflect underlying NY interaction dynamics. Therefore, detailed calculations along the lines outlined in this study are highly desirable.

REFERENCES

1. B. Mecking *et al.*, CEBAF Proposal PR-89-045, 1989.
2. F. M. Renard and Y. Renard, Nucl. Phys. B **1**, 389 (1967).
3. R. A. Adelseck and L. E. Wright, Phys. Rev. C **39**, 580 (1989); X. Li and L. E. Wright, J. Phys. G **17**, 1127 (1991); S. R. Cotanch and S. Hsiao, Nucl. Phys. A **450**, 419 (1986); T.-S. H. Lee *et al.*, Nucl. Phys. A **639**, 247 (1998); H. Yamamura *et al.*, nucl.-th/9907029, V. 2.
4. S. V. Bashinsky and R. L. Jaffe, Nucl. Phys. A **625**, 167 (1997).
5. J. C. David *et al.*, Phys. Rev. C **53**, 2613 (1996).
6. G. F. Chew *et al.*, Phys. Rev. **106**, 1345 (1957).
7. M. Gourdin *et al.*, Nuovo Cimento **37**, 525 (1965).
8. F. Gross, Phys. Rev. C **10**, 1875 (1974); W. W. Buck and F. Gross, Phys. Rev. D **20**, 2361 (1979).
9. B. L. G. Bakker *et al.*, Yad. Fiz. **43**, 1508 (1986) [Sov. J. Nucl. Phys. **43**, 982 (1986)]; B. Kerbikov *et al.*, Nucl. Phys. A **480**, 585 (1988).
10. D. P. Heddle and L. Kisslinger, Phys. Rev. C **30**, 965 (1984).
11. R. L. Jaffe and F. E. Low, Phys. Rev. D **19**, 2105 (1979).
12. F. Rouvier, *Etude de la photoproduction d'etrangete sur le deuton. These* (Univ. Claude Bernard, Lyon, 1997).
13. S. P. Verma and D. P. Sural, Phys. Rev. C **22**, 229 (1980).

Synchrotron Radiation of Photino Pairs

A. V. Kurilin and A. I. Ternov[1]

Moscow State Open Pedagogical University, Malaya Pirogovskaya ul. 1, Moscow, 119882 Russia
Received June 11, 1999; in final form, October, 18, 1999

Abstract—The probability of photino-pair emission by an electron moving in an external electromagnetic field $(e \longrightarrow e\tilde{\gamma}\tilde{\gamma})$ is calculated within the minimal supersymmetric extension of the Standard Model. This process is analyzed in two different cases: the production of massless photinos is studied first, and the effect of a finite photino mass is taken into account after that. The results of the calculations are applied to the theory of stellar evolution. In particular, the photino emissivity of a neutron star due to the above reaction is calculated. A comparison of the rate of star cooling induced by photino emission with the rates associated with other competing mechanisms of energy losses makes it possible to set a new constraint on the selectron mass: $M_{\tilde{e}_R} = M_{\tilde{e}_L} \geq 96.3$ GeV. © 2000 MAIK "Nauka/Interperiodica".

1. INTRODUCTION

Among various modern attempts at constructing a theoretical scheme that would extend, in a natural way, the commonly accepted Standard Model of elementary-particle physics, those that rely on the idea of supersymmetry (SUSY) [1–5] play a special role. An important advantage of SUSY theories consists in that they improve the ultraviolet properties of the Standard Model, providing a beautiful solution to the well-known hierarchy problem [6, 7]. In addition, field-theoretical models featuring $N = 1$ global SUSY appear to be a natural low-energy approximation of supergravity and superstring theories presently laying claim to the role of a universal paradigm for unifying all fundamental interactions, including gravity.

In the minimal supersymmetric extension of the Standard Model (MSSM) [8, 9], the most popular theory at present indeed, the idea of SUSY is realized in the most economical way. The minimal list of new particles predicted by this model incorporates scalar superpartners to all known leptons and quarks (sleptons and squarks)—two particles, $\tilde{f}_R$ and $\tilde{f}_L$, per fermion species f of standard $SU(3) \otimes SU(2) \otimes U(1)$ theory. In addition, spinor superpartners to the gauge vector bosons γ^0, Z^0, $W^\pm$, and g—these superpartners are generically referred to as gauginos—are introduced in the consideration. The gauginos include the photino $\tilde{\gamma}^0$, zino $\tilde{Z}^0$, the winos $\tilde{W}_1^\pm$ and $\tilde{W}_2^\pm$, and the gluino $\tilde{g}$, which form, upon a spontaneous breakdown of $SU(2)$ symmetry, new mass states of the neutralinos $\tilde{\chi}_1^0$ and $\tilde{\chi}_2^0$ and of the charginos $\tilde{\chi}_1^\pm$ and $\tilde{\chi}_2^\pm$. As to the Higgs sector, two chiral doublets that have opposite hyper-

charges and which ensure cancellation of Adler–Bell–Jackiw triangle anomalies are present in the MSSM, yielding an entire family of scalar Higgs particles, both charged ($H^\pm$) and electrically neutral (H^0, h^0, A^0) ones.

Since the masses of all these hypothetical superpartners are expected to be about a few TeV or below, it is highly probable that they will be experimentally detected in the near future at the LHC collider being presently constructed at CERN. At the same time, it should be noted that, within the MSSM, supersymmetry is realized under the assumption that there is additional discrete symmetry between ordinary particles and their superpartners, which is referred to as R parity. This new quantum number is given by

$$R = (-1)^{2S + 3B + L},$$

where S, B, and L are, respectively, the spin, the baryon number, and the lepton number corresponding to a given particle in the MSSM. Since all superpartners differ in spin by 1/2 from their conventional analogs, their R parities are of opposite signs. In the case where R parity is a strictly conserved quantum number (and where the baryon and lepton quantum numbers B and L are also conserved), the interactions of conventional particles can therefore produce superparticles only in pairs.

This circumstance toughens significantly requirements for next-generation accelerators: such accelerators must ensure that the c.m. energies of colliding particles will be at least twice as great as the masses of the sought superpartners.

For the same reason, the modern constraints on the masses of hypothetical particles in the SUSY sector of the MSSM are very lenient: these masses must be about 45 GeV for superpartners involved in weak interactions and about 150 GeV for strongly interacting particles.

In connection with what was said above, it would be very interesting to find some indirect manifestations of

---

[1] Moscow Institute for Physics and Technology, Institutskiĭ proezd 9, Dolgoprudnyĭ, Moscow oblast, 141700 Russia.
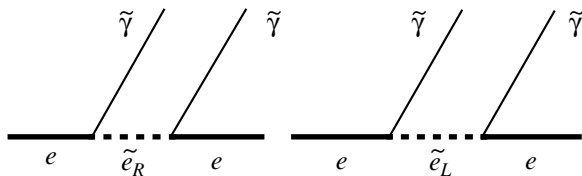
Fig. 1. Diagrams describing the production of photino pairs in an electromagnetic field.

SUSY. In particular, attempts were made to obtain constraints on the MSSM parameters by requiring that the theoretical predictions for some low-energy processes be consistent with the measured probabilities of these processes [10–12]. Unfortunately, many such constraints are disabled if the distinctions between the masses of supersymmetric particles of the same type are comparatively small. There exists, however, another line of searches for SUSY signatures and of derivation of constraints on the masses of superpartners. We mean here the approach that was proposed in [13–17] and which is associated with studying the manifestations of SUSY in the presence of extremely strong electromagnetic fields. It is well known that quantum processes occurring in ultrastrong electromagnetic fields differ substantially from analogous processes in a vacuum. In particular, many reactions that are forbidden under conventional conditions can proceed in a strong external field, which lifts some constraints and opens new channels for quantum processes.

In the present study, we consider the production of a photino pair by an electron (or by another charged lepton) in an external electromagnetic field: $e \longrightarrow e\tilde{\gamma}\tilde{\gamma}$. This reaction has an interesting application in the theory of stellar evolution. Many authors emphasized that, at certain values of matter density in the region of comparatively low temperatures, the energy of stars may be dissipated primarily through various channels of the production of light neutral particles. The reason for this is that weakly interacting neutral particles produced at the center of a star may leave it almost immediately, carrying away sizable amounts of energy. Electromagnetic radiation, which is a competing mechanism of energy losses, does not contribute considerably to the energy-removal process at high matter densities peculiar to later stages of stellar evolution: the motion of photons formed within a star to its surface is severely damped because of multiple scattering and absorption in a nontransparent stellar gas.

In the present study, we analyze one possibility associated with the production of light neutral particles. The ensuing exposition is organized as follows. In Section 2, we calculate the probability of the reaction $e \longrightarrow e\tilde{\gamma}\tilde{\gamma}$ in an external field. In Section 3, we investigate the photino-mass effect on the probability of the bremsstrahlung emission of a photino pair by an electron and assess the region of parameter values where the pair production of photinos via the reaction

$e \longrightarrow e\tilde{\gamma}\tilde{\gamma}$ proceeds at a rate higher than that of the competing decay process $e \longrightarrow \tilde{e}\tilde{\gamma}$. In Section 4, we evaluate the photino emissivity of neutron stars, relying on the results obtained in the preceding sections. At relatively low temperatures, in which case the electron gas of stellar matter is in a strongly degenerate state, we compute the rate of energy losses via photino-pair production per unit volume of the neutron star (Q) and compare it with rate of other processes removing energy. By comparing our results with known expressions for the neutrino emissivity of stars (the latter is associated with the processes $e \longrightarrow e\nu_e\bar{\nu}_e$, $e \longrightarrow e\nu_\mu\bar{\nu}_\mu$, and $e \longrightarrow e\nu_\tau\bar{\nu}_\tau$—see, for example, [18]), we set some new constraints on the masses of the scalar electrons ($\tilde{e}_L$, $\tilde{e}_R$), whose virtual states mediate the emission of photino pairs (see Fig. 1).

2. PROBABILITY OF PHOTINO-PAIR PRODUCTION BY AN ELECTRON

Within the MSSM, the matrix element of the process $e \longrightarrow e\tilde{\gamma}\tilde{\gamma}$ is described by two Feynman diagrams in Fig. 1. In addition, the fact that the photino is a Majorana particle makes us consider two cases where the outgoing fermion lines are interchanged. In line with the up-to-date experimental constraints on the selectron mass [19], we use the effective four-fermion Lagrangian (in the MSSM, it arises in the limit M_R, $M_L \gg M_{\tilde{\gamma}}, m_e$)

$$\mathcal{L}_{\text{eff}} = \frac{e^2}{2M_R^2}\overline{\psi}(1 + \gamma^5)\lambda\bar{\lambda}(1 - \gamma^5)\psi$$
$$+ \frac{e^2}{2M_L^2}\overline{\psi}(1 - \gamma^5)\lambda\bar{\lambda}(1 + \gamma^5)\psi, \tag{1}$$

where $M_R \equiv M_{\tilde{e}_R}$ and $M_L \equiv M_{\tilde{e}_L}$ are the masses of, respectively, the right-handed and the left-handed selectron; ψ and λ are the wave functions of, respectively, the selectron and the photino; and $\gamma^5 = -i\gamma^0\gamma^1\gamma^2\gamma^3$. The effect of the external field in (1) is taken into account by using exact solutions to the Dirac equation in an external magnetic field for the initial- and final-electron wave functions (ψ, $\overline{\psi}$) [20]. Here, we restrict our consideration to the semiclassical approximation; this corresponds to comparatively small values of the field strength:

$$F_{\mu\nu}F^{\mu\nu} \ll m_e^4/e^2, \quad \tilde{F}_{\mu\nu}F^{\mu\nu} \ll m_e^4/e^2. \tag{2}$$

The condition in (2) is essentially equivalent to the so-called crossed-field approximation ($|\mathbf{H}| = |\mathbf{E}|$, $\mathbf{H} \perp \mathbf{E}$; see [21]). In this case, the Volkow solutions to the Dirac equation in a constant uniform crossed field [22] can be used for the wave functions describing the initial and the final electron state.

The probability of the process $e \longrightarrow e\tilde{\gamma}\tilde{\gamma}$ in an external field is obtained by integrating the squared modulus of the matrix element over the phase space of the final states of particles. (The general computational scheme can be found, for example, in [16, 23].) By performing summation over the spin states of the photino and the electron, we find that the total probability of the photino-pair production by an electron per unit time can be represented as

$$P(e \longrightarrow e\tilde{\gamma}\tilde{\gamma}) = \frac{\alpha^2 m_e^2 \chi^2}{12\pi^2 p_0}\left(\frac{m_e}{M_L}\right)^2\left(\frac{m_e}{M_R}\right)^2$$

$$\times \int_0^1 du \int_0^1 dv \frac{v^2}{(1-v)}[\Phi_1(z)A(u, v) \tag{3}$$

$$+ [z^3\Phi_1(z) + z^2\Phi'(z)]B(u, v) + z\Phi(z)C(u, v)],$$

where

$$A(u, v) = 4\beta[2 - 2v + v^2(1 - 2u + 2u^2)], \tag{4}$$

$$B(u, v) = \beta[2 - 2v + v^2 - u(1 - u)(6 - 6v + 5v^2)]$$

$$- 3(z_0/z)[(1 + 2\beta)(1 - v) + \beta v^2$$

$$- 12(1 + \beta)(1 - v)u(1 - u) - 5\beta v^2 u(1 - u)] \tag{5}$$

$$+ 3(z_0/z)^2[2(1 + \beta)(1 - v) + \beta v^2$$

$$- 12(1 + \beta)(1 - v)u(1 - u) - 4\beta v^2 u(1 - u)],$$

$$C(u, v) = \beta[8 - 8v + 4v^2 - u(1 - u)$$

$$\times (30 - 30v + 17v^2)] + 3(z_0/z)$$

$$\times [(1 - 2\beta)(1 - v) - \beta v^2 + 8(1 + 2\beta)(1 - v) \tag{6}$$

$$\times u(1 - u) + 5\beta v^2 u(1 - u)],$$

$$z = \frac{\lambda^2(1 - v) + v^2 u(1 - u)}{u(1 - u)[\chi v^2(1 - v)]^{2/3}}, \tag{7}$$

$$z_0 = \chi^{-2/3}\left(\frac{v}{1 - v}\right)^{2/3},$$

$$\beta = \frac{1}{2}\left[\left(\frac{M_R}{M_L}\right)^2 + \left(\frac{M_L}{M_R}\right)^2\right], \quad \lambda = \frac{M_{\tilde{\gamma}}}{m_e}. \tag{8}$$

The integrand in (3) is the differential probability for the process $e \longrightarrow e\tilde{\gamma}\tilde{\gamma}$; there, integration is performed with respect to the Lorentz-invariant variables u and v given by

$$u = \left[\sqrt{\frac{(F^{\mu\nu}p_\nu)^2}{(F^{\mu\nu}q_\nu)^2}} - \sqrt{\frac{(F^{\mu\nu}p_\nu')^2}{(F^{\mu\nu}q_\nu)^2}}\right]^{-1},$$

$$\tag{9}$$

$$v = 1 - \sqrt{\frac{(F^{\mu\nu}p_\nu')^2}{(F^{\mu\nu}p_\nu)^2}},$$

where p_ν and p_ν' are the momenta of the initial and the final electron, respectively; q_ν is the momentum of one of the photinos; and $\alpha = e^2/4\pi$ is the fine-structure constant. The effect of an intense electromagnetic field is absorbed in the dependence of the probability in (3) on the dimensionless Lorentz-invariant parameter

$$\chi = em_e^{-3}\sqrt{-(F_{\mu\nu}p^\nu)^2}, \tag{10}$$

which appears in the argument z (7) of the Airy functions

$$\Phi(z) = \int_0^\infty dt \cos\left(zt + \frac{t^3}{3}\right), \quad \Phi'(z) = \frac{d\Phi(z)}{dz},$$

$$\Phi_1(z) = \int_z^\infty \Phi(x)dx,$$

which often enter into expressions describing processes in crossed fields. The general expression (3) is rather complicated, so that it is hardly possible to perform analytically integration with respect to the variables u and v (9).

In order to obtain physically interesting predictions, we will first investigate the case where the photino mass is so small that it can be disregarded against the electron mass and slepton masses ($M_{\tilde{\gamma}} \ll m_e$, $M_{\tilde{\gamma}} \ll M_L, M_R$). This means that we can set the parameter λ (8) to zero in all formulas. As a result, the probability of photino-pair emission by an electron can be approximated as

$$P(e \longrightarrow e\tilde{\gamma}\tilde{\gamma}) = \frac{\alpha^2 m_e^2 \chi^2}{36\pi^2 p_0}\left(\frac{m_e}{M_L}\right)^2\left(\frac{m_e}{M_R}\right)^2\int_0^1 dv \frac{v^2}{(1-v)}$$

$$\times \{8\beta(3 - 3v + v^2)\Phi_1(z_0) \tag{11}$$

$$+ [9(1 - v) + \beta(3 - 3v + 2v^2)][z_0^3\Phi_1(z_0) + z_0^2\Phi'(z_0)]$$

$$+ [21(1 - v) + \beta(15 - 15v + 2v^2)]z_0\Phi(z_0)\}.$$

The analytic representation (11) can be further simplified if we consider the region of comparatively weak electromagnetic fields; this corresponds to small values of the parameter χ (10). Under the assumption that $\chi \ll 1$, the asymptotic estimate of expression (11) is given by

$$P(e \longrightarrow e\tilde{\gamma}\tilde{\gamma}) = \frac{119\alpha^2 m_e^2 \chi^5}{72\pi\sqrt{3}p_0}\left(\frac{m_e}{M_L}\right)^2\left(\frac{m_e}{M_R}\right)^2$$

$$\times \left[\frac{27}{17} + \left(\frac{M_L}{M_R}\right)^2 + \left(\frac{M_R}{M_L}\right)^2\right]. \tag{12}$$

It should be noted that the dependence of the probability in (12) on the parameter χ coincides with the corresponding χ dependence of the probability of

bremsstrahlung neutrino-pair emission (see [24, 25]). This is because the reactions $e \longrightarrow e\tilde{\gamma}\tilde{\gamma}$ and $e \longrightarrow e\nu_e\bar{\nu}_e$ are kinematically similar, which is typical of many three-body decays in an external electromagnetic field (see, for example, [26]). At the same time, the probability in (12) is proportional to χ^5, significantly differing from the corresponding probabilities for reactions like $l \longrightarrow \tilde{l}\tilde{\gamma}$ and $e \longrightarrow \tilde{W}\nu$, which are exponentially suppressed under analogous conditions (see, for example, [16, 27]).

In order to obtain results for ultrastrong electromagnetic fields (and high electron energies), we estimate the asymptotic behavior of the probability for our process [see (11)] in the limit $\chi \gg 1$. The result is

$$P(e \longrightarrow e\tilde{\gamma}\tilde{\gamma})$$
$$= \frac{\alpha^2 m_e^2 \chi^2}{27\pi p_0}\left[\left(\frac{m_e}{M_R}\right)^4 + \left(\frac{m_e}{M_L}\right)^4\right]\left(\ln\frac{\chi}{\sqrt{3}} - \gamma_E - \frac{5}{6}\right), \quad (13)$$

where $\gamma_E = 0.577$ is the Euler constant. Comparing the last expression with the corresponding result for bremsstrahlung neutrino emission [24, 25], we notice that the aforementioned analogy between the reactions $e \longrightarrow e\tilde{\gamma}\tilde{\gamma}$ and $e \longrightarrow e\nu_e\bar{\nu}_e$ remains in force. A similar dependence on the parameter χ is characteristic of some other processes involving three particles in the final state—for example, $\nu \longrightarrow \nu e^+e^-$ [26] or $\mu \longrightarrow e\nu_e\bar{\nu}_\mu$ [21].

3. ROLE OF THE PHOTINO MASS

In this section, we analyze the case of a nonzero photino mass, using formula (3). As was discussed, for example, in [16], the case of $\lambda = M_{\tilde{\gamma}}/m_e > 1$ corresponds to an unclear phenomenological situation where the probabilities of two competing photino-production processes, $e \longrightarrow e\tilde{\gamma}\tilde{\gamma}$ and $e \longrightarrow \tilde{e}\tilde{\gamma}$, are commensurate. This is because, for $\lambda \neq 0$, the probability of pair photino emission significantly changes the form of dependence on the external-field-strength parameter χ in the region of its small values. The probability of massive-photino production in the reaction $e \longrightarrow e\tilde{\gamma}\tilde{\gamma}$, $P(e \longrightarrow e\tilde{\gamma}\tilde{\gamma})$, can be estimated by the saddle-point method, which makes it possible to construct the asymptotic expansion of the double integral in (3) for $\chi \longrightarrow 0$. The leading term of the asymptotic expansion has the form

$$P(e \longrightarrow e\tilde{\gamma}\tilde{\gamma}) = \frac{\alpha^2 m_e^2 \chi^{5/2}}{\sqrt{\pi} p_0}\left(\frac{m_e}{M_L}\right)^2\left(\frac{m_e}{M_R}\right)^2$$
$$\times \left(\frac{M_L}{M_R} + \frac{M_R}{M_L}\right)^2 G(\lambda)\exp\left[-\frac{n(\lambda)}{\chi}\right]. \quad (14)$$

The dependence of the probability in (14) on the photino mass $M_{\tilde{\gamma}} = \lambda m_e$ is described by the functions $n(\lambda)$ and $G(\lambda)$ that are given by

$$n(\lambda) = (\lambda/2)\sqrt{48 + 6\lambda(\lambda^2 + 8)^{3/2} + 120\lambda^2 - 6\lambda^4}, \quad (15)$$

$$G(\lambda) = \frac{512[\sqrt{\lambda^2 + 8} + \lambda]^{1/4}[5\sqrt{\lambda^2 + 8} + 11\lambda]}{(\lambda^2 + 8)^{1/4}[\sqrt{\lambda^2 + 8} + 3\lambda]^{7/4}[\sqrt{\lambda^2 + 8} + 7\lambda]^{9/2}}\left(\frac{\lambda}{\sqrt{6}}\right)^{5/2}. \quad (16)$$

The values of the function $n(\lambda)$ determine the applicability range of formula (14) for relatively weak electromagnetic fields satisfying the condition $\chi \ll n(\lambda)$ (smallness of χ). The graphs of the functions $n(\lambda)$ and $G(\lambda)$ are displayed in Figs. 2 and 3, respectively. It should be noted that the function $n(\lambda)$, which appears in the exponential function on the right-hand side of (14), has a crucial effect on the probability of photino pair emission. Although the preexponential factor $G(\lambda)$ has a sharp maximum at $\lambda = 0.364$, the probability $P(e \longrightarrow e\tilde{\gamma}\tilde{\gamma})$ decreases monotonically with increasing photino mass at any fixed value of the parameter χ from the applicability range of the asymptotic formula (14).

Comparing expression (14) with the result presented in (12) for the massless photino, we highlight the presence of the exponential factor $e^{-n/\chi}$, which is peculiar to many processes forbidden in a vacuum. This factor of exponential suppression stems from the fact that the total energy of particles appearing in the final-state of the reaction $e \longrightarrow e\tilde{\gamma}\tilde{\gamma}$ exceeds the energy of the initial electron, which has to produce a pair of massive photinos by deriving energy from the external electromagnetic field. From this point of view, the photino-emission process can be considered as the tunneling of an electron through the potential barrier whose transparency is determined by the well-known semiclassical formula involving the imaginary action functional in the exponent. The height of the potential barrier is directly related to the energy of virtual photons absorbed by an initial electron from the surrounding electromagnetic field.

As the strength of the external electromagnetic field increases, the energy of the original electron becomes higher with the result that the exponential suppression factor becomes insignificant; therefore, the process of photino emission proceeds without tunneling for $\chi \gg n(\lambda)$. In the region of strong electromagnetic fields, the probability of the reaction $e \longrightarrow e\tilde{\gamma}\tilde{\gamma}$ proves to be so great that this process can be observed experimentally under laboratory conditions. By way of example, we

indicate that, even in the case of very heavy photinos, $\lambda \gg 1$, there is the domain of χ values ($\lambda^2 \ll \chi \ll \lambda^3$) where the probability of photino emission by an electron grows monotonically with increasing field strength according to the asymptotic estimate

$$P(e \longrightarrow e\tilde{\gamma}\tilde{\gamma})$$

$$= \frac{\alpha^2 m_e^2 \chi^2}{9\pi p_0}\left[\left(\frac{m_e}{M_R}\right)^4 + \left(\frac{m_e}{M_L}\right)^4\right]\left[\ln\left(\frac{\chi}{\lambda^2\sqrt{3}}\right) - \gamma_E - \frac{7}{4}\right]. \quad (17)$$

The calculations show that, as the parameter χ grows further, effects associated with a finite photino mass become negligibly small. If the electron energy and the strength of the external-field strength increase to an extent that the condition $\chi \gg \lambda^3$ is satisfied, the asymptotic behavior of expression (3) coincides with that for the massless-photino case [see (13)].

4. PHOTINO EMISSIVITY OF NEUTRINO STARS

The results of our analysis have an interesting application in the theory of the evolution of neutron stars.

Neutron stars are exotic astrophysical objects formed at very high temperatures ($T > 10^{11}$ K) in the core of a supernova burst. The modern theory of neutron-star cooling (see, for example, [28, 29]) is based on the so-called URCA processes where a significant part of the star energy is carried away by neutrinos. Since neutrino interaction with matter is extremely weak, almost all neutrinos produced in the interior of a neutron star can escape directly from its core nearly without additional losses of energy.

At the same time, the presence of magnetic fields of strength $H = 10^{11}$–10^{13} G is a feature peculiar to neutron stars. Such strong magnetic fields lead to the emergence of some new specific mechanisms of neutron-star cooling that are capable of exerting a decisive effect on the rate at which stars lose energy. Among other things, many authors investigated the synchrotron emission of neutrino pairs ($e \longrightarrow e\nu\bar{\nu}$) that occurs only in the presence of an external field. It was shown that, under specific conditions, this reaction can become a dominant mechanism of the cooling of a neutron star as soon as its temperature falls below 10^9 K.

The last circumstance gives impetus to searches for analogous processes that must be analyzed and taken into account in detail in order to construct the general pattern of the evolution of neutron stars. It is also of interest to investigate the influence of new physics on the energy balance and rate of cooling of magnetized objects such as neutron stars.

In this section, we calculate the rate of cooling of a neutron star via the emission of supersymmetric particles, photinos, relying on the results obtained in [17, 23] for bremsstrahlung photino production by electrons in an external field ($e \longrightarrow e\tilde{\gamma}\tilde{\gamma}$).

The rate of energy losses per unit volume of a neutron star by photino emission is related to the differen-
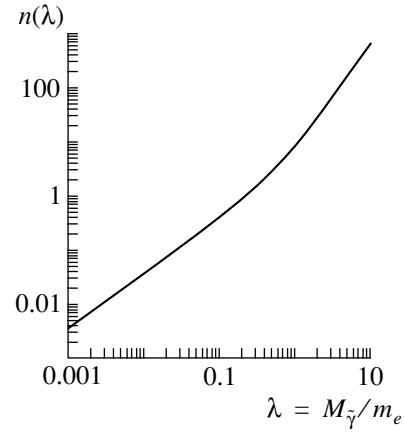

Fig. 2. Function $n(\lambda)$ appearing in the probability (14) of the process $e \longrightarrow e\tilde{\gamma}\tilde{\gamma}$ versus the photino mass for $\chi \ll 1$ [see equation (15)].
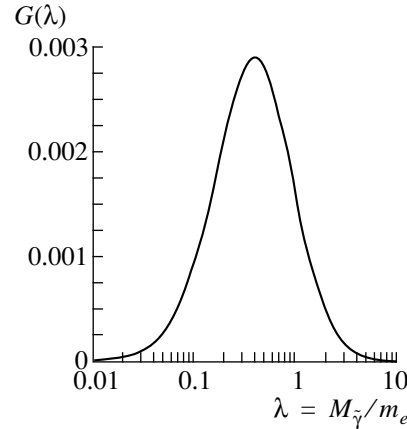

Fig. 3. Function $G(\lambda)$ appearing in the probability (14) of the process $e \longrightarrow e\tilde{\gamma}\tilde{\gamma}$ versus the photino mass for $\chi \ll 1$ [see equation (16)].

tial probability $W(p, q_1, q_2)$ [see expressions (3)–(9)] by the equation:

$$Q = 2\int \frac{d^3 p}{(2\pi)^3}\int d^3 q_1 \int d^3 q_2 (q_{10} + q_{20})$$

$$\times W(p, q_1, q_2)n_F(1 - n_F'). \quad (18)$$

As in (3)–(9), p and p' are the four-momenta of the electron in the initial and in the final state, respectively, and q_1 and q_2 are the photino four-momenta. The Fermi–Dirac distribution functions

$$n_F = \frac{1}{\exp\left(\dfrac{p_0 - \mu}{T}\right) + 1},$$

$$1 - n_F' = \frac{1}{\exp\left(\dfrac{\mu - p_0'}{T}\right) + 1}, \quad (19)$$

which appear in (18), describe the density of the initial electron states in a neutron star (n_F) and the effect of the reduction of the final-electron phase space by the Pauli exclusion principle ($1 - n_F'$).

Physically, the most interesting case corresponds to the region of low temperatures of a star, in which case the electron gas is in a strongly degenerate state. All electrons contributing to photino emissivity will then have momenta close to the Fermi momentum ($|\mathbf{p}| \approx |\mathbf{p}'| \approx p_F = \sqrt[3]{3\pi^2 n_e}$). Estimates show that the density of electrons in a neutron star, n_e, must exceed the value of 10^{30} cm^{-3}. This indicates that all electrons involved in the reaction $e \longrightarrow e\tilde{\gamma}\tilde{\gamma}$ are relativistic ($p_0, p_0' \gg m_e$). In this case, the presence of the blocking factors $n_F(1 - n_F')$ in expression (18) for emissivity results in that the reaction phase space reduces to a narrow layer near the surface of the Fermi sphere in the momentum space, the width of this layer decreasing sharply as the temperature of the star decreases. From the mathematical point of view, this circumstance can be used by approximating the blocking factors in the phase space by the Dirac delta function as (see, for example, [18, 30])

$$n_F(1 - n_F') \approx \delta(p - p_F)\frac{\omega}{e^{\omega/T} - 1}, \qquad (20)$$

where $\omega = p_0 - p_0'$ with $p_0 = \sqrt{\mathbf{p}^2 + m_e^2} \approx p$.

In (18), we go over from q_1 and q_2 to the invariant variables of integration u and v [see (9)]. Considering that, in the relativistic case, we can set the photino and the final-electron energy to

$$p_0' \approx p_0(1 - v) \quad \text{and} \quad q_{10} + q_{20} \approx p_0 v, \qquad (21)$$

respectively, we reduce expression (18) to the form

$$Q = 2\int\frac{d^3 p}{(2\pi)^3}\int_0^1 dv\, p_0 v W(p, v) n_F(1 - n_F'), \qquad (22)$$

where $W(p, v)$ is the differential probability of the reaction $e \longrightarrow e\tilde{\gamma}\tilde{\gamma}$ with respect to the spectral variable v. This differential probability is obtained by integration with respect to the photino momenta and coincides with the integrand in expression (11).

By using rule in (20) for the change in the electron phase space for the case of a strongly degenerate electron gas and going over to spherical coordinates to perform integration in the momentum space of the initial electrons, we find that expression (22) can be recast into the form

$$Q = \frac{2p_F^4}{(2\pi)^2}\int_0^\pi \sin\theta\, d\theta \int_0^1 dv\, v^2 \frac{W(v, \theta)}{e^{v p_F/T} - 1}, \qquad (23)$$

where $W(v, \theta)$ is the aforementioned differential probability of the reaction $e \longrightarrow e\tilde{\gamma}\tilde{\gamma}$ with respect to spectral variables v at

$$p_0 \approx p = p_F,$$

$$\chi = \frac{e}{m_e^3}\sqrt{-(F_{\mu\nu}p^\nu)^2} = \frac{e p_F H}{m_e^3}\sin\theta.$$

In Eq. (23), we go over to a new variable of integration and retain only the leading terms of the expansion in temperature; as a result, the final expression for the rate of energy losses of a neutron star by photino emission takes the form

$$Q = \frac{\alpha^2 m_e^5}{48\pi^4}\left(\frac{p_F}{m_e}\right)^{10}\left(\frac{eH}{m_e^2}\right)^7\left(\frac{m_e}{M_R}\right)^2\left(\frac{m_e}{M_L}\right)^2$$

$$\times \int_0^\pi d\theta \sin^8\theta \int_0^\infty dz'\, z'^{13/2}\left[\exp\left(\frac{e p_F^2 H}{m_e^3 T}z'^{3/2}\sin\theta\right) - 1\right]^{-1} \qquad (24)$$

$$\times \{\Phi_1(z')[24\beta + z'^3(9 + 3\beta)]$$

$$+ z'^2\Phi'(z')(9 + 3\beta) + z'\Phi(z')(21 + 15\beta)\}.$$

Here, we have used the notation introduced in (3) with the only difference that the new argument of the Airy functions, z', is given by

$$z' = \left(\frac{v}{\chi_F \sin\theta}\right)^{2/3}, \quad \chi_F = \frac{e p_F H}{m_e^3}.$$

Let us consider expression (24) in some limiting cases.

In the case of weak magnetic fields, $H \ll \dfrac{m_e^3 T}{e p_F^2}$, we obtain

$$Q = \frac{400\alpha^2 m_e^5}{189\pi^3}\left(\frac{p_F}{m_e}\right)^8\left(\frac{H}{H_0}\right)^6\left(\frac{T}{m_e}\right)$$

$$\times\left[\left(\frac{m_e}{M_L}\right)^4 + \left(\frac{m_e}{M_R}\right)^4 + \frac{42}{25}\left(\frac{m_e}{M_L}\right)^2\left(\frac{m_e}{M_R}\right)^2\right], \qquad (25)$$

where $H_0 = m_e^2/e$.

Since the right-hand side of (25) is proportional to temperature, the efficiency of photino emission during the cooling of a neutron star does not decrease so fast as for URCA processes, whose rate is proportional to T^8. Under the assumption that $H \ll \dfrac{m_e^3 T}{e p_F^2}$ and $s_W^2 = \sin^2\theta_W = 0.23124(24)$ (see [19]), the same temperature dependence is characteristic of the synchrotron emission of neutrino pairs via the reaction $e \longrightarrow e\nu\bar{\nu}$, which provides a dominant mechanism of energy

removal at later stages of the evolution of neutron stars [18],

$$Q(e \longrightarrow e\nu\bar{\nu})$$

$$= \frac{32 G_F^2 m_e^9}{63\pi^5}\left(\frac{p_F}{m_e}\right)^8\left(\frac{H}{H_0}\right)^6\left(\frac{T}{m_e}\right)\left[\left(s_W^2 - \frac{1}{12}\right)^2 + \frac{223}{288}\right]. \quad (26)$$

We note that neutrino synchrotron emission plays a leading role not only in weak magnetic fields but also in sufficiently strong fields obeying the condition $H \gg \frac{m_e^3 T}{e p_F^2}$. In that case, however, the energy-removal rate decreases more sharply (in proportion to T^5), but this is quite sufficient for the reaction $e \longrightarrow e\nu\bar{\nu}$ to dominate over URCA processes (see [18]). Specifically, we have

$$Q(e \longrightarrow e\nu\bar{\nu})$$

$$= \frac{8\zeta(5)}{3\pi^5} G_F^2 m_e^9\left(\frac{H}{H_0}\right)^2\left(\frac{T}{m_e}\right)^5\left[\left(s_W^2 - \frac{1}{12}\right)^2 + \frac{17}{144}\right], \quad (27)$$

where $\zeta(5) \approx 1.0369$ and where it is assumed that $H \gg \frac{m_e^3 T}{e p_F^2}$.

For the aforementioned reaction of photino-pair emission in strong magnetic fields ($H \gg m_e^3 T/e p_F^2$), the photino emissivity per unit volume of a neutron star behaves in the same way as the neutrino emissivity; that is, it decreases in proportion to T^5 with decreasing temperature. The exact formula following from (24) has the form

$$Q = \frac{16\zeta(5)}{9\pi^3}\alpha^2 m_e^5\left(\frac{H}{H_0}\right)^2\left(\frac{T}{m_e}\right)^5\left[\left(\frac{m_e}{M_R}\right)^4 + \left(\frac{m_e}{M_L}\right)^4\right]. \quad (28)$$

We now use the above relations to analyze the energy losses of a neutron star under conditions where the synchrotron emission of neutrino pairs dominates over all other mechanisms. The rate of the synchrotron losses, $Q(e \longrightarrow e\nu\bar{\nu})$, was calculated by many authors, but the most comprehensive calculations, which also improve some errors of earlier studies, were performed by Kaminker and his colleagues (see, for example, [18]). In particular, expressions (26) and (27) from the present study are the transformed results of the calculations with three neutrino generations from [18].

From a comparison of (25) and (26), it can clearly be seen that, in the case where the masses of the left- and right-handed scalar electrons (M_L, M_R) are anomalously small, the rate of photino emission can be much higher than the rate of neutrino losses. Because of this, the characteristic period of neutron-star cooling can become overly small, in contradiction with various data from astrophysical observations.
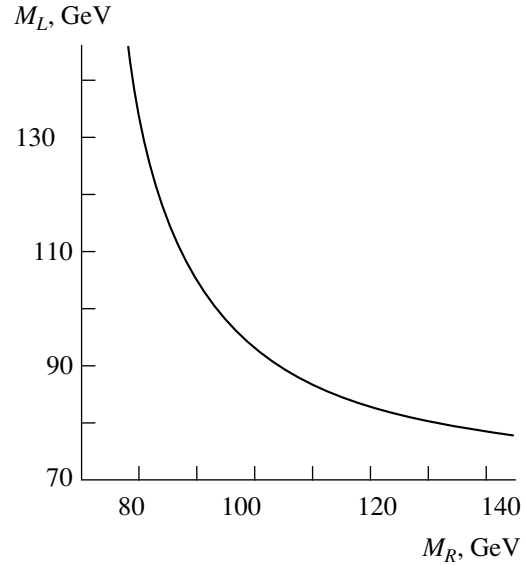
Fig. 4. Boundary of the admissible values of the scalar-electron masses (the allowed mass values lie above the curve on the graph).

If we are to remain within the modern standard model of neutron-star cooling, we must therefore require that the contribution of the reaction $e \longrightarrow e\tilde{\gamma}\tilde{\gamma}$ to the total rate of the energy losses not be observable or, at least, not exceed the rate of the synchrotron emission of neutrino pairs:

$$Q(e \longrightarrow e\tilde{\gamma}\tilde{\gamma}) < Q(e \longrightarrow e\nu\bar{\nu}). \quad (29)$$

This relation sets some constraints on the masses of the selectrons participating in the photino-emission process. In the plane spanned by the parameters M_L and M_R, the inequality in (29) singles out the domain of admissible values of the selectron masses, which lies above the curve in Fig. 4. For the case where the scalar selectrons $\tilde{e}_R$ and $\tilde{e}_L$ have the same mass $M_{\tilde{e}}$, the condition in (29) yields the constraint

$$M_{\tilde{e}} > 96.33 \text{ GeV}.$$

If one of the scalar electrons is much heavier that the other (for example, $M_R \gg M_L$), then a weaker constraints on the mass of the lighter selectron follows from (29):

$$M_L > 69.55 \text{ GeV}.$$

5. CONCLUSION

Relying on the minimal supersymmetric extension of the Standard Model—recall that it is commonly known as minimal supersymmetric SM (or merely MSSM)—we have considered some new physical phenomena occurring in a strong electromagnetic field. In particular, we have calculated the probability of the

synchrotron emission of photino pairs via the process $e \longrightarrow e\tilde{\gamma}\tilde{\gamma}$ at various values of the electron energy and of the external-electromagnetic-field strength. A systematic analysis of the probability of this reaction predicts that massive photinos can be produced with a high probability only in extremely strong fields ($\chi \propto \lambda^2$). At present, such fields can hardly be generated under actual experimental conditions. In the region of weaker fields, the emission of photino pairs is suppressed exponentially: this is because the final-state energy of the quantum system in question must be much greater here than the initial-state energy. The required amount of energy is insignificant in the case of massless photinos, and this is highly promising from the phenomenological point of view. Assuming that $M_{\tilde{\gamma}} \longrightarrow 0$, we arrive at the conclusion that the reaction $e \longrightarrow e\tilde{\gamma}\tilde{\gamma}$ can become accessible to experimental investigations in the near future.

Nonetheless, the results of our investigations have interesting applications in the theory of stellar evolution. It is well known that, at later stages of star evolution, many astrophysical objects can undergo strong compression, in which case the strength of the magnetic fields already present in their interiors at earlier stages of evolution is expected to increase substantially. In this connection, mention should be made above all of neutron stars and white dwarfs, which exhibit extremely strong magnetic fields ($H \geq 10^8$–10^{13} G). In the presence of such strong magnetic fields, many unusual reactions forbidden in a vacuum become possible. By way of example, we can indicate neutrino emission by an electron via the process $e \longrightarrow e\nu_e\bar{\nu}_e$, which is of great importance for astrophysics—it was established in [18, 31] that, under certain conditions, synchrotron neutrino radiation comes to be a dominant channel through which stars dissipate energy during their evolution. If supersymmetry does indeed exist in nature, synchrotron photino emission via the process $e \longrightarrow e\tilde{\gamma}\tilde{\gamma}$, which is similar in many respects to neutrino emission, may become a competing mechanism of the cooling of a neutron star. Therefore, this mechanism may increase considerably, at specific values of the density and temperature of stellar matter, the rate at which stars lose energy. It follows that supersymmetric particles could change noticeably the standard scenario of stellar evolution at its last stage. Within the modern theory of the cooling of stars [28, 29], where reactions involving supersymmetric particles are unobservable, it is natural to assume at the same time that the contribution of the process $e \longrightarrow e\tilde{\gamma}\tilde{\gamma}$ is rather small in relation to the neutrino-emission contribution. Relying on these premises and comparing the calculated photino emissivity per unit volume of a neutron star (see above) with known results for the neutrino emissivity, we have obtained new astrophysical constraints on the scalar-

electron masses. These constraints are more stringent than those available so far [19] (see Section 4 of the present article).

REFERENCES

1. P. Fayet and S. Ferrara, Phys. Rep. **32**, 249 (1977).

2. A. Salam and J. Strathdee, Fortschr. Phys. **26**, 57 (1978).

3. V. I. Ogievetskiĭ and L. Mezincescu, Usp. Fiz. Nauk **117**, 637 (1975) [Sov. Phys. Usp. **18**, 960 (1975)].

4. A. A. Slavnov, Usp. Fiz. Nauk **124**, 487 (1978) [Sov. Phys. Usp. **21**, 240 (1978)].

5. M. I. Vysotskiĭ, Usp. Fiz. Nauk **146**, 591 (1985) [Sov. Phys. Usp. **28**, 667 (1985)].

6. E. Gildener, Phys. Rev. D **14**, 1667 (1976).

7. E. Gildener and S. Weinberg, Phys. Rev. D **13**, 3333 (1976).

8. H.-P. Nilles, Phys. Rep. **110**, 1 (1984).

9. H. E. Haber and G. L. Kane, Phys. Rep. **117**, 75 (1985).

10. J. Ellis and D. V. Nanopoulos, Phys. Lett. **110B**, 44 (1982).

11. F. Gabbiani and A. Masiero, Nucl. Phys. B **322**, 235 (1989).

12. J. Hagelin, S. Kelley, and T. Tanaka, Nucl. Phys. B **415**, 293 (1994).

13. P. A. Éminov, Yad. Fiz. **51**, 542 (1990) [Sov. J. Nucl. Phys. **51**, 346 (1990)].

14. V. Ch. Zhukovskiĭ and P. A. Éminov, Yad. Fiz. **52**, 1473 (1990) [Sov. J. Nucl. Phys. **52**, 931 (1990)].

15. A. V. Kurilin, Phys. Lett. B **249**, 455 (1990).

16. A. V. Kurilin, Yad. Fiz. **57**, 1129 (1994) [Phys. At. Nucl. **57**, 1066 (1994)]; Int. J. Mod. Phys. A **9**, 4581 (1994).

17. A. V. Kurilin and A. I. Ternov, Pis'ma Zh. Éksp. Teor. Fiz. **63**, 305 (1996) [JETP Lett. **63**, 311 (1996)].

18. A. D. Kaminker, K. P. Levenfish, and D. G. Yakovlev, Pis'ma Astron. Zh. **17**, 1090 (1991) [Sov. Astron. Lett. **17**, 450 (1991)].

19. Particle Data Group, Eur. Phys. J. C **3**, 1 (1998).

20. V. B. Berestetskiĭ, E. M. Lifshitz, and L. P. Pitaevskiĭ, *Quantum Electrodynamics* (Nauka, Moscow, 1989; Pergamon, Oxford, 1982).

21. V. I. Ritus, Tr. Fiz. Inst. Akad. Nauk SSSR **111**, 5 (1979).

22. D. M. Volkow, Zh. Éksp. Teor. Fiz. **7**, 1286 (1937); Z. Phys. **94**, 250 (1935).

23. A. V. Kurilin and A. I. Ternov, Phys. Lett. B **381**, 185 (1996).

24. V. N. Baĭer and V. M. Katkov, Dokl. Akad. Nauk SSSR **171**, 313 (1966) [Sov. Phys. Dokl. **11**, 947 (1967)]; V. I. Ritus, Zh. Éksp. Teor. Fiz. **56**, 986 (1969) [Sov. Phys. JETP **29**, 532 (1969)].

25. I. M. Ternov, V. N. Rodionov, and A. I. Studenikin, Yad. Fiz. **37**, 1270 (1983) [Sov. J. Nucl. Phys. **37**, 755 (1983)].

26. A. V. Borisov, A. I. Ternov, and V. Ch. Zhukovskii, Phys. Lett. B **318**, 489 (1993).

27. G. G. Likhachev, A. I. Studenikin, and I. M. Ternov, Yad. Fiz. **53**, 1614 (1991) [Sov. J. Nucl. Phys. **53**, 990 (1991)].

28. V. M. Lipunov, *Astrophysics of Neutron Stars* (Nauka, Moscow, 1987).

29. S. L. Shapiro and S. A. Teukolsky, *Black Holes, White Dwarfs and Neutron Stars: The Physics of Compact Objects* (Wiley, New York, 1983; Mir, Moscow, 1985).

30. A. V. Borisov and V. Yu. Grishina, Zh. Éksp. Teor. Fiz. **106**, 1553 (1994) [JETP **79**, 837 (1994)].

31. J. D. Landstreet, Phys. Rev. **153**, 1372 (1967); V. Canuto, H. Y. Chiu, C. K. Chou, and L. Fassio-Canuto, Phys. Rev. D **2**, 281 (1970).

Translated by A. Isaakyan